Influence of urban water surfaces on human thermal environments
–
an obstacle resolving modelling approach

Dissertation

zur Erlangung des Doktorgrades der Naturwissenschaften

an der Fakultät für Mathematik, Informatik und Naturwissenschaften

Fachbereich Geowissenschaften der Universität Hamburg

vorgelegt von

Jana Fischereit

aus Hamburg

Hamburg, 2018

Tag der Disputation: 04.12.2018

Folgende Gutachter empfehlen die Annahme der Dissertation:
Prof. Dr. K. Heinke Schlünzen
Prof. Dr. Bernd Leitl
Dr. Ir. Gert-Jan Steeneveld

Vorsitzender des Fachpromotionsausschusses Geowissenschaften:
Prof. Dr. Dirk Gajewski

Zusammenfassung

Hitze in Städten kann den Komfort, die Gesundheit und die Leistungsfähigkeit von Menschen negativ beeinflussen. Im Rahmen dieser Arbeit wird das Potential von Wasserflächen als Maßnahme zur Reduktion von Hitze mit einem hindernisauflösenden Modell (ORM) untersucht. Zwei thermische Indizes, die Physiologische Äquivalenttemperatur (Physiological Equivalent Temperature (PET)) und der Universelle Thermische Klimaindex (Universal Thermal Climate Index (UTCI)), werden genutzt, um die thermische Umwelt in der Stadt, wie sie vom Menschen wahrgenommen wird, zu untersuchen.

PET und UTCI wurden aus 165 begutachteten Indizes ausgewählt, da sie global in ihrer momentanen Form angewendet werden können, um die thermische Umwelt des Menschen in der Stadt, wie sie vom Menschen wahrgenommen wird, in hindernisauflösenden Modellen zu bewerten. PET und UTCI unterscheiden sich unter anderem in Bezug auf ihre Behandlung von Kleidung und Aktivität, die Vollständigkeit des thermo-physiologischen Modells und der bewerteten Reaktion des Menschen. Aus diesem Grund kann es sein, dass sie die gleiche meteorologische Situation in Bezug auf die Wirkung auf den Menschen unterschiedlich bewerten. Um diese Unterschiede zu charakterisieren, wird die Sensibilität von PET und UTCI gegenüber ihrer meteorologischen, ihrer bebaute-Umwelt-bezogenen und ihrer personenbezogenen Eingangsgrößen (dies nur für PET) untersucht. Die Ergebnisse zeigen, dass PET und UTCI am sensibelsten auf Lufttemperatur reagieren, sowohl für sommerliche als auch für winterliche Bedingungen. Beide Indizes sind sehr sensibel gegenüber Windgeschwindigkeit, wobei der Einfluss auf UTCI stärker ist. Von den personenbezogenen Variablen reagiert PET am stärksten auf Änderungen der metabolischen Rate und der Kleidungsisolation, vor allem im Winter. PET, und in geringerem Maße auch UTCI, reagiert auch auf Änderungen der mittleren Strahlungstemperatur und dementsprechend bebaute-Umwelt-bezogene Variablen im Sommer.

Um die Empfindlichkeit der thermischen Indizes gegenüber der mittleren Strahlungstemperatur berücksichtigen zu können, wird das hindernisauflösende Modell MITRAS erweitert, um die Berechnung von Strahlung in der Hindernisschicht zu verbessern. Das erweiterte Modell wird angewendet, um zu analysieren, wie unterschiedliche Arten von Wasserflächen in ihrer Umgebung die thermische Umwelt des Menschen beeinflussen. Untersucht wird jeweils der Einfluss eines Kanals und eines großen Sees auf eine kleine idealisierte Stadt für unterschiedliche meteorologische Situationen, die wolkenfreie Bedingungen in Hamburg repräsentieren. Die Ergebnisse zeigen, dass im Vergleich zu einem

Kanal, ein großer See tagsüber in Bezug auf UTCI und PET im Mittel fünf mal so stark kühlt. Darüber hinaus zieht diese kühlere Luft weiter in die Stadt, wenn diese neben einem See anstelle eines Kanals liegt. Höhere Windgeschwindigkeiten erhöhen sowohl diese Eindringtiefe als auch die Stärke des Kühlungseffekts des Sees. Auf den Einfluss des Kanals auf die Stadt wirken sich die meteorologischen Bedingungen weniger stark aus. Beide Wasserflächen wärmen die Stadt hinsichtlich PET und UTCI in der Nacht. Die Stärke dieser Erwärmung ist ungefähr halb so groß wie die Stärke der Kühlung tagsüber. Nichtsdestotrotz zeigen die Ergebnisse, dass Wasserflächen trotz ihres großen Kühlungspotentials am Tag auf Grund ihrer nächtlichen Wärmeeffekte nicht uneingeschränkt zur Gestaltung von thermisch komfortablen Städten empfohlen werden können.

Abstract

Heat in urban areas can negatively affect people's comfort, health and performance. In this thesis, the potential of urban water surfaces as a heat reduction measure is investigated using an obstacle resolving modelling (ORM) approach. Two thermal indices, the Physiological Equivalent Temperature (PET) and the Universal Thermal Climate Index (UTCI), are applied to characterise the thermal environment within the urban area in human relevant terms.

PET and UTCI have been selected out of 165 reviewed thermal indices, as they can be used globally in the current form to evaluate outdoor urban human thermal environments in ORM applications. PET and UTCI differ i.a. with respect to the treatment of clothing and activity, the comprehensiveness of the thermo-physiological model and the assessed human response. Hence, for the same meteorological situation, they may assess the human thermal environment differently. To characterise these differences, the sensitivity of PET and UTCI to their meteorological, built-environment-related and personal input variables (only for PET) is assessed. The results show that PET and UTCI are most sensitive to air temperature for both summer and winter conditions. Both indices also indicate a high sensitivity to wind speed, with UTCI being more sensitive. Out of the personal variables, PET is most sensitive to metabolic heat and clothing insulation, especially for winter. PET, and to a lesser extent UTCI, are also sensitive to mean radiant temperature and consequently to built-environment-related variables for summer.

To account for the sensitivity of the thermal indices to mean radiant temperature, the ORM MITRAS is extended to improve the calculation of radiation within the obstacle layer. This extended model is applied to assess how different kinds of urban water surfaces affect the human thermal environment in their surroundings. The influence of a canal and a large lake on a small idealised urban area was investigated for different meteorological situations that represent cloudless summer conditions in Hamburg. The results indicate that, compared to a canal, a large lake provides on average five times stronger cooling in terms of UTCI and PET during daytime. Furthermore, this cooled air penetrates further into the urban area when it is close to a lake rather than a canal. Larger wind speeds increase both the penetration depth and the magnitude of the cooling for the lake. In the canal scenario meteorological conditions affect the water influence less. Both water bodies warm the urban area in terms of PET and UTCI during the night. The magnitude of this warming is about halved compared to the daytime cooling. Nevertheless, these results

indicate that despite the enormous cooling potential during the day, water surfaces cannot be recommended unconditionally for thermal comfortable designs due to the night-time warming.

Contents

List of Figures

List of Tables

1 Introduction

More than half of the world's population lives in urban areas (54 % in 2014, UN, 2015) – a fraction that is projected to increase to two-thirds in 2050 (UN, 2015). To accommodate the increasing number of urban residents, the natural landscape is replaced by transport infrastructure and buildings. This process of urbanisation changes the radiative, thermal, moisture and aerodynamic characteristics of the landscape (Oke, 1987; Oke et al., 2017) causing well known urban climate modifications such as enhanced turbulence (Arnfield, 2003), increased air pollution (Oke, 1987) and elevated air temperatures especially at night (i.e. the Urban Heat Island (UHI), Arnfield, 2003).

Elevated temperatures are a severe health hazard, since the autonomous thermo-regulative system of the human body has to ensure core temperatures within a narrow range around 37 °C by adjusting the amount of heat exchanged by respiration, evaporation, convection and radiation to avoid heat stroke or even death (Kovatas and Hajat, 2008; ASHRAE, 2001). Even within this range, productivity deteriorates during thermal stress (Parsons, 2014) or due to missing relief from day time stress during hot nights (Libert et al., 1988). Residents of urban areas might face higher risks compared to people in rural areas due to the UHI in addition to the global temperature rise (Gabriel and Endlicher, 2011). This might differ, however, for different background climates (Kovatas and Hajat, 2008; O'Neill and Ebi, 2009; Burkart et al., 2011), personal disposition, gender and age (Kovatas and Hajat, 2008; Ye et al., 2012; Åström et al., 2011). Elderly people and young children are especially vulnerable as they cannot thermo-regulate as well as healthy young adults (Kovatas and Hajat, 2008; Schellen et al., 2010; Thorsson et al., 2014). Since the ageing of the world's population is expected to accelerate in the future (Lutz et al., 2008), appropriate strategies to mitigate heat stress are required.

One option for heat stress mitigation is to develop thermally comfortable outdoor designs (Chen and Ng, 2012). In addition to changes of the streets' aspect ratio, materials, the size and position of canopies and vegetation (Müller et al., 2014; Chatzidimitriou and Yannas, 2016; Perini and Magliocco, 2014; Hong and Lin, 2015; Ali-Toudert and Mayer, 2006; Schrijvers et al., 2016), urban open water surfaces have been proposed as possible thermal comfortable design elements (Coutts et al., 2013; Burkart et al., 2016; Žuvela-Aloise et al., 2016). Open water surfaces are present in many cities since cities traditionally have been built close to rivers or lakes to ensure water supply for households or agriculture (Kummu et al., 2011) or for economical reasons of trading routes (Morris, 1994; Hägerskog et al., 2015). Nowadays, still more than half of the world's population lives less than about 3 km from open freshwater areas (Kummu et al., 2011).

Water surfaces have a high thermal heat capacity, small roughness length, a time-dependent albedo and a strong potential for evaporation (Kuttler, 1991). Therefore, they influence all parameters – air temperature, wind, radiation and humidity – that impact the heat exchange mechanisms of a person. How strongly open water surfaces influence the thermal conditions in the surrounding urban areas – both in terms of intensity and extent – depends on several factors, which can be grouped into three categories: (1) meteorological factors (e.g. wind direction, air temperature), (2) characteristics of the water surface (e.g. extent, shape, depth, temperature) and (3) surrounding urban morphology (e.g. height and orientation of buildings, presence of vegetation, surrounding orography). Although several studies have investigated the effect of individual factors on the influence of water surfaces (Hathway and Sharples, 2012; Žuvela-Aloise et al., 2016; Ashie et al., 2005), they often do not systematically control for the other factors. Additionally, most studies focus on air temperature as a target variable, although the human body responds to all parameters together. The potential benefits of water surfaces for mitigating day-time heat stress might reverse during the night, when water surfaces have been found to warm the surrounding city (Steeneveld et al., 2014) and thus deteriorate important night-time thermal comfort. Considering these aspects, the guiding research question of this thesis is

GRQ *How strongly do different kinds of urban water surfaces affect their thermal surroundings under various meteorological situations and urban scenarios during different times of the day?*

To address this question, idealised simulations with an Obstacle Resolving micro-scale model (ORM) are performed for different meteorological situations, water extents and urban morphologies. ORMs are useful to evaluate different outdoor design strategies for thermal comfort, since different designs can be investigated for several meteorological situations relatively easily. ORM simulations typically cover a domain between 0.1 and 5 km^2 with a spatial resolution of 0.1 to 100 m (Blocken, 2015). Therefore, in addition to resolving buildings and vegetation explicitly, ORMs simulate the thermal conditions on spatial and also temporal scales which people actually experience. To assess those conditions in human-relevant terms, thermal indices are applied. Thermal indices quantify perceived subjective temperatures objectively by combining the effects of temperature, humidity, wind and radiation on the human body into one quantity. By combining the effects of these environmental variables with the human specific variables metabolic heat and clothing insulation, thermal indices quantify the human thermal environment a person experiences. Overall more than 165 indices have been proposed (de Freitas and Grigorieva, 2017). However, not all of them can be applied to assess outdoor thermal comfort, because they neglect important parameters such as solar radiation or wind speed and not all of them can be used in combination with ORMs as they are designed for temporal or spatial scales different from those in ORMs. Therefore, before the guiding research question (GRQ) can be addressed, first the following question has to be considered:

RQ 1 *Which thermal indices can be used globally in their current form to evaluate the outdoor urban thermal environment in ORM applications?*

To do so, criteria for suitable thermal indices for application in ORMs are derived based on the characteristics of thermal indices, of outdoor urban environments and of ORMs. This derivation together with a detailed description of the underlying characteristics is presented in Chapter 2 and serves as theoretical background of this thesis.

In order to apply the suitable thermal indices effectively in ORMs, the sensitivity of the indices to their input variables, i.e. temperature, humidity, wind and radiation, has to be known. This allows the identification of those processes that have to be simulated accurately in ORMs for thermal comfort studies in urban areas and the derivation of the achievable accuracy of thermal indices in urban areas in the face of uncertain input parameters. Therefore Chapter 4 addresses the question:

RQ 2 *How sensitive are selected thermal indices to their input variables?*

For this sensitivity analysis two of the suitable thermal indices are selected – the Physiological Equivalent Temperature (PET) and the Universal Thermal Climate Index (UTCI). To derive the sensitivities, several different meteorological situations and urban configurations have to be evaluated. Therefore, a computationally efficient model for the urban environment is required. Consequently, within this thesis the Simple Urban Radiation Model (SURM) has been developed, which is introduced and evaluated in Chapter 3.

Since the sensitivity analysis indicates that both thermal indices are sensitive to changes in radiation in addition to changes in air temperature and wind, the radiation field within the applied ORM for research question GRQ should be accurately simulated, especially as all those parameters interact. Therefore the Microscale Transport and Stream model (MITRAS) (Schlünzen et al., 2003; Salim et al., 2018) is extended to better represent radiative processes in urban areas. MITRAS has been selected as the ORM of the current study, since the source code is available. Furthermore, it has been shown to fulfil the test cases of the Association of German Engineers (Verein Deutscher Ingeneure (engl. Association of German Engineers) (VDI), VDI (2005)) for obstacle resolving micro-scale models (Grawe et al., 2013), thus providing a good foundation for further developments. MITRAS is described along with the implemented and validated extensions in Chapter 5.

Using this extended model system and the knowledge gathered from research question RQ 1 and RQ 2, the guiding research question of this thesis (GRQ) is addressed in Chapter 6. Final conclusions for this thesis are drawn in Chapter 7.

Parts of this thesis are accepted for publication (Chapter 2; Fischereit and Schlünzen, 2018) or are already published (parts of Appendix M, Wiesner et al., 2018). The journal articles are reproduced here. To facilitate reading, the abstracts and introductions as well as parts of the conclusions are left out and all references are summarised at the end of the thesis. Furthermore, all texts are transferred to British English and cross references to other sections of this thesis have been added where appropriate.

2 Evaluation of thermal indices for their usability in obstacle resolving meteorology models

Preface

This chapter has been published in **Fischereit J. and Schlünzen K. H.** (2018): Evaluation of thermal indices for their applicability in obstacle resolving meteorology models. *International Journal of Biometeorology*, volume 62(10):pages 1887–1900. ISSN 1432-1254. `http://dx.doi.org/10.1007/s00484-018-1591-6` under the terms of the Creative Commons Attribution 4.0 International License (`http://creativecommons.org/licenses/by/4.0/`). For this thesis the introduction and parts of the conclusions have been left out. Additional paragraphs have been added, which serve as a theoretical background of this thesis; those additions are indicated in italics. References to other chapters of this thesis have been added where applicable and Figure 2.1 has been added for illustrative purposes. To be consistent with the other parts of this thesis American English has been changed to British English and symbols have been replaced by their respective counterparts used in this thesis. References have been combined at the end of this thesis. The appendices of the original publication are given in Appendix A to Appendix C. Due to the structure of this thesis sections in the original paper have been replaced by subsections and so forth. K. Heinke Schlünzen provided some ideas regarding the methods used and the structure of the original paper.

2.1 Introduction

To select suitable thermal indices for modelling of outdoor thermal comfort in urban areas, this chapter identifies criteria based on a literature analysis regarding the characteristics of thermal indices, of human environmental heat exchange, of outdoor urban environments and of ORMs (Section 2.2). The derived criteria are applied to all 165 thermal indices listed in a catalogue by de Freitas and Grigorieva (2015) by reviewing their original literature and using the existing literature review by de Freitas and Grigorieva (2017) (Section 2.3). The analysis focuses on the typical urban resident and thus the results might not be directly applicable to outdoor workers or tourists. Section 2.4 discusses the results and indicates prospects for further developments regarding thermal comfort modelling in urban areas.

2.2 Thermal indices and application demands

This section describes characteristics of human environmental heat exchange and the related concept of thermal indices (Section 2.2.1), characteristics of outdoor urban environment (Section 2.2.2) and characteristics of ORMs (Section 2.2.3). Based on these characteristics, criteria for suitable thermal indices in ORM applications are derived along with additional features of suitable indices (Section 2.2.4).

2.2.1 Thermal indices and related definitions

2.2.1.1 Human thermal environments and thermal indices

The human body exchanges heat with its surroundings by different processes: radiation, convection, evaporation, respiration and, if a significant area is in direct contact with solid material, via conduction (Fiala and Havenith, 2015, *Figure 2.1*). How much heat is exchanged via the different processes depends on four environmental variables, namely air temperature (T_a), humidity (H), wind speed (FF) and long- and shortwave radiation (Q^*, often summarised in the integrating variable mean radiant temperature, T_{mrt}), and two human-related factors: activity and clothing. Activity controls the amount of heat produced by the body, and clothing insulation determines the resistance to heat exchange. All six factors together are referred to as the "six basic parameters" (Parsons, 2014). The specific combination of the six basic parameters makes up the human thermal environment a person experiences. How a person feels in such a human thermal environment is defined as thermal sensation, e.g. hot, cold or neutral. Thermal sensation cannot be expressed directly in physical or physiological terms as it is a psychological phenomenon. However, thermal sensations have been shown to correlate with environmental conditions and physiological responses of the human body (Parsons, 2014).

A useful technique for the assessment of a thermal environment is the thermal index. The term "thermal index" is rarely defined in literature. Parsons (2014) defines an assessment of the thermal environment as an index, if it maps the factors that influence the human response to thermal environments to a single value that varies with the human response. This definition is applied in the present study.

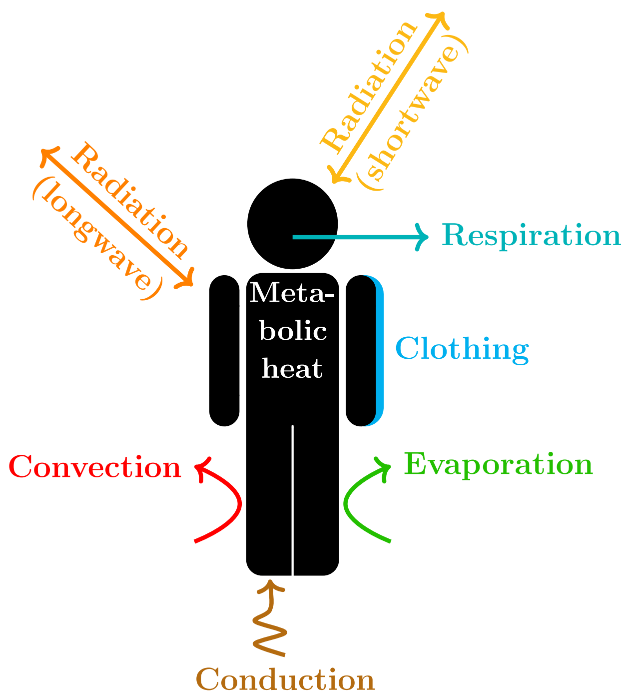

Figure 2.1: *Heat fluxes from and to the human body to be taken into account for exchange with the environment.*

2.2.1.2 Categories of thermal indices

Based on the measured human response, indices can be categorised into comfort or stress indices. Thermal comfort is defined as "that condition of mind which expresses satisfaction with the thermal environment" (ASHRAE, 2001), whereas thermal stress quantifies the effect of the six basic parameters in terms of thermal strain experienced by the person (Parsons, 2014).

Another possibility to categorise thermal indices has been proposed by MacPherson (1962), who discriminates direct, empirical and rational indices. Direct indices are based on direct measurements of environmental variables, either by using integrated measurement devices, which model a human body, or by combining measured meteorological parameters using an algebraic weighted expression (MacPherson, 1962; Eissing, 1995). In contrast, empirical indices are developed by exposing people to different environmental conditions (e.g. in a climate chamber) and measuring physiological parameters such as heart rate or rectal temperature. By means of multiple regression analysis the different environmental conditions and possibly different clothing and activities are linked to the physiological reactions (MacPherson, 1962). The third category, rational indices, formalise the heat exchange mechanisms of the human body (Section 2.2.1.1) to yield the heat balance equation (Eq. (2.1)) of the human body (ASHRAE, 2001; VDI, 2008):

$$M + w_m + Q^* + Q_H + Q_L + Q_{sw} + Q_{Re} + S = 0 \tag{2.1}$$

where M denotes metabolic heat, w_m mechanical work accomplished, Q^* radiation budget, Q_H, Q_L and Q_{sw} the turbulent flux of sensible heat, of latent heat by diffusion and of latent heat by sweat evaporation, Q_{Re} the respiratory heat flux (sensible and latent), and S the rate of storage of heat. Individual heat fluxes are calculated from gradients between physiological variables such as skin temperature and environmental variables. *Those heat fluxes transport approximately 85 % of the generated* 100 W *body heat of a non-active human (ASHRAE, 2001) to the environment. The human body can control this heat transfer to a certain extent through the active system of thermoregulation (Kovatas and Hajat, 2008; Wölki and van Treek, 2013; Parsons, 2014). It regulates the exchanged amount in warm environments by sweating and vasodilatation (increased skin blood flow (ASHRAE, 2001)) and in cold environments by shivering and vasoconstriction (reduced skin blood flow). Skin blood flow regulation is a continuous process, whereas shivering and sweating are threshold processes. The regulative processes are controlled by different parts of the hypothalamus (ASHRAE, 2001; Parsons, 2014) with warm and cold receptors on the skin and in the brain (Parsons, 2014) signalling the current state. The active system aims to keep the core temperature relatively constant at* 37 °C*, varying between* 36.7 °C *in the morning and* 37.5 °C *during the day (Havenith, 2005). Although during heavy exercise core temperature may reach* 40 °C *(Havenith, 2005), stronger deviation to above* 45 °C *or below* 18 °C *may be fatal (ASHRAE, 2001). Additionally to this active system, a passive system exists that consists of different layers of bones, muscles, fat and skin and influences the heat exchange.*

The regulation mechanisms are simulated with different complexity in one-node, two-node, multi-node and multi-element models (Cheng et al., 2012). Individual differences, such as gender and age (ASHRAE, 2001; Rida et al., 2014), but also acclimatisation (Froehle, 2008) have been noted to influence the physiological thermoregulation. In addition to the thermoregulatory system of the body, people adapt to a stressful environment by changing their behaviour (e.g. change in activity or exposure, Jendritzky and de Dear (2009)). Rational indices either refer to equilibrium conditions ($S = 0$), or to dynamic, transient conditions, or changing activities ($S \neq 0$). Out of the three categories of indices, they have the most objective basis, since they are based on the first law of thermodynamics. However, empirical relationships are used to calculate the regulation mechanisms within the body (ASHRAE, 2001).

Many indices apply the concept of a standard or reference environment. These thermal indices calculate the air temperature that would result in the ‘equivalent effect’ for a person as the actual environment does, which consists of the six basic parameters (Parsons, 2014). What is defined as ‘equivalent effect’ depends on the individual index, e.g. some require the core temperature to be equal in both environments. These so-called equivalent temperatures have the same unit as air temperature and, can therefore be understood by laypeople (Höppe, 1999).

2.2.1.3 Assessment scales for indices

A thermal index value itself is not necessarily meaningful, since it depends on the assumptions of the underlying equations. It is not clear, for instance, whether an equilibrium temperature of 10 °C is desirable in terms of thermally optimal design, or a value of 25 °C is better. Therefore, an assessment scale is needed that maps individual index values into categories of similar and generally understood thermal sensations or thermal stresses.

Different types of assessment scales can be identified: based on (1) strain reactions of the human body (Bröde et al., 2012), (2) regression between accepted scales from climate chambers and index values (Matzarakis and Mayer, 1996), or (3) regression between thermal sensation votes (denoted Thermal Sensation Vote (TSV) in the following) from surveys and index values (Watanabe et al., 2014). The first two scales aim to predict the value of the thermal index for a clearly defined reference person who chooses a place freely without specific expectations and before it adapts to this particular thermal environment (Staiger et al., 2011). In contrast, scales derived from TSVs represent the thermal perception after adaptation and include cultural norms and expectations for people attending the place at a specific time without free choice (Staiger et al., 2011). Although TSVs are important to identify regional particularities, they are unsuitable for ORM applications, since they are valid only for the regional climatic context where they have been derived The standardisation initiative of thermal comfort studies (Johansson et al., 2014) may lead to a globally standardised data base of TSVs. Those may be dense enough to be used in ORM applications, however, people deliberately avoiding the place due to uncomfortable environmental conditions are still not included in the TSVs and thus TSVs may lead to skewed results (Staiger et al., 2011).

2.2.2 Outdoor urban environments

2.2.2.1 *Characteristics of urban climate for thermal comfort*

Urban areas develop a unique climate, which differs from the regional background climate due to artificial materials, vertical structures and pollutant and heat emission (Oke et al., 2017). This urban climate concerns all aspects of climate, e.g. wind, radiation, temperature, water and atmospheric composition, and thus in turn the thermal environment a human being is exposed to. Buildings on the one hand increase turbulence but on the other hand decrease the mean wind speed due to an increased surface roughness. This decreased wind speed in general increases thermal stress in warm conditions (e.g. heat stress) due to reduced convection (Eq. (2.1), Figure 2.1) except if air temperatures are higher than skin temperatures. In contrast the shade provided by buildings reduces heat stress (Jendritzky et al., 2007). Multiple reflection of radiation both in the longwave and shortwave spectral range traps radiation within the urban canopy (Best and Grimmond, 2014, Section 2.2.2.3), which increases surface temperatures and consequently air temperatures. Air temperatures are also affected by a storage of heat in the urban fabric during the day and a slow heat release during the night due to the lower albedo and larger heat capacity of artificial building materials compared to natural surfaces. Those processes, in addition to anthropogenic heat release, cause the well known UHI effect in urban areas (Arnfield, 2003). The elevated temperatures especially deteriorate night-time thermal comfort. Also the changed water budget with increased run-off and less infiltration contributes to increased air temperatures and heat stress, since incoming solar radiation is transformed into sensible heat rather latent heat (Best and Grimmond, 2014). The changed atmospheric composition due to pollutants can effect the radiation budget and thus thermal stress, but more importantly directly influences the health of urban residents.

2.2.2.2 Outdoor air temperature range

Outdoor thermal environments exhibit a much wider range of environmental parameters than controlled indoor environments (Jendritzky and de Dear, 2009). To derive the air temperature range people are exposed to when being outdoors, two data sets have been combined. First, a global data set of observation-based monthly mean 2-m-air-temperature values (T_a) over land covering the period from 1986 to 2015 (Fan and van den

Dool, 2008), and second, a global data set for the population count (P) for the year 2000 (CIESIN, 2005). Both data sets have a resolution of 0.5°×0.5°. To estimate the air temperature range people are exposed to, an air temperature weighted population distribution is derived by calculating the population exposed (PE, Eq. (2.2)) to a specific 5K-ΔT_a-range between 1986 and 2015:

$$PE(T_{a,\min}) = \frac{1}{N}\left(\sum_{m=1}^{M}\sum_{i=1}^{N} f(T_{a,\min}) \cdot P_i\right) \tag{2.2}$$

with

$$f(T_{a,\min}) = \begin{cases} 1 & T_{a,\min} \leq T_a < T_{a,\min} + 5\mathrm{K} \\ 0 & \text{else} \end{cases} \tag{2.3}$$

M is the number of months (m) between January 1986 and December 2015 ($M = 360$), N is the number of grid cells (index i), and $T_{a,\min}$ is varied between -60 °C and 60 °C in 5 K-steps. For the air temperature data from 1986 to 2015 T_a lay between -55.0 °C and 62.6 °C. Due to slight differences in the land-sea-mask of the two data sets, about 2 million people (0.03 % of the world population) could not be considered in the analysis. Most of them live on islands in the Pacific Ocean. Figure 2.2 shows PE for each ΔT_a-range. Only few people exposed to monthly mean air temperature values below -25 °C or above 40 °C (less than 0.1 % of the worlds population per range). 95 % of the world population lives in an air temperature range of -5 °C to 35 °C. The hatched bars in Figure 2.2 mark the two ranges enclosing 95 % of the population.

2.2.2.3 Radiation fluxes and wind speed

A particular feature of outdoor environments is the presence of direct solar shortwave radiation fluxes. These include direct, diffuse and reflected radiation fluxes. In an urban environment, longwave radiation is not only emitted from the sky and the ground, but also from surrounding building walls. These walls, in turn, can shade areas and shield people from direct shortwave radiation. The mean radiant temperature (T_{mrt}), which is usually applied to express the effect of radiation Kántor and Unger (2011), is the most variable parameter within an urban street canyon (Ali-Toudert and Mayer, 2006; Chen et al., 2016; Jendritzky et al., 2007; Lee et al., 2016, 2014; Mayer et al., 2008). The second most variable parameter is the wind speed due to drag and advection effects. Radiation and wind are also those parameters that can best be modified for a thermally comfortable design (Barry and Blanken, 2016) and affect thermal perception most (Moonen et al., 2012).

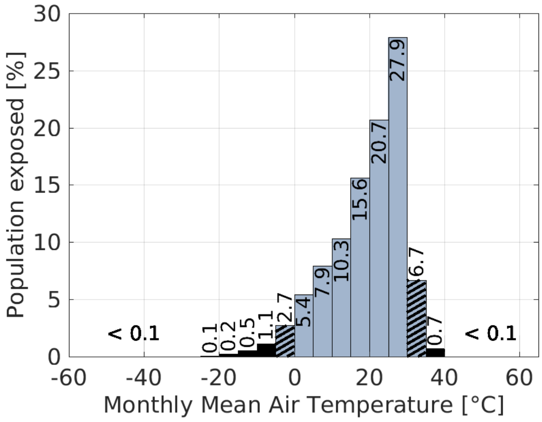

Figure 2.2: Percentage of the world population exposed to a specific 5 K monthly mean 2-m-air-temperature range. To each range below -25 °C and above 40 °C less than 0.1 % of the world's population is exposed. Grey-coloured bars indicate 95 % of world population; hatched bars indicated the range containing the accumulated upper and lowermost 2.5 % of the world population and black-coloured bars the outer 5 % of world population. Basic data have been taken from GHCN Gridded V2 data Fan and van den Dool (2008) and the Gridded Population of the World dataset, Version 3 (see text).

2.2.2.4 Urban activities and clothing behaviour

Urban activities include standing, e.g. while smoking or talking, or walking, e.g. while shopping or commuting. Although activities vary for different types of urban spaces (Thorsson et al., 2007a), in the current study standing and walking are considered as typical urban activities as they reflect the typical behaviour outside parks.

Clothing behaviour in urban areas has been shown to vary seasonally (Havenith et al., 2012; Nikolopoulou et al., 2001) but within certain limits: even in hot conditions a minimum of 0.2 clo (1.0 clo is equivalent to a thermal resistance of clothing of 0.155 $m^2\,K\,W^{-1}$, ASHRAE, 2001) has been observed, which corresponds for instance to short-sleeve shirt and short trousers (de Freitas, 1987). Those limits might be due to cultural rules and norms Knez et al. (2009). Urban clothing behaviours may differ significantly from clothing of beach tourists or workers wearing special protective clothes. Therefore, the indices selected in this study might not be applicable for those groups.

2.2.2.5 Persistence of outdoor environmental conditions

Today many urban activities usually take place indoors: in most industrialised countries people spend about 90 % of their time inside buildings (Höppe, 2002). Thus, the time spent outdoors is usually too short to achieve thermal equilibrium, especially as people tend to stray between different microclimates (Thorsson et al., 2007a). Furthermore, the meteorological conditions are changing: A quasi-steady state, e.g. a state for which the thermal conditions of the body per time unit change only marginally, may be achieved for a certain microclimate within 2 hours if the weather is constant, but not only the person might move, usually also the meteorological situation changes in that time (e.g. diurnal cycle). Therefore, an index considering dynamic conditions would be most suitable (Section 2.2.1.2). However, such an index strongly depends on the thermal history of a person, e.g. exiting from a sauna or from an air-conditioned building. Therefore, to evaluate a certain design, simulations of an ensemble of people with different thermal histories would be required. However, getting that kind of information is difficult, and even then ensemble simulations are computationally intensive. Therefore, although dynamic indices are more realistic, steady state indices offer advantages for urban planning applications.

2.2.3 Obstacle resolving atmospheric models (ORMs)

2.2.3.1 Time scales

ORMs simulate thermal and dynamic atmospheric processes by numerically solving partial differential equations for conservation of energy, mass and momentum. These so called Navier-Stokes equations cannot be solved directly due to computational limitations (Blocken, 2015). Hence, the equations are filtered and approximated. Nowadays the time and space averaged so called Reynold-Averaged-Navier-Stokes Equations (Reynolds-Averaged-Navier–Stokes equations (RANS)) are used for simulating flows within urban areas (Blocken, 2015). Those RANS models simulate the temporal mean flows in detail but with a typical time average of 10 to 20 minutes that mainly results from the parameterisation of turbulent motion. The spatial resolution depends on the grid size used. RANS models are applied for studying urban areas (e.g. Ali-Toudert and Mayer, 2006; Salim et al., 2015). For specific applications quality guidelines are established (Franke et al., 2011; VDI, 2017).

2.2.3.2 Input variables for thermal indices

By solving the RANS equations, ORMs simulate the temporal evolution and spatial distribution of several meteorological variables (e.g. air temperature and flow field; Bohnenstengel et al., 2004), which can then serve as input for thermal indices. For the two human-related factors, clothing insulation and activity, standardised input tables have been established (e.g. ASHRAE, 2001) which can be used to derive input values. In contrast, physiological input parameters such as heart rate or rectal temperature would require expert knowledge or a suitable thermophysiological model. Only if such a model exists for a particular index, it can be used in ORM applications.

2.2.3.3 Calculation of thermal indices in ORM applications

The calculation of thermal indices from ORM outputs requires either a set of equations or a suitable calculation program since the manual estimation of index values from nomograms or tables is not feasible due to the high number of grid points in ORMs. In the past, several integrated measurement devices have been proposed for a convenient estimation of direct indices (Section 2.2.1.2). Indices derived from those devices can be used in ORMs if either a methodology to model the device within the ORM or an equation fitted from standard meteorological parameters exists.

Indices can be calculated either on-line during the simulation or off-line using model output. From a physical point of view an on-line calculation would only be necessary, if the heat released by a person impacts the surrounding atmosphere. Outdoors, a person's impact on the thermal environment is small because the wind speed is large and the air is often well mixed. Indoors, the impact of persons on the air is commonly larger due to smaller exchange rates of air, and thus on-line coupling is attempted (e.g. Cropper et al., 2010). From a computational point of view, off-line calculation is favourable because the effect of a set of meteorological conditions can be estimated for different personal characteristics without the need to rerun the ORM. However, Buzan et al. (2015) showed for global simulations that infrequent model output can cause an underestimation of thermal stress experienced. To avoid this effect in ORMs the output needs to be frequent enough to reflect the changing air temperature and wind conditions (e.g. about 20 minutes). The output might have to be even more frequent to capture changes in meteorology if the

ORM is nested (Schlünzen et al., 2011b).

2.2.3.4 Fields of application for ORM

ORMs are applied for design and performance analysis of building components, pollutant dispersion and wind and thermal comfort (Moonen et al., 2012). In terms of thermal comfort, various studies assess the impact of different urban features (vegetation, albedo, etc.) or building configurations on the human thermal environment (Jänicke et al., 2015; Lee et al., 2016; Moonen et al., 2012). To do so, it is essential that the index can evaluate the thermal environment at a specific location (not only relative to a different location) for a specific meteorological situation (no climate average values required as inputs). Frequently applied thermal indices allow for a comparison of thermally comfortable designs in different climatic zones.

2.2.4 Evaluation procedure for suitable indices

From the characteristics described in Section 2.2.1 to Section 2.2.3, the following 11 selection criteria for determining indices suitable for ORM application are derived. A pre-condition for all indices selected is that they shall provide only one output value (Section 2.2.1.1). The criteria cover input demands (C1, C2), calculation demands (C3–C9) and interpretation demands on the index (C10, C11). The numbering follows the order how an index would be applied in an ORM application:

- C1 The input of the index is retrievable from ORMs or from standardised tables (i.e. for activity and clothing; Section 2.2.3.2).
- C2 The index exploits meteorological input values on the same temporal scale as typical for output time scales of ORMs (Section 2.2.3.4).
- C3 The index is computable using a formula or a numerical model (Section 2.2.3.3).
- C4 The index assesses the local thermal environment at a specific location within an urban area (Section 2.2.3.4).
- C5 The index considers the influence of all six basic parameters (Temperature (T_a), humidity (H), wind speed (FF) and radiation (Q^*), clothing and activity) in the calculation and includes both longwave and shortwave radiative fluxes (Section 2.2.1.1 and Section 2.2.2.3).

C6 The index considers longwave radiative fluxes from all directions (Section 2.2.2.3).

C7 The index considers the average air temperature range in which a large proportion of mankind lives (-5 °C to 35 °C, Section 2.2.2.2).

C8 The index considers typical clothing behaviour and activities of urban residents (Section 2.2.2.4).

C9 The index assesses thermal conditions for an exposure time of 10 minutes and more; instantaneous reactions should not be assessed (Section 2.2.3.1).

C10 An assessment scale exists for the thermal index (Section 2.2.1.3).

C11 The assessment scale of the index is not derived from thermal sensation votes in a specific region (Section 2.2.1.3).

The criteria are applied in the order given above (C1 to C11) to the 165 indices listed in the catalogue by de Freitas and Grigorieva (2015), which is the most comprehensive list of indices existing so far. If an index does not fulfil a specific criterion, subsequent criteria are not further assessed. To assess the criteria, the original literature of the indices has been reviewed. For 21 indices the original literature could not be obtained and therefore secondary sources have been used. In our review of the original literature differences have been found compared to the review by de Freitas and Grigorieva (2017). Those differences are described in Appendix B. For the analysis, indices are evaluated according to our review. For three indices ("Perceived Temperature according to Linke", "Physical saturation deficit" and "Thermal Insulation of Clothing according to Aizenshtat") the cited reference by de Freitas and Grigorieva (2017) did not contain such an index. Therefore, those indices had to be excluded from the analysis (Appendix B). For the index "Respiratory Heat Loss" neither the original publication nor sufficient secondary literature could be obtained. Here the review by de Freitas and Grigorieva (2017) was used, although it only allows an evaluation of some criteria (Appendix A). For criterion C7 the air temperature ranges given by de Freitas and Grigorieva (2017) are used for all indices.

After the 11 criteria are applied, for all remaining indices, 6 additional index features, also derived from Section 2.2.1 to Section 2.2.3, are analysed:

F1 Unit of the thermal index (Section 2.2.1.2)

F2 Type of human response evaluated by the index (Section 2.2.1.2)

F3 Temporal resolution considered (Section 2.2.2.5)

F4 Implementation of index calculation in ORM applications (Section 2.2.3.3)

F5 Available methods for the calculation of the index (Section 2.2.3.3)

F6 Application frequency of the index in ORMs (Section 2.2.3.4)

The features F1 to F5 serve as information, but do not lead to an exclusion of an index. The features are assessed by reviewing the original literature of the indices. For F6 a systematic literature review was performed using the databases "Scopus" (`https://www.scopus.com/home.uri`) and "Web of Science" (`https://apps.webofknowledge.com`) with the key-words "numerical model", "thermal index", "urban" including all fields in Scopus and the topic in Web of Science on 15th November 2016. A total of 116 publications between 2000 and 2016 were obtained of which 106 were left after duplicates had been removed. By screening, 74 records were excluded because of at least one of the following reasons: (1) no ORM application, (2) study of a different spatial scale, (3) did not estimate a thermal index or (4) were not published in a peer reviewed journal. In total, 32 studies with different thermal indices remained to evaluate the application frequency (F6). The flow diagram and the 32 studies ordered by applied indices and by climatic zone are shown in Appendix C.

2.3 Results

The assessment criteria derived in Section 2.2 are applied using the method described in Section 2.2.4 in order to identify suitable thermal indices for ORM applications.

2.3.1 Application of criteria

From the 165 analysed indices, two entries do not meet the definition of thermal indices used in this paper (Section 2.2.1.1), since they provide more than one output (precondition for selected index): the Predicted effects of heat acclimatisation (Givoni and Goldman, 1973) and the Predicted Heat Strain (Malchaire et al., 2001). Therefore, they are not further analysed.

All indices excluded because of criterion C1 to C7 are shown in Appendix A including their abbreviations, references, equations for their calculation as far as possible as well as reasons for their exclusion. As noted before, the criteria are applied in the order given in

Section Section 2.2.4. If an index fails a criterion, subsequent criteria are not assessed. Figure 2.3 shows the number of indices excluded by C1 to C7 and the remaining number indices. Most indices do not consider all six basic parameters (C5). After C1 to C7 are applied, 13 indices remain. For those indices, the air temperature design ranges and restrictions for other meteorological variables are shown in Table 2.1.

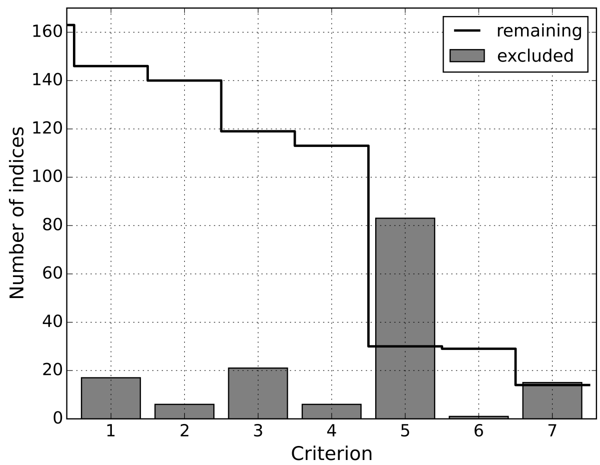

Figure 2.3: Number of indices excluded by criterion C1 to C7 (bars) and remaining number of indices (line). A detailed table of excluded indices is given in Appendix A.

Table 2.1: Air temperature design ranges (ΔT_a) of thermal indices meeting criteria C1 to C7. Ranges of wind speed in persons height (v) or 10 m (v_{10}), relative humidity (RH) and mean radiant temperature (T_{mrt}) are indicated as far as documented in the original publications. Air temperature ranges have been taken from de Freitas and Grigorieva (2017).

ΔT_a **range** [°C]	**Index**	**Other ranges**	**Reference**
$-25 \leq T_a \leq 35$	**He**at **B**udget **I**n**dex** (HEBIDEX) **S**kin **T**emperature **E**nergy **B**alance **I**n**dex** (STEBIDEX)		de Freitas (1985); de Freitas, C. R. (1986); de Freitas and Symon (1987)
$-40 \leq T_a \leq 40$	**Ph**ysiological **S**train (PhS), **S**ubjective **T**emperature **I**ndex (STI)		Błażejczyk (2005)
	Predicted **M**ean **V**ote – **o**utdoors ($\mathrm{PMV_o}$)		Jendritzky and Nübler (1981)
	Physiological **S**ubjective **T**emperature (PST)	$FF \leq 22\ \mathrm{m\,s^{-1}}$	Błażejczyk et al. (2012); Błażejczyk and Matzarakis (2007)
$-40 \leq T_a \leq 50$	**P**erceived **T**emperature ($\mathrm{PT_J}$)		Błażejczyk et al. (2012); Staiger et al. (2011)
$-50 \leq T_a \leq 50$	**P**hysiological **E**quivalent **T**emperature (PET)		Höppe (1999); Mayer and Höppe (1987)
	Universal **T**hermal **C**limate **I**ndex (regression, look-up table version; $\mathrm{UTCI_{app}}$)	$0.5 \leq FF_{10} \leq 30.3\ \mathrm{m\,s^{-1}}$, $-30 \leq T_{mrt} - T_a \leq 70$ °C, $5 \leq RH \leq 100$ %	Bröde et al. (2012); Jendritzky et al. (2012)

ΔT_a **range** [°C]	**Index**	**Other ranges**	**Reference**
$-90 \leq T_a \leq 37$	**Th**ermal **Bal**ance (balance version, see Appendix A; $\mathrm{ThBal_b}$)		Rusanov (1981)
$-90 \leq T_a \leq 60$	**O**utdoor **T**hermal **E**nvironment **I**ndex (OTEI, ETVO)		Nagano and Horikoshi (2011)
	Universal **T**hermal **C**limate **I**ndex (UTCI)		Bröde et al. (2012); Jendritzky et al. (2012)
	Standard **E**ffective **T**emperature **Out**doors (OUT_SET*)		Pickup and de Dear (2000)

All 13 remaining indices (Table 2.1) clearly cover the air temperature range of -5 °C to 35 °C (C7), where 95 % of the world population lives (Section 2.2.2.2). For PST and $\mathrm{UTCI_{app}}$additional restrictions concerning wind speed (both), relative humidity and mean radiant temperature were found. Although no restrictions for the other indices were found, it is likely that their application range is also constrained, since the underlying parameterisations have been derived only for a limited number of conditions. C8 to C11 are applied to the indices in Table 2.1 (Table 2.2). Since all remaining indices are rational indices based on thermophysiological models for the human heat budget, they can be applied for every combination of clothing and activity. Therefore, no index is excluded due to criterion C8.

Table 2.2: Indices excluded from further analysis due to criterion (C). Full index names and references are shown in Table 2.1.

C	**Index**	**Reason**
9	PhS	Evaluates reaction of body immediately after exposure to an environment Błażejczyk (2011, 2005). Thus, PhS evaluates time scales shorter than 10 minutes, which cannot be resolved with ORMs
9	STI	Same as PhS
10	OTEI	No assessment scale defined
10	$\mathrm{ThBal_b}$	No assessment scale defined. An assessment scale is defined for a regression version, but that does not include longwave radiation (C5, Appendix A)
11	HEBIDEX	Assessment scale is derived from thermal sensation votes of beach tourists Błażejczyk (2005)
11	STEBIDEX	Same as HEBIDEX
11	OUT_SET*	Contradicting assessment scales derived from thermal sensation votes for different locations by different authors (Tsitoura et al. (2014); Spagnolo and de Dear (2003); Watanabe et al. (2014))

After assessing the indices with respect to C1 to C11, five indices, $\mathrm{PMV_o}$, Perceived Temperature ($\mathrm{PT_J}$), PET, PST and UTCI (and $\mathrm{UTCI_{app}}$) are found suitable for applications in ORMs. Since $\mathrm{PT_J}$ is an extension of $\mathrm{PMV_o}$ and improves the limited humidity-sensitivity in warm situations Staiger et al. (2011), $\mathrm{PMV_o}$ is excluded from further analysis.

2.3.2 Evaluation of index features

The indices PT_J, PET, PST, $UTCI_{app}$and UTCI are analysed with respect to their additional features (F1 to F6); the results are compared in Table 2.3. All remaining indices have a temperature unit (°C, F1). PT_J uses PMV to measure the equivalent effect and is therefore comfort-based (F2). Additionally, PT_J was linked to stress categories (Table 2.4, Staiger et al., 2011). PET and UTCI also evaluate thermal stress (F2) since they use strain reactions to measure the equivalent effect in the reference environment and in the actual environment. PET is linked to the PMV scale via a linear regression (Matzarakis and Mayer, 1996) and can therefore also be viewed as comfort-based (Błażejczyk et al., 2012). The validity of the regression method was questioned (e.g. Lee and Mayer (2016)). Consequently for PET other scales from TSVs have been derived for various climates (e.g. Lin and Matzarakis, 2008; Holst and Mayer, 2010; Kántor et al., 2012; Cohen et al., 2013). However, these scales differ from the original scale (Section 2.2.1.3) in terms of their implications. The categories of the UTCI assessment scale (Table 2.4) are derived from occurrence of strain reactions such as the onset of shivering (Bröde et al., 2012). PST estimates thermal sensation (F2), but in contrast to the other indices is not an equilibrium temperature. Instead, PST is defined as the temperature established around the skin surface (under clothing) after 15-20 min of adaptation to maintain homeothermy. Therefore, the temporal resolution (F3) considered for PST is much more detailed than for UTCI (average over two hours), and PT_J and PET, which estimate steady state conditions.

Table 2.3: Thermal indices for ORM applications fulfilling criteria C1 to C11. For entries related to features F1 to F6 the corresponding feature is given. The following abbreviations are used: A_{Du} is body surface area, BF is body fat content, e is water vapor pressure, e_a is water vapour pressure under actual conditions (related to reference environments) , H is a general measure for humidity with specification such as relative humidity (RH), h_p is height, I_{clo} is clothing insulation, M is metabolism, m is weight, T_a is air temperature, T_c is core temperature, T_{mrt} is mean radiant temperature, T_{sk} is skin temperature, FF is wind speed in person's height, v_w is walking speed, FF_{10} is wind speed in 10 m, w_m is work metabolism. Superscripts have the following meaning a: Regression version of UTCI, b: Look-up-table version of UTCI and c: full model version of UTCI. For index abbreviations see Table 2.1.

Index	**PT$_\mathbf{J}$**	**PET**	**PST**	**UTCI**
Unit (F1)	°C	°C	°C	°C
Definition	Equilibrium temperature: same thermal perception (measured by PMV)	Equilibrium temperature: same T_{sk} and T_c	Temperature that is formed around skin surface (under clothing) after 15-20 min of adaptation to maintain homeothermy	Equilibrium temperature: same strain evaluated by same dynamic response of the physiological model
Reference conditions	$T_{mrt} = T_a$ $H = \begin{cases} RH = 50\ \% & \text{warm} \\ e = e_a & \text{else} \end{cases}$	$T_{mrt} = T_a$ $e = 12$ hPa	Not applicable	$T_{mrt} = T_a$ $H = \begin{cases} e = 20\text{hPa} & T_a > 29\ °\text{C} \\ RH = 50\ \% & \text{else} \end{cases}$

Index	$\mathbf{PT_J}$	**PET**	**PST**	**UTCI**
	$FF = 0.1\ \mathrm{m\,s^{-1}}$	$FF = 0.1\ \mathrm{m\,s^{-1}}$		$FF_{10} = 0.1\ \mathrm{m\,s^{-1}}$
Reference person	$M = 135\ \mathrm{W\,m^{-2}}$ $(v_w = 4\ \mathrm{km\,h^{-1}})$ $I_{clo} = \begin{cases} 1.75\ \mathrm{clo} & \text{winter} \\ f(T_a) & \text{else} \\ 0.5\ \mathrm{clo} & \text{summer} \end{cases}$ Male, 35 years $m = 75$ kg $A_{Du} = 1.9\ \mathrm{m^2}$ $h_p = 1.75$ m	$M \approx 86\ \mathrm{W\,m^{-2}}$ $(w_m = 80\ \mathrm{W})$ $I_{clo} = 0.9$ clo Male, 35 years $m = 75$ kg $A_{Du} = 1.9\ \mathrm{m^2}$ $h_p = 1.75$ m	$M = 135\ \mathrm{W\,m^{-2}}$ $(v_w = 4\ \mathrm{km\,h^{-1}})$ $(v_w = 4\ \mathrm{km\,h^{-1}})$ $I_{clo} = \begin{cases} 3\ \mathrm{clo} & T_a < -30 \\ f(T_a) & \text{else} \\ 0.6\ \mathrm{clo} & T_a > 25 \end{cases}$	$M = 135\ \mathrm{W\,m^{-2}}$ $I_{clo} = f(T_a)$ (Havenith et al., 2012) $BF = 14$ % $m = 73.4$ kg $A_{Du} = 1.85\ \mathrm{m^2}$
Measure of assessment scale (F2)	Thermal perception; Thermophysiological stress, directly linked to PMV-scale	Thermophysiological stress, related to PMV-scale	Thermal Sensation	Thermal Stress
Temporal resolution (F3)	Steady state	Steady state	After 15 to 20 min exposure	Average over 2 hours

Index	PT_J	PET	PST	UTCI
Thermo-physiological model (related to F4)	Klima-Michel-Model (KMM), parameterisations derived from a two-node model Gagge et al. (1986)	Munich Energy Balance Model for Individuals (MEMI), two-node	Man-ENvironment heat EXchange model (MENEX), one-node	UTCI-Fiala Model, multi-element
Coupling (F4)	On-line / off-line	Off-line	On-line /off-line	On-line[a], off-line[b,c]
Code availability (F5)	VDI (2008)	VDI (2008)	No	Version a,b via ISB Comission 6 ISB Comission 6 (2012)
Software (examples, F5)	Free Software RayMan (Matzarakis and Fröhlich, 2009; Matzarakis et al., 2007, 2010), sub-module BioMet of the commercial version of ENVI-met (Bruse and Team, 2015)	Free Software Package RayMan (Matzarakis and Fröhlich, 2009; Matzarakis et al., 2007, 2010), sub-module Bio-met of the commercial version of ENVI-met (Bruse and Team, 2015)	Free Software BioKlima (Błażejczyk, 2010)	Free Software Package RayMan (Matzarakis and Fröhlich, 2009; Matzarakis et al., 2007, 2010) and BioKlima (Błażejczyk, 2010), sub-module Bio-met of the commercial version of ENVI-met (Bruse and Team, 2015)
Assessment scale (F6)	See Table 2.4			

Index	$\mathbf{PT_J}$	**PET**	**PST**	**UTCI**
Ranges of meteorological inputs	See Table 2.1			
References	Jendritzky et al. (1990); Staiger et al. (2011)	Mayer and Höppe (1987); Höppe (1999)	Błażejczyk and Matzarakis (2007); Błażejczyk et al. (2012)	Bröde et al. (2012); Jendritzky et al. (2012)

Whether an index is capable to be applied on-line (F4) depends primarily on the computational cost required for the calculation. The computational cost can be estimated from the evaluated temporal state (e.g. more calculations are needed to reach thermal equilibrium) and the complexity of the thermophysiological model (e.g. more complex multi-elements models require more calculations). Temporal state, the thermophysiological models and the derived on-line or off-line application type are shown in Table 2.3. The thermophysiological model of PST (MENEX) is a one-node model. Due to the nature of a one-node model, PST cannot account for thermophysiological regulation processes within the body, e.g. heat exchange between different body parts. To consider these processes at least two nodes are necessary (Section 2.2.1.2) as considered in thermophysiological models of PET and PT_J. Out of the thermophysiological models of four suitable indices, the UTCI-Fiala model most sophisticated. Due to its multi-element structure it predicts the state of individual body parts, although the UTCI index itself currently represents an entire body value.

The software (F5) to calculate the indices is indicated in Table 2.3. The source code is only publically available for $UTCI_{app}$. For PET and PT_J source code is available from VDI (2008).

Table 2.4: Assessment scales of thermal indices suitable for ORM applications based on criteria C1 to C11. For index abbreviations see Table 2.1. Physiological stress categories refer to PT_J, PET and UTCI but not to PST.

Thermal sensation	**PST** [°C]	**PT_J**[°C]	**PET** [°C]	**UTCI** [°C]	**Physiological Stress**
+5 sweltering	$\geq$ 54				
+4 Very hot	44 to 54	$\geq$ 38	$\geq$ 41	> 46	Extreme heat stress
				38 to 46	Very strong heat stress
+3 Hot	34 to 44	32 to 38	35 to 41	32 to 38	Strong heat stress
+2 Warm	24 to 34	26 to 32	29 to 35	26 to 32	Moderate heat stress
+1 Slightly warm		20 to 26	23 to 29		Slight heat stress
0 Neutral (comfortable)	14 to 24	0 to 20	18 to 23	9 to 26	No thermal stress
-1 Slightly cool		-13 to 0	13 to 18	0 to 9	Slight cold stress
-2 cool	4 to 14	-26 to -13	8 to 13	-13 to 0	Moderate cold stress
-3 cold	-16 to 4	-39 to -26	4 to 8	-27 to -13	Strong cold stress
-4 very cold	-36 to -16	$\leq$ -39	$\leq$ 4	-40 to -27	Very strong cold stress
-5 frosty	$\leq$ -36			< -40	Extreme cold stress

PT_J, PET, PST and UTCI not only differ with respect to the index features but also regarding the treatment of clothing and activity (criterion C8). PET uses a fixed clothing insulation of 0.9 clo for the definition of the assessment scale (Table 2.3). Hence, it is a purely climatic index independent of individual behaviour (Höppe, 1999). However, other clothing values may be used in Munich Energy Balance Model for Individuals (MEMI), although the assessment scale is technically applicable only for 0.9 clo. The three other indices account for a behavioural adjustment of clothing. In the calculation of UTCI a full clothing model is incorporated (Havenith et al., 2012), which considers typical clothing behaviour of urban residents, derived from studies in Europe and Russia. By considering adjustable clothing, behavioural adaptation (Section 2.2.1.2) is accounted for. For the wide range of atmospheric conditions experienced outdoors, fixed clothing is unlikely to represent the clothing behaviour of the population during all seasons. However, to be able to compare thermal climates at two locations, fixed clothing may be preferred. PET considers a very light activity (standing still), which represents the lowest expected outdoor body heat production under normal circumstances. The three other indices consider walking at 4 $\mathrm{km\,h^{-1}}$. The UTCI index is currently further developed to include other clothing and activity levels (Bröde et al., 2016).

The indicated assumptions and limitations of individual indices must be kept in mind by the user when applying these indices. Despite the differences between the indices, they have been shown to be strongly correlated (e.g. Błażejczyk et al., 2012; Staiger et al., 2011; Park et al., 2014; Matzarakis et al., 2014; Fröhlich and Matzarakis, 2015). The correlations, however, were found to be regime dependent (Staiger et al., 2011; Fröhlich and Matzarakis, 2015) because of the sensitivity of the indices to specific meteorological parameters and the different clothing models.

For the evaluation of F6, a systematic literature review was conducted as described in Section 2.2.4. Figure 2.4 shows the results of the 32 identified studies (references are given in Appendix C). PET is the most widely applied index in ORM applications (Figure 2.4a). It remained popular even after the development of UTCI in 2012. Similar results were obtained by Coccolo et al. (2016), who did not focus on the microscale. PET has been applied in all three climatic zones, whereas most other indices have been applied only in some zones (Figure 2.4b). Most studies have been conducted for the subtropics, followed by temperate climate and the tropics. No study for polar climate was found in the systematic review.

This statistical analysis shows that of the selected indices in this study only PET has been applied in different climatic zones. PET is also the most frequently applied index. Therefore, PET is most suitable for comparing simulation results for different cities around the globe. No studies were found to apply PST or $\mathrm{PT_J}$, although with PMV a precursor of $\mathrm{PT_J}$ was applied. The two indices without a rational basis (THI, WBGT; Appendix A) are least frequently applied; Morakinyo et al. (2016) use them in addition to PET.

(a) **(b)**

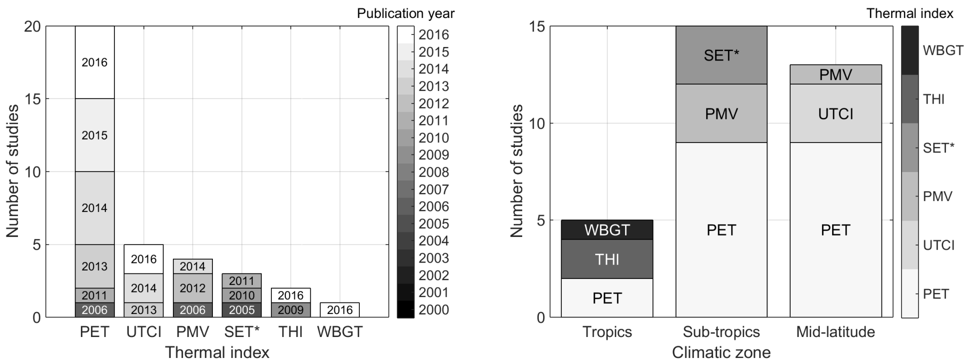

Figure 2.4: Number of ORM applications using the different indices (a) published in different years (grey-coloured) and (b) per climate zone (indices grey-coloured). Appendix C summarises the studies included in the analysis derived from the method in Section 2.2.4. For abbreviations of indices see Appendix A and Table 2.1. Note that some studies applied several indices and that PMV and SET* are used here to summarise studies that apply these indices in their original or derived form.

2.4 Discussion

In this chapter, thermal indices suitable for ORM applications in urban environments for evaluating thermally comfortable designs *are identified.* Indices not selected in this analysis are not "bad", but not targeted for the intended type of application. Indices developed in form of nomograms, for instance, can be transformed to a program but that would require extra work from the user (C3). This may change, however, if the index is further developed. The indices selected in this study were targeted for the average urban resident with typical urban clothing and activity. To assess the thermal environment of beach tourists or workers wearing special protective clothes, different indices may be needed than those selected in this study. Additionally, only those indices were selected that can be applied to an air temperature range of -5 °C to 35 °C. This range was determined to cover the climatic air temperature range 95 % of the world population experiences. If only warm conditions shall be thermally assessed, all indices discarded by C7 in Appendix A might be usable. For those indices criteria C8 to C11 should be evaluated before use. Besides the temperature design range also the ranges for humidity, wind and radiation to which the world population are exposed to should be evaluated. However, only for very few indices the applicable design ranges for those parameters are given in the original literature. Therefore, this has not been attempted here. For future index developments, the design range of all input parameters should be clearly defined.

In urban planning a design should result in thermal comfort for the average population. The thermal indices selected in this study assess the average population by considering a reference person (Table 2.3). As a result, however, the individual perception of a specific environment may differ from the assessment calculated by the index. Individual perception depends on the thermal history (Section 2.2.2.5), the expectations of an individual and the interaction with other stressors such as noise or odours. Although important, this multitude of factors currently cannot be taken into account when designing thermal comfortable spaces for the general population. However, with increasing computational power and increased knowledge on human behaviour, new methods for thermal environmental assessment in ORM applications in the context of urban planning may be established. Computational power may favour application of turbulence resolving ORMs, for which a suitable index should be able to consider the unsteadiness of the flow. Furthermore, ensemble simulations for individuals with different personal characteristics and thermal histories could be used to evaluate the environment dynamically, as recommended for outdoor applications by Höppe (2002) and Coccolo et al. (2016). First steps in this direction have been taken by Bruse (2007). In the modelling framework of urban system models all those interactions could be combined to model health-related urban well-being. By extending studies such as by Hoffmann et al. (2018) to realistic cases, ORMs along with the found suitable thermal indices can make up one component in a suite of different multi-sectorial models to model the entire urban system.

3 The Simple Urban Radiation Model (SURM) for estimating mean radiant temperature in idealised street canyons

The suitable thermal indices (Chapter 2) can be used in an ORM application to determine the influence of water surfaces on thermal comfort. However, for the interpretation of the results, the sensitivity of the indices to their input parameters has to be known to differentiate between a non-existing change due to a non-sensitivity of the index and a non-existing change in meteorological parameters. The most important input variable of a thermal index during sunny conditions is the T_{mrt}, which summarises the impact of radiative fluxes in both the shortwave and the longwave spectral range on the human body into one quantity. T_{mrt} is defined as the uniform temperature of a fictive black-body radiation enclosure in which a subject would experience the same net-radiation energy exchange as in the actual more complex radiation environment (Kántor and Unger, 2011; Dai and Schnabel, 2014). During the day T_{mrt} can be about 30 K higher than air temperature, T_a, and even in shaded locations T_{mrt} is higher than T_a by several degrees due to diffuse and reflected solar radiation components. In urban areas, the radiation field – and hence the distribution of T_{mrt} – is very complex due to sun-shading, shortwave absorption and reflection, longwave emission of walls and ground, etc. (Dai and Schnabel, 2014). Consequently, T_{mrt} varies more strongly between shaded and sunny areas within a street canyon than air temperature (Jendritzky et al., 2007). The exact pattern of T_{mrt} within a street canyon is intricate and has been shown to depend on building height, street widths, orientation, etc. (Ali-Toudert and Mayer, 2006; Holst and Mayer, 2011; Dai et al., 2012; Dai and Schnabel, 2013b,a, 2014). To derive the sensitivity of T_{mrt} to those variables and consequently the sensitivity of the thermal indices, a large number of meteorological situations and urban scenarios have to be investigated. To that end a computationally effective model for the radiation modification in the urban environment is required. Therefore, this chapter presents the newly developed Simple Urban Radiation Model (SURM), which is then used in Chapter 4 to derive the sensitivities.

The development of SURM was motivated by existing models for T_{mrt} being either full microscale models (e.g. ENVI-met (Bruse, 1999; Huttner, 2012)), which are computationally demanding, or being designed for realistic urban areas with complex input data and for being not open source so that they cannot be used in an integrated model framework (e.g. SOLWEIG (Lindberg et al., 2008; Lindberg and Grimmond, 2011), RayMan or SkyHelios (Matzarakis et al., 2007, 2010; Matzarakis and Gulyás, 2011)). Additionally, Staiger (2014) showed that parameterisations for shortwave radiation used in RayMan are outdated and therefore should be replaced by newer algorithms for better agreement with observations. Furthermore, SOLWEIG approximates the standing person as a cylinder, which does not fit well to their actual geometry (Vorre et al., 2015). Last but not least, SURM is developed as a preliminary stage for the implementation of person-to-surface and surface-to-surface radiation interaction in MITRAS Chapter 5 to test different algorithms.

SURM uses undisturbed rural radiation fluxes from measurements or from the output of a mesoscale model and modifies those to take into account the effect buildings. These radiation modification routines are realised both in FORTRAN90 and in MATLAB and can therefore be coupled to existing model systems. Furthermore, parameterisations for radiative fluxes based on standard meteorological parameters are included in the MATLAB version of SURM to be able to use the radiation modification routines even if radiative fluxes are not available. The parameterisations are based on VDI (1994); Gierisch (2011); Schlünzen et al. (2012b) and Staiger (2014). The best performing combination of parameterisations for Hamburg, Germany, is evaluated in this chapter. SURM has been applied so far to estimate the heat stress of commuters in combination with a traffic model by Hoffmann et al. (2018) as part of an urban system model.

In this chapter, the scientific background for the calculation of T_{mrt} (Section 3.1.1) is shortly introduced. Then the realisation of the radiation modification scheme by buildings in SURM is described (Section 3.1.2) together with the radiation parameterisations (Section 3.1.3). Validation results for the view factor calculations (Section 3.2.1), for the parameterisations of the radiative fluxes for rural areas (Section 3.2.3) and for the radiation modification effects by buildings (Section 3.2.4) are presented. Section 3.3 provides possible ideas for future developments of the model.

3.1 Model description

3.1.1 Scientific background

The amount of radiation reaching a person is derived by dividing their surroundings into N isothermal surfaces ($i = g$ (ground) or $i = w$ (wall)), each having a surface temperature T_i, an emission coefficient ε_i and an albedo α_i and thus emitting longwave radiation fluxes

(LW_i) and reflecting shortwave radiation fluxes ($SW_{diff,i}$). Additionally, diffuse shortwave and longwave radiation from the sky ($i = s$) has to be considered. The amount of diffuse radiation from i depends on the view factors between the person, p, and i. In general a view factor between two arbitrary surfaces i and j describes the "fraction of uniform diffuse radiation leaving a surface [i with size A_i] that directly reaches another surface [j with size A_j]" (Howell et al., 2016) and is denoted $VF_{i \to j}$ in this thesis:

$$J_{e,i} \cdot A_i \cdot VF_{i \to j} = E_{e,j} \cdot A_j. \tag{3.1}$$

$J_{e,i}$ is the radiosity of surface i, describing the radiant flux leaving A_i per unit area. $E_{e,j}$ the irradiance flux density, and thus the radiant flux received by surface i per unit area of A_j. The view factor $VF_{i \to j}$ depends only on the geometry of the two surfaces – size, distance and orientation towards each other (Howell et al., 2016). The view factors of the two surfaces are linked via the reciprocity theorem (note the change of $VF_{j \to i}$ to $VF_{i \to j}$, Howell et al., 2016)

$$A_j \cdot VF_{j \to i} = A_i \cdot VF_{i \to j}. \tag{3.2}$$

Eq. (3.2) can be applied to Eq. (3.1) to arrive at

$$\begin{gathered} J_{e,i} \cdot A_j \cdot VF_{j \to i} = E_{e,j} \cdot A_j \\ J_{e,i} \cdot VF_{j \to i} = E_{e,j} \end{gathered} \tag{3.3}$$

Hence, the incoming radiant flux at j ($E_{e,j}$) can be calculated from the outgoing flux at i ($J_{e,i}$) and the view factor $VF_{j \to i}$, which thus describes fraction of the total incoming flux at j that originates from i. In this way, the total incoming diffuse longwave flux at the person can be calculated from $E_{e,p} = \sum_{i=1}^{N} VF_{p \to i} \cdot LW_i$.

In addition to the diffuse radiation fluxes, incoming direct shortwave radiation (SW_{dir}) has to be considered. This is done by weighing the incoming radiation by a projection factor (f_p), which adjusts the incoming radiation according to the person's geometry. How much of the diffuse and direct radiative fluxes are actually absorbed by the person depends on the shortwave absorption coefficient (a_k) and the longwave absorption coefficient, which, according to Kirchhoffs law, is equivalent to the emissivity (ε_p) of the person. Therefore, the total radiation flux density (S_{Str}) absorbed by the human body can be described by (Kántor and Unger, 2011):

$$S_{str} = \varepsilon_p \sum_{i=1}^{N} VF_{p \to i} \cdot LW_i + a_k \sum_{i=1}^{N} VF_{p \to i} \cdot SW_{diff,i} + a_k \cdot f_p \cdot SW_{dir} \tag{3.4}$$

According to the definition of T_{mrt}, the radiation flux density (S_{str}) is equal to the absorbed part of the emitted radiant energy, $\sigma \cdot T_{mrt}^4$, of a isothermal black body enclosure ($\varepsilon = 1$) with temperature T_{mrt}:

$$S_{str} = \varepsilon_p \cdot \sigma \cdot T_{mrt}^4 \tag{3.5}$$

which leads to (VDI, 2008)

$$T_{mrt} = \sqrt[4]{\frac{1}{\sigma} \cdot \sum_{i=1}^{n} VF_{p \to i} \cdot \left(LW_i + \frac{a_k}{\varepsilon_p} \cdot SW_{diff,i} \right) + \frac{f_p \cdot a_k \cdot SW_{dir}}{\varepsilon_p \cdot \sigma}}. \tag{3.6}$$

Therefore, buildings affect T_{mrt} due to two different processes. First, the view factors ($VF_{p \to i}$) determine the fraction of emitted longwave and reflected shortwave radiation by the surfaces that reaches the person and, second, they influence SW_{dir} by shading the person from the sun. The following sections describe how this radiation modification effect by buildings is considered in SURM (Section 3.1.2) and how the outgoing radiative fluxes from the surfaces and the sky are parameterised (Section 3.1.3).

3.1.2 Radiation modification by buildings in SURM

The complex building morphology found in cities around the world is simplified in SURM by approximating it as an isolated, infinitely long, symmetric, non-vegetated street canyon of width W, street orientation ω_s and building height H (Figure 3.1). The buildings are assumed to be homogeneous in their radiative properties (e.g. albedo and emissivity), being grey surfaces and therefore reflecting and emitting radiation diffusely (Howell et al., 2016). All surfaces are assumed to have homogeneous but different surface temperatures in lit and shaded areas (Section 3.1.3).

The advantage of such a street canyon lies in the simplification of being able to express relatively large areas on a person by only one view factor ($VF_{p \to i}$). SURM distinguishes between the sky view factor ($VF_{p \to s}$), the ground view factor ($VF_{p \to g}$) and the wall view factor ($VF_{p \to w}$), with view factors for ground and wall divided into lit (lit) and shaded parts (sha).

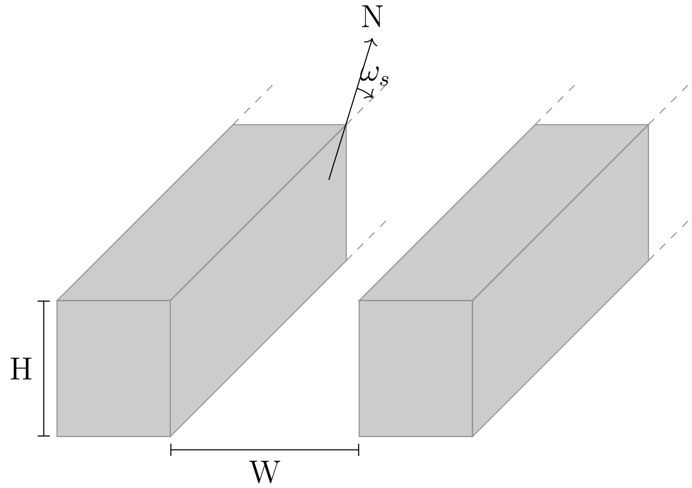

Figure 3.1: Idealised street canyon as used in SURM indicating building height (H), street width (W) and street orientation (ω_s).

In general, the view factors ($VF_{p\to i}$) of a person to a rectangle with edges a and b, which is oriented in such a way that a surface normal (n) of one corner of the rectangle transects a person (Figure 3.2), can be calculated from (Fanger, 1970, p. 164, Gennusa et al., 2008):

$$VF_{p\to i} = \begin{cases} \frac{1}{\pi}\int_{x/y=0}^{x/y=a/c}\int_{z/y=0}^{z/y=b/c} \frac{f_p}{\left[1+\left(\frac{z}{y}\right)^2+\left(\frac{x}{y}\right)^2\right]^{1.5}} d\left(\frac{z}{y}\right) d\left(\frac{x}{y}\right) & \text{for a vertical surface} \\ \frac{1}{\pi}\int_{x/z=0}^{x/z=a/c}\int_{y/z=0}^{y/z=b/c} \frac{f_p}{\left[1+\left(\frac{y}{z}\right)^2+\left(\frac{x}{z}\right)^2\right]^{1.5}} d\left(\frac{y}{z}\right) d\left(\frac{x}{z}\right) & \text{for a horizontal surface} \end{cases} \tag{3.7}$$

with f_p being the surface projection factor of a rotational symmetric standing person, since the orientation of a person within a street canyon is in general not known. f_p can be calculated from (Matzarakis et al., 2010; VDI, 2008; Jendritzky et al., 1990):

$$f_p = 0.308 \cdot \cos\left[\alpha \cdot \left(0.998 - \frac{\alpha^2}{50000}\right)\right]. \tag{3.8}$$

with the elevation angle α depending on the surface type:

$$\alpha = \begin{cases} \arctan\left(\frac{z/y}{\sqrt{(x/y)^2+1}}\right) & \text{for vertical surface} \\ \arctan\left(\frac{1}{\sqrt{(x/z)^2+(y/z)^2}}\right) & \text{for horizontal surface} \end{cases} \tag{3.9}$$

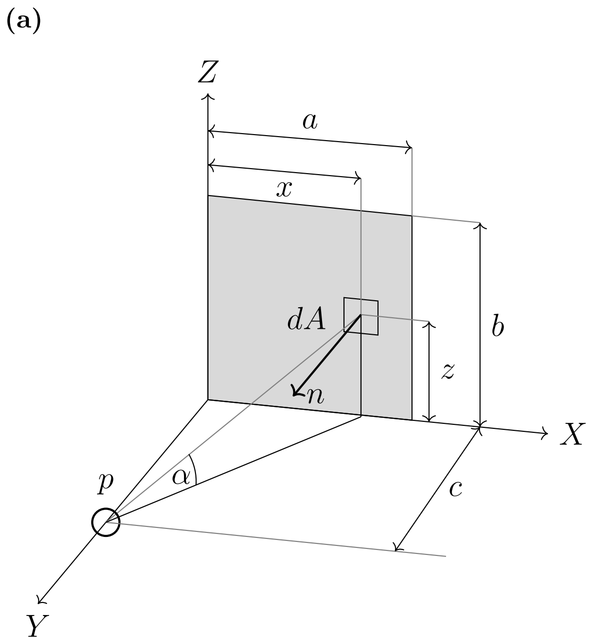

Figure 3.2: Sketch of relevant angles and distances for the view factor calculation of a person p to a surface i ($VF_{p \to i}$) for a vertical rectangle ((a), grey) and a horizontal rectangle ((b), grey) both of size $a \times b$ in distance c to a person p (circle). α indicates the elevation angle needed for the calculation of the surface projection factor (f_p), dA is the surface element located at (x, y, z) and n the a normal vector on that surface element.

Since Eq. (3.7) assumes that the person's centre is located on a normal through a surface's corner point, view factor algebra has to be used in cases where shaded and lit areas do not conform with that requirement. Figure 3.3 shows an exemplary situation for an infinitely long wall of which only the upper half is illuminated by the sun. The view factor of the lit part of the wall ($VF_{p \to w,lit}$) can be estimated from:

$$VF_{p \to w,lit} = 2 \cdot VF_{p \to 1} = 2 \cdot (VF_{p \to 1\&2} - VF_{p \to 2}) \tag{3.10}$$

where the factor 2 is due to a separate estimation of the view factor to the left and to the right of the person. In a similar way, view factors to all lit and shaded areas can be derived.

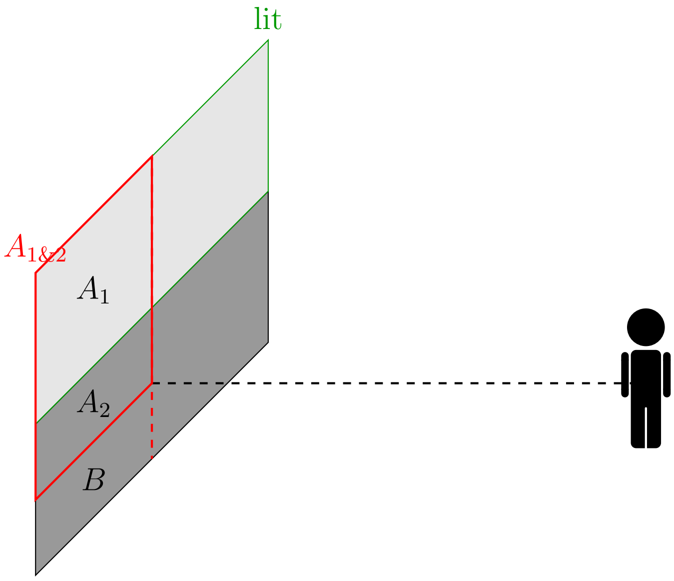

Figure 3.3: Sketch for the view factor calculation of a partly lit wall (light grey).

For the numerical integration of the integral in Eq. (3.7) different possibilities exist in SURM. The most accurate results can be obtained by integrating the equation numerically with very fine grid spacing (method denoted as 'Fanger'). However, since the computational time increases non-linearly with decreased grid spacing, other calculation methods are implemented in SURM: a two-dimensional Simpson method (Vorre et al., 2015, denoted 'Fangerfast') and a fitted polynomial expression (Cannistraro et al., 1992, denoted 'Cannistraro'). The impact of the different integration methods and the grid spacing is evaluated in Section 3.2.1.

With those view factors the absorbed amount of diffuse shortwave and longwave radiation fluxes from all directions can be calculated from Eq. (3.11) and Eq. (3.12). Here w_j with $j \in \{lit, sha, shae\}$ and g_j with $j \in \{lit, sha\}$ denote the differentiated parts of wall and ground surfaces, respectively. $VF_{w_j \to s}$ and $VF_{g_j \to s}$ denote the view factor of the respective surface to the sky to characterise the amount of reflected diffuse radiation from the sky at the surface (Section 3.1.3.3). η_w and η_g denote the angle between the surface normal (of wall and ground, respectively) and sun and is calculated according to Eq. (3.20).

$$\begin{aligned}\frac{a_k}{\varepsilon_p}\cdot\sum_{i=1}^{n} VF_{p\to i}\cdot SW_{diff,i} = \frac{a_k}{\varepsilon_p}\cdot\Big(&VF_{p\to w,lit}\cdot a_w\cdot SW_{dir}\cdot\cos(\eta_w)\\ &+\sum_{j=1}^{3}\Big[VF_{p\to w,j}\cdot VF_{w,j\to s}\cdot a_w\cdot SW_{diff,s}\Big]+VF_{p\to g,lit}\cdot a_g\cdot SW_{dir}\cdot\cos(\eta_g)\\ &+\sum_{j=1}^{2}\Big[VF_{p\to g,j}\cdot VF_{g,j\to s}\cdot a_g\cdot SW_{diff,s}\Big]+VF_{p\to s}\cdot SW_{diff,s}\Big)\end{aligned} \tag{3.11}$$

$$\begin{aligned}\sum_{i=1}^{n} VF_{p\to i}\cdot LW_i = &\sum_{j=1}^{3}\Big[VF_{p\to w,j}\cdot LW_{w,j}\Big]+\sum_{j=1}^{2}\Big[VF_{p\to g,j}\cdot LW_{g,j}\Big]\\ &+VF_{p\to s}\cdot LW_s+\sum_{j=1}^{3}\Big[VF_{p\to w,j}\cdot VF_{w,j\to s}(1-\varepsilon_w)\cdot LW_s\Big]\\ &+\sum_{j=1}^{2}\Big[VF_{p\to g,j}\cdot VF_{g,j\to s}(1-\varepsilon_g)\cdot LW_s\Big]\end{aligned} \tag{3.12}$$

If no buildings exist ($H = 0$), the view factors to the sky ($VF_{p\to s}$) and to the ground ($VF_{p\to g}$) are both set to 0.5 and correspondingly $VF_{p\to w} = 0$. If buildings exist, the lit and shaded fractions of wall ($f_{lit,w}$) and ground ($f_{lit,g}$) surfaces have to be determined to correctly derive the view factors. Those fractions are calculated from

$$f_{lit,w} = \begin{cases}(\tan(\alpha)\cdot x)/H & \text{if } \alpha < H/x \quad \text{(floor is dark)}\\ 1 & \text{else and } x<\infty \quad \text{(wall entirely lit)}\\ 0 & \text{if } x=\infty \quad \text{(sun parallel to canyon)}\end{cases} \tag{3.13}$$

$$f_{lit,g} = \begin{cases}0 & \text{if } \alpha < H/x \quad \text{(floor is dark)}\\ 1-(H\cdot x)/\tan(\alpha) & \text{else and } x<\infty \quad \text{(wall entirely lit)}\\ 1 & \text{if } x=\infty \quad \text{(sun parallel to canyon)}\end{cases} \tag{3.14}$$

with x being the length of the cross section of the canyon in the direction of the sun, where ψ denotes the azimuth angle of the sun (Eq. (3.19)):

$$x = \frac{W}{|\cos(\psi-\omega_s+90^\circ)|} \tag{3.15}$$

Using the absolute value ensures that the lit wall is selected automatically during different times of the day.

Whether a person standing within the street canyon receives direct radiation (relevant for Eq. (3.6)) is calculated by the boolean l_{lit}

$$l_{\text{lit}} = f_{lit,g} \geq 0.5 + (0.5 - x_{\text{rel}}) \cdot \text{sign}(\cos(\psi - \omega_s + 90°)), \tag{3.16}$$

where x_{rel} is the distance of the person's position to the eastern wall relative to the overall street width.

All the above calculations assume northern hemispheric conditions; an application to the southern hemisphere has not been tested.

3.1.3 Radiative flux parameterisations in SURM

The calculation of the radiation modification by buildings (Section 3.1.2) requires radiative fluxes from sky, wall and ground (Eq. (3.6)) as input. If those are not available, either from measurements or from mesoscale model calculations, parameterisations are needed to estimate shortwave and longwave fluxes from standard meteorological parameters such as air temperature (T_a), relative humidity (RH) and wind speed (FF). These are available in SURM. The parameterisations have been mainly taken from the microscale model MITRAS (Gierisch, 2011; Schlünzen et al., 2012b; Salim et al., 2018), the VDI Guideline 3789 (VDI, 1994) and the recommended parameterisations by Staiger (2014). All parameterisations are only valid for clear sky conditions. Those conditions have been selected, because it is then that T_{mrt} is most relevant. However, due to the modular structure of SURM, other parameterisations can be easily incorporated (Section 3.2.4). The validation of the parameterisations are shown in Section 3.2.

3.1.3.1 Shortwave Radiation

Astronomical parameters of solar radiation

The amount of solar radiation at the top of the atmosphere varies during the course of the year: to account for that, the mean solar constant I_∞=1367 W m^{-2} is varied according to an annual cycle (VDI, 1994) to determine the solar constant for a specific time (I_0):

$$I_0 = I_\infty \cdot (1 + 0.03344) \cdot \cos(0.9856 \cdot jd - 2.72)) \tag{3.17}$$

To estimate the fraction of the solar constant received at a given latitude (ϕ), Julian day (jd) and hour (h_t), we need the solar elevation angle (α) or zenith angle (Θ, Eq. (3.18)) and the solar azimuth angle (ψ, Eq. (3.19)):

$$\sin(\alpha) = \sin(\delta) \cdot \sin(\phi) + \cos(\delta) \cdot \cos(\phi) \cdot \cos(\omega) = \cos(\Theta) \tag{3.18}$$

$$\psi = \arccos\left(\cos(\psi)\right) = \arccos\left(\frac{\sin(\alpha) \cdot \sin(\phi) - \sin(\delta)}{\cos(\alpha) \cdot \cos((\phi)}\right) \cdot \text{sign}(\omega) \tag{3.19}$$

where ω is the hour angle of the sun: $\omega = (h_t - 12) \cdot 15$ (VDI, 2001, p.54) and δ is the declination of the Earth. To calculate δ two different options are available in SURM[1]. One (denoted 'vdi3789') is based on VDI (2001), the other is taken from MITRAS (denoted 'MITRAS') (Schlünzen et al., 2012b). Both apply the trigonometric functions on the current Julian day but differ in the used coefficients. Details are given in Appendix D.1.

Direct radiation

Three different parameterisation options for direct shortwave radiation in beam direction are implemented in SURM[2]: 'MITRAS' (Gierisch, 2011, after Bruse, 1999) uses an empirical turbidity coefficient to characterise the amount of shortwave radiation extinct in the atmosphere. In contrast, 'VDI1994' (VDI, 1994) and 'ESRA' (Rigollier et al., 2000; Remund et al., 2003 following Staiger (2014) without accounting for atmospheric refraction) parameterise the extinction by $T_{L,am2}$, the Linke Turbidity factor of relative optical air mass 2. $T_{L,am2}$ is defined as the integral optical thickness of a turbid and wet atmosphere relative to a Rayleigh atmosphere under standard conditions (Kasten, 1996) and combines the effect of Rayleigh and Mie-scattering and absorption of shortwave radiation by molecules and aerosols. The relative optical air mass 2 corresponds to the relative optical air mass at α=30° (Kasten, 1996, details on the relative optical air mass are given in Appendix D.2). 'VDI1994' and 'ESRA' differ in the coefficients used to derive the different parameters for the extinction parameterisation. All options are described in detail in Appendix D.2.

The radiation in beam direction has to be adjusted to derive the amount of radiation received by a surface i taking into account its orientation, characterised by the azimuth angle of the surface (ψ_i), and its inclination, characterised by the zenith angle of the

[1]switch BASIS_DECLIN_CALC

[2]switch BASIS_DIR_RAD

surface (i.e. the inclination of the surface with respect to the horizontal, β_i). This is expressed by an angle η_i between the surface normal and the sun (VDI, 1994, p.16):

$$\cos(\eta_i) = \cos(\beta_i) \cdot \sin(\alpha) + \sin(\beta_i) \cdot \cos(\alpha) \cdot \cos(\psi_i - \psi) \tag{3.20}$$

The zenith angle for vertical walls is $\beta_w = 90°$ and for horizontal ground surfaces $\beta_g = 0°$. The azimuth angle of ground surfaces is equal to the azimuth angle of the sun ($\psi_i = \psi$). The azimuth angle of the walls for the simple geometry of the street canyon used in SURM (Figure 3.1) can be calculated by the following algorithm, which automatically selects the lit wall based on the street orientation (ω_s) at a specific time:

$$\psi_w = \begin{cases} \omega_s + 90° & \text{if } \omega_s - \psi < 0 \\ ((\omega_s - 90° + 180°) \mod 360) - 180 & \text{if } 0 < \omega_s - \psi < 180 \\ ((\omega_s + 90° + 180°) \mod 360) - 180 & \text{if } \omega_s - \psi > 180 \\ \text{NaN} & \text{else, sun parallel to canyon (e.g. } \omega_s = 0) \end{cases} \tag{3.21}$$

The modulo function ensures that the algorithm works for street orientations greater than 360°.

Diffuse radiation

The three parameterisation options ('MITRAS', 'VDI1994' and 'ESRA') for diffuse radiation in SURM[3] correspond to their direct counterparts and are described in detail in Appendix D.3

3.1.3.2 Longwave radiation

Longwave radiation from the sky

For clear sky conditions, longwave radiation from the sky is determined by the amount of water vapour in the atmosphere. As the humidity is largest close to the ground, humidity and temperature at 2 m are used in all three implemented parameterisations[4] ('MITRAS', 'Iso1981' and 'vdi3789') but with different weighting coefficients (Appendix D.4).

[3] switch BASIS_DIFF_RAD
[4] switch BASIS_LW_SKY

Longwave radiation from the ground and wall surfaces

Longwave radiation emitted from ground ($i = g$) and wall ($i = w$) surfaces is calculated from the Stefan-Boltzmann law using the ground and wall surface temperature (T_g and T_w), respectively:

$$LW_i = \varepsilon_i \cdot \sigma \cdot T_i^4 \tag{3.22}$$

The surface temperatures can be determined in two different ways in SURM[5], using either prescribed temperatures or prognostic calculated temperatures in immediate equilibrium of the energy fluxes. Details are given in Appendix D.5.

3.1.3.3 Surface-to-surface view factors

The short and longwave radiation balances at the different surfaces (Appendix D.5) as well as the amount of radiation received by the person (Eq. (3.11) and Eq. (3.12)) require surface-to-surface view factors of lit and shaded parts of the walls. In general, view factors between two surfaces can be derived numerically from Eq. (3.23) (Figure 3.4), since the view factors only depend on geometric properties of the surfaces. This can be calculated according to Howell et al. (2016) by

$$VF_{d1\rightarrow 2} = \frac{\int_{A_2} \cos\theta_1 \cdot (\cos\theta_2 dA_1/S^2) dA_2}{\pi I_1 dA_1} = \int_{A_2} \frac{\cos\theta_1 \cos\theta_2}{\pi S^2} dA_1 \tag{3.23}$$

where A_2 is the area of a finite element, dA_1 is the differential area of a differential element, S is the distance between the surfaces and θ_1 and θ_2 are the respective angles between the surface normal and the line connecting the two differential elements (Figure 3.4).

For simple geometries, however, analytic expressions have been derived, which allow a faster calculation. For the simple geometry of the idealised street canyon (Figure 3.1), such analytic expressions exist. For the calculation of view factors between perpendicular surfaces (e.g. view factors between ground and wall), the equation for two infinitely long plates (1 and 2) of unequal width without a common edge with an included angle α (Eq. (3.24)) is applied. Figure 3.5 shows as an example the view factor between the shaded part of the ground ($W(1 - f_{lit,g})$) and the lit part of the wall $f_{lit,w} \cdot H$ together

[5]switch BASIS_TS

with the corresponding notation of Eq. (3.24).

$$F_{1-2} = \frac{1}{2 \cdot (x_2 - x_1)} \{ (x_1^2 - 2x_1 y_2 \cos\alpha + y_2^2)^{1/2} + (x_2^2 - 2x_2 y_1 \cos\alpha + y_1^2)^{1/2} \\ - (x_2^2 - 2x_2 y_2 \cos\alpha + y_2^2)^{1/2} - (x_1^2 - 2x_1 y_1 \cos\alpha + y_1^2)^{1/2} \} \tag{3.24}$$

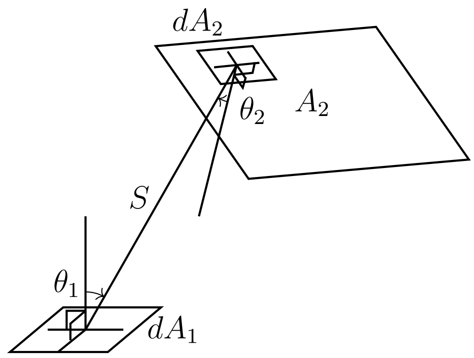

Figure 3.4: Sketch of view factor calculation between a differential element (dA_1) and a finite area (A_2) set apart by S and having orientation θ_1 and θ_2. Figure based on Howell et al. (2016).

Note that for the idealised street canyon, shown in Figure 3.1, $f_{lit,g}$ and $f_{lit,w}$ do not differ from zero or one at the same time, since either part of the wall is lit and the entire street is shaded or parts of the street is lit and the wall shaded (Eq. (3.13) and Eq. (3.14)). Eq. (3.24) can also be applied to other surface-to-surface view factors by permuting W and H and all corresponding fractions. Therefore, most view factors of the idealised street canyon can be calculated with Eq. (3.24) and by use of the summation theorem (Eq. (3.25)), which states that in an enclosure, the fractions of energy leaving one surface and reaching other surfaces of that enclosure must total to one (Howell et al., 2016).

$$VF_{k-1} + VF_{k-2} + VF_{k-3} + \cdots + VF_{k-k} + \cdots + VF_{k-N} = \sum_{j=1}^{N} VF_{k-j} = 1 \tag{3.25}$$

Only for the wall view factor between the entirely shaded wall and the shaded and lit parts of the illuminated wall an additional analytic equation is required (Eq. (3.26)). Figure 3.6 shows as an example the situation of the view factor of the entirely shaded wall to the shaded part of the lit wall. Other wall-to-wall view factors can be calculated analogously by replacing 1 and 2.

$$F_{1-2} = \frac{L_2 + L_3 - L_1 - W}{2 \cdot H_{shawe}} \tag{3.26}$$

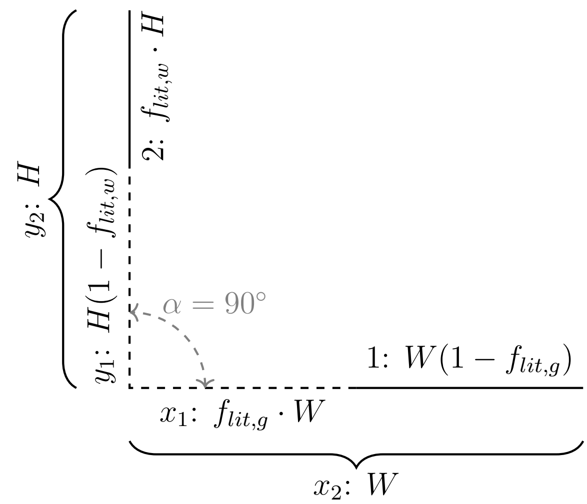

Figure 3.5: View factors for two infinitely long plates (1 and 2) of unequal width ($W(1-f_{lit,g})$) and $f_{lit,w} \cdot H$, respectively) without a common edge with an included angle α (in this case 90°) after C-5a in Howell (2010) using a notation corresponding to sun from the right.

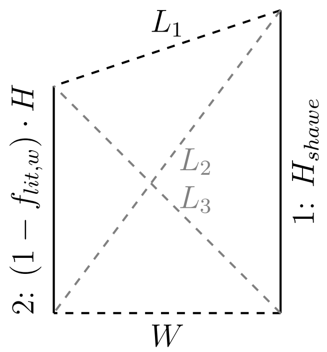

Figure 3.6: View factors for two infinitely long parallel plates 1 and 2 of different width contained in parallel planes after C-2a in Howell (2010).

3.2 Evaluation of SURM

SURM is evaluated with respect to different aspects. In Section 3.2.1 the different calculation methods for person-to-surface view factors ($VF_{p \to i}$) are evaluated. The plausibility tests performed for surface-to-surface view factor and for T_{mrt} calculations are shown in Section 3.2.2. In Section 3.2.3 radiative flux parameterisations are validated for a sub-urban location in Hamburg, Germany (53 °N) (Section 3.2.3) and in Section 3.2.4 the radiation modification routines by buildings are evaluated.

3.2.1 Calculation methods for person-to-surface view factors

In SURM different calculation methods for person-to-surface view factors are available (Section 3.1.2). They differ in complexity but also in their computational costs, ranging from a fitted polynomial expression (method 'Cannistraro'), over a 2-dimensional Simpson method (method 'Fangerfast') to a simple numerical integration of Eq. (3.7) (method 'Fanger'). Figure 3.7 shows the impact of those methods on $VF_{p \to i}$ for surfaces i of different sizes as in Figure 3.2 for a vertical (Figure 3.7a) and a horizontal (Figure 3.7b) surface. The calculated values in general agree with those presented in Fanger (1970), which indicates that the calculation methods have been implemented correctly. Among each other the different calculations methods agree as well, but only up to $a/c = 5$. For higher ratios, 'Cannistraro' (plus and dotted lines) deviates from the other methods, likely because it has been developed only from the ranges displayed in Fanger (1970). Therefore, 'Cannistraro' is not applicable for outdoor conditions with very large ratios of a/c. Hence, 'Cannistraro' should not be used in the current version of SURM, where an infinite long street canyon ($a = \infty$) is assumed (Figure 3.1).

For Figure 3.7 for 'Fanger' and 'Fangerfast' a grid spacing of 0.01 m was used. As indicated by Vorre et al. (2015) for seated persons with specific orientation a grid spacing of 0.05 gives sufficiently accurate results with reasonable computational costs. Figure 3.8 evaluates the difference in $VF_{p \to i}$ for grid spacing of 0.01 m and 0.1 m (stars, very close to zero), 0.01 m and 0.5 m (circles) and 0.01 m and 1 m (triangles) for 'Fangerfast' for both horizontal (solid line) and vertical surfaces (dashed line) with different surface dimensions (colour coded). The impact of a resolution of 0.1 m is small ($< 10^{-6}$) and almost independent of a/c and b/c (not visible in Figure 3.8). A resolution of 0.5 m changes the view factors on average by $< 5 \cdot 10^{-4}$ with slightly higher differences for small b/c. Larger differences of up to $8 \cdot 10^{-3}$ are visible for $\Delta x = 1$ m. The computational costs

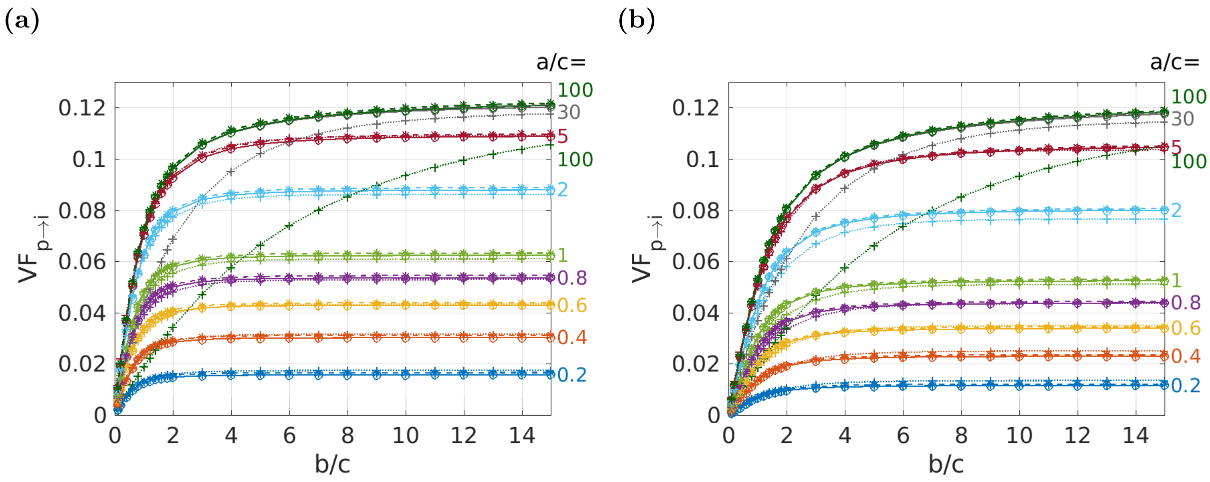

Figure 3.7: $VF_{p \to i}$ calculated with method (Section 3.1.2) 'Fanger' (stars and dashed line), 'Fangerfast' (circles and solid line) and 'Cannistraro' (plus and dotted line) for different wall sizes and distances (as shown in Figure 3.2) for a (a) vertical surface and for (b) a horizontal surface. Note that $a/c = 30$ is almost identical to $a/c = 100$ for 'Fanger' and 'Fangerfast'.

reduce from about 20 s (0.01 m) over 0.30 s (0.1 m) to 0.1 s (0.5 m) and 0.06 s (1 m). Therefore, a grid spacing of 0.5 m reduces the computational costs drastically and is still accurate enough for the application in SURM. A further increase in grid spacing does not significantly improve performance but increases the error. With this grid spacing of $\Delta x = 0.5$ m not all a/c and b/c configurations can be evaluated if the ratio is too small (e.g. $a/c = 2$ m/10 m). In those cases, the necessary grid spacing is calculated from $\min(0.5, \lfloor(x \cdot y)\rfloor/y)$, where $x = a/c$ or $x = b/c$ depending on the integral in question and $y = 10^{-\lfloor(\log_{10}(x))\rfloor}$.

SURM assumes infinite lengths for walls and ground (i.e. $a = \infty$, Figure 3.1). To decide which a/c is sufficient to approximate infinite conditions, Figure 3.9 shows for different a/c (colours) and b/c (abscissa) the difference in $VF_{p \to i}$ to $a/c = 300$ for vertical surfaces (stars) and horizontal surfaces (circles). Vertical and horizontal surfaces are equally influenced by a change in dimensions. By changing from $a/c = 30$ to $a/c = 70$ the differences to $a/c = 300$ are smaller than $5 \cdot 10^{-4}$ for relevant values of b/c and therefore have a similar order of magnitude as a change in grid spacing from 0.01 m to 0.5 m. Therefore, the error is acceptable and thus a is defined by $a = 70 \cdot c$ in SURM, where c is the distance to the closer wall for the person.

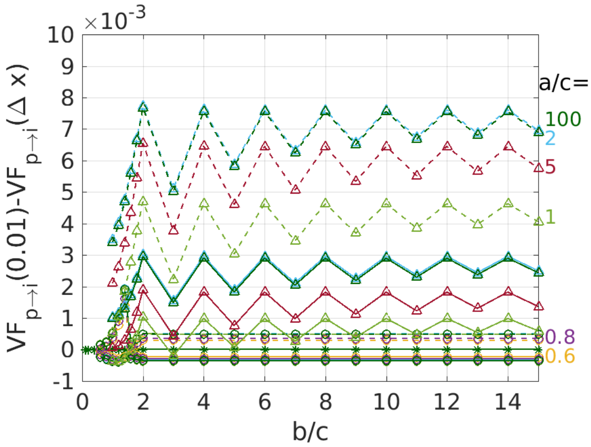

Figure 3.8: Impact of grid spacing (Δx) on $VF_{p\rightarrow i}$ for 0.01 m$-$0.1 m (stars), 0.01 m$-$0.5 m (circles) and 0.01 m $-$ 1 m (triangle) for 'Fangerfast' for vertical (dashed line) and horizontal (solid line) surfaces of different surface dimensions (as shown in Figure 3.2).

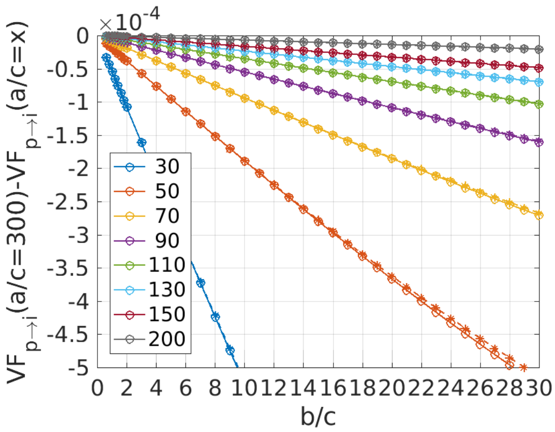

Figure 3.9: Impact of surface size dimensions (as shown in Figure 3.2) on $VF_{p\rightarrow i}$ with Δx = 0.5 m for 'Fangerfast' for vertical (stars and dashed line) and horizontal (circles and solid line) as difference $VF_{p\rightarrow i}(a/c = 300)$-$VF_{p\rightarrow i}(a/c = x$ [colours]).

3.2.2 Plausibility tests for surface-to-surface view factors and T_{mrt}

The simple geometry in SURM (Figure 3.1) allows to validate simulation results not only against measurements (Section 3.2.3) but also against known results for idealised test cases. The surface-to-surface view factors in SURM are calculated from Eq. (3.24) and Eq. (3.26) and the summation theorem (Eq. (3.25)) for the last missing view factor. To ensure that the obtained view factor is correct, it is validated against a view factor calculated from an analytic expression. To ensure that the T_{mrt} calculation works as desired, two plausibility tests are performed for which the results are known. Table 3.1 and Table 3.2 show the results for the set-up of the different test cases, the expected and actual results for the surface-to-surface view factor tests and the T_{mrt} tests, respectively.

Table 3.1: Tests for surface-to-surface view factor ($VF_{j \to i}$) calculation.

	Set-up	Expected result	Result
(1)	$H = 10$, $W = 5$, $f_{lit,g} = 0$, $f_{lit,w} = 0$	$VF_{g-w,sha} \overset{!}{=} 1/2 \cdot (1 + (H/W) - \sqrt{1 + (H/W)^2}) \overset{!}{=} VF_{g-w,shae}$ (Two infinitely long plates of unequal width H and W, having one common edge and having an angle of 90° to each other, Howell et al., 2016)	$VF_{g-w,sha} = 0.382 = VF_{g-w,shae}$
(2)	see (1)	$VF_{w,sha-w,shae} \overset{!}{=} \sqrt{1 + (W/H)^2} - W/H \overset{!}{=} VF_{w,shae-w,sha}$ (two infinite long, directly opposed parallel plates of the same finite width, Howell et al., 2016)	$VF_{w,sha-w,shae} = 0.618 = VF_{w,shae-w,sha}$
(3)	see (1) but with $f_{lit,w} = 1$	$VF_{g-w,lit} \overset{!}{=} 1/2 \cdot (1 + (H/W) - \sqrt{1 + (H/W)^2}) \overset{!}{=} VF_{g-w,shae}$ (see (1))	$VF_{g-w,lit} = 0.382 = VF_{g-w,shae}$
(4)	see (3)	$VF_{w,lit-w,shae} \overset{!}{=} \sqrt{1 + (W/H)^2} - W/H \overset{!}{=} VF_{w,shae-w,lit}$ (see (2))	$VF_{w,lit-w,shae} = 0.618 = VF_{w,shae-w,lit}$

Table 3.2: Plausibility tests for T_{mrt}. LST refers to Local Solar Time.

	Set-up	Expected result	Result
(1)	$H = 0$, 12:00 LST, W and ω_s varying	T_{mrt} does not change with varied W and ω_s	Differences are zero
(2)	$H = 10$, $W = 10$, ω_s varying between 0 and 360	opposite orientations result in same T_{mrt} for $x_{\mathrm{rel}} = 0.5$ for the entire day	T_{mrt} Difference for opposite direction is smaller than 10^{-8}

3.2.3 Validation of the radiative flux parameterisations

The performance of the different shortwave and longwave radiative flux parameterisations is evaluated with five error measures; each of these evaluates a different error type. All errors use a predicted value, denoted by P_i, and an observed value, denoted by O_i, with their corresponding means ($\overline{P}$, $\overline{O}$) and standard deviations (σ_P, σ_O (Schlünzen and Sokhi, 2008). The Standard Deviation of Error ($STDE = \sqrt{\frac{1}{N}\sum_{i=1}^{N}\left[(P_i - \overline{P}) - (O_i - \overline{O})\right]^2}$) evaluates the non-systematic part of the error whereas the average difference ($BIAS = \frac{1}{N}\sum_{i=1}^{N} P_i - O_i$) evaluates the systematic part of the error. The Root Mean Square Error ($RMSE = \sqrt{\frac{1}{N}\sum_{i=1}^{N}(P_i - O_i)^2}$) combines both errors. The correlation coefficient ($r = \left(\frac{1}{N}\sum_{i=1}^{N}\left[(P_i - \overline{P}) - (O_i - \overline{O})\right]\right)/\sigma_P\sigma_O$) evaluates the correct timing of the parameterisation and the hit rate ($HR = \frac{1}{N}\sum_{i=1}^{N} 1$ for $|P_i - O_i| \leq DA$ and 0 else) is used as a measure that is less affected by outliers and considers a absolute desired accuracy, DA, for the different variables (Table 3.3). DA values are taken from the 'observation breakthrough goal for nowcasting' of the World Meteorological Organisation (WMO, 2018) and for T_{mrt} from ISO 7726 (1998) in Staiger (2014). The latter corresponds to the accuracy requirements for class thermal stress (stress) and thermal comfort (comf).

Table 3.3: Desired accuracy (DA) for the hit rate calculation for global radiation (G), longwave radiation from sky (LW_s), ground surface temperature T_g and mean radiant temperature T_{mrt}. For details see text.

	G	LW_s	T_g	T_{mrt} (stress)	T_{mrt} (comf)
DA	10 W m^{-2}	10 W m^{-2}	1 °C	5 °C	2 °C

The simulated radiative fluxes are compared against measurements conducted at the

Hamburg Weathermast operated by the Meteorological Institute, University of Hamburg between 01.04.2004 and 29.02.2016 (`https://wettermast.uni-hamburg.de`). Since currently the parameterisations in SURM are only applicable to clear sky conditions, cloudfree days have been selected for the evaluation. They are defined as days with a cloud cover $N \leq 1$ for all 10 minute average values of one day. In total 160 cloudfree days could be identified covering all seasons. 10 minute averages of air temperature (T_a), relative humidity (RH) and wind (FF) of those days have been used as inputs for SURM along with the station characteristics of the Weathermast (Table 3.4) for which the monthly average $T_{L,am2}$ values have been taken from SoDa Service (2017). SURM is applied for each minute within a 10-minute averaging interval and then averaged to be compared to the 10-minute measurement average. Higher temporal resolution is especially necessary during sunrise and sunset.

Table 3.4: Initial conditions for validating the radiative flux parameterisations in SURM. T_{a2} and RH_2 are air temperature and relative humidity in 2 m, FF_{10} is wind speed in 10 m, $T_{L,am2}$ is the Linke Turbidity factor of relative optical air mass 2, H is the building height, Bo is the Bowen ratio of surface and a_g is the albedo of ground surface. 'meas' indicates measured values are used as inputs.

T_{a2}	RH_2	FF_{10}	Latitude	$T_{L,am2}$	H [m]	Bo	a_g
meas	meas	meas	53 °N	monthly average	0	0.5	0.21

3.2.3.1 Validation of shortwave parameterisations

All available parameterisations for shortwave radiation (Section 3.1.3) are able to reproduce the diurnal cycle of global radiation, G, as indicated by the high value for r (Table 3.5). However, with respect to the other error measures a more diverse picture emerges with large BIASes. Negative BIASes are indicated in Table 3.5 in blue, positive BIASes in red. Darker colours indicate worse performance. The best parameterisation is shown in light green. Only daytime values are used as inputs for the error measures. Overall the combination of the parameterisations 'vdi3789' for declination angle, 'esra' for direct radiation and 'esra' for diffuse radiation performs best, which supports the findings by Staiger (2014) regarding the clear sky model.

Table 3.5: Standard deviation of error (STDE), average difference (BIAS), root mean square error (RMSE), correlation coefficient (r) and hit rate (HR) for global radiation (G) of SURM model compared to measurements for different parameterisations for declination (δ), direct (SW_{dir}) and diffuse shortwave radiation ($SW_{diff,s}$).

δ	SW_{dir}	$SW_{diff,s}$	STDE [W m^{-2}]	BIAS [W m^{-2}]	RMSE [W m^{-2}]	r	HR
vdi3789	esra	esra	39.3	-8.0	40.1	0.99	0.34
vdi3789	esra	MITRAS	43.0	-44.1	61.6	0.99	0.13
vdi3789	esra	vdi1994	39.1	-13.2	41.3	0.99	0.27
vdi3789	MITRAS	esra	43.4	48.4	65.1	0.99	0.13
vdi3789	MITRAS	MITRAS	44.0	27.2	51.7	0.99	0.21
vdi3789	MITRAS	vdi1994	39.4	-9.8	40.6	0.99	0.33
vdi3789	vdi1994	esra	40.4	-9.5	41.5	0.99	0.33
vdi3789	vdi1994	MITRAS	43.2	-46.7	63.6	0.99	0.11
vdi3789	vdi1994	vdi1994	39.1	-13.3	41.3	0.99	0.27
MITRAS	esra	esra	39.7	-8.5	40.6	0.99	0.34
MITRAS	esra	MITRAS	43.3	-44.6	62.2	0.99	0.13
MITRAS	esra	vdi1994	39.5	-13.7	41.8	0.99	0.27
MITRAS	MITRAS	esra	43.8	47.9	64.9	0.99	0.14
MITRAS	MITRAS	MITRAS	44.2	26.7	51.7	0.99	0.21
MITRAS	MITRAS	vdi1994	39.7	-10.3	41.0	0.99	0.32
MITRAS	vdi1994	esra	40.8	-10.0	42.0	0.99	0.33
MITRAS	vdi1994	MITRAS	43.5	-47.2	64.2	0.99	0.11
MITRAS	vdi1994	vdi1994	39.5	-13.8	41.8	0.99	0.27

Although even the best parameterisation option for G still has systematic and non-systematic errors (Table 3.5), the resulting difference in T_{mrt} is small. Figure 3.10 shows the difference between T_{mrt} as derived from the best parameterisations ('vdi3789', 'esra', 'esra') and T_{mrt} with assumed correct simulation of SW_{dir} by SURM and derived diffuse radiation from measurements by $SW_{diff,s} = G_{\text{meas}} - SW_{dir} \cdot \cos(\eta_i)$. The fact that radiation measurements were only available on global scales necessitate this approach. Large deviations at about 15:00 are caused by a shading of the measurement device. The error measures (STDE=1.9 K, BIAS=-0.3 K, RMSE=2 K, r=1 and HR_{stress}=0.98, HR_{comf}=0.83) confirm the visual impression of Figure 3.10 that the resulting difference in T_{mrt} is small. Therefore, the parameterisation yields sufficiently accurate results for the calculation of T_{mrt} under clear sky conditions.

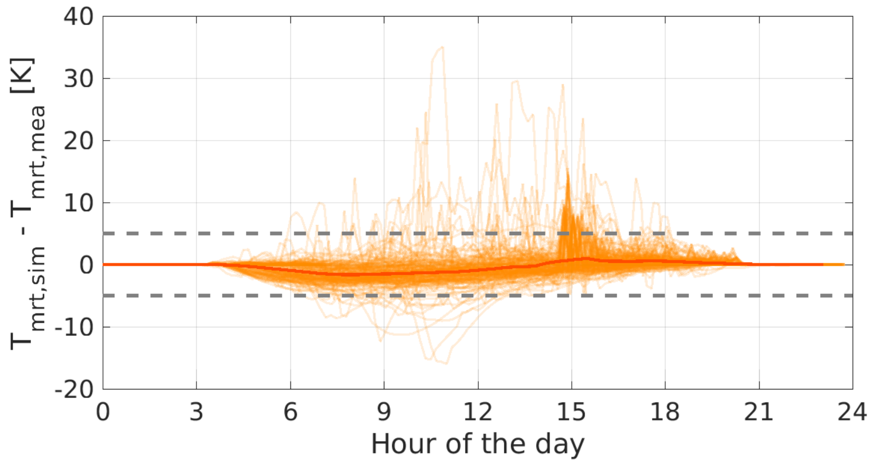

Figure 3.10: Difference of T_{mrt} values calculated from simulated G with SURM and T_{mrt} values calculated from simulated SW_{dir} but derived diffuse radiation from $SW_{diff,s} = G_{\text{meas}} - SW_{dir} \cdot \cos(\eta_i)$ using the best combination of parameterisation (Table 3.5). Dashed lines indicate desired accuracy for stress classes of T_{mrt} (Table 3.3). The thick line indicates a running mean over 10 minutes over all days.

3.2.3.2 Validation of longwave parameterisations

To validate the longwave radiation parameterisation in SURM, the parameterisation settings for the best performing shortwave radiation are used (Section 3.2.3.1) and the parameterisation options for longwave downward radiation from sky (LW_s) and for ground surface temperature (T_g) are varied. Note that for the 'prescribed' option for T_g, air temperatures have been used for both lit and shaded areas as ground temperatures. The parameterisation 'vdi3789' for longwave radiation from sky highly overestimates LW_s (Table 3.6, using same colour coding as described in Section 3.2.3.1) especially during the day, indicating that a parameterisation solely depending on temperature is not sufficient. 'Idso1981' performs better than 'MITRAS' in terms of non-systematic error (STDE) but has a stronger systematic positive BIAS, leading to worse RMSE and HR. Thus, overall 'MITRAS' performs best.

Table 3.6: As Table 3.5 but for longwave radiation from sky (LW_s).

LW_s	STDE [W m^{-2}]	BIAS [W m^{-2}]	[W m^{-2}]	r	HR
MITRAS	14.6	3.1	14.9	0.96	0.57
Idso1981	12.4	12.7	17.7	0.96	0.32
vdi3789	26.2	19.5	32.6	0.92	0.30

The diurnal cycle of $LW_{ssim} - LW_{smea}$ (Figure 3.11) shows that 'MITRAS' is close to the observations during the night and slightly overestimates LW_s during the day.

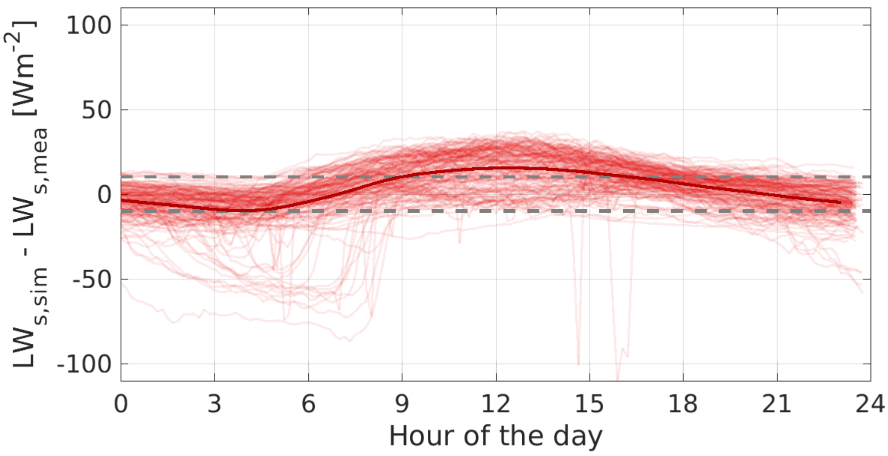

Figure 3.11: Difference in longwave radiation from sky (LW_s) calculated with parameterisation 'MITRAS' compared to measurements. Dashed lines indicate desired accuracy for LW_s (Table 3.3). The thick line indicates running mean over 10 minutes over all days.

In contrast to the longwave radiation from the sky, the longwave radiation from the ground, evaluated in terms of the ground surface temperature T_g, shows larger differences to observations. However, for the comparison one has to take into account that the measured ground surface temperatures refer to equilibrium radiant temperatures, whereas the prognostically calculated ground surface temperatures in SURM refer to temperatures above the viscose sub-layer. Therefore, a difference between observation and simulation results is to be expected. During the night a positive bias between observations and simulated values exist (Figure 3.12). However, during the day prognostically calculated T_g values on average are consistent with observations (Figure 3.12a). Therefore, the prognostic calculation of ground surface temperatures clearly improves the simple and obviously wrong assumption that surfaces temperatures equal air temperatures (Figure 3.12b, option 'prescribed'). Since the deviations from observations for prescribed T_g as air temperatures almost compensate during different times of the day (Figure 3.12b), a small BIAS is calculated. The other error measures indicate worse correspondence to observations (Table 3.7).

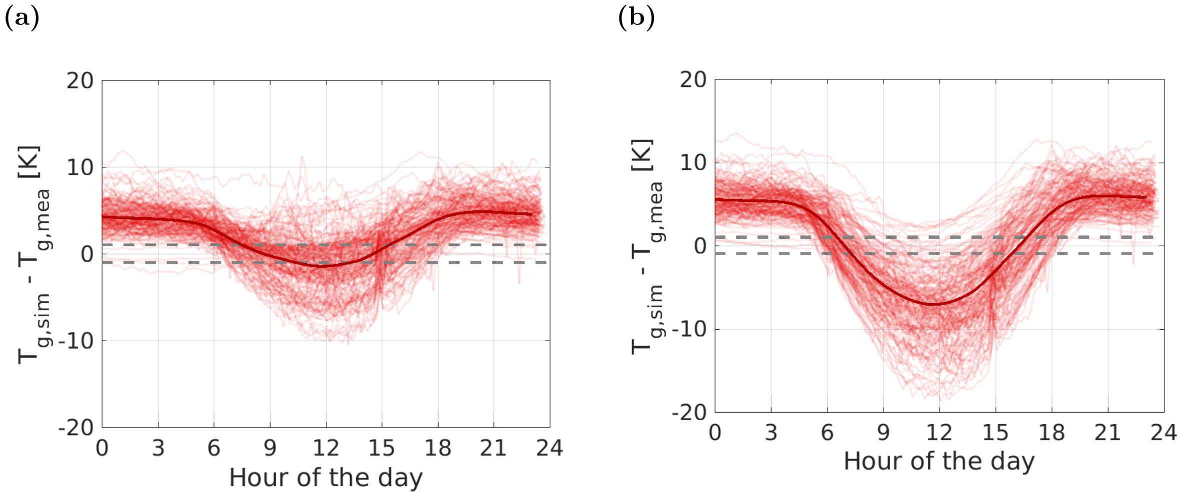

Figure 3.12: Same as Figure 3.11 but for ground surface temperature (T_g) for calculating the ground temperature 'prognostically' (a) and using 'prescribed' values (b).

The differences of LW_s and T_g compared to observations only slightly influence the calculated value of T_{mrt} when the best combination ('MITRAS' for LW_s and 'prognostic' for T_g) is used (STDE=1.8 K, BIAS=-0.2 K, RMSE=1.8 K, r=1 and HR_{stress}=0.98, HR_{comf}=0.78). However, the differences result in an abrupt change in T_{mrt} differences just after sunrise and before sunset (Figure 3.13), which has to be further investigated. The negative BIAS for some simulations during the night is caused by deviations in simulated LW_s from measured ones, likely because some clouds have not been filtered by the

Table 3.7: As Table 3.5 but for ground surface temperature (T_g).

T_g	LW_s	STDE [K]	BIAS [K]	RMSE [K]	r	HR
prognostic	MITRAS	3.2	2.3	4.0	0.98	0.14
prognostic	Idso1981	3.3	2.5	4.1	0.98	0.14
prognostic	vdi3789	3.2	2.5	4.0	0.98	0.14
prescribed	MITRAS	5.8	1.0	5.9	0.92	0.08
prescribed	Idso1981	5.8	1.0	5.9	0.92	0.08
prescribed	vdi3789	5.8	1.0	5.9	0.92	0.08

criterion ($N \leq 1$).

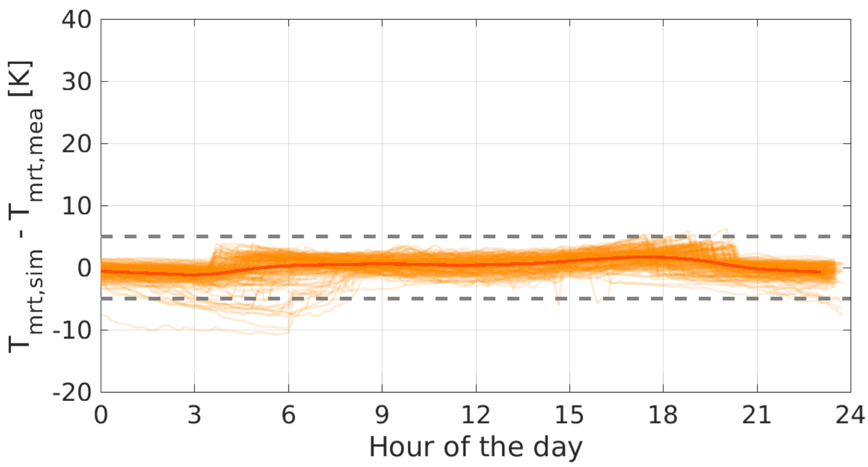

Figure 3.13: As Figure 3.10 but using measured values for ground surface temperature and longwave radiation from the sky.

3.2.3.3 Overall impact of radiation parameterisations on T_{mrt}

The overall impact of calculating T_{mrt} entirely from the parameterisations compared to values for T_{mrt} that are largely based on measured data from a suburban area is shown in Figure 3.14. As described in Section 3.2.3.1 and 3.2.3.2 not all input radiation fluxes for the calculation of T_{mrt} were available as measured data. For the T_{mrt} entirely calculated from parameterisations and for the missing fluxes from observations the overall best parameterisation combination has been used ('vdi3789' for declination angle, 'esra' for direct radiation and 'esra' for diffuse radiation, 'MITRAS' for longwave radiation from the sky and 'prognostic' ground temperatures).

The desired accuracy of ±5 °C for stress classes of T_{mrt} is met for 92 % of the cases and for comfort classes (±2 °C) still for 64 %. Although some systematic and non-systematic errors exist (STDE=2.8 K, BIAS=-0.5 K, RMSE=2.8 K), the diurnal cycle is reproduced well (r=0.99). Some deviations are caused by clouds, which are not filtered by the criterion $N \leq 1$, and by the presence of the measurement mast. In consequence, the overall quality of the parameterisations is considered good and these are therefore used for further investigations in this thesis.

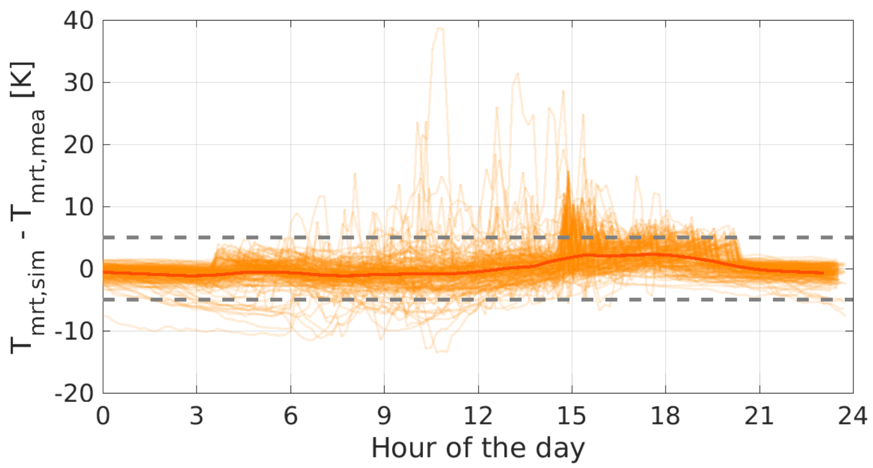

Figure 3.14: As Figure 3.10 but for difference of T_{mrt} from T_g, LW_s and G simulated with SURM and T_{mrt} calculated from corresponding measured fluxes.

3.2.4 Evaluation of the radiation modification by buildings

To validate the radiation modification by buildings as implemented in SURM, the measurement station 'Hafencity' is used, which is located in an urban street canyon in Hamburg (53.5 °N) and is part of the measurement network Hamburg Urban Soil Climate Observatory (HUSCO, Wiesner et al., 2014). The geometric situation at the station consists of a complex mixture of buildings with different heights and urban street trees (Figure 3.15) and is thus much more complex than the idealised canyon used in SURM (Figure 3.1). Since the aim of this validation is not to evaluate whether SURM can represent the situation in every detail but whether it can reproduce the principle timing of shading, the complex situation is transferred in a simplified way to SURM (Figure 3.16).

For the meteorological situation, the same cloudfree days as in Section 3.2.3 are used since no cloud measurements were available at the station. However, since the measurements at

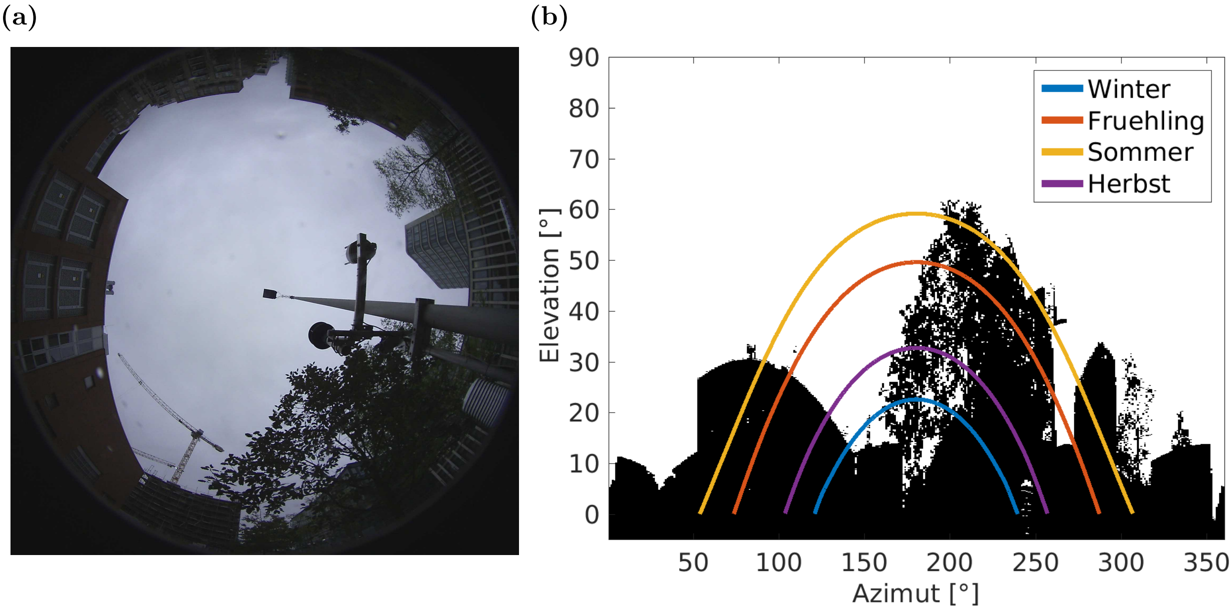

Figure 3.15: (a) Fish-eye photograph of measurement station 'Hafencity' and (b) derived panorama for different azimuth and elevation angles with the theoretical average of global radiation per season. ('Fruehling' is German for spring, 'Sommer' is German for summer, 'Herbst' is German for autumn.) Figures by Corinna Jensen (Jensen, 2017); reprinted with permission.

'Hafencity' started only in June 2014, only three of the determined cloudfree days within the period are available for detailed validation (04.09.2014, 04.10.2014, 02.07.2015). Since all these days fall within the vegetation period, the crown of the tree can be approximated to act as a solid wall. Therefore, only the right part of the street canyon up to the tree in Figure 3.16 was used for the model domain of SURM. Radiative fluxes are calculated using the best parameterisation combination (Section 3.2.3.3).

Figure 3.17 shows the simulation results (dots) compared to measurements (solid) for (a) global radiation and (b) ground surface temperature. Considering the simplifications of the actual street canyon (Figure 3.16), the timing of shading and solar illumination agree well, especially for the July case, when the sun is highest. For the other days, shading around 12:00 LST begins too late in SURM. Changing the orientation of the street canyon to better capture the relative orientation of the crown to the station, yields better results for those days but worse results for the July case (not shown), indicating that shading by lower branches of the tree causes the differences. Peaks in measured global radiation

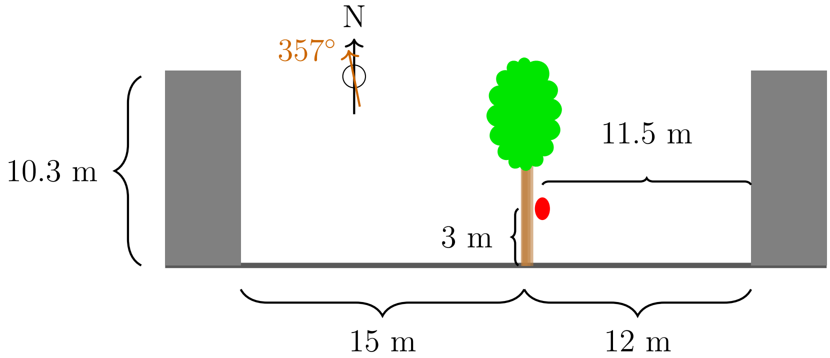

Figure 3.16: Sketch of the measurement station 'Hafencity' used for the urban validation test case for SURM. The red dot indicates the location of the measurement station; the brown arrow the street orientation chosen.

during the afternoon are due to solar radiation penetrating through the tree canopy, which cannot be captured with SURM. When the station is shaded, incoming diffuse radiation is overestimated by SURM (morning and evening). Reducing the Linke turbidity factor, $T_{L,am2}$, leads to smaller errors during those times of the day but worsens the midday results. Coste and Eftimie (2010) found for Brasov (Romania) that $T_{L,am2}$ varies during the day in the city with high values during the morning and smaller ones during the night. Therefore, the monthly climatic $T_{L,am2}$ might have to be adjusted for urban applications or a different parameterisation for direct shortwave radiation, e.g. 'MITRAS', should be used, which yields better results.

The measured ground surface temperature (solid lines in Figure 3.17b) differs from measured air temperature (dashed lines). This deviation is generally well captured in SURM (dots), although the actual values are overestimated during midday. If the Bowen ratio is reduced better agreements between measured and simulated T_g can be achieved (not shown). Therefore, the local conditions at the measurement station should be taken into account when SURM is applied. Slight deviations in timing might be due to ground temperatures being measured with an infra-red remote temperature sensor (Wiesner et al., 2014), which measures ground temperature over a larger area and not directly below the station. In contrast, for simulated values of T_g in Figure 3.17b the values in shade have been used if the station is shaded and vice versa when the station is lit.

The high correlation coefficients (Table 3.8) confirm that the timing is quite well captured in SURM both for G and T_g. Large errors for G can be explained by slight offsets in timing of shading and illuminating due to the simplifications made for the street canyon.

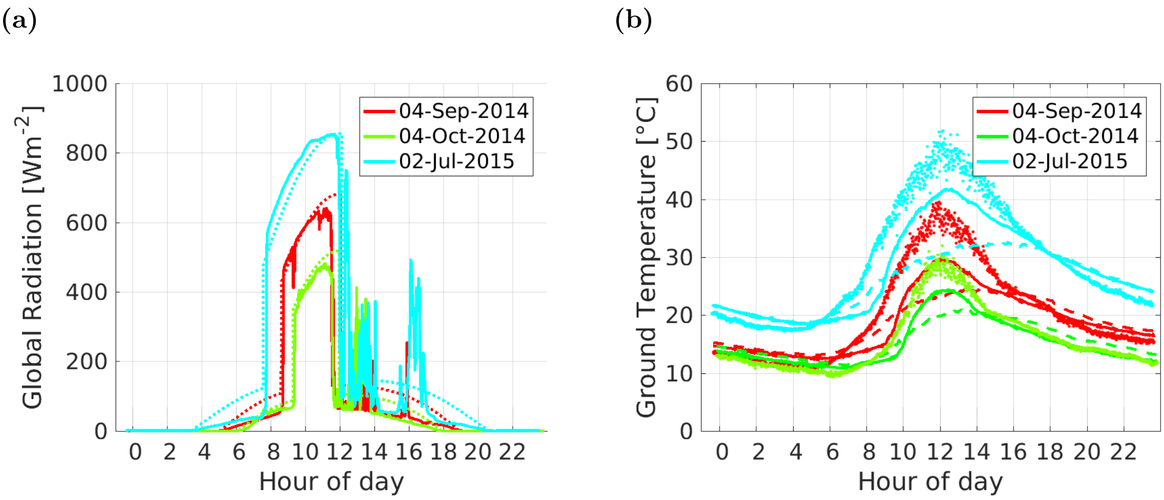

Figure 3.17: Comparison of (a) global radiation and (b) ground temperature simulated by SURM and measured at 'Hafencity' for three cloudfree days. Solid lines indicate measured values; dotted lines indicate simulated values. Dashed lines in (b) show measured air temperature.

Therefore, in general the radiation modification routines work as desired.

Table 3.8: As Table 3.5 but for global radiation (G) and ground surface temperature (T_g) for an urban street canyon. Hit rates include both day and night times.

Variables	STDE	BIAS	RMSE	r	HR
G	85.9 $\mathrm{W\,m^{-2}}$	17.6 $\mathrm{W\,m^{-2}}$	87.7 $\mathrm{W\,m^{-2}}$	0.92	0.48
T_g	3.1 K	1.3 K	3.3 K	0.96	0.33

3.3 Conclusions and prospects for future developments

In this chapter, the open source model SURM for calculating T_{mrt} in idealised urban street canyons is presented. SURM will be made open source and has a modular structure, making it easy to be extended or adjusted to specific needs; some examples are given in the following. For more complex urban environments, the view factor calculation between the person and walls and ground could be generalised to non-parallelepiped environments (Gennusa et al., 2008) or sedentary persons (e.g. in an restaurant, Rizzo et al., 1991). SURM currently focuses on clear sky conditions when both the radiation modification by buildings on T_{mrt} is most important and heat stress is largest. For cloudy conditions a modification by clouds may be taken into account for instance by using the algorithm developed by Reindl et al. (1990) together with the clearness index as suggested by Staiger (2014). Additionally, the anisotropic part of diffuse radiation could be included in the future (Staiger, 2014). A quite simple method for the prognostic calculation of wall and ground temperatures has been implemented in SURM. As Lee et al. (2016) pointed out, in urban areas this method could be improved whereas the parameterisation provides sufficient accuracy for the calculation of T_{mrt} at least in rural areas (Staiger, 2014). To account for the effect of heat storage, a simple force-restore approach (Deardorff, 1978) could be used. For wall temperatures the method discussed in Salim et al. (2018) could be applied. Multiple reflections could be included using the Gebhart factor (Saneinejad et al., 2014). For finite street canyons, the surface-to-surface view factors can be adjusted using the expressions cited in Howell (2010).

For this thesis the current development state of SURM is sufficient, since it focuses on clear sky conditions and more complex urban situations will be investigated with a full microscale ORM. The model development of SURM was used to identify relevant processes for radiation exchange in the urban environment and hence to aid the model development of the ORM.

4 Sensitivities of selected thermal indices in urban environments

4.1 Introduction

In Chapter 2 thermal indices have been identified that can be used to assess the thermal environment in ORMs simulation results. To appraise how accurate this assessment is, the sensitivity of the thermal index to its input variables has to be known: if an index is very sensitive to an input variable, but this variable is not precisely known, the overall thermal assessment is relatively inaccurate. Or, to put it the other way round, all processes that determine the input variable to which the index is sensitive to, have to be accurately represented in the ORM to calculate the thermal index with a specific accuracy. Those thereby identified important input variables and processes are consequently effective ways to develop thermal comfortable designs, as a small change on this variables provides a large change in the human thermal environment. Last but not least, the sensitivities aid the interpretation of the ORM simulation results, since a non-existing change of thermal conditions can be distinguished from a non-existing change of the thermal index due to its insensitivity to that changed input. Considering these beneficial aspects of knowing the sensitivities of the thermal indices, this chapter addresses RQ 2 "How sensitive are selected thermal indices to their input variables?".

The identified suitable thermal indices (PET, PT_J, UTCI and PST) all use as input variables air temperature (T_a), vapour pressure (e), wind speed (FF) and radiation, mostly in form of mean radiant temperature (T_{mrt}). For PET, PT_J and UTCI, the sensitivities to those variables have been determined for a certain range of meteorological conditions (e.g. Fröhlich and Matzarakis, 2015; Provençal et al., 2015) but the consequential accuracy requirements of the input variables has not been investigated. Furthermore, in an urban environment, the meteorological variables are influenced by the three-dimensional structure of buildings and the used construction materials (Section 2.2.2). Therefore, if the thermal indices are applied to assess the thermal environment in an urban area, additional influencing variables have to be considered. Those built-environment-related variables, such as building height (H), street width (W), orientation (ω_s) and albedo and emissivity of wall and ground surfaces (a, ε), can change the achievable accuracy of the thermal indices, if they are poorly known. Schoetter et al. (2013) considered those variables to analyse the required input accuracy for the thermal index PT_J when using a non-obstacle resolving mesoscale model for summer conditions in Hamburg. However, on the microscale, for other seasons and other thermal indices the accuracy requirements might differ. Since PT_J is only seldom applied for microcscale studies (Figure 2.4), the frequently applied Physiological Equivalent Temperature (PET) and Universal Thermal Climate Index (UTCI) are selected in the present study. Those two indices differ in several ways (e.g. complexity of the thermal-physiological model, reference conditions; Table 2.3) and thus are likely differently sensitive to their inputs. Furthermore, personal characteristics such as age (A), gender (gn), height (h_p), weight (m), work metabolism (M_w) and clothing insulation (I_{clo}), are known to affect the thermo-physiological processes within the body (e.g. ASHRAE, 2001; Schellen et al., 2010; Wölki and van Treek, 2013; Rida et al., 2014). Since for PET these characteristics of the reference person can be modified, within the present analysis the sensitivity of PET to those personal variables is also derived.

To determine the sensitivities of the thermal indices to the meteorological, to the built-environment-related and to the personal variables, four different sensitivity analysis methods are applied in order to get reliable results (Section 4.2). The influence of the built-environment-related variables on T_{mrt} are considered by applying SURM (Chapter 3). The sensitivities are derived separately for summer and winter conditions in Hamburg to best consider the range each meteorological variable takes. The results of this analysis is presented in Section 4.3. The robustness and generality of the results are discussed along with required input accuracies and possible implications for thermal comfortable design and ORM development in Section 4.4.

4.2 Used thermal indices and sensitivity analysis methods

4.2.1 Thermal indices investigated

The sensitivities of two thermal indices are derived in the present analysis, the Universal Thermal Climate Index (UTCI, Bröde et al., 2012) and the Physiological Equivalent Temperature (PET, Höppe, 1999). UTCI is based on the recently developed thermo-physiological model UTCI-Fiala (Table 2.3), which represents the thermo-regulatory processes within the body by multiple elements. In contrast, PET is based on a simple two-node thermo-physiological model (MEMI), which approximates the thermo-regulatory processes within the body by exchanges between only two elements – the body core and the skin. Both indices use a reference environment for their derivation: the value of the thermal index is equal to the temperature of a clearly defined reference environment, in which a reference person experiences the same thermal strain as in the actual environment (Chapter 2.2.1, Table 2.3). PET uses same skin and core temperature in both environments as a measure of thermal strain, whereas UTCI uses a combination of seven different body-related variables (Bröde et al., 2012).

For the UTCI-Fiala model the source code is not openly available. Instead two official approximation calculations have been made available: a polynomial regression and a look-up table (Bröde et al., 2012). In the present analysis the regression version is used, since it is commonly applied in the investigated ORM applications (Section 2.3.2). For the calculation of PET at least two different algorithms are used in the reviewed literature (Table C.1). First an algorithm, which is based on MEMI and was published by VDI (2008). This version with small changes by Holst and Mayer (2011) was provided for this analysis by Holst (2016, personal communications) and is termed PET as VDI version ($\mathrm{PET_{vdi}}$) within this thesis. The other version is included in the Bio-met module of ENVI-met ($\mathrm{PET_{env}}$) and is based on the instationary version of MEMI (Instationary Munich Energy balance Model, IMEM). Due to the in-stationarity, the equilibrium temperature in IMEM has to be derived iteratively. For that the numerical method Regular-Falsi is used. Additionally, in contrast to $\mathrm{PET_{vdi}}$, heat losses by transpiration and diffusion are recalculated for the reference environment using the reference humidity and the air velocity in $\mathrm{PET_{env}}$ (enviadmin, 2017). This version was provided by Bruse (2016, personal communications) as Pascal source code and was transferred to Fortran for the analyses within this thesis. The two versions are compared in Section 4.3.1. The sensitivity of both PET versions is investigated with the edge-based analysis method (Section 4.2.2.1). For the full-space analysis method (Section 4.2.2.2) only $\mathrm{PET_{vdi}}$ is used, since it is the published version, is much less computationally demanding and is, based on the current knowledge, likely confirmed as a standard in an updated version of VDI (2008).

The availability of the source codes for PET enables to derive not only the sensitivities of PET to the meteorological and built-environment related input variables but also to the used characteristics of the reference person. Since PET is defined officially for a specific set of personal characteristics of the reference person, Physiological Equivalent Temperature with changed personal parameters (PET^*) is used in the following to denote PET values that are calculated with personal characteristics deviating from the standard set (Table 2.3).

4.2.2 Sensitivity analysis

Sensitivity analysis in general refers to attribution of variation in model output to its input variables (Pianosi et al., 2016). This is done typically by calculating sensitivity indices (S_i), which measure the importance of a specific input variable i (Pianosi et al., 2016). The sensitivity indices can be derived by different methods, which can be roughly categorised into local and global methods (see Frey and Sumeet, 2002; Iooss and Lemaître, 2015; Norton, 2015; Song et al., 2015; Borgonovo and Plischke, 2016; Pianosi et al., 2016 for reviews on possible methods). Local methods explore the sensitivity of the model to small variations around reference points, whereas global methods consider variation within the entire input range of the variable. Thus, global methods have, compared to local methods, the advantage that the derived sensitivity indices refer to the entire input space, whereas the validity of the sensitivity indices from a local analysis can only be assumed to refer to the entire input space if the model is known to be linear and additive (Saltelli and Annoni, 2010; Norton, 2015; Pianosi et al., 2016). Since the thermo-physiological modes of PET and UTCI are not linear and additive, in the present analysis different global methods are applied.

Due to the complexity of the thermo-physiological models, the sensitivity indices cannot be derived analytically. Instead, they are numerically approximated by calculating the thermal indices for a set of sampled input conditions. Different sampling strategies exist that can be categorised in One-At-a-Time (OAT) input variable variation, for which one input variable is varied while all other variables are kept fixed, and All-At-a-Time (AAT) input variable variation, for which all input variables are varied at the same time (Pianosi et al., 2016). Due to the simultaneous variation of all input variables in AAT methods, not only the direct influence of one variable on the output variable (referred to as the main effect in the following) can be derived but also the influence of one input variable on the output due to interactions with other variables (i.e. second order effects for the interactions of two variables). AAT methods have the drawback that a large number of model calculations are needed to derive those indices. Consequently, in the present analysis an One-At-a-Time (OAT)-based method is applied to get an impression of the sensitivities for the thermal indices (Section 4.2.2.1), followed by an AAT-method (Section 4.2.2.2).

In the first analysis method (Section 4.2.2.1) the entire input range of each variable is reduced its extreme values. By using those minimum and maximum values for each input variable i, an m-dimensional hyper-cuboid is generated that contains all possible combinations of input variables, where m refers to the number of input variables. Figure 4.1 shows a 3-dimensional cuboid as an example. The thermal indices are calculated for corner points of the hyper-cuboid (dots) as well as for variation of one variable along the edge of the hyper-cuboid, while the other variables are kept fixed at their values of one corner point. Therefore, both approaches reduce the entirely possible input space within the hyper-cuboid to its edges. Consequently, in this chapter this analysis method is referred to as "edge-based method".

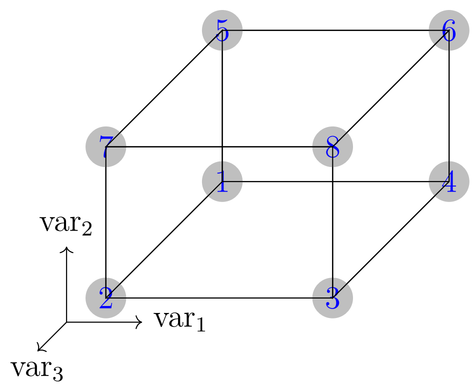

Figure 4.1: Visualisation of a 3-dimensional hyper-cuboid.

By reducing the entire possible input space of the different variables to the edges of the hyper-cuboid in the edge-based method, the input space is in principal fully covered. However, only the extreme situations are explicitly calculated. Furthermore, these extreme situations might not even occur in reality, if for instance the actually occurring situations form an ellipsoid. To overcome these limitations, in the second analysis method the input space is sampled based on the probability density function (PDF) of each variable (Section 4.2.2.2). Since this method can better represent the actually occurring conditions and thus explores the input space more thoroughly, this method is referred as "full-space method" in this chapter. How sensitivity indices can be derived from the two methods is described in detail in Section 4.2.2.1 and Section 4.2.2.2, respectively.

4.2.2.1 Edge-based analysis method

From the edge-based method, for which situations along the edges of the hypercube are calculated, sensitivity indices can be derived in two ways. The first method only uses the corner points of the hyper-cuboid. This complies to a two-level (i.e. minimum and maximum value) factorial design method (Saltelli and Annoni, 2010) and therefore sensitivity indices calculated with this method are denoted by f. For this method the main effect sensitivity index (S_{if}), i.e. the direct contribution from an individual input variable to the model output variability, can be derived by subtracting the expected value (E) of I_t for all situations with minimum x_i ($x_i = \min(x_i)$) from all situations with maximum x_i ($x_i = \max(x_i)$) (Saltelli and Annoni, 2010):

$$S_{if} = \frac{E(I_t|x_i = \max(x_i)) - E(I_t|x_i = \min(x_i))}{\Delta I_t} \tag{4.1}$$

The intermediate samples along each axis of the hyper-cuboid (Figure 4.1) can be used to calculate the sensitivity indices from a fitted linear regression:

$$I_t|_{x_{\sim i}=\text{const}} = a_i + s_i \cdot x_i + R_i \tag{4.2}$$

where $x_{\sim i}$ refers to all other variables except i, which are held constant at one of the corner-point values, and R_i refers to a minimised residuum. The linear regression coefficient in Eq. (4.2) corresponds to a non-standardised sensitivity index (s_i) (Pianosi et al., 2016), since it represents how much I_t changes with x_i. To be able to compare the sensitivities for inputs with different units, the sensitivity indices of the regression analysis are standardised to obtain the main sensitivity indices from the regression method (index r, S_{ir}). For the standardisation the varied ranges ($\Delta x_i := \max(x_i) - \min(x_i)$) and the calculated variation of the thermal index for all situations ($\Delta I_t := \max(I_t) - \min(I_t)$) are used:

$$S_{ir} = s_i \frac{\Delta x_i}{\Delta I_t} \tag{4.3}$$

Since S_{ir} can be derived for each corner point value of $x_{\sim i}$, the importance of non-linear effects can be inferred: if S_{ir} is the same for all values of $x_{\sim i}$, no non-linear effects with other variables exist.

To derive S_{if} and S_{ir} for the meteorological and personal variables, two separate m-dimensional hyper-cuboids are constructed. The meteorological 4-dimensional hyper-cuboid consists of the variables air temperature, relative humidity, wind speed and mean radiant temperature ($i \in \{T_a, RH, FF_{10}, T_{mrt}\}$); the personal 5-dimensional hyper-cuboid consists of the personal variables age, height, weight, work metabolism and clothing insulation of the reference person in PET ($i \in \{A, h_p, m, M_w, I_{clo}\}$). The derivation of the corner points for the two hyper-cuboids are described in the following.

a) Meteorological hyper-cuboid

To derive the limits of the meteorological 4-dimensional hyper-cuboid consisting of $i \in \{T_a, RH, FF_{10}, T_{mrt}\}$, the climatological limits of the variables are derived for Hamburg, Germany, from measurements for summer (June, July, August) and winter (December, January, February) between 01.01.1950 and 31.12.2015 (Table 4.1). Since T_{mrt} cannot be directly measured, it has to be derived from other measured quantities. For the present analysis T_{mrt} is derived from hourly measured air temperature, wind, humidity and cloudiness together with the Linke turbidity factor using the program by Staiger (2016, personal communication). This program uses for cloudless conditions the same parameterisations as SURM (Section 3.1.3.1) except for applying changed coefficients according to Remund et al. (2003). However, it also can consider the effects of clouds by a cloud modification factor (Kasten, 1983 and Reindl et al., 1990). Downward longwave radiation is modelled according to Konzelmann et al. (1994) with adjusted coefficients (Marty and Philipona, 2000). Upward longwave radiation is parameterised with the same method as in SURM (Eq. (D.18)).

Table 4.1: Used observations at Fuhlsbüttel, Hamburg (location is shown in Figure M.2) operated by the German Meteorological Service (DWD).

Variable	Period	Height [m]
Air Temperature (T_a)	01.01.1949 – 31.12.2015	2.0
Relative humidity (RH)	01.01.1949 – 31.12.2015	2.0
Wind speed (FF)	01.01.1950 – 10.07.1968	14.7
	11.07.1968 – 31.12.2015	10.0
Cloud fraction (N) estimated from a meteorological observer	01.01.1949 – 31.12.2015	not applicable

Figure 4.2 shows combinations of measured T_a, RH, FF_{10} and T_{mrt} within the measurement period for different seasons (colours). The solid boxes indicate the limits used for the meteorological hyper-cuboid. The limits for relative humidity and wind speed deviate from the climatological extremes, since the UTCI regression calculation restricts the input variable space to $e < 50$ hPa and $0.5 \leq FF_{10} \leq 17\ \mathrm{m\,s^{-1}}$ (Bröde et al., 2012; ISB Comission 6, 2012). In order to make the results for PET and UTCI comparable, the input space is restricted accordingly for both indices. However, since summer and winter conditions are analysed separately, some excluded humidity conditions for summer are covered by the range for winter (Figure 4.2).

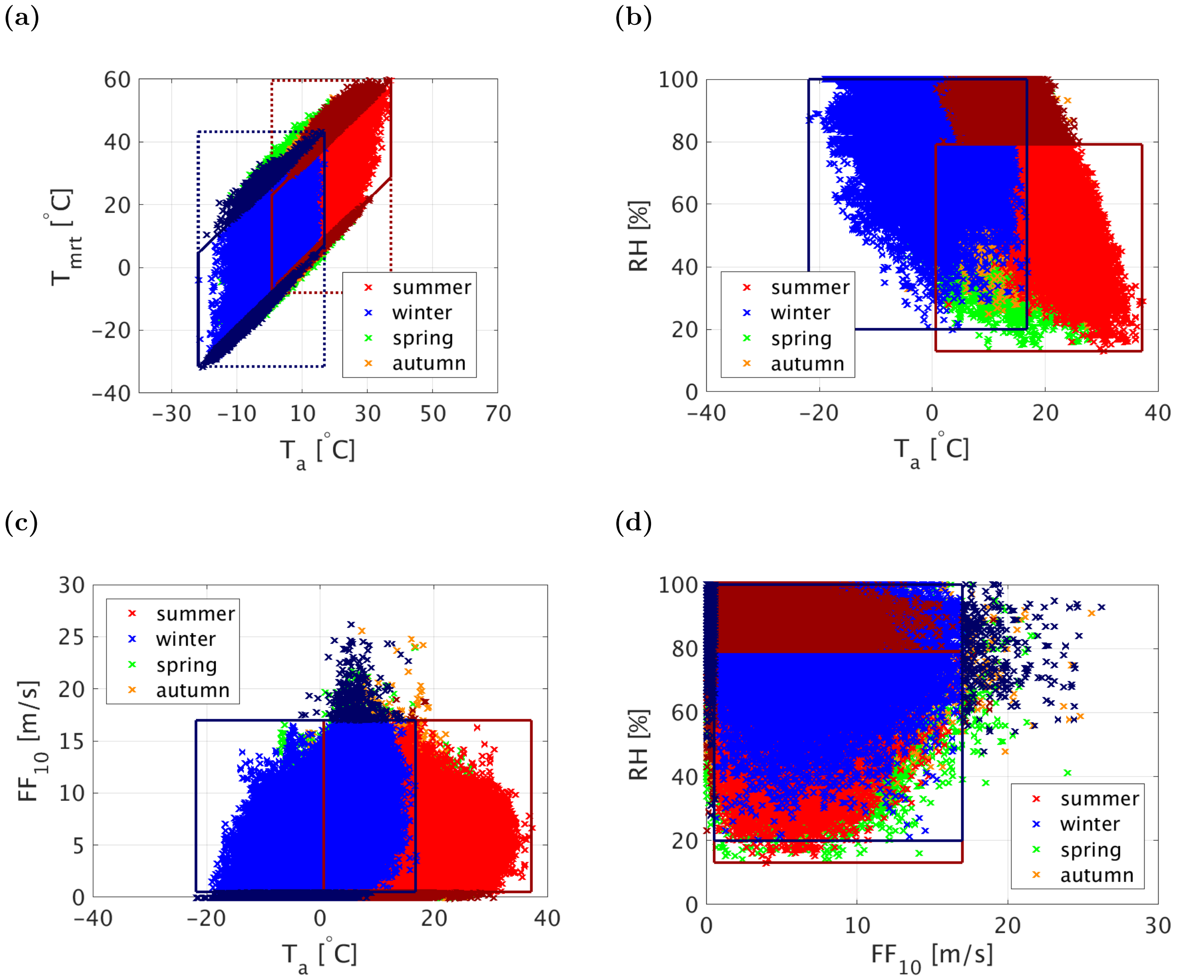

Figure 4.2: Observed hourly values for combination of (a), (b), (c) mean radiant temperature (T_{mrt}), relative humidity (RH), wind speed at 10 m height (FF_{10}) and air temperature (T_a) and (d) FF_{10} and RH. The colours denote different seasons.

Figure 4.2a shows that T_a and T_{mrt} are closely linked. Therefore, if the climatological limits would be used for the edge-based analysis (dotted lines in Figure 4.2a) very non-physically and unrealistically combinations would be included in the hyper-cuboid, e.g. $T_{mrt} = -32$ °C but $T_a = 16.8$ °C. To avoid that, T_a and T_{mrt} are not treated as independent dimensions of the hyper-cuboid but as linked ones (solid parallelogram in Figure 4.2a). Consequently, the range of T_{mrt} values differs for different values of T_a. For instance for winter the corner points of the hyper-cuboid for the T_{mrt} dimension are not -32 °C and +42 °C but -32 °C and +5 °C for minimum T_a and 7 °C and 43 °C for maximum T_a.

Formally the new hyper-cuboid, which accounts for this relationship, can be expressed by a change of bases from the base of the original hyper-cuboid

$$\vec{e}_{T_a} = (1,0,0,0); \quad \vec{e}_{RH} = (0,1,0,0); \quad \vec{e}_{FF_{10}} = (0,0,1,0); \quad \vec{e}_{T_{mrt}} = (0,0,0,1) \tag{4.4}$$

to a new base

$$\vec{e}_{T_{mrt} \text{ and } T_a} = (1,0,0,1); \; \vec{e}_{RH} = (0,1,0,0); \; \vec{e}_{FF_{10}} = (0,0,1,0); \; \vec{e}_{T_{mrt}} = (0,0,0,1). \tag{4.5}$$

As a consequence of this change of bases, one dimension of the hyper-cuboid now consists of a simultaneous variation of T_{mrt} and T_a by the same coefficient (indicated by $\vec{e}_{T_{mrt} \text{ and } T_a} = (1,0,0,1)$ in Eq. (4.5)) and the other $T_{mrt} - T_a$-related dimension of a temperature dependent variation of T_{mrt}. For T_a and RH a similar method could have been applied to take into account that air at a specific temperature has a certain limiting saturation vapour pressure. However, to facilitate interpretation of the results only the most prominent relationship of T_a and T_{mrt} is taken into account. In the full-space sensitivity analysis method, vapour pressure is used instead of RH as a more independent humidity variable (Section 4.2.2.2).

The used limits for the meteorological hyper-cuboid are summarised in Table 4.2. Each variable is varied for the regression method (Eq. (4.2)) by 11 steps between its extreme values. Since PET assumes that the input values refer to values in body height FF_{10} is convert to 1 m values assuming a logarithmic wind profile over grass. Measured temperature and humidity in 2 m are assumed to be equal to those in 1 m and are thus used directly for the calculation of UTCI and PET.

Table 4.2: Limits of the hyper-cuboid for the different variables. T_a is the air temperature, RH is the relative humidity, FF_{10} is the wind speed at 10 m and T_{mrt} is the mean radiant temperature. T_{mrt} is varied depending on T_a (see text).

	Summer		Winter	
	Min	Max	Min	Max
T_a [°C]	0.60	37.20	-21.90	16.80
RH [%]	13.00	79.10	20.00	100.00
FF_{10} [m/s]	0.50	17.00	0.50	17.00
T_{mrt} [°C]	$T_a - 8.60$	$T_a + 22.40$	$T_a - 9.72$	$T_a + 26.48$

From the described meteorological hyper-cuboid, the non-standardised sensitivity indices, s_i, of $i \in \{T_{mrt} \text{ and } T_a, RH, FF_{10}, T_{mrt}\}$ are derived from Eq. (4.2). As T_a is never varied separately due to the base change (Eq. (4.5)), s_{T_a} cannot be derived directly. Instead, s_{T_a} has to be derived from $s_{T_{mrt}}$ and $s_{T_{mrt} \text{ and } T_a}$ by

$$s_{T_a} = s_{T_{mrt} \text{ and } T_a} - s_{T_{mrt}}. \tag{4.6}$$

Eq. (4.6) was derived in the following way: The regression of Eq. (4.2) defines an affine (i.e. a linear map with a constant a) map $I_t'(\vec{x}) := \vec{s} \cdot \vec{x} + a$ that approximates I_t, where $\vec{s}$ is the vector of the non-standardised sensitivity indices s_i and $\vec{x}$ is the vector of the meteorological variables x_i. I_t' can be transferred to a linear map by subtracting a: $I_t'' := I_t' - a = \vec{s} \cdot \vec{x}$. Using the calculated sensitivity indices $I_t''(\vec{e}_{T_{mrt} \text{ and } T_a}) = s_{T_{mrt} \text{ and } T_a}$, where T_{mrt} and T_a are varied equally, and $I_t''(\vec{e}_{T_{mrt}}) = s_{T_{mrt}}$, where the T_{mrt} values are varied depending on T_a, and the fact that $\vec{e}_{T_{mrt} \text{ and } T_a} = \vec{e}_{T_{mrt}} + \vec{e}_{T_a}$ we arrive at

$$s_{T_{mrt} \text{ and } T_a} = I_t''(\vec{e}_{T_a \text{ and } T_{mrt}}) = I_t''(\vec{e}_{T_{mrt}} + \vec{e}_{T_a}) = I_t''(\vec{e}_{T_a}) + I_t''(\vec{e}_{T_{mrt}}) = s_{T_a} + s_{T_{mrt}},$$

which can be rearranged to Eq. (4.6).

b) hyper-cuboid of personal variables

For the derivation of the sensitivity indices of the meteorological variables, the standard characteristics of the reference person are used for PET (Table 2.3). However, the defined values for age (A), gender (gn), height (h_p), weight (m), work metabolism (M_w) and clothing insulation (I_{clo}) influence the heat exchange mechanisms in MEMI. Table 4.3 summarises their influence on the heat exchange processes; details on the underlying equations are given in Höppe (1984) and Höppe (1999).

To investigate how strongly the characteristics of the reference person influence PET, the personal variables of the reference person are varied. Since PET is defined for the standard set of characteristics of the reference person (Table 4.4), PET* denote all PET values in this chapter that are calculated with deviating values for the personal variables. Since gender is a discrete variable, it is not included in the personal-hypercuboid itself. Instead the $m = 5$-dimensional hyper-cuboid of personal variables ($i \in \{A, h_p, m, M_w, I_{clo}\}$) is evaluated twice – once for a male and once for a female. The same ranges of the personal variables have been used for the male and the female. Table 4.4 shows these ranges as well as the variation steps and the characteristics of the standardly applied reference person (male) for PET. Since MEMI considers activity in form of work metabolism (M_w), the indicated total metabolisms are indicative only as those have been derived for the characteristics of the standard reference person in terms of skin area (A_{Du}) and basal rate.

Table 4.3: Influence of the characteristics of the reference person on heat exchange processes in MEMI.

Variable	Influenced property	Influenced heat fluxes
Age	basal rate	internal energy
Gender	basal rate, sweating	internal energy, physiological possible latent heat flux by sweating
Height	skin area, basal rate	effective radiation area and heat fluxes through clothing, internal energy
Weight	skin area, basal rate	effective radiation area and heat fluxes through clothing, internal energy
Metabolic heat	Metabolism added to basal rate	respiratory heat flux and internal energy
Clothing insulation	fraction of bare and clothed skin, clothing resistance	all sensible and radiative heat fluxes

To detect, whether the sensitivity to the personal variables changes with the considered meteorological condition, the male and female hyper-cuboid is evaluated for each meteorological conditions represented by the corner point of the 4-dimensional meteorological hyper-cuboid described above. To be able to detect this influence, but limit the number of calculations, the variations along the edges of the personal hyper-cuboid is not calculated for every corner point. Instead each personal variable is varied between its extremes for 3 conditions of the other personal variables: minimum value, maximum value and standard value for the reference subject. For a 3-dimensional hyper-cuboid (Figure 4.1) this would correspond to corner points 1 and 8, as well as to a point relatively close to the centre.

The different meteorological situations are referenced by numbers, which correspond to the meteorological situations indicated in Figure 4.3. The smaller number at each dot refers minimum values of the missing variable in the three-dimensional representation of the hyper-cuboid (i.e. T_{mrt} in Figure 4.3a and FF_{10} in Figure 4.3b), whereas the higher number refers to its maximum values. Note that the effect of the personal variables height, weight and activity on the projection factor used in T_{mrt} (Eq. (3.6)) is neglected in this chapter, since the effects are small compared to the direct effect of the variables on the heat exchange processes.

Table 4.4: Characteristics of the reference person for the calculation for the sensitivity of PET* to the personal variables.

Variable	Range	Step	Standard
Height (h_p [m])	1.5 – 2	0.1	1.75
Weight (m [kg])	60 – 100	5	75
Age (A [yr])	15 – 100	5	35
Clothing Insulation (I_{clo}, [clo])	0.1 – 2	0.2	0.9
Work metabolism (M_w [W]; (corresponding total metabolism [$\mathrm{W\,m^{-2}}$]))	0 – 300 ($\approx$ 44 – 202)	20 ($\approx$ 10.5)	80 ($\approx$ 86)

As the personal variables are changed both for the actual and for the reference environment in accordance with the structure of MEMI, this analysis investigates how much PET* changes with the choice of the characteristics of the reference person under investigation. It cannot detect, how much PET or PET*, respectively, differs if for the actual environment a person with a different characteristic would be used than for the reference environment.

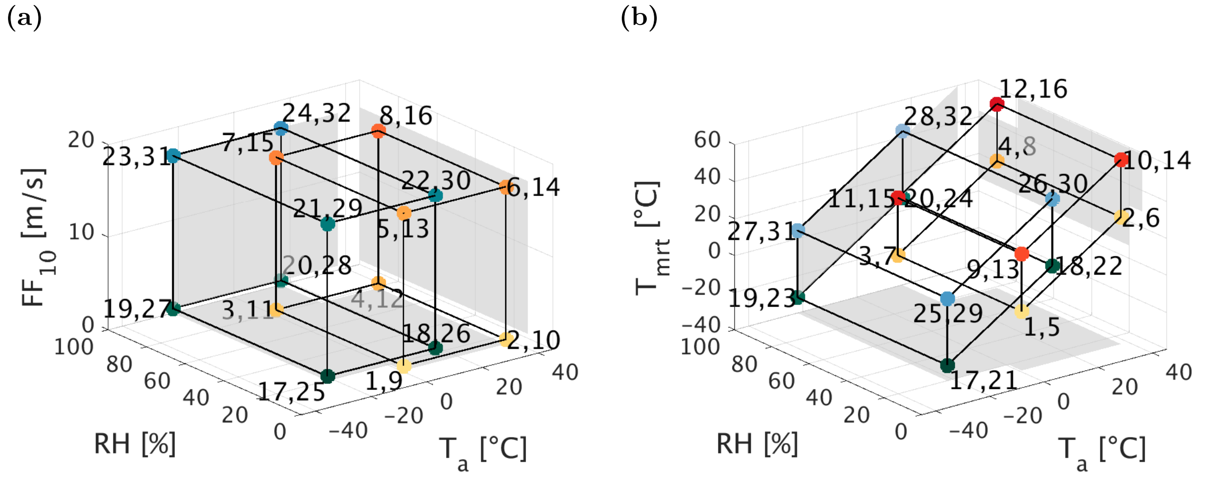

Figure 4.3: Three-dimensional representation of the four-dimensional hyper-cuboid of the meteorological variables for summer (reddish dots) and winter (blueish dots). Numbers indicate the different meteorological situations used for the sensitivity analysis of the personal variables.

4.2.2.2 Full-space analysis method

In the edge-based method the thermal indices are only calculated along the edges of the hyper-cuboid. Thus, although in principle the entire input space is covered, it is not thoroughly explored as the indices may behave differently anywhere within the cuboid. In addition in the edge-based method several situations are considered that do not occur in reality (Figure 4.2). Therefore in the full-space method, the samples are drawn from the probability density function (PDF) of each variable. To better detect interactive effects of personal and meteorological variables compared to the edge-based analysis method, those two groups are varied together, e.g. All-At-a-Time (AAT). In addition, in the full-space analysis method a third group of input variables, built-environment related variables, are included as additional input variables for the sensitivity analysis. Although the built-environment in principle affects all meteorological variables, especially large effects exist on mean radiant temperature (T_{mrt}) due to large differences in shaded and lit areas. To take that into account in the full-space method, the effect of the built-environment on mean radiant temperature is simulated with SURM (Chapter 3). Out of the various parameterisation options available in SURM, the best options as identified in Section 3.2, which among others includes prognostic wall and ground temperatures.

Due to the use of SURM a two-step modelling approach is used in the full-space analysis.

In the first step, meteorological variables and built-environment variables are used to derive T_{mrt} with SURM and in the second step, these T_{mrt} values are used together to calculate the thermal indices. This two-step modelling approach ensures that the strong link between air temperature T_a and T_{mrt} (Section 4.2.2.1) is adequately considered in the full-space method. Figure 4.4 shows the applied two-step modelling approach with meteorological variables (blue; air temperature (T_a), vapour pressure (e), wind speed in 10 m height (FF_{10})), built-environment variables (grey; building height (H), street width (W), street orientation (ω_s), albedo and emissivity of all surfaces (a, ε) and relative position of the person within the street canyon (x_{rel}), Figure 4.5) and personal variables (orange; height (h_p), weight (m), age (A), gender (gn), clothing insulation (I_{clo}) and work metabolism (M_w) of the person). The personal variables are only varied for PET and not for UTCI (Section 4.2.1). Since PET is defined for a standard set of personal variables (Table 2.3), PET* is used to indicate that deviating personal variables from the standard set are applied. For the meteorological variables hourly varying values are used to account for a diurnal cycle. For the built-environment-related variables as well as personal variables time-independent values are used.

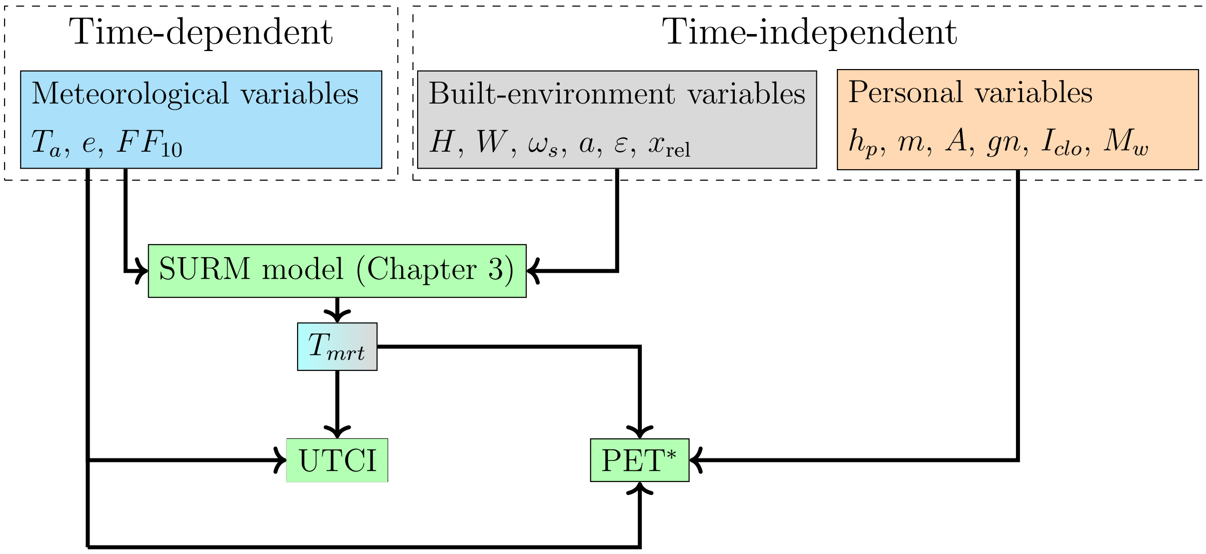

Figure 4.4: Two-step modelling approach for the full-space method. Step 1 accounts for effects of the built-environment on T_{mrt}. Step 2 is the calculation of UTCI and PET*. For variables see text.

The values of the different input variables are sampled quasi-randomly from predefined PDFs using a Latin-hypercube-sampling. Such a quasi-random sampling strategy is ap-

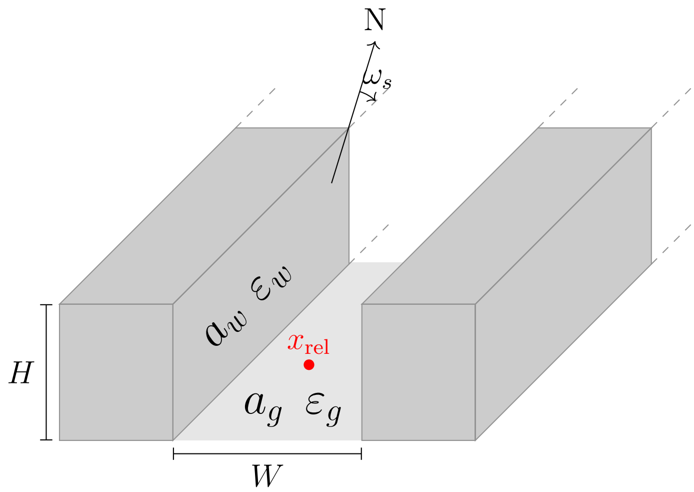

Figure 4.5: Varied built-environment-related properties within an idealised street canyon of SURM with infinite length, height H and width W. Other variables are explained in the text.

plied, as it has been shown to provide a better coverage of the input space than a fully random sampling technique (Zhang et al., 2015b; Spiessl and Becker, 2015). To derive sensitivity indices from such a set of samples, several techniques have been developed (Pianosi et al., 2016). In the present analysis two techniques are applied: (1) a variance-based method and (2) an Elementary Effect Test (EET).

Variance-based sensitivity indices use the explained output variance due to variation of the input variables as a measure for sensitivity. Sensitivity indices of different orders can be calculated from the variance-based method. A first-order or main effects variance-based sensitivity index describes the direct contribution from an individual input variable to the model output variability. Therefore, this index corresponds to S_{i_f} and S_{i_r} in the edge-based method. Formally, the variance-based main sensitivity index assess, how much the output variance (V) of the thermal index is expected to reduce for a fixed input (x_i), while all other inputs $x_{\sim i}$ can vary (Pianosi et al., 2016):

$$S_i = \frac{V_{x_i}\left[E_{x_{\sim i}}(I_t|x_i)\right]}{V(I_t)}, \tag{4.7}$$

In addition to this main effect index, from the variance-based method also a total-order or total effects index ($S_{i,T}$) can be defined. $S_{i,T}$ (Eq. (4.8)) assesses in addition to the direct effect of a variable, the contribution of one input variable to the effect of other factors (Pianosi et al., 2016). Since $S_{i,T}$ takes into account both the direct effect of a variable and the indirect effect due to interactions with other input variables, a total-order index of zero is a necessary and sufficient condition for non-influential input factors.

$$S_{i,T} = \frac{E_{x_{\sim i}}\left[V_{x_i}(I_t|x_{\sim i})\right]}{V(I_t)}. \tag{4.8}$$

The variance-based sensitivity indices cannot be calculated analytically; instead Monte-Carlo integrals must be used (Nossent et al., 2011). For these, different approximations have been suggested (Saltelli and Annoni, 2010). For the present analysis the approximations by Jansen (1999) in Saltelli and Annoni (2010) are used.

The second technique (Elementary Effect Test (EET)) calculates the main effects sensitivity index by varying an input variable x_i by Δ_i, while keeping all other input variables $x_{\sim i}$ fixed. By dividing the resulting differences in the output (ΔI_t) by the varied input range (Δ_i) finite difference quotients ('Elementary Effects', $EE_{i,m}$, Eq. (4.9)) can be calculated. These quotients are aggregated over the entire input space n and scaled by a factor $c_i = \Delta x_i$ to yield comparable mean elementary effects for the different input variables (Pianosi et al., 2016).

$$\begin{aligned} EE_{i,m} &= \frac{1}{n}\sum_{j=1}^{n} EE_i^j \\ &= \frac{1}{n}\sum_{j=1}^{n} \frac{I_t\left(\overline{x}_1^j, ..., \overline{x}_i^j + \Delta_i^j, ...\overline{x}_m^j\right) - I_t\left(\overline{x}_1^j, ..., \overline{x}_i^j, ...\overline{x}_m^j\right)}{\Delta_i^j} \cdot c_i \end{aligned} \tag{4.9}$$

This technique is very similar to the finite differences used in the edge-based method. However, as the starting values x_i are chosen quasi-random using Latin-hypercube sampling the input space is much better covered.

In contrast to the variance-based sensitivity indices, no total sensitivity index can be defined for the EET. Instead the standard deviation of the 'Elementary Effects' (Eq. (4.10)) is used to assess the degree of interaction between the i-th input variable and the others (Pianosi et al., 2016).

$$EE_{i,std} = std(EE_i^j) \tag{4.10}$$

Note, that the absolute values of $EE_{i,m}$ and $EE_{i,std}$ are not meaningful; only the relative difference in $EE_{i,m}$ and $EE_{i,std}$ between the variables is relevant.

To be able to derive the elementary effects and the variance-based sensitivity indices from a set of samples, a specific sampling strategy is required. The variance-based indices require a tailored two-stage procedure (Pianosi et al., 2016). In this procedure first two independent sets of $n = 8000$ base samples are drawn quasi-randomly from defined input

PDFs. These two base samples are recombined to additional $m{\cdot}n$ samples, by choosing one block of n input values from base sample 1, except for the i-th column, which is used from base sample 2 (Pianosi et al., 2015, 2016). The EET requires a similar sampling strategy: each sample sub-set, for which the elementary effect is calculated, consists of $(m+1)\cdot m$ samples, for which in each row, one of the m input variables is varied by Δ_i, whereas for the other variables the value is the same for all rows in this sample sub-set. Thus, the generated samples by the tailored two-stage procedure for the variance-based indices can restructured to the sampling strategy for the EET. This has the advantage that the two applied sensitivity calculation techniques can use the same samples and thus the thermal indices have been calculated only once for both techniques. To generate the samples and derive the sensitivity indices of the full-space analysis the SAFE toolbox (Pianosi et al., 2015, available at `http://www.bris.ac.uk/cabot/resources/safe-toolbox/`) is applied using an extension to transfer the tailored two-stage procedure for the variance based indices to the sampling strategy of the EET (Pianosi et al., 2018).

The base samples are selected from the PDFs of the input variables. For the personal and built-environment variables, uniform continuous and uniform discrete PDFs (for age and gender) are used. The personal variables are varied in the same range as for the edge-based method (Table 4.4); the ranges for the built-environment related variables are shown in Table 4.5.

Table 4.5: Input ranges for the built-environmental variables for the full-space analysis method. Variables are indicated in Figure 4.5

Variable	Range	Literature source for range
Building height (H)	0 m – 40 m	Schlünzen et al. (2011a)
Street width (W)	5 m – 50 m	Schlünzen et al. (2011a)
Street orientation (ω_s)	0° – 180°	
Albedo of ground and wall a_g=a_w	0.15 – 0.6	Dai et al. (2012); Schrijvers et al. (2016)
Emissivity of ground and wall ε_g=ε_w	0.85 – 0.95	Schrijvers et al. (2016)
Relative position of the person within the street canyon (x_{rel})	$0.1\cdot W$ – $0.9\cdot W$	

The input PDFs of the meteorological variables are derived from measurements. Since the effect of the built-environment on T_{mrt} are largest during clear sky conditions the already the measurements have been filtered for cloudless days. For that hourly measurements in Fuhlsbüttel (Table 4.1) and 10 minutes averages at the Hamburg Weathermast (Table 4.6) located in the east of Hamburg (Figure M.2) are filtered for days for which each observation fulfills $N \leq 1$ for the Weathermast data (as in Section 3.2.3) and $N \leq 2$ for the Fuhlsbüttel data. The threshold value differs for the two stations due to the different measurement methods: the meteorological observer at Fuhlsbüttel takes into account the entire sky to define N. Therefore, if $N > 0$ the clouds are not necessarily present above the measurement station. In contrast the ceilometer scans the sky immediately above the station. Therefore, a stricter value for Weathermast compared to Fuhlsbüttel is used. Even stricter criteria cannot be used, as otherwise too few observations are left. In total for summer 142 days (50 days at the Weathermast and 92 in Fuhlsbüttel) and for winter 73 days (11 days at the Weathermast and 62 in Fuhlsbüttel) with cloudless conditions have been identified. Hereof, 23 days in summer and 6 days in winter are the same for Weathermast and Fuhlsbüttel. In addition, some of those selected days are consecutive to each other. Therefore, the sampled conditions are not independent from each other, this has to be kept in mind, when interpreting the results.

Table 4.6: Used observations at Weathermast, Hamburg (Figure M.2), operated by the Meteorological Institute of the University of Hamburg.

Variable	Period	Height [m]
Air Temperature (T_a)	01.04.2004–29.02.2016	2.0
Relative humidity (RH)	01.04.2004–29.02.2016	2.0
Wind speed (FF)	01.04.2004–29.02.2016	10.0
Cloud fraction (N) estimated from a Ceilometer	01.04.2004–29.02.2016	not applicable

Since the measurements are conducted at legal time, which does not completely reflect the position of the sun, the closest observation to each hour in Local Solar Time between 01:00 LST and 23:00 LST was used. 00:00 LST could not be used, since entire days have been used for the filtering of cloudless days; observations later than 23:30 LST have been attributed to 23:00 LST.

For every hour 17 different parametric PDFs are fitted to each T_a, e and FF_{10} using the matlab file exchange function 'allfitdist' (Sheppard, 2012). From these the four best representing PDFs for the observations based on the Bayesian information criterion are derived. For those four PDFs a Kolmogorov-Smirnoff-test and an Anderson-Darling-test are conducted to test, whether the underlying empirical function can indeed be represented by the PDFs. These two tests have been chosen, since they assess different aspects of the distributions. The distribution with the highest combined p-value of the two tests is assumed to best represent the empirical data. The chosen PDFs for all hours for summer and winter are summarised in Appendix E. Since the regression function for UTCI can only be applied for wind speeds between 0.5 $\mathrm{m\,s^{-1}}$ and 17 $\mathrm{m\,s^{-1}}$ (Bröde et al., 2012; ISB Comission 6, 2012), similarly to the edge-based analysis, random sampled values outside these limits have been replaced by the limit values (0.5 $\mathrm{m\,s^{-1}}$ and 17 $\mathrm{m\,s^{-1}}$) both for UTCI and PET. For PET the wind speed is rescaled to the input height of 1 m as described in Section 4.2.2.1.

To limit the computational cost, all other input variables than the three meteorological variables, the six built-environment variables and six personal variables (Figure 4.4) are fixed for the simulations (Table 4.7). The simulations are carried out for average summer and winter radiation days. These days have been derived by calculating the average theoretical amount of incoming solar radiation received in Hamburg for each season assuming no absorption of radiation in the atmosphere. The two days with incoming solar radiation closest to these average theoretical amounts are selected (Table 4.7).

Table 4.7: Fixed input factors for the full space analysis method.

Parameter	Value
Street length	infinite
Shortwave absorption coefficient of the body	0.7
Emissivity of the body	0.97
Latitude	53.5 °
Date	28.07. (summer), 26.01 (winter)

4.3 Results for sensitivities of selected thermal indices

4.3.1 Comparison of PET versions

For the present analysis two different version (PET_{env} and PET_{vdi}) to calculate PET are available (Section 4.2.1). To assess, how much the PET values differ between these two versions, PET_{env} and PET_{vdi} are calculated for the meteorological situations of the edge-based analysis (Section 4.2.2.1, Figure 4.3). Figure 4.6 shows that PET values differ by about 14 K for the investigated situations. Large differences are calculated especially for those situations for which sweating is simulated. If the ENVI-met version is modified in such a way that the actual conditions are used to derive the latent heat fluxes in the reference environment – as done in the VDI version (Section 4.2.1) – differences in PET vanish (crosses in Figure 4.6). This indicates that the differences between the versions is related to the handling of the latent heat fluxes.

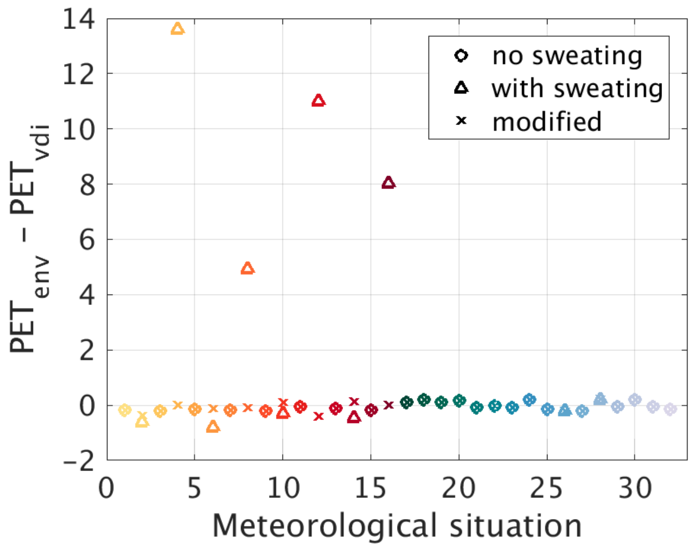

Figure 4.6: Differences in PET_{env} and PET_{vdi} for different meteorological situations indicated by numbers referring to Figure 4.3. 'modified' indicates a version of PET_{env}, where the latent heat fluxes in the actual environment are used in the reference environment.

4.3.2 Edge-based analysis

4.3.2.1 Sensitivity to meteorological inputs

The results of the edge-based analysis show that PET and UTCI overall increase with increasing T_{mrt}, RH and T_a and decrease with increasing FF_{10} (Figure 4.7 to Figure 4.9). Thus, in general the thermal indices reflect the effects of sensible, latent and radiative heat exchange mechanisms of the human body (Figure 2.1, Section 2.2.1). However, when assessed in detail differences between the thermal indices and the different meteorological variables become apparent.

All investigated thermal indices strongly depend on T_a and T_{mrt} (figure a in Figure 4.7 to 4.9), with highest slopes for high wind speed cases for UTCI (Figure 4.9a). All thermal indices seem to be approximately linearly linked to T_{mrt}. In contrast, RH influences the thermal indices little, except for warm conditions with sweating (Figure 4.7 to Figure 4.9 (b) and (d)). UTCI decreases almost linearly with increasing FF_{10} for hot conditions, but non-linearly for cold conditions (Figure 4.9c). PET changes for both versions linearly with FF_{10} for situations with minimum T_{mrt} but non-linearly for other situations (Figure 4.7 to Figure 4.8 (c)). For one meteorological situation ($RH_{\min}$, $T_{mrt\min}$ and $T_{a\max}$) PET of both versions increases with increasing FF_{10}. In this situation the ambient air temperature is high (37.2 °C) but the heat gain by radiation is small (T_{mrt} = 28.6 °C) and thus the temperature of the clothing surface (T_{cl}) is smaller than air temperature causing a heat gain from the environment at the clothed surface part (A_{cl}) of the body:

$$Q_{H cl} = A_{cl} \cdot h_a \cdot (T_a - T_{cl}) \tag{4.11}$$

With increasing wind speed this heat gain slightly increases, causing an increase in PET.

As expected from the analysis of the two PET versions (Section 4.3.1), PET_{env} increases abruptly above a certain RH threshold. A closer analysis of the heat fluxes shows that for those conditions sensible heat loss is maximal (vasodilatation is maximal) and that the skin is fully wet with higher physiological possible sweat rates than potentially possible sweat rate due to the humidity gradient to the environment. Thus, much of the sweat drops from the body unused for the heat loss causing an abrupt increase in skin and core temperature. In the reference environment humidity is lower. Thus, PET_{env}, which recalculates the latent heat fluxes in the reference environment calculates much higher sweat rates in the reference environment. As PET is defined by equally high core and skin temperatures in the actual and in the reference environment, a high air temperature is required to balance the large sweat rates but keeping the high core and skin temperatures. Since per definition the air temperatures of the reference environment equal the calculated PET value (Section 4.2.1), very high PET values are calculated. Since $\mathrm{PET_{vdi}}$ does not recalculate the sweating in the reference environment, lower air temperatures of the reference environment are sufficient to balance the high core and skin temperatures. This leads to the lower values for $\mathrm{PET_{vdi}}$ compared to $\mathrm{PET_{env}}$.

The finding that the influence of one meteorological input variable changes depending on the state of the other inputs indicates that interactions between the variables are important. This is also reflected in the difference in mean and maximum sensitivity indices (Table 4.8) as derived from the regression analysis (Eq. (4.3), S_r): the mean S_r coefficient over all edges over the hyper-cuboid is very similar to the standardised sensitivity indices of the factorial design (S_f), which is derived from the differences of all corner points together (Eq. (4.1)). This indicates that on average the variables influence the thermal indices linearly. However, the maximum values of S_r that is found along a specific edge of the hyper-cuboid, differs largely from the corresponding means, indicating non-linear effects. These results for interactions with other meteorological variables are investigated in more detail in the full-space analysis (Section 4.3.3).

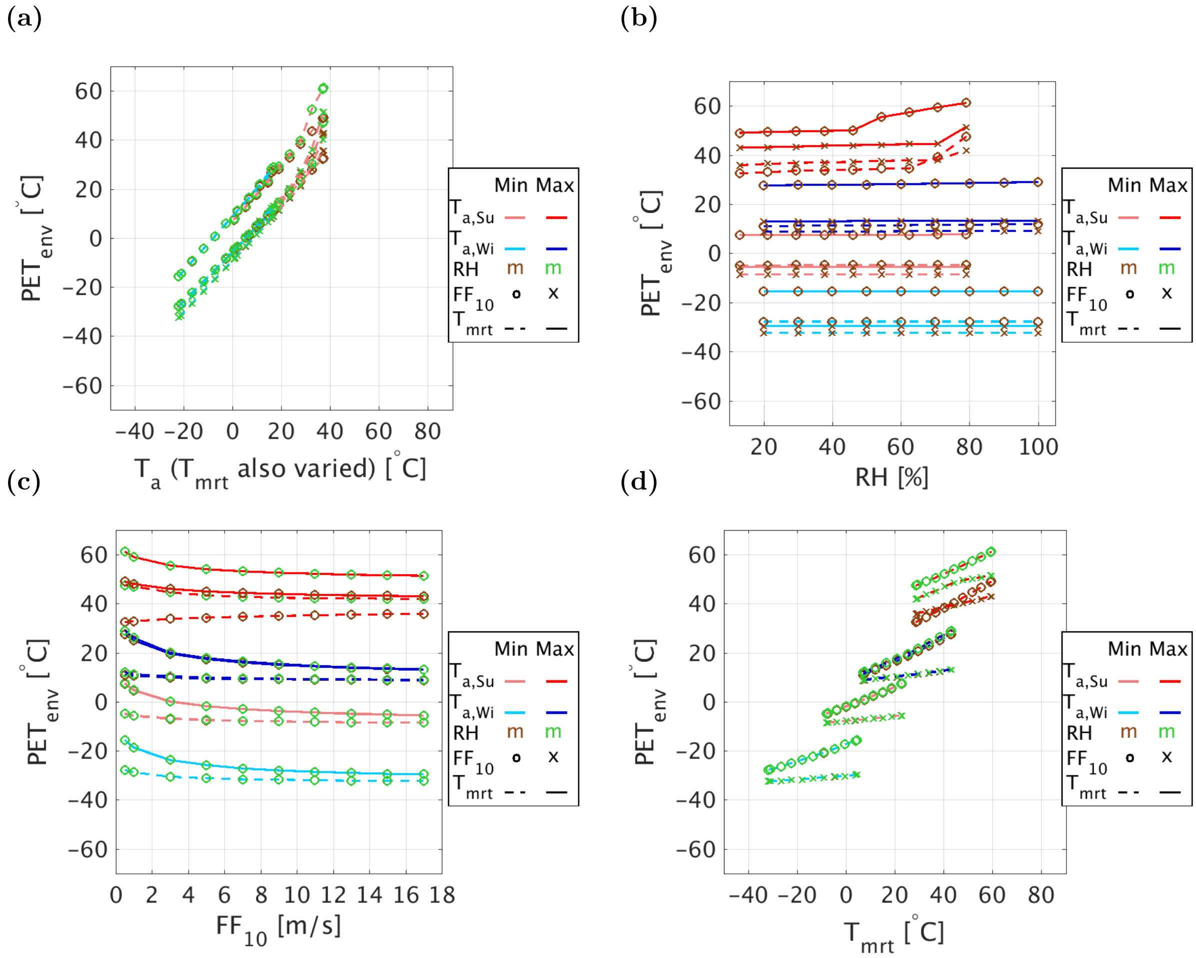

Figure 4.7: Simulated $\mathrm{PET}_{\mathrm{env}}$ for different meteorological conditions: Varied meteorological variables are shown on the abscissa, all other variables are kept fixed at there climatological limits (Table 4.2). Line colours indicate summer ('Su', red) and winter ('Wi', blue), brighter (darker) colours indicate climatological minimum (maximum) values for air temperature (T_a). Brown (green) markers ('m') indicate minimum (maximum) values of relative humidity (RH), circles (crosses) indicate minimum (maximum) values for wind speed (FF_{10}) and dashed (solid) lines indicate minimum (maximum) values for mean radiant temperature (T_{mrt}). Please note that for (a) both T_a and T_{mrt} are varied.

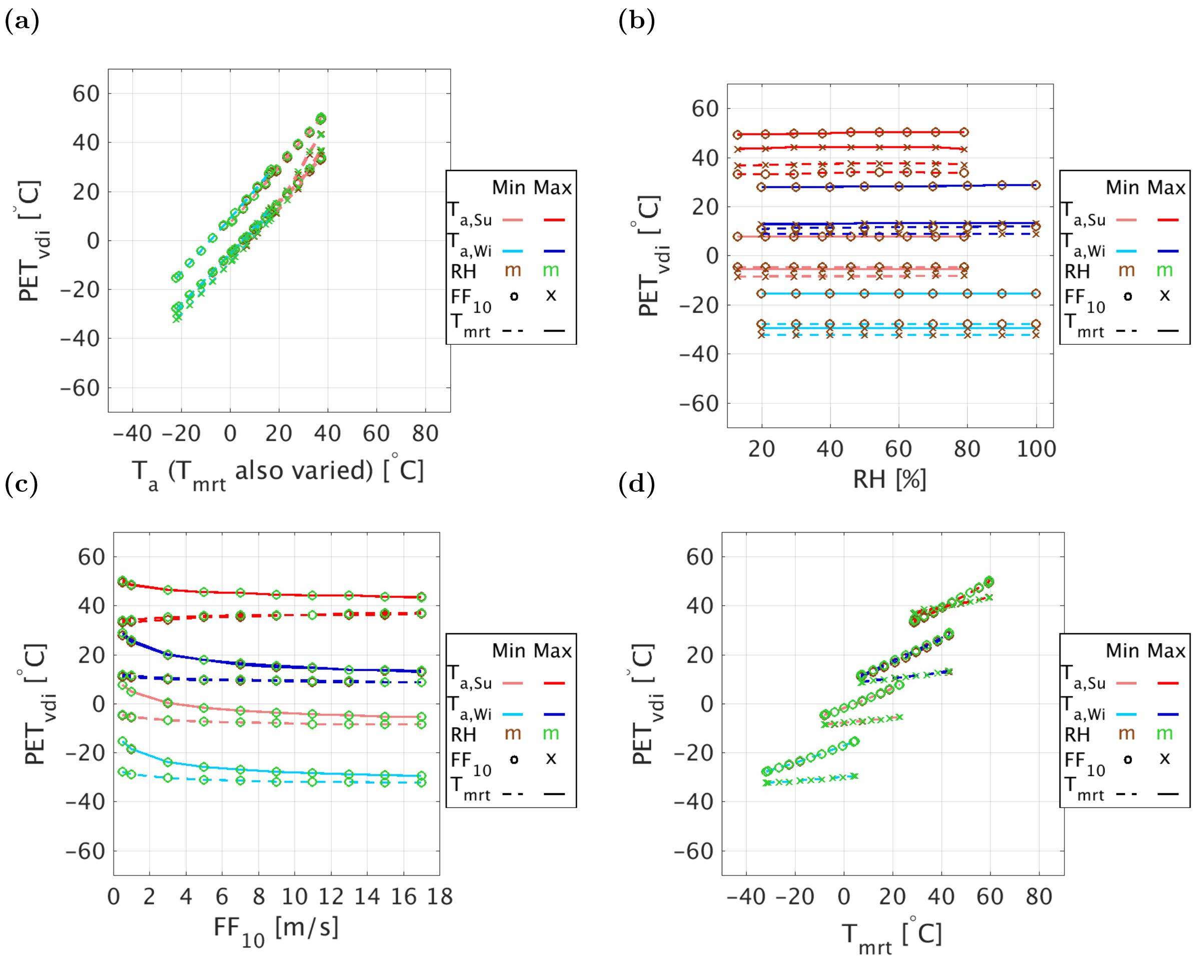

Figure 4.8: Same as Figure 4.7 but for $\mathrm{PET_{vdi}}$.

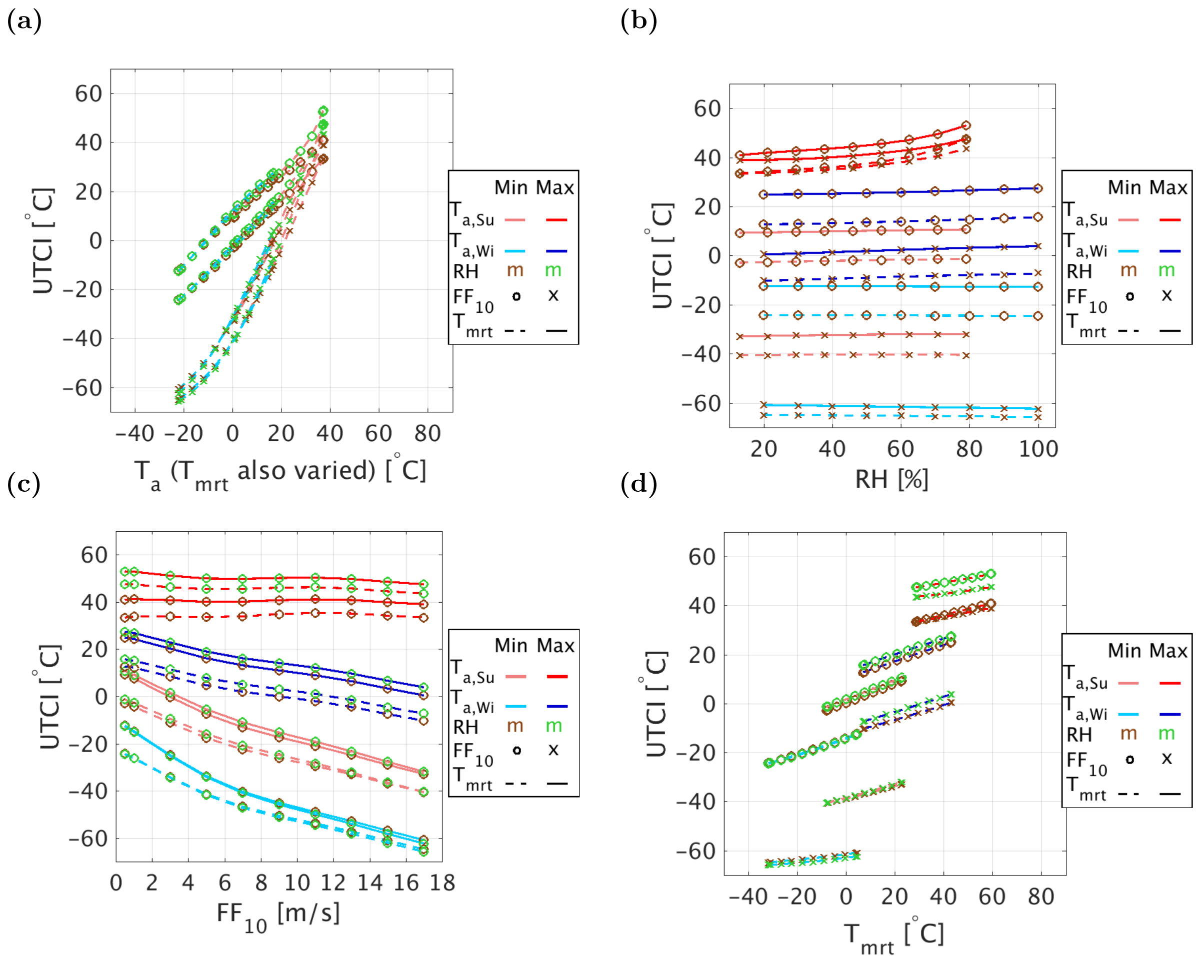

Figure 4.9: Same as Figure 4.7 but for Universal Thermal Climate Index (UTCI).

Table 4.8: Mean and maximum (Max) sensitivity indices (s not standardised and S standardised for regression method (index r) and factorial design method (index f), Section 4.2.2.1) of air temperature (T_a), relative humidity (RH), wind speed at 10 m height (FF_{10}) and mean radiant temperature (T_{mrt}) for the thermal indices Physiological Equivalent Temperature ($\mathrm{PET_{env}}$) and $\mathrm{PET_{vdi}}$ and the Universal Thermal Climate Index (UTCI) for Summer and Winter as derived from the local sensitivity analysis.

		PET_{env}				PET_{vdi}				UTCI			
		Summer		Winter		Summer		Winter		Summer		Winter	
		Mean	Max	Mean	Max	Mean	Max	Mean	Max	Mean	Max	Mean	Max
T_a	s [K/K]	0.96	1.21	0.83	1.04	0.87	1.22	0.83	1.04	1.33	2.12	1.02	1.50
T_a	S_r [ ]	0.50	0.63	0.52	0.65	0.55	0.76	0.52	0.66	0.52	0.83	0.42	0.62
T_a	S_f [ ]	0.55	-	0.53	-	0.58	-	0.53	-	0.54	-	0.43	-
RH	s [K/%]	0.07	0.20	0.00	0.02	0.01	0.01	0.00	0.01	0.09	0.20	0.01	0.04
RH	S_r [ ]	0.07	0.19	0.01	0.02	0.01	0.02	0.01	0.02	0.06	0.14	0.01	0.04
RH	S_f [ ]	0.08	-	0.01	-	0.00	-	0.01	-	0.07	-	0.01	-
FF_{10}	s [K/ms^{-1}]	-0.31	-0.64	-0.44	-0.78	-0.24	-0.64	-0.44	-0.76	-1.26	-2.51	-2.00	-2.89
FF_{10}	S_r [ ]	-0.07	-0.15	-0.12	-0.21	-0.07	-0.18	-0.12	-0.21	-0.22	-0.44	-0.35	-0.51
FF_{10}	S_f [ ]	-0.09	-	-0.15	-	-0.08	-	-0.15	-	-0.23	-	-0.37	-
T_{mrt}	s [K/K]	0.31	0.54	0.25	0.47	0.31	0.53	0.25	0.47	0.25	0.39	0.27	0.34
T_{mrt}	S_r [ ]	0.14	0.24	0.15	0.28	0.16	0.28	0.15	0.28	0.08	0.13	0.10	0.13
T_{mrt}	S_f [ ]	0.14	-	0.15	-	0.16	-	0.15	-	0.08	-	0.10	-

Figure 4.10 summarises the results for the edge-based analysis for the meteorological variables. The thermal indices are most sensitive to air temperature in both seasons. The sensitivity to RH is small in general, except for UTCI and PET_{env} for summer. But even then the sensitivity is smaller than the sensitivity to FF_{10} and T_{mrt} and much smaller than the one to T_a. In contrast to both versions of PET, UTCI is more sensitive to FF_{10} and less to T_{mrt}. Both PET versions are similarly sensitive to FF_{10} and T_{mrt}. For all indices the wind speed dependence is larger in winter; this is most pronounced for UTCI.

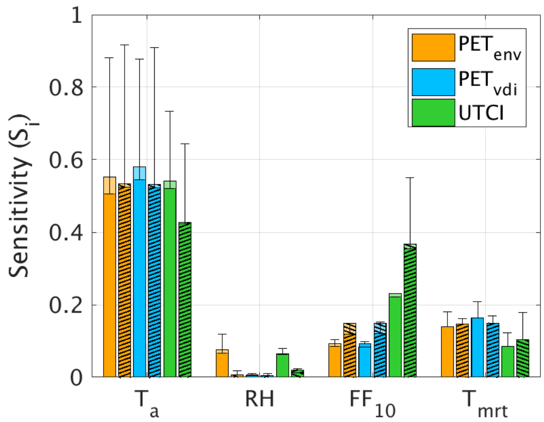

Figure 4.10: Absolute values of standardised sensitivity indices (S_i) from edge-based analysis for meteorological variables (i) air temperature (T_a), relative humidity (RH), wind speed at 10 m height (FF_{10}) and mean radiant temperature (T_{mrt}) for summer conditions and winter conditions (hatched bars) for regression method (darker colours and upward hatched) and factorial method (brighter colours and downward hatched; behind regression bars). Winkers indicate maximum standardised sensitivities for regression method.

4.3.2.2 Sensitivity to personal inputs

For the derivation of the sensitivity of PET to the meteorological variables, the standard set personal variables for the reference subject has been used (Table 4.4). In this section the influences of deviating personal variables are calculated. Since PET is only defined for the standard set of personal variables, PET* is used in this section to indicate that PET has been calculated with deviating personal variables.

Overall PET* is less sensitive to changes in personal variables than to changes in meteorological conditions for both PET-versions. Since slopes are linear and often close to zero, the variations of the personal variables along the edges of the hyper-cuboid are not shown. Instead the derived standardised sensitivity indices (S_{ir}) based on the regression method (Eq. (4.3)) are shown in Figure 4.11 for $\mathrm{PET}^*_{\mathrm{env}}$ and Figure 4.12 for $\mathrm{PET}^*_{\mathrm{vdi}}$. In these figures, circles refer to S_{ir} derived by linear regression fitting along axis i of the hyper-cuboid with all other variables at those for the standard reference subject in PET (i.e. close to the centre of the hyper-cuboid); stars refer to conditions with all other variables at minimum value (e.g. similar to corner point 1 in Figure 4.1) and triangles to conditions with all other variables at maximum conditions (e.g. similar to corner point 8 in Figure 4.1). Orange markers refer to a female reference subject, black ones to a male reference subject. The considered meteorological condition is shown colour coded along the axes using the colour code in Figure 4.7 to Figure 4.9.

For all personal variables, except work metabolism, $|S_i|$ is smaller than 0.1 for both versions of PET^*, irrespective of the considered meteorological condition and conditions of the other personal variables. Furthermore, the results for S_{ir} for both versions of PET^* are very similar, except for hot situations with sweating (e.g meteorological situation 4 and 8). Height, weight and age show little impact for all meteorological situations ($S_i = \pm 0.02$). This can be expected as those variables influence in MEMI only the basal rate and slightly the skin area (Table 4.3). In contrast, work metabolism and clothing insulation (I_{clo}) influence heat fluxes directly (Table 4.3) and consequently show larger impacts (figure a and b in Figure 4.11a and Figure 4.12a).

In the following, first the conditions with all other personal variables at standard conditions (circles) of the reference subject are analysed in detail. In those situations, with increasing clothing insulation PET^* increases for winter, because the body is cooled less by convection. For summer PET^* both increases and decreases, depending on whether cool or warm summer conditions are experienced: for cool conditions with high wind speeds higher I_{clo} suppresses heat loss by convection and during warm conditions I_{clo} shields the body from heat gains from radiation and convection in the reference environment. With increasing I_{clo} skin and core temperature increase only slightly in the actual environment for those warm conditions but in the reference environment heat gains are suppressed by the higher insulation. Comparing the sensitivity indices for male and females (black and orange markers for each situation), it becomes apparent that gender influences $\mathrm{PET}^*_{\mathrm{env}}$ and $\mathrm{PET}^*_{\mathrm{vdi}}$ little. Largest differences in sensitivity indices for a male and for a female are visible for $\mathrm{PET}_{\mathrm{env}}$ for situations with sweating, where differences up to 0.07 in standardised sensitivity indices. Maximum differences for sensitivity indices for males and females for $\mathrm{PET_{vdi}}$ are about 0.01.

Work metabolism has the largest impact on PET* with sensitivity indices comparable to those of T_{mrt} and FF_{10} in cold conditions (Figure 4.11b and Figure 4.12b). For those conditions PET* decreases linearly with increasing work metabolism (Figure 4.13). This non-intuitive behaviour can be explained by the requirement of equal skin and core temperatures in the actual and the reference environment in combination with integrating until energy balance for the different fluxes is achieved (Section 4.2.1): for low work metabolisms heat losses by convection and radiation are small ($\mathcal{O}(30)$ W) both in the actual and in the reference environment. With increasing work metabolism higher heat losses in the actual environment are simulated to balance the large internal energy. This causes smaller skin and core temperatures as for lower work metabolisms. In accordance with the definition of PET the same skin and core temperatures are used in the reference environment. However, to facilitate those temperatures, very small air temperatures (and consequently PET* values) in the reference environment are required. For very low work metabolism values and extreme cold conditions even negative skin and core temperatures are simulated in the actual environment. In reality those negative values would not be experienced since the exposure time to those conditions are usually smaller than 75 hours, which is required to calculate equilibrium of heat fluxes.

If for the other personal variables not the standard characteristics of the reference subject but the maximum conditions are used (triangles in Figure 4.7 and Figure 4.9, Table 4.4), PET* decreases less with increasing work metabolism, since the higher clothing insulation suppresses heat losses by convection and radiation and increases skin temperature. Also the impact of other personal variables on PET* changes if minimum or maximum conditions are used for the other fixed personal variables. This indicates that interactions between the personal variables are also important for determining PET*.

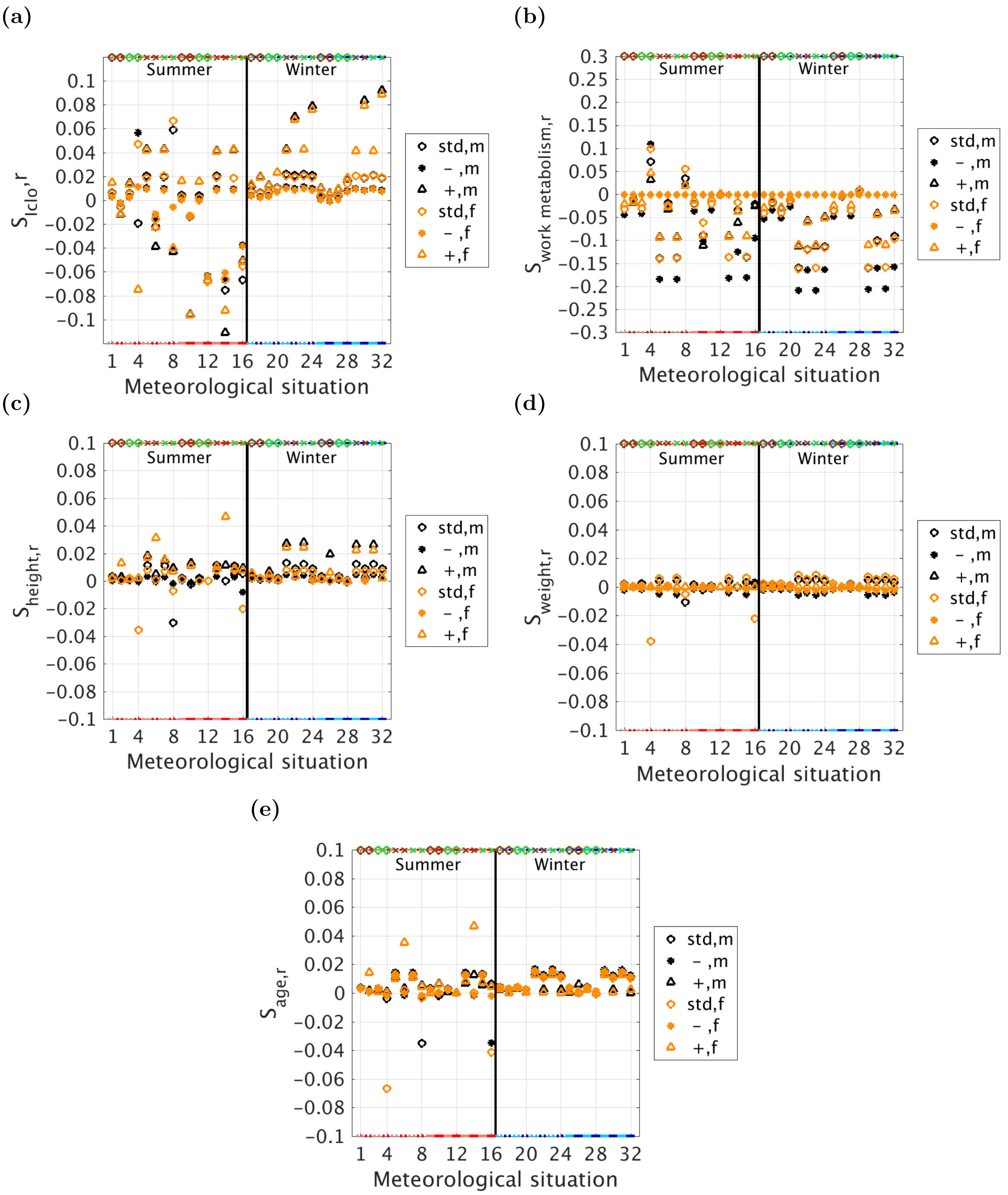

Figure 4.11: Standardised sensitivity indices from the regression method for PET_{env} for different personal variables ((a) to (e)). Different meteorological situations are denoted with numbers corresponding to Figure 4.3 and colour coded along the axes as in Figure 4.7 for male (black) and female (orange) subjects with all other variables at standard ('std') conditions (circles), at minimum conditions (stars), maximum conditions (triangles). Note the different ordinate in (b).

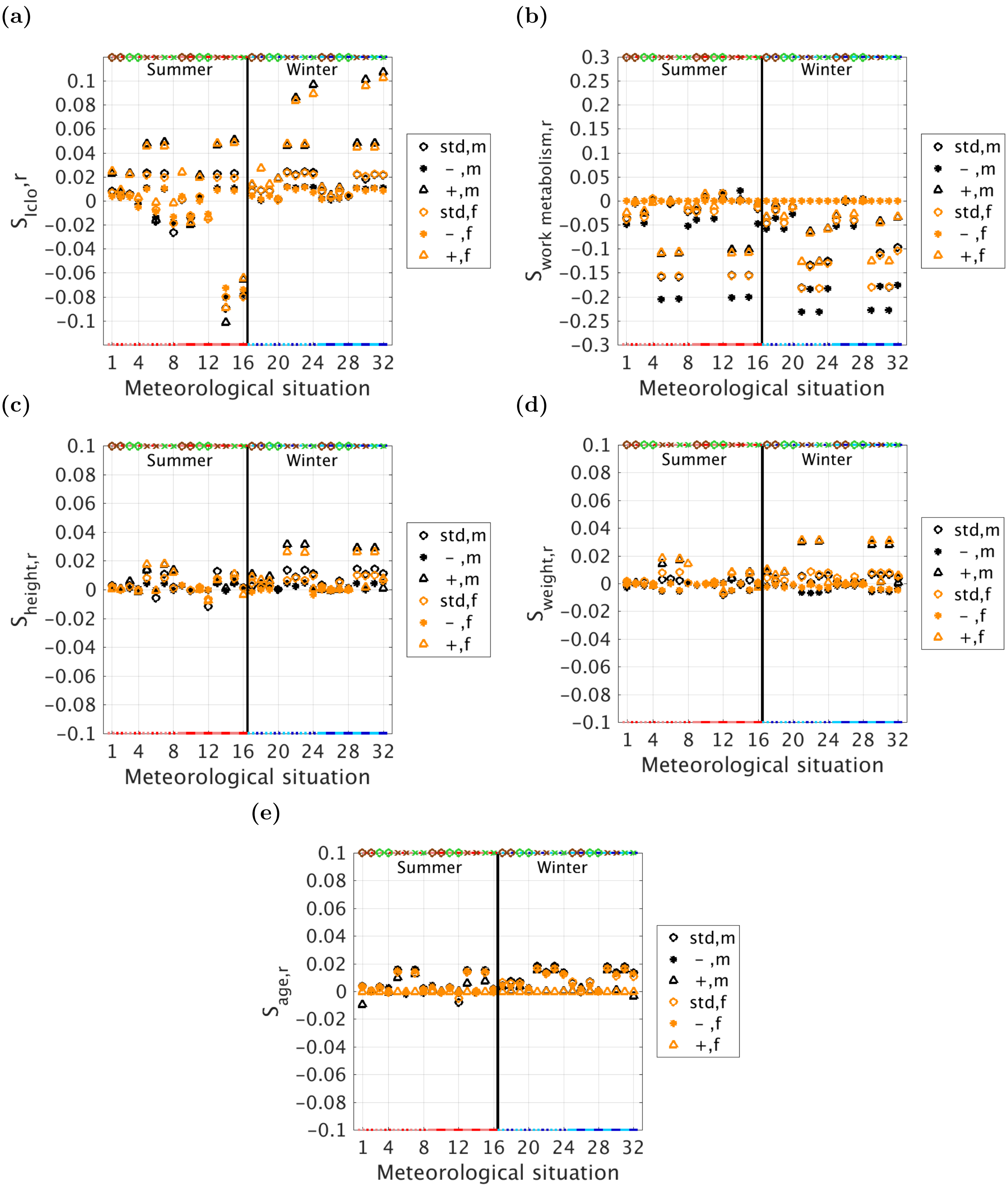

Figure 4.12: Same as Figure 4.11 but for PET_{vdi}.

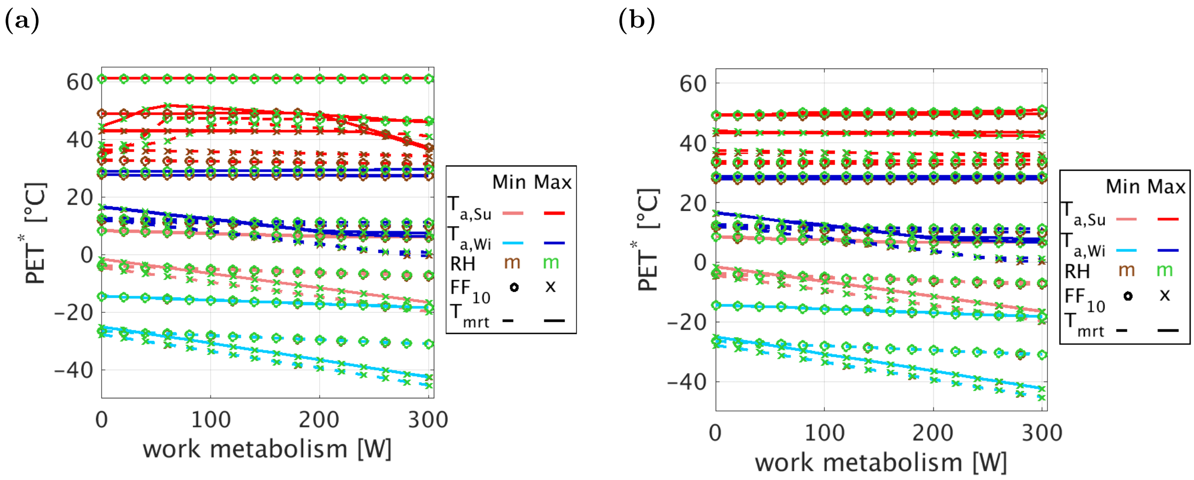

Figure 4.13: Impact of changing work metabolism on (a) $\mathrm{PET}^{*}_{\mathrm{env}}$ and (b) $\mathrm{PET}^{*}_{\mathrm{vdi}}$ with colour code as in Figure 4.7 for a male. All other personal variables are at standard conditions for the reference subject (Table 4.4).

4.3.3 Full-space analysis

The main effects sensitivity indices of the full-space analysis S_i (Eq. (4.7)) and $EE_{i,m}$ (Eq. (4.9)) reflect the direct contribution of a variable to the variability in the output value of the thermal indices. Therefore, they represent the full-space equivalents of the edge-based analysis main effects sensitivity indices S_{if} and S_{ir}. S_i and $EE_{i,m}$ are shown for $\mathrm{PET}^{*}_{\mathrm{vdi}}$ on the left in Figure 4.14 (i.e. a, c,e,g) and for UTCI on the left in Figure 4.15 (i.e.) a,c,e,g). Note that as in the full-space method all variables including the personal variables are varied together $\mathrm{PET}^{*}_{\mathrm{vdi}}$ is used everywhere to indicate that PET values were not obtained with the standard set of personal variables for the reference subject (Table 4.4). The S_i and $EE_{i,m}$ generally support for both seasons the ranking of influencing variables for $\mathrm{PET}^{*}_{\mathrm{vdi}}$ and UTCI from S_{if} and S_{ir} (Section 4.3.2). $\mathrm{PET}^{*}_{\mathrm{vdi}}$ is mostly determined by air temperature (T_a) in both seasons followed by wind speed (FF_{10}) in summer and work metabolism (M_w) in winter. UTCI is mostly determined by T_a followed by FF_{10} in summer and vice versa in winter, i.e. FF_{10} is more important than T_a in winter.

The full-space analysis additionally shows how the main sensitivities vary within one day: In summer for $\mathrm{PET}^{*}_{\mathrm{vdi}}$ the sensitivity to T_a decreases after sun rise and the built-environment-related variables including the persons' position within the street canyon

(x_{rel}) become more influential (Figure 4.14a,c). This can be seen more clearly for $\mathrm{PET}^{*}_{\mathrm{vdi}}$ than for UTCI, since the built-environment variables only influence T_{mrt} via SURM (Chapter 3) and $\mathrm{PET}^{*}_{\mathrm{vdi}}$ is more sensitive to T_{mrt} (Figure 4.10). For $\mathrm{PET}^{*}_{\mathrm{vdi}}$ also the sensitivity to FF_{10} increases during the day, especially in winter (Figure 4.14e,g). This increase in sensitivity is on the one hand caused by a direct influence of wind, as wind speed increases during the day in the simulated conditions. On the other hand it is caused by the influence of wind speed on surface temperature in SURM (Eq. (D.18) and Eq. (D.24)) and consequently T_{mrt}, which is used in the two-step modelling approach (Figure 4.4). In contrast to summer, in winter the built-environment-related variables affect $\mathrm{PET}^{*}_{\mathrm{vdi}}$ and UTCI less (a,c,e,g in Figure 4.14 and Figure 4.15). This is caused by overall smaller values of T_{mrt} in winter. However, the general diurnal cycle is the same in summer and winter, except that the sensitivity to T_a slightly increases during midday.

In contrast to the edge-based sensitivity analysis the importance of one input variable on I_t due to interactions with other input variables, can be easily assessed in the full-space analysis with the total sensitivity indices ($S_{i,T}$, Eq. (4.8)) and the standard deviations of the elementary effects ($EE_{i,std}$, Eq. (4.10)). $S_{i,T}$ includes both the main effect of one variable on the thermal index and the effect due to the interactions with other variables, whereas $EE_{i,std}$ only indicates the importance of interactions. $S_{i,T}$ and $EE_{i,std}$ are shown in the right column in Figure 4.14 and Figure 4.15, i.e. figures b,d,g,h). Both measures indicate that the built-environment-related variables, including also the relative position of the subject within the street canyon (x_{rel}, Figure 4.5, Section 3.1.2), mostly come into play due to interactions with other variables, whereas T_a (and FF_{10} in case of UTCI) mostly influence the thermal indices directly.

Comparing the results obtained from the two different full-space sensitivities, that is S_i and $EE_{i,m}$ for the main effect sensitivity (a and c for summer and e and f for winter in Figure 4.14 and Figure 4.15) and $EE_{i,std}$ and $S_{i,T}$ for the importance of interactions (b and d for summer and g and h for winter in Figure 4.14 and Figure 4.15), shows that both approaches consistently identify the most influential variables. However, they differ in their ranking for the less influential variables. For instance, neither UTCI nor $\mathrm{PET}^{*}_{\mathrm{vdi}}$ are sensitive to humidity in both summer and winter according to the variance-based indices, whereas the elementary effects indicate a slight direct influence for UTCI and an effect through interactions for $\mathrm{PET}^{*}_{\mathrm{vdi}}$. This vanishing influence of humidity might be due to almost zero meteorological situations for which limitations in sweating are relevant for determining heat stress in the simulated input space obtained from the condition in

Hamburg: although high humidity conditions are experienced in Hamburg, sensible heat fluxes are still effective to reduce heat stress as seldom very high humidity levels together with very high air temperatures are encountered.

Neither a direct nor an indirect effect through interactions is detected for albedo (a) and emissivity (ε) for UTCI for both seasons. For $\mathrm{PET}^*_{\mathrm{vdi}}$ only a slight influence through interactions in summer was detected and only by $EE_{i,std}$ and not by $S_{i,T}$. No effect was also detected for all personal variables except clothing insulation (I_{clo}) and work metabolism M_w for $\mathrm{PET}^*_{\mathrm{vdi}}$. The small sensitivity to the personal variables is in line with the results of the edge-based sensitivity analysis (Section 4.3.2), which indicates that the influence of the reference subject on $\mathrm{PET}^*_{\mathrm{vdi}}$ is almost solely determined by I_{clo} and M_w. The high influence of M_w in winter, which is mostly due to the definition of core temperature and skin temperature being equal in the reference and in the actual environment (Section 4.3.2), is also clearly visible in the full-space sensitivity results. This non-intuitive response with increasing M_w should be investigated in more detail and if possible be corrected in the future for instance by changing the definition of PET.

To check the reliability of the obtained sensitivity indices from the full-space analysis, bootstrapping with 500 randomly drawn samples is used. Figure 4.16 exemplary shows detailed results for 12:00 LST. The 95 %-interval, that is the interval in which the inner 95 % of all values lie, is very close to the mean of the bootstrapped results, especially for the total sensitivity indices ($S_{i,T}$, orange and green in Figure 4.16a,b) and means of the elementary effects ($EE_{i,m}$, abscissa in Figure 4.16c,d). Therefore, obtained mean results for 12:00 LST are relatively robust. Since the 95 %-intervals of the more influential variables do not overlap, the previously discussed ranking of the input variables is relatively certain. In contrast, the overlapping 95 %-intervals for the less influential variables indicate that a ranking of the importance of those input variables is not possible. For some variables, especially those with almost no influence, 95 %-intervals extend to negative values for S_i (Figure 4.16a,b) due to the approximation equations for Eq. (4.7).

In contrast to the mean of the elementary effects ($EE_{i,m}$) the estimation of their standard deviation ($EE_{i,std}$), i.e. the amount of interaction with other variables, is less certain for 12:00 LST as indicated by the large 95 %-intervals for the ordinate derived from the bootstrapping (Figure 4.16c,d). Especially the 95 %-intervals of $EE_{i,std}$ for x_{rel} in winter are very large (light purple). This is due to large differences in received shortwave radiation at midday in sun and shade: if a person at a specific position is exposed to the sun due to a change in building height or street orientation, T_{mrt} and consequently the thermal index changes drastically. In contrast, in other situations, for instance for street orientations of 0° or 180°, the person is lit irrespective of the position at 12:00 LST and consequently the interaction with other variables is zero. As indicated by Figure 4.14 and Figure 4.15 for other hours of the day the interaction of x_{rel} with other variables is less important. This is likely due smaller differences in received shortwave radiation in shaded and lit areas and due to smaller unshaded parts of the canyon.

Since Figure 4.16 shows only exemplary results for 12:00 LST, standard deviations for the sensitivity indices are derived from the bootstrapping for all hours and are shown in Appendix F. The standard deviations for other variables indicate that, in general, the obtained results are quit certain during the entire day (S_i within ± 0.02, $S_{i,T}$ within ± 0.015, $EE_{i,m}$ within ± 1.5 and $EE_{i,std}$ within ± 10 except for a few outliers).

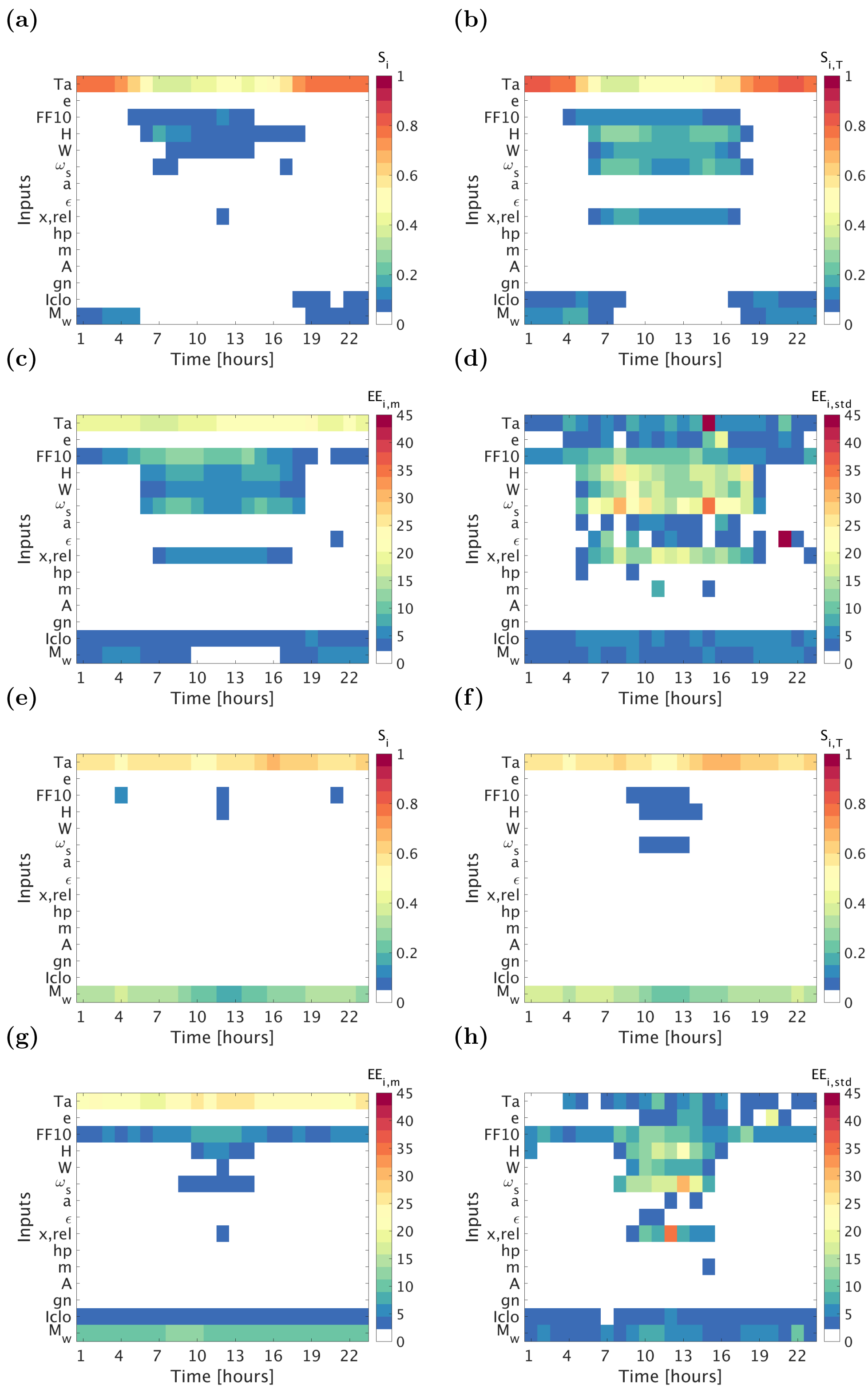

Figure 4.14: Global sensitivity for $\mathrm{PET}^*_{\mathrm{vdi}}$ in form of (a), (e) main sensitivity indices (S_i) and (b), (f) total sensitivity indices ($S_{i,T}$) and (c), (g) mean elementary effects ($EE_{i,m}$) and (d), (h) standard deviation of elementary effects ($EE_{i,std}$) for (a) to (d) summer and (c) to (h) winter. For variables see Table 4.4 and Table 4.5.

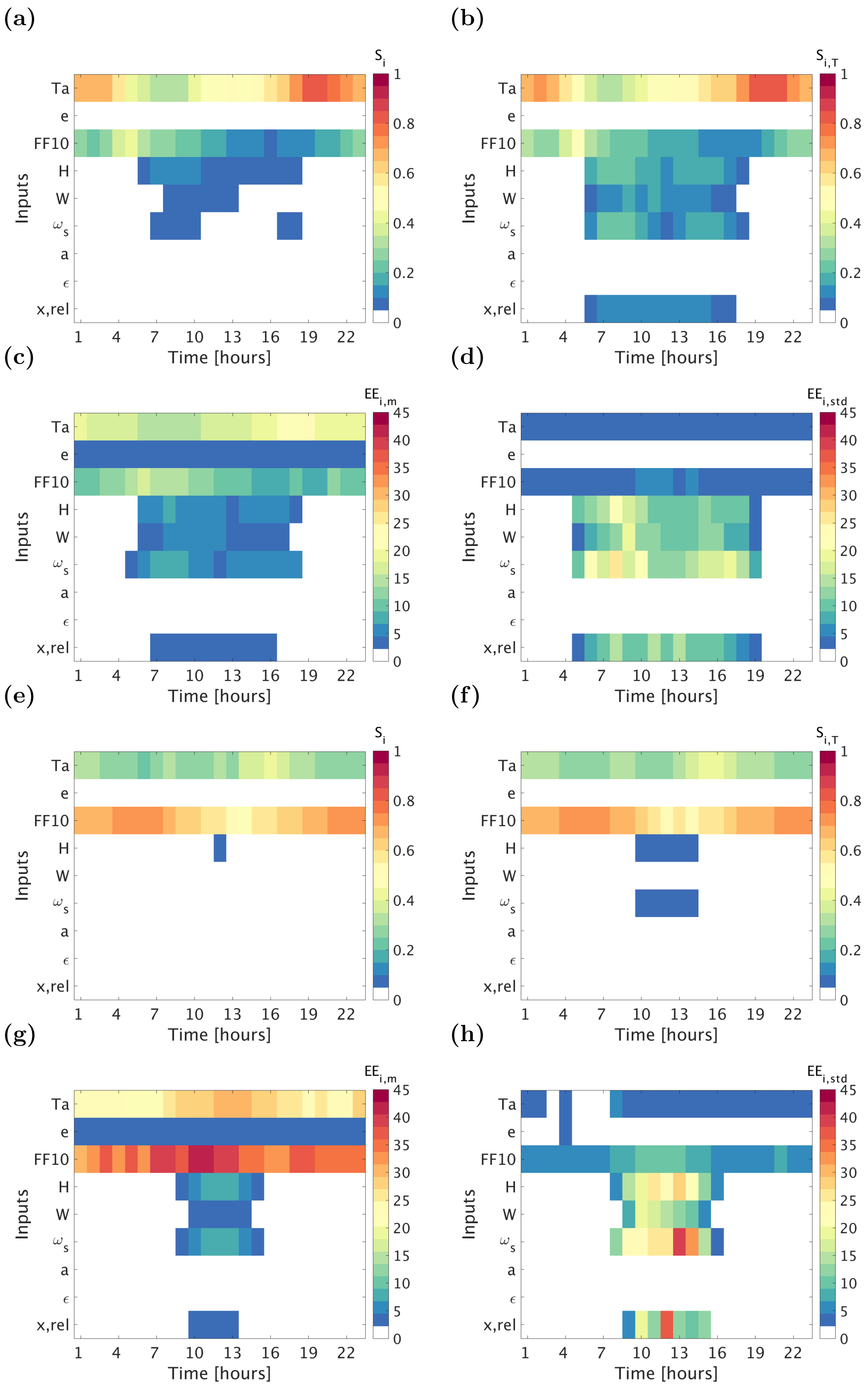

Figure 4.15: Same as Figure 4.14 but for UTCI.

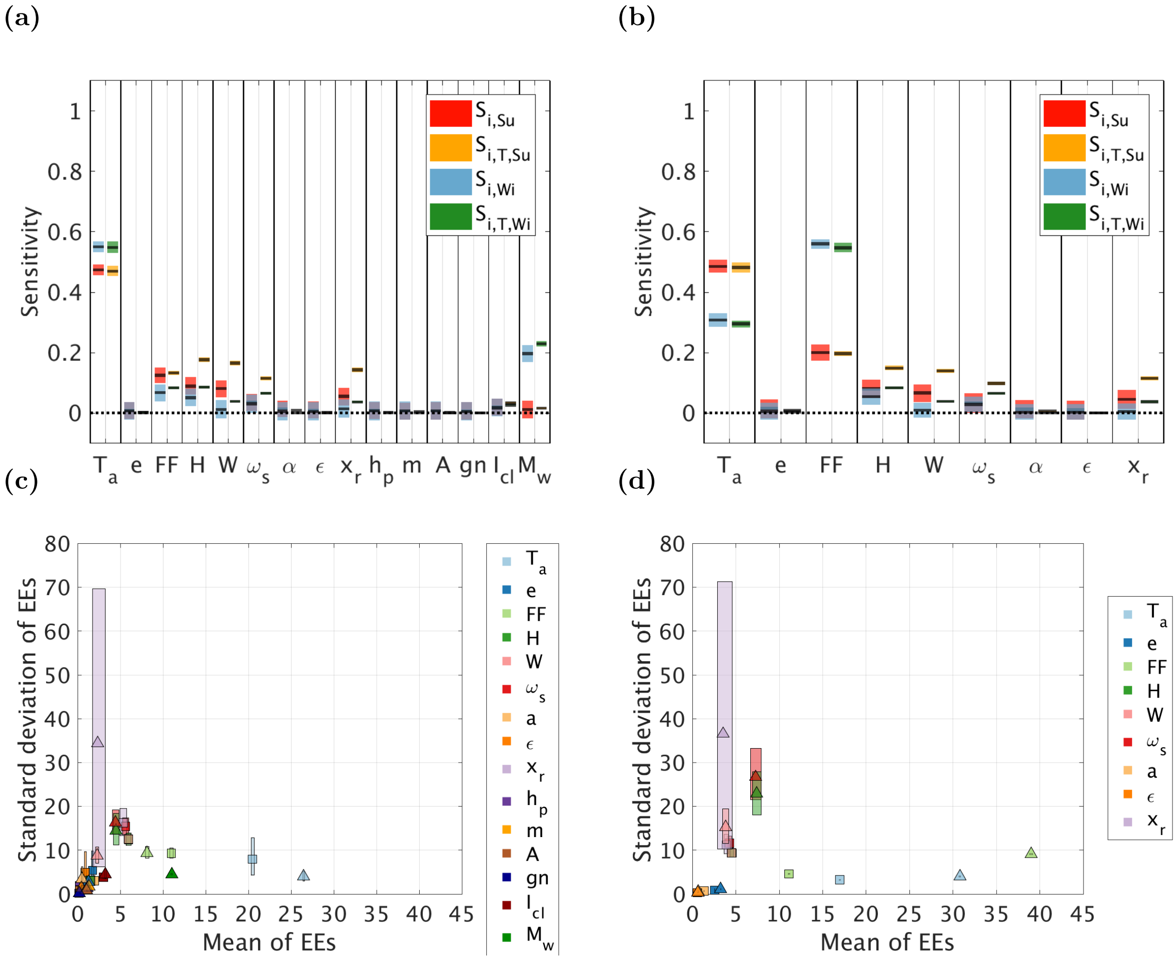

Figure 4.16: Bootstrap results for (a), (b) variance-based sensitivity indices and (c), (d) elementary effects for (a), (c) for $\mathrm{PET}^*_{\mathrm{vdi}}$ and (b), (d) for UTCI for 12:00 LST. Box plot range in (a) and (b) and width and height of bars in (c) and (d) indicate intervals in which 95 % of all values lie. Seasons are colour coded in (a) and (b) and indicated by squares (summer) and triangles (winter) in (c) and (d). Note that x_{rel} has been shortened to x_r, I_{clo} to I_{cl} and FF_{10} to FF in the figures.

4.4 Discussion of the sensitivity results

In this chapter, the sensitivity of two thermal indices, PET and UTCI is explored with respect to meteorological, built-environment and for PET* also with respect to personal variables for both non-urban and urban environments for climatological summer and winter conditions derived from Hamburg, Germany. The robustness and generality of these results, their consequence for required input accuracies, for urban planning and for Obstacle Resolving micro-scale model (ORM) development are discussed in this section.

4.4.1 Robustness and generality of the sensitivities

The sensitivities to the different input variables have been derived using four different methods – two edge-based and two full-space ones. All methods yield consistent results regarding the importance of the meteorological variables and personal variables (only for PET*): UTCI is mostly determined by T_a and during winter at least equally by FF_{10}. PET is most influenced by T_a both in summer and winter followed by FF_{10} in summer and M_w in winter. This result is consistent for both considered versions of PET. This indicates that the sensitivity of the thermal indices to one meteorological variable depends on the state of the other meteorological variables. The sensitivity to the built-environment-related variables has been investigated only within the full-space analysis. However, the bootstrapping results provide confidence to conclude that H, W, ω_s and x_{rel} (Figure 4.5) influence both indices strongly during the day with amplitudes comparable to those of FF_{10}. Since the influence of the built-environment variables in the two-step modelling approach applied in the full space analysis solely influence T_{mrt} as calculated by SURM (Figure 4.4), this indicates that the thermal indices are sensitive to T_{mrt} during the day. This result is supported by the edge-based analysis, for which T_{mrt} is included as an additional variable and equally high main sensitivity indices as for FF_{10} are calculated.

The determined relevances for the different input variables agree well with the results obtained in other studies for PET (meteorological variables: Bröde et al. (2012); Lee et al. (2016); Provençal et al. (2015); Fröhlich and Matzarakis (2015); built-environment-related variables: Andreou (2013); Schrijvers et al. (2016) in terms of street orientation and aspect ratio and Molenaar et al. (2015); He et al. (2015); Lee et al. (2016) in terms of SVF). The present analysis, however, extends those results in terms of higher number of input variables and more general street canyon designs. Furthermore, in contrast to other studies, here a global sensitivity analysis is performed to cover the full input space.

Additionally, in contrast to the other studies also interaction with other variables and the effect of personal variables on PET are investigated in the present analysis.

To complement the present analysis in addition to the variance-based sensitivity method a moment-independent method (Pianosi and Wagener, 2015) could be applied. This would have the advantage that daytime summer conditions could be better investigated. During those conditions the distribution function of the thermal indices is slightly skewed and therefore the variance is not the best suited moment to describe and determine the PDF of sensitivities. However, as the additionally applied elementary effect method does not rely on those assumptions, the obtained results are relatively robust. The derived main sensitivity indices are calculated according to the approximation method by Jansen (1999). If a different approximation method is used, as suggested by Saltelli et al. (2010), similar mean indices are obtained but 95 %-intervals are larger.

The meteorological variables are not fully independent of each other (Figure 4.2). Therefore, an independent sampling of those variables can result in unrealistic combinations. To avoid that, the strongest link between T_a and T_{mrt}, has been accounted for in the present analysis by the two-step modelling approach (Figure 4.4). For the other variables a dependent sampling strategy using the methods suggested by e.g. Kucherenko et al. (2012) and Zhang et al. (2015a) could be used to avoid unrealistic combinations of the meteorological variables.

The meteorological conditions selected in this study correspond to the climatological conditions experienced in the mid-latitude city of Hamburg. Due to its climatological location almost no heat stress due to restriction in heat loss by sweating in combination with restrictions in sensible heat loss are experienced. This can be seen in the full-space analysis, where the samples have been selected according to their probability of occurrence. In contrast, in the edge-based method, very high humidity levels in combination with high temperatures are simulated (Figure 4.2), higher sensitivities of the indices to humidity are calculated. Therefore, if the full-space analysis would be performed for a location in the tropics with high frequencies of combinations of high temperature and high humidity levels, higher variance-based sensitivities to water vapour are expected. Hence, one can conclude that for moderate warm conditions UTCI and PET_{env} are not sensitive to humidity, but for even warmer conditions the process of heat loss limitations by sweating is well included. In contrast PET_{vdi} seems to be insensitive to humidity regardless of the temperature input range.

The present analysis was carried out only for average radiation days in summer in winter. For days and locations with larger shortwave radiation even higher sensitivities to built-environment-related variables are expected and smaller one for lower radiation amounts or cloudy conditions. For the edge-based sensitivity analysis both cloudy and cloudless conditions are investigated. Therefore, the determined sensitivities to T_{mrt} are not expected to differ as much as the sensitivities to the built-environment-related variables for other regions. Since the regression version of UTCI is only applicable for $0.5 \leq FF_{10} \leq 17\ \mathrm{m\,s^{-1}}$ (ISB Comission 6, 2012), the meteorological input space has been reduced accordingly for all thermal indices to use comparable conditions for all thermal indices. Therefore, for very small or large wind speeds the sensitivity might be different. Additionally, also for the look-up-table version of UTCI different results might be obtained.

The sensitivity of $\mathrm{PET_{env}}$ has been investigated only within the edge-based analysis and thus the results are less robust than those for $\mathrm{PET_{vdi}}$. Since the two versions of PET calculate very different values in certain meteorological situations (Section 4.3.1), in applications it should be clearly indicated, which version is used. Additionally, the unexpected behaviour of decreasing PET^* values with increasing work metabolism in cold conditions should be further investigated and corrected. The small sensitivities of PET^* to the other personal variables is related to the simplified inclusion of the influence of the personal variables on the thermo-physiological processes in MEMI. Therefore, for more complex thermo-physiological models the sensitivity to changes in personal variables might be greater.

4.4.2 Required input accuracy

The sensitivity indices indicate whether and how strong an input variable influences the resultant thermal index I_t. However, also the accuracy required for the different input variables in order to calculate the thermal indices with a specific accuracy can be derived. This is relevant to derive how certain calculated thermal indices are, if the input variables are not known very accurately. For the present analysis the accuracy requirements to calculate the thermal indices within 1 kelvin is investigated.

Since the sensitivity indices are non-dimensional, they cannot be used directly to derive the required input accuracies. Instead two different methods are used to derive them from the edge-based and full-space analyses results. For the edge-based analysis, the determined regression coefficients (s_i, Eq. (4.2)) for each variation k along the edge of the hyper-cuboid can be used to derive the required accuracy of input i to calculate the thermal index with an accuracy of 1 K by

$$Acc_i(k) = \frac{1\ \mathrm{K}}{s_i(k)} \tag{4.12}$$

For the full-space sensitivity results the elementary effects ($EE_{i,m}$) for the different times of the day (t) can be used:

$$Acc_i(t) = \frac{1\ \mathrm{K}}{\frac{EE_{i,m}(t)}{\Delta x_i}} \tag{4.13}$$

For both methods both median and maximum accuracy are derived for the edge-based sensitivity analysis with respect to all cases (k) and for the full-space analysis with respect to all hours (t). Additionally, the median absolute derivations over all cases (Eq. (4.12)) or hours (Eq. (4.13)) have been derived, to determine how much the accuracy results differ for the different cases. Table 4.9 summarise the maximum required input data accuracy. The median required accuracies are shown Table G.1 in the Appendix.

Table 4.9: Maximum input data accuracy required to calculate Physiological Equivalent Temperature (PET*) with versions ENVI-met (PET_{env}) and VDI (PET_{vdi}) and the Universal Thermal Climate Index (UTCI) with an accuracy of 1 K. Summer and winter accuracies are given derived from the regression-based ('Regr', Eq. (4.12)) and the elementary-effect-based (EE, Eq. (4.13)) sensitivity analysis. Mean results have been derived for the regression-based accuracies as average over all edges of the hyper-cuboid and for the elementary-effect-based method as average over all times of the day. The median absolute derivations (±) are derived according.

	$\text{PET}^*_{\text{env}}$		$\text{PET}^*_{\text{vdi}}$				UTCI				Range
	Summer	Winter	Summer		Winter		Summer		Winter		
	Regr	Regr	Regr	EE	Regr	EE	Regr	EE	Regr	EE	
T_a [K]	0.8 ± 0.2	1.0 ± 0.2	0.8 ± 0.3	1.0 ± 0.06	1.0 ± 0.2	1.2 ± 0.08	0.5 ± 0.3	1.2 ± 0.1	0.7 ± 0.3	1.2 ± 0.06	
e [hPa]				13 ± 1.6		6.0 ± 0.7		4.7 ± 1.7		2.5 ± 0.1	
RH [%]	5.1 ± 6.6	57 ± 133	67 ± 242		80 ± 893		5.0 ± 20		23 ± 18		
FF_{10} [m/s]	1.6 ± 1.8	1.3 ± 1.6	1.6 ± 1.2	1.0 ± 0.6	1.3 ± 1.7	2.0 ± 0.4	0.4 ± 0.05	0.7 ± 0.2	0.3 ± 0.2	0.4 ± 0.03	
T_{mrt} [K]	1.9 ± 0.8	2.1 ± 3.2	1.9 ± 1.5		2.1 ± 3.3		2.5 ± 1.5		3.0 ± 0.2		
h_p [m]	0.10 ± 0.9	0.2 ± 0.8	0.3 ± 1.9	1.1 ± 0.3	0.2 ± 0.9	0.4 ± 0.01					1.5–2.0
m [kg]	8.1 ± 70	14 ± 87	23 ± 122	93 ± 26	14 ± 48	32 ± 0.5					50–100
A [y]	12 ± 128	42 ± 57	49 ± 125	172 ± 37	43 ± 19	78 ± 1.1					16–100
gn []				5.8 ± 1.2		4.9 ± 0.10					1– 2
I_{clo} [clo]	0.2 ± 0.6	0.2 ± 0.7	0.2 ± 0.9	0.4 ± 0.07	0.2 ± 0.8	0.6 ± 0.04					0.1–2.0
M_w [W]	14 ± 40	12 ± 35	14 ± 101	62 ± 22	12 ± 32	26 ± 0.2					0–300
H [m]				5.0 ± 3.2		8.8 ± 11		5.9 ± 2.5		5.4 ± 5.1	0–40
W [m]				7.3 ± 11		20 ± 55		9.1 ± 10		12 ± 16	5–50
ω_s [°]				18 ± 5.4		41 ± 9.7		22 ± 5.5		25 ± 5.2	0–180
a []				0.2 ± 0.2		0.9 ± 0.5		0.3 ± 0.3		0.7 ± 0.3	0.2–0.6
ε []				0.05 ± 0.01		0.2 ± 0.01		0.1 ± 0.02		0.2 ± 0.01	0.85–0.95
x_{rel} []				0.2 ± 0.3		0.3 ± 3.2		0.2 ± 0.3		0.2 ± 0.8	0.1–0.9

For determining the thermal indices with an accuracy of 1 K, air temperature has to be known with an accuracy of about 1 K (Table 4.9 and G.1). This is a robust result since the accuracy differs only slightly between the different methods and for median and maximum calculations. Humidity has to be known only roughly: if only the direct impact of humidity on the thermal indices is considered – as done in the edge-based analysis – the highest accuracy in relative humidity is required in summer with about 5 %; variations are large. The accuracy demands are smaller in winter. In the full-space analysis the vapour pressure directly affects the thermal indices but also T_{mrt} as it is used for the parameterisations of longwave radiation from the sky in SURM. This effect seems to dominant in winter, since higher accuracy requirements are determined for winter than for summer. The accuracy requirements for wind speed vary greatly between the indices: UTCI requires an accuracy of about 0.3 $\mathrm{m\,s^{-1}}$ in winter, which can hardly be reached by measurements or ORM simulations. For PET values with an accuracy of about 1 $\mathrm{m\,s^{-1}}$ are sufficient, which is achievable. The requirements for T_{mrt} have been derived from the edge-based sensitivity analysis. The results indicate that for the two seasonal representative radiation days, T_{mrt} has to be known with an accuracy of about 2 K.

The accuracy requirements for the personal variables indicate that gender, age, height and weight have not to be known to derive PET* with an accuracy of 1 K. In contrast, clothing insulation in both seasons and work metabolism in winter have to been known relatively accurate (I_{clo} within 0.2 clo and M_w within ($\mathcal{O}(10)$ W)). Since the last is so relevant it should again be stressed that the decreasing PET values with increasing work metabolism should be investigated and corrected.

In winter the accuracy requirements for albedo and emissivity exceed the varied range of the parameters indicating that those are unimportant during this season. The position of the person within the street canyon (x_{rel}) has to be known quite accurately (within $0.2 \cdot W$), since huge differences exist between shaded and unshaded areas in summer. Building height and street widths have to be known with an accuracy of about 5 m and 7 m, respectively. Those determined values are less accurate than those determined by Schoetter et al. (2013) for the mesoscale in summer to calculate the thermal index $\mathrm{PT_J}$ with an accuracy of 1 K, which might be due to the different simulation days chosen. The requirements for the built-environment-related variables are likely smaller in overcast situations as indicated by smaller sensitivities during the night.

If not actual values for the thermal indices but thermal stress classes are of interest, the accuracy requirements for all variables are likely higher, since a small change in one variable might cause a class change due to the discrete scale. Additionally, the accuracy requirements might change, if in addition to the effects of buildings on the radiation field other urban effects are considered. To consider for instance the effect of flow channelling by buildings or surface albedo effects on air temperature, a full ORM could be applied as discussed in the next section (Section 4.4.3).

4.4.3 Indications for urban planning and obstacle resolving models

The results of this chapter indicate that the most effective way to change thermal conditions at a specific location is to alter air temperature, since both indices investigated are very sensitive to it. However, air temperature cannot be influenced as easily as radiation and wind (Barry and Blanken, 2016). Since all indices are also sensitive to those variables, modifying those parameters could also be used to create thermally comfortable conditions. Based on this study the modification of a shaded area by, for instance, changing building height is the most effective measure to change T_{mrt}. Higher buildings would also decrease wind speed and thus reduce cold stress in winter (Molenaar et al., 2015). However, the access to sun light is also an important aspect of quality of life and should not be entirely disregarded to favour thermally comfortable designs. Furthermore, one has to keep in mind that in urban systems many processes are coupled (von Szombathely et al., 2017) and thus an increase in aspect ratio may cause more traffic jams and thus longer exposure times to uncomfortable conditions (Hoffmann et al., 2018).

Changes for albedo and emissivity also show an effect on T_{mrt} (maximum changes due to variation in albedo in this study where 8 K), but these changes are much smaller compared to the effect of shading, which is in line with results obtained by Andreou (2013) and Schrijvers et al. (2016). The influence of albedo could increase slightly if multiple reflections would be accounted for in SURM as done in the model applied by Schrijvers et al. (2016). Since in the present study only considered the influence of buildings on the radiation field with SURM, the effects of the built-environment on other meteorological variables could not be accounted for. For instance, a change in albedo not only influences T_{mrt} but also air temperature, which might increase the sensitivity of the thermal indices to albedo. However, previous studies (e.g. Schrijvers et al., 2016) suggest that when both effects are considered the increase in T_{mrt} exceeds the positive effect of reduced air temperature. To investigate those effects in detail a full Obstacle Resolving microscale model (ORM) could be applied, which could be also used to consider more complex urban morphologies e.g. crossings, asymmetrical canyons or street-trees as those factors may influence the required input accuracy.

For the development of such obstacle resolving models the present study indicates that in addition to air temperature and average wind speed the radiative fluxes have to be accurately simulated in order match the required accuracy of the input variables to calculate thermal indices with an accuracy of 1 K.

5 Extending MITRAS for modelling human thermal environments

With the knowledge of the sensitivities of the selected thermal indices (Chapter 4), they can be applied in an Obstacle Resolving micro-scale model (ORM) to study the influence of urban water surfaces on the thermal environment in a city. In this thesis, the Microscale Transport and Stream model MITRAS is used, since on the one hand it has been shown to fulfil the test cases of the Association of German Engineers (VDI) guidelines (VDI, 2005) for obstacle resolving micro-scale models (Grawe et al., 2013) and on the other hand the source code of MITRAS is documented and available (Salim et al., 2018), which allows to extend the model and include the missing features for modelling human thermal environments in urban areas. Within this thesis the radiation parameterisation of MITRAS was extended to account for important effects of buildings and vegetation on radiation as described in Section 2.2.2 (Section 5.2), since the sensitivity analysis indicated that the thermal indices are sensitive to T_{mrt} (Chapter 4). The entire model system consisting of pre- and post-processors has been extended to easily calculate thermal indices from MITRAS model output (Section 5.3). A new pre-processor is developed that creates based on desired building types, street widths, areas of specific surface cover classes and vegetation, an idealised domain. Details on the preprocessor PREMASK (PREMASK) are given in Appendix I.

As a basis for those extensions, Section 5.1 describes the general characteristics of MITRAS, the representation of water surfaces, the treatment of explicit obstacles and the initialisation procedure. The radiation parameterisations are introduced along with the further developments in Section 5.2.1. Further details are summarised in Appendix H, Schlünzen et al. (2012b) and Salim et al. (2018). The chosen parameterisations for this thesis are listed in Appendix K.

5.1 Obstacle resolving model MITRAS

MITRAS is a 3-dimensional, non-hydrostatic, prognostic numerical model based on the fundamental principles of conservation for momentum, mass and heat, water or other tracers. It was initially developed in the Tropospheric Research Program (TFS) (Schlünzen et al., 2003) and has been applied so far both to non-urban environments, e.g. biogenic emissions in a forest (Schlüter, 2006) and wind turbines (Linde, 2011), and to urban environments, e.g. to investigate the role of urban trees (Salim et al., 2015), pollutant dispersion (Schlünzen et al., 2003) or the thermal effects of a single isolated building (Gierisch, 2011).

To represent atmospheric conservation processes, MITRAS employs the Navier-Stokes equations, the continuity equation and the conservation equations for scalar properties together with the ideal gas law and the equations for potential temperature, which form a closed set of equations. To reduce computational costs, the equations are not solved directly but filtered by the Reynold's averaging method that integrates the equations in space and time (Schlünzen et al., 2012b). Those Reynolds-Averaged-Navier–Stokes equations (RANS) are further approximated by the anelastic, the Boussinesq and the domain constant Coriolis parameter approximation to reduce the computational costs without neglecting important details (Appendix H). The filtered and approximated equations are discretised and solved numerically on the Arakawa-C-grid to accurately represent divergences using different numerical schemes for the meteorological quantities (see Schlünzen et al., 2012b; Salim et al., 2018 for details). MITRAS employs an orography-following coordinate system by transforming all model equations from the Cartesian coordinate system to a non-orthogonal coordinate system. This transformation is advantageous for numerical calculation, since the lowest model height corresponds to the ground of the model area. MITRAS supports non-uniform grids both vertically and horizontally to resolve interesting areas in detail but still keeping computational costs to a minimum.

To represent the effect of different ground surfaces on the atmosphere, surface sub-grid scale fluxes for momentum and scalar quantities are used by employing the surface layer similarity theory by Monin and Obukhov (Schlünzen et al., 2012b, p. 18). Within this theory, the turbulent fluxes are described by typical scaling values: u_* for momentum and χ_* for scalar quantities such as temperature (ϑ_*) and humidity (q_*) as described in Appendix H.5. If more than one surface cover class (SCC) is present in a grid cell, the quantities have to be averaged and weighted according to their proportion in the grid cell. For that the parameter averaging method is employed in the current study, since for a resolution of $\mathcal{O}$(m) sub-grid scale variations in surface cover are small (Appendix K).

The most important SCC for this thesis is water, since its effects within an urban area are investigated. Due to its particular properties (Section 6.1), water physically differs from other SCCs and is therefore treated differently compared to other SCCs (Section H.5). For water surfaces, a constant surface temperature is assumed in MITRAS. This is a valid assumption, since for well mixed water bodies, the surface temperature changes little within one day. Figure 5.1 shows the mean diurnal cycle of $T_{\mathrm{wat}} - \overline{T}_{\mathrm{wat}}$ for different seasons (colours) for the lake Alster (Figure 5.1a) and for the river Elbe (Figure 5.1b) averaged over the period 01.01.2002 to 31.12.2017. Standard deviation bounds are shaded and based on 10-minutes average values. The locations of the stations are shown in Figure M.2. Days with at least one missing value have been excluded. Note that for averaged diurnal cycles deviations differ between 00:00 and 23:50 due to days with increasing or decreasing temperature throughout the day. The water temperature of Elbe and Alster changes within one summer day on average by ±0.1 K to ±0.3 K, respectively. Changes in other seasons are smaller, diurnal cycles in winter are well below ±0.11 K on average. Compared to other surfaces, these changes are small and therefore a constant water temperature can be assumed.

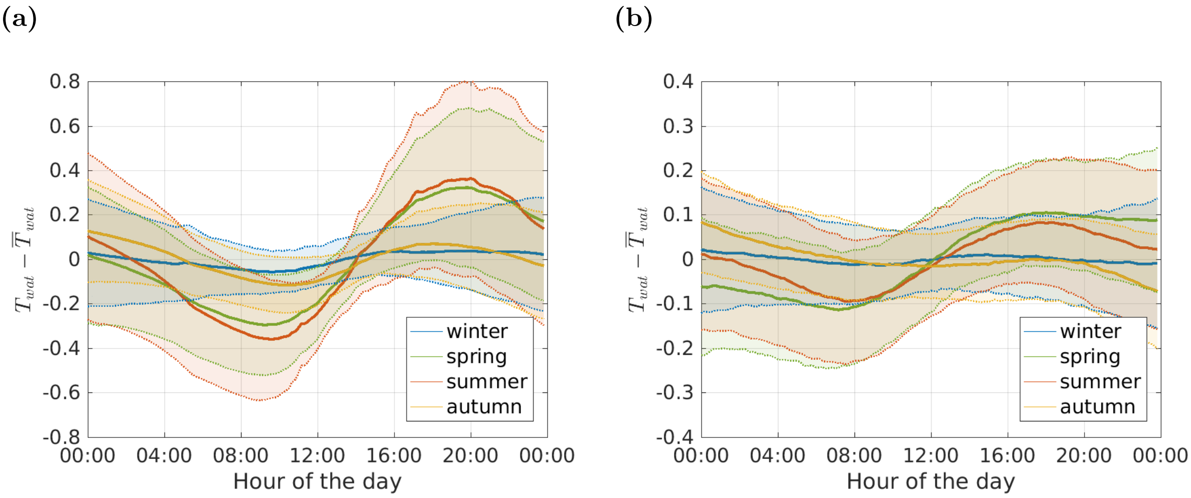

Figure 5.1: Mean diurnal cycle of the deviations of the water temperature (T_{wat}) in a depth of about 1 m from the daily mean ($T_{\mathrm{wat}} - \overline{T}_{\mathrm{wat}}$) for winter (blue), spring (green), summer (red) and autumn (orange) for ((a)) the lake Alster (station Lombardsbrücke) and ((b)) the river Elbe (station Seemanshöft). Values are averaged over the period 01.01.2002 to 31.12.2017 with standard deviation bounds shaded.

The albedo of water surfaces changes depending on the zenith angle (Θ) of the sun:

$$a_{\text{wat}} = \min \begin{cases} \max \begin{cases} -0.0139 + 0.0467 \cdot \tan\Theta \\ 0.03 \end{cases} \\ 0.999 \end{cases} \tag{5.1}$$

a_{wat} is small during midday and large during morning and evening (Figure 5.2, light blue). Since the water temperature is held constant throughout the day, the non-reflected part of the radiation is lost. The reflected radiation is added to the same grid cell, although water surfaces reflect specularly, i.e. mirror-like. The effect of this simplification is discussed within in Section 5.2.3.

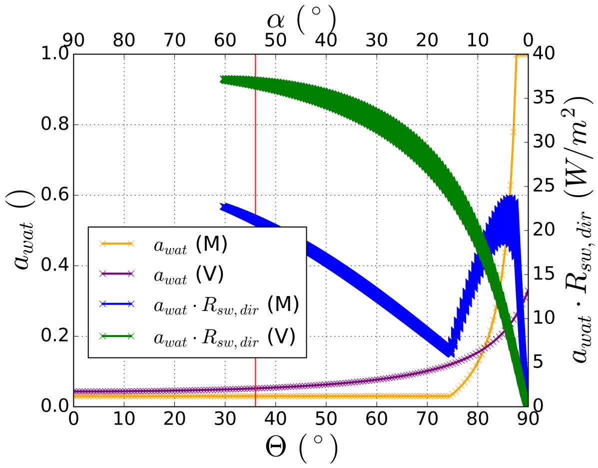

Figure 5.2: Albedo of water surfaces (a_{wat}, orange and purple, left y-axis) and reflected radiation flux density ($a_{\text{wat}} \cdot SW_{dir}$, blue and green, right axis) for different zenith angles (Θ, lower x-axis) and corresponding elevation angles (α, upper x-axis) for the parameterisation used in MITRAS (denoted M, orange and blue) and a parameterisation of VDI (1994) (denoted V, purple and green). The red line highlights an elevation angle of 53°.

Compared to a parameterisation in the VDI guideline (VDI, 1994) (Figure 5.2, purple), higher values for a_{wat} are calculated in MITRAS (orange) during the morning and smaller values for $\Theta < 80°$. For the atmosphere, the amount of reflected radiation is of interest. To estimate the reflective radiative flux during the course of a year for ϕ=53°, SURM is used with the 'MITRAS' parameterisation option for about one minute resolution. Compared to incoming radiation, the reflected radiation is small (Figure 5.2, blue and green). During most part of the day only 3 % of the incoming radiation is reflected and during the remaining times incoming radiation amount is small. Although the general course of a_{wat} is similar in both parameterisations, the parameterisation in MITRAS (blue) leads to a non-monotonic reflected radiation. The parameterisations should be compared to measurements to decide, which parameterisation option is better. For this thesis the 'MITRAS' parameterisation option is kept.

The roughness length of water surfaces depends on the wind velocity, since the surface roughness increases with swell. In MITRAS the momentum roughness length of water surfaces is calculated following Clarke (Schlünzen et al., 2012b, p. 22):

$$z_{0,\mathrm{water}} = \max \begin{cases} 0.0185 \cdot {u_*}^2/g \\ \min \begin{cases} 7 \cdot 10^{-5}\ \mathrm{m} \\ \max \begin{cases} 0.032 \cdot {u_*}^2/g \\ 1.5 \cdot 10^{-5}\ \mathrm{m} \end{cases} \end{cases} \end{cases} \tag{5.2}$$

The different properties of the SCC (Schlünzen et al., 2012b) enable to account for the effect of smaller obstacles (e.g. grass) on the meteorological quantities. Larger obstacles such as buildings, vegetation and wind turbines can be resolved explicitly in MITRAS (Salim et al., 2018). Within this thesis only buildings and vegetation are used.

Buildings

Buildings are represented in MITRAS by the mask method (Salim et al., 2018): impermeable grid cells defined by weighting factors `vol`, `weight_x`, `weight_y`, `weight_z` (Figure 5.3) are placed at the location of buildings using the preprocessor GRIMASK (Salim et al., 2018). `vol` describes the atmospheric volume fraction of the grid cell, whereas the `weight`-variables describe the atmospheric surface fraction of the grid cell. The two structures are used for the blocking approach as factor within the equation for scalar and vector quantities, due to the Arakawa-C-grid (Salim et al., 2018). Building surfaces next to scalar grid points (brown cells in Figure 5.3) are defined by type (1: east or west, 2: north or south and 3: roof) and direction (e.g. 1: east and -1 west) to account for the internal boundary effect of building surfaces.

The building surface temperature influences the ambient air temperature due to a sensible heat flux, which is represented by a source or sink term (Q_Θ) in the equation for turbulent fluxes of heat (Eq. (H.12)):

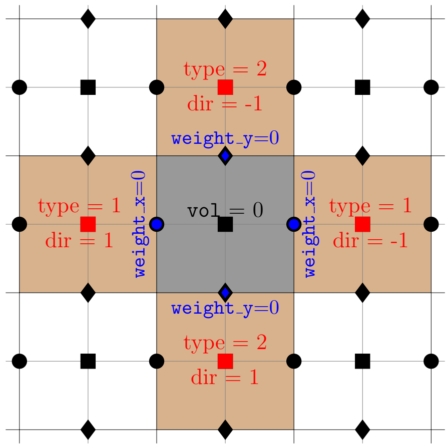

Figure 5.3: Representation of a building (grey) on an Arakawa-C-grid using the weighting factors. Scalar grid points are shown as ■, vector grid points in x-direction are shown as ● and vector grid points in y-direction are shown as ◆. Atmospheric grid cells adjacent to a building are shown in brown with their surface cell characteristics in red.

$$Q_\Theta = -u_*^b \vartheta_*^b = \kappa \frac{|v_b|}{\ln\left(\frac{d_b}{z_{0,b}}\right)} \cdot \kappa \frac{(\overline{\Theta}_{d_b} - \Theta_b)}{\ln\left(\frac{d_b}{z_{0,b,\Theta}}\right)} \tag{5.3}$$

with the friction velocity u_*^b, the scaling variable for potential temperature ϑ_*^b, the roughness length for momentum $z_{0,b} = 10^{-3}$ m and temperature, $z_{0,b,\Theta}$, the wind speed parallel to the building wall at the adjacent atmospheric grid cell, v_b, the distance between building and scalar grid cell, d_b and the von Karman constant, κ. The building surface temperature of an infinitesimal slab of the façade, T_b is calculated from

$$\frac{\partial T_b}{\partial t} = \frac{1}{c_w D}\left[SW_{net} + \underbrace{LW\downarrow - \varepsilon\sigma T_b^4}_{LW_{net}} + \underbrace{c_p \rho u_*^b \vartheta_*^b(T_b)}_{Q_H} - \underbrace{C(T_b - T_{\mathrm{room}})}_{Q_{\mathrm{cond}}}\right] \tag{5.4}$$

where SW_{net} and LW_{net} denote the shortwave (Eq. (5.6)) and longwave radiation balance (Eq. (5.7)), Q_H the sensible heat flux density and Q_{cond} the conductive heat flux through building wall to indoor air. c_w is the volumetric heat capacity of the building wall and D is the wall thickness (Table K.2). C is the heat transfer coefficient of the building wall. Latent heat fluxes are neglected in MITRAS, which is a valid assumption if walls are not watered or vegetated.

Eq. (5.4) is similar to Eq. (D.24) in SURM but considers sensible heat fluxes from buildings to air more sophisticated and, most importantly, considers a time-dependence in Eq. (5.4). Therefore, it accounts for the effect of heat storage. Eq. (5.4) is solved using an implicit scheme (Salim et al., 2018):

$$
\begin{aligned}
&{T_b}^{t+\Delta t} = {T_b}^{t} \\
&+ \frac{SW_{net} + LW\downarrow - \varepsilon\sigma {T_b}^{t4} - c_p \rho u_*^b \frac{\kappa}{\ln\left(\frac{d_b}{z_{0,b,\Theta}}\right)} \left({T_b}^{t}\left(\frac{100000}{p}\right)^{R_0/c_p} - \overline{\Theta}_{d_b}\right) - C({T_b}^{t} - T_{\mathrm{room}})}{\frac{c_w D}{\Delta t} + C + 4\varepsilon\sigma {T_b}^{t3} + c_p \rho u_*^b \frac{\kappa}{\ln\left(\frac{d_b}{z_{0,b,\Theta}}\right)} \left(\frac{100000}{p}\right)^{R_0/c_p}}
\end{aligned} \tag{5.5}
$$

The shortwave radiation balance at wall surfaces, SW_{net}, is calculated during the day from Eq. (5.6), in which the diffuse radiation is weighted by a sky view factor ($VF_{w\to s}$):

$$
SW_{net} = (1 - a_w) \cdot SW_{diff} \cdot VF_{w\to s} + \begin{cases} 0 & \text{shaded} \\ (1 - a_w) \cdot SW_{dir} \cdot \cos(\eta_i) & \text{unshaded} \end{cases} \tag{5.6}
$$

In the original version, before the further developments in this thesis, $VF_{w\to s}$ was set to 0.5 for all walls and to 1 for roofs. Hence, originally MITRAS treated buildings as isolated. Shading and inclined surfaces ($\cos(\eta_i)$) are accounted for as described in Section 5.2.1.1. The sky view factor is also used to account for the fraction of incoming longwave radiation: half of the longwave radiation originates from the ground and the other half from the sky:

$$
LW_{net,w} = (1 - VF_{w\to s}) \cdot \varepsilon\sigma T_g^4 + VF_{w\to s} \cdot \varepsilon\sigma T_{a,k}^4 \cdot (a - b \cdot 10^{-c\cdot e_{a,k}}) \tag{5.7}
$$

Since a wall grid cell receives longwave radiation from several ground cells with potentially different surface temperatures, MITRAS weighs several ground surface cells to calculate the effective T_g in Eq. (5.7). These weighting factors weigh (a) cells closer to the walls higher than cells further away and (b) cells with an acute angle higher than cells with an obtuse angle (Gierisch, 2011). For the calculation of the weighting factors cells are treated as point-like emitters not accounting for the area of the cells. Both the weighting factors and $VF_{i \to s}$ have been changed in this thesis to account for radiative surface-surface interaction (Section 5.2.3).

Vegetation

Vegetation is also explicitly modelled in MITRAS. Instead of resolving individual leafs, which would require a very fine grid, the principle structure of a tree is resolved. Smaller scale tree effects on the flow field are parameterised from the porous media or viscosity approach (Schlüter, 2006; Salim et al., 2015, 2018). The fine scale structures of vegetation are represented by the Leaf Area Index (LAI), which describes the area of the leafs per ground surface area, and the Leaf Area Density (LAD), which describes the area of the leafs per volume of air. These two parameters are linked by:

$$LAD(z) = LAI(z+1) - LAI(z) \tag{5.8}$$

The effect of vegetation on temperature is parameterised by the vertical flux divergence of shortwave radiation, since vegetation reduces penetrating direct shortwave radiation:

$$Q_{\Theta} = \frac{1}{\rho c_p} \frac{\partial SW_{net}}{\partial z} \tag{5.9}$$

The reduction is parameterised by

$$\tau(z) = e^{-0.5 \cdot LAI(z)}. \tag{5.10}$$

The factor -0.5 is empirically chosen based on literature (Schlüter, 2006). The reduction of direct solar radiation is included in the original version per column. Partial shading of grid cells adjacent to vegetated grid cells was not accounted for and is newly introduced in this thesis (Section 5.2.4).

Initial data and initialisation

To apply MITRAS four steps are necessary: (1) Creation of the model domain with the preprocessor GRIMASK, (2) definition of initial conditions, (3) generation of one-dimensional initial profiles using a one-dimensional version of MITRAS and (4) application of the profiles to the three-dimensional domain for model initialisation. Steps (1) and (3) are modified within this thesis. GRIMASK for calculation of view factors for radiation as explained in Section 5.2 and Section 5.3. The one-dimensional version of MITRAS to derive solar input fluxes for shallow model domains (Section 5.2.2.1).

As input for a one-dimensional version of MITRAS, initial values of air temperature, relative humidity, large scale wind, stratification and pressure at initialisation time have to be defined (step 2). Additionally, initial values for soil and water temperature representing averages of a few days around the initialisation day have to be prescribed, which are used as boundary values for the temperature calculation. Those initial and boundary values are used together with the model domain from GRIMASK to generate balanced background and initial profiles for the three-dimensional model. This is done by the following procedure: assuming hydrostatic equilibrium, a layer-wise constant temperature gradient and the ideal gas law, profiles for pressure, potential temperature and density are determined. Within the one-dimensional model, the wind profiles are integrated until stationarity without considering changes in the scalar quantities. To account for dry periods before the initialisation, after stationarity is achieved for the wind profiles the model is integrated further until the defined number of drying days are reached. For that, temperature and humidity are calculated with a time-dependent energy balance at the ground. If drying days are needed, the balanced profiles for wind and the initial profiles for temperature and humidity are kept to initialise the 3-dimensional model. The changed surface values due to the dry period are used as initial values for the three-dimensional model calculations.

In step 4, the one-dimensional stationary profiles are expanded horizontally homogeneous over the three-dimensional model area by initially neglecting all orography. The orography heights increase during the initialisation phase of the three-dimensional model using the diastrophism method (Schlünzen et al., 2012b). After several thousand integration time-steps the model can be assumed to independent from the initialisation. For the microscale simulation this takes only a few minutes due to the very small model time step (well below one second).

5.2 Extension of the radiation parameterisations

In MITRAS two radiation parameterisations are available. In the two-stream approach upward and downward propagating radiative fluxes are solved for each grid cell in the model domain (Figure 5.4a) to calculate a change in potential temperature within the atmosphere (Eq. (5.11)). Neighbouring columns do not interact (black and grey arrows in Figure 5.4a), since radiation is exchanged only vertically and therefore all transmitted or diffuse reflected shortwave or longwave radiation is either upward or downward.

$$\left.\frac{\partial\overline{\Theta}(k)}{\partial t}\right|_{\text{rad}} = \frac{SW\downarrow(k+1) - SW\downarrow(k) + SW\uparrow(k-1) - SW\uparrow(k)}{c_p\rho dz} + \frac{-LW\downarrow(k) + LW\downarrow(k+1) - LW_{\uparrow}(k) + LW_{\uparrow}(k-1)}{c_p\rho dz} \tag{5.11}$$

In the vertically integrated approach, radiation fluxes are not calculated explicitly within the atmosphere. Instead the effect of absorption and scattering of longwave and shortwave fluxes within the atmosphere are parameterised to estimate the incoming and outgoing fluxes at the ground (Figure 5.4b). The temperature change within the atmosphere is parameterised by using (Eq. (5.12)). Hence, this scheme is similar to the Simple Urban Radiation Model (SURM) described in Chapter 3.

$$\left.\frac{\partial\overline{\Theta}(z)}{\partial t}\right|_{\text{rad}} = -\frac{\Theta_{\text{loss}}}{86400}\cdot e^{\frac{-(\eta-z_0)}{600}} \tag{5.12}$$

with $\Theta_{\text{loss}} = 2$ K during day time and 3 K during night time.

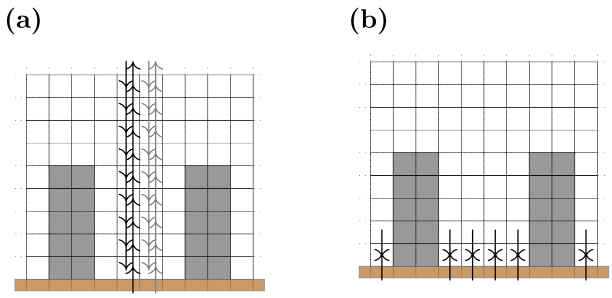

Figure 5.4: Sketches of the two radiation parameterisations: (a) the two-stream approach and (b) the vertically integrated approach. Grey grid cells symbolise buildings.

At the begin of this thesis, the two radiation parameterisations were not consistent in the model (Table 5.1): Shading is not considered in the two-stream approach, whereas shading by buildings is accounted for in the vertically integrated approach (Eq. (5.21)). Diffuse radiation, which is essential for the calculation of T_{mrt} (Chapter 3), does not exist in the two-stream approach. However, the two-stream approach takes into account the reduction of shortwave radiation by vegetation, can calculate incoming radiation for all heights and is overall physically more sound. Therefore, within this thesis the two-stream approach is extended to account for the presence of buildings including radiative surface-surface interaction to better represent the urban heat island effect (Section 2.2.2) and partial shading of vegetation. Figure 5.5 schematically shows the initial situation (Figure 5.5a,c,e) and the final model (Figure 5.5b,d,f). The outline of the extensions is given here, details will be given in Section 5.2.2 to Section 5.2.4.

Table 5.1: Comparison between the two radiation schemes used in MITRAS with respect to the of relevant aspects for modelling the human thermal environment.

	Two-stream approach	Vertically integrated approach
Effect by obstacles		
- vegetation	shortwave radiation reduced Eq. (5.10); no shading of neighbouring grid cells	Not considered
- buildings	Not considered	Shading of ground considered (Eq. (5.21))
Effect on obstacles	Not considered	
- Buildings	Not considered	$LW_s(k=0)$ and $SW\downarrow(k=0)$ for walls at all model heights; longwave effect of ground on walls (Section 5.1, Section 5.1)
Diffuse radiation	Not considered	Considered, Eq. (D.10)
Domain height	200 m / 10 km	Not applicable
Inclined surfaces	Not considered	Considered, Eq. (5.20)

Since buildings were only accounted in the vertically integrated approach, downward shortwave radiation at ground had to be used for wall grid cells in all heights (Figure 5.5a). Inherent to the two-stream approach is a height dependence of radiation that is now used ($SW\downarrow(k)$, Figure 5.5b). An interaction of wall grid cells with ground cells was considered only for longwave radiation and only using a simplified view factor based on points without accounting for the grid cell area ($VF_{wi\rightarrow gj}$, Section 5.1, Section 5.1). The sky view factor of all vertical wall grid cells was $VF_{w\rightarrow s}$=0.5 and therefore, radiation exchange with other buildings was not considered. Those issues are resolved by implementing a sophisticated scheme to calculate view factors between wall and ground grid cells ($VF_{wi\rightarrow gj}$) and between wall grid cells ($VF_{wi\rightarrow wj}$), which leads to individual sky view factors for each surface cell ($VF_{w\rightarrow s}(k)$). Those view factors are applied not only to longwave radiation but also to diffusely reflected shortwave radiation (Section 5.2.3.3).

For shading the minimum elevation angle of the lowest grid cell above ground or building i, j ($\alpha_{\min}$) was used for all heights within a column above i, j ($\alpha_{\min} = c$, Eq. (5.21)); indicated by the shifted dashed line in Figure 5.5a. Therefore, building cells higher up received direct radiation at the same time as that lowest grid cell. To correct that, shading has been introduced to the two-stream approach (Section 5.2.3.1) with different minimum elevation angles for different heights ($\alpha_{\min}(k)$). Shading is not only applied at surfaces as before but also within the atmosphere. The newly introduced diffuse radiation (Section 5.2.2.2) ensures that shortwave radiation is received even in shaded areas.

For ground cells no wall view factors ($VF_{gi\rightarrow wj}$) were defined before this thesis (Figure 5.5c). Hence, for all ground cells an unobstructed sky was assumed ($VF_{g\rightarrow s}$=1). To correct this, within this thesis wall view factors for ground surfaces are introduced ($VF_{gi\rightarrow wj}$, Figure 5.5d).

A reduction of shortwave radiation by vegetation was included in the two-stream approach (Eq. (5.10), Figure 5.5e, Schlüter (2006)). However, no distinction was made between direct and diffuse radiation, all components were reduced. Additionally, the upward reflected radiation was reduced following the same equation. Thus, radiation increased with height below vegetation. These issues have been addressed by introducing diffuse radiation (Section 5.2.2.2), which is assumed to be unaffected by vegetation. Since all reflected fluxes, except those reflected by water surfaces, are assumed to be diffuse (Section 5.2.3.3), upward reflected radiation is unaffected by vegetation. To be able to account for a reduction of radiation for solar elevation angles other than 90°, partial shading by vegetation of a neighbouring grid cell has been introduced (Section 5.2.4). Thereby, direct solar radiation in beam direction is partially absorbed by leafs and therefore a reduced amount of direct radiation and reflected upward radiation exist in the shaded volume of vegetation (smaller orange arrows, Figure 5.5f).

Details on the extensions are described in Section 5.2.2 to Section 5.2.4. The validation of these extensions is shown in Section 5.2.5. As background information for these extensions, the two radiation parameterisations are introduced in Section 5.2.1 in the form used in Salim et al. (2018).

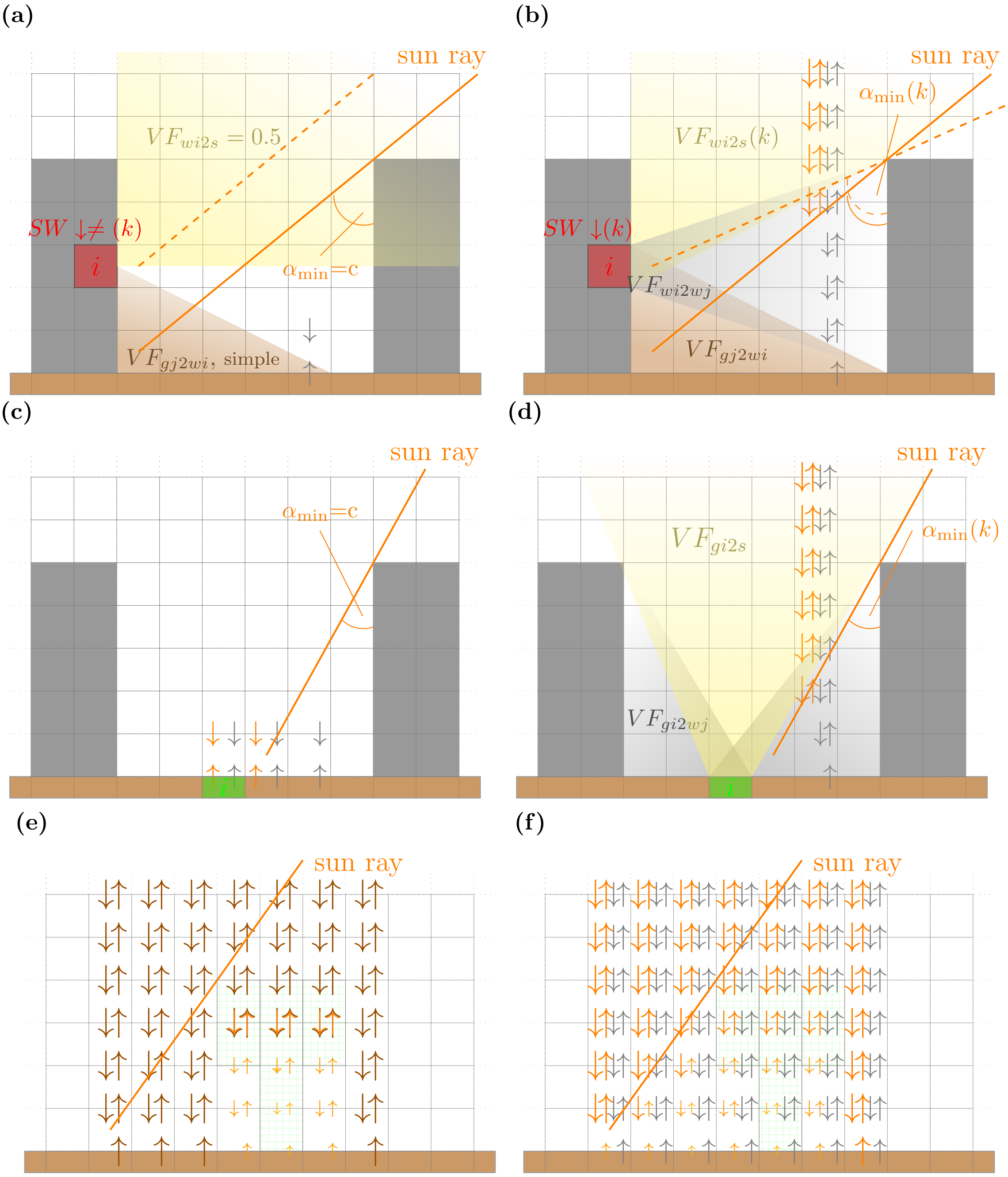

Figure 5.5: Sketch for (a), (b) radiation between buildings (grey), (c), (d)) with ground surfaces (brown) and (e), (f) with explicit vegetation (green). (a),(c),(e) show the status of MITRAS as in Salim et al. (2018) and (b), (d), (f) the extensions made in this thesis. View factors (VF) are indicated as shaded areas for sky (yellow), buildings (grey) and ground (brown). Radiation fluxes are shown as arrows in grey (diffuse), orange (direct) and brown orange (global, only (e)). Wall (red) and ground (green) grid cell i are exemplary surface cells. Minimum elevation angle ($\alpha_{\min}$) are indicated by orange lines.

5.2.1 Previous radiation parameterisations in MITRAS

5.2.1.1 Shortwave radiation parameterisations

Two-stream approach In the two-stream approach, the propagation of two radiation streams – one downward and one upward (black and blue in Figure 5.6) – is calculated from the same equation: transmitted (tr) shortwave radiation flux at each layer is calculated as a product of several transmission factors (T_A, T_L, T_V and T_R) to account for absorption and scattering by aerosols, liquid water and water vapour and Rayleigh scattering, respectively. For the upward flux in Eq. (5.13) a unity flux is used, i.e. $I_\infty = U = 1$ (Figure 5.6). At each layer, a fraction (a_r) of the downward (upward) propagating radiation is reflected upward (downward) ($a_r(k) \cdot I_\infty$ or $a_r(k) \cdot U \uparrow$).

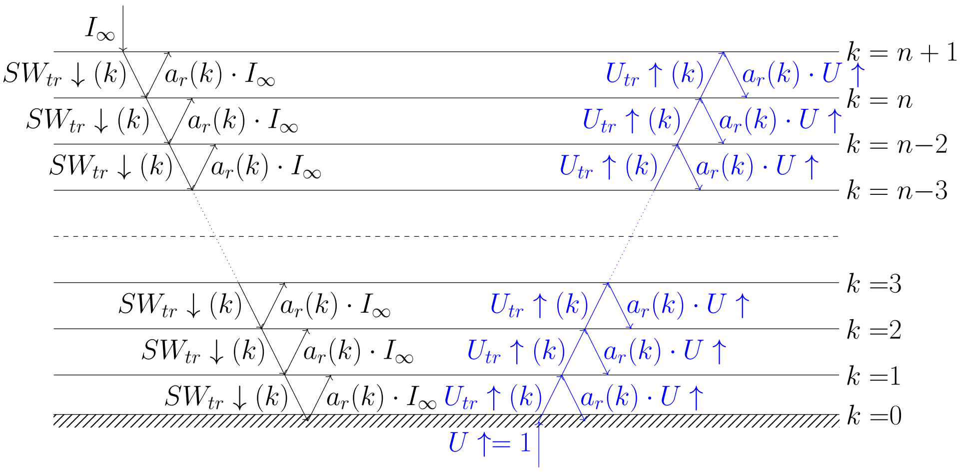

Figure 5.6: Sketch of downward (black) and upward (blue) shortwave fluxes and their respective reflected fluxes. Arrows are shown inclined to illustrate the reflection; radiation is actually treated as perpendicular to each model layer.

If clouds are present, transmission factors cannot be calculated for the entire shortwave spectral range. Therefore, the equation is solved for two ranges: visible range ($\lambda < 0.75$ µm, denoted 1 in the following) and a near infrared ($\lambda > 0.75$ µm, denoted 2 in the following). The solar constants of the two ranges are set to $I_{\infty 1} = 707\ \mathrm{W\,m^{-2}}$ and $I_{\infty 2} = 660\ \mathrm{W\,m^{-2}}$. Currently, the solar input fluxes at the top of the atmosphere are weighted by the zenith angle (Eq. (5.13)). However, such a weighting is only valid for solid horizontal surfaces and not for the atmosphere. This approach leads to an underestimation of the shortwave fluxes within the atmosphere and has been corrected within this thesis (Section 5.2.2.1).

$$SW_{tr} \downarrow (k) = I_{\infty} \cdot \cos(\Theta) \cdot T_A(k) \cdot T_R(k) \cdot T_L(k) \cdot T_V(k). \tag{5.13}$$

Most transmission factors are set to one in the model ($T_{R2} = T_{V1} = T_{A1} = T_{A2} = 1$). Therefore, no scattering or absorption by aerosols is included in the current parameterisation. In the visible range, only $T_{R1} \neq 1$ and $T_{L1} \neq 1$ and in the near infrared range $T_{V2} \neq 1$ and $T_{V2} \neq 1$. Scattering is parameterised in the visible range as $1 - T_{tot}$ and in the near infrared only scattering by cloud droplets are taken into account. Details on the calculation of the transmission factors can be found in Schlünzen et al. (2012b) or Bakan (1994).

The reflected fraction of shortwave radiation at each layer is derived from a reflectivity coefficient $a_r(k)$. $a_r(k)$ is an integral value that describes for the downward radiation flux an integral value from the ground ($\ell = 1$) up to layer k. For the upward radiation flux the flux from the model top ($\ell = K$) up to layer k for downward propagating radiation or from the ground up to layer k. Therefore, the total incoming reflected radiation at each layer is calculated from the reflectivity coefficient and the fluxes at the model top for downward radiation (I_{∞}) and ground for upward radiation ($U \uparrow$):

$$SW_{rf,tot} \uparrow (k) = \sum_{\ell=1}^{k} a_r(\ell) \cdot I_{\infty} \tag{5.14}$$

$$U_{rf,tot} \downarrow (k) = \sum_{\ell=K}^{k} a_r(\ell) \cdot U \uparrow \tag{5.15}$$

In addition to this single reflection, reflections of already reflected radiation are accounted for in the scheme. To do so, a correction factor is calculated: a fraction of reflected shortwave radiation at ground, represented by U, is reflected back to the ground at layer 1 (termed R in Figure 5.7). At the ground a fraction of R is reflected according to the ground albedo (a). A fraction of the radiative flux aR is then again reflected in the atmosphere ($R \cdot (aR)$) and at the ground ($(aR)^2$) and so forth. The total fraction of reflected radiation at the ground is therefore

$$1 + aR + (aR)^2 + ... = \sum_{0}^{\infty} (aR)^n = \frac{1}{1 - aR} \tag{5.16}$$

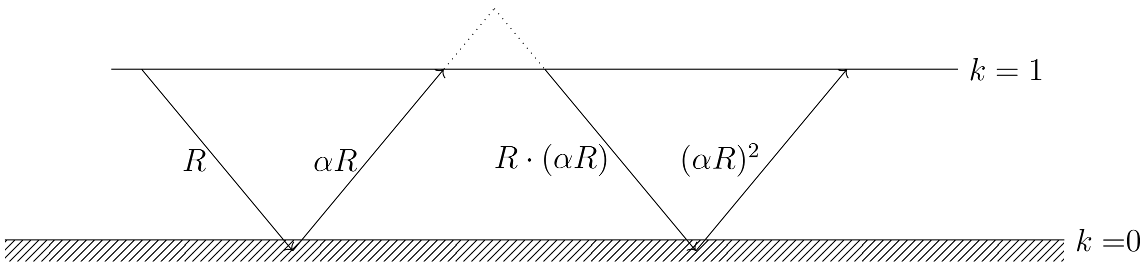

Figure 5.7: Multiple reflections in the two-stream approach. Arrows are inclined only for illustrative purposes; radiation is actually treated as perpendicular to each model layer.

Eq. (5.16) is used to correct the fluxes at each layer for multiple reflections:

$$f_a = \frac{a \cdot SW_{tr} \downarrow (k = 1)}{1 - a \cdot U_{rf,tot} \downarrow (k = 1)} \tag{5.17}$$

Using f_a, the total global radiation, $G(k)$, in beam direction is calculated in the model as

$$\begin{aligned} G(k) &= SW_{tr} \downarrow (k) & +f_a \cdot U_{rf,tot} \downarrow (k) \\ &= I_\infty \cdot \cos(\Theta) \cdot T_A(k) \cdot T_R(k) \cdot T_L(k) \cdot T_V(k) & +f_a \cdot U_{rf,tot} \downarrow (k) \end{aligned} \tag{5.18}$$

and similarly the upward reflected radiation flux from

$$SW \uparrow (k) = SW_{rf,tot} \uparrow (k) \quad +f_a \cdot U_{tr} \uparrow (k) \tag{5.19}$$

Vertically integrated approach The calculation of shortwave radiation of the vertically integrated approach is implemented and presented in SURM (Chapter 3) for direct radiation (Eq. (D.3)) and diffuse radiation (Eq. (D.10)). In contrast to SURM, MITRAS does not account for the annual cycle of I_∞ (Eq. (3.17)). Instead a fixed value of I_∞=1370 W m^{-2} is used.

Inclined surfaces are treated similar as in SURM (Eq. (3.20)), except that the definition of the azimuth angle in MITRAS is positive towards east and negative towards west and therefore opposite to the definition used in SURM. Hence, the corresponding equation reads:

$$\cos(\eta_i) = \cos(\beta_i) \cdot \sin(\alpha) + \sin(\beta_i) \cdot \cos(\alpha) \cdot \cos(\psi - \psi_{in}) \tag{5.20}$$

Figure 5.8 shows the difference in annual mean shortwave radiation received by a horizontal surface ($SW_{in,p}$) compared to a surface inclined by β_i ($SW_{in,i}$) for different elevation angles (α) as calculated with the 'MITRAS' option in SURM. Please note, that the parameterisation of shortwave absorption within the atmosphere in MITRAS is only valid for Northern Germany (Eq. (D.3)) and therefore, the actual values of incoming shortwave radiation amount in Figure 5.8 should be viewed with care for elevation angles not existing in Northern Germany.

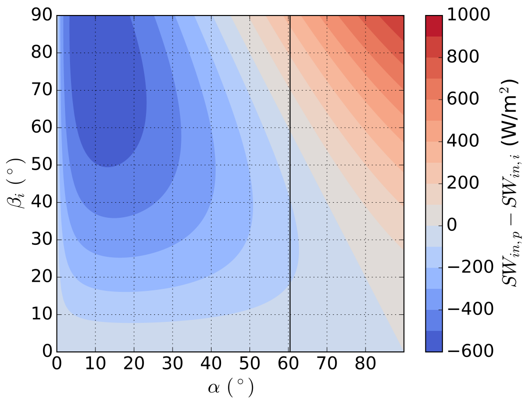

Figure 5.8: Difference in annual mean incoming shortwave radiation between radiation received at horizontal surfaces ($SW_{in,p}$) and inclined surfaces ($SW_{in,i}$) with angle β_i. Results are for different elevation angles (α).

Surfaces with large β_i receive more radiation for most elevation angles. This is indicated by differences below zero and thus $SW_{in,p}$ smaller than $SW_{in,i}$. For small elevation angles (e.g. about 15°), the incoming radiation is more than 500 W m^{-2} larger in the annual mean. Horizontal surfaces only receive more radiation compared to vertical surfaces for elevation angles larger than 45° with different values depending on β_i. Absolutely, horizontal surfaces receive more radiation than vertical surfaces, since for larger elevation angles the atmosphere absorbs less radiation (e.g. about 900 W m^{-2} for elevation angles of 90°). The black line indicates the maximal elevation angle reached in the city of Hamburg at 53 °N. In Hamburg walls (β_i=90°) receive almost always more radiation than ground surfaces.

A minimum elevation angle of the sun is calculated to determine, if a grid cell at location i, j, k is shaded from direct radiation. This is pre-calculated in the initialisation phase of MITRAS for n = 12 different azimuth sectors (ψ_n; each being 30°), which describe how high the sun has to be for direct radiation to reach the cell. During integration of the model, the actual elevation angle is compared to the minimum angle for the actual azimuth sector to decide whether the grid cell is shaded.

Before this thesis, this minimum angle α_{min} (Eq. (5.21)) was calculated using the difference in building height at grid cell j ($H_{i,j}$) and a grid cell l in direction of the ψ_n ($H_{i',j'}$) and the horizontal distance between the two grid points Δs:

$$\alpha_{\text{min}j}(\psi_n) = \max\left(\arctan\frac{H_{i',j'} - H_{i,j}}{\Delta s}, 0\right). \tag{5.21}$$

However, Eq. (5.21) uses an absolute building height, which is independent if of the vertical level k of the grid cell of interest. However, if not the lowest atmospheric grid cell above ground or building is of interest, the difference between the absolute building heights in the two grid cells is not a meaningful value to use. For instance, for a ground grid cell ($k = 0$) $H_{i,j} = 0$. Thus, $H_{i',j'} - H_{i,j}$ adequately describes the elevation height, the sun has to reach before the grid cell is lit. However, for a grid cell within the atmosphere ($k \neq 0$), the difference between $H_{i',j'}$ and the height above ground of j (z_j) is important and not the fact that the $H_{i,j} = 0$. To adequately consider shading of atmospheric grid cell, Eq. (5.21) has been changed within this thesis (Section 5.2.3.1). Furthermore, only the building height, not the difference in orography height is taken into account in MITRAS. This has also been added within this thesis.

5.2.1.2 Longwave radiation parameterisations

Two-stream approach Longwave radiation fluxes in the atmosphere are parameterised in the two-stream approach with the Planck function (B) for 9 different spectral ranges, considering absorption by CO_2 ($13 \leq \lambda \leq 18$ µm), liquid water absorption in the atmospheric window ($8.33 \leq \lambda \leq 11.11$ µm) and absorption of water vapour and liquid water inside and outside these ranges. Details on the calculation of B_{win} and B_{CO_2} are given in Schlünzen et al. (2012b).

Using the Planck functions, the upward longwave radiation flux for a grid cell at height k is calculated from

$$LW_{\uparrow}^{+}(k) = LW_{\uparrow}^{-} \cdot e^{-\beta\sigma_a\Delta z} + B^{+} - B^{-} \cdot e^{-\beta\sigma_a\Delta z} - \frac{(1 - e^{-\beta\sigma_a \cdot 0.5\Delta z})}{\beta\sigma_a}\frac{\partial B}{\partial z} \cdot (e^{-\beta\sigma_a \cdot 0.5\Delta z}) \tag{5.22}$$

with "+" indicating the locations at the upper boundary and "-" at the lower boundary of the grid cell, β being the diffusivity parameter (β=1.66) and σ_a the total absorption coefficient. This absorption coefficient consists of the volume extinction coefficient of water vapour and liquid water, which are calculated differently for the different spectral ranges.

The downward longwave radiation flux is similarly calculated using $LW\downarrow^{+}$ instead of $LW_{\uparrow}^{-}$ (Schlünzen et al., 2012b).

At the upper and lower boundary, the Planck functions are averaged over the neighbouring levels ($k+1$ and $k-1$, respectively):

$$B_{k^+} = 0.5 \cdot (B_{k+1}(T_{k+1}) + B_k(T_k)) \tag{5.23}$$

$$B_{k^-} = 0.5 \cdot (B_k(T_k) + B_{k-1}(T_{k-1})) \tag{5.24}$$

Vertically integrated approach In the vertically integrated approach, downward and upward longwave radiation fluxes are calculated according to Eq. (D.13) and Eq. (3.22), respectively.

5.2.2 Adjustment of the radiation transfer parameterisation within the atmosphere

5.2.2.1 Adjusted solar radiation fluxes at domain top

The two-stream approach was initially developed for the mesoscale model Mesoscale Transport and Stream model (METRAS). Therefore, the solar constants for the two regimes ($I_{\infty 1} = 707\ \mathrm{W\,m^{-2}}$ and $I_{\infty 2} = 660\ \mathrm{W\,m^{-2}}$) were defined for the top of the model atmosphere at about 14 km above sea level. For microscale simulations, however, the model domain is usually quite low. Therefore, the solar radiation fluxes at the model domain top have to correspond to that lower height. Otherwise the radiative fluxes would be overestimated. To adjust the input fluxes, an additional one-dimensional model simulation is performed. For this simulation, an artificial grid cell is created, which represents the average grid cell surface cover composition of the model area. With a domain height extended to 10 km, step 3 of the model's initialisation is performed (Section 5.1). The model time is set to the initial time of the three-dimensional model and the one-dimensional model is integrated for a user defined period starting. Within this simulation, the solar radiation is calculated at each height using the two-stream radiation approach and prognostic surface boundary conditions (Appendix H.5). The solar radiation fluxes are also determined at the height of the lower model domain and are then used as upper boundary incoming radiation values within the two-stream radiation scheme in the three-dimensional model.

Adjusting the solar radiation fluxes by multiplication with $\cos\Theta$ at the model top and then using these values within the atmosphere (Eq. (5.13)) is not helpful. This multiplication is necessary to adjust the radiation in beam direction to the amount received by a solid surface. For walls, however, the radiation can be much larger (Figure 5.8). Therefore, Eq. (5.13) is changed to:

$$SW_{tr}\downarrow(k) = I_\infty \cdot T_A(k) \cdot T_R(k) \cdot T_L(k) \cdot T_V(k). \tag{5.25}$$

5.2.2.2 Inclusion of diffuse radiation

The present two-stream approach did not differentiate between direct and diffuse radiation. However, for archiving realistic surface temperatures in the shade and to calculate T_{mrt}, diffuse radiation is required. Therefore, the diffuse radiation is extracted from the global radiation by assuming at each layer that radiation is scattered both backward to the sky and forward to the ground. In addition the downward reflected radiation of the upward flux (Eq. (5.18)) is assumed to be fully diffuse. Therefore, the full downward radiation flux can no be written as:

$$G(k) = \underbrace{SW_{tr}\downarrow(k)}_{\text{direct radiation}} + \underbrace{0.5 \cdot SW_{re} + f_a \cdot U_{rf,tot}\downarrow(k)}_{\text{diffuse radiation}} \tag{5.26}$$

5.2.2.3 Transmission factor for Rayleigh scattering

The transmission factor for Rayleigh scattering for range 1 (T_{R1}) is calculated as an integral value for both the upward and downward flux according to

$$T_{R1} = 1.041 - 0.16 \cdot \sqrt{\frac{0.962 \cdot p/p_0 + 0.051}{\cos\Theta}}, \tag{5.27}$$

where $1/1.66$ is used instead of $\cos\Theta$ for the upward flux (Bakan, 1994). In the downward direction p/p_0 increases and therefore T_{R1} decreases, leading to a decreasing transmitted flux towards the ground. However, applying the same equation upward, the transmitted flux increases with height. This non-physical result has been corrected by using a layer-wise transmission factor and assuming an equal upward and downward transmission through each layer. The layer-wise transmission factor ($T_{R1}(k)$) is calculated during the calculation of the downward flux from

$$T_{R1}(k) = \frac{T_{R1,k+1}}{T_{R1,k}} \tag{5.28}$$

and integrated from the ground ($T_{R1,k}$) for the upward radiation by

$$T_{R1,k} = \prod_{i=1}^{i=k} T_{R1}(i) \tag{5.29}$$

5.2.2.4 Planck functions close to the ground

In the two-stream approach longwave radiation is parameterised using Planck functions (Section 5.2.1). At the lowest model level above ground ($k = 1$), the Planck function at the lower boundary (B_{1^-}, Eq. (5.24)) uses the air temperature at $k = 0$ ($T_{a,k=0}$) to parameterise the upward flux. However, $T_{a,k=0}$ is not the actual surface temperature but the boundary value and has therefore been replaced by T_g.

For the longwave downward flux at $k = 1$, B_{1^-} is changed to only include the air temperature at $k = 1$ ($T_{a,k=1}$) and not the ground temperature (T_g), since the downward flux at the lowest model level should not depend on the surface condition.

5.2.3 Inclusion of surface to surface radiative fluxes

Three effects of buildings on radiation have been added to the previous MITRAS version (Figure 5.5) in the further developments of this thesis: shading of ground surfaces and atmospheric grid cells by buildings, vertical impact of buildings on incoming and outgoing longwave and shortwave radiation and radiative exchange between two building surfaces and between building surfaces and ground surfaces (Figure 5.5).

5.2.3.1 Shading by buildings

The shading algorithm of MITRAS (Eq. (5.21)) is extended to account for a height dependence of the minimum elevation angle, $\alpha_{\min}$, and orography. A height dependence of $\alpha_{\min}$ is needed to account for the fact that atmospheric grid cells in the vicinity of a building above the lowest atmospheric grid cell in a vertical column are earlier and longer lit as the lowest grid cell. This has so far not been accounted for, as only the building height difference between two cells was used and not the height of the current atmospheric cell above the lowest atmospheric cell, i.e. above ground or above building. Therefore, the height, z_j above ground or building, of a certain grid cell j is used in Eq. (5.30). In addition, not only the difference in building height but also an effect of orography is taken newly accounted for. To do so, both differences in elevation and building height of a grid cell j to a certain grid cell l is used ($\Delta(h + H)$):

$$\alpha_{\min j}(\psi_n) = \max\left(\arctan\frac{(h_l + H_l) - (h_j + H_j + z_j)}{\Delta s}, 0\right) \tag{5.30}$$

The shading considered only of surface cells, existed in the previous model version (Salim et al., 2018). Now shading of atmospheric grid cells is considered: in shaded atmospheric grid cells the downward transmitted direct radiation (Eq. (5.13)) and the reflected diffuse radiation component from that layer, $SW_{rf,tot} \uparrow$ and $U_{rf,tot} \downarrow$, are set to zero. This ensures that shaded grid cells neither transmit nor reflect direct radiation. The incoming diffuse shortwave radiation is unaffected at that layer.

The radiation fluxes within the atmosphere are used to calculate the incoming radiation at surfaces (e.g. building, ground, humans), but not for the change in atmospheric temperature due to differences in radiative fluxes (Eq. (5.11)). The changes in radiation cannot be directly considered here, since temperature changes are calculated from flux divergences, which are very high at the transition from a sunny to a shaded grid cell, leading to unrealistically high heating rates. Since the temperature changes due to radiation are usually small if no clouds or fog exist, heating rates by shading should not lead to drastically unrealistic results.

5.2.3.2 Vertical interaction of buildings and radiation

Consistent with the immersed boundary method used in MITRAS (Salim et al., 2018), the building roof is set as the lower boundary of a radiation column for the two-stream approach: all upward and downward short- and longwave flux calculations start (or stop) at roof height, ensuring that radiation fluxes within buildings are zero. For the longwave radiation flux (Section 5.2.1), roof temperature is used instead of ground temperature is used. For the shortwave radiation flux the roof albedo instead of the ground albedo is used as the lower boundary value as well as for the correction factor (Eq. (5.17)).

5.2.3.3 Radiative exchanges between surfaces

Radiative exchange between surfaces is essential to simulate radiative trapping (Section 2.2.2) and its effects on air and surface temperatures, which in turn affects the amount of longwave radiation received by a person and hence the thermal comfort. Since this radiative exchange between surfaces was not or only simplified considered in MITRAS (Figure 5.5) and is very relevant for thermal comfort, it has been further developed in this thesis.

a) Background

Most surfaces can be approximated as "grey" in MITRAS. Their optical roughness, the ratio of the root mean-square roughness height to the radiation wavelength (Howell et al., 2016), is high and irregular enough to increase diffuse reflection and small enough to neglect multiple reflections (Hottel and Sarofim, 1967). Grey surfaces uniformly emit the same radiation intensity over all directions. The spectral emissivity and absorptivity of such surfaces does not depend on the wavelength (Howell et al., 2016). The only non-grey surface in MITRAS are water surfaces, since they reflect radiation specularly. These surfaces are treated in a different part of this section.

The radiation exchanged between two grey surfaces depends on their view factors, as described in the section on SURM (Section 3.1.1). Thereby, the fraction of total incoming radiant flux at j, $E_{e,j}$, emitted from surface i, $J_{e,i}$, can be described by $J_{e,i} \cdot VF_{j\to i} = E_{e,j}$ (Eq. (3.3)). In this way, in MITRAS the total irradiance at surface grid cell j can be calculated by

$$E_{e,j} = \sum_{i}^{N} J_{e,i} \cdot VF_{j\to i}, \tag{5.31}$$

with N being all visible cells from j.

In general view factors have to be calculated numerically by integrating Eq. (3.23). However, if many surfaces exist within the domain, this can be computationally very demanding. Therefore, view factor algebra is often applied to derive view factors from already known ones. View factor algebra summarises a set of rules describing the relationships between view factors, for instance, the reciprocity theorem (Eq. (3.2)), the summation theorem (Eq. (3.25)) or the symmetry method (Figure 5.9, Eq. (5.32), taken from Howell et al., 2016). The symmetry method describes that if A_1, $VF_{1\to 2}$ and A_3 are known, $VF_{3\to 4}$ can be estimated from those values; and vice versa $VF_{1\to 2}$ from A_1, $VF_{3\to 4}$ and A_3. See (Howell et al., 2016, p.171 ff) for derivation of Eq. (5.32).

$$A_1 \cdot VF_{1\to 2} = A_3 \cdot VF_{3\to 4}. \tag{5.32}$$

b) View factors for building and ground surfaces

Since buildings are represented in MITRAS on a grid (Figure 5.3), only view factors between rectangular areas are required, if a flat ground is assumed. This is an advantage, since for rectangular surfaces analytic expression for view factors have been derived,

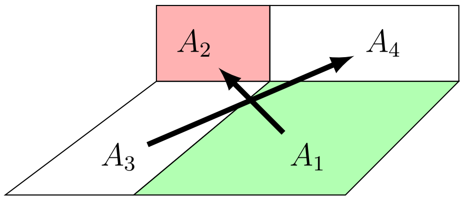

Figure 5.9: Sketch of using symmetry methods to derive a relationship between the view factors $VF_{1\to 2}$ and VF_{3-4}. Figure following Howell et al. (2016).

allowing a faster calculation of view factors than by integrating Eq. (3.23) numerically. Depending on their relative orientation view factors between two buildings can be described by rectangle to rectangle view factors in either perpendicular or parallel planes. View factors in perpendicular planes can be calculated from Eq. (5.33) using Eq. (5.34). The equation has been taken from Ehlert and Smith (1993) and is visualised in Figure 5.10a. View factors in parallel planes can be calculated from Eq. (5.33) with Eq. (5.35). Eq. (5.35) has been taken from Howell (2010, sec. C-13) and is visualised in Figure 5.10b.

$$VF_{1\to 2} = \frac{1}{(x_2 - x_1)(y_2 - y_1)} \sum_{l=1}^{2}\sum_{k=1}^{2}\sum_{j=1}^{2}\sum_{i=1}^{2} \left[(-1)^{(i+j+k+l)} G(x_i, y_i, \eta_k, \xi_l)\right] \tag{5.33}$$

$$G = \frac{1}{2\pi}\left\{(y-\eta)(x^2+\xi^2)^{1/2}\arctan K - \frac{1}{4}\left[(x^2+\xi^2)-(y-\eta)^2\right]\cdot \ln\left(x^2+\xi^2\right)+(y-\eta)^2\right\} \tag{5.34}$$

with $K = (y-\eta)/(x^2+\xi^2)^{1/2}$.

$$\begin{aligned} G = \frac{1}{2\pi}\Bigg\{&(y-\eta)\left[(x-\xi)^2+z^2\right]^{1/2}\arctan\frac{y-\eta}{\left[(x-\xi)^2+z^2\right]^{1/2}} \\ &+(x-\xi)\left[(y-\eta)^2+z^2\right]^{1/2}\arctan\frac{x-\xi}{\left[(y-\eta)^2+z^2\right]^{1/2}} \\ &-\frac{z^2}{2}\ln\left[(x-\xi)^2+(y-\eta)^2+z^2\right]\Bigg\} \end{aligned} \tag{5.35}$$

The expression for rectangles in perpendicular planes, Figure 5.10c, fails if the rectangles share a common edge. In MITRAS this is the case for a wall facade grid cell adjacent to ground cell. In this case, the Eq. (5.36) has to be used with $W = (x_2 - x_1)/(y_2 - y_1)$ and $H = (z_2 - z_1)/(y_2 - y_1)$. The equation has been taken from Howell et al. (2016):

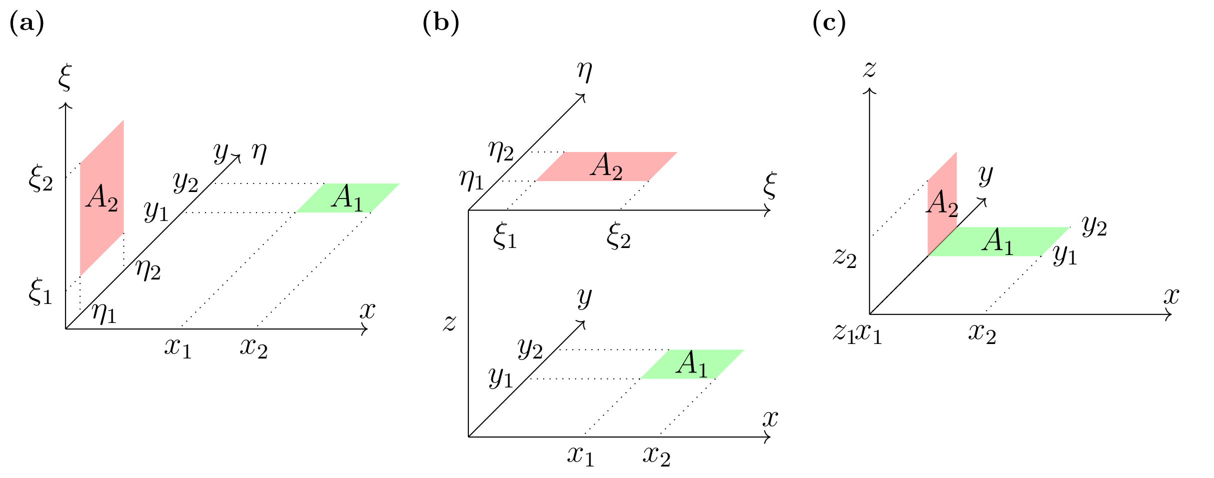

Figure 5.10: Variables used for view factor calculation between (a) two rectangles in perpendicular planes, (b) parallel planes and (c) sharing a common edge.

$$
\begin{aligned}
VF_{1\to 2} = \frac{1}{\pi W} \Bigg\{ & W \arctan\frac{1}{W} + H\arctan\frac{1}{H} - \sqrt{H^2+W^2}\arctan\frac{1}{\sqrt{H^2+W^2}} \\
& + \frac{1}{4}\ln\left(\frac{(1+W^2)(1+H^2)}{1+W^2+H^2}\cdot\left[\frac{W^2(1+W^2+H^2)}{(1+W^2)(W^2+H^2)}\right]^{W^2}\cdot\left[\frac{H^2(1+H^2+W^2)}{(1+H^2)(H^2+W^2)}\right]^{H^2}\right)\Bigg\}
\end{aligned}
\tag{5.36}
$$

Eq. (5.34) also fails, if $x_1 = 0$ and $\xi_1 = 0$, e.g. a situation similar to Figure 5.9. In that case, an expression can be derived from view factor algebra by only using the common edge case (Eq. (5.36)):

$$
\begin{aligned}
VF_{(2+4)-(1+3)} &\overset{\text{Summation}}{=} VF_{(2+4)-1} + VF_{(2+4)-3} \\
&\overset{\text{Reciprocity}}{=} \frac{A_1}{A_2+A_4}VF_{1-(2+4)} + \frac{A_3}{A_2+A_4}VF_{3-(2+4)} \\
&\overset{\text{Summation}}{=} \frac{A_1}{A_2+A_4}VF_{1-2} + \frac{A_1}{A_2+A_4}VF_{1-4} + \frac{A_3}{A_2+A_4}VF_{3-2} + \frac{A_3}{A_2+A_4}VF_{3-4} \\
&\overset{\text{Symmetry}}{=} \frac{A_1}{A_2+A_4}VF_{1-2} + \frac{A_1}{A_2+A_4}VF_{1-4} + \frac{A_3}{A_2+A_4}VF_{3-2} + \frac{A_1}{A_2+A_4}VF_{1-2} \\
\Rightarrow VF_{1-2} &= \frac{1}{2A_1}\left[(A_2+A_4)VF_{(2+4)-(1+3)} - A_1 VF_{1-4} - A_3 VF_{3-2}\right]
\end{aligned}
\tag{5.37}
$$

Assuming the cells 1 and 2 (Figure 5.9) are separated by a wall grid cell, A_6, and a ground grid cell, A_5, additional grid cells have to be taken into account in Eq. (5.37). By doing so, Eq. (5.38) has been derived.

$$VF_{1-2} = \frac{1}{2A_1}\Big[(A_2 + A_6 + A_4)VF_{(2+6+4)-(1+5+3)} - (A_4 + A_6)VF_{(4+6)-(1+5)} - (A_2 + A_6)VF_{(2+6)-(5+3)} + A_5 VF_{5-6}\Big] \quad (5.38)$$

Eq. (5.37) and Eq. (5.38) are used in addition to Eq. (5.36) to compliment Eq. (5.34). Once all surface-to-surface view factors are known, the sky view factor of surface i ($VF_{i\to s}$) can determined from

$$VF_{i\to s} = 1 - \sum_{j=1}^{N} VF_{i\to j} \quad (5.39)$$

j denotes all ground and wall surfaces affecting i. Buildings facing the boundary of the domain are assumed to face an open space. If buildings are placed too close to the model boundary, $VF_{i\to s}$ will be overestimated since only a limited number of ground cells exist up to the model boundary.

c) Use of view factors

The view factor calculation for building and ground surfaces is performed in the preprocessor GRIMASK, since the view factors are fixed for the entire model simulation. Since basically any two surface cells within the model domain can interact, a 4-dimensional array consisting of ground indices and building indices would be required. Even larger arrays (five dimensions) would be necessary for the view factors for T_{mrt}, since these are also calculated in the atmosphere (Section 5.3.1). To use the same structure for all view factors, the multi-dimensional array is split into three arrays: two arrays containing for each building cell a vector of ground surface indices i and j, and one array containing the corresponding view factors (`w2gvf`). Similar structures are used for wall to wall (`w2wvf`) and wall to ground view factors (`g2wvf`).

d) Detection of obscured surfaces

In theory every pair of surfaces in the model domain can exchange radiation, if their faces are parallel up to perpendicular to each other. However, due to the presence of other buildings within the domain, a specific surface might be obscured. An algorithm has been implemented that detects those cases and sets the corresponding view factors to zero. The algorithm makes use of the line equation between the centre points of the two surfaces ($\vec{p}$ and $\vec{q}$) in parameter form:

$$\begin{pmatrix} x \\ y \\ z \end{pmatrix} = \begin{pmatrix} p_1 \\ p_2 \\ p_3 \end{pmatrix} + S \begin{pmatrix} q_1 - p_1 \\ q_2 - p_2 \\ q_3 - p_3 \end{pmatrix} \tag{5.40}$$

S indicates the distance to $\vec{p}$ along the line. The algorithm works as follows:

1. the coordinate direction with the largest distance between $\vec{p}$ and $\vec{q}$ is determined (e.g. x direction in Figure 5.11).
2. in coordinate directions, the coordinates for every scalar grid point between $\vec{p}$ and $\vec{q}$ are determined. These are used to determine s from Eq. (5.40).
3. This value for s is used in Eq. (5.40) to calculate the coordinates of the other directions, e.g. coordinate direction y in Figure 5.11 shown as blue diamonds.
4. The closest scalar grid point to the newly calculated coordinates is determined (e.g. $y_{sc,i}$ in Figure 5.11). If the scalar grid point is located within a building (red grid cell in Figure 5.11), the view factor is set to zero for this and of further away in a flat terrain visible grid points. Otherwise the algorithm uses the second next scalar grid point and so on.

This algorithm simplifies the actual diffuse radiation exchange between surfaces, as only the exchanged is reduced to one direction connection between the surfaces, i.e. a ray, without taken into account the actual areas of the surfaces. Since only the closest scalar grid point is used to detect buildings (step 4), buildings that in reality would influence the radiative exchange, if the area is taken into account, are not detected to obscure the view between $\vec{p}$ and $\vec{q}$ (e.g. green building in Figure 5.11). To determine obscured obstacles more accurately with the current method the resolution has to be increased.

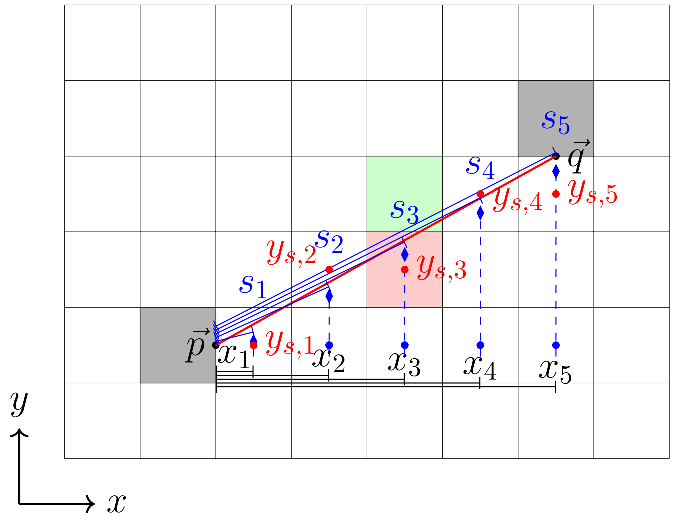

Figure 5.11: Sketch of the algorithm to detect obscured surfaces for a uniform grid. Black dots at buildings (grey) indicate centre of the surfaces ($\vec{p}$ and $\vec{q}$), which exchange radiation along the direct connection between the two points (red). Corresponding to each x_i, s_i describes the scaling factor (Eq. (5.40)) and the blue diamonds the calculated y values. Red dots indicate closest scalar grid point ($y_{s,i}$). The red building obscures the visibility between $\vec{p}$ and $\vec{q}$. The green building is not resolved and does not influence the visibility between $\vec{p}$ and $\vec{q}$ based on the implemented algorithm (see text).

e) Truncation value

$VF_{1\to 2}$ decreases with increasing distances between surfaces 1 and 2. As the influence surfaces further away is small, a truncation value for relevant view factors is defined.

The amount of outgoing shortwave and outgoing longwave radiation fluxes from a surface are considered, to derive the truncation value. To illustrate the methodology, Figure 5.12 shows the incoming shortwave radiation for the entire year at latitude 0 °N in dark red for wall surfaces and in light red for road surfaces as calculated from SURM using the 'MITRAS' parameterisation. Latitude 0 °N has been chosen to show the full range of elevation angles, although the 'MITRAS' parameterisation is only valid for Northern Germany. For latitude 53 °N the overall elevation angles are limited to α=60 ° (blue line).

As expected from the difference in annual mean incoming shortwave radiation between a horizontal and an inclined surface (Figure 5.8), more radiation is received by walls (Fig-

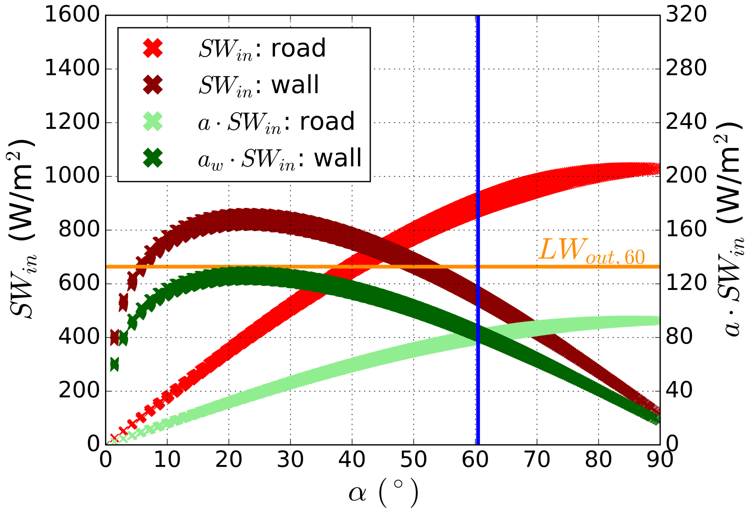

Figure 5.12: Incoming shortwave radiation (SW_{in}, left ordinate) at walls (dark red) and roads (light red) for different elevation angles (α) as simulated for one year by SURM using the parameterisation option 'MITRAS' for latitude 0 °N and corresponding outgoing shortwave radiation (green, right axis) assuming $a = 0.09$ and $a_w = 0.15$. The blue line indicates the maximal elevation angle encountered at latitude 53 °N and the orange line the longwave outgoing radiation amount for $T_g = 60$ °C (left ordinate).

ure 5.12, dark red) compared to ground surfaces (Figure 5.12, light red) for low elevation angles α. For the truncation value, the outgoing radiation ($a \cdot SW_{in}$) is important. Assuming a road albedo of $a = 0.09$, which corresponds to the SCC asphalt in MITRAS, and a wall albedo of $a_w = 0.15$, as defined for walls in MITRAS (Table K.2), a maximum outgoing shortwave radiation of about 120 W m^{-2} for elevation angles of $\alpha = 25°$ is obtained for wall surfaces (dark green line, right ordinate). The reflected shortwave radiation from the ground is lower due to the smaller albedo values and smaller incoming radiation (light green line).

A surface temperature of 60 °C and an emissivity of ε=0.95 are assumed, to estimate the limit of outgoing *longwave* radiation from a surface. This outgoing longwave radiation would amount to $LW_{out} = 663$ W m^{-2} (orange line in Figure 5.12, left ordinate). Hence, the outgoing longwave radiation is much larger compared to the outgoing shortwave radiation and thus is most relevant for determining the truncation value of the view factors. The emitted radiation accumulates over the day and, therefore, also the error due to a truncated view factor accumulates. Considering this, view factors up to 10^{-5} are considered in MITRAS, allowing for a maximal error of about $6 \cdot 10^{-3}$ W m^{-2} per time step. A sensitivity test to assess the relevance of the truncation value is performed in Section 5.2.5 by using a smaller value (10^{-6}) and assessing the differences.

f) Application of view factors in MITRAS

The incoming shortwave radiation from the sky at each surface ($SW_{in,s,i}$) can be calculated using the sky view factor (Eq. (5.39)) from

$$SW_{in,s,i} = VF_{i \to s} \cdot SW_{diff} + l_{\text{lit}} \cdot SW_{dir} \cdot \cos\theta \tag{5.41}$$

with l_{lit} being 1, if the surface is in the sun and 0 otherwise.

Using $SW_{in,s,i}$, the shortwave reflected radiation from another surfaces to a ground surface gi from a wall surface wj can be calculated from Eq. (5.42):

$$SW_{in,refl,t,gi} = \sum_{wj} VF_{gi \to wj} \cdot a_w \cdot SW_{in,s,wj} \tag{5.42}$$

For a wall surface, wi, the reflected radiation is calculated as

$$\begin{aligned} SW_{in,refl,t,wi} &= \sum_{wj} VF_{wi \to wj} \cdot a_w \cdot SW_{in,s,wj} \\ &+ \sum_{j} \sum_{gj} VF_{wi \to gj} \cdot \left\{ (1 - \delta_{j,\text{wat}}) \cdot f_j \cdot a_j \cdot SW_{in,s,gj} + \delta_{j,\text{wat}} \cdot f_j \cdot a_j \cdot VF_{i \to s} \cdot SW_{diff} \right\}. \end{aligned} \tag{5.43}$$

$\delta_{j,\text{wat}}$ denotes the Kronecker delta switch for water surfaces to consider that water surfaces do not reflect diffusely (see next section):

$$\delta_{j,\text{wat}} = \begin{cases} 1 & \text{if } j \in \text{ `water'} \\ 0 & \text{if } j \notin \text{ `water'} \end{cases} \tag{5.44}$$

The total incoming shortwave radiation flux per surface grid cell is

$$SW_{in,t,i} = SW_{in,s,i} + SW_{in,refl,t,i}. \tag{5.45}$$

Using the described method, MITRAS takes only one reflection from surfaces into account. This is a valid first assumption since the albedo of walls in MITRAS is a_w=0.15 and therefore at the second reflection only about 2 % of the original incoming radiation flux would be reflected. Thus, from the results in Figure 5.12 the maximum error is about 1.8 W m^{-2} per time step. This error is larger than the one made by the truncation value for the view factors. However, this amount of short wave radiation is only received by a certain surface for a short time, as for Figure 5.12 the value is assumed to be directly perpendicular to the beam direction of the sun. Furthermore, during the night this error is not present. Nevertheless, the error is not negligible and thus in further developments of MITRAS, multiple reflections could be included for instance by the method discussed in Section 5.4.

Longwave radiation fluxes are handled similar to the shortwave radiation fluxes: Using the incoming longwave radiation amount from the sky ($LW_{in,s,i}$) at each surface,

$$LW_{in,s,i} = VF_{i\to s} \cdot LW_{s,i}, \tag{5.46}$$

the total incoming longwave radiation at ground surfaces can be determined from

$$LW_{in,t,gi} = LW_{in,s,g} + \sum_{wj} VF_{gi\to wj} \cdot \left[(1-\varepsilon_w)\cdot LW_{in,s,wj} + \varepsilon_w \sigma T_{wj}^4\right]. \tag{5.47}$$

Eq. (5.47) takes into account the longwave emission of building walls and longwave reflection at building walls, $(1-\varepsilon_w)$, which is, however, very small. T_{wj} is the building wall's temperature of the previous model time step, since the actual temperature is not available in the model's time integration for calculating $LW_{in,t,gi}$. However, the model time step in MITRAS is generally small (well below 1 s). Therefore, using T_{wj} from the previous time step is an approximation that does not lead to large errors.

Using the ground temperature of the actual time step, the incoming longwave radiation at building surfaces is calculated from:

$$\begin{aligned} LW_{in,t,wi} = LW_{in,s,w} &+ \sum_{wj} VF_{wi\to wj} \cdot \left[(1-\varepsilon_w)\cdot LW_{in,s,wj} + \varepsilon_w \sigma T_{wj}^4\right] \\ &+ \sum_{gj} VF_{wi\to gj} \cdot \left[(1-\varepsilon)\cdot LW_{in,s,gj} + \varepsilon \sigma T_{gj}^4\right] \end{aligned} \tag{5.48}$$

The emissivity of the ground surfaces is set for all js to the value as for the walls, i.e. ε=0.95 Table K.2.

g) Handling of reflection by water surfaces

Due to the smooth surface of water bodies, water surfaces reflect radiation specularly in MITRAS instead of diffusely as assumed for other surfaces. Depending on the time of the day, incoming direct radiation would be reflected from a water surface to different atmospheric cells: around noon (large elevation angles) radiation is reflected to the atmospheric cell above the ground cell, whereas after sunrise and before sunset (small elevation angles) radiation is reflected to adjacent atmospheric cells. The two-stream approach only allows for a reflection to the grid cell above the ground cell. The 'critical' angle, for which is approximation is valid, depends on the resolution. For the resolution used in the present study (3 m horizontally (Δx) and 2 m vertically (Δz) in the inner domain, Section 6.2.2), reflected radiation reaches neighbouring grid cells for $\arctan(\Delta z/\Delta x) = \alpha < 53°$. From Figure 5.2 it can be gathered that the maximum increase due to reflected radiation from water surfaces amounts to maximal 25 $\mathrm{W\,m^{-2}}$ in the neighbouring grid cell (red line). Compared to the direct downward radiation, this additional input is small (only 3 % $(=a_{\mathrm{wat}})$) of the direct incoming radiation. Hence, the two-stream approach is not altered with respect to the reflection of water surfaces and all reflected radiation goes into the grid cell vertically above. Since the view factors for radiative surface-to-surface interaction are only valid for diffuse radiation, they are applied for water surfaces only to the diffuse shortwave component and the longwave component.

5.2.4 Inclusion of partial shading by vegetation

To introduce partial shading of neighbouring grid cells by vegetation (Figure 5.5), the shading calculation for buildings (Eq. (5.30)) is extended for vegetation. The most exact approach for partial shading would be the application of a ray tracing scheme that sums up the leaf area densities (LAD) along the beam. However, such a scheme increases the computational costs and the required storage. Therefore, a simplified version of such a scheme is developed in this thesis.

For elevation angles smaller than the minimum elevation angle of shading by solid obstacles, α_{min}, no effect of vegetation is considered, since the solid shading obscures the sun for the vegetation (Figure 5.13a). If α_{min} is smaller for a certain grid cell than the elevation angle to vegetation, $\alpha_{\mathrm{min},t}$, a reduction in shortwave radiation is considered (Figure 5.13b). For that a reduction factor, τ, is used. The reduction factor takes into account the summed LAD along a particular ray j of transected grid cells i:

$$\tau_j = e^{-0.5 \cdot \sum_{i=1}^{N} LAD_i}. \tag{5.49}$$

To limit the number of calculations, τ is calculated for $\alpha_{\mathrm{min},t}$ with a step of 10° for each azimuth sector (Figure 5.13b, black lines).

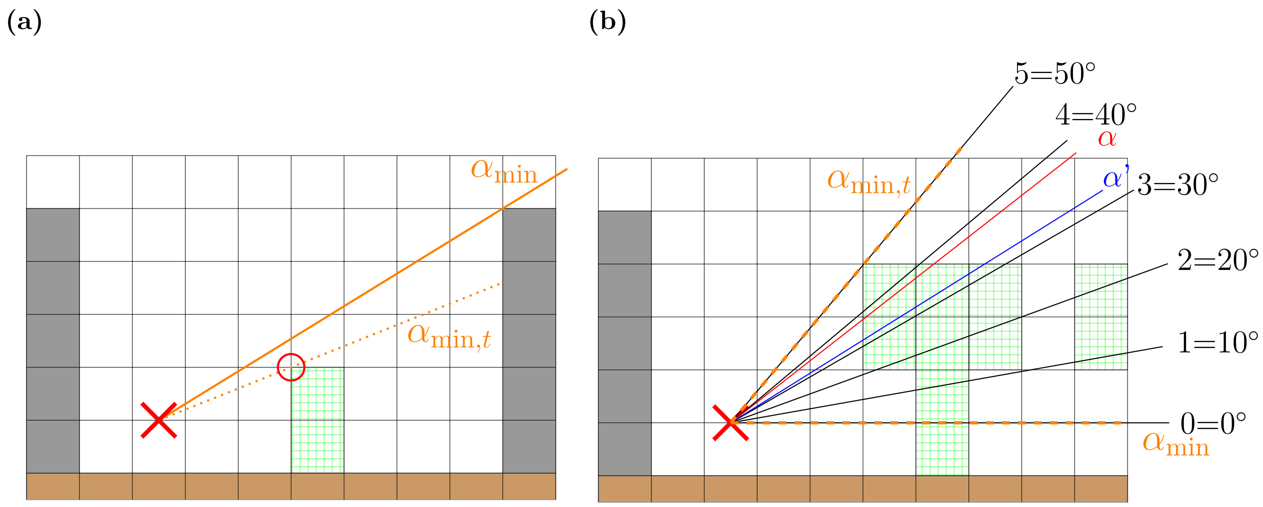

Figure 5.13: Sketch of determining partial shading by vegetation for (a) solid shading by building exceeds partial shading by vegetation and (b) no shading by building. α_{min} is the minimum elevation angle for solid shading by obstacles and $\alpha_{\mathrm{min},t}$ the minimum elevation angle for vegetation. The blue and red line indicate solar rays for different times. Black lines indicate considered sectors of equal shading.

To determine, which grid cells are transacted by the ray, a two-dimensional version of the algorithm to determine obscured surfaces (Figure 5.11) is used:

1. For the centre line of each azimuth sector (ψ_{nc}) the x and y coordinates of the closest grid cell centres are derived for different distances with the two-dimensional algorithm. The coordinate direction for the calculation depends on the azimuth sector: the x-direction is chosen for azimuth sectors between 90±30° and 270±30° and y otherwise.

2. For each thereby determined grid cell centre in the horizontal plane, the centre

point of the grid cell closest to every 10° elevation angle is determined with the two-dimensional algorithm and LAD summed up.

3. The reduction factor τ_j corresponds to the elevation angle closest to the actual elevation angle and azimuth sector of the sun. For example, for the blue line in Figure 5.13b the reduction factor along line 3 (30°) are used. For the red line the reduction factor along line 4 (40°) is used.

Below vegetation no partial shading is calculated, since direct radiation is already reduced for those grid cells by the two-stream radiation approximation (Eq. (5.10)).

5.2.5 Validation of model extensions

5.2.5.1 Adjusted solar radiation fluxes at domain top

For the evaluation of adjusted solar radiation fluxes at shallow domains (Section 5.2.2.1), the derived shortwave radiation fluxes at model top are compared to those existing for an earlier version of MITRAS for 200 m height (Table 5.1). These input fluxes have been calculated for the latitude and longitude of Jülich (50.927608°, 6.374128°) for a domain consisting mainly of forest by Schlüter (2006). Using similar initial conditions (Table 5.2) and a domain consisting entirely of forest, the solar radiation fluxes at the top of the model domain are derived for 14.07.2013.

Table 5.2: Initial conditions for validation simulation for solar radiation fluxes at lower domain top at 14.07.2013.

Parameter	Value	Reason
Air temperature	21 °C	Fig. 3.3 in Schlüter (2006)
Relative humidity	49 %	Fig. 3.4 in Schlüter (2006)
Geostrophic wind (u_g, v_g)	3.5 $\mathrm{m\,s^{-1}}$, 6.5 $\mathrm{m\,s^{-1}}$	Not given in Schlüter (2006), randomly selected
Stratification	0.035 $\mathrm{K\,m^{-1}}$	Not given in Schlüter (2006), randomly selected

The derived fractions of the solar constants at 200 m above ground are shown in Figure 5.14 from the extended model version of this thesis are shown as solid blue line for spectral range 1 and solid green line for spectral range 2. The fractions derived by a model version, which does not include the corrections for the elevation angle (Eq. (5.25)) are shown as blue dashed line (range 1) and green dashed line (range 2). The values used by Schlüter (2006) are shown as blue dots for range 1 and green dots for range 2. The values are each shifted to one hour later, because those values were not calculated in LST.

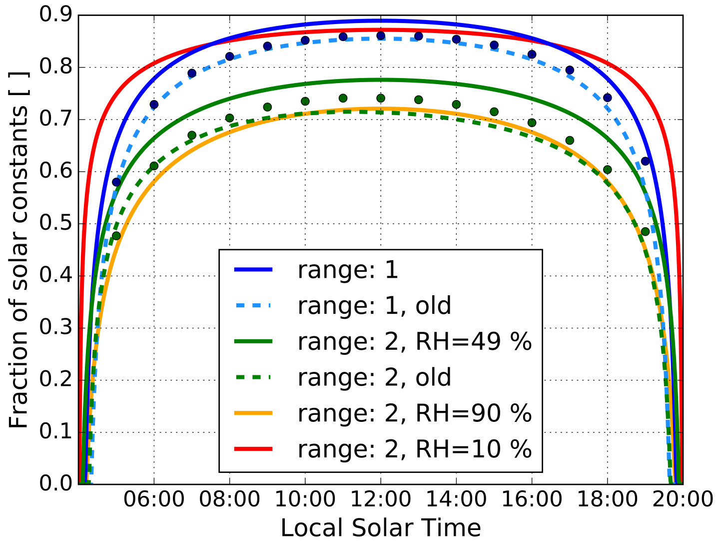

Figure 5.14: Fraction of solar constants at 200 m height above ground during the day using initial conditions similar given in Table 5.2. Results for the extended model version in this thesis are shown as solid blue (range 1) and green (range 2) lines. Results without elevation correction in Eq. (5.25) are shown as dashed blue (range 1) and dashed green (range 2). Dots indicate values used by Schlüter (2006) shifted to one hour later. Orange line refers to initially 90 % relative humidity and red lien to initially 10 % relative humidity.

The values for range 1 before the necessary correction for the elevation angles (blue dashed line), agreed well for those determined by Schlüter (2006) (blue dots). The values for range 2 (green dashed line) are overestimated compared to those by Schlüter (2006) (green dots). This might be due to a different vertical humidity distribution compared to the simulations by Schlüter (2006), since the near infrared range is sensitive to humidity. With the correction for the elevation angle (Eq. (5.25)) higher values are calculated (solid blue and green lines) compared to those without the correction (dashed blue and green lines). This is expected from the correction.

To test the sensitivity of the solar fractions to humidity, two additional simulations, with 10 % (red) and 90 % relative humidity (orange) have been performed with the extended model version. The results indicate that the solar radiation fluxes are sensitive to the humidity conditions. Therefore, the current implementation only works, if the humidity conditions above the actual used 3-dimensional model domain are similar. If fog or precipitation locally develop in the 3-d simulation, the reduction factors of the solar constants are different. For the simulations carried out in this thesis no large deviations from the 1-dimensional simulations are anticipated, since the simulations are calculated without clouds.

5.2.5.2 Radiation modelling within the obstacle layer

The extensions for the modelling of radiation within the obstacle layer have to be validated, before the new model version can be used to study the effect of urban water surfaces. The validation consists of two aspects. First, it has to be ensured that implementation of the calculation for surface-to-surface view factors is correct and second that the extensions lead to plausible results within the atmosphere. The implementation of the surface-to-surface view factors can be checked against theoretical values, since the view factor values only depend on geometric relations between surfaces. The performed tests along with their results are described in detail in Appendix J. For the validation of the extensions in MITRAS there is no simple test case with "expected" values. Therefore, a different approach is used. Idealised test cases are simulated that differ in the applied model physics. Differences between the test cases can be used to detect errors in the model. The performed test cases and results are described below.

a) Definition of validation test cases

Eight simulations with different model versions and/or boundary conditions are performed (Table 5.3) for one domain (Figure 5.15) and a specific set of initial conditions (Table 5.4). For the different model versions, git branches are created to ensure the validation is reproducible.

Table 5.3: Basic test cases with MITRAS.

Case	Setting
`50inital`	Initial version of MITRAS without model extensions of this thesis. Surface energy budget solved with interaction of building and ground. MITRAS as described in Salim et al. (2018)
`51`	MITRAS as described in this thesis (reference simulation)

Case	Setting
`50`	Model version including radiative interactions of buildings as presented in this thesis but using the vertically integrated approach for radiation within the atmosphere (Section 5.2.1.1)
`51vf0`	As case `51`, but all wall view factors are set to 0 manually and view factors are set as follows: $VF_{g\to s} = 1$, $VF_{w\to s} = 0.5$ and $VF_{wi\to gj} = 0.5 \cdot VF_{wi\to gj,init}$
`5`	As case `50`, but no surface energy budget at walls. The wall temperature is fixed, no radiative interaction exists
`51nodiff`	As case `51`, but no diffuse radiation. Global radiation is used instead of diffuse and direct radiation being separated
`51wT`	As case `51` and inclusion of trees. A model domain with a tree in the courtyard is used Figure 5.15
`51vfcrit`	As case `51`, but the truncation criterion for the view factors is 10^{-6} instead of 10^{-5} for all other cases

The initial conditions (Table 5.4) are chosen to correspond to average clear sky conditions in summer. They have been derived from cloudfree days at the weather station Fuhlsbüttel using the methodology described in Section 4.2.2.2). The day with the average solar input flux in summer (28.07.2013) has been chosen for the simulations (Section 4.2.2.2 and Chapter 4).

Table 5.4: Initial condition for MITRAS validation simulations. T_a is air temperature, RH is relative humidity, e is vapour pressure, DD and FF are wind direction in ° and wind speed in $\mathrm{m\,s^{-1}}$ at 10 m height, u_g and v_g are geostrophic wind components in $\mathrm{m\,s^{-1}}$ and T_{wat} and T_{soil} are water temperature and soil temperature, respectively, both in °C.

Time	Day	T_a	RH	e	DD	FF	u_g	v_g	$\partial\Theta/\partial z$	T_{wat}	T_{soil}
04:00	28.07.	16.00	81.00	14.70	180	1.27	1.00	2.00	3.50	21.5	15.00

The expected differences between the simulations are known qualitatively for different times of the day (Table 5.5), which allows to compare the simulated difference to the expected ones.

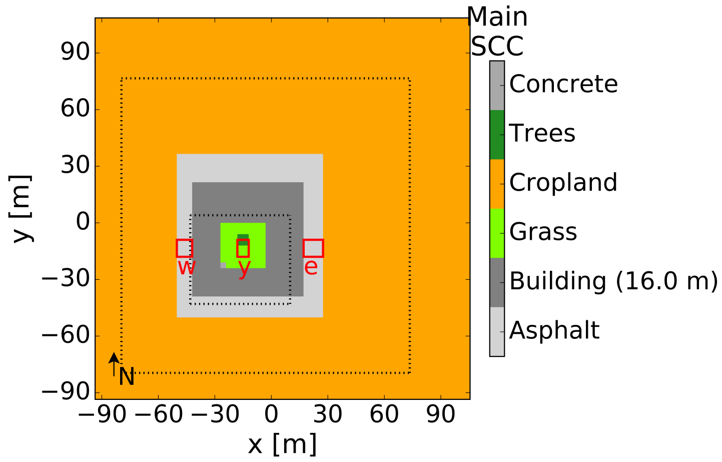

Figure 5.15: Surface cover classes (SCC) of idealised domain for MITRAS validation test cases. Explicit vegetation (tree within courtyard) is only considered in one simulation (`51wT`). Building height is given in brackets for the SCC "building". Red areas mark the averaging domains 'east' (e), 'yard' (y) and 'west' (w).

Table 5.5: Comparisons of the test case results (Table 5.3) to validate the extensions of MITRAS.

No	Difference of test cases	Target to assess	Expected results
A	`50initial - 51`	all implemented model changes	Higher temperatures within the courtyard. Largest differences between sunrise and sunset.
B	`50 - 51`	two-stream approach compared to vertically integrated scheme	Small difference at night, large ones during the day
C	`51vf0 - 51`	radiative wall-wall and wall-surface interaction and realistic surface-wall interaction	Large differences within the courtyard and in areas next to sunny building walls

No	Difference of test cases	Target to assess	Expected results
D	`5 - 51`	(1) as validation B, (2) as validation C, (3) prognostic building wall temperature	see B and C; large differences close buildings walls, which heat up strongly during the day
E	`51nodiff - 51`	diffuse radiation	Without diffuse radiation colder in shade
F	`51wT - 51`	shading by explicit vegetation	During the day building temperature is smaller in shade; no difference at night
G	`51vfcrit - 51`	truncation criterion (Section 5.2.3.3)	No significant differences

b) Results of the validation

Validation test A shows the overall influence of the extensions in this thesis on the simulation results. During the morning after sunrise (Figure 5.16a), the atmosphere close to the ground is warmer in case `50inital` compared to case `51`. At about 08:40 LST the pattern reverses to higher temperatures in case `51` (Figure 5.16b at 14:40 LST). Largest differences are in the courtyard (Figure 5.16b). This is to be expected as the radiative interactions between the surfaces is largest there.

The time series in Figure 5.17 shows the difference in air temperature between the two simulations for day and night time for the three averaging areas (Figure 5.15). The results show that for these areas air temperature difference of up to 3.5 K between the simulations exist. This value is larger than the required accuracy of 1 K for the thermal PET and UTCI (Table 4.9). This indicates that the extensions lead to significant different results for PET and UTCI and are therefore necessary.

The time series in Figure 5.17 shows gaps. Here data have been removed that occurred due to erroneous outputs at restarts of the model. The missing data for the restart of the model has been included for the final simulations for the influence of water surfaces (Chapter 6). Thus, idealised test cases like these help to detect such inconsistent model behaviour and are therefore worth to be applied.

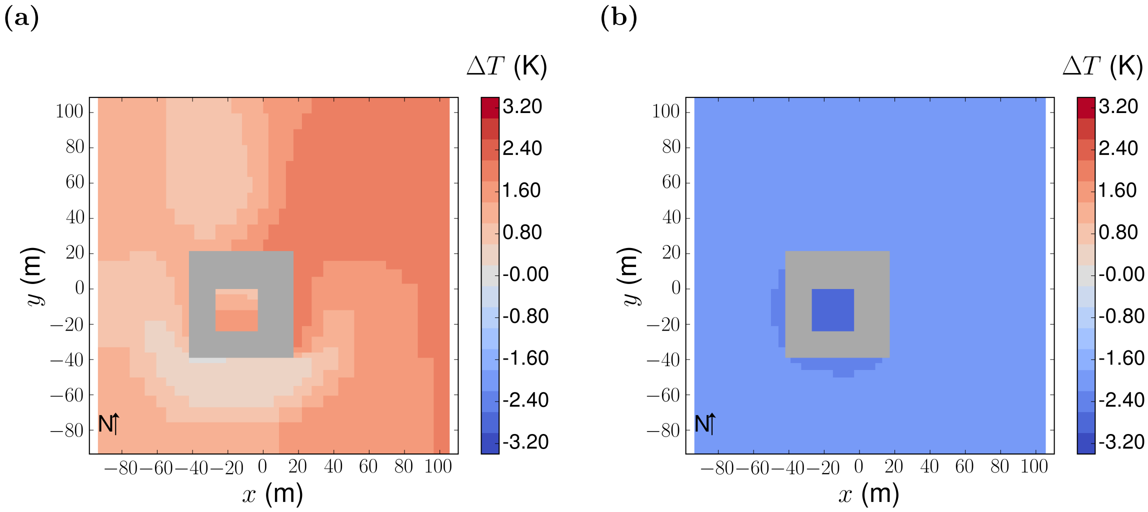

Figure 5.16: Air Temperature (T_a) difference for case `50initial - 51` (validation case A) at 1 m height for (a) 04:20 LST and (b) 14:40 LST.

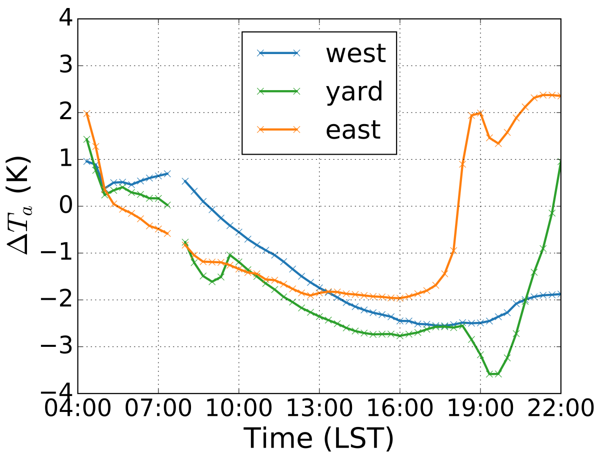

Figure 5.17: Time series of air Temperature (T_a) difference for validation test case A at 1 m height for the three areas indicated in Figure 5.15.

Differences for validation case B indicate the influence of calculating radiation with the two-stream approach instead of the vertically integrated approach (Section 5.2.1.1). The simulated differences for $SW\downarrow$ are generally small in shade during morning for 'west' and during evening for 'east' and everywhere during midday (below 60 W m^{-2}, Figure 5.18a). Differences in shade are due to larger diffuse radiation in the two-stream approach especially at low solar elevation angles. The large differences after sunrise are caused by a abrupt large increase in direct radiation in test case 50 (not shown). Test case 50 uses the vertically integrated scheme to calculate radiative fluxes within the atmosphere (Section 5.2.1.1). Such a large increase is unrealistic. Therefore, the more comprehensive two-stream modelling approach should be applied for further studies with MITRAS.

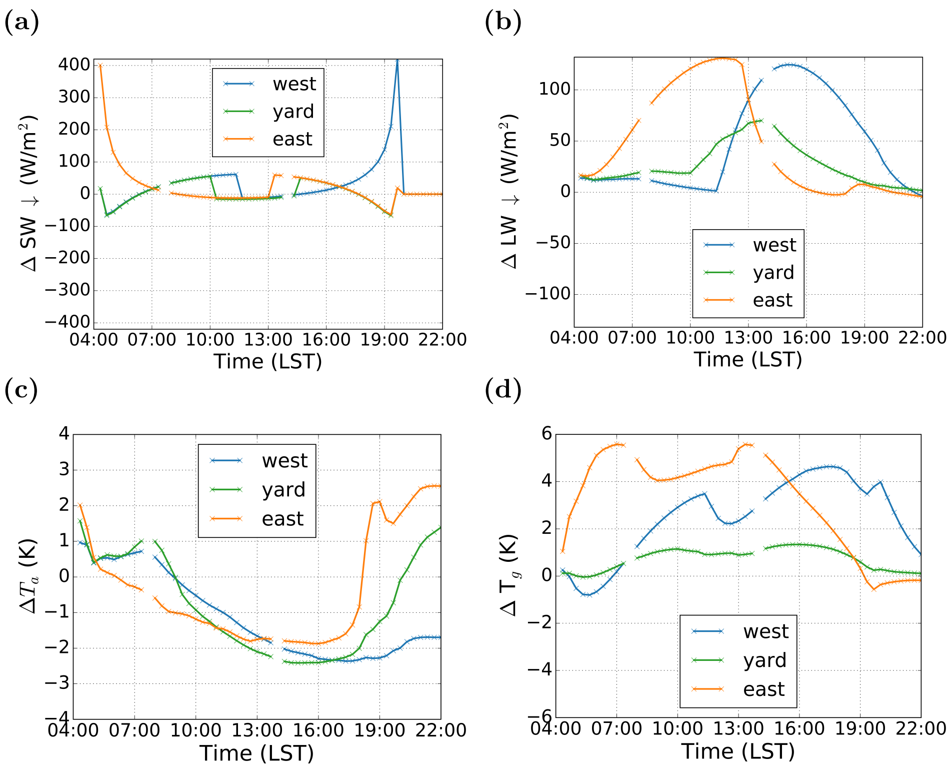

Figure 5.18: Results for validation case B (a)) total downward shortwave radiation ($SW\downarrow$), (b) downward longwave radiation flux ($LW\downarrow$), (c) air temperature (T_a) and (d) ground surface temperature (T_g). All values for the lowest model level above ground and for the three domains in Figure 5.15.

Longwave radiation ($LW\downarrow$) is simulated similarly by both radiation parameterisations during the night but differs by more than 100 W m^{-2} in sunny areas during the day (Figure 5.18b). The differences in radiative fluxes are reflected in higher ground temperatures (T_g, Figure 5.18d) and building temperatures in test case 50 (not shown). In contrast to surface temperatures, air temperatures are higher in test case 51 due to the explicit calculation of the effect of radiation on air temperature in the atmosphere (Eq. (5.11)). Figure 5.18c shows this results for 1 m above ground level. However, higher air temperatures are calculated in all heights. Overall the difference in the radiative fluxes follow the expectations in Table 5.3 with small differences at night and larger ones during the day (except for shortwave radiation for morning and evening).

The validation test B can already explain much of the difference found in Figure 5.17, especially for 'west' and 'east'. Within the courtyard ('yard') the radiative exchange between surfaces is especially relevant (Section 5.1). To analyse the influence of using sophisticated view factors compared to simplified ones (e.g. 0.5 for walls and 1 for ground surfaces; Table 5.3), test cases `51vf0` and `51` are jointly analysed in validation test C. Note that the calculation in `51vf0` differs from the calculation method in Gierisch (2011), which takes into account weighting factors for ground cells (Section 5.1).

The view factors in test case `51vf0` have only a small effect on air temperature for 'west' and 'east' (Figure 5.19a), since view factors are only changed slightly for those walls. The effect of these changes are better reflected in building surface temperature of the outer walls (Figure 5.19d). In Figure 5.19d, the three-dimensional building is reduced to a two-dimensions by plotting the surfaces in form of a net: walls are arranged in a plane that can be folded along edges (dashed lines) to become the building wall faces in three dimensions. For the outer wall, the ground surface is located along the edges of the figure and the roof is located in the centre between the dashed line and the white courtyard (indicated by the arrows 'roof'). For the inner walls (Figure 5.19c), the ground is located in the centre of the figure and the roof is located along the figure's edges. At the outer walls a horizontal pattern emerges: wall grid cells, which actually have smaller ground view factors than 0.5 are warmer in test case `51vf0` than in test case `51`. The heating is opposite for cells with larger ground view factors. As expected, the roof temperature is the same in both simulations, since $VF_{i \to s}$=1 in both cases.

The largest differences between the two test cases are visible for air temperature in the courtyard (Figure 5.19a) and for wall temperatures facing the courtyard (Figure 5.19c). The large differences are due to the neglected wall-to-wall surface interaction in test case `51vf0`. For midday the wall temperatures differ by more than 14 K for all shaded walls. The air temperature difference is largest during the time when solar radiation does not reach directly into the canyon (Figure 5.19a). Also the ground temperature is affected by using simplified view factors (Figure 5.19b), since due to the absence of $VF_{gi \to wj}$, less longwave radiation is received in sunny areas.

In general, the effects of simplified view factors are larger than expected from the overall changes (Figure 5.17), probably due to the different view factor implementation in

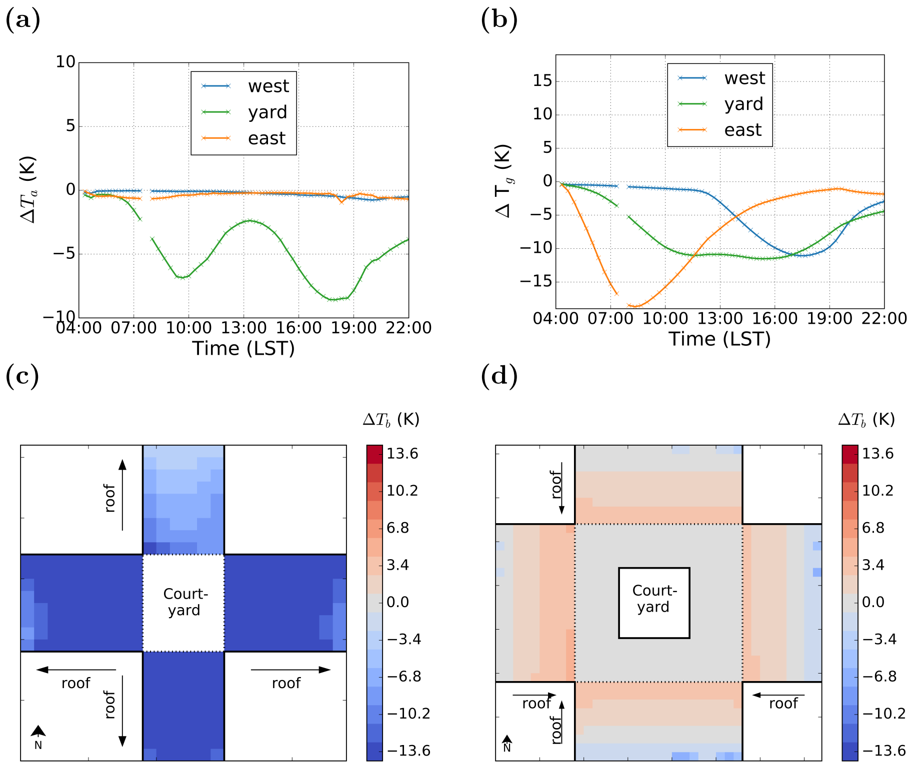

Figure 5.19: Results of validation test case C for (a) air temperature (T_a) and (b) ground temperature (T_g) for the three domains indicated in Figure 5.15; (c) shows wall surface temperatures at 12:00 LST for the inner walls and (d) for outer walls.

`50initial` and due to a partial compensation of the impacts by using the vertically integrated radiation scheme. Altogether, the changes introduced by the model extensions follow the expectations (Section 5.5). Hence, the implementation of the extensions is assumed to be correct.

Validation test case D assess the importance of calculating building surface temperatures prognostically compared to using fixed building temperatures. In test case `5` the wall temperature is held fixed at the 04:00 LST air temperatures of neighbouring atmospheric grid cells (about 16 °C), and no radiative exchange is simulated (Table 5.5). In general, results for validation test D (Figure 5.20) and validation test B (Figure 5.18c) are similar. This indicates that the used radiation parameterisation exceeds the effect of prognostically calculated temperatures as both `50` and `5` use the vertically integrated radiation scheme (Section 5.2.1.1). Differences are, however, visible in the enclosed courtyard. Walls facing the courtyard heat up stronger during the day due to the smaller wind speed within the courtyard.

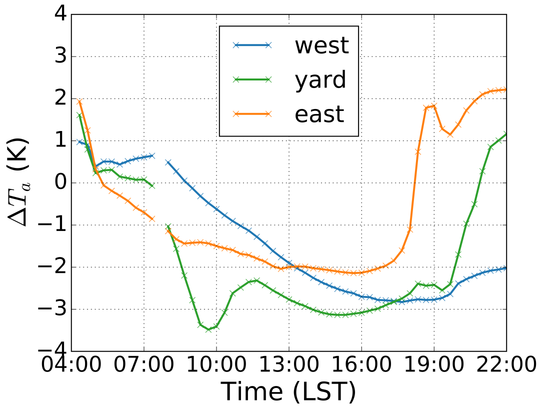

Figure 5.20: Same as Figure 5.18c but for validation test case D.

The importance of separating diffuse and direct radiation is evaluated by validation test E by comparing a simulation neglecting diffuse radiation with model version as extended in this thesis. Since diffuse radiation is calculated at all heights (Eq. (5.26)), the downward radiation flux differs for the entire atmosphere (Figure 5.21a). The difference depends on the time of the day and peaks in early morning and evening (Figure 5.21a,b). Whether this peak is realistic should be determined from measurements. In comparison to these differences of simulating diffuse radiation at all, the differences between sunny and shaded areas is one order of magnitude smaller, e.g. at 17:00 LST in shaded areas 'yard' (green) and 'east' (orange) $SW \downarrow$ is about 5 $\mathrm{W\,m^{-2}}$ larger than in 'west' (blue), which is lit Figure 5.21a.

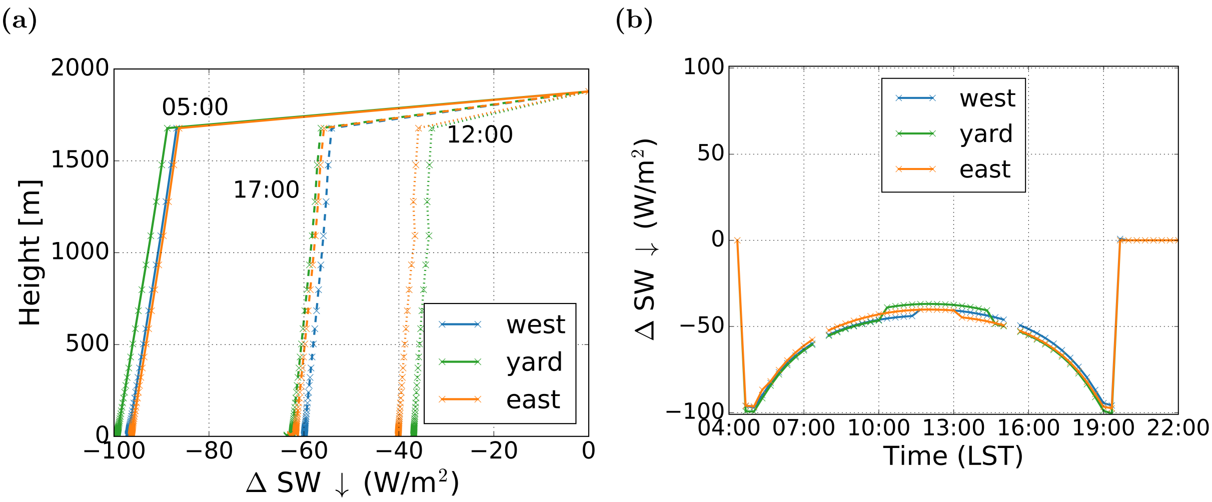

Figure 5.21: Validation test case E for difference in total downward radiation ($SW \downarrow$) for a profiles at 05:00 LST, 12:00 LST and 17:00 LST and (b) time series of the differences at the averaging areas in 1 m height.

Validation test case F is used to evaluate the partial shading by the vegetation (Section 5.2.4) using the tree within the courtyard (Figure 5.15). As expected lower surface temperatures are calculated for shaded building wall and ground grid cells (Figure 5.22a to Figure 5.22d). Which wall grid cells are shaded, varies in accordance with the azimuth angle of the sun during the course of the day. This indicates that the partial shading has been implemented correctly.

Since heating and cooling rates within the atmosphere are unchanged by the shading (Section 5.2.4), atmospheric grid cells are not directly cooled by tree. On the contrary, the absorption of direct radiation within the vegetated canopy grid cells increase air temperature directly (Eq. (5.9)) and over time warm the entire courtyard (Figure 5.22f). This effect exceeds the cooling by the cooler surfaces. The amplitude of warming by the tree canopy might be too high as Schlüter (2006) determined from comparisons with measurements. Possible improvements are discussed in Section 5.4.

Validation case G evaluates the sensitivity of the simulation results to the truncation value of 10^{-5} for the view factor calculation (Section 5.2.3). Table 5.6 shows maximum and relative difference between 04:20 LST and 22:00 LST between the two simulations. The differences are very small for all variables (note the units). Hence, including view factors up to 10^{-6} (`51vfcrit`) yields almost the same result as using only view factors up to 10^{-5} (`51`). Therefore, the used truncation value is sufficient. However, as the maximum differences are that small, probably larger a truncation value of could be also sufficient 10^{-4}.

Table 5.6: Maximum differences for validation test case G for the entire domain in the lowest model level between 04:20 LST and 22:00 LST. T_a is the air temperature, T_g is the ground surface temperature, $LW\downarrow$ is the downward longwave radiation flux.

	T_a [K]	T_g [K]	$LW\downarrow$ [W m^{-2}]
Difference	$1.1 \cdot 10^{-3}$	$2 \cdot 10^{-3}$	$15.1 \cdot 10^{-3}$
Relative difference [%]	0.005	0.003	0.005

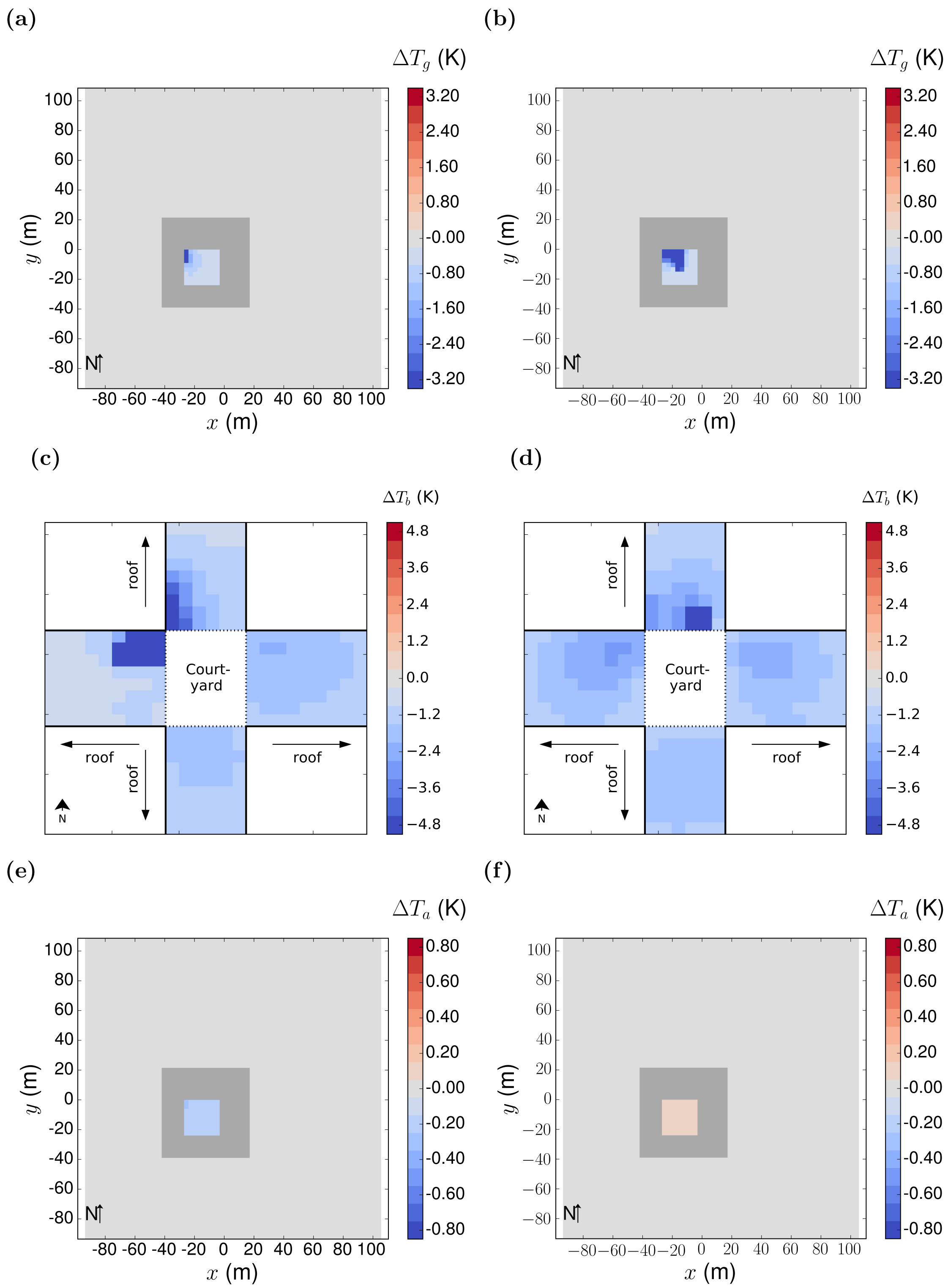

Figure 5.22: Results for validation test case F for (a,b) differences in ground temperature (T_g), (c,d) differences in surface temperature of building walls (T_b) and (e,f) differences in air temperature at 1 m height (T_a) for (a, c, e) 8:40 LST and (b, d, f) 12:40 LST. For the location of the tree see Figure 5.15.

5.3 Model extension for deriving thermal indices

To derive thermal indices from MITRAS model output, in addition to air temperature, humidity and wind speed also the mean radiant temperature T_{mrt} is required. To derive the amount of reflected shortwave and longwave radiation from the building walls and ground surfaces, person-to-wall and person-to-ground view factors ($VF_{p \to i}$) are required. $VF_{p \to i}$ are pre-calculated in GRIMASK together with the surface-to-surface view factors. These and the model results are used in a newly developed post-processor PERCEIVED to calculate T_{mrt} and the thermal indices PET, UTCI, $\mathrm{PT_J}$ (see Chapter 2 and Chapter 4 for details on the indices). The calculation is done offline, to have the opportunity to change personal variables for PET, without having to rerun the atmospheric model.

5.3.1 Calculation of person-to-surface view factors

According to the definition of T_{mrt} (Eq. (3.6), Section 3.1.1), incoming longwave and diffuse shortwave radiation have to be weighted by a view factor ($VF_{p \to i}$) to derive the radiation amount actually received by a person. $VF_{p \to i}$ are calculated following Fanger (1970, p. 164) as shown in Section 3.1.2 by integrating Eq. (3.7) numerically with $d\,(x/y) = d\,(z/y) = d\,(x/z) = d\,(y/z) = 0.01$.

The view factors are calculated at scalar grid points. Ground and wall surfaces are located at vector grid points (Figure 5.3). Since Eq. (3.7) is only applicable if the normal of a surface at one corner passes through the scalar grid point (Figure 3.2), view factors for entire grid cells have to be calculated using view factor algebra (e.g. Eq. (3.25)). Figure 5.23 shows an exemplary situation for view factors between a person and a wall. View factors between a person and a ground surfaces is calculated in analogy.

To calculate the view factor ($VF_{p \to i}$) of a person, visualised as red dot in Figure 5.23, standing in front of a wall consisting of several grid cells, three cases have to be distinguished: (1, red) grid cell directly in front of the person, (2, blue) grid cell directly above or directly to the right or left of the person (3) other grid cells:

1. The view factor to the red grid cell is $VF_{p2{\color{red}\blacksquare}} = 4 \cdot VF_{p2\boxtimes}$
2. The view factor to any bordering blue grid cell is $VF_{p2{\color{blue}\blacksquare}} = 2 \cdot (VF_{p2\boxslash} - VF_{p2\boxtimes})$. For all other blue grid cells, the view factor to grid cells in between has to be subtracted to derive the view factor.

3. The view factor to a diagonally bordering grid cell is $VF_{p2\blacksquare} = VF_{p2\square} - VF_{p2\boxbslash} - VFp2\boxslash + VF_{p2\boxtimes}$. The view factor to any other grid cell (green, grey or yellow in Figure 5.23) can be calculated by subtracting the view factor to all grid cells in between.

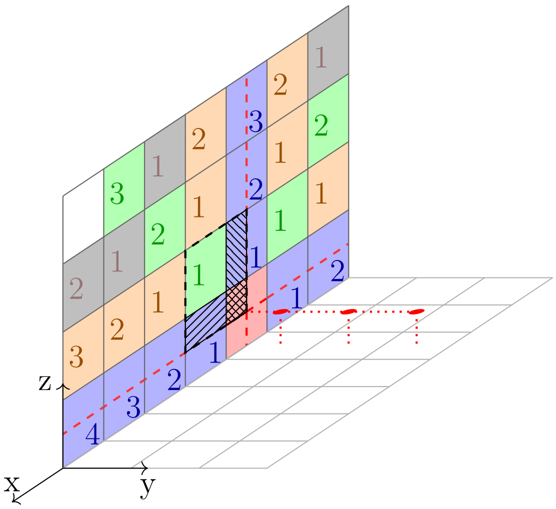

Figure 5.23: Sketch of view factor calculation for person at different distances to wall (red dots) to different wall grid cells (coloured cells).

Based on Table 5.6 a truncation value of 10^{-4} is deemed sufficient to account for all relevant cells for $VF_{p \to i}$. Obscured surfaces are detected by the same algorithm as for surface-to-surface view factors (Section 5.2.3.3, Figure 5.11) and the same method is used to store these view factors (Section 5.2.3.3).

5.3.2 Validation of the person-to-surface view factor calculation

Similarly to the surface-to-surface view factors the implementation of the calculation is validated against known values. The used tests and results are shown in Appendix J.2.

5.4 Discussion of the extensions for MITRAS

The extensions for modelling of radiation within the obstacle layer have been validated using idealised simulations. These simulations differ in their model version and/or in their boundary conditions. A comparison between the simulations indicates that the model extensions show the desired effects. To increase the confidence in the extensions, comparisons with measurements could be conducted in the future.

The extensions could be improved regarding the effect of partially obscured surfaces and multiple reflections of shortwave radiation. The current algorithm to detect obscured surfaces is based on point to point visibility that cannot take into account that the view between two surfaces is partially obscured (Figure 5.11). To improve that visibility polygons for each surface could be derived. For a more accurate representation of the urban heat island, multiple reflections between walls and ground surfaces should be taken into account. This could be done effectively by replacing the view factors by Gebhart factors as suggested by (Saneinejad et al., 2014).

A ray-tracing scheme is an alternative to the view factors calculation as applied in this thesis. In this scheme explicit rays are simulated within the atmosphere to derive the amount of radiation exchanged between buildings. On a rectangular grid, view factors as implemented in this thesis are an accurate and computationally cheap method to account for diffuse radiative exchange between buildings. To achieve the same simulation results using a ray-tracing scheme a sufficient number of rays is required that cover the entire grid cell area, which might be computationally demanding. If such a scheme would be implemented in MITRAS, the implemented view factor calculation within this thesis could serve as validation of the ray tracing scheme. A ray tracing scheme has the advantage that specular surfaces such as water surfaces or windows could be included easier than for the view factor scheme of the current thesis. In addition, absorption and scattering within the atmosphere in the obstacle layer could be accurately accounted for, since rays pass through the actual grid cells. Existing ray-tracing schemes in other obstacle resolving models (e.g. PALM Resler et al., 2017 or ENVI-met Huttner, 2012) neglect this interaction.

A ray-tracing scheme could also improve the partial shading algorithm for vegetation developed in this thesis as discrete elevation sectors (Section 5.2.4) would not be necessary. Modelling of explicit vegetation could also be improved regarding evapotranspiration. Currently, direct short wave radiation absorption by vegetation is directly linked to an increase in air temperature (Eq. (5.9)). Simulations by Schlüter (2006) indicated that this might cause an overheating of the crown. To resolve this, a surface temperature of a tree could be calculated from a full energy balance prognostically. However, results by Lee et al. (2016) indicated that shading by trees is more important than evapotranspiration from grass alone. Therefore, the more important effect has been implemented in this thesis.

6 Modelling the influence of urban water surfaces

The extended and validated MITRAS modelling system (Chapter 5) can be applied to address the guiding research question (GRQ) of this thesis "How strongly do different kinds of urban water surfaces affect their thermal surroundings under various meteorological situations and urban scenarios during different times of the day?". To do so, in Section 6.1 is identified, which meteorological variables, urban and water characteristics affect the influence of urban water surfaces on the thermal environment. As a consequence of this identification, the water influence is simulated for different meteorological situations, which together represent average cloudless summer conditions in Hamburg (Section 6.2.1). The water influence is then analysed for different scenarios both in terms of the size of the water surface and for a different urban morphology (Section 6.2.2). The evaluation methods to quantify the effect of different meteorological conditions and scenarios on the influence of water surfaces are presented in Section 6.3. Using the described methodology, the simulation results are analysed in Section 6.4 and discussed in Section 6.5.

6.1 Thermal effect of water surfaces

Water surfaces affect the thermal environment through energy fluxes from and to the water surface. Eq. (6.1) shows the energy balance of the surface layer of a water body, extending to a depth where the vertical heat transfer is zero (Oke, 1987 and Oke et al., 2017):

$$Q^* = Q_H + Q_E + \Delta Q_S (+\Delta Q_A)(+Q_G) \tag{6.1}$$

where Q^* is the net allwave radiation balance with $Q^* = LW_{net} + SW_{net}$, Q_H is the sensible heat flux density, Q_E is the latent heat flux density, ΔQ_S is the net heat storage and ΔQ_A is the net advective heat flux by currents and Q_G is the ground heat flux density.

Figure 6.1 visualises these energy fluxes from the perspective of the atmosphere for a standing water body (i.e. $\Delta Q_A = 0$). During the day, incoming shortwave radiation (SW, yellow) is in parts reflected according to an albedo (a_{wat}) that changes during the course of the day (Eq. (5.1), Figure 5.2) and with the turbidity of the water (Hathway and Sharples, 2012). The non-reflected part as well as incoming longwave radiation ($LW \downarrow$, black) is absorbed either by the water body itself, leading to a storage of heat, ΔQ_S, or by the underlying soil (Q_G, brown) if the water body is shallow (d, Oke, 1987). In contrast to other surfaces, the surface water temperature (T_{wat}) does not change much in response to those radiation fluxes (Figure 5.1). The lack of this thermal response is due to (1) penetration of shortwave radiation to greater depth and therefore diffuse heating over a large volume, (2) mixing within the water (black arrows), (3) evaporative cooling, which decreases water temperature close to the surfaces and thus destabilises the water column and enhances mixing, and (4) the large thermal heat capacity of water (Oke, 1987).

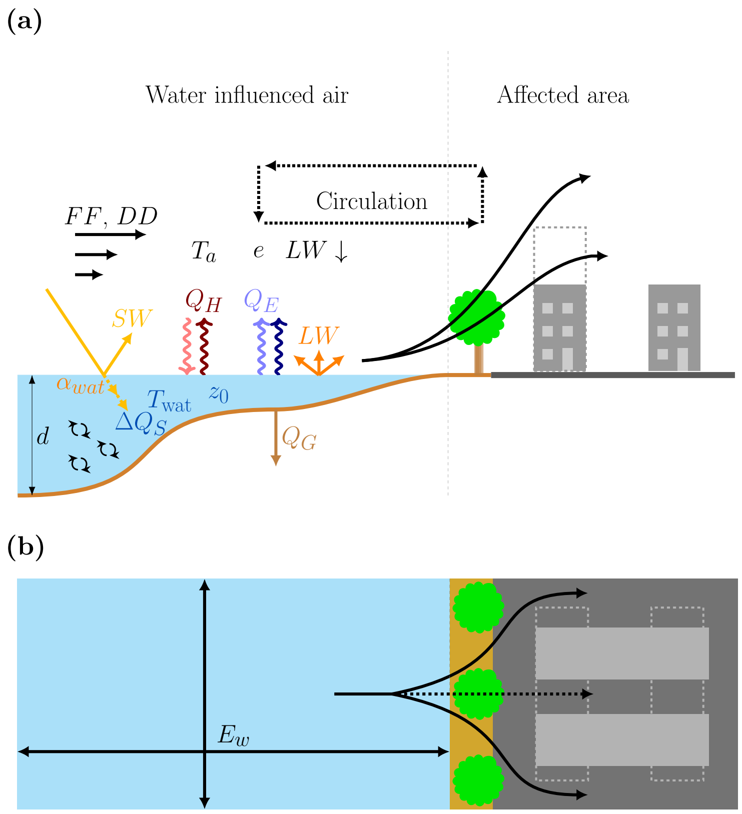

Figure 6.1: (a) cross section and (b) plane view of processes and variables affecting the thermal impact of water surfaces on an adjacent urban area. Circulation and brighter red and blue arrows indicate daytime behaviour.

The water surfaces exchanges heat with the atmosphere predominantly by turbulent latent (Q_E, blue) and sensible (Q_H, red) heat fluxes and to a smaller part by longwave radiation (LW, orange). The direction and strength of the turbulent heat fluxes depend on the wind speed (FF) and the gradients of air temperature (T_a) and humidity (depicted as vapour pressure e) between the water and the atmosphere for sensible and latent heat fluxes, respectively (Oke et al., 2017). The latent heat flux is directed from the water to the atmosphere both day (brighter blue) and night (darker blue). In contrast, the sensible heat flux is usually directed from the atmosphere to the water body during the day (when the air is warmer than the water; bright red) and reversed during the night (dark red), although during different meteorological conditions the water may be colder or warmer the entire day. A cooling during the day and a warming during the night is used as the default for the following discussion, since the lake Alster and river Elbe on average behave in this way. Figure 6.2 shows the difference between air temperature and water temperature during different hours of the day for different seasons (colours) averaged over the period 01.01.2002 to 31.12.2017. The figure is based on 10 min averages measured for Alster (solid line) and Elbe (dotted line). Note that the peak in $T_{air} - T_{\mathrm{wat}}$ at Alster for late afternoon in summer, spring and autumn are due the air temperature measurement device being exposed to solar radiation during these times. During all seasons the water surfaces cool the atmosphere during the afternoon. This is indicated by a positive difference during that time and thus T_{air} being larger than T_{wat}. The exact period differs for the different seasons and the two types of water surfaces. During morning and night, on average the water surface warms the atmosphere in Hamburg. Therefore, water surfaces can intensify the Urban Heat Island (UHI) close to the shoreline and thus deteriorate important night-time thermal comfort (Chapter 1). Such a warming effect have been noted in many studies (e.g. Böttcher, 2017; Broadbent et al., 2017; Hathway and Sharples, 2012; Schlünzen et al., 2010; Steeneveld et al., 2014; Žuvela-Aloise et al., 2016).

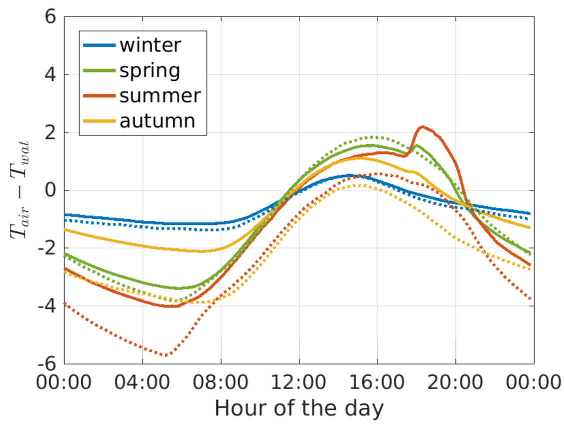

Figure 6.2: Mean diurnal cycle of the difference between air temperature (T_{air}, 3 m above ground) and water temperature (T_{wat}, in 1 m depth) for winter (blue), spring (green), summer (red) and autumn (orange). Solid lines refer to lake Alster (station Lombardsbrücke) and dotted lines to the river Elbe (station Seemanshöft). Values are averaged over the period 01.01.2002 to 31.12.2017.

The air locally cooled or warmed by the water surface is transported downwind (wind direction DD in Figure 6.1a). Thus, the influence of the water surface is largest if the wind direction is perpendicular to the urban environment (Broadbent et al., 2017). According to the reviewed literature (Appendix L) the downwind cooling effect is between 10 m and 1000 m. The encountered temperature change was found to be between 1 K and 6 K. These huge differences for the extent and magnitude of the water surfaces are due to different definitions for "water-influenced air" and due to different characteristics of the investigated water surface, urban environment and meteorological conditions in the different studies.

The meteorological variables (T_a, e, FF, DD, Q^*) and water temperature directly affect the energy fluxes (Eq. (6.1)) and thus the cooling effect of the water surface. Larger wind speeds increase on the one hand latent and sensible heat fluxes, but on the other hand, decrease the time spent above the water surface. This decreased time can cause a smaller cooling during the day, especially for small water surfaces (Hathway and Sharples, 2012; Murakawa et al., 1991). The size of the water body (E_w in Figure 6.1b) is thus an important characteristic for the cooling effect, since it determines the time an air parcel spends above the water surface. For instance, Syafii et al. (2017) noted that a larger pond cools stronger during the day than a smaller water body. In addition, for larger water bodies a thermal circulation can develop (Crosman and Horel, 2010). This is especially important for coastal cities, where an extensive sea breeze can be an important cooling source during the day (Lopes et al., 2011). In addition to the size of the water body, also the water depth (d in Figure 6.1a) influences the cooling of the water surface during the day. The water temperature in shallow water bodies increases more rapidly during the day, which decreases the cooling effect (Hathway and Sharples, 2012). Heusinkveld et al. (2014) estimated the cooling rate of a water column of less than one metre to be even lower than that of asphalt.

In addition to the meteorological condition and water characteristics, the surrounding urban morphology affects the water influence: Depending on the building orientation, height and density (i.e. height to width ratio, dashed buildings in Figure 6.1), air cannot be well transported into the surrounding urban environment (Ashie et al., 2005; Hathway and Sharples, 2012; Murakawa et al., 1991; Tominaga et al., 2015). Furthermore, depending on the used building materials, the cool air from the water body may heat fast in the urban environment (Hathway and Sharples, 2012). Water-side vegetation have been found to support the cooling effect (Hathway and Sharples, 2012; Kuttler, 1991) due to evapotranspiration.

Most studies, and thus also the above discussion, focused on air temperature as a target variable to define the influence of water surfaces. However, the human body responds to all meteorological variables (T_a, e, FF, Q^*) together (Section 2.2.1). Therefore, for people in the vicinity of an urban water surface, the influence of the water surface on other meteorological variables is also important. Due to the small roughness length of water surfaces (Eq. (5.2)) wind speeds are higher close to the shoreline than in the urban surroundings. Although higher wind speeds could decrease the cooling effect of water surfaces in terms of air temperature, as discussed above, they might overall positively affect human thermal comfort as sensible and latent heat fluxes are increased (if the air temperature is below the skin temperature). The latent heat fluxes increase humidity in the surroundings of the water body. For very warm regions this effect might dampen the cooling effect due to air temperature as discussed in Chapter 4. Due to the relatively low water temperatures compared to building materials, longwave radiation fluxes from water bodies are smaller compared to those from buildings and thus decrease mean radiant temperature. However, shortwave radiation can be larger close to the shoreline, if no shading exits. Due to the diurnal cycle of albedo, reflected shortwave radiation is small during the day (Figure 5.2). Overall, this discussion indicates that if all meteorological variables that affect the human thermal environment are taken into account, water surfaces could both positively or negatively affect the human thermal environment close to the shoreline and within the city. Hence, in this chapter the influence of water surface is investigated in human relevant terms in form of thermal indices.

6.2 Performed model simulations

To address the question of this chapter, model simulations are performed with MITRAS for an idealised domain. Idealised simulations are used to derive general conclusions for different urban morphologies. In total 60 different meteorological situations are investigated to derive the sensitivity of the water influence to the meteorological conditions. The situations are described in Section 6.2.1. For three out of the 60 meteorological situations different urban morphologies are investigated. All simulations are carried out both for a canal and a lake to determine the influence of the size of the water surface on the water influence. The different urban and water scenarios are described in Section 6.2.2. The set-up of the MITRAS simulations are depicted in Section 6.2.3.

6.2.1 Meteorological situations

The investigated meteorological situations represent clear sky summer conditions in Hamburg. Those situations have been selected, since the cooling influence of water surfaces during these days is most important. To assess, whether heat stress conditions are relevant in Hamburg, the frequency of threshold days (e.g. hot days) as well as changes in stress classes for the Physiological Equivalent Temperature (PET) are investigated for the airport station Fuhlsbüttel. The analyses indicate that although the bio-climatic conditions in Hamburg are generally mild, the frequency of heat stress situations has increased in the past (detailed results are given in Appendix M). For the future, a similar trend is expected (Hoffmann et al., 2016; Trusilova and Riecke, 2015) and thus heat stress situations are worth to be investigated. Furthermore, by using idealised simulations the results are not specific for the situations in Hamburg and might thus be transferable to other regions, which encounter more frequent heat stress situations.

Air temperature (T_a), humidity (here used as relative humidity RH), wind speed (FF) and the temperature difference of daily mean air and water temperature ($\overline{T}_a - \overline{T}_{\mathrm{wat}}$) are identified as important variables for the influence of water surfaces in Section 6.1. Consequently, the 60 meteorological situations differ for these variables. All other meteorological input variables, such as soil temperature or initial stratification, are the same for all simulations. To derive the ranges of values for T_a, RH, FF and $\overline{T}_a - \overline{T}_{\mathrm{wat}}$ for cloudless summer conditions in Hamburg, measurements for the Hamburg Weathermast, for Fuhlsbüttel and for the Lombardsbrücke (Alster) are used (Table 6.1). The measurements have been filtered for entirely cloudless days using the same method as for the full-space sensitivity analysis of the thermal indices (Section 4.2.2.2).

In total 142 entirely cloudless days are found for summer at Weathermast (50 days) and Fuhlsbüttel (92 days). Those days are not entirely independent, as consecutive days as well as same days at Weathermast and Fuhlsbüttel are included in the set of conditions. Nevertheless all days have been used to derive the initial conditions for the meteorological situations. For each of the 142 cloudless days, the diurnal average water temperature and air temperature at Lombardsbrücke (Alster) is used to derive the ranges for the water-air temperature difference. Daily averages for the water temperature are sufficient, since the water temperature is constant in MITRAS (Section H.5).

Similar to the sensitivity analysis for the thermal indices (Chapter 4), the determined

Table 6.1: Measurement periods and characteristics of the used data sets for the derivation of initial conditions for the simulations. Locations of the stations are shown in Figure M.2.

Variable	Weathermast	Fuhlsbüttel	Lombardsbrücke
Air Temperature	01.04.2004–29.02.2016 (2 m, 10 minutes average)	01.01.1950–31.12.2015 (2 m, hourly)	01.11.2002–31.12.2017 (daily average)
Relative humidity	01.04.2004–29.02.2016 (2 m, 10 minutes average)	01.01.1950–31.12.2015 (2 m, hourly)	-
Wind speed	01.04.2004–29.02.2016 (height levels in m: 10, 50, 110, 175, 250, 280, 10 minutes average)	01.01.1950–31.12.2015 (10 m, hourly), zero wind speed treated as missing value	-
Cloudiness	01.04.2004–29.02.2016 (Ceilometer, 10 minutes average)	1950 (by a meteorological observer, hourly)	-
Water temperature	-	-	01.11.2002–31.12.2017 (daily average)
Soil temperature	-	01.01.1961–31.12.2017 (depth levels in cm 20, 50 and 100; aggregated to daily averages)	-

input space of each variable is sampled according to its frequency distribution (Section 4.2.2.2). For the analysis in this chapter, only the distributions at the initialisation time of the simulations at 04:00 LST are required. Figure 6.3 shows the frequency distributions for $T_{a,4}$, $FF_{10,4}$, $\overline{T}_a - \overline{T}_{\mathrm{wat}}$ and RH_4 along with the four parametric PDF with the highest Bayesian information criterion. The chosen distributions based on the Kolmogorov-Smirnoff-Test and the Anderson-Darling-Test indicated by stars (see Section 4.2.2.2 for details on the methodology). For $\overline{T}_a - \overline{T}_{\mathrm{wat}}$ the parametric PDF with the third highest p-value had to be used, for the higher scored functions no inverse function is available in MATLAB. The chosen distribution functions for air temperature and wind speed are the same as for the sensitivity analysis (Appendix E). For the difference between water and air temperature ($\overline{T}_a - \overline{T}_{\text{wat}}$) a generalised extreme value function with parameters -0.17 K, 1.56 K and -0.4 is determined to fit the measurements best. For relative humidity an extreme value function with parameters 88.82 % and 6.36 % is used.

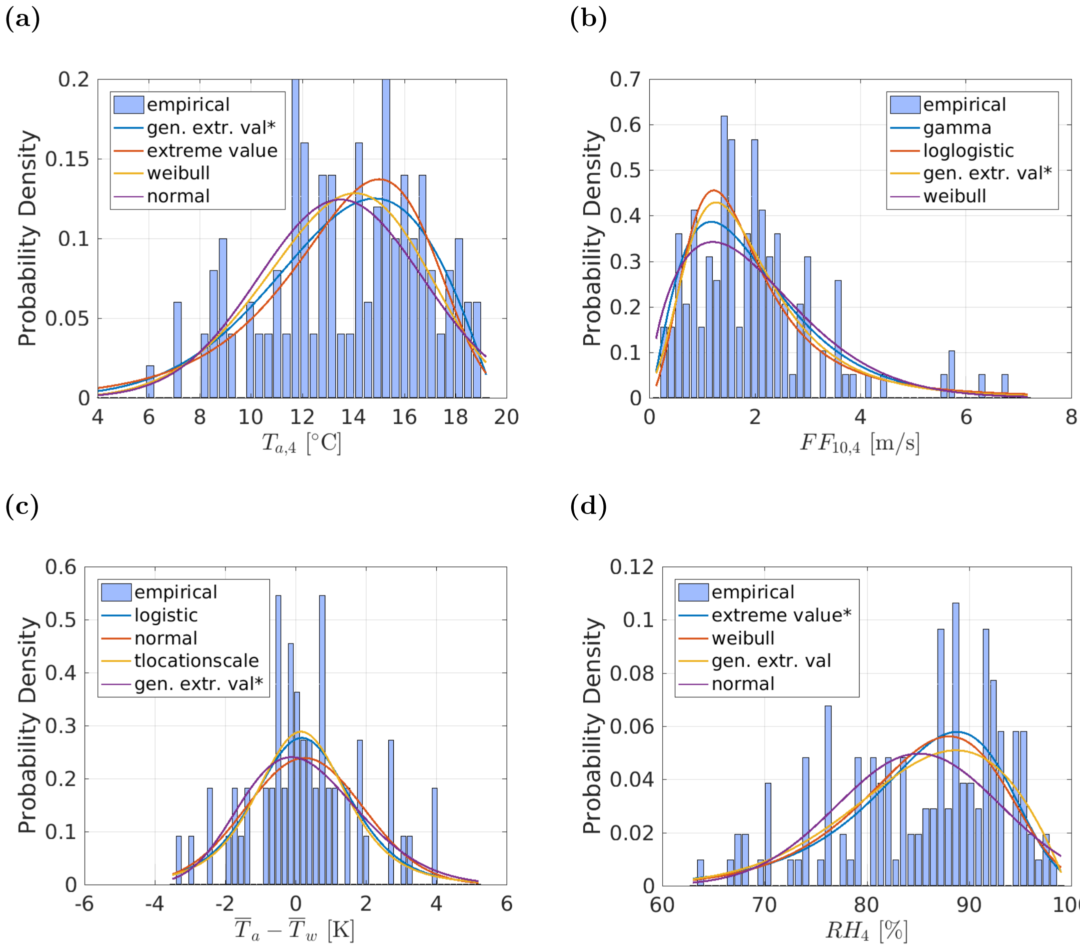

Figure 6.3: Measured probability density function (blue bars) and fitted distributions (lines) for (a) air temperature, (b) wind speed in 10 m, (c) temperature difference between air and water and (d) relative humidity for 04:00 LST. 'gen. extr. val' refers to a generalised extreme value distribution. Please note the different scales of the ordinates.

To be able to apply the elementary effect test (EET, Section 4.2.2.2) to analyse the impact of the different meteorological variables, the samples are drawn from the parametric distributions functions using the radial-based design (details are given in Section 4.2.2.2). EET uses finite difference quotients to measure the sensitivity of an output variable to a change in one input variable. In total $r = 12$ different values have been sampled for each of the $M = 4$ meteorological variables, which results in a total number of $r \cdot (M + 1) = 60$ meteorological situations. Figure 6.4 shows the sampled situations (red) along with the observations for Weathermast (blue) and Fuhlsbüttel (black). Green circles indicate a subset of samples used to investigate the impact of different urban scenarios on the water influence (Section 6.2.2). The samples reproduce the observations well; even the observations for vapour pressure are quit well met, despite T_a and RH having been sampled.

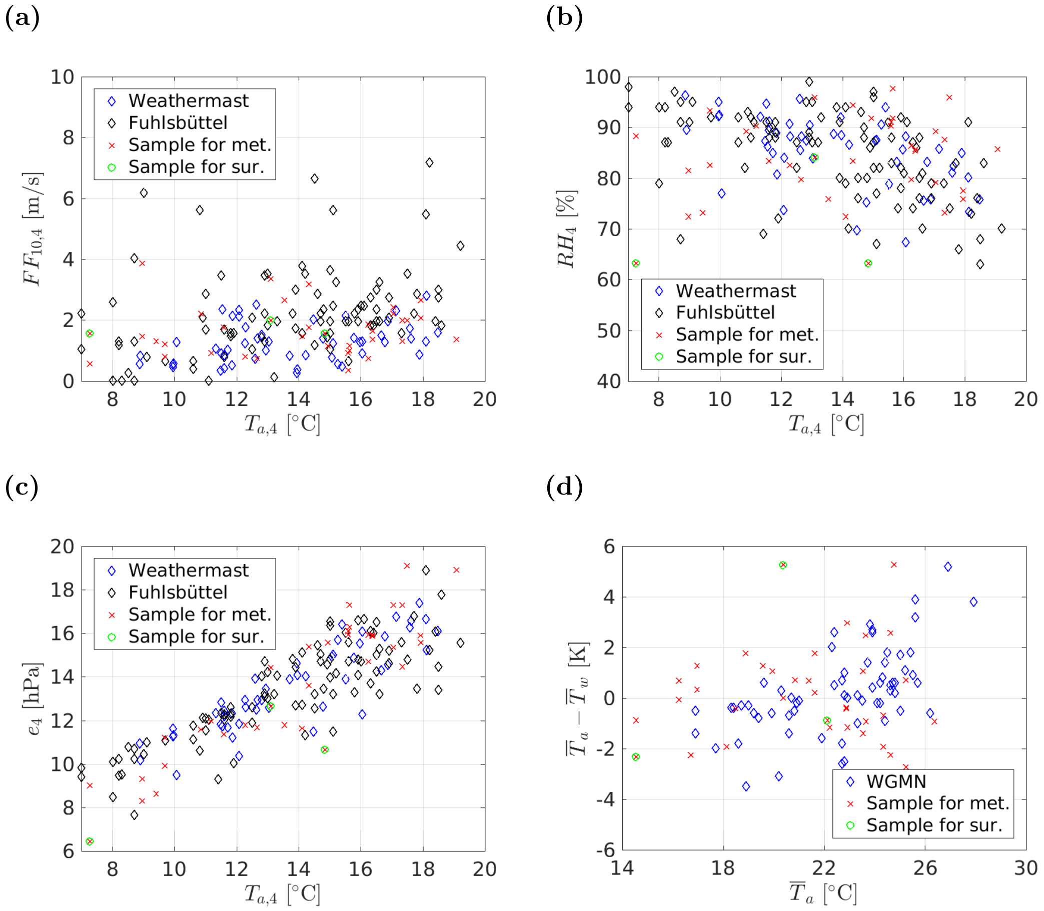

Figure 6.4: Scatter plots of measured (blue and black) and sampled values (red for entire sample set and green sub-set for urban scenarios) for (a), (b) and (c) air temperature ($T_{a,4}$) to wind speed in 10 m ($FF_{10,4}$), to relative humidity (RH_4) and to vapour pressure (e_4) all at 04:00 LST and (d) diurnal mean air temperature ($\overline{T}_a$) to daily average temperature difference between air and water ($\overline{T}_a - \overline{T}_{\text{wat}}$).

For the initial values, the $\overline{T}_a - \overline{T}_{\text{wat}}$ is converted to a water-air temperature difference for 04:00 LST. To do so, the difference between daily average air temperature and air temperature at 04:00 LST ($\overline{T}_a - T_{a,4}$) for the 142 cloudless days has been calculated for the Weathermast and Fuhlsbüttel (Figure 6.5). The median (7.3 K) of this distribution is used to convert the diurnal mean air temperature values to initial values for air temperature at 04:00 LST and diurnal mean water temperature: $\overline{T}_{\text{wat}} = -(\overline{T}_a - \overline{T}_{\text{wat}}) + T_{a,4} + 7.3$. This equation has also been used to convert the sampled values of $T_{a,4}$ to $\overline{T}_a$ in Figure 6.4d.

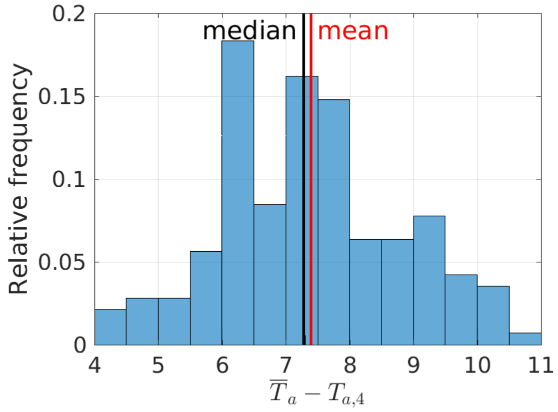

Figure 6.5: Relative frequency of difference between daily average air temperature ($\overline{T}_a$) and air temperature at 04:00 LST ($T_{a,4}$) for the 142 cloudless days.

The sub-set of meteorological conditions to investigate the effect of urban morphologies on the influence of the water surfaces (green in Figure 6.4) is selected to represent meteorological conditions with a high potential of latent, sensible and combined latent and sensible heat flux: maximal latent heat flux potential is defined by minimal RH combined with maximal $FF_{10,4}$ (meteorological situation number 59 in Appendix N); maximal absolute sensible heat flux by maximal $\overline{T}_a - \overline{T}_{\mathrm{wat}}$ combined with maximal $FF_{10,4}$ (meteorological situation number 20 in Appendix N) and the highest potential of both fluxes by selecting the situation for which both criteria are large (situation number 57 in Appendix N).

Besides initial conditions for T_a, RH and FF and boundary conditions for T_{wat}, MITRAS also uses the day of the year to determine incoming shortwave radiation, initial stratification and initial wind direction and soil temperature and moisture as initial and boundary conditions (Section 5.1). The 28.07. is chosen as the simulation day as for this day the average solar radiation amount for summer is received for the latitude of Hamburg (Section 4.2.2.2). The initial stratification is chosen from the potential temperature profiles derived from the 50 cloudless days at the Weathermast (Figure 6.6a). The frequency of normalised potential temperature differences between 2 m and 280 m (and 250 m if no measurements in 280 m were available) is presented for different 2 m air temperatures in Figure 6.6b. The frequencies do differ systematically for the 2 m air temperatures ranges. Therefore, median stratification of 0.027 $\mathrm{K\,m^{-1}}$ is used for all simulations up to 300 m. Above, due to a lack of more detailed information, a slightly stable standard atmosphere (0.035 $\mathrm{K\,m^{-1}}$) is used.

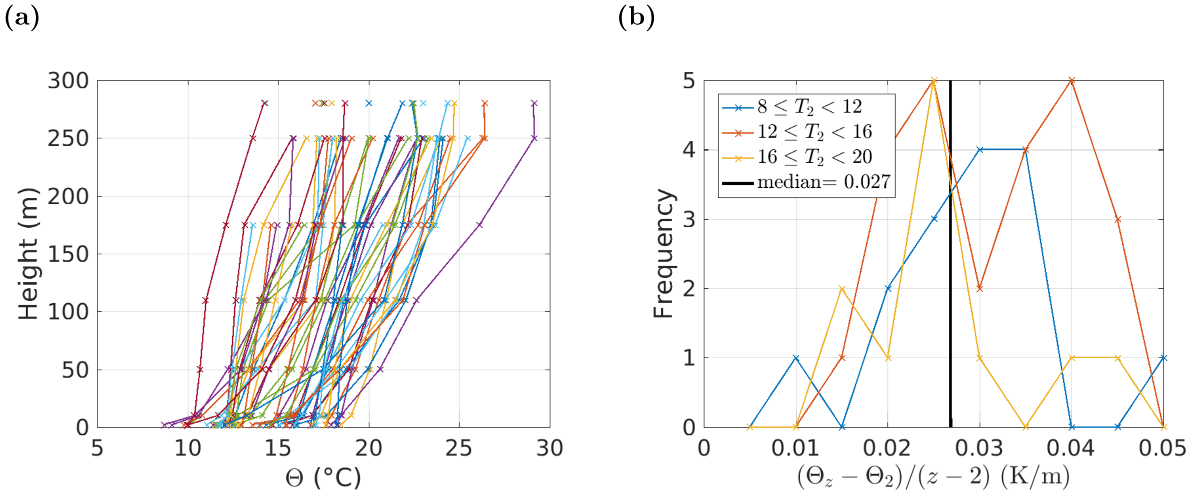

Figure 6.6: (a) potential temperature (Θ) change with height for 04:00 LST for 50 cloudless days at the Weathermast and (b) frequency of potential temperature differences between z = 280 m (or z = 250 m if 280 m was not available) and 2 m normalised with the Δz for three different 2-m air temperature (T_2) ranges (colours).

The predefined soil temperature in MITRAS represents a longer term average around the initialisation day (Section 5.1). Therefore, a climatological summer average soil temperature is used to derive the conditions. Figure 6.7 shows the soil temperature in three depths at Fuhlsbüttel for June, July and August between 1961 and 2017. Overall soil temperatures increased since the beginning of the measurements. Since the variability on an annual basis exceeds this trend, the average soil temperature in 20 cm, 18.1 °C, is used for the simulations. As initial conditions for soil moisture two days without precipitation preceding the initial day of the simulations are assumed.

The initial wind direction is set to south for the wind in 10 m height, to ensure that the wind initially flows over the water surface into the urban environment. As for the simulations open lateral boundary conditions for the wind are used (Appendix K), the wind direction can change during the simulation day. This has the advantage that in MITRAS thermal circulations with ageostropic winds can develop.

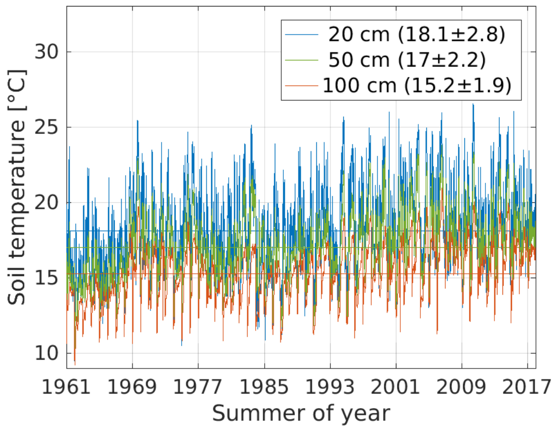

Figure 6.7: Soil temperature for months June, July and August between 1961 and 2017 in different depths (colours) at Fuhlsbüttel. Numbers in brackets indicate averages and standard deviations over the entire measurement period.

6.2.2 Urban and water scenarios

An idealised model domain is constructed to investigate the influence of water surfaces under the different meteorological situations. The domain consists of a water surface to the south of the urban area of interest. Two different water surface sizes are investigated, a large open water surface with a width of more than 220 m inspired by the lake Alster in Hamburg (scenario termed `e220` in this chapter) and a canal with a width of 30 m, which is a typical width encountered for canals in Hamburg (`e30`). The two types of water surfaces are shown in Figure 6.8a and Figure 6.8b, respectively. Buildings are placed regularly to the north of the lake and both to the north and south of the canal. Two different building types are investigated block buildings (`bb`, Figure 6.8a) and terraced buildings (`bt`, Figure 6.8b). These two building types are placed at the same locations in the different scenarios to derive how such a subtle change in building morphology could impact the influence of water surfaces. Most simulations are carried out without waterside vegetation (`v0`); in some simulations waterside vegetation is present (`v1`, Figure 6.8a). The built-up urban area is surrounded by cropland (Figure 6.8) to increase the roughness of the surface without placing buildings explicitly.

Figure 6.8 shows only two out of the investigated scenarios; Table 6.2 summarises all scenarios. The impact of different meteorological situations on the influence of water surfaces is investigated only for the scenario without waterside vegetation and with block

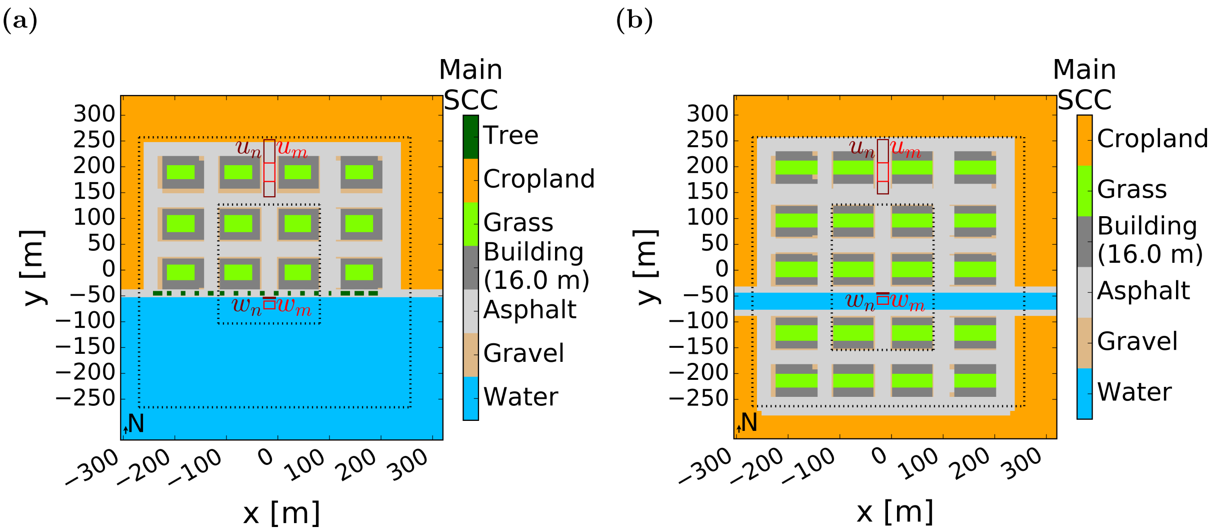

Figure 6.8: Model domain for (a) `e220v1bb` and (b) `e30v0bt`. Dotted lines indicate uniform areas; red areas u and w indicate averaging areas (Section 6.3.2).

buildings but both for the canal (`e30v0bb`) and the lake (`e220v0bb`). The impact of terraced buildings instead of block buildings and the presence of waterside vegetation is analysed only for three meteorological situations (green in Figure 6.4).

Table 6.2: Performed MITRAS simulations with number of meteorological (shortened 'met.') situations.

Impact of...	influence of canal	influence of lake
meteorology on...	`e30v0bb`, 60 met. situations	`e220v0bb`, 60 met. situations
building morphology on...	`e30v0bt`, 3 met. situations	`e220v0bt`, 3 met. situations
vegetation on...	`e30v1bb`, `e30v1bt`, 3 met. situations	`e220v1bb`, `e220v1bt`, 3 met. situations

The characteristics of the different scenarios are summarised in Table 6.3. The relative position of buildings, their heights and extents have been chosen based on Local Climate Zone (LCZ) characteristics. Local Climate Zones (LCZs) categorise different urban morphologies by defining "regions of uniform surface cover, structure, material, and human activity that span hundreds of meters to several kilometers in horizontal scale" (Stewart and Oke, 2012). Each LCZ is defined by ranges of 7 characteristics: sky view factor, average aspect ratio, building surface fraction, pervious surface fraction, impervious surface fraction, roughness height and terrain roughness class.

Table 6.3: Properties of the different urban scenarios `e30`, `e220`, `v0`, `v1`, `bt`, `bb`. See text for the meaning of the abbreviations.

Property	`e30`	`e220`	`v0`	`v1`	`bt`	`bb`
Building height [m]	16					
Street width [m]	30					
Building width [m]	15					
Built-up floor area [m]	80 × 60					
Water extent [m]	30	220				
Vegetation			No	17 m high		
Courtyard size [m]					30 × 80	30 × 50

The urban scenarios for this study are chosen in such a way that all correspond to the same LCZ. Thereby, the variability of human thermal environments in the same LCZ but different building configurations can be assessed. LCZ 5 is used for all scenarios, because it is the most frequent class for the inner city of Hamburg (Bechtel et al., 2015). Table 6.4 summarises the derived values of the urban scenarios for the different LCZ characteristics. In the vegetated scenarios only the pervious and impervious fraction of the surface change slightly.

To represent the explicit vegetation in the scenarios with waterside vegetation (`v1`), the three-dimensional LAD is used (Section 5.1). The vertical distribution of LAD is specified by Eq. (6.2). Eq. (6.2) is based on an empirical relation derived by Lalic and Mihailovic (2004) and uses vegetation height (h_v), maximum Leaf Area Density (LAD_m) and height of maximum Leaf Area Density (h_{LAD_m}) to define the LAD.

$$LAD(z) = LAD_m \left(\frac{h_v - h_{LAD_m}}{h_v - z} \right) \exp \left[n \cdot \left(1 - \frac{h_v - h_{LAD_m}}{h_v - z} \right) \right] \tag{6.2}$$

The parameter n is used to define the shape of the tree:

$$n = \begin{cases} 6 & 0 \leq z \leq LAD_m \\ 0.5 & LAD_m \leq z \leq h_v \end{cases} \tag{6.3}$$

Table 6.4: Evaluation of the characteristics of the urban scenarios for the different Local Climate Zone (LCZ) characteristics.

Characteristic	`e30v0bt`	`e30v0bb`	`e220v0bt`	`e220v0bb`	LCZ 5	LCZ 6
Sky view factor	0.7	0.7	0.7	0.7	0.5–0.8	0.6–0.9
Aspect ratio	0.53	0.53	0.53	0.53	0.3–0.75	0.3–0.75
building surface fraction	0.2	0.2	0.2	0.3	0.2–0.4	0.2–0.4
Impervious fraction	0.5	0.5	0.5	0.5	0.3–0.5	0.2–0.5
Pervious fraction	0.3	0.3	0.3	0.2	0.2–0.4	0.3–0.6
Roughness height [m]	16	16	16	16	10–25	3–10
Roughness class	6 − 7	6 − 7	6 − 7	6 − 7	5 − 6	5 − 6

For all waterside trees the same parameters are used (h_v=17 m, h_{LAD_m}=12 m, LAD_m=1.6 m^2 m^{-3}). The surface below the trees is grass.

6.2.3 Model set-up

The model domain is represented both horizontally and vertically by a non-uniform grid. The horizontal resolution increases from 3 m in the inner domain (inner dotted rectangle in Figure 6.8) to 9 m in the outer domain (outer dotted rectangle in Figure 6.8). The vertical resolution is 2 m up to a height of 42 m and increases above to 200 m up to the model top at about 2500 m height. This height is chosen based on the one dimensional simulations for the boundary conditions of short and longwave radiation (Section 5.2.5.1). The simulations indicate that this height should be above the boundary layer.

The simulations are carried out for one continuous day in order to evaluate daytime and nighttime influence of the water surfaces. The initial meteorological conditions at 04:00 LST have been described in Section 6.2.1 and are summarised in Appendix N. The used parameterisations, boundary conditions and numerical schemes in this study are presented in Appendix K. All simulations are performed without considering condensation of water vapour. This process has been left out, as the reviewed thermal indices currently cannot evaluate discomfort due to the presence of water droplets from fog or precipitation on the skin.

In two simulations (`e220v0bb_18` and `e220v0bb_62`) the initially stable stratification (Figure 6.6) in combination with high wind speeds lead to numerical instabilities at about 500 m height at about 07:00 LST. To avoid those instabilities, in those simulations a 7-point filter was applied for all wind components for all heights above two building heights (Appendix O). Therefore, for those simulations the model physics differs from the other simulations. However, as those simulations are not compared directly to another simulation but are used in a statistical way, both simulations have been included in the analysis. For all simulations domain average values for the three wind components, air temperature and absolute humidity for every model time step have been investigated to detect, whether in any simulation instabilities develop. The results indicate that the simulations in general not exhibit any unreasonable behaviour.

Water surfaces are presented in MITRAS as standing surfaces with zero depth and constant water temperature. Therefore, ΔQ_S in Eq. (6.1) is not explicitly simulated.

6.3 Analysing methods

6.3.1 Applied thermal indices

To evaluate the influence of urban water surfaces on the human thermal environment, the Physiological Equivalent temperature (PET) and the Universal Thermal Climate Index (UTCI) are calculated from the simulation results. For the calculation of PET the standard characteristics of the reference person are used (Table 2.3). For the present analysis the VDI version of PET ($\mathrm{PET}_{\mathrm{vdi}}$) is used, since it corresponds to the published version of PET and is, based on the current knowledge, to be confirmed as a standard in the updated version of VDI (2008). Since $\mathrm{PET}_{\mathrm{vdi}}$ is not sensitive to humidity (Chapter 4), the effect of humidity on the human thermal environment can only be evaluated with UTCI. In this chapter, PET is used short for $\mathrm{PET}_{\mathrm{vdi}}$.

UTCI requires wind speeds in 10 m height as input. Thus, the simulated values in 1 m height are converted to 10 m by using a logarithmic wind profile. UTCI converts wind speeds in 10 m height with the same approach to 1 m height. In some simulations wind speeds below 0.5 $\mathrm{m\,s^{-1}}$ are calculated for the converted wind speed to 10 m height. Since the regression version of UTCI cannot be applied for such small wind speeds, $FF_{10} = 0.5$ is used those situations (Bröde et al., 2012).

For meteorological situations with very high relative humidity values at 04:00 LST, relative humidity values above 100 % have been calculated before sunrise. Since the simulations are preformed without considering condensation of water vapour (Section 6.2.3) no fog develops during those situations. For the calculation of both thermal indices during those times $RH = 100$ % is used.

6.3.2 Assessment of water influence

The strength of the influence of the water surface (shortened as "water influence" in the following) is assessed in terms of the penetration depth of the influence into the urban environment and the magnitude of the influence. The magnitude characterises the difference of a variable between the water influenced air and a non- or little influenced air. Both aspects of the water influence are evaluated for PET and UTCI as well as for their meteorological input variables air temperature (T_a), vapour pressure (e), wind speed (FF) and mean radiant temperature (T_{mrt}). By doing so, the influence of the water surfaces on the thermal indices can be compared to their input variables. χ is used representative for all variables ($\chi \in \{T_a, e, FF, T_{mrt}, PET, UTCI\}$). All values are evaluated at 1 m height, as this is the relevant height for humans. In the following the methods to derive the penetration depth and magnitude of the water influence for the different χ are described.

6.3.2.1 Penetration depth of the water influence

To define the penetration depth of the water influence two normalised indices are defined. Those indices describe to which fraction γ a variable χ is influenced by the water surface at a certain location and time. For the normalisation a water reference area w and an urban reference area u (Figure 6.9) are used to define a fully water influenced state of χ ($\chi_w(t)$) and a mostly urban influenced state ($\chi_u(t)$). In between, $\chi(y,t)$ varies due to the influence of both the water and the urban area. The normalisation has the advantage that γ can be defined in the same way for all χ. This enables to objectively compare the penetrations depths for the different variables and urban scenarios, without having to choose arbitrary threshold values for each quantity.

The monotonic index for the penetration depth, γ_m, assumes that χ changes monotonically from the water to the urban reference area (Figure 6.9, red). Thereby, the fraction γ_m is defined by

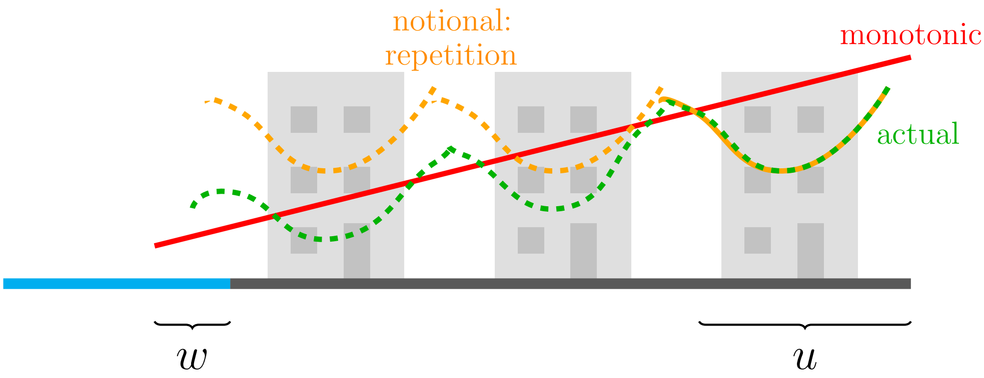

Figure 6.9: Cross section through an urban area along a road to illustrate the monotonic (red) and notional (orange) method to derive the penetration depth of the influence of a water surface (blue) for a specific quantity (green). u and w indicate an urban and water reference domain.

$$\gamma_m(y,t) = \frac{\chi(y,t) - \overline{\chi}_{um}(t)}{\overline{\chi}_w(t) - \overline{\chi}_{um}(t)}. \tag{6.4}$$

The averaged values of a quantity χ over the urban and water reference areas, $\overline{\chi}_u(t)$ and $\overline{\chi}_w(t)$ are time-dependent. In Figure 6.8, the averaging domains for the monotonic method are depicted as u_m and w_m.

For some quantities a monotonic change from the water edge to the urban reference cannot be expected. For instance, shortwave radiation, and consequently T_{mrt}, shows an alternating pattern of high and low values due to shaded and unshaded areas by buildings. To isolate the water influence for such type of χ a notional course of χ is constructed. This course reflects how χ would vary along the street canyon under the same meteorological conditions, if no water surface exists (Figure 6.9, orange). This course is constructed by using the pattern at the last street canyon as a proxy of an uninfluenced urban street canyon. The course is repeated up to the water edge. The difference between this notional course and the actual course can be used to derive $\gamma_n(y,t)$, by normalising the difference with the difference at the water edge:

$$\gamma_n(y,t) = \frac{\chi(y,t) - x \cdot \chi_{uf}(y,t)}{\chi_w(t) - \chi_{uf}(y,t)}. \tag{6.5}$$

$\chi_{uf}(y,t)$ represents the course of χ in the uninfluenced street canyon and x the number of street canyons up to the water edge. For the actual model domain (Figure 6.8) the north-most street canyon is used (u_n) and therefore $x = 3$. Since u_n is located in the non-uniform part of the domain, the values are interpolated to the nearest grid point of a uniform grid with $\Delta y = 3$ m.

Both γ_m and γ_n represent averages across the street, i.e. in x-direction. This is done to take the situation within the entire street canyon into account. In y-direction γ_m and γ_n are smoothed by a running mean over 3 grid cells. If $\overline{\chi}_w(t) - \overline{\chi}_u(t)$ is below a certain threshold, γ_m and γ_n are not calculated for that time. This is due to small absolute deviations resulting in very high relative differences due the normalisation. For all temperature related variables ($\chi \in \{PET, UTCI, T_a, T_{mrt}\}$) a threshold of 0.5 K is used. For FF the maximum of 0.1 m s^{-1} and $0.05 \cdot \sqrt{u_g^2 + v_g^2}$ is used to take into account the larger scale wind speed (u_g, v_g). e has not been filtered as differences are overall small.

γ_m and γ_n are calculated for each location y between the water and urban reference areas. To compare γ_m and γ_n for the different meteorological situations and urban scenarios (Table 6.2), the location y, where the water influence falls below a threshold of 30 %, $y(\gamma = 0.3)$, is defined as the penetration depth of the influence of the water surface. That is, the water influence on χ at that location is just below on-third. Different values for this threshold value have been tested. All yield similar results but naturally different penetration depths.

6.3.2.2 Magnitude of the water influence

As a measure for the magnitude of the water influence (Γ) on χ, the difference between the value at a certain location y and the value in the urban average area u_m (Figure 6.8) is used:

$$\Gamma(t) = \chi_y(t) - \chi_{u,m}(t) \tag{6.6}$$

The maximum magnitude of the water influence is defined at a location 4.5 m onshore (Γ_{sh}). To derive the magnitude of the water influence further within the city, the magnitude at the penetration depth, $\Gamma_{0.3} = \chi_{0.3} - \chi_{u,m}$ is used. Please note that the location $y(\gamma = 0.3)$ can vary during the course of the day.

6.3.3 Meteorological influence via Elementary Effect Test

The Elementary Effect Test (EET) is applied to assess the meteorological impact on the penetration depth, $y(\gamma = 0.3)$, and the magnitude Γ_{sh} and $\Gamma_{0.3}$ of the water influence. The EET is described in detail in Section 4.2.2.2; Eq. (4.9) is reproduced in Eq. (6.7) for convenience. It calculates how much the aforementioned three target values, I_w, differ in response to a change in one initial variable $i \in \{T_{a,4}, RH_4, FF_{10,4}, \overline{T}_a - \overline{T}_{\text{wat}}\}$. All other input variables are fixed for this calculation. The finite difference quotients are scaled with the sampled input range for each variable to make them comparable for the different input variables. The finite difference quotients are referred to as Elementary Effects for a variable i for a certain situation j, EE_i^j. The sum over all meteorological situations j of EE_i^j, $EE_{i,m}$, defines the direct or main effect of one input variable i on the variability of I_w. The standard deviation of EE_i^j ($EE_{i,std}$, Eq. (4.10)) can be used to assess the importance of interactions between the different variables to determine the variability in I_w. The actual values of $EE_{i,m}$ and $EE_{i,std}$ are not meaningful; instead the relative differences between the variables can be interpreted to rank different input variables i according to the sensitivity of I_w to i.

$$\begin{aligned} EE_{i,m} &= \frac{1}{n}\sum_{j=1}^{n} EE_i^j \\ &= \frac{1}{n}\sum_{j=1}^{n} \frac{I_w\left(\overline{x}_1^j, ..., \overline{x}_i^j + \Delta_i^j, ...\overline{x}_m^j\right) - I_w\left(\overline{x}_1^j, ..., \overline{x}_i^j, ...\overline{x}_m^j\right)}{\Delta_i^j} \cdot c_i \end{aligned} \tag{6.7}$$

6.4 Simulation results for the influence of water surfaces

In Section 6.4.1 a meteorological situation is selected to analyse the general influence of a lake and a canal on the human thermal environment in the urban area. In Section 6.4.2 the impact of different meteorological situations on the water influence is assessed. In Section 6.4.3 the impact of different urban morphologies is determined.

6.4.1 General influence of urban water surfaces

Detailed simulation results are presented for the meteorological situation `57` that is characterised by the highest combined potential for sensible and latent heat fluxes at 04:00 LST (Section 6.2.1). The initial conditions at 04:00 LST for the four varied meteorological input variables are $T_{a,4} = 15$ °C, $RH_4 = 63$ %, $T_{\text{wat}} = 23$ °C, $FF_{10,4} = 1.6\ \text{m s}^{-1}$ (Appendix N). This meteorological situation is selected for detailed investigations, because of all samples it has the highest combined potential for latent and sensible heat flux (Section 6.2.1) and thus both aspects of the thermal influence can be analysed. This situation was simulated for all urban morphology scenarios. Here the building block scenario without water-side vegetation `v0bb` is selected, since for this scenario the meteorological impact on the water influence is determined (Table 6.2). Both the results for the lake (`e220v0bb_57`) and the canal (`e30v0bb_57`) are discussed.

6.4.1.1 Simulated human thermal environments

Figure 6.10 shows simulation results for PET at 1 m height for the lake on the left (`e220v0bb_57`; Figure 6.10a,c,e,g) and the canal on the right (`e30v0bb_57`; Figure 6.10b,d,f,h). Figure 6.10a,b show the results for 08:00 LST, Figure 6.10c,d for 12:00 LST, Figure 6.10e,f for 16:00 LST and Figure 6.10g,h for 20:00 LST. The colours reflect thermal stress classes: blue is slight cold stress, green is no stress, yellow is slight heat stress, orange is moderate heat stress and red colours refer to various categories of very and extreme heat stress with very dark red colours exceeding the usually PET scale (Table 2.4). Therefore, the scale is extended by two heat stress categories, 41–45 °C and 45–50 °C, according to Matzarakis and Fröhlich (2015).

PET shows a clear diurnal cycle with higher values around noon (Figure 6.10c,d) compared to morning (Figure 6.10a,b), afternoon (Figure 6.10e,f) and evening (Figure 6.10g,h). Shading by buildings is clearly visible by smaller PET values during morning in the west, at noon in the north and during afternoon in the east of buildings. Although the lake and the canal exhibit the same meteorological conditions at 04:00 LST, very different human thermal environments develop during the day: PET values are much higher in the urban environment in the canal scenario. This is mainly caused by an reduced inner city wind speed and corresponding higher building wall temperatures in the canal scenario. In the lake scenario much higher wind speeds are simulated due to a sea breeze during the day, which is driven by the thermal contrasts between the urban area and the lake. As for the simulations open boundary conditions are used for the wind components, the lake implicitly extends to the south of the model domain. Due to the low roughness length of the water surface, the average wind speed increases during the simulation. In contrast, for the canal no such thermal circulation can develop, since the size of the water surface is too small. Instead a flow through and around the urban area develops. After sunset at about 19:30 LST the human thermal environment remains warmer in the canal scenario due to the smaller wind speeds and larger building wall temperatures.

Figure 6.11 shows the same simulation results but for UTCI. The colour coding reflects the stress classes of UTCI, which has a larger range for comfortable conditions (green). Overall PET values take a much wider range both in terms of actual values and in terms of stress classes. For UTCI mostly no thermal stress or slight heat stress is simulated, except for midday and afternoon. These differences between the thermal indices are caused by the thermal indices being sensitive to different degrees to the meteorological variables (Chapter 4). PET is more sensitive to T_{mrt} than UTCI. In the simulations very high building wall temperatures above 100 °C are calculated, which result in a high longwave heat flux that increases T_{mrt}.

The unrealistically high wall temperatures are likely caused by (1) a small volumetric heat capacity of the building wall, (2) an underestimated sensible heat flux and (3) a relatively small wall albedo. MITRAS uses 1000 $\mathrm{J\,m^{-3}\,K^{-1}}$ for the volumetric heat capacity of building walls. This value is similar to the value of air. c_w values for building materials are usually higher by one order of magnitude, i.e. 2000 $\mathrm{kJ\,m^{-3}\,K^{-1}}$ (Kusaka et al., 2001). The sensible heat flux between the building wall and the atmosphere is likely too small as the building friction velocity in Eq. (5.3) is parameterised based on the mean wind speed in the atmospheric grid cell adjacent to the wall. By using this approach, larger temporary wind speeds due to turbulence and upwinds close the wall are not included. The wall albedo in MITRAS is 0.15. This value is relatively small compared to values used for instance in Schrijvers et al. (2016). A higher albedo would increase reflection of shortwave radiation and thus decrease the absorbed amount. Tests performed by Gierisch (2011) for an older version of MITRAS that did not include the effect of heat storage indicated that higher albedo values result in more realistic building wall temperatures.

Despite these high wall temperatures, the simulations can still be used to derive the influence of water surfaces under different meteorological situations and urban scenarios. This is due to several reasons. First, only the central street of the model domain (Figure 6.8) is used for the analysis in this chapter and highest building wall temperatures are simulated within the courtyards of the block buildings. The wall temperatures are maximal in the courtyard, since the wind speed is small in the courtyard and thus sensible heat flux is suppressed even more. Furthermore, the newly introduced radiation exchange between buildings amplifies the increase in wall temperature. Second, air temperature values are generally reasonable due to the small sensible heat fluxes from the building walls. Third, the mean radiant temperature, which is directly affected by the wall temperatures, has maximal values of about 70 °C within the central street canyon at noon. Although this is likely too high, T_{mrt} values above 60 °C have been measured for instance in Göteborg, Sweden, in July (Thorsson et al., 2007b). Therefore, the values are not much too high. Fourth, the present analysis focusses on the difference of the variables between the water edge and the urban reference area. Even if the absolute values are wrong, these differences should be reasonable for all variables, except maybe for T_{mrt} during noon. After sunset plausible wall temperatures with maximum temperatures of about 25 °C are simulated. Hence, during night-time the simulations are reliable.

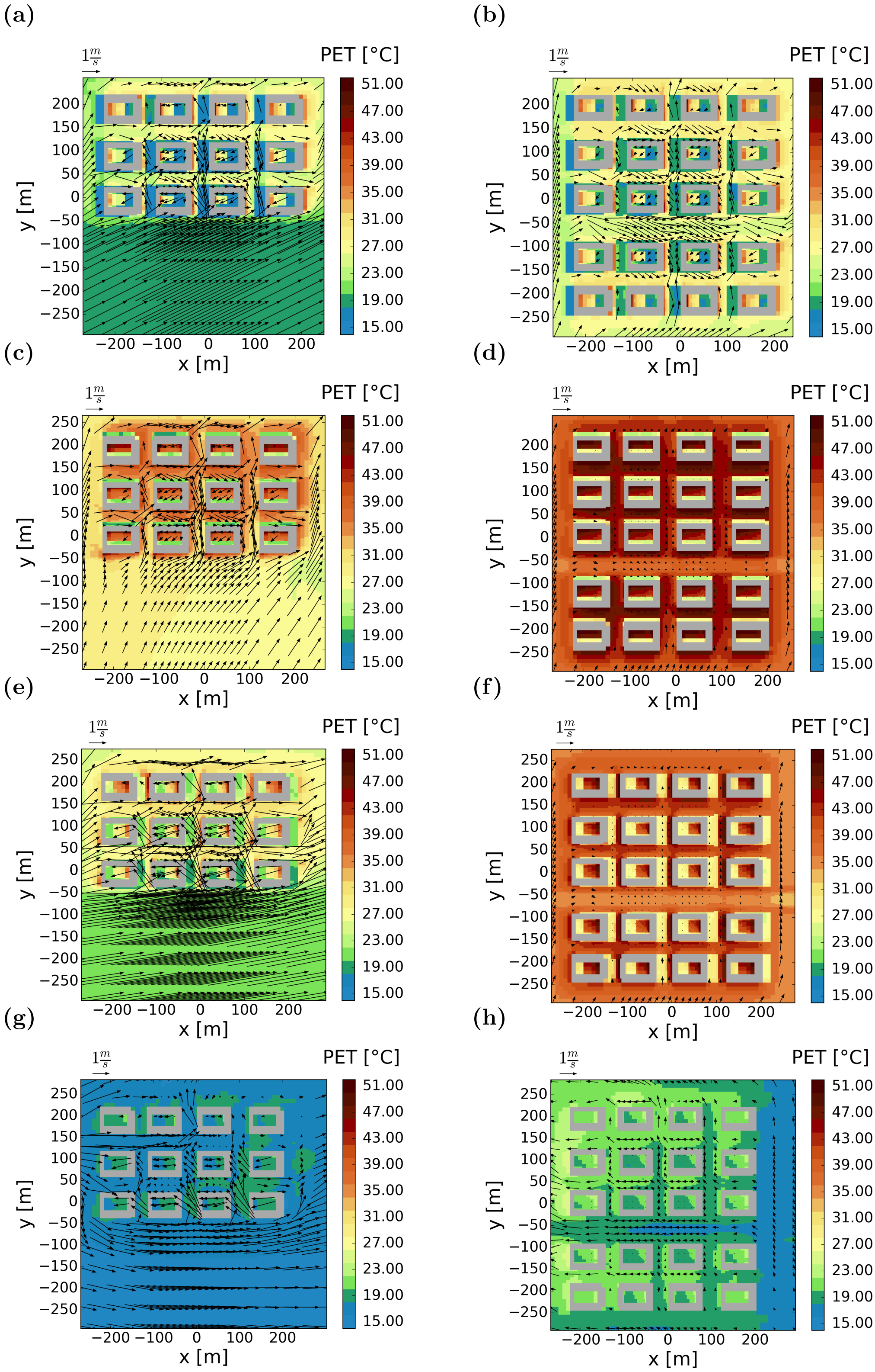

Figure 6.10: PET (colours) and wind (arrows) for (a), (c), (e), (g) for `e220v0bb_57` and (b), (d), (f), (h) for `e30v0bb_57`. (a) and (b) show results for 08:00 LST, (c) and (d) for 12:00 LST, (e) and (f) for 16:00 LST and (g) and (h) for 20:00 LST. Every 5th wind vector is shown.

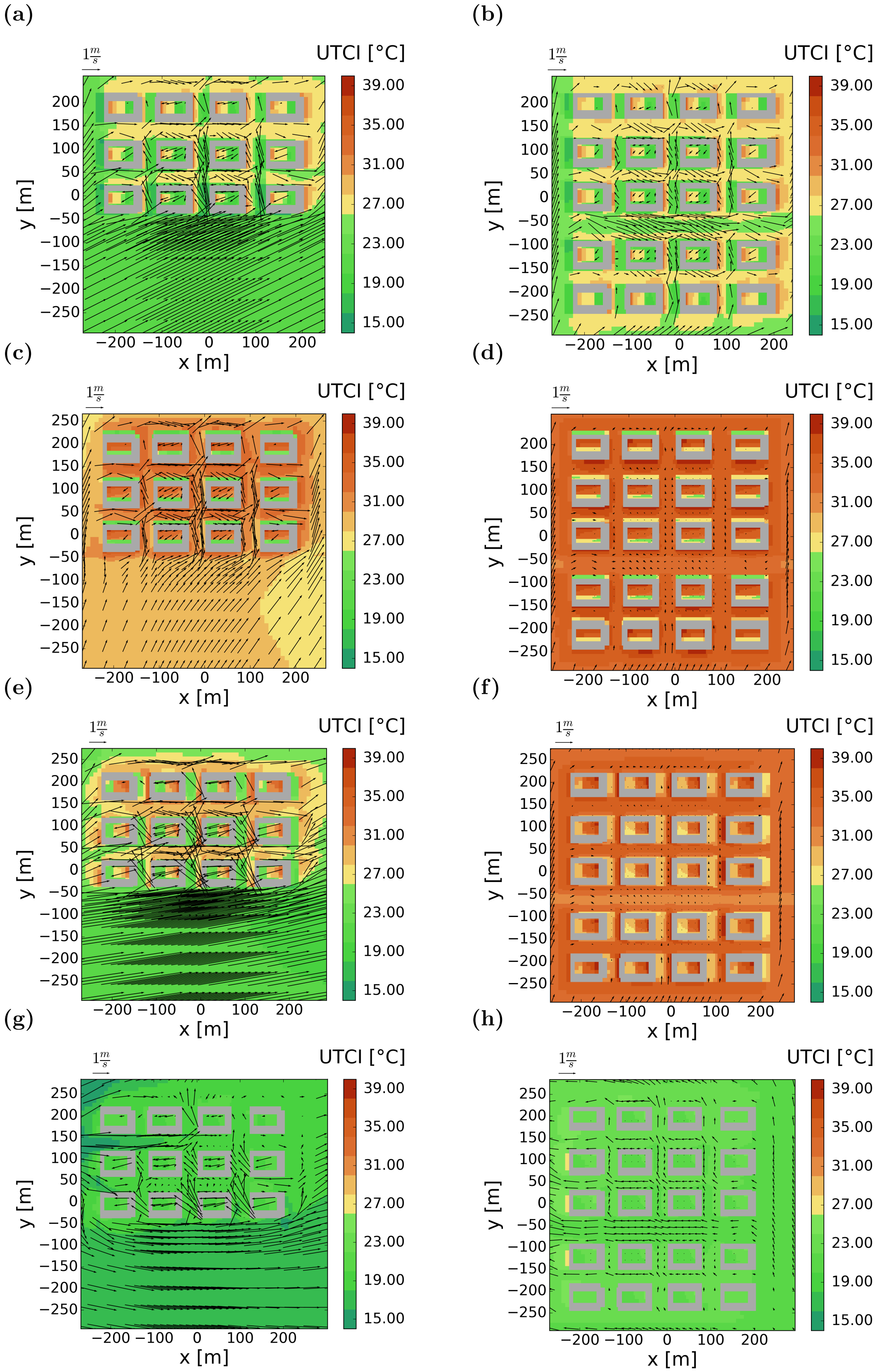

Figure 6.11: Same as Figure 6.10 but for UTCI.

6.4.1.2 Penetration of the water influence

The change of penetration of the water influence into the urban environment during the day is investigated for the different meteorological variables using the normalised indices γ_m and γ_n. Figure 6.12 and Figure 6.13 shows the derived values colour coded for the lake scenario (e220v0bb_57) in form of Hovmöller diagrams (Hovmöller, 1949). In this type of diagram time is on the ordinate and location is on the abscissa. The left column in each figure (a, c, e) shows the results for the monotonic method (γ_m, Eq. (6.4)), the right column (b, d, f) the results for the notional city method (γ_n, Eq. (6.5)). The input variables for the thermal indices are shown in Figure 6.12a to Figure 6.13b (Figure 6.12a,b for T_a, Figure 6.12c,d for e, Figure 6.12e,f for FF, Figure 6.13a,b for T_{mrt}). The thermal indices are shown in Figure 6.13c,d for PET and Figure 6.13e,f for UTCI. Only the domain to the north of the water surface is shown. Buildings are indicated as grey vertical and grey horizontal lines along the axis and averaging areas as black horizontal lines along the axis. White colours indicate areas for which no values have been calculated, because they lie in the average domains (Figure 6.8) or the minimum thresholds between water and urban area have not been reached (Section 6.3.2.1). As an indication for the overall wind situation at a specific time, wind direction and wind speed are shown as arrows every 40 minutes at two locations: south of the shoreline (green) and north of the last building. The green dashed lines indicate sunrise, sunset and midnight. As γ_m and γ_n are normalised, the values should vary between 0 and 1 if the water influence is the dominant process. Negative values or values above 1 indicate local influences being more important than the water influence. Note that all values above 1.1 and below 1.1 have the same colour coding.

The penetration of the water influence differs strongly during daytime and night-time for all variables. In the following, first penetrations during daytime are discussed.

Both γ_m and γ_n indicate (Figure 6.12a,b) a clear monotonic decrease in water influence from the shore-line to the urban area for air temperature and vapour pressure. Such a behaviour is defined as a direct influence of the water surface as it is independent of local processes within the urban environment. The penetration depth, that is the location where the water influence falls below 30 %, $y(\gamma = 0.3)$, generally decreases for water vapour during the day. This is due to less advection of evaporated water vapour from the water surface into the urban environment induced by a turning of the wind from onshore to parallel to the shore over the course of the day (Figure 6.10). In contrast, for T_a the penetration depth is almost constant.

For FF very small penetration depths are simulated between 06:40 LST and midday and between 13:30 LST and sunset (Figure 6.12e,f): both γ_m and γ_n drop below 10 % at the location, where the building begins. Deeper in the canyon γ_m and γ_n increase again. This pattern can be explained by a flow channelling effect by the presence of the building. Therefore, this building induced local influence on the flow field is clearly an important process during the day. However, in the second and third building row (included in γ_n) no such maximum is encountered. This is due to a smaller wind speed and a differently approaching wind direction. Therefore, an indirect influence of the water surface on wind speed is encountered. This indirect influence comes into play because of the local flow channelling processes. As flow patterns in street canyons vary with different street geometries and flow directions (Hunter et al., 1990), this indirect effect likely differs for different meteorological situations and urban scenarios, as further discussed in Section 6.4.2 and Section 6.4.3. In early morning, between 04:40 LST and 06:20 LST, a monotonic change from the shoreline towards the urban environment and thus a direct influence of the water surface on wind speed is calculated. The direct influence is visible during this time of the day, as the wind direction is still mainly parallel to the street canyon and thus the higher wind speed over the water surface penetrates into the first building row independent of the exact building structure. Around noon a third pattern is observed that strongly differs from the two previously described situations. This pattern is an artefact of a small urban to water wind speed difference (see Figure 6.14c in Section 6.4.1.3). This difference is just above the minimal calculation threshold (Section 6.3.2) and causes large differences due the normalisation of γ_m and γ_n. Therefore, the results are not interpreted.

T_{mrt} (Figure 6.13a,b) is, similar to FF, also strongly influenced by local effects due to the presence of buildings. For T_{mrt} shading is the most important determinant of γ_m between 06:00 LST and 09:00 LST and between 15:00 LST and 18:00 LST as indicated by meandering patterns of large positive and negative values (Figure 6.13a). γ_n takes this general pattern into account and thus only calculates values outside 0 and 1, when the last street canyon behaves differently compared to the other street canyons. This is the case for instance during early morning, when the sun shines into the last street canyon, whereas all other street canyons are still shaded. Around midday, monotonic changes from the shoreline towards the urban reference domain are calculated for T_{mrt}. This indicates a direct influence of the water surface on T_{mrt} during these hours. The direct influence is due to the around 30 K smaller water temperatures of the lake compared to the surface temperatures of asphalt. Thus, a person close to the shoreline receives less longwave radiation from the water. In addition, overall surface temperatures of wall and ground surfaces are smaller within the first street canyon compared to the urban reference canyon. This is due to (1) smaller air temperatures close to the lake, which increases sensible heat flux, and (2) the smaller longwave radiation fluxes from the lake received by the buildings compared to radiation fluxes only from asphalt for the other canyons.

The penetration of the water influence for the thermal indices PET and UTCI (Figure 6.13d to Figure 6.13f) clearly reflects the pattern of the different input variables. This is visible most clearly for the influence of T_{mrt} in the monotonic method, γ_m (Figure 6.13c,e). The penetration depth derived by the notional city method, γ_n (Figure 6.13d,f), accounts for this behaviour and thus shows smoother patterns. Overall, for both thermal indices a monotonic decrease in water influence is calculated around midday, which can be attributed to a direct influence of the water surface.

After sunset a local maximum and minimum develop for the different variables. The maximum for T_a (Figure 6.12a,b) is due to the first building row receiving more direct shortwave radiation shortly before sunset compared to the other building rows, which are already shaded. The larger shortwave radiation fluxes increase building wall and ground temperature in the first street canyon. These higher surface temperatures warm the atmosphere by sensible heat fluxes. The sensible heat fluxes are increased locally by a local maximum in wind speed from a flow channelling effect during the night (Figure 6.12e,f). The larger surface temperatures are visible in local maxima of T_{mrt} during the night (Figure 6.13a,b). The thermal indices (Figure 6.13c,f) also appraise the local maxima, as they reflect their input variables.

Since all variables assume local maxima during the night, the influence of the water surface during this time seems to be mainly caused by indirect processes due to interaction with the building structure. Thus, the night-time influence can be expected to vary for the different meteorological situations and urban scenarios (Section 6.4.2 and Section 6.4.3). However, the trigger for these indirect influences during the night is a direct influence of the water surface on incoming shortwave radiation due to the absence of shading, which comes into play only after sunset.

In contrast to the other meteorological variables, for vapour pressure a local minimum develops within the first two rows of buildings from the shoreline (Figure 6.14c,d). This local minimum is likely an artefact of the small model domain: in general humidity decreases from the water surface towards the city. However, as the urban area is surrounded by cropland that can transpire, water vapour pressure is higher in the last building row. Since these values are used to normalise the indices γ_m and γ_n, a local minimum is obtained for the inner city. Therefore, the simulation results correspond to a situation that will be experienced in small coastal towns. For larger coastal towns with an urban averaging domain uninfluenced by rural humidity conditions, a general decrease in γ from the shoreline towards the inner city is expected also during the night.

All presented results only referred to the lake scenario. However, for the canal overall similar results are obtained (Appendix P), except that the penetration of the water influence for all variables is much smaller. In addition, the differences between the conditions above water surface and in the urban averaging domain are often small, especially for wind speed and air temperature, and thus the normalised indices (γ_m and γ_n) are not calculated.

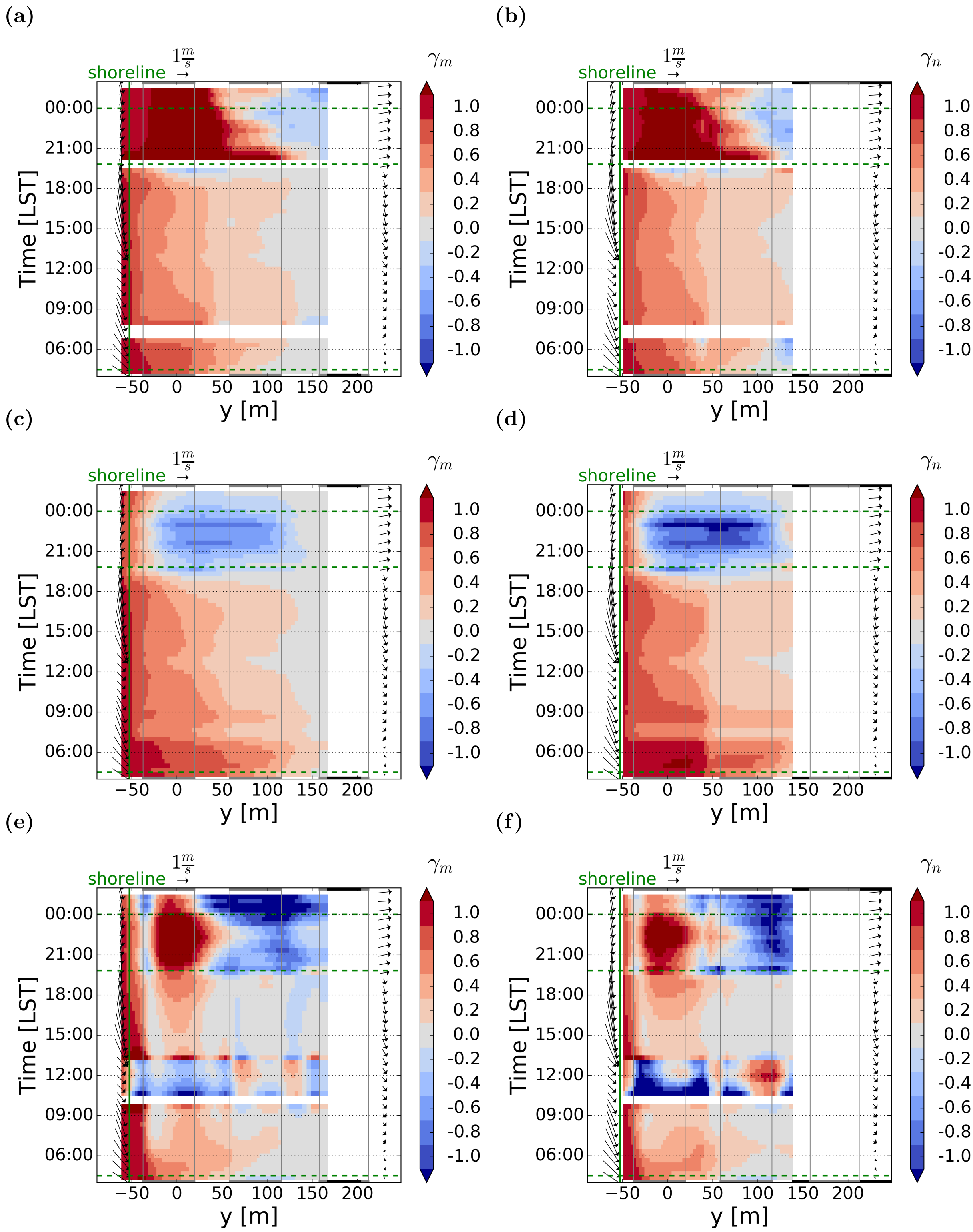

Figure 6.12: Hovmöller diagrams for `e220v0bb_57` for γ in (a), (c) and (e) according to monotonic method (γ_m, Eq. (6.4)) and (b), (d) and (f) according to notional city method (γ_n, Eq. (6.5)) for (a) and (b) T_a, (c) and (d) e, (e) and (f) FF.

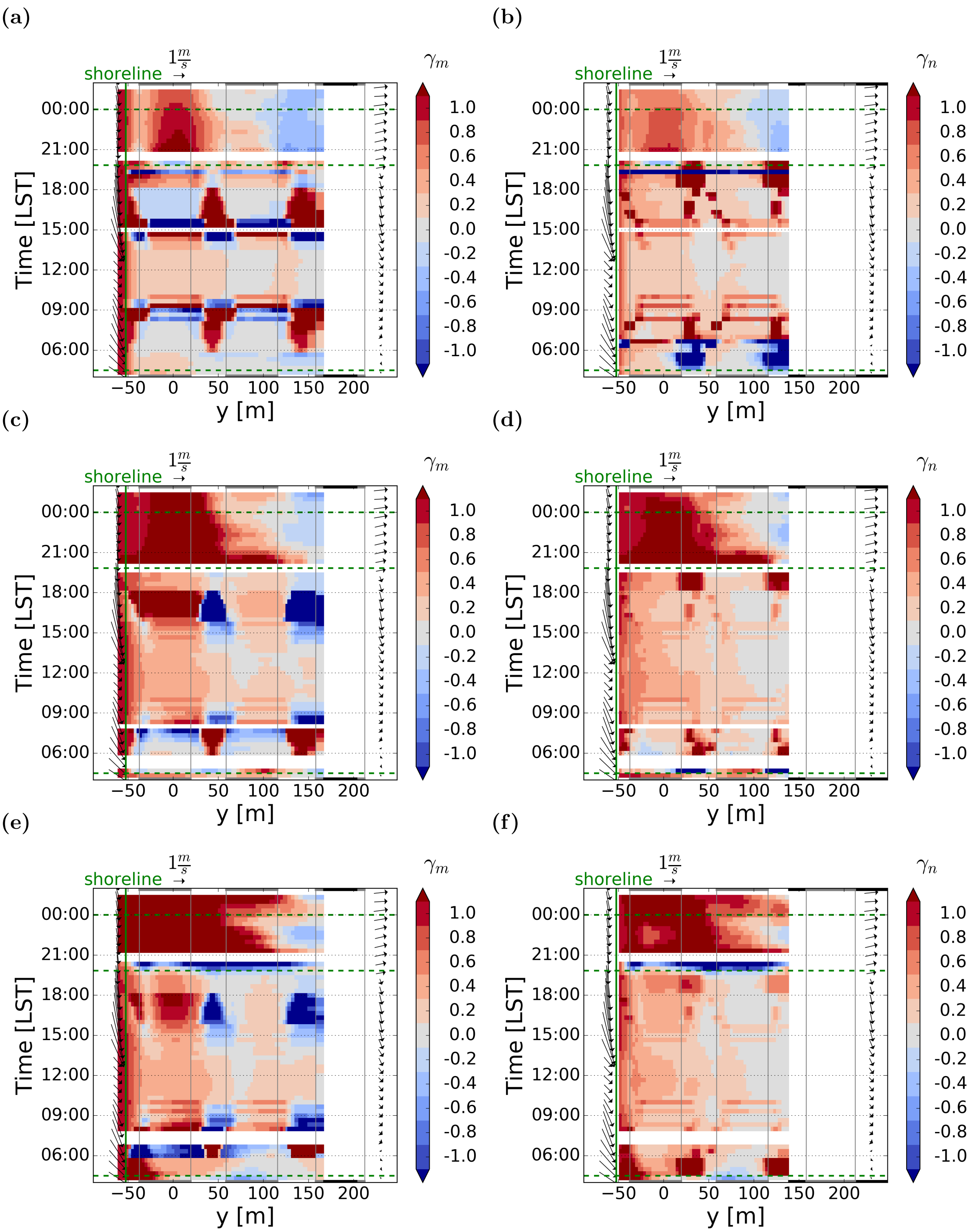

Figure 6.13: Same as Figure 6.12 but for (a) and (b) T_{mrt}, (c) and (d) PET, (e) and (f) UTCI.

6.4.1.3 Magnitude of the water influence

Figure 6.14 shows the change of the magnitude of the water influence, Γ (Section 6.3.2.2), during the day at different locations in the form of Hovmöller diagrams for the lake scenario (`e220v0bb_57`). Subfigure (a) shows air temperature, T_a, (b) vapour pressure, e, (c) wind speed, FF, (d) mean radiant temperature, T_{mrt}, (e) Physiological Equivalent Temperature, PET, and (f) Universal Thermal Climate Index, UTCI. The black lines indicate the penetration depths derived from the analysis in Section 6.4.1.2. The penetration depths are defined as the locations where γ_m (solid line) and γ_n (dashed line) fall below the threshold value of 30 % (Section 6.3.2.1). For the meaning of lines and wind arrows see Section 6.4.1.2.

The magnitudes in Figure 6.14 visualise the discussed reasons for different the penetration depths during the day (Section 6.4.1.2). For instance the local maxima for FF during the day (Figure 6.14c) and of all variables except water vapour during the night are clearly visible (Figure 6.14a and Figure 6.14c,d,e,f). In addition also the maxima of T_{mrt} in non-shaded areas during the day (Figure 6.14d) and consequently PET (Figure 6.14e) and UTCI (Figure 6.14f) are clearly visible. This pattern corresponds to γ_m and not to γ_n, since the average of the urban reference area u_m (Figure 6.8) is used to define the magnitude of the water surface.

In addition to the analysis of the penetration of the water influence, Figure 6.14 also indicates the sign of the influence. For instance, for air temperature (Figure 6.14a) it is clearly visible that the 23 °C warm water heats the atmosphere during morning and night and cools the air during the day. Even at a distance of about 180 m the air is cooler by 0.5 K during noon than further within the city. Therefore, the water surface also contributes directly, in addition to the discussed indirect influence of water surfaces on a higher air temperature close to shoreline during the night (Section 6.4.1.2).

The warming during the morning is not visible in UTCI (Figure 6.14f) due to the larger wind speeds at this time of the day (Figure 6.14c). As PET is more sensitive to T_{mrt}, positive differences are calculated for PET between 06:00 LST and 09:00 LST and between 16:00 LST and 18:00 LST. This is because the person in u_m is shaded on average, whereas it is exposed to sunlight close to the shoreline. PET and UTCI also differ in the maximum cooling effect calculated for midday at the shoreline. This difference is caused by the maximum in vapour pressure difference of more than 5 hPa (Figure 6.14b) during this time: UTCI considers that high humidity values under warm conditions are stressful, as latent heat fluxes by sweating are reduced (Chapter 4). This process is not included in the VDI-version of PET (Chapter 4). In the early afternoon, when the humidity influence of the water surface is smaller, also large cooling effects are calculated for UTCI close to the shoreline.

Overall maximum cooling of the water surface during the day is larger for both thermal indices than for T_a. PET shows maximum cooling effects of 10 K (exceeding the scale in Figure 6.14e), UTCI of 7 K and T_a of 4 K. For both thermal indices the maximum cooling influence of the water surface exceeds the range of one stress class (except for the larger comfort class for UTCI). Thus, at the most, the presence of water surfaces can decrease heat stress by up to 2 stress classes close to the shoreline during the day. Further within in the urban area, for instance at the penetration depth location (black lines in Figure 6.14), cooling effects are within the range of one stress class. During the night both indices simulate a warming of up to about 4 K for UTCI and 5 K for PET. Hence, this warming effect is smaller than the cooling effect during the day and lies within the range of one stress class. It may, nonetheless, deteriorate important night-time thermal comfort (Chapter 1). However, the magnitude might be slightly overestimated, since the surface temperatures and thus longwave emission from buildings and resulting air temperatures are overall too high in the current simulations.

The magnitude of the water influence for the canal (`e30v0bb_57`) is smaller than for the lake (Figure 6.15, note that for all variables the scale has been halved). The maximum cooling effect is about -3.7 K for UTCI (Figure 6.15f) and about -7.2 K for PET (Figure 6.15e). Therefore, even for the canal the cooling effect for PET exceeds the range of one stress class. For UTCI the cooling effect is about halved compared to the lake scenario. The warming effect during the night in terms of air temperature (Figure 6.15a) and PET (Figure 6.15e and Figure 6.15f) is not as far reaching as for the lake. For UTCI the warming effect of about 0.5 K extends up to 90 m onshore. This is due to higher humidity values during night-time. After midnight the stratification changes from neutral to stable, which is accompanied by a change in wind direction from east to north-west. Thus the previous outflow boundary becomes the inflow boundary so that warmer air is advected back into the model are due to the applied adaptive boundary conditions. Since the wind speeds are higher over the canal and the surrounding cropland area (Figure 6.15c), warmer air is advected faster in those areas. This causes a relative cooling effect of the denser urban area for all temperature related variables (Figure 6.15a,d,e,f).

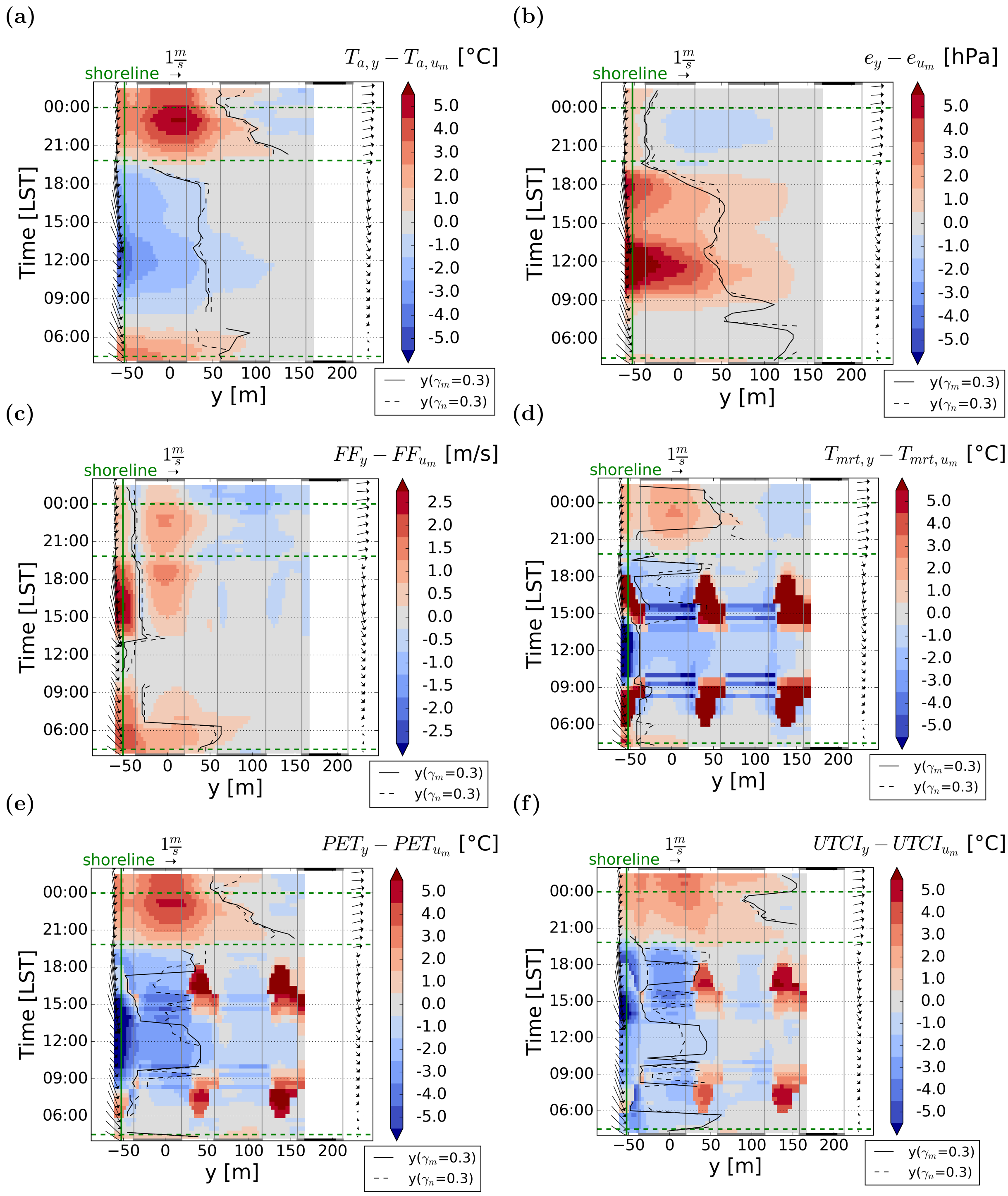

Figure 6.14: Hovmöller diagrams of differences between the value at y and the urban reference area for the lake scenario `e220v0bb_57` for (a) air temperature, T_a), (b) vapour pressure, e, (c) wind speed, FF, (d) mean radiant temperature, T_{mrt}, (e) Physiological Equivalent Temperature, PET and (f) Universal Thermal Climate index, UTCI. Note the different scale for wind speed.

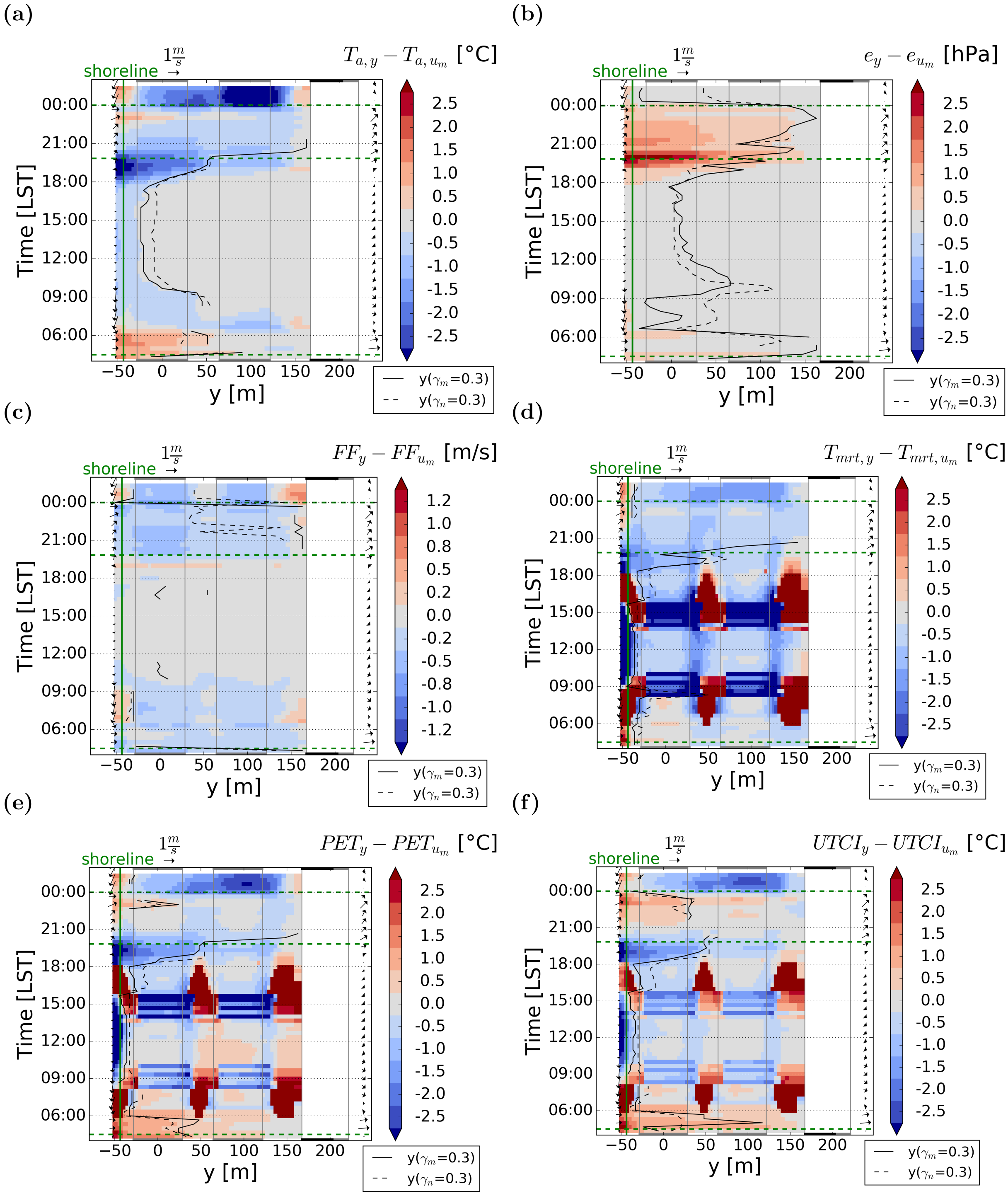

Figure 6.15: Same as Figure 6.14 but for canal scenario e30v0bb_57. Note that for all variables the scale has been halved.

6.4.1.4 Comparison of the methods for the penetration depth

γ_m (Eq. (6.4)) and γ_n (Eq. (6.5)) yield overall similar penetration depth for T_a, e, FF and T_{mrt} for the lake (Figure 6.12) and the canal (Figure 6.15) and for PET and UTCI for the canal (Figure 6.15). Therefore, for the following analyses only results for one method, γ_n, are presented. γ_n can capture urban induced effects better due to the notional city used for its construction.

6.4.2 Sensitivity of water influence to meteorology

In this section, it is assessed whether the obtained results for the magnitude, Γ_{sh} and $\Gamma_{0.3}$, and penetration depth of the water influence, $y(\gamma_n = 0.3)$, in Section 6.4.1 are valid for all cloudless summer situations. To do so, γ_n and Γ are calculated for all 60 meteorological situations (Table N.1). Results for the penetration depth are presented in Section 6.4.2.1. The results for magnitude in Section 6.4.2.2.

6.4.2.1 Sensitivity of the penetration depth of the water influence to meteorology

The impact of meteorological situations on the penetration depth of the water influence, $y(\gamma = 0.3)$, for air temperature is presented in Figure 6.16 in form of a one-dimensional Hovmöller diagram. Figure 6.16a shows the results for the lake and Figure 6.16b the results for the canal. The meteorological situations have been categorised and are colour-coded in the figures. Orange-brown colours indicate situations with negative air-water-temperature differences ($\overline{T}_a - \overline{T}_{\mathrm{wat}} < -0.5$ K; i.e. a warming of the water surface on the diurnal average; denoted $H+$), greenish colours almost no differences ($-0.5 \leq \overline{T}_a - \overline{T}_{\mathrm{wat}} \leq 0.5$ K; denoted $H0$) and bluish colours a cooling effect ($\overline{T}_a - \overline{T}_{\mathrm{wat}} > 0.5$ K; denoted $H-$). Darker colours in each category refer to initial air temperatures at 04:00 LST larger than 14 °C (denoted $T+$). Every second colour refers to situations with an initial relative humidity smaller than 80 % and thus a relatively large latent heat flux potential (denoted $L+$). The markers in each colour refer to the initial wind speeds: circular markers refer to relatively low wind speeds ($FF_{10,4} < 1.5$, denoted $FF-$), whereas crosses and triangles refer to higher wind speeds (denoted $FF+$). Filled markers, that is dots for $FF-$ and triangles for $FF+$, indicate situations, for which a local maximum ($\gamma_n > 1$) or minimum ($\gamma_n < 0$) was encountered before the threshold value of 30 % of the water influence was reached. In the legend the different meteorological situations are shown as lines without markers to reduce the number of entries. Marker symbols are denoted in the legend in black to indicate that they apply to all colours. Note that in each category more than one simulation might be present. Missing values are due to small overall differences during that time (Section 6.3.2.1). The results for all variables are given in detail in Appendix P.2.

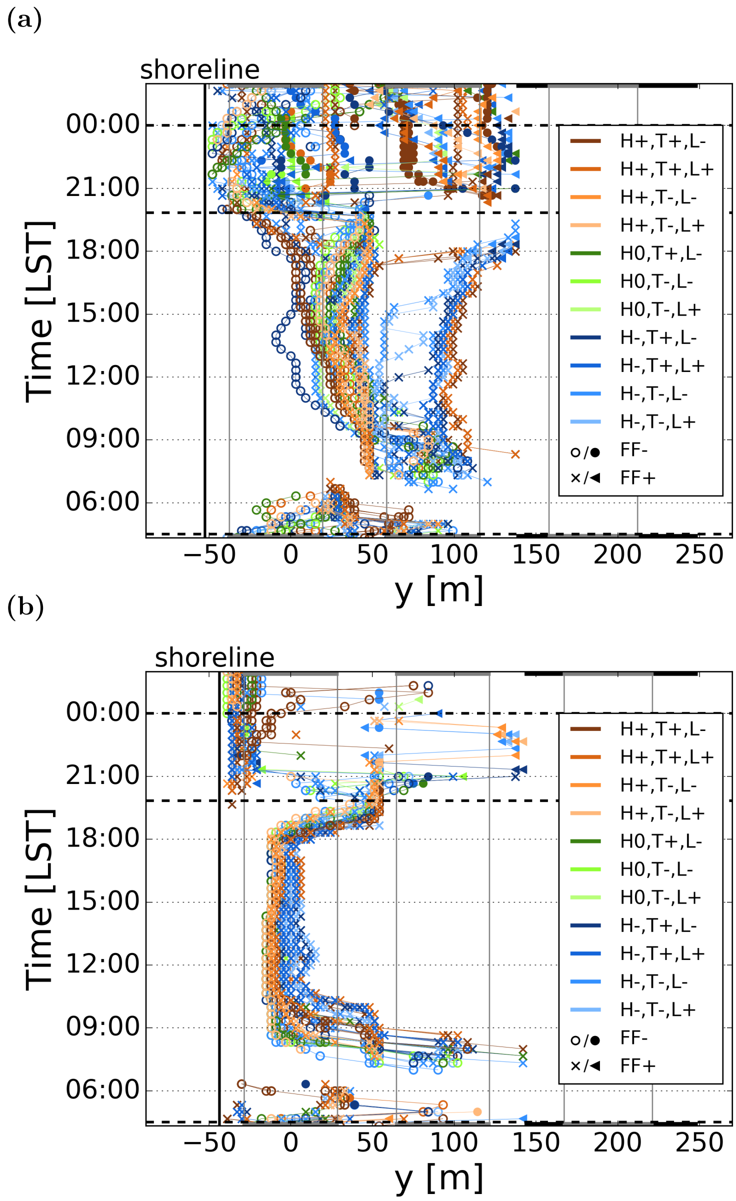

Figure 6.16: Penetration depth of the water influence ($y(\gamma_n = 0.3)$) for different meteorological conditions (colour and marker coded) for air temperature for (a) the lake scenario (`e220v0bb`) and (b) the canal scenario (`e30v0bb`). See text for the colour coding.

For the lake (Figure 6.16a) the penetration depths differ by up to 100 m for the different meteorological conditions during the day; during the night the spread is even larger. This large spread during the night is expected: depending on the exact wind direction the influence of the water surface at night can be direct, if the wind direction is more perpendicular to the canyon, or indirect due to an interaction with a flow channelling effect (Section 6.4.1.2). If the water influence is indirect, local maxima in the normalised index γ_n are calculated. In Figure 6.16a larger penetration depths are visible during the night after a local maximum or minimum was calculated (filled dots or filled triangles). During the day two clusters of penetration depths are identified: most situations with higher wind speeds penetrate deeper into the urban environment (crosses). This can be explained by a stronger advection during situations with high wind speeds. For the canal (Figure 6.16b) similar penetration depths are simulated during all meteorological situations. The range of encountered penetration depth is only within about 20 m during the day in contrast to 100 m for the lake. During the night equally large spreads in penetration depths as for the lake are calculated.

Figure 6.17 summarises those results for the penetrations depth for T_a and for the other variables in the form of box plots: for each variable for MORNING (04:20 LST to 06:00 LST, blue), NOON (10:00 LST to 13:00 LST, red) and NIGHT (20:00 LST to 02:00 LST, green) the median and the lower and upper quartile of the all calculated penetration depths are shown as boxes. Whiskers indicate the closest value to 1.5 times the interquartile range and are a measure of the data spread. Values outside this range are marked by stars as outliers. Dark blue, dark red and dark green refer to the canal scenario; brighter colours represent to the lake scenario, i.e. left result for each colour. Note that for the canal only very few data points were available for FF as differences were overall small (Figure P.3f).

The meteorological situation influences the penetration depth of the water influence for almost all variables for the lake strongly: depending on the meteorological situation either very small penetration depth of a few metre or penetration depth up to the urban reference domain in about 190 m are observed. Penetration depth for T_{mrt} do not vary as much as for the other variables. This is because penetration depths for T_{mrt} are strongly influenced by the local shading by buildings (Section 6.4.1.2) and all simulations are performed for the same day of the year. However, penetration depth might be overall underestimated for T_{mrt} due to the large wall temperatures encountered.

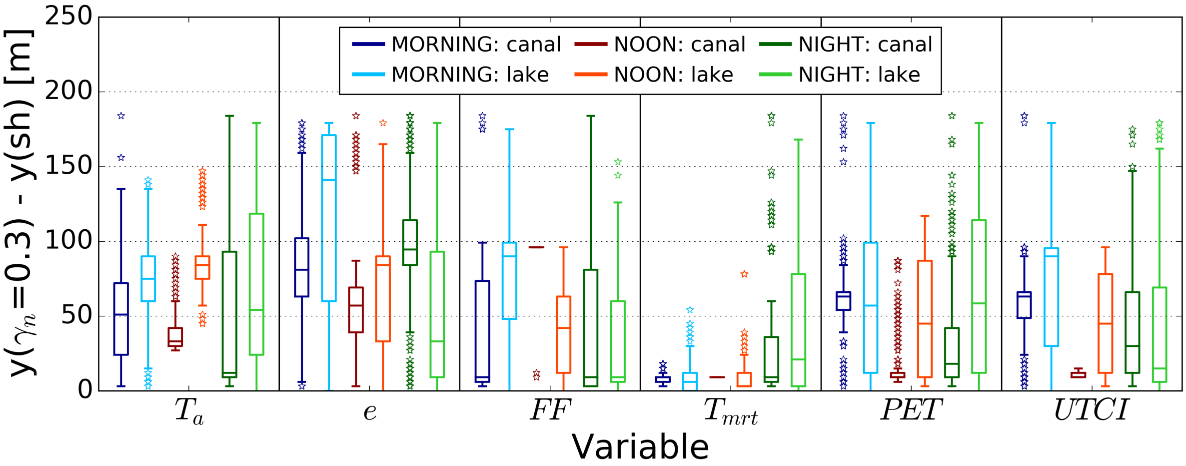

Figure 6.17: Box plots over all meteorological situations for the penetration depth of the water influence from the shoreline (sh, i.e. $y(\gamma_n = 0.3) - y(sh)$) for MORNING (04:20 LST to 06:00 LST, blue), NOON (10:00 LST to 13:00 LST, red) and NIGHT (20:00 LST to 02:00 LST, green) for T_a air temperature, e vapour pressure, FF wind speed, T_{mrt} mean radiant temperature, PET Physiological Equivalent Temperature and UTCI Universal Thermal Climate Index.

In general, for the canal smaller penetration depths are calculated than for the lake. Additionally, the spread of penetration depth due to different meteorological situations is also smaller for the canal. This is indicated by a smaller extent of the box and whiskers. Therefore, the meteorological situation influence the penetration depths of the water influence less for the canal than for the lake.

Median penetration depth during NOON are smaller for the thermal indices PET and UTCI (about 55 m for the lake and 10–15 m for the canal) than for T_a and e. The mean penetration depth for the lake for both T_a and e is about 90 m. For the canal the mean penetration depth amounts to 30 m for T_a and 55 m for e. Therefore, by using T_a as a proxy of the penetration depth of the water influence, the penetration is likely overestimated in terms of the influence on the human thermal environment.

During NIGHT (green in Figure 6.17) the whisker ranges span for almost all variables the entire urban area up to the urban reference domain both for the lake and the canal. However, the one-dimensional Hovmöller diagram for T_a for the canal (Figure P.3b) shows that the penetration depths cluster at locations between buildings. This is caused by the interaction of the water influence with local processes of flow channelling, which leads to local maxima for γ_n, as discussed above. Similar clusters are calculated for almost all variables (Figure P.3 and Figure P.4).

Mean elementary effects ($EE_{i,m}$) are used to derive the sensitivity of the penetration depths to the meteorological situations at 04:00 LST. Elementary effects in general use finite difference quotients to derive how much the output variable differs if input variables are varied (Section 6.3.3, Eq. (6.7)). Figure 6.18 shows the diurnal course of $EE_{i,m}$ values for the different variables air temperature at 04:00 LST, $T_{a,4}$, wind speed in 10 m at 04:00 LST, $FF_{10,4}$, the temperature difference between diurnal average air temperature and diurnal average water temperature, $\overline{T}_a - \overline{T}_{\text{wat}}$, and relative humidity at 04:00 LST, RH_4. On The left (i.e. Figure 6.18a,c,e,g,i,k) the results for the lake are shown and on the right (i.e. Figure 6.18b,d,f,h,j,l) the results for the canal. Figure 6.18a,b show results for T_a, Figure 6.18c,d for e, Figure 6.18e,f for FF, Figure 6.18g,h for T_{mrt}, Figure 6.18i,j for PET and Figure 6.18k,l for UTCI). The actual values of the $EE_{i,m}$ have no particular meaning, they only indicate the relative importance between the different variables.

The $EE_{i,m}$ for air temperature (Figure 6.18a) confirms that for the lake wind speed is the most influential variable for the penetration depth. Figure 6.18a,c,e,g,i,k show that $FF_{10,4}$ also strongly influences the penetration depths of all other variables for the lake scenario. T_{mrt} is an exception, as it is more influenced by the local conditions as discussed above. As for the canal penetration depths are not much influenced by the meteorological situation, only for T_a, e and PET influential variables are determined during daytime (Figure 6.18b,d, j). For those variables, the penetration depth is also mostly determined by $FF_{10,4}$. After sunset, for both the canal and the lake scenario more influential variables are determined. This is due to local effects being more important than the overall meteorological situation. However, a bootstrapping with 10 randomly drawn samples indicates that results are less certain during the night (not shown).

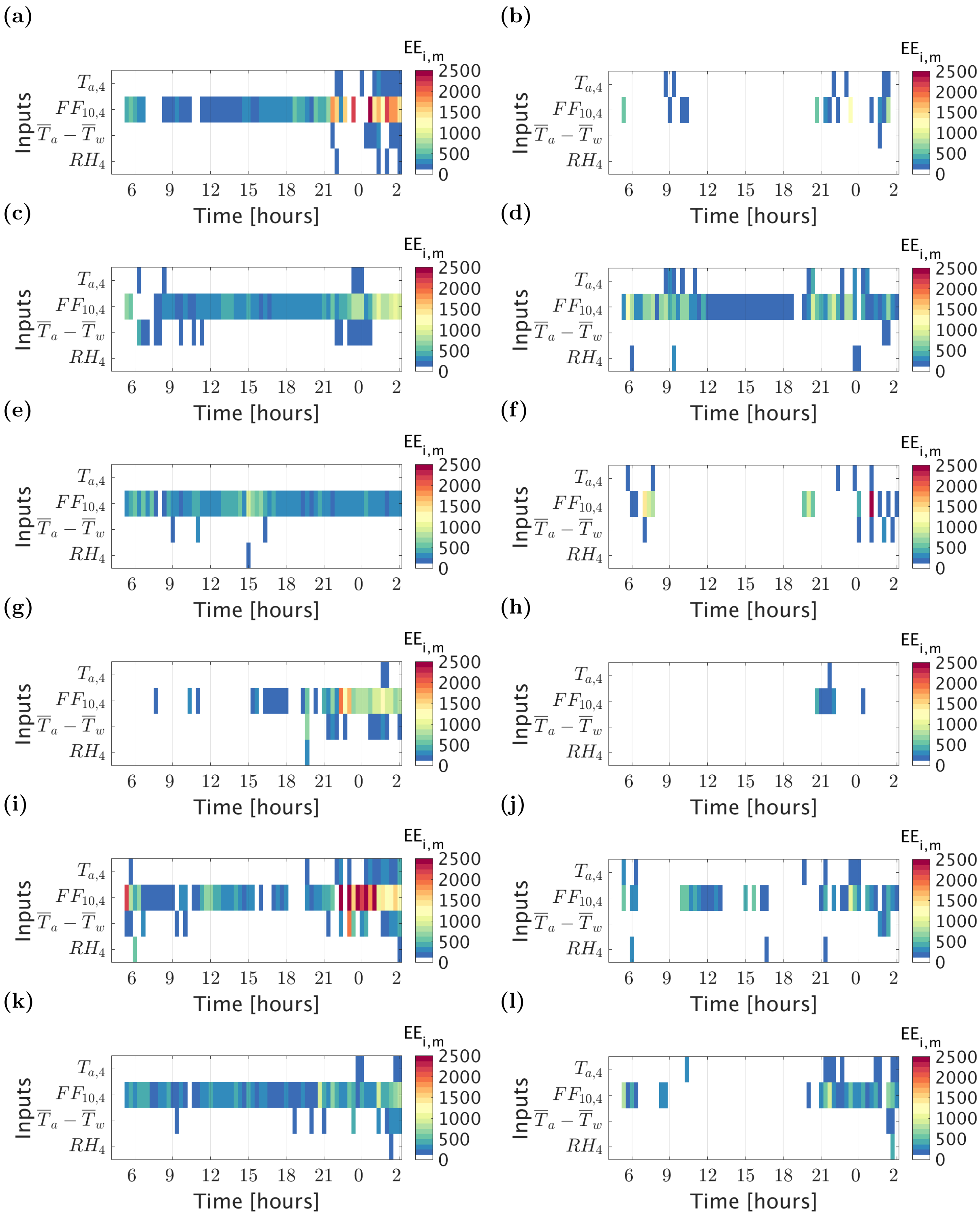

Figure 6.18: Mean Elementary Effects ($EE_{i,m}$) for the penetration depth of the water influence ($y(\gamma_n = 0.3)$) of the sampled input variables (Section 6.2.1) for (a) and (b) T_a, (c) and (d) e, (e) and (f) FF, (g) and (h) T_{mrt}, (i) and (j) PET, (k) and (l) UTCI for (a),(c),(e),(g),(i),(k) for the lake (`e220v0bb`) and for (b),(d),(f),(h),(j),(l) for the canal (`e30v0bb`).

6.4.2.2 Sensitivity of the magnitude of the water influence to meteorology

The meteorological situation at 04:00 LST influences the magnitude, Γ, of the water influence. In Figure 6.19 detailed results are presented for the magnitude of the water influence for the lake (`e220v0bb`) at the shoreline, that is $\Gamma_{sh} = \chi_{sh} - \chi_{u,m}$. Figure 6.19a shows results for air temperature, T_a, Figure 6.19b for vapour pressure, e, Figure 6.19c for wind speed, FF, Figure 6.19d for mean radiant temperature, T_{mrt}, Figure 6.19e for Physiological Equivalent Temperature, PET, and Figure 6.19f for Universal Thermal Climate Index, UTCI, all at 1 m height. The same colour coding as in Figure 6.16 is used.

In general, for all temperature related variables, air temperature (Figure 6.19a), mean radiant temperature (Figure 6.19d), Physiological Equivalent Temperature Figure 6.19e and Universal Thermal Climate Index Figure 6.19f, similar diurnal cycles as for the exemplary situation `57` are calculated (Figure 6.19, Section 6.4.1.3): the water surface cools the atmosphere during the day and can warm it during morning and night. However, the meteorological situations influence the magnitude of this cooling and warming and may even induce a cooling during the entire day. The abrupt changes in T_{mrt} (Figure 6.19d) and consequently the thermal indices (Figure 6.19e,f) are due to different timings in shading of the urban reference area and the shoreline. The shoreline receives earlier and longer solar radiation than the urban average area, which is located in a street canyon (Figure 6.8). The step-wise changes are caused by the averaging in x-direction over the street canyon.

Under the same meteorological conditions, the cooling in terms of PET and UTCI (Figure 6.19e,d) exceeds the cooling effect in air temperature (Figure 6.19a) by up to 10 K in case of UTCI. This indicates that cooling effects in terms of air temperatures, as often used in the reviewed literature (Section 6.1), underestimate the cooling effect in human relevant terms at least for a large lake. For UTCI larger spreads are encountered for the different conditions compared to PET due the larger sensitivity to wind speed (Chapter 4), since wind speed differs strongly between the simulations (Figure 6.19c). In contrast, T_{mrt} differs less for different meteorological situations (Figure 6.19d) and as PET is more sensitive to T_{mrt} than to FF in summer (Chapter 4), the spread between the meteorological conditions is smaller.

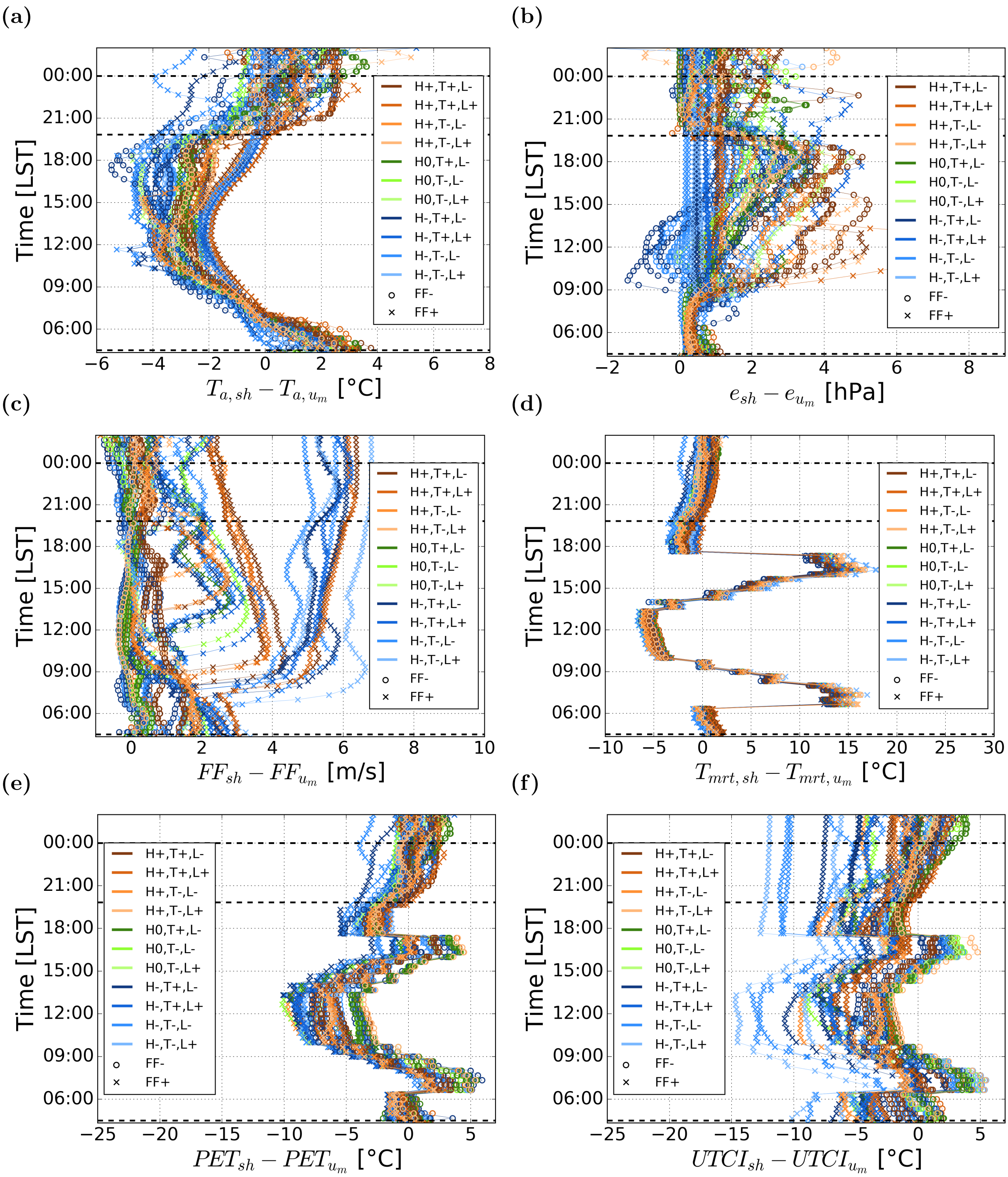

Figure 6.19: Magnitude of the water influence at shoreline ($\Gamma_{sh} = \chi_{sh} - \chi_{u,m}$) for different meteorological situations (colour coded and marker coded) for the lake (`e220v0bb`) for (a) air temperature (T_a), (b) vapour pressure (e), (c) wind speed (FF) for (d) T_{mrt}, (e) Physiological Equivalent Temperature (PET) and (f) Universal Thermal Climate Index (UTCI) all at 1 m height. See Figure 6.16 for colour coding.

Overall the maximum cooling effect varies between about 3.5 K and 10 K for PET and between about 2.5 K and 15 K UTCI. Hence, the derived maximum cooling effect of more than two stress classes in Section 6.4.1.3 for the meteorological situation 57 is not representative of all cloudless summer conditions. Smaller cooling effects are simulated in situations with small wind speeds at 04:00 LST. The second most influential parameter seems to be daily water to air temperature difference ($\overline{T}_a - \overline{T}_{\mathrm{wat}}$): During situations with a cooling effect of the water surface on the daily average air temperature, higher cooling effects of the water surface are encountered. This is caused by two processes: (1) the cooler water surface cools the air close to the shoreline directly and (2) the cooler water surface increases the temperature difference between the water surface and the urban land surface, which causes a stronger thermal circulation. Further within the city at $y(\gamma_n = 0.3)$ a smaller cooling, i.e. between 1.8 K and 4 K in terms of PET and between 0.5 K and 5 K in terms of UTCI, is calculated (Figure 6.20). Note that the location $y(\gamma_n = 0.3)$ varies throughout the day and the different meteorological situations and lies between about 20 and 100 m within the city (Figure P.3b). Large positive differences during morning and afternoon are due to u_m being mostly shaded, whereas $y(\gamma_n = 0.3)$ is not.

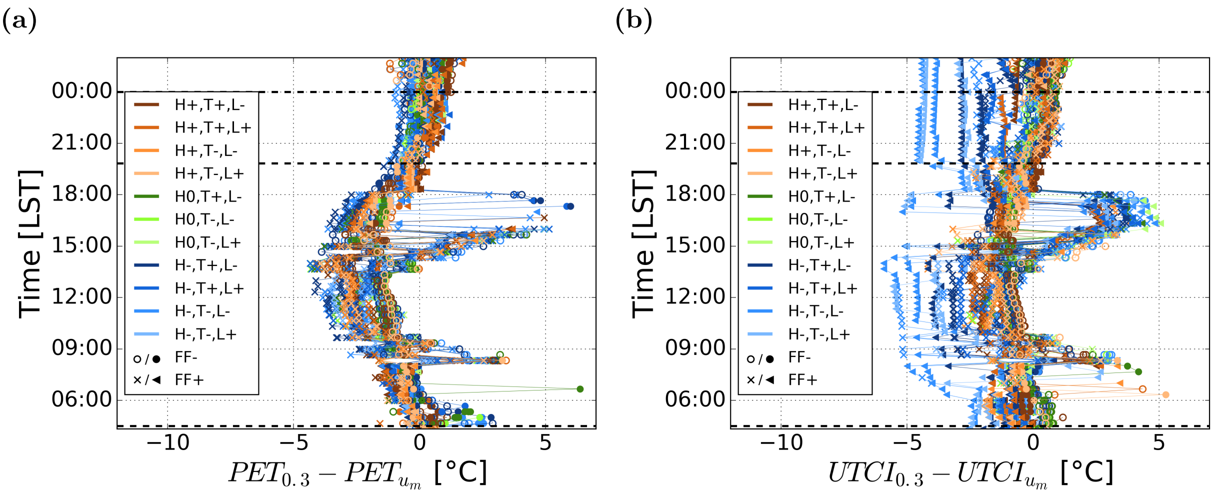

Figure 6.20: Same as Figure 6.19e and Figure 6.19f but at $y(\gamma_n = 0.3)$.

For vapour pressure (Figure 6.19c) only some meteorological situations produce the same diurnal cycle as for the exemplary situation 57, which has smaller values at about 15:00 LST. However, during most meteorological situations, larger values for vapour pressure close to the shoreline are simulated during the day compared to morning and night as in the exemplary situation 57 (Figure 6.14b). In large wind speed situations with a large cooling potential during the day (H^{-}, blue with crosses) no diurnal cycle is simulated. For the same meteorological situations but with small wind speeds (blue with circles) and relative small potential for latent heat fluxes (L^{-}, dark blue and median blue) vapour pressure close to the shore is even smaller than in the urban reference area. This is caused by transpiration of the cropland surrounding the model domain (Figure 6.8), which increases the humidity locally, and small latent heat fluxes over the water area.

For exemplary situation 57 smaller wind speed differences between the shoreline and the urban reference area were simulated during midday compared to morning, afternoon and night (Figure 6.19d). This diurnal cycle is only simulated for very few meteorological situations. The spread of $FF_{sh} - FF_{u,m}$ during the day varies from 0 to 7 $\mathrm{m\,s^{-1}}$. In some simulations, especially those with high initial wind speeds and a strong cooling potential of the atmosphere (H^{-}, blue with crosses), wind speed increase during the entire day. This is caused by a strong sea breeze circulation during the day and the open boundary conditions, which implicitly assume the water surface to extend far to the south of the actual model domain (Section 6.4.1.3).

In Figure 6.21 the magnitude of the water influence at the shoreline for the lake scenario is compared to that of the canal scenario. The colour coding is the same as in Figure 6.17. The comparison indicates that overall smaller magnitudes are simulated for the canal compared to the lake. In addition, the spread due to different meteorological situations is smaller for the canal compared to the lake. Therefore, as for the penetration depth (Section 6.4.2.1), the meteorological situations affect the magnitude of the water influence less.

For PET the magnitude of the water influence for the canal at NOON (dark red) differs by about 4 K for different meteorological situations. In contrast, for UTCI the spread is smaller. This is due to the wind speed being below 0.5 $\mathrm{m\,s^{-1}}$ in 10 m height (the input height for wind speed for UTCI) for most meteorological situations and thus almost all values are calculated with the minimum wind speed of 0.5 $\mathrm{m\,s^{-1}}$. Since UTCI is very sensitive to wind speed, the missing variability in wind speed causes the small spread. Since in urban areas often small wind speeds are encountered, the regression version of UTCI seems less suitable to be applied there.

Mean Elementary Effects ($EE_{i,m}$, Section 6.3.3) for the magnitude of the water influence at the shoreline, $\chi_{sh} - \chi_{u,m}$, are calculated over all meteorological situations for all variables

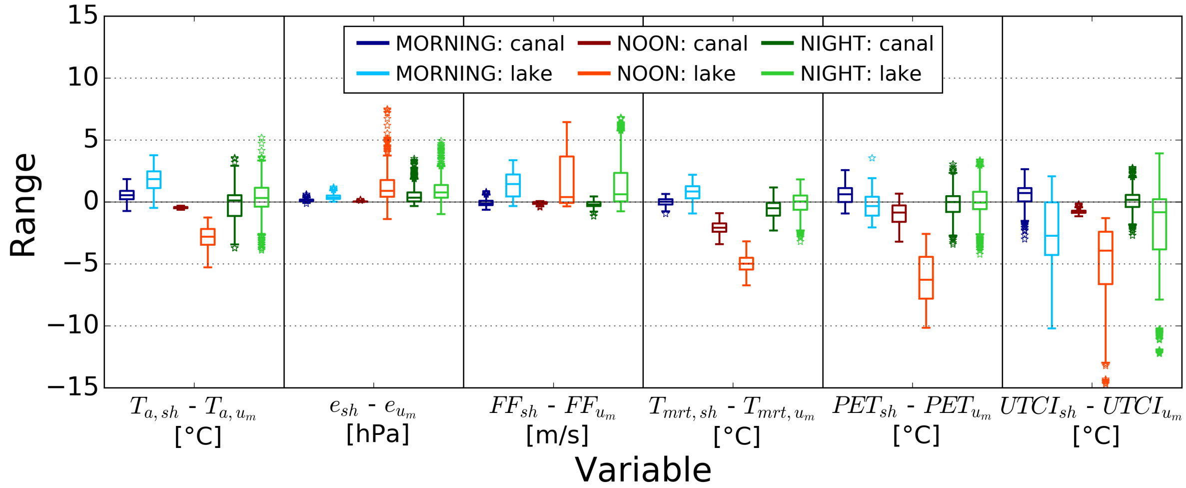

Figure 6.21: Box plots for the magnitude of the water influence at the shoreline $\chi_{sh} - \chi_{u,m}$) for different meteorological variables for MORNING (04:20 LST to 06:00 LST, blue), NOON (10:00 LST to 13:00 LST, red) and NIGHT (20:00 LST to 02:00 LST, green).

and for the two water body scenarios to derive the sensitivity of the magnitude to the meteorological conditions at 04:00 LST. The diurnal course of $EE_{i,m}$ values is shown in Figure 6.22 with the same arrangement as in Figure 6.18, i.e. Figure 6.22a,b for T_a, Figure 6.22c,d for e, Figure 6.22e,f for FF, Figure 6.22g,h for T_{mrt}, Figure 6.22i,j for PET and Figure 6.22k,l for UTCI. Results for the lake are presented on the left, i.e. in Figure 6.22a,c,e,g,i,k, and for the canal on the right, i.e. in Figure 6.22b,d,f,h,j,l.

The $EE_{i,m}$ values for the different variables indicate that the magnitude of the water influence at the shoreline is most sensitive to $FF_{10,4}$ for all variables both for the lake and the canal. Hence, wind speed is the most important determinant for both the penetration depth and magnitude of the water influence. For the lake also the air temperature at ($T_{a,4}$) and the difference of diurnal average water and air temperature ($\overline{T}_a - \overline{T}_{\mathrm{wat}}$), influence several variables during the day. This is owing to their influence on the developing sea breeze circulation as discussed above.

Since for the canal the magnitude of T_a and e only depends on the meteorological condition during MORNING and NIGHT (Figure 6.21, Figure P.5), no influential variables are derived during midday (Figure 6.22b,d). The small $EE_{i,m}$ values during midday for UTCI (Figure 6.22l) are due to the use of the minimum wind speed level of 0.5 m s^{-1} in almost all situations in the calculation of UTCI as discussed above. Largest sensitivities for the canal are calculated during midday and afternoon for T_{mrt} (Figure 6.22h) and PET (Figure 6.22j) due to their larger variability at that time (Figure P.5d,e).

Standard deviations from the bootstrapping over 10 random samples (not shown) indicate that the obtained results are quite certain. The standard deviations $EE_{i,std}$, which indicate the importance of interactions between input variables on the output variability (Section 6.3.3), are very similar to $EE_{i,m}$ and are thus not shown. This indicates that the $FF_{10,4}$ does not only directly influence the magnitude of water influence but also indirectly through interactions with other variables.

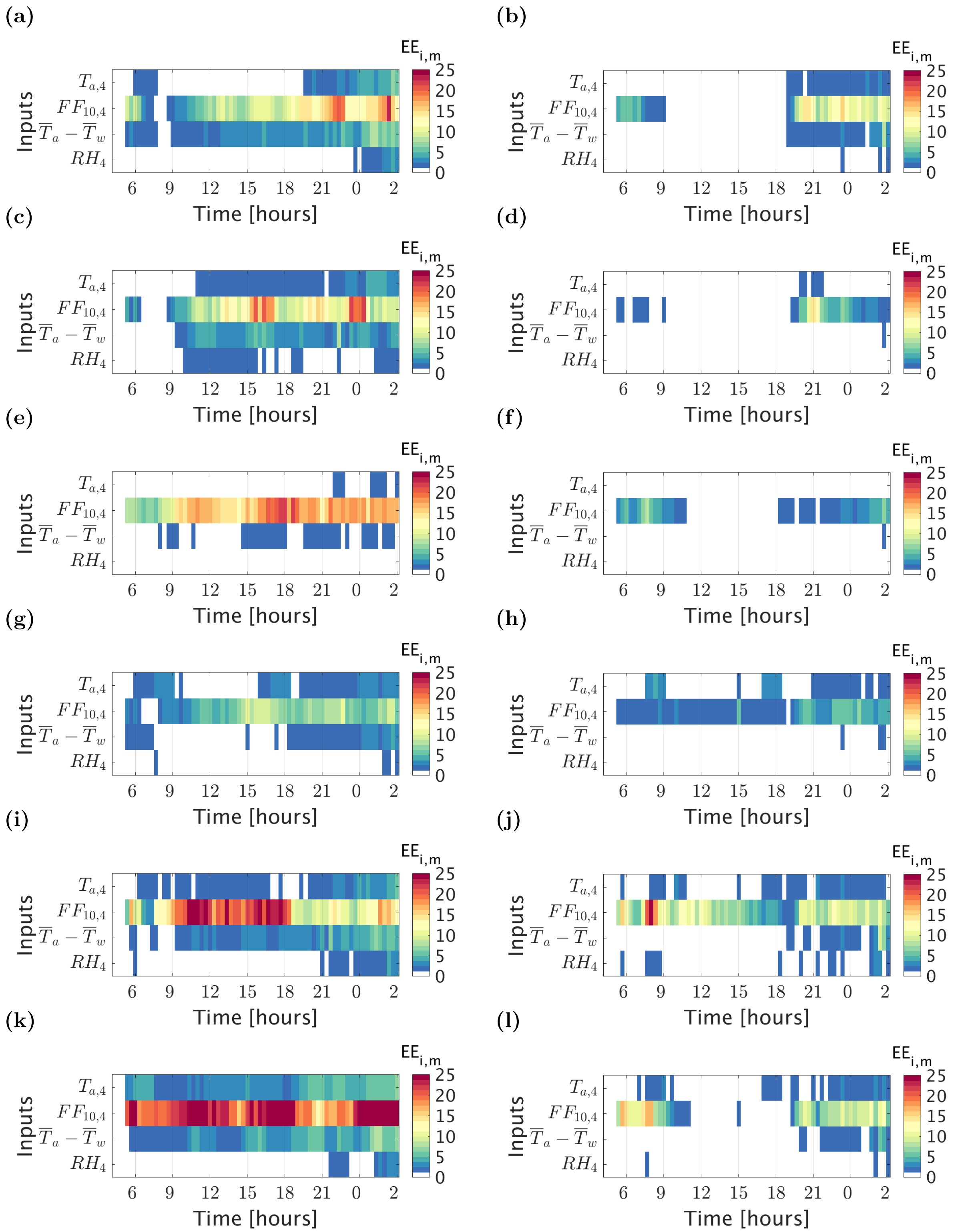

Figure 6.22: Same as Figure 6.18 but for magnitude of the water influence at the shoreline ($\chi_{sh} - \chi_{u,m}$).

6.4.3 Sensitivity of water influence to building structure and water-side vegetation

In this section, the sensitivity of the penetration depth, $y(\gamma_n = 0.3)$, and magnitude, Γ_{sh}, to the building structure and water-side vegetation is assessed. To that end, γ_n and Γ are calculated for the simulations with terraced buildings, `bt`, and water-side vegetation, `v1` (Section 6.2.2), for the three meteorological situations detailed in Table N.2. Results for the penetration depth are shown in Section 6.4.3.1, results for the magnitude of the water influence in Section 6.4.3.2.

6.4.3.1 Sensitivity of the penetration depth to morphology

Figure 6.23 shows the time-dependent variation of the location where the water influence γ_n falls below 30 % ($y(\gamma_n = 0.3)$, Section 6.3.2.1) in the form of one-dimensional Hovmöller diagrams for the lake scenario (`e220`). Figure 6.23a show penetration depths for T_a, Figure 6.23b for e, Figure 6.23c for FF, Figure 6.23d for T_{mrt}. Figure 6.24 the results for the thermal indices Figure 6.24a for PET and Figure 6.24b for UTCI. The different urban scenarios (Section 6.2.2) are colour coded. Purple and pink colour refers to the reference scenario `v0bb`, which has been used to derive the sensitivity to meteorological conditions in Section 6.4.2. Green colours refer to scenario `v1bb`, which has the same building type (block buildings `bb`) but includes water-side vegetation (`v1`). Orange and brown colours refer to the scenario `v0bt`, which has no riverside vegetation (`v0`) and consists of terraced buildings (`bt`). Blue colours refer to the scenario `v1bt`, which includes riverside vegetation (`v1`) and terraced buildings (`bt`). Different shades of colours in each category characterise the different meteorological situations (Table N.2). Bright colours refer to situation `59`, which is characterised by a large latent heat flux potential (RH_4=63 %). Medium colours in each category refer to meteorological situation `20`, which is characterised by a large sensible cooling potential of the water surface in terms of daily mean temperatures ($\overline{T}_a - \overline{T}_{\text{wat}}$=5.2 K). Dark colours indicates meteorological situation `57`, which has both a large potential for latent and sensible heat fluxes (RH_4=63 %, $\overline{T}_a - \overline{T}_{\text{wat}}$=-0.9 K) but in contrast to situation `20` warms the atmosphere on average. Triangle markers indicate that a local maximum or minimum in γ_n was calculated before the threshold of 0.3 was reached (for details see Section 6.4.2.1); crosses are used otherwise. The symbols are not shown in the legend to reduce the number of entries. For each variable the actual penetration depth is shown on the left of each figure and on the right the difference between the penetration depth for the different scenarios and the reference scenario ($y_{\text{scen}}(\gamma_n = 0.3) - y_{\texttt{v0bb}}(\gamma_n =$

0.3)). For details on the other lines see Figure 6.19.

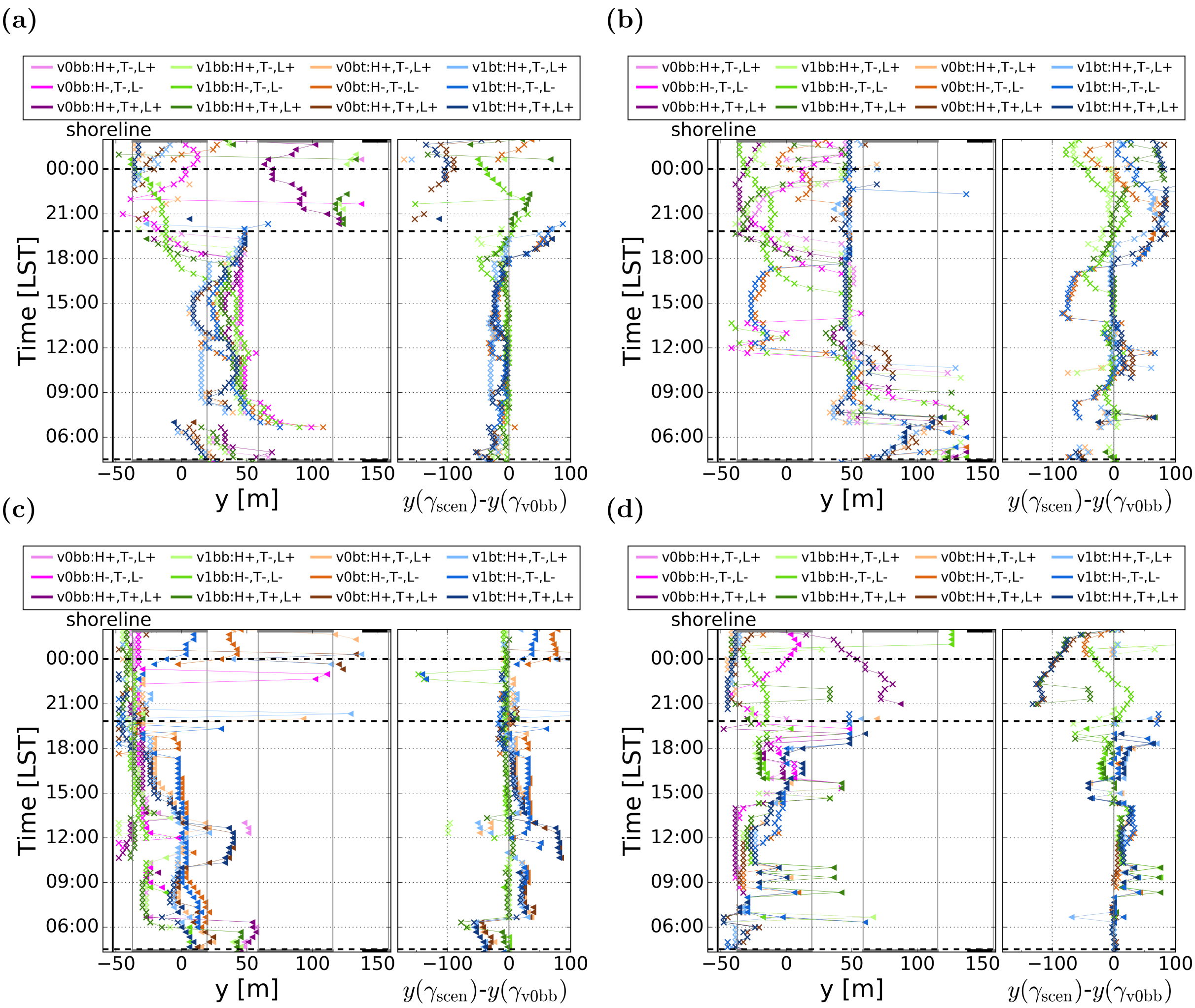

Figure 6.23: Penetration depth of the water influence ($y(\gamma_n = 0.3)$) for different scenarios (colour coded) and meteorological conditions (colour and marker coded) for the lake scenario `e220` for (a) air temperature, (b) vapour pressure, (c) wind speed, (d) mean radiant temperature. In each figure on the left the actual penetration depths are shown and on the right the difference in penetration depth between each scenario and the reference scenario ($y_{\mathrm{scen}}(\gamma_n = 0.3) - y_{\mathtt{v0bb}}(\gamma_n = 0.3)$). See text for the colour coding.

In general, the differences between the scenarios and the reference scenario are mostly within ±40 m for daytime (right sub-figures in Figure 6.23). Larger differences are encountered during daytime only if a local minimum or maximum is calculated for γ_n for any scenario (indicated by triangles). During the night differences are larger, since often

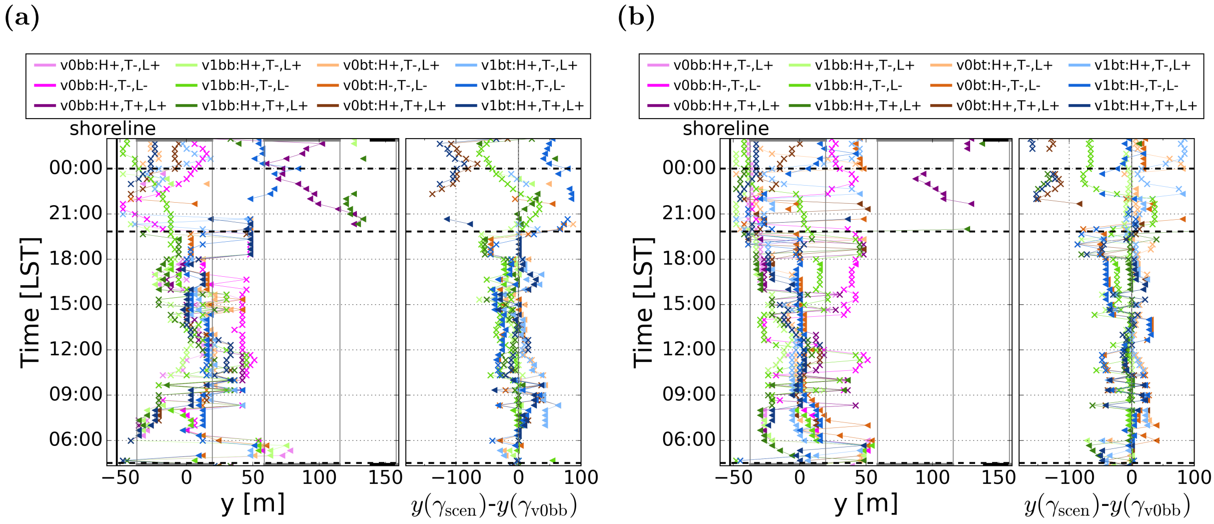

Figure 6.24: Same as Figure 6.23 but for (a) PET and (b) UTCI.

local maxima or minima for γ_n develop. Larger differences during the night than during the day are expected from Section 6.4.1.2, as the effect of water surfaces during the night is indirect via a flow channelling effect in the first building row. As the flow channelling effect depends on the street geometry and the exact wind direction and speed, local maxima or minima for γ_n are calculated only in some scenarios and situations.

For daytime for T_a (Figure 6.23a) and e (Figure 6.23b) smaller penetration depths are calculated for terraced building scenarios (`v0bt`, orange-brown, and `v1bt`, blue) than for building block scenarios (`v0bb`, pink-purple and `v1bb`, green). This is caused by a stronger advection of lower temperatures from over the lake into the urban environment by the flow channelling of the block building. For the terraced buildings the flow channelling is interrupted and walls warm the air locally. The small impact of riverside vegetation (`v1bb`, green) is due to the fact that vegetation only directly influences the radiation and flow field in MITRAS, which of course indirectly influences temperature. The process of evapotranspiration is not included in the simulations. If evapotranspiration was included a larger impact on T_a and e is expected.

For FF (Figure 6.23c) for simulations with vegetation (green, blue) slightly smaller penetration depth are typically calculated compared to their non-vegetated counterparts (pink-purple, orange-brown). Since explicit vegetation reduces wind speed in MITRAS (Salim et al., 2018), the higher wind speeds from over the lake cannot penetrate as far into the city. Therefore, closer to the shoreline wind speeds similar to those in the urban reference area are calculated, leading to smaller penetration depths. Systematic larger penetration depths are encountered for the terraced building scenarios (blue, orange-brown). This is due to the different flow channelling effects of the two building types: In the building block scenario a strong flow channelling is simulated in all street canyons up to the urban reference canyon. In contrast, in the terraced building scenario flow channelling is much stronger in the first terraced building compared to the reference street canyon due to higher wind speeds from the lake. Therefore a local maximum is derived in the notional city method (γ_n).

The effects of vegetation on the radiation field are visible in the differences for T_{mrt} (Figure 6.23d): during midday smaller T_{mrt} values extend farther from the shore into the urban environment if riverside vegetation provides shading. Thus slightly larger penetration depths are simulated for the `v1bb` scenario (green). If the elevation angle of the sun is smaller, i.e. around 09:00 LST and between 16:00 LST and 18:40 LST, the shading by the riverside trees induces a discontinues pattern for T_{mrt}. Thus, penetration depth with vegetation (green, blue) are calculated after a local minimum for γ_n has been reached (triangles).

Of all meteorological variables, the thermal indices PET (Figure 6.24a) and UTCI (Figure 6.24b) show the largest impact of the different morphologies during the day. This is to be expected, as they include the effect of all the different morphologies on all input variables. However, no clear pattern of the influences of the different building types and the presence of riverside vegetation is visible. This is because a similarly large variability due to different meteorological situations and local maxima or minima encountered for γ_n.

In Figure 6.25 the differences in penetration depth due to different urban morphologies ($y_{\mathrm{scen}}(\gamma_n = 0.3) - y_{\mathtt{v0bb}}(\gamma_n = 0.3)$, darker colours, that is, left box of each colour) are compared to the differences due to the different meteorological situations ($y_{\mathrm{met}}(\gamma_n = 0.3) - y_{\mathrm{H^+T^-L^+}}(\gamma_n = 0.3)$, brighter colours, that is, right box of each colour). For the differences due to different meteorological conditions only the spread of penetration depths is of interest. Thus, the reference meteorological situation $\mathrm{H^+T^-L^+}$ is chosen arbitrarily, any of the two other situation could have been used. Different colours indicate different times of the day: blue is MORNING (04:20 LST to 06:00 LST), red is NOON (10:00 LST to 13:00 LST) and green is NIGHT (20:00 LST to 02:00 LST). Median, interquartile range and outliers are shown in the same way as in Figure 6.17. Results are presented for the lake (e220) in Figure 6.25a and for the canal (e30) in Figure 6.25b. Note that overall differences between the water and the urban reference area were often small for the canal. Thus, γ_n was not always calculated due to the required minimum difference thresholds (Section 6.3.2.1). The results for the canal scenario are therefore less certain.

(a)

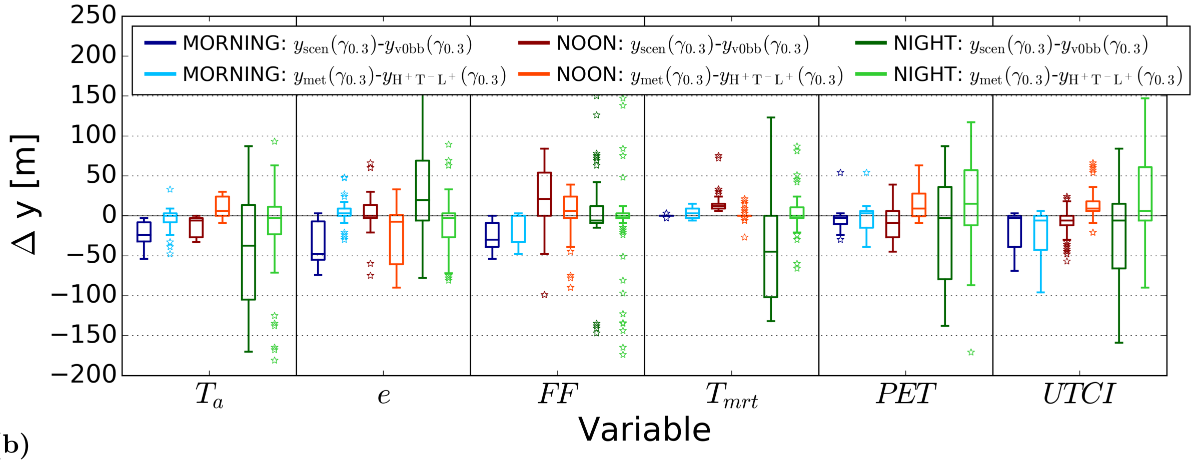

(b)

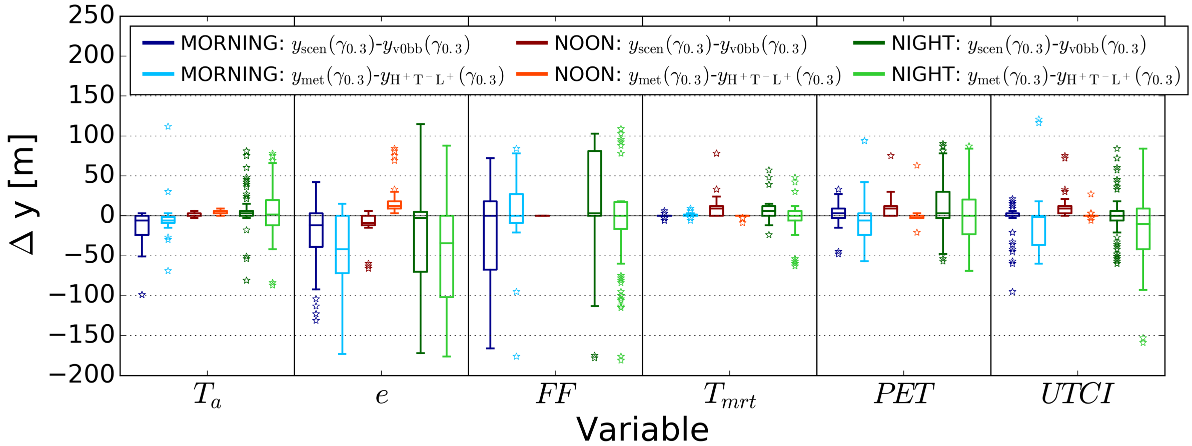

Figure 6.25: Box plots for the difference in penetration depth of the water influence due to different morphologies (darker colours, left box of each colour) and different meteorological situations (brighter colours, right box of each colour) for MORNING (04:20 LST to 06:00 LST, blue), NOON (10:00 LST to 13:00 LST, red) and NIGHT (20:00 LST to 02:00 LST, green) for (a) the lake (e220) and (b) the canal scenario (e30).

Focusing on the lake scenario (Figure 6.25a), the reduced penetration depth of air temperature and the larger penetration depth due to a local maximum in γ_n in the terraced building scenario are visible during NOON (dark red) and during MORNING for T_a (dark blue). For MORNING and NOON also the non-systematic differences in penetration depth due to different morphologies for PET and UTCI are visible. The non-systematic difference can be explained by the large differences caused by different meteorological conditions (orange): the calculated ranges of the variability due to meteorological conditions and urban morphologies are equally large (NOON) or larger (MORNING). Large differences in T_a induced by different meteorological situations during NOON are due to only $H^+T^-L^+$ having a different effect on `v1bt` compared to all other situations during most of NOON (Figure 6.23a). During NIGHT the influence of the urban morphologies is equally large or larger for the different variables due to the difference in penetration depth dominated by local effects.

For the canal scenario (Figure 6.25b) the influence of the meteorological conditions is equally large as or even larger than the influence of the urban morphology for almost all variables during all average times (detailed Hovmöller diagrams are shown in Figure P.6). During NOON the variability in T_{mrt} and UTCI due to different scenarios is larger than the variability due to different meteorological conditions. For PET the smaller extent of the box also indicates stronger influence of the morphology compared to the meteorology during NOON. The strong variabilty due to different scenarios is caused by shading provided by vegetation. This can be gathered from Figure P.6d to Figure P.6f showing the penetration depth for T_{mrt}, PET and UTCI to be systematically larger for scenarios with vegetation (blue and green lines in Figure P.6). For FF neither the different meteorological situations nor the different urban morphologies have an effect on the penetration depth of the influence during NOON, since the water influence is mainly small (Section 6.4.2.1).

Overall, recommendations for building designs to favour large penetration depth cannot be derived based on the simulations and methodology used here. On the one hand, variations due to meteorological conditions are equally large and on the other hand, local maxima or minima in γ_n are calculated for some simulations and meteorological conditions. However, the local maxima and minima depend on both the meteorological situation and urban morphology. Further analysis and more simulations are required to disentangle these effects fully and derive general conclusions.

6.4.3.2 Sensitivity of the magnitude to morphology

The magnitude of the water influence at the shoreline is for all variables equally strong influenced by different meteorological situations and urban morphologies for the lake, except T_{mrt} at NOON. This can be seen in Figure 6.26a, which shows the difference in magnitude of the water influence due to different morphologies and different meteorological situations with the same colour coding as Figure 6.25a.

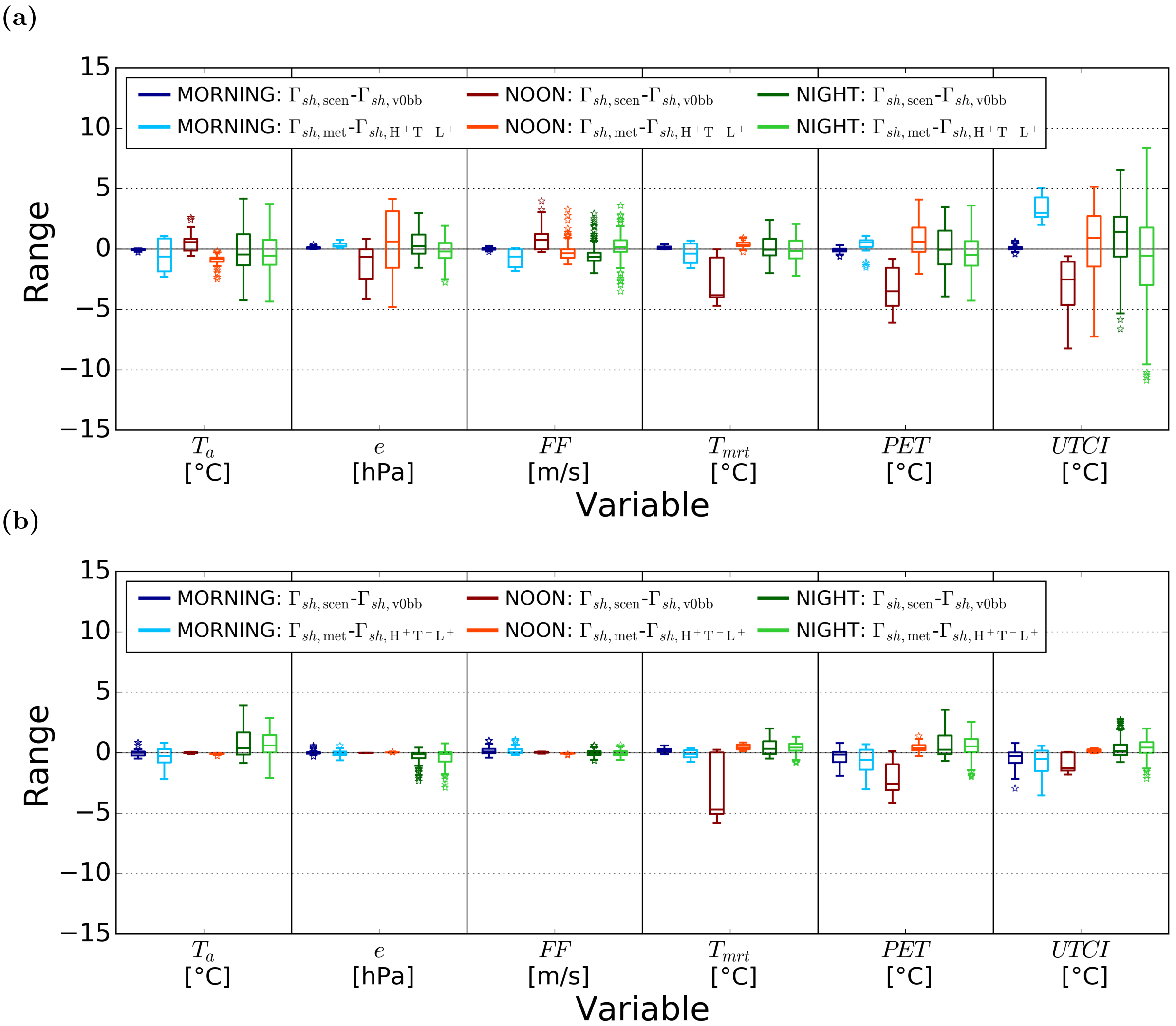

Figure 6.26: Same as Figure 6.25 but for the magnitude of the water influence at the shoreline, $\Gamma = \chi_{sh} - \chi_{u,m}$.

Despite the large variability of the magnitude of the water influence due to different meteorological situations, systematic differences exist between the different urban morphologies. This can be seen in Figure 6.27. It shows the magnitude of the water influence at the shoreline ($\chi_{sh} - \chi_{u,m}$) for the different meteorological variables for the lake scenario on the left of each sub-figure and the difference of the various scenarios to `v0bb` on the right of each sub-figure, using the same colour coding as Figure 6.27. Overall higher wind speeds are simulated in the terraced building scenarios (Figure 6.27c). This is due to the atmosphere being less stable over the lake and thus more downward mixing of higher wind speeds. The higher wind speeds lead to a stronger advection of water influenced air into the urban area. As the urban averaging area is also influenced by this advection typically smaller differences between the shoreline and the urban reference area are calculated for T_a (Figure 6.27a) and e (Figure 6.27b). The higher wind speeds at the shoreline in the terraced building scenarios cause on average more cooling in terms of PET (Figure 6.27e) and UTCI (Figure 6.27f). The strongest cooling during the day is calculated for each meteorological condition for `v1bt` (blue). This scenario includes besides terraced buildings also vegetation. Due to the shading of the vegetation generally smaller T_{mrt} values are encountered near the shoreline and thus a larger difference is calculated (Figure 6.27d, blue and green). The differences are also present at midday, as the average across the street canyon is used to derive the differences and thus parts of the averaging region are fully shaded (Figure 6.8).

In contrast to the lake scenario, in the canal scenario different urban morphologies do not cause large differences in the magnitude of the water influence (Figure 6.26b). This is due to usually smaller magnitudes of the water influence in the canal (Figure P.7). An exception are all variables that take radiation into account, i.e. T_{mrt} and the thermal indices PET and UTCI. For those variables systematically stronger cooling for scenarios with vegetation is simulated (blue and green colours in Figure P.7d to Figure P.7f).

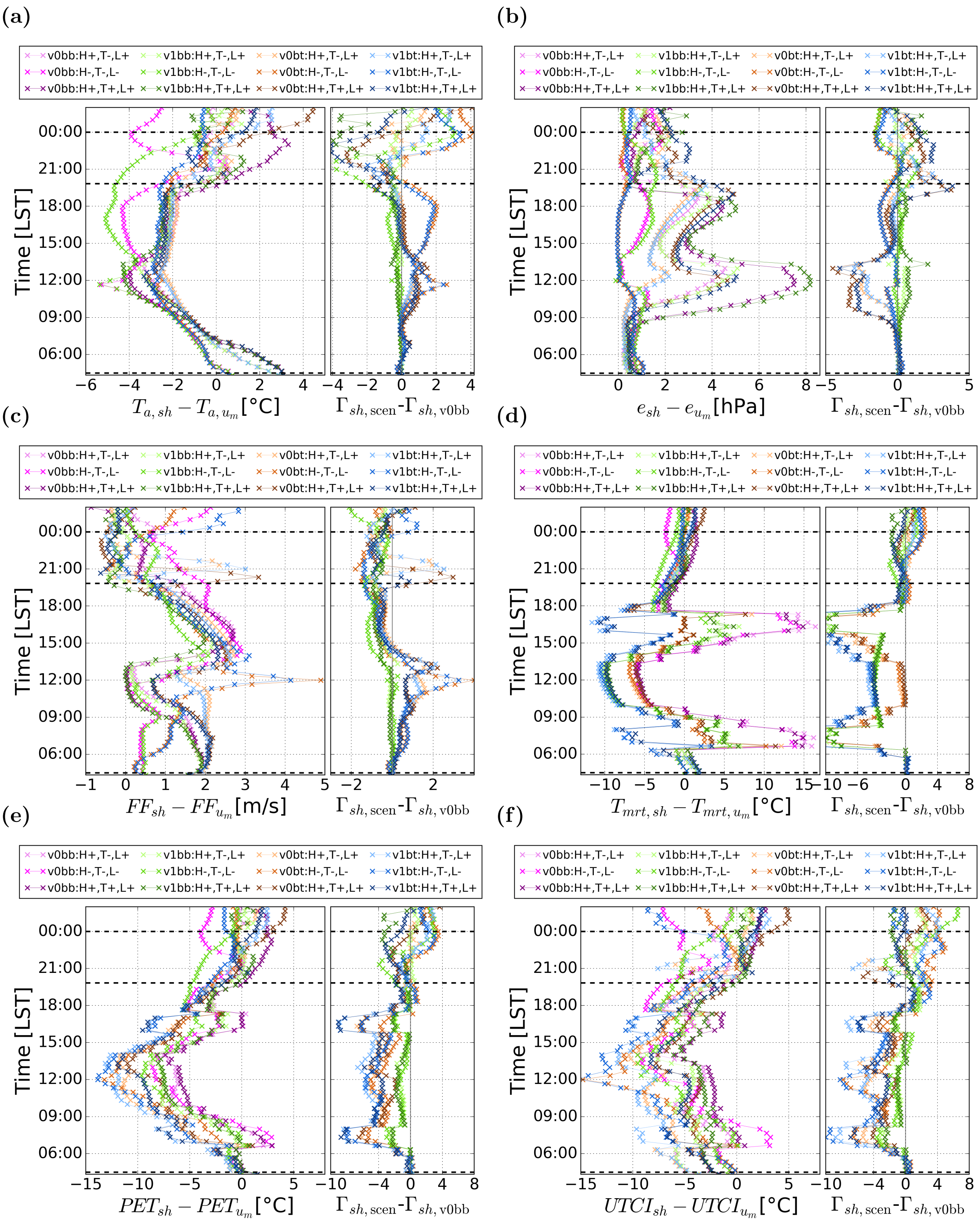

Figure 6.27: Same as Figure 6.23 but for the magnitude of the water influence at the shoreline, $\Gamma = \chi_{sh} - \chi_{u,m}$.

6.5 Discussion of the influence of water surfaces

In this chapter, the influence of water surfaces on the thermal conditions within a neighbouring urban area was assessed. The analysis was made both in terms of penetration depth and magnitude of the water influence for the meteorological variables air temperature (T_a), vapour pressure (e), wind speed (FF) and mean radiant temperature (T_{mrt}) as well as the thermal indices Physiological Equivalent Temperature (PET) and Universal Thermal Climate Index (UTCI).

The results indicate that penetration depths of the water influence into the urban environment differ for the different meteorological variables. In general, the water influence penetrates further into the urban environment for T_a and e than for the thermal indices during the day. In contrast, the magnitude of the water influence indicates stronger cooling during the day in terms of thermal indices PET and UTCI compared to T_a. Hence, air temperature, which is often used as an indicator of the cooling influence of a water surface (Table L.1), cannot fully capture the effect of water surfaces in human-relevant terms.

In early morning and during the night, the water surface typically warms the atmosphere in the investigated meteorological situations both in terms of air temperature and in terms of PET and UTCI. The warming is up to 4 K for the thermal indices and thus lies within the range of one thermal stress class of the indices (Table 2.4). Depending on the meteorological situation and building morphology, the warming during the night is not only a direct warming in terms of sensible heat fluxes but may also come into play indirectly: the building row closest to the shoreline receives shortwave radiation longer before sunset compared to building rows further away from the shoreline, which are already shaded by other buildings during that time. This causes higher surface temperatures of building walls and ground surfaces closer to the shoreline. Depending on the exact geometry and wind conditions, flow channelling is simulated in the street canyons. This flow channelling increases sensible heat fluxes from the warmer building walls, which in turn increases air temperature and consequently the thermal indices. Therefore, in addition to a direct warming of the lake during the night, a local maximum further within the urban environment is observed for the lake. However, as the flow channelling is sensitive to building morphology and exact meteorological conditions, for other meteorological situations and other building types this effect is not present in this form.

During daytime, typically larger penetration depths and magnitudes of the water influence are calculated for a lake compared to a canal: the lake cools the atmosphere close to the shoreline during the day by more than two stress classes of the thermal indices (15 K for UTCI and 10 K for PET). Therefore, this cooling is one stress class larger than the warming during the night. Further within the city, that is at the location of the penetration depth, PET and UTCI are cooler by between 0.5 K and 5 K than within the urban reference area. For the canal the maximum cooling of PET is about 3.5 K close to the shoreline during the day and lies therefore within one stress class. For the lake the water influence penetrates up to 130 m into the urban environment for PET and up to 90 m for UTCI. Therefore, to cool an urban environment more strongly and over a larger area during the day, larger water surfaces are better. However, in already existing urban areas there is often not enough space is available for such extensive water surfaces. Nevertheless cooling effect of almost one stress class for PET indicates that even a small water surface can provide a small relief from daytime heat stress.

The above mentioned values for PET and UTCI indicate that the magnitude of the water influence differs not only between the thermal indices and their input variables, but also between different thermal indices. This is due to different sensitivities of the thermal indices to their input variables. UTCI has the advantage over PET that it considers a reduction in cooling due to high humidity in warm conditions. However, the disadvantage of UTCI becomes apparent for the canal scenario: even if wind speeds from 1 m height are re-scaled to the 10 m input height for UTCI for wind, wind speeds are often below 0.5 $\mathrm{m\,s^{-1}}$ for a compact city. During such situations for the regression version (and also the look-up table version) of the UTCI the lower boundary value of 0.5 m has to be used, so that the variability within the urban area is lost. Thus, for the present analysis UTCI values do not differ for different meteorological conditions in the canal scenario. This seems to be a general issue as mean wind speeds are often small in urban areas due to the higher roughness of the buildings.

The influence of the water surface is affected by the general meteorological conditions during the day. The most influential variable is wind speed: For larger wind speeds larger penetration depths are simulated for all variables. The magnitude of the water influence is smaller for large wind speeds, whereas the magnitude of the thermal indices is larger. For the lake, in addition to wind speed, also the temperature difference between diurnal mean air temperature and diurnal mean water temperature ($\overline{T}_a - \overline{T}_{\mathrm{wat}}$) as well as air temperature itself are important determinants of the magnitude of the water influence. In contrast, the penetration depth and magnitude during the day for the canal are less sensitive to meteorological conditions at 04:00 LST. Nevertheless, wind speed is also the most influential variable for the canal. During the night, local effects become more important than during the day and thus large differences in penetration depths are simulated.

The urban morphology also affects the influence of the water surface especially in terms of its magnitude. A systematically stronger cooling for the thermal indices was derived for terraced buildings compared to block buildings for the lake scenario due to different atmospheric stability, which led to more downward mixing and thus larger wind speeds in the terraced building scenario. This indicates that towns close to a large lake could potentially increase the cooling potential of the water surface at the shoreline by using terraced buildings. However, more simulations are required to derive whether this is a generally valid result and if this would also be observed in larger urban areas. No clear recommendations could be derived for building scenarios that increase the penetration depth of the water influence. This is because the variability between the simulations for different meteorological situations is large and due to the used methodology as discussed below. Furthermore, the investigated urban morphologies only differ slightly as block buildings have been replaced by terraced buildings. The motivation for that was to test whether a small change could already cause a notable difference in the influence of the water surface. Larger effects might be found if for instance terraced buildings perpendicular to the urban environment are used, a different LCZ is investigated, the characteristics of the buildings are modified, i.e. albedo and emissivity, or the building height is changed.

For the lake, shoreline vegetation impacts the water influences less than a change in building structure. Close to the shoreline vegetation increased the magnitude of the water influence due to the shading. In contrast, for the canal, the influence of vegetation is larger compared to the building structure, because the penetration depth is overall smaller and thus not reaches far into the build-up area. In vegetated scenarios stronger cooling and larger penetration depths are simulated. Despite that, the influence of vegetation might still be underestimated in the current simulation as only the effect of shading and wind speed reduction and not the effect of evapotranspiration is accounted for (Chapter 5). Although Lee et al. (2016) indicated that the effect of shading by trees on human thermal environments is larger than the effect of evotranspiration by grass alone, evapotranspiration should be included in further investigations.

A relatively small model domain is chosen to balance physical insights and computational costs. Due to the limited extent of the domain the entire model domain is influenced by the presence of the water surface: assuming a wind speed of 1 $\mathrm{m\,s^{-1}}$, within 10 min an air parcel is transported through the entire 600 m large domain. Therefore, also the urban reference area is influenced by the water surface. Consequently, the derived penetration depth for the water influence are a lower limit. Furthermore, the small model domain in combination with the open boundary conditions for wind speed represent the situation of a small town close to a lake. As a consequence some conclusions might differ for larger urban areas; for instance the smaller humidity during the night within the inner urban area for the lake scenario. In comparison to forced boundaries, the open boundary conditions have the advantage that thermally driven circulations can develop within the model domain and thus might reflect more realistic results than forced boundary conditions. The chosen resolution of 3 m cannot capture every detail of the flow field (e.g. at building edges). However, as the thermal indices only account for mean wind speeds and not for turbulence, the resolution is deemed to be sufficient for the purpose of this study.

The applied method to derive the penetration depths of the water influence has the advantage that the penetration depth for different variables and scenarios can be compared. However, as a specific value is used for the threshold, in some situations a meandering pattern for each 20 min output interval is calculated. This could be improved by requiring that the influence falls below the threshold for a certain number of grid cells rather than one grid cell as currently implemented. Furthermore, the penetration depth for the present analysis has been defined as the location where the value of a particular variable approaches the urban reference value by 70 %, i.e. the water influence falls below 30 %. For other threshold values obviously other penetration depths of the water influence are derived. This has to be kept in mind for the interpretation of the presented results. Furthermore, local maxima and minima are calculated due to the normalisations of the indices for the penetration depth. These extrema indicate that an additional process impacts the influence of the water surface, e.g. flow channelling or shading. However, the actual influence of the water surface might reach further into the city and only interacts with the local process. This cannot be derived by this method and should be further investigated. For instance, instead of a fixed value of the fraction of the water influence a fixed distance could be used and for that location the fraction of the water influence could be derived. This would have the advantage that the cooling and warming effect further within the urban area can be assessed more clearly as the location does not vary during the day.

The idealised city structure allows drawing general conclusions regarding block- and terraced buildings are possible. However, even for this idealised structure slightly different wind directions can lead to a different flow channelling effect, which in turn influences the penetration depth of the water influence. In realistic urban domains local effects like these are even more important and can lead to a more complicated pattern of the water influence. Furthermore, in the present analysis only the influence along a main street perpendicular to the shoreline has been investigated. To fully assess the influence of water surfaces, also the situation in parallel streets and in courtyards should be investigated, especially for the terraced building scenario.

The initial conditions for the sensitivity of the water influence to meteorological conditions have been selected in such a way that they represent cloudless summer conditions in Hamburg. Although the sample size of only 60 different meteorological conditions is relatively small, the bootstrap results for the Elementary Effects indicates that the main sensitivity of the water influence to wind speed is relatively certain. However, as situations with overall small differences between the urban reference area and the water reference area are excluded from the analysis, the Elementary Effects are not always derived from all 60 simulations. The frequency of $\overline{T}_a - \overline{T}_{\text{wat}}$ (Figure 6.3c), which was used as an input for EET method was derived from daily averaged values of air and water temperature. Unfortunately from spring to autumn, the measurement of air temperature was affected by solar radiation in the afternoon due to a wrong attachment of the measurement device (Figure 6.2). No correction of these values has been attempted in this study. Therefore, the frequency of higher $\overline{T}_a - \overline{T}_{\text{wat}}$ values might be overestimated in the current study. Furthermore, the samples are drawn for each variable independently. Although in general also for a pair-wise comparison the distributions are relatively well met (Figure 6.4), for further analyses a dependent sampling strategy as suggested by e.g. Kucherenko et al. (2012) and Zhang et al. (2015a) could be applied to account for this dependence.

Although the meteorological situations are selected to represent cloudless summer conditions in Hamburg, the conclusions of this study are transferable to other urban areas at similar latitudes and for similar city structure. In the tropics, where air temperatures are higher than in the simulated input space, the evaporation of the water surface might increase heat stress due to higher humidity. Even for the conditions in Hamburg, a reduced cooling was derived for UTCI during the day (Figure 6.14). Furthermore, only one initial wind direction and one orientation of the urban area relative to the sun and the water surface has been investigated. Due to the influence of solar radiation, the results are not symmetric for other orientations. Since parts of the street canyon will be shaded during midday in other situations, the largest differences now observed for midday might shift to other hours of the day. However, this has to be investigated in more detailed analyses. In addition, during cloudy situations and during winter smaller influences of the water surface are expected as the temperature difference between the water surface and the urban area is smaller.

The building wall surface temperatures are too high in the simulations. This is due to (1) a too small volumetric heat capacity of the building wall, (2) an underestimated sensible heat flux and (3) a relatively small wall albedo (Section 6.4.1.1). The high surface temperatures influence especially the penetration depths calculated for T_{mrt}. Also other variables are influenced by the high wall temperatures. However, as in this study only differences to an urban reference area are investigated, the impact on the derived results is not that large. Finally, T_{mrt} within the investigated street canyon are not much too high as the wall temperatures are highest within the courtyards.

The current results reflect a standing water surface, which has the same height as the neighbouring urban area and has a constant water temperature throughout the day. Although all these assumptions are not unreasonable, they affect the results. For instance for river Elbe and the lake Alster water temperatures are smaller during early morning and midday than the diurnal average (Figure 5.1). Thus, the warming during early morning might be smaller if a diurnal cycle of the water temperature was included in the simulations. For a water surface, which is deeper than the urban environment, the cooling effect might be different as exposed building materials for canals might heat up during the day. Finally, a moving water surface could change the results as for instance for small wind speeds rural air could be transported in the urban environment by the water surface (Kuttler, 1991).

7 Conclusions

Elevated temperatures in urban areas together with the observed global temperature rise pose a severe health risk to society. To reduce this risk, thermally comfortable designs are required. Within this thesis, the potential of urban water surfaces as such a design element is investigated by Obstacle Resolving micro-scale model (ORM) simulations. Thus, the thesis is guided by the question (GRQ) "*How strongly do different kinds of urban water surfaces affect their thermal surroundings under various meteorological situations and urban scenarios during different times of the day?*"

To derive the influence of water surfaces on the thermal environment in human-relevant terms, thermal indices are used. Thermal indices quantify subjective perceived temperatures objectively by taking into account heat fluxes between the human body and the environment. Altogether, more than 165 thermal indices with different characteristics and targets have been developed in the past (de Freitas and Grigorieva, 2015). As not all of them can be applied to evaluate outdoor human thermal environments in obstacle resolving models, research question one was posed (RQ 1): "*Which thermal indices can be used globally in their current form to evaluate the outdoor urban thermal environment in ORM applications?*" To identify suitable indices, 11 criteria and 6 index features are derived based on the characteristics of human environmental heat exchange, the characteristics of outdoor urban environments and the characteristics of ORMs. The application of the criteria and features showed that out of the 165 proposed thermal indices only four fulfil all criteria. These thermal indices, Perceived Temperature (PT_J), Physiological Equivalent Temperature (PET), Physiological Subjective Temperature (PST) and Universal Thermal Climate Index (UTCI), differ with respect to the comprehensiveness of the thermo-physiological model, the assessed human response, the treatment of clothing and activity, the computational costs and their application frequency in ORM studies. PET and UTCI are applied more frequently compared to the other indices and are thus selected in this thesis to derive the influence of water surfaces on human thermal environments.

PET and UTCI differ in various aspects. Thus, for the same meteorological situation, they may yield different results. RQ 2, "*How sensitive are selected thermal indices to their input variables?*", addresses these differences. The sensitivity of PET and UTCI was assessed for meteorological input variables (air temperature, vapour pressure, wind speed and radiation in form of mean radiant temperature (T_{mrt})), personal input variables (age, gender, height, weight, work metabolism and clothing insulation) and built-environment-related input variables (building height, street width, street orientation, albedo and emissivity of the ground and wall surfaces). The analysis indicates that both PET and UTCI are most sensitive to air temperature in both summer and winter. The second most influential variable for UTCI is wind speed, which is almost as important as air temperature in winter. For PET, wind speed and mean radiant temperature are important input variables in summer, while in winter PET is sensitive to work metabolism. The analysis showed that PET decreases with increasing work metabolism in winter. This is an unexpected result as higher work metabolisms increase internal energy and thus should lead to higher PET values. The counter-intuitive behaviour of PET is related to its definition as a steady state index and the requirement of equal skin and core temperature in the actual and the reference environment. Thus, the definition of PET should be revised in the future for applications in cold environments.

Two different versions for calculating PET have been investigated: (1) a version provided by VDI (2008), which is based on the stationary thermo-physiological model MEMI and (2) a version used in ENVI-met, which is based on the instationary model IMEM that is integrated until energy balance is achieved. In cold and moderate environments both versions agree well. Both show the counter-intuitive behaviour with respect to metabolism. However, in hot environments, they differ by up to 14 K in the investigated situations due to the different treatment of latent heat fluxes by sweating. Because of its treatment of latent heat fluxes the VDI version of PET is not sensitive to humidity. In contrast, the ENVI-met version of PET and UTCI are slightly sensitive to humidity in warm conditions.

For the assessment of the sensitivities of PET and UTCI to the built-environment-related input variables, the Simple Urban Radiation Model (SURM) was developed. SURM calculates mean radiant temperatures for clear sky conditions in urban environments. As SURM is relatively fast, a large number of building scenarios could be investigated. The results indicate that building height, street width, street orientation and the position of the person within the street canyon all influence both thermal indices during daytime in summer. However, PET is more strongly influenced by these variables because it is more sensitive to the mean radiant temperature. These results are in line with those of earlier studies (e.g. Bröde et al., 2012; Fröhlich and Matzarakis, 2015; Schrijvers et al., 2016), which investigated the sensitivities for other meteorological situations and for a selected number of building orientations. Since only the direct influence of buildings on the radiation field is considered in SURM, non-linear effects in terms of air temperature or flow channelling are not accounted for. Therefore, the influence of built-environment-related variables on the thermal indices might be underestimated.

As a meteorology and built-environment-related variable, T_{mrt} is an important input variable for the thermal indices in summer. Therefore, MITRAS, the ORM applied in this thesis, is extended to improve the modelling of radiation within the obstacle layer and thus T_{mrt}. To be able to account for radiative surface-to-surface interaction between buildings and the ground, view factors between all surfaces are derived and used for radiation calculations. Furthermore, diffuse radiation was newly introduced in MITRAS to be able to calculate T_{mrt} directly from the simulation. Only with this inclusion radiation within the shade of buildings can be correctly calculated. The extended MITRAS version now also accounts for partial shading by vegetation. Here the Leaf Area Density is used. The extensions have been validated with idealised model simulations, which indicated that the extensions provide the desired effects.

The extended model is applied to address the guiding research question (GRQ) of this thesis, i.e. "*How strongly do different kinds of urban water surfaces affect their thermal surroundings under various meteorological situations and urban scenarios during different times of the day?*". The influences of a canal and a large lake for a small idealised urban area were investigated for different meteorological situations which represent cloudless summer conditions in Hamburg. The results indicate that large water surfaces can decrease thermal stress by more than two stress classes for UTCI and PET (VDI-version) close to the shoreline during the day compared to an urban reference area further away from the shoreline. Due to the small model domain, this reference area is also influenced by the water surface through advection. Within the urban canopy layer PET and UTCI are still up to about 5 K cooler a in a distance of 120 m from the shoreline than in the reference area. However, both the penetration depth and the magnitude of the cooling depends on the meteorological conditions: higher wind speeds lead to a cooling effect that is both stronger and noticeable further away from the shoreline than lower wind speeds. For the canal scenario, penetrations depths reach only up to 90 m and are thus smaller than for the lake case. Furthermore, close to the canal the median cooling effect over all meteorological situations is for PET about one sixth of the cooling effect of the lake and for UTCI about one quarter of the cooling effect of the lake. Different meteorological conditions barely influence the cooling effect of a canal. As these results have been derived for an idealised urban domain more simulations are necessary to determine whether similar cooling effects are detectable in more complex urban environments. In addition, other orientations of the water surface with respect to the urban area might change the results. This is due to different solar irradiations during different times of the day, which lead to a different warming of the urban environment for different orientations. However, it can be already concluded that larger water bodies have a more wide reaching influence.

Water surfaces provide a more far-reaching cooling effect in terms of air temperature than in terms of PET and UTCI as they are more strongly influenced by the urban morphology. In contrast, the magnitude of the water influence close to the shoreline is larger in terms of PET and UTCI due to higher wind speeds at this location. Thus, air temperature, which is often used as a proxy for the influence of water surfaces, cannot fully capture the influence in human-relevant terms. Due to different sensitivities to their input variables, PET and UTCI evaluate the cooling effect differently. UTCI is more sensitive to wind speed, so that higher wind speeds lead to a stronger cooling for UTCI than for PET in the lake scenario. In the canal scenario wind speeds within the urban area are generally small. As the regression version of UTCI is only applicable to wind speeds larger than 0.5 $\mathrm{m\,s^{-1}}$ at 10 m height, the wind speed variability in compact cities cannot be captured with this thermal index. This is a clear disadvantage of UTCI compared to PET. However, in contrast to the VDI version of PET, which is insensitive to humidity, UTCI indicates reduced cooling during daytime for very warm and humid situations, when latent heat fluxes by sweating become ineffective. Therefore, it is worthwhile to apply several thermal indices to characterise the human thermal environment and thereby use the strength of each index.

Further investigations are necessary to fully assess how different building types, i.e. block buildings and terraced buildings, alter the water influence. First results in this thesis indicate that meteorological conditions influence the penetration depth more than building types. The magnitude of the water influence was found to increase close to the shoreline of a lake during daytime for terraced buildings due to systematically different atmospheric stability and thus wind speed. However, this result should be confirmed for more meteorological situations and building scenarios with different height and be reproduced in measurements. The presence of waterside vegetation increased the cooling of the water surface close to the water edge due to shading for both a lake and a canal. However, the influence of vegetation might be underestimated in the current study: vegetation only influences shading and wind speed directly and not temperature and humidity by evapotranspiration as heat storage by trees is not accounted for. If this process was included the cooling effect might be even more enhanced (Kuttler, 1991).

In addition to improvements for modelling vegetation, the calculation of building surface temperatures should be improved. Unrealistically high building wall temperatures were calculated due to (1) a too small volumetric heat capacity of the building wall, (2) an underestimated sensible heat flux and (3) a relatively small wall albedo. The radiative interactions of building walls newly introduced in this thesis amplify the issue of the too high wall temperatures. However, this effect is strongest within courtyards, which are not assessed in the current study. In addition, the derived results for the influence of water surfaces are expected to be reasonable as (1) T_{mrt} values are quite plausible during the day, (2) air temperature is little affected by the higher wall temperature and (3) only the difference of the thermal environment and an urban reference area, rather than the respective absolute value, is of interest. Nevertheless, for further applications, building wall temperatures in MITRAS should be improved by changing the volumetric heat capacity and wall albedo. To improve the effect of the close-to-wall wind speed an adaptive temperature wall function can be introduced that accounts for the effect of buoyancy by solar heating (Allegrini et al., 2012). During the night, building wall temperatures are altogether quite reasonable.

The cooling of the water surfaces during daytime shifts to a warming during the night for most of the investigated meteorological situations. This night-time warming effect is up to 5 K in terms of PET and UTCI close to the shoreline of the lake. In other words, the warming during the night is within one stress class for both thermal indices compared to the daytime cooling of the two thermal indices by two stress classes. However, this indicates that close to the shoreline the positive effect of urban water surface in terms of providing thermally more comfortable conditions during the day is associated with the drawback of a night-time warming. This means that during the night water surfaces contribute to the urban heat island and deteriorate important night-time thermal comfort. This result is in line with a study by Steeneveld et al. (2014) and mesoscale urban climate investigations for Hamburg (e.g. Schlünzen et al., 2010; Böttcher, 2017) and indicates that water surfaces cannot be recommended unconditionally for thermally comfortable designs.

For a holistic assessment of the influence of urban water surfaces on the well-being of urban dwellers other aspects should be taken into account in addition to the water surfaces' influence on human thermal environments in summer. Due to higher deposition rates of air pollutants caused by higher humidity levels and the possible spray over water surfaces (Kuttler, 1991), water surfaces can improve air quality (Sander and Zhao, 2015).

Furthermore, on calm days moving water surfaces can transport cleaner rural air into the urban area (Kuttler, 1991). As heat wave events are often accompanied by strong air pollution (Kovatas and Hajat, 2008), water surfaces could improve both aspects. This is at least true for hygroscopic particles and water soluble gases. In addition, water surfaces are important during heavy precipitation events. As urban areas are often mostly sealed, water from precipitation runs off rather than infiltrates into the ground. Water surface can decrease the risk of flooding as they are often lower and thus can gather the excess water. Therefore, water-sensitive urban designs (Coutts et al., 2013) can also improve the resilience against heavy precipitation events. Finally, open water surfaces act as therapeutic landscapes (Foley and Kistemann, 2015; Völker and Kistemann, 2011, 2015), which provide relaxation, improve mental (Völker and Kistemann, 2011) and overall health and well-being (Krefis et al., 2018) and promote physical activity (Völker and Kistemann, 2015). Considering these aspects, multi-sectoral urban system models (von Szombathely et al., 2017) should be applied to combine the findings of this study regarding the influence on human thermal environments with other aspects of human well-being.

Acknowledgements

Several people supported and helped me during my PhD-project. I would like to use this opportunity to thank them personally.

First and foremost I would like to thank my supervisors Prof. Dr. K. Heinke Schlünzen and Prof. Dr. Bernd Leitl. Thank you, Heinke, for given me the flexibility to shape my own project and supporting me in numerous ways during the different stages of my work. Thank you, Bernd, for always encouraging me to be on a good path during my panel meetings. In this regard, I would also like to thank Dr. Frank Lunkeit for chairing my panel meetings and given advices for my PhD-project.

I am grateful for the stimulating working environment both in the UrbMod-project and in the MEMI working group. Thank you, Peter, for numerous advices both scientifically and personally and for letting me profit from your experience. Thank you, Marita, for offering distractions from work during coffee and lunch breaks but also for the fruitful discussions about modelling the atmosphere and MITRAS in particular. Thank you, David, for being ever available for all kinds of technical and scientific questions and creating a fun working environment. To all present and former members during my PhD-project: thank you for generating such vivid working conditions.

I gratefully acknowledge financial support through the UrbMod project, financed by the city of Hamburg. I am also grateful for the support by the School of Integrated Climate System Sciences, which helped to broaden my horizon on the various facets of climate research through their stimulating interdisciplinary environment.

I would like to thank Prof. Dr. Lutz Katzschner, who helped me getting started with the topic of human thermal environments. I would also like to thank Dr. Ingo Lange and Dr. Sarah Wieser, who provided the measurement data for the validation of SURM and the initialisation of the simulations in this thesis. The Climate Data Center of the German Meteorological Service and the Wassergütemessnetz Hamburg Service Portal are acknowledged for meteorological and water data for Hamburg. Dr. Jutta Holst, Prof. Dr. Michael Bruse and Dr. Henning Staiger are acknowledged for providing programs for calculating the thermal index PET and the mean radiant temperature from weather data. I would also like to thank Corinna Jensen for agreeing to reprint a figure from her master's thesis.

Last but not least, I would like to thank my friends and family for their fond support. Thank you, Rike, for many nice lunch and ice cream breaks and sharing life at SICSS. Thank you especially for proof-reading parts of my thesis. Thank you, Mu, for having a sympathetic ear during various stages of my PhD-project and for proof-reading parts of my thesis. I would also like to thank my mother, Marita, my father, Klaus, and my sister, Lenia, for their encouraging support throughout these years. Marita is particularly acknowledged for helping me to convert some tables from MS Word to LaTeX. Finally I would like to thank my partner, Arne, for his continuous, unconditional encouragement and support, which helped me to finish this thesis.

List of Acronyms

AAT	All-At-a-Time
BIAS	Average difference
DWD	German Meteorological Service
EET	Elementary Effect Test
GRIMASK	GRIMASK
HR	Hit rate
HUSCO	Hamburg Urban Soil Climate Observatory
IMEM	Instationary Munich Energy balance Model
LCZ	Local Climate Zone
LST	Local Solar Time
MEMI	Munich Energy Balance Model for Individuals
METRAS	Mesoscale Transport and Stream model
MITRAS	Microscale Transport and Stream model
OAT	One-At-a-Time
ORM	Obstacle Resolving micro-scale model
PDF	probability density function
PERCEIVED	Perceived temperatures postprocessor
PET	Physiological Equivalent Temperature
PET^*	Physiological Equivalent Temperature with changed personal parameters
PET^*_{env}	PET^* as Envi-met version
PET^*_{vdi}	PET^* as VDI version
PET_{env}	PET as Envi-met version

PET_{vdi}	PET as VDI version
PREMASK	PREMASK
PREMASK	PREMASK
PT_J	Perceived Temperature
r	Correlation Coefficient
RANS	Reynolds-Averaged-Navier–Stokes equations
RMSE	Root Mean Square Error
SCC	surface cover class
STDE	Standard Deviation of Error
SURM	Simple Urban Radiation Model
TSV	Thermal Sensation Vote
UHI	Urban Heat Island
UTCI	Universal Thermal Climate Index
VDI	Verein Deutscher Ingeneure (engl. Association of German Engineers)

List of Symbols

Greek Letters

α	[$^{\circ}$]	elevation angle of the sun
α^{*}	[m^3]	grid volume
$\alpha_{\min}$	[$^{\circ}$]	minimum elevation angle for grid point to receive direct radiation
$\alpha_{\min,t}$	[$^{\circ}$]	minimum elevation angle for grid point to receive direct radiation if explicit vegetation is present
α_q	[ ]	soil water availability
β	[ ]	diffusivity parameter
θ	[$^{\circ}$]	zenith angle of inclined surface
χ	[ ]	scalar quantity
χ_*	[ ]	scaling flux of a scalar quantity (χ)
δ	[ ]	declination of the Earth
$\delta_{j,\mathrm{wat}}$	[ ]	water switch, $\delta_{j,\mathrm{wat}}$=1 for j=‘water’
δ_{R0}	[ ]	vertical optical thickness of the clean and dry standard atmosphere
ε_p	[ ]	emissivity of the human body
ε	[ ]	emissivity
ε_g	[ ]	emissivity of ground surfaces
ε_w	[ ]	emissivity of wall surfaces
η	[ ]	Vertical coordinate
η_i	[$^{\circ}$]	angle between surface normal and sun
Γ	[ ]	Magnitude of the water influence
γ_m	[ ]	Normalised water influence based on a monotonic method
γ_n	[ ]	Normalised water influence based on notional city method
γ	[ ]	Normalised water influence
κ	[ ]	von Karman constant
λ	[m]	wave length
∇	[ ]	Nabla operator
ν_s	[$\mathrm{m}^2\,\mathrm{s}^{-1}$]	thermal conductivity

Ω	[rad/s]	Earth's angular velocity
ω	[seconds since midnight]	hour angle of the sun
ω_s	[°]	street orientation
Φ	[m]	geopotential
ϕ	[ ]	latitude
ψ	[°]	azimuth angle of the sun
ψ_i	[°]	azimuth angle of surface i
ψ_{nc}	[°]	centre angle of azimuth sector n
ψ_{in}	[°]	azimuth angle of inclined surface
ψ_n	[°]	azimuth angle of sector n
ψ_m	[ ]	stability function
ρ	[$\mathrm{kg\,m^{-3}}$]	air density
ρ_0	[$\mathrm{kg\,m^{-3}}$]	large scale air density
$\widetilde{\rho}$	[$\mathrm{kg\,m^{-3}}$]	microscale air density
ρ_w	[$\mathrm{kg\,m^{-3}}$]	absolute humidity
σ	[$\mathrm{W\,m^{-2}\,K^{-14}}$]	Stefan-Boltzmann constant
σ_a	[1/m]	total absorption coefficient
τ	[ ]	coefficient for reduction of shortwave radiation by vegetation
Θ	[°]	zenith angle of the sun
β_i	[°]	angle between the normal of a surface and the sun
$\mathit{\Theta}$	[K]	potential temperature
θ	[°]	angle between the surface normal and a line to a different element
ϑ_*	[ ]	scaling flux of temperature
ϑ_*^b	[ ]	scaling flux of temperature at buildings
$\mathit{\Theta}_b$	[K]	potential surface temperature of the building
ζ	[°]	rotation angle of coordinate system against North
Latin Letters		
B	[$\mathrm{W\,sr^{-1}\,m^{-3}}$ sort]	Planck function
d_b	[m]	distance between building and scalar grid cell
A	[yr]	age
a	[ ]	albedo
A_1	[$\mathrm{m^2}$]	area of finite element
A_2	[m^2]	area of finite element

A_{Du}	[m^2]	body surface area
a_g	[ ]	albedo of ground surface
a_j	[ ]	albedo of surface cover class j
a_k	[m^{-1}]	absorption coefficient of human body surface
a_r	[ ]	Reflectivity in vertical resolved shortwave radiation
$\overline{ASP}$	[ ]	average aspect ratio
a_w	[ ]	albedo of wall surface
BF	[%]	body fat content
Bo	[ ]	Bowen ratio of surface
b_{terr}	[ ]	comprehensive parameter for physical properties of ground
C	[$\mathrm{Wm^{-2}K^{-1}}$]	C-value, heat transfer coefficient of the building wall
c_p	[$\mathrm{J\,kg^{-1}\,K^{-1}}$]	Specific heat at constant pressure
c_w	[$\mathrm{J\,m^{-3}\,K^{-1}}$]	volumetric heat capacity of the building wall
D	[ ]	wall thickness
d	[m]	water depth
DA	[ ]	Desired accuracy for Hit rate calculation
dA_1	[m^2]	differential area of differential element
DD	[$^\circ$]	wind direction
E	[ ]	expected value
e	[Pa]	vapour pressure
e_4	[Pa]	vapour pressure at 04:00 LST
$e_{a,k=2m}$	[Pa]	Vapour pressure at 2 m height
$e_{a,k}$	[Pa]	Vapour pressure at height k
E_e	[$\mathrm{W/m^2}$]	irradiance flux density
$EE_{i,m}$	[ ]	mean elementary effect (EE_i^j) of input i
$EE_{i,std}$	[ ]	standard deviation of EE_i^j of input i
EE_i^j	[ ]	elementary effect of input i at point j
e_s	[Pa]	saturation vapour pressure
E_w	[m]	water extent
f	[$\mathrm{rad\,s^{-1}}$]	coriolis parameter ($2\Omega\sin\phi$)
f'	[$\mathrm{rad\,s^{-1}}$]	coriolis parameter ($2\Omega\cos\phi$)
$\overline{F}_1$	[$\mathrm{m^2\,s^{-2}}$]	subgrid scale turbulent momentum flux in x-direction
$VF_{1\to 2}$	[ ]	view factor between A_1 and A_2
$\overline{F}_2$	[$\mathrm{m^2\,s^{-2}}$]	subgrid scale turbulent momentum flux in y-direction

$\overline{F}_3$	$[\mathrm{m^2\,s^{-2}}]$	subgrid scale turbulent momentum flux in z-direction
f_a	[ ]	function of albedo
f_b	[ ]	building surface fraction
$\overline{F}_{\overline{\chi}}$	[ ]	subgrid scale turbulent scalar flux
F_d	[ ]	diffuse angular function
$VF_{d1\to 2}$	[ ]	view factor between dA_1 and A_2
FF	$[\mathrm{ms^{-1}}]$	wind speed
FF_{10}	$[\mathrm{ms^{-1}}]$	wind speed at 10 m
$FF_{10,4}$	$[\mathrm{ms^{-1}}]$	wind speed at 10 m at 04:00 LST
f_{iper}	[ ]	impervious surface fraction
f_j	[ ]	fraction of j
$f_{lit,g}$	[ ]	fraction of ground lit
$f_{lit,w}$	[ ]	fraction of wall lit
F_m	[N]	Molecular forces
f_p	[ ]	surface projection factor
f_{per}	[ ]	pervious surface fraction
G	$[\mathrm{W\,m^{-2}}]$	global radiation
g	$[\mathrm{m\,s^{-2}}]$	Gravitational acceleration
gn	[ ]	gender
H	[m]	building height
h	[m]	elevation height
h_a	$[\mathrm{W\,m^{-2}\,K^{-1}}]$	heat transfer coefficient between surface and atmosphere
h_{LAD_m}	[m]	height of maximum Leaf Area Density
h_p	[m]	height of a person
h_t	[hour]	current hour
h_ϑ	[m]	depths of daily temperature wave
h_v	[m]	vegetation height
I_0	$[\mathrm{W\,m^{-2}}]$	solar constant for a specific time
I_{clo}	[clo]	clothing insulation
I_t	[ ]	thermal index
I_∞	$[\mathrm{W\,m^{-2}}]$	mean value of the solar constant
j	[ ]	surface cover class
jd	[rad]	Julian day number
J_e	$[\mathrm{W/m^2}]$	radiosity of a surface

k	[ ]	vertical index of model layer
k_s	[$\mathrm{m^2 s^{-1}}$]	thermal diffusivity
L	[m]	Monin-Obukhov length
l_{21}	[$\mathrm{J\,kg^{-1}}$]	Specific heat of vaporisation ($2.5 \cdot 10^6\ \mathrm{J\,kg^{-1}}$)
LAD	[$\mathrm{m^2\,m^{-3}}$]	Leaf Area Density
LAD_m	[$\mathrm{m^2\,m^{-3}}$]	maximum Leaf Area Density
LAI	[ ]	Leaf Area Index
l_{lit}	[ ]	logical parameter; 1 if point is lit, 0 otherwise
LW	[$\mathrm{W\,m^{-2}}$]	longwave radiation flux
$LW\downarrow$	[$\mathrm{W\,m^{-2}}$]	downward longwave radiation flux
LW_i	[$\mathrm{W\,m^{-2}}$]	longwave radiation emitted from surface i
$LW_{in,s,i}$	[$\mathrm{W\,m^{-2}}$]	incoming longwave radiation from sky
$LW_{in,t,gi}$	[$\mathrm{W\,m^{-2}}$]	total incoming longwave radiation at ground i
$LW_{in,t,wi}$	[$\mathrm{W\,m^{-2}}$]	total incoming longwave radiation at wall i
LW_{net}	[$\mathrm{W\,m^{-2}}$]	longwave radiation balance
$LW_{net,g}$	[$\mathrm{W\,m^{-2}}$]	longwave radiation balance of ground surface g
$LW_{net,w}$	[$\mathrm{W\,m^{-2}}$]	longwave radiation balance of walls
LW_{out}	[$\mathrm{W\,m^{-2}}$]	outgoing longwave radiation
LW_s	[$\mathrm{W\,m^{-2}}$]	longwave radiation from sky
$LW_{\uparrow}$	[$\mathrm{W\,m^{-2}}$]	upward longwave radiation flux
M	[$\mathrm{W\,m^{-2}}$]	Metabolic heat production
m	[kg]	weight of a person
m_{r0}	[ ]	relative optical air mass
M_w	[W]	work metabolism
N	[ ]	cloudiness
p	[hPa]	pressure
p_0	[hPa]	pressure of standard atmosphere at sea level
p_1	[hPa]	hydrostatic part of pressure
p_2	[hPa]	dynamic part of pressure
q	[ ]	specific humidity, short for q_1^k with k=1
Q^*	[$\mathrm{W\,m^{-2}}$]	net allwave radiation balance
q_*	[ ]	scaling flux of humidity
q_1^k	[ ]	Concentration of atmospheric water; k=1,2,3 is vapour, liquid and solid phase, respectively
ΔQ_A	[$\mathrm{W\,m^{-2}}$]	net advective heat flux

Q_χ	[ ]	sources and sinks of χ
Q_{cond}	$[\mathrm{W\,m^{-2}}]$	conductive heat flux
Q_G	$[\mathrm{W\,m^{-2}}]$	ground heat flux density
Q_H	$[\mathrm{W\,m^{-2}}]$	sensible heat flux density
Q_L	$[\mathrm{W\,m^{-2}}]$	latent heat of diffusion
Q_E	$[\mathrm{W\,m^{-2}}]$	latent heat flux density
Q_{Re}	$[\mathrm{W\,m^{-2}}]$	heat flux from respiration (latent and sensible)
ΔQ_S	$[\mathrm{W\,m^{-2}}]$	net heat storage
Q_{sw}	$[\mathrm{W\,m^{-2}}]$	latent heat of sweating
Q_Θ	$[\mathrm{W\,m^{-2}}]$	source or sink of Θ
RH	[ ]	relative humidity
RH_4	[ ]	relative humidity at 04:00 LST
R_i	$[\mathrm{kg\,m^2\,s^{-2}\,mol^{-1}\,K^{-1}}]$	individual gas constant
R_{se}	$[\mathrm{m^2\,K\,W^{-1}}]$	thermal resistance of outer facade
SW_{dir}	$[\mathrm{W\,m^{-2}}]$	Direct shortwave radiation
S	$[\mathrm{W\,m^{-2}}]$	storage of heat
S_i	[ ]	Main effect sensitivity index of variable i
s_i	[ ]	Not standardised sensitivity index of variable i
$S_{i,T}$	[ ]	Total-order effect sensitivity index of variable i
std	[ ]	Standard deviation
SVF	[ ]	sky view factor
SW	$[\mathrm{W\,m^{-2}}]$	shortwave radiation
SW_{diff}	$[\mathrm{W\,m^{-2}}]$	Diffuse shortwave radiation
$SW_{diff,i}$	$[\mathrm{W\,m^{-2}}]$	Diffuse shortwave radiation from direction i
$SW_{diff,s}$	$[\mathrm{W\,m^{-2}}]$	Diffuse shortwave radiation from sky
$SW\downarrow$	$[\mathrm{W\,m^{-2}}]$	total downward shortwave radiation
$SW_{in,s,i}$	$[\mathrm{W\,m^{-2}}]$	incoming shortwave radiation from sky
$SW_{in,t,i}$	$[\mathrm{W\,m^{-2}}]$	total incoming shortwave radiation
SW_{net}	$[\mathrm{W\,m^{-2}}]$	shortwave radiation balance
$SW_{net,g}$	$[\mathrm{W\,m^{-2}}]$	shortwave radiation balance of ground surface
$SW_{net,w}$	$[\mathrm{W\,m^{-2}}]$	shortwave radiation balance of wall surface
$SW_{rf,tot}\uparrow$	$[\mathrm{W\,m^{-2}}]$	total upward reflected shortwave radiation incoming at specific height
$SW\uparrow$	$[\mathrm{W\,m^{-2}}]$	upward shortwave radiation
T	[K]	temperature

t	[s]	Time
T_A	[ ]	Transmission factor due to scattering and absorption by aerosols
T_a	[K]	air temperature
$\overline{T}_a$	[K]	diurnal mean air temperature
$T_{a,k=2m}$	[K]	air temperature at 2 m height
$T_{a,k}$	[K]	air temperature at height k
$T_{a,4}$	[K]	air temperature at 04:00 LST
T_c	[K]	core temperature
T_{cl}	[K]	temperature of the clothing surface
T_R	[ ]	Transmission factor due to Rayleigh scattering
T_g	[K]	ground surface temperature
T_{room}	[K]	room air temperature
TKE	[$\mathrm{m^2\,s^{-2}}$]	Turbulent Kinetic Energy
T_L	[ ]	Transmission factor due to scattering and absorption by liquid water
T_L	[ ]	height corrected Linke Turbidity factor of relative optical air mass 2
$T_{L,am2}$	[ ]	Linke Turbidity factor of relative optical air mass 2
$T_{\max}$	[K]	maximum temperature at 2 m height
$T_{\min}$	[K]	minimum temperature at 2 m height
T_{mrt}	[K]	mean radiant temperature
T_{rd}	[ ]	diffuse transmission function
T_{sk}	[K]	skin temperature
T_{soil}	[K]	soil temperature
T_{tot}	[ ]	total transmission
T_V	[ ]	Transmission factor due to water vapour absorption
T_b	[K]	surface temperature of building; used to denote T_w for MITRAS calculations
T_w	[K]	wall surface temperature; used to denote T_b for SURM calculations
$\overline{T}_a - \overline{T}_{\mathrm{wat}}$	[K]	daily average temperature difference between air and water
T_{wat}	[K]	water temperature

U	$[\mathrm{W\,m^{-2}\,K^{-1}}]$	U-value, total heat transfer coefficient of the building wall
u	$[\mathrm{m\,s^{-1}}]$	wind component in x-direction
u_*	$[\mathrm{m\,s^{-1}}]$	friction velocity
u_*^b	$[\mathrm{m\,s^{-1}}]$	friction velocity at buildings
u_g	$[\mathrm{m\,s^{-1}}]$	U-component of geostrophic wind
$U_{rf,tot} \downarrow$	$[\mathrm{W\,m^{-2}}]$	total downward reflected shortwave radiation of unity flux $U \uparrow$ incoming at specific height
$U \uparrow$	$[\mathrm{W\,m^{-2}}]$	upward unity flux for two-steam approach
V	[ ]	variance
$\vec{v}$	$[\mathrm{m\,s^{-1}}]$	three-dimensional wind velocity
v	$[\mathrm{m\,s^{-1}}]$	wind component in y-direction
v_b	$[\mathrm{m\,s^{-1}}]$	wind speed parallel to the building wall at the adjacent atmospheric grid cell
$VF_{g \to s}$	[ ]	ground grid cell to sky view factor
$VF_{gi \to wj}$	[ ]	ground to wall view factor
$VF_{i \to j}$	[ ]	view factor from surface i to surface j
$VF_{p \to i}$	[ ]	view factor from person p to surface i
$VF_{i \to s}$	[ ]	sky view factor of surface i
$VF_{j \to i}$	[ ]	view factor of surface j to surface i
$VF_{p \to g}$	[ ]	view factor from person p to ground g
$VF_{p \to s}$	[ ]	view factor from person p to sky
$VF_{p \to w}$	[ ]	view factor from person p to wall w
$VF_{w \to s}$	[ ]	wall grid cell to sky view factor
$VF_{wi \to gj}$	[ ]	wall to ground view factor of surface i to ground j
$VF_{wi \to wj}$	[ ]	view factor of wall surface i to wall surface j
v_g	$[\mathrm{m\,s^{-1}}]$	V-component of geostrophic wind
v_{gr}	$[\mathrm{m\,s^{-1}}]$	wind speed parallel to ground in lowest model height (z_1)
v_i	$[\mathrm{m^3\,kg^{-1}}]$	specific volume of dry air ($i = 0$) and water ($i = 1$)
v_w	$[\mathrm{m\,s^{-1}}]$	walking speed
W	[m]	street width
w	$[\mathrm{m\,s^{-1}}]$	wind component in z-direction
w_m	$[\mathrm{W\,m^{-2}}]$	mechanical work accomplished
WVF	[ ]	wall view factor

WVF_i	[ ]	wall view factor of wall i
$\dot{x}_1$	[ ]	first direction of topography following coordinate system
$\dot{x}_2$	[ ]	second direction of topography following coordinate system
$\dot{x}_3$	[ ]	third direction of topography following coordinate system
x_{rel}	[ ]	relative position of person within street canyon
z_0	[m]	surface roughness length
$z_{0,b}$	[m]	surface roughness length of the building surface
$z_{0,b,\Theta}$	[m]	surface roughness length of the building surface for temperature
$z_{0,\Theta}$	[m]	surface roughness length for temperature
$z_{0,\mathrm{water}}$	[m]	surface roughness length of water
$z_{0,q}$	[m]	surface roughness length for humidity
z_1	[m]	height of the lowest model level

Appendix A

Preface

This appendix has been published as supplementary material in **Fischereit J. and Schlünzen K. H.** (2018): Evaluation of thermal indices for their applicability in obstacle resolving meteorology models. *International Journal of Biometeorology*, volume 62(10):pages 1887–1900. ISSN 1432-1254. `http://dx.doi.org/10.1007/s00484-018-1591-6` under the terms of the Creative Commons Attribution 4.0 International License (`http://creativecommons.org/licenses/by/4.0/`). For this thesis references to other chapters of this thesis have been added where applicable. To be consistent with the other parts of this thesis American English has been changed to British English, symbols have been replaced by their respective counterparts used in this thesis and the citation method of this thesis is used. References have been combined at the end of this thesis. Other changes made in comparison to the original supplementary material are marked italic.

Table A.1 shows the indices excluded by C1 to C7, their abbreviation, references and the reason for their exclusion.

Table A.1: Indices excluded from further analysis with the first criterion (C) they do not meet. Indices are given with their abbreviations (Abbr.) and reference in alphabetical order per failed criterion. Reasons for exclusion and comments include equations for the calculation of the indices if they are short enough. Indices for which differences are found in our literature review and the one by de Freitas and Grigorieva (2016) are marked with a star (*). Details on the differences are given in Appendix B. The air temperature design range of indices (ΔT) are taken from de Freitas and Grigorieva (2016). The following abbreviations of human body related parameter are used: I_{clo} is clothing, E_{sk} is evaporative heat loss from skin surface, HR is heart rate, HB is heart beats, M is metabolic heat, PEx is physical exertion, R is thermal resistance of clothing, SR is sweat rate, T_b is body temperature, T_c is core temperature, T_{rect} is rectal temperature, T_{sk} is skin temperature, $T_{sk,init}$ is initial skin temperature, TS is thermal sensation, WL is water loss. Additional parameters: a is a general function, e is water vapour pressure, e_s is saturation water vapour pressure, f is vapour tension of air, F is vapour tension at 36.5 °C [mmHg], h_t is hour of the day, h_a is convective heat transfer coefficient, LW is longwave radiation, h is elevation, N is cloudiness, p is pressure, P is precipitation, p_d is diurnal pressure range, ρ_w is absolute humidity, SW is solar radiation, T_a is air temperature, T_d is diurnal temperature range, T_{dp} is dew-point temperature, T_{gl} is globe temperature, T_g is ground temperature, T_m is mean temperature of surroundings, T_w is wall temperature, T_{wb} is wet-bulb temperature, Tu is turbulence intensity, FF is wind speed.

C	Index	Abbr.	Reference	Reason / Comments
1	Air Cooling Power	ACP	McPherson (1992)	Requires T_{sk}
1	Cold strain Index	CSI	Moran et al. (1999)	Requires T_c, T_{sk}
1	Cumulative Heat Strain index	CHSI	Frank et al. (1996)	Requires HB, HR, T_{rect}
1	Grade of Heat strain	GHSI	Hubač et al. (1989)	Requires HR
1	Heat tolerance index	HTI	Hori (1978)	Requires T_{rect}, salt loss, WL

C	Index	Abbr.	Reference	Reason / Comments
1	Increment Temperature Equivalent to Radiation Load	ITER	Lee and Vaughan (1964)	Requires SR
1	Index of Physiological Effect	$\mathrm{E_P}$	Robinson et al. (1944)	Requires HR, T_{sk}, T_{rect}, SR
1	Maximum Exposure Time	MET_B	Brauner and Shacham (1995)	Requires $T_{sk,init}$
1	Perceptual Hyperthermia Index*	PHI	Gallagher et al. (2012)	Requires TS, PEx or T_c
1	Perceptual strain index*	PeSI	Tikuisis et al. (2002)	Requires TS, PEx
1	Physiological index of Strain	Is	Hall and Polte (1960)	Requires HR, T_{rect}, SR
1	Physiological Strain Index	PSI	Moran et al. (1998)	Requires HR, T_{rect}
1	QS-index (correct name: ΔQd-index, see Table B.1)*		Rublack et al. (1981)	Requires T_{sk}
1	Quotient of heat stress	$\mathrm{Q}_{dif,H}$	Hubač et al. (1989)	Requires HR
1	Skin Temperature	SKT	Mehnert et al. (2000)	Requires T_{rect}
1	Skin wettedness	SkW	Gonzalez et al. (1978)	Requires E_{sk} / in original publication measurements were used. However, E_{sk} could be estimated from thermophysiological models (e.g. Gagge et al., 1986) including all six variables. Nonetheless the index characterises stress only for warm conditions and is thus rejected due to C7

C	Index	Abbr.	Reference	Reason / Comments
1	Required Clothing Insulation	I_{req}	Holmer (1988)	Requires T_{sk} and SR / Except for minimum I_{req} ($I_{req,\min}$), which is calculated for T_{sk}= 30 °C and SR = 0.06. However, design range ($-35 \leq \Delta T \leq 10$) is smaller than required (rejected due to C7)
2	Climate Index	CI	Becker (2000)	Requires monthly averages of hot and cold days estimated from Predicted Mean Vote values
2	Heat Stress Index	HSI_{WK}	Watts and Kalkstein (2004)	Requires, among others, daily maximum and minimum Apparent Temperature values and numbers of consecutive days of heat stress
2	Mahoney scale	MS	Koenigsberger et al. (1971)	Requires monthly mean air temperature and humidity to estimate daytime and nighttime thermal stress
2	Spatial Synoptic Classification	SSC	Kalkstein and Nichols (1996); Sheridan (2002)	Requires long-term input (about 30-year) to determine seed days for weather classification
2	Summer Severity Index	SSI /I_o	McLaughlin and Shulman (1977)	Requires, among others, air temperature deviations from a 30-year average period
2	Weather Stress Index	WSI	Kalkstein and Valimont (1986)	Requires deviations from 40-year average of Apparent Temperature
3	Black sphere actinograph		Poschmann cited by Brüner (1959)	No fitted equation
3	Classification of Weather in Moments	CWM / KPM	Golovina and Rusanov (1993)	No fitted equation / Table to read weather classification from T_a, RH, N, FF
3	Comfort Index	CI	Terjung (1966, 1968)	No fitted equation / Only available as nomogram
3	Corrected Effective Temperature	CET	Bedford (1964)	No fitted equation / Only available as nomogram

C	Index	Abbr.	Reference	Reason / Comments
3	Cylinder		Brown and Gillespie (1986)	No fitted equation
3	Daily Weather Types	DWT	Lecha and B. (1998)	No fitted equation / Table to read weather classification from T_a, e, N, P
3	Ellipsoid Index		Błażejczyk et al. (1998)	No fitted equation
3	Eupathescope		Brüner (1959); Dufton (1929)	No fitted equation
3	Evans Scale	ES	Evans (1980)	No fitted equation / Table to read comfort conditions from T_a, RH; comfort ranges derived from FF, M, I_{clo}
3	Frigorimeter		Thilenius and Dorno (1925)	No fitted equation
3	Metal man (Thermal-manikin)		Pedersen (1948) cited by Brüner (1959)	No fitted equation
3	Modified Effective Temperature	MET$_S$	Smith (1952)	No fitted equation / Only available as nomogram
3	Resultant thermometer		Missenard (1935) cited by Brüner (1959)	No fitted equation
3	Thermal Resistance of Clothing	TRC /R$_{t,wa}$	Jokl (1982)	If $T_a \neq T_{mrt}$, h_a must be read from a diagram. Otherwise TRC is only a function of FF and the number of clothing layer (rejected due to C5)
3	Thermo-integrator		Winslow et al. (1935)	No fitted equation
3	Effective Temperature	ET	Houghten and Yaglo-glou (1923) cited by Givoni (1976)	No fitted equation / Only available as nomogram
3	Heat Tolerance Limits	HTL	Vogt et al. (1982)	No fitted equation / Only available as nomogram

C	Index	Abbr.	Reference	Reason / Comments
3	Mean Equivalence Lines	MEL	Wenzel (1978)	No fitted equation / Only available as nomogram
3	Predicted four hour sweat rate	P4SR	McArdle et al. (1947)	No fitted equation / Basic four hour sweat rate (input of P4SR) only available as nomogram
3	Still Shade Temperature	SST	Burton and Edholm (1955); Parsons (2014)	No fitted equation / The insulation decrement is only available in a table
3	Wind Effect Index	WEI	Terjung (1966)	No fitted equation / Only available as nomogram
4	Acclimatization Thermal Strain Index	ATSI	de Freitas and Grigorieva (2009)	Thermal stress due to abrupt change of climates / $ATSI = 100(Q_{rh} - Q_r')/Q_{rh}$ Q_{rh} is respiratory heat loss at home and Q_r' at destination
4	Adaptation Strain index	ASI	Blazejczyk and Vinogradowa (2014)	Thermal stress due to abrupt change of climates
4	Bioclimatic Contrast Index	BCI	Błażejczyk (2011)	Thermal stress due to abrupt change of climates / $BCI = (\Delta UTCI + \Delta PST + \Delta WL + \Delta I_{clp})/4$ for parameter names see this table
4	Bioclimatic Distance Index	BDI	Mateeva and Filipov (2003) cited by Błażejczyk (2011)	Thermal stress due to abrupt change of climates / $BDI = (ECI_h - ECI)/13 \cdot 100$ ECI is effective clothing insulation, h indicates home location
4	Integral Load Index	ILI	Matyukhin and Kushnirenko (1987)	Thermal stress due to abrupt change of climates /methodology can be used for different meteorological parameters
4	Weather-Climate-Contrasts	WCC	Rusanov	Thermal stress due to abrupt change of climates /difference in clo-units between two climates in relation to maximum difference
5	Air Enthalpy	AirE, i	Gregorczuk (1968)	Does not consider all 6 variables / $i = 0.24\left(T_{wb} + \frac{1.555}{p} \cdot e\right)$
5	Air temperature		MacPherson (1962)	Does not consider all 6 variables / Considers T_a

C	Index	Abbr.	Reference	Reason / Comments
5	Apparent Temperature, Atrocity of weather	AT	Arnoldy (1962)	Does not consider all 6 variables / Considers T_a, FF
5	Apparent Temperature* or Heat Index	AT/HI	Steadman (1979, 1984)	Does not consider all 6 variables / Considers T_a, e, FF, SW, M, I_{clo}
5	Belgian Effective Temperature	BET/TEL	Bidlot and Ledent (1947) cited by Brüner (1959); Eissing (1995)	Does not consider all 6 variables / $TEL = 0.9T_{wb}[°C] + 0.1T_a[°C]$
5	Bioclimatic Index of the Severity of Climatic Regime	BISCR	Belkin (1992)	Does not consider all 6 variables / Considers T_a, p, FF, RH, h
5	Biometeorological Comfort Index	BCI	Rodriguez et al. (1985)	Does not consider all 6 variables / $BCI = \frac{t_a+T_{wb}}{2}$, $t_a = t_a(T_b, T_a, FF)$
5	Bodman's Weather-Severity Index	BWSI/S	Bodman (1908)	Does not consider all 6 variables / $S = \frac{k(T_a,FF)}{k(T_{a,0},FF_0)} = \frac{506\cdot(1-0.04T_a)(1+0.272\cdot FF)}{506}$ Heat loss for specific situation $k(T_a, FF)$ compared to reference situation $k(T_{a,0}, FF_0)$; usually $T_{a,0}$= 0 °C, $FF_0 = 0\ \mathrm{m\,s^{-1}}$
5	Body-atmosphere Energy Exchange Index	BIODEX	de Freitas and Ryken (1989)	Does not consider all 6 variables / Considers T_a, e, FF, SW, M, I_{clo}
5	Clothing Insulation	I_c	Mount and Brown (1985)	Does not consider all 6 variables / Considers T_a, FF, SW, N, P
5	Clothing Thickness	Clo	Steadman (1971)	Does not consider all 6 variables / Considers T_a, FF, SW
5	Comfort Chart	CmCh	Mochida (1979)	Does not consider all 6 variables / Considers T_a, e, FF, LW, I_{clo}, M, Calculates T_{mrt} from surrounding walls

C	Index	Abbr.	Reference	Reason / Comments
5	Comfort Vote	CmV/S	Bedford (1936, 1961)	Does not consider all 6 variables / $S = 11.16 - 0.0556T_a\,[°F] - 0.538T_{gl}\,[°F] - 0.0372e\,[mmHg] + 0.00144FF^{0.5}\left[\frac{ft}{\min}\right](100 - T\,[°F])$ From questionnaires in winter season in Great Britain for sedentary activity, only indoors
5	Cumulative Discomfort Index	CumDI	Tennenbaum et al. (1961)	Does not consider all 6 variables / $\sum_{h=1}^{h_{end}} \frac{T_a(h)-T_{wb}(h)}{2} - 24$ Hourly summation over period
5	Dew point temperature		Bruce (1916) cited by Brüner (1959); Eissing (1995)	Does not consider all 6 variables / Considers T_{dp}
5	Discomfort Index	DI_K	Kawamura (1965) cited by Ono and Kawamura (1991)	Does not consider all 6 variables / $DI_K = 0.99T_a[°\mathrm{C}] + 0.36T_{dp}[°\mathrm{C}] + 41.5$ Based on DI_T
5	Discomfort Index or Temperature Humidity Index	DI_T / THI	Thom (1957) and Thom (1958) cited by Landsberg (1972); Tromp (1966)	Does not consider all 6 variables / $THI = T_a[°F] - (0.55 - 0.55 \cdot RH)(T_a[°F] - 58)$; $DI_T = 0.4(T_a[°F] + T_{wb}[°F]) + 15$; $DI_T = 0.4(T_a^{\circ}F + T_{wb}[°F]) + 4.8$
5	Draught Risk Index* /Percent dissatisfied	PD	Fanger et al. (1988)	Does not consider all 6 variables / $PD = 3.143(34 - T_a) \cdot (FF - 0.05)^{0.6223} + 0.3696FF \cdot Tu(34 - T_a)(FF - 0.05)^{0.6223}$
5	Effective Temperature	ET_M	Missenard (1933) cited by Gregorczuk and Cena (1967)	Does not consider all 6 variables / $ET = T_a[°\mathrm{C}] - 0.4(T_a[°\mathrm{C}] - 10)(1 - \frac{RH}{100})$
5	Environmental Stress Index	ESI	Moran et al. (2001)	Does not consider all 6 variables / $ESI = 0.63T_a - 0.03RH + 0.002SW + 0.0054(T_a \cdot RH) - 0.073(0.1 + SW)^{-1}$

C	Index	Abbr.	Reference	Reason / Comments
5	Equatorial Comfort Index or Singapore Index	ECI	Webb (1959)	Does not consider all 6 variables / $ECI = 0.574T_a + 0.488 \cdot e - 0.231FF^{0.5} + 21.23$ Sensations for Singapore climates indoors
5	Equivalent Effective Temperature	EET	Aizenshtat and Aizenshtat (1974)	Does not consider all 6 variables / $EET = T_a[1 - 0.003(100 - RH)] - 0.385FF^{0.59}[(36.6 - T_a) + 0.662(FF - 1)] + (0.0015FF + 0.0008)(36.6 - T_a) - 0.0167](100 - RH)$
5	Equivalent Rectal Temperature	ERT / T_{rec}	Givoni and Goldman (1972)	Does not consider all 6 variables / Considers T_a, e, FF, M, I_{clo}
5	Equivalent Temperature*	EqT	Bedford (1936, 1951)	Does not consider all 6 variables / $EqT = 0.522T_a[°F] + 0.478T_{mrt}[°F] - 0.01474\sqrt{FF}[\frac{ft}{min}](100 - T_a[°F])$ T_{mrt} from T_{gl} or Eupatheoscope
5	Equivalent Warmth*	EqW	Bedford (1936)	Does not consider all 6 variables / $EqW = 9.979 - 0.1495x^2 - 2.89$, $x = 0.0556T_a + 0.0538T_w + 0.0372e_s - 0.00144\sqrt{FF}(100 - T_a)$
5	Exposed skin Temperature*	EST	Brauner and Shacham (1995)	Does not consider all 6 variables / Considers T_a, FF, SW
5	Globe Thermometer Temperature	T_{gl}	Dimiceli et al. (2011); Vernon and Warner (1932)	Does not consider all 6 variables / Considers T_{gl}, or in approximation equation T_a, FF, e, SW
5	Heart Rate Index	HRI_G	Givoni and Goldman (1973)	Does not consider all 6 variables / Considers T_a, e, FF, M, I_{clo}
5	Heat Stress Index*	HSI_{BH}	Belding and Hatch (1955)	Does not consider all 6 variables / Does not explicitly account for solar radiation in the equation for radiative balance.

C	Index	Abbr.	Reference	Reason / Comments
5	Heat Stress Prediction Model / Heat Strain Model	HSPM / ARIEM	Cadarette et al. (1999); Pandolf et al. (1985)	Does not consider all 6 variables / Considers T_a, e, FF, M, I_{clo} Different versions for laptop, pocket calculator and desktop exist. Based on HRI$_G$ and T_{rec}
5	Humidex	HD	Masterson and Richardson (1979)	Does not consider all 6 variables / $HD = T_a[°\text{C}] + \frac{5}{9}(e[mbar] - 10)$
5	Humisery		Weiss (1982)	Does not consider all 6 variables / Humisery= $T_a + a(T_{dp}, FF, h)$
5	Humiture		Pepi (1999); Weiss (1982)	Does not consider all 6 variables / Humiture= $T_a + T_{dp} - 18[°\text{C}]$; Humiture=$\frac{T_a - T_{dp}}{2}$; Humiture=$T_a[°F] + e[mbar] - 10[°F]$ Different versions exist
5	Index of Clothing required for Comfort*	CLODEX	de Freitas, C. R. (1986); de Freitas and Symon (1987)	Does not consider all 6 variables / $CLODEX = \frac{T_s - T_a}{H} - \frac{I_a(H+SW)}{H}$ with $T_s = 33$ °C, $H = 0.75 \cdot M$ and $1/I_a = [0.61 + 0.19(FF \cdot 100)^{0.5}]H$
5	Index of Pathogenicity of Meteorological Environment	IPME	Latyshev and Boksha (1965) cited by Kobyscheva et al. (2008)	Does not consider all 6 variables / Considers T_a, T_d, e, FF, h, SW, p_d
5	Index of Sultriness Intensity	ISI	Aikimovich and Balalla (1971)	Does not consider all 6 variables / Classes of e only
5	Index of thermal sensation	ITSN	Rohles and Nevis (1971)	Does not consider all 6 variables / Considers T_a, RH Further developments link sensations also to new ET* and FF (Rohles et al., 1975, 1974)
5	Index of thermal stress*	ITS$_{GIV}$	Givoni (1976)	Does not consider all 6 variables / LW is not considered

C	Index	Abbr.	Reference	Reason / Comments
5	Index of thermal stress	ITS_K,N	Kondratyev (1957) cited by Rusanov (1981)	Does not consider all 6 variables / $N = \frac{0.16(T_{sk}-T_a)}{\frac{R}{0.175}+\frac{5.7}{a(FF)}}$, $N = 0.78\frac{M}{100}$
5	Insulation Predicted index*	I_{clp}	Błażejczyk (2011)	Does not consider all 6 variables / $I_{clp} = 0.082 \cdot \frac{[91.4-(1.8 \cdot T_a+32)]}{2.3274} - [1/0.61 + 1.9FF^{0.5}]$
5	Integral Index of Cooling Conditions	IICC	Afanasieva et al. (2009)	Does not consider all 6 variables / $IICC = 73.882 - 0.60361T_a + 1.3096FF - 9.1985I_c - 0.15527M$
5	Kata thermometer		Hill and Hargood-Ash (1919); Maloney and Forbes (2011)	Does not consider all 6 variables / Approximation equations considers T_a, FF, RH, SW
5	Maximum Recommended Duration of Exercise*	MRDE	Young (1979)	Does not consider all 6 variables / Considers T_a, RH, SW and I_{clo}, M
5	Meteorological Health Index	MHI	Bogatkin and Tarakanov (2006)	Does not consider all 6 variables / Considers T_a, RH, FF, N, P, p, T_d, p_d
5	Modified Discomfort Index	MDI	Moran et al. (2001)	Does not consider all 6 variables / $MDI = 0.75T_{wb} + 0.3T_a$
5	Modified (Reduced) Temperature /Equivalent facial skin temperatures*	MTTR / T_{pr}	Adamenko and Khairullin (1972)	Does not consider all 6 variables / Considers T_a, FF
5	Natural Wet Bulb Temperature	NWBT / T_n	Maloney and Forbes (2011)	Does not consider all 6 variables / $T_n = 0.85T_a + 0.17RH - 0.61FF^{0.5}0.0016SW - 11.62$

C	Index	Abbr.	Reference	Reason / Comments
5	New Wind Chill Temperature Index	NWCI /WCET /WCI	OFCM (2003); Osczevski and Bluestein (2005)	Does not consider all 6 variables / $WCT[°C] = 13.12 + 0.6215T_a[°C] - 11.37FF^{0.16}[km/h] + 0.3965FF^{0.16}[km/h]$
5	Oxford Index /Wet-Dry Index*	OxI / WD	Lind (1956) cited by Bedford (1957); Lind and Hellon (1957)	Does not consider all 6 variables / $WD = 0.15T_a + 0.85T_{wb}$
5	Operative Temperature	OpT / T_o	Winslow and Herrington (1949); Winslow et al. (1937)	Does not consider all 6 variables / Summarises effect of dry heat exchange; Considers T_a, FF, T_{mrt} in original form T_w
5	Outdoor Apparent Temperature	OAT	Steadman (1984, 1994)	Does not consider all 6 variables / Considers T_a, e, FF, SW, M, I_{clo}; regression version is more frequently used than complete model version
5	Physiological Heat Exposure Limit Chart	PHEL	Dasler (1977)	Does not consider all 6 variables / Considers time-weighted-mean of WBGT and M
5	Radiation Equivalent Effective Temperature	REET	Sheleihovskyi (1948) cited by Rusanov (1981)	Does not consider all 6 variables / Considers T_a, e, FF, SW
5	Relative Heat Strain*	RHS	Lee and Henschel (1966)	Does not consider all 6 variables / Considers T_a, e, FF, LW and I_{clo}, M
5	Relative Humidity Dry Temperature	RHDT	Wallace et al. (2005)	Does not consider all 6 variables / $RHDT = 0.9T_a + 0.1RH$
5	Respiratory Heat Loss	RHL/Q_R	Rusanov (1989) cited by de Freitas and Grigorieva (2016)	Does not consider all 6 variables / C1 to C4 not checked since required literature could not be obtained. Considers T_a, e, p, h, M

C	Index	Abbr.	Reference	Reason / Comments
5	Resultant Temperature or Net Effective Temperature	RT/ NET	Missenard cited by Landsberg (1972)	Does not consider all 6 variables / $NET = 37 - (37 - T_a) \cdot (0.68 - 0.0014RH + \frac{1}{1.76+1.4FF^{0.75}})^{-1} - 0.29T_a(1 - \frac{RH}{100})$
5	Saturation deficit		Fluegge (1912) cited by Brüner (1959)	Does not consider all 6 variables / Considers q
5	Severity Rating	S	Osokin (1968) cited by Rusanov (1981)	Does not consider all 6 variables / $S = (1 - 0.06T_a)(1 + 0.20FF)(1 + 0.0006h)K_b(RH)A_c(T_d)$
5	Standard Operative Temperature	To'/T_{SO}	Gagge et al. (1973)	Does not consider all 6 variables / Considers T_a, FF, T_{mrt}; T_{sk} can be calculated from provided model
5	Subjective Temperature	T_{sub}	McIntyre (1973)	Does not consider all 6 variables / $T_{sub} = 0.44T_r + 0.56(5 - \sqrt{10FF}(5 - T_a))(0.44 + 0.56\sqrt{10FF})^{-1}$
5	Summer Simmer Index	SSI	Pepi (1987, 1999); Tzenkova et al. (2007)	Does not consider all 6 variables / $SSI = T[°F] - (0.55 - 0.0055 \cdot RH[\%]) \cdot (T[°F] - 58)) - 56.83$, Different versions exist (further developments)
5	Sultriness value		Scharlau (1943)	Does not consider all 6 variables / Considers e
5	Survival Time Outdoors in Extreme Cold*	STOEC	de Freitas and Symon (1987)	Does not consider all 6 variables / Considers T_a, e, FF, SW and I_{clo}, M
5	Temperature Humidity Index	THI_S	Schoen (2005)	Does not consider all 6 variables / $THI = T_a - 1.0799e^{0.03755T_a}(1 - e^{0.0801(T_{dp}-14)})$
5	Temperature-Wind Speed-Humidity Index	TWH	Zaninović (1992)	Does not consider all 6 variables / Considers T_a, FF, e_s

C	Index	Abbr.	Reference	Reason / Comments
5	Thermal Acceptance Ratio	TAR	Ionides, Plummer and Siple (1945) cited by Auliciems and Szokolay (2007)	Does not consider all 6 variables / Considers T_a, e, LW, M
5	Thermal Balance	ThBal$_r$ /Q$_S$	Rusanov (1981)	Does not consider all 6 variables / 2 versions exist: full heat balance version that includes all terms (ThBal$_b$, Table 2.1) and a regression version based on EET, which does not consider longwave radiation and is applicable only for nude persons (ThBal$_r$) but has an assessment scale
5	Thermal Insulation Characteristics of Clothing	TICC /R	Kondratyev (1957) cited by Rusanov (1981)	Does not consider all 6 variables / $R = 3.36\frac{T_{sk}-T_a}{M} - \frac{0.99}{a(FF)}$, T_{sk} set to 33 °C
5	Thermal Insulation of Clothing	TIC$_B$	Budyko and Cicenko (1960); Liopo and Cicenko (1971)	Does not consider all 6 variables / Regression equation considering T_a, FF, SW and M fitted by Liopo and Cicenko (1971) to full heat balance equation by Budyko and Cicenko (1960) and related derived nomograms
5	Thermal Insulation of Clothing	TIC$_R$	Rusanov (1981)	Does not consider all 6 variables / Is based on ThBal$_r$ and therefore does not consider longwave radiation
5	Thermal Insulation of Protective Clothing	TIPC	Afanasieva (1977)	Does not consider all 6 variables / Considers T_a, FF and M. Designed especially for winter conditions (SW-input is assumed very small)
5	Thermal Sensation Index*	TSNI	dePaula Xavier and Lamberts (2000)	Does not consider all 6 variables / Regression equation developed for indoors; coefficient of T_o is probably different if solar radiation is included. $S = 0.219T_o + 0.012RH - 0.547FF - 5.83$

C	Index	Abbr.	Reference	Reason / Comments
5	Thermal Strain Index	TSI /G	Lee (1958)	Does not consider all 6 variables / $G = a\left[\frac{(M-w_m)-\frac{5.55(34-T_a)}{I_a(FF)+I_C}-0.00033(46-e)}{\frac{c-e}{r_a(FF)+r_c}}\right]^d$
5	Total Thermal Stress*	TTS	Auliciems and Kalma (1981)	Does not consider all 6 variables / Does not consider LW
5	Tropical summer index	Tsi	Bureau of Indian Standards (1987) cited by Auliciems and Kalma (1981)	Does not consider all 6 variables / $Tsi = 0.308T_{wb} + 0.745T_{gl} - 2.06\sqrt{FF + 0.841}$
5	Wet Bulb Dry Temperature	WBDT	Wallace et al. (2005)	Does not consider all 6 variables / $WBGT = 0.4T_{wb} + 0.6T_a$
5	Wet Bulb Globe Temperature	WBGT	Auliciems and Kalma (1981); Yaglou and Minard (1957)	Does not consider all 6 variables /$WBGT = 0.7T_{wb} + 0.2T_g + 0.1T_a$
5	Wet Bulb Temperature	T$_{wb}$	Brüner (1959); Eissing (1995); Stull (2011)	Does not consider all 6 variables / Approximation equation considers T_a, RH
5	Wet Kata Cooling Power by Hill	WKCP / H$_w$	Hill and Hargood-Ash (1919)	Does not consider all 6 variables / $H = (0.27 + 0.49\sqrt{FF})(36.5 - T_a) + (0.85 + 0.102FF^{0.3})(F - f)^{4/3}$
5	Wind Chill Equivalent Temperature	WCT$_{wc}$ / Twc	Falconer (1968)	Does not consider all 6 variables / Under sunshine cooling is reduced $Twc[°F] \approx -(\sqrt{FF \cdot 100} + 10.45 - FF)(91.4 - T_a[°F]) \cdot (\sqrt{1.34 \cdot 100} + 10.45 - 1.34) + 91.4)^{-1}$
5	Wind Chill Equivalent Temperature	WCET	Steadman (1971)	Does not consider all 6 variables / Considers T_a, FF, LW, M, I_{clo}; LW, M and I_{clo} are assumed fixed
5	Wind Chill Index	WCI	Siple and Passel (1945)	Does not consider all 6 variables / Considers T_a, FF

C	Index	Abbr.	Reference	Reason / Comments
6	Thermal Sensation	TS_{GIV}	Givoni et al. (2003)	Does not consider longwave radiation from all directions / $TS_{GIV} = 1.7 + 0.1118T_a + 0.0019SW - 0.322FF - 0.0073RH + 0.0054T_{gr}$ For fixed clothing + activity; considers only longwave radiation from ground
7	Body Temperature Index	BTI	Dayal (1974)	Air temperature range smaller than -5 °C to 35 °C / Designed for $30 \leq \Delta T_a \leq 42$; Equation for T_{mrt} from T_{gl}-measurements might be needed to be adapted to consider solar influence
7	Effective Heat Strain Index	EHSI	Kamon and Ryan (1981)	Air temperature range smaller than -5 °C to 35 °C / Designed for $27 \leq \Delta T_a \leq 36$; Equation for T_{mrt} from T_{gl}-measurements might be needed to be adapted to consider solar influence
7	Heart Rate Index	HRI_D	Dayal (1974)	Air temperature range smaller than -5 °C to 35 °C / Designed for $30 \leq \Delta T_a \leq 42$; Equation for T_{mrt} from T_{gl}-measurements might be needed to be adapted to consider solar influence
7	Heat Strain Decision Aid Model	HSDA	Cadarette et al. (1999); Santee and Wallace (2003)	Air temperature range smaller than -5 °C to 35 °C / Designed for $18 \leq \Delta T_a \leq 43$
7	Humid Operative Temperature	HToh /T_{oh}	Gagge et al. (1973, 1971)	Air temperature range smaller than -5 °C to 35 °C / Designed for $10 \leq \Delta T_a \leq 40$
7	New Effective Temperature	ET*	Gagge et al. (1973, 1971)	Air temperature range smaller than -5 °C to 35 °C / Designed for $10 \leq \Delta T_a \leq 40$
7	Predicted Mean Vote - indoors	PMV	Fanger (1970)	Temperature range smaller than -5 °C to 35 °C / Designed for $15 \leq \Delta T_a \leq 45$ [indoors]
7	Predicted Mean Vote - outdoors*	PMV*	Gagge et al. (1986)	Air temperature range smaller than -5 °C to 35 °C / Designed for $0 \leq \Delta T_a \leq 50$

C	Index	Abbr.	Reference	Reason / Comments
7	Predicted Mean Vote - Fuzzy	PMV_F	Hamdi et al. (1999)	Air temperature range smaller than -5 °C to 35 °C / Designed for $-10 \leq \Delta T_a \leq 32$; Fuzzy logical estimation of PMV. Designed for indoors; Rules for T_{mrt} may require adjustment if used outdoors
7	Predicted Percentage Dissatisfied	PPD	ASHRAE (2001); Fanger (1970)	Air temperature range smaller than -5 °C to 35 °C / Designed for $15 \leq \Delta T_a \leq 45$ [indoors]
7	Reference Index	RI	Pulket et al. (1980)	Air temperature range smaller than -5 °C to 35 °C / Designed for $30 \leq \Delta T_a \leq 40$; Originally included only LW; but expected to work if SW is included as based on heat balance principles
7	Required Sweat Rate	Req SR /S_r	Vogt et al. (1981)	Air temperature range smaller than -5 °C to 35 °C / Designed for $20 \leq \Delta T_a \leq 60$
7	Standard Effective Temperature	SET*	Gagge et al. (1973); Gonzalez et al. (1974)	Air temperature range smaller than -5 °C to 35 °C / Designed for $0 \leq \Delta T_a \leq 50$
7	Thermal Discomfort	DISC	Gagge et al. (1986)	Air temperature range smaller than -5 °C to 35 °C / Designed for $10 \leq \Delta T_a \leq 50$; calculated from 2-node model
7	Thermal Work Limit	TWL	Brake and Bates (2002)	Air temperature range smaller than -5 °C to 35 °C / Designed for $36 \leq \Delta T_a \leq 40$; developed for indoors but uses heat balance equations with T_{mrt} so SW can be included

Appendix B

Preface

This appendix has been published as supplementary material in **Fischereit J. and Schlünzen K. H.** (2018): Evaluation of thermal indices for their applicability in obstacle resolving meteorology models. *International Journal of Biometeorology*, volume 62(10):pages 1887–1900. ISSN 1432-1254. `http://dx.doi.org/10.1007/s00484-018-1591-6` under the terms of the Creative Commons Attribution 4.0 International License (`http://creativecommons.org/licenses/by/4.0/`). For this thesis references to other chapters of this thesis have been added where applicable. To be consistent with the other parts of this thesis American English has been changed to British English, symbols have been replaced by their respective counterparts used in this thesis and the citation method of this thesis is used. References have been combined at the end of this thesis. Other changes made in comparison to the original supplementary material are marked italic.

To evaluate the criteria for the different indices in Section 2.3, the original publication of the indices were reviewed. For some indices our analysis of the indices differed from the results by de Freitas and Grigorieva (2017). This might be in some cases due to the use of secondary literature by de Freitas and Grigorieva (2017). In other cases we interpret the same publication differently, indicating that indices are not always thoroughly documented. The found differences of index characteristics are documented in Table B.1. As evidence for our interpretation citations or equations are given.

Table B.1: Index characteristics found in our literature review of the thermal indices and used in the present study compared to the ones by de Freitas and Grigorieva (2017). Atmosphere-related variable inputs are denoted ”A“ and body-related variable inputs are denoted ”B“. The following abbreviations are used: clo is clothing, e is vapour pressure, e_s is saturation vapour pressure, $e_{s,sk}$ is saturated water vapour pressure at T_{sk}, HR is heart rate, I_{clo} is clothing insulation, LW is longwave radiation, M is metabolic rate, PE is physical exertion, RH is relative humidity, r_b is body tissue thermal resistance, SW is solar radiation, T_a is air temperature, T_c is core temperature, T_{gl} is globe temperature, T_g is ground temperature, T_{mrt} is mean radiant temperature, T_{sk} is skin temperature, T_m is mean temp of surroundings, T_{wb} is wet bulb temperature, TS is thermal sensation, Tu is turbulence intensity, FF is wind speed.

Index (Abbreviation)	Variable inputs considered according to de Freitas and Grigorieva (2017) (cited reference)	Variable inputs considered according to our review (reference)	Evidence, Comments
Apparent Temperature (AT) or Heat Index (HI)	A: T_a, e, SW B: clo, M (Steadman, 1979, 1984)	A: T_a, e, FF, SW B: No (Steadman, 1979, 1984)	Using the nomenclature of this paper the publication by Steadman (1984) reads: ”The apparent temperature of a set of meteorological conditions T_a, e, FF, SW may be defined as equal to dry-bulb temperature at FF=SW=0, and at a base vapor pressure of moderate humidity, which would require the same thermal resistance, in a walking adult, as this set of conditions“. Clothing and activity are considered in AT but fixed and are therefore no variable inputs. From the full model regression equations were developed, which are used far more frequently. In the final development stage Steadman (1979) the scope of the index ”has been enlarged to cover the range of dry-bulb temperatures from -40 to +50 °C“. This range is larger than +20 to +60 °C mentioned by de Freitas and Grigorieva (2017)

Index (Abbreviation)	Variable inputs considered according to de Freitas and Grigorieva (2017) (cited reference)	Variable inputs considered according to our review (reference)	Evidence, Comments
Draught Risk Index (PD; Percent dissatisfied)	A: T_a, FF B: No (Fanger et al., 1988)	A: T_a, FF, Tu B: No (Fanger et al., 1988)	The full equation reads: $PD = 3.143(34 - T_a) \cdot (FF - 0.05)^{0.6223} + 0.3696FF \cdot Tu(34 - T)(FF - 0.05)^{0.6223}$ Thus, turbulent intensity Tu is included as input.
Equivalent Temperature (EqT)	Not considered	A: T_a, FF, T_m B: No (Bedford, 1936, 1951)	EqT is mentioned by de Freitas and Grigorieva (2015) but not analyzed by de Freitas and Grigorieva (2017). The definition reads: $EqT = 0.522T_a[^\circ F] + 0.478T_{mrt}[^\circ F] - 0.01474\sqrt{FF}[\frac{ft}{min}](100 - T_a[^\circ F])$
Equivalent Warmth (EqW)	A:T_a, T_{mrt}, e B: T_{sk} (Bedford, 1936 cited by Auliciems and Szokolay, 2007)	A:T_a, T_m, e_s, FF B: No (Bedford, 1936)	The definition is: $EqW = 9.979 - 0.1495x^2 - 2.89$, $x = 0.0556T_a + 0.0538T_w + 0.0372e_s - 0.00144\sqrt{FF}(100 - T_a)$
Exposed skin Temperature (EST)	A: T_a, FF, SW B: M (Brauner and Shacham, 1995)	A: T_a, FF, SW B: No (Brauner and Shacham, 1995)	The equation reads: $\frac{T_c - T_{sk}}{r_b} = \frac{T_c - T_a}{r_b + 1/h_c}$ Fixed $M = 58\ \mathrm{W\,m^{-2}}$ (comfortable steady state condition) is used for calculating r_b: "The body tissue thermal resistance, r_b, can be estimated from Eq. 7 by introducing known values of thermal comfort in a normal temperature room [...]. Under such conditions [...], the metabolic heat production while sitting at rest is approximately equal to 50 kcal $\mathrm{h^{-1}}$m−2 (58 $\mathrm{W\,m^{-2}}$), and [...]. Thus, is approximately 0.08 kca1^{-1} h °C $\mathrm{m^2}$ [...]." (Brauner and Shacham 1995)
Heat Stress Index (HSI_{BH})	A: T_a, T_{gl}, e, FF B: clo, M (Belding and Hatch, 1955)	A: T_a, T_{gl}, e, FF B: M (Belding and Hatch, 1955)	"Clothing is the third variable fixed for the estimate, and it is unfortunate that limitations of available knowledge make it necessary to fix on a no-clothing basis." (Belding and Hatch 1955)

Index (Abbreviation)	Variable inputs considered according to de Freitas and Grigorieva (2017) (cited reference)	Variable inputs considered according to our review (reference)	Evidence, Comments
Index of Clothing Required for Comfort (CLODEX)	A: T_a, FF, e, LW, SW B: clo, M (de Freitas, C. R., 1986; de Freitas and Symon, 1987)	A: T_a, FF, SW B: M (de Freitas, C. R., 1986; de Freitas and Symon, 1987)	The definition is $CLODEX = \frac{T_s - T_a}{H} - \frac{I_a(H+SW)}{H}$ with $T_s = 33$ °C, $H = 0.75 \cdot M$ and $1/I_a = [0.61 + 0.19(FF \cdot 100)^{0.5}]H$. Thus, humidity and longwave radiation is not considered and clothing is not a variable input
Index of thermal Stress (ITS_{GIV} or I.T.S.)	A: T_a, e, FF, SW, LW B: clo, M (Givoni, 1976)	A: T_a, e, FF, SW B: clo, M (Givoni, 1976)	"The I.T.S. does not as yet separately cover the factor of longwave radiation" (Givoni, 1976)
Insulation Predicted index (I_{clp})	A: T_a, FF B: M (Błażejczyk, 2011)	A: T_a, FF B: No (Błażejczyk, 2011)	The definition is $I_{clp} = 0.082 \cdot \frac{[91.4-(1.8 \cdot T_a+32)]}{2.3274} - [1/0.61 + 1.9FF^{0.5}]$ Thus, no variable metabolic heat is considered
Maximum Recommended Duration of Exercise (MRDE)	A: T_a, e, SW B: M (Young, 1979)	A: T_a, RH, SW B: clo, M (Young, 1979)	"The MRDE is determined by the level of exercise, the ambient temperature and humidity, the solar radiation and the clothing worn" (Young, 1979)
Modified (Reduced) Temperature (MTTR, T_{pr})	A: T_a, FF, SW B: No (Adamenko and Khairullin, 1972)	Not found in cited reference, however for Θ_{rf} cited in reference: A: T_a, FF B: No (Adamenko and Khairullin, 1972)	In the publication cited by de Freitas and Grigorieva (2017) for the index MTTR no temperature termed Modified (Reduced) Temperature could be found. Instead an equivalent facial skin temperature (Θ_{rf}) derived only from T_a and FF is presented in the publication.

Index (Abbreviation)	Variable inputs considered according to de Freitas and Grigorieva (2017) (cited reference)	Variable inputs considered according to our review (reference)	Evidence, Comments
Oxford Index (OxI)/Wet-Dry Index (WD)	A: T_a, T_{wb} B: No (Lind and Hellon, 1957)	Not found in cited reference, however from secondary literature: A: T_a, T_{wb} B: No (Lind et al. (1956) cited by Bedford (1957); Lind and Hellon (1957))	The cited publication is wrong: in the publication cited by de Freitas and Grigorieva (2017) for the Oxford Index no index termed Oxford Index or Wet-Dry Index could be found. However, from the book review by Bedford (1957) of "Lind A.R., Weiner J.S., Hellon R.F., Jones R.M., Fraser D.C. (1956) Reactions of Mines-Rescue Personal to Work in Hot Environments, Medical Research Memorandum No 1" the equation given in Table 1 could be retrieved and therefore the variable inputs could be confirmed.
Perceptual strain index (PeSI)	A: T_a, e B: T_c, HR (Tikuisis et al., 2002)	A: No B: No (Tikuisis et al., 2002)	The definition is $PeSI = 5 \cdot \frac{TS_t - 7}{6} + 5 \cdot \frac{PE_t}{10}$. Thus, only thermal sensation and physical exertion are needed.
Perceptual Hyperthermia Index (PHI)	A: No B: T_c, HR (Gallagher et al., 2012)	A: No B: T_c (Gallagher et al., 2012)	"The development of the PHI consisted of calculating PeSI values for all RPE-RTS combinations. [...] Next, the mean T_c coincident with each calculated PeSI value was determined. These T_c values subsequently replaced the PeSI values on the constructed figure therefore linking the perceptual variables of RPE and RTS with the physiological criterion of T_c." (Gallagher et al., 2012) Thus, PHI can be estimated either from TS and PE or from T_c. Heart rate was measured and found to be well correlated with TS and PE but is not further integrated into the calculation of PHI ranges.
Perceived Temperature (PT_L)	A: T_a, FF, LW B: No (Linke, 1926 cited by Eissing, 1995)	Not found (Linke, 1926)	In the publication cited by de Freitas and Grigorieva (2017) for PT_L no such index could be found. Instead an equation to calculate the heat input from radiation measured with a specific kind of a black globe thermometer is presented in the publication.

Index (Abbreviation)	Variable inputs considered according to de Freitas and Grigorieva (2017) (cited reference)	Variable inputs considered according to our review (reference)	Evidence, Comments
Physical saturation deficit	A: e B: No (Thilenius and Dorno, 1925 cited by Eissing, 1995)	Not found (Thilenius and Dorno, 1925)	In the publication cited by de Freitas and Grigorieva (2017) for the index physical saturation deficit (Thilenius and Dorno (1925) cited by Eissing, 1995) the following definition is given "Difference between the vapour pressure of the ambient air and the vapour pressure of exhaled air". However in the original publication (Thilenius and Dorno, 1925) no such index is described. Instead the Frigorimeter (Table A.1) is described.
Relative Heat Strain (RHS)	A: T_a, T_{wb}, e, FF B: clo, M (Lee and Henschel, 1966)	A: T_a, e, FF, LW B: clo, M (Lee and Henschel, 1966)	"The equation just cited includes terms for air temperature, humidity, air movement, radiant heat, metabolic rate and clothing"(Lee and Henschel 1966)
Skin wettedness (SkW, w)	A: T_a, T_m B: No (Gonzalez et al., 1978)	A: e B: E_{sk}, $e_{s,sk}$ (Gonzalez et al., 1978)	"Skin wettedness (w), defined as the fraction of the subjects' body surface area covered by evaporative moisture, was determined as a ratio of the observed E_{sk} to maximum evaporation ($E_{\max}$) possible to the environment, assuming a subject's entire surface is completely wet." (Gonzalez et al., 1978) $w = \frac{E_{sk}}{E_{\max}} = \frac{E_{sk}}{h_e(e_{s,sk}-e)}$. h_e is the evaporative heat transfer coefficient
Survival Time Outdoors in Extreme Cold (STOEC)	A: T_a, FF, SW B: M (de Freitas and Symon, 1987)	A: T_a, e, FF, SW B: M (de Freitas and Symon, 1987)	STOEC includes e to estimate respiratory heat loss (using the nomenclature of this paper): $E_{res} = 1.73 \cdot 10^{-3} M(44 - e)$ Clothing is taken into account for convective heat exchange but fixed ($I_{clo} = 4$ clo).
Thermal Insulation of Clothing (TIC$_A$)	A: T_a, e, FF, SW, LW B: No (Aizenshtat, 1964)	Not found (Aizenshtat, 1964)	In the publication cited by de Freitas and Grigorieva (2017) for the index TICA (Aizenshtat, 1964) no index TICA could be found. Instead this paper describes how a globe thermometer can be used to evaluate the thermal balance of a person.

Index (Abbreviation)	Variable inputs considered according to de Freitas and Grigorieva (2017) (cited reference)	Variable inputs considered according to our review (reference)	Evidence, Comments
Thermal Sensation Index (TSNI)	A: T_a, e, FF, T_{mrt} B: clo, M (dePaula Xavier and Lamberts, 2000)	A: T_a, e, FF, T_{mrt} B: No (dePaula Xavier and Lamberts, 2000)	"The activity was constant (school activity) and not considered to be an independent variable influencing the sensation of thermal comfort. In our studies, we do not treat the thermal insulation of clothes as an independent variable but as dependent on the external temperature" (dePaula Xavier and Lamberts, 2000): $S = 0.219T_o + 0.012RH - 0.547FF - 5.83$ Thus, clothing and metabolic heat are not variable inputs.
Total Thermal Stress (TTS)	A: T_a, e, FF, SW, LW B: No (Auliciems and Kalma, 1981)	A: T_a, e, FF, SW B: No (Auliciems and Kalma, 1981)	"The net gain of shortwave solar radiation must be incorporated [...]. $(Q+q)_m$ is the sum of net direct (Q) and diffuse (q) radiation falling upon man" (Auliciems and Kalma, 1981). Includes only direct and diffuse radiation and no longwave radiation
Q_S-index Correct name: ΔQ-index	A: T_a, e, FF, LW B: clo, M, T_{sk} (Rublack et al., 1981 cited by Graveling et al., 1988)	A: T_a, e, FF, LW B: clo, M, T_{sk} (Rublack et al., 1981)	The Q_S-index cited by Graveling et al. (1988) should be named Δq-index since Qs according to the original publication (Rublack et al., 1981) describes only the longwave component in Δq: $\Delta Q = Q_M + Q_c + Q_s - Q_{v,max}(e)$

Appendix C

Preface

This appendix has been published as supplementary material in **Fischereit J. and Schlünzen K. H.** (2018): Evaluation of thermal indices for their applicability in obstacle resolving meteorology models. *International Journal of Biometeorology*, volume 62(10):pages 1887–1900. ISSN 1432-1254. `http://dx.doi.org/10.1007/s00484-018-1591-6` under the terms of the Creative Commons Attribution 4.0 International License (`http://creativecommons.org/licenses/by/4.0/`). For this thesis references to other chapters of this thesis have been added where applicable. To be consistent with the other parts of this thesis American English has been changed to British English, symbols have been replaced by their respective counterparts used in this thesis and the citation method of this thesis is used. References have been combined at the end of this thesis. Other changes made in comparison to the original supplementary material are marked italic.

A systematic literature review using the databases “Scopus” and “Web of Science” was conducted to identify which thermal indices have been used in the past with ORMs. Figure C.1 shows the flow diagram corresponding to the method described in Section 2.2.4. Table C.1 shows the 32 studies included in the analysis for F6 ordered by thermal index and climatic zone.

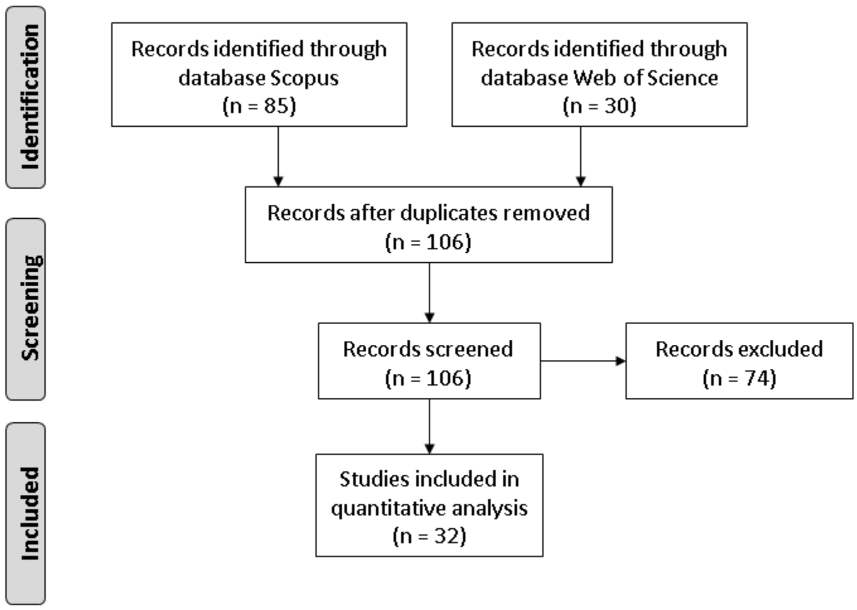

Figure C.1: Flow Diagram for the systematic literature review adapted from the standardized Preferred Reporting Items for Systematic Reviews and Meta-Analysis (PRISMA) flow diagram (Moher et al., 2009) with changes.

Table C.1: Cited studies to evaluate application frequency of indices. Studies have been selected according to the method in Section 2.2.4. For abbreviations of indices see Table A.1 and Table 2.3.

Index	Zone	References
PET	Tropics	Qaid et al. (2016),Morakinyo et al. (2016)
	Sub-tropics	Morakinyo and Lam (2016),Taleghani et al. (2016),Yang et al. (2015),Lopes et al. (2011),Yahia and Johansson (2014),Chen and Ng (2013),Peng and Jim (2013),Yang et al. (2011),Ali-Toudert and Mayer (2006)
	Mid-latitudes	Žuvela-Aloise et al. (2016),Lobaccaro and Acero (2015),Acero and Herranz-Pascual (2015),Taleghani et al. (2015),Ketterer and Matzarakis (2015),Minella et al. (2014)
PMV	Sub-tropics	Hedquist and Brazel (2014) (PMV),Stavrakakis et al. (2012) (PMV (extended version)), Zhang et al. (2012) (PMV (extended version))
	Mid-latitudes	Robitu et al. (2006) (PMV*)
SET*	Sub-tropics	He and Hoyano (2010) (OUT_SET*), He (2011) (OUT_SET*), Huang et al. (2005) (SET*)
THI	Tropics	Morakinyo et al. (2016), Kakon et al. (2009)
UTCI	Mid-latitudes	Goldberg et al. (2013), Schrijvers et al. (2016), Tumini et al. (2016), Park et al. (2014), Minella et al. (2014)
WBGT	Tropics	Morakinyo et al. (2016)

Appendix D

D.1 Calculation of declination (BASIS_DECLIN_CALC)

Parameterisation options for the calculation of the Earths declination:

(a) vdi3789 (VDI, 2001)

$$\begin{aligned}\delta = &\arcsin(\\ &0.3978 \cdot \sin((0.9856 \cdot jd - 2.72) - 77.51 + 1.92 \cdot \sin(0.9856 \cdot jd - 2.72))))\end{aligned} \tag{D.1}$$

(b) MITRAS (Schlünzen et al., 2012b)

$$\begin{aligned}\delta = 0.006918 &- 0.399912 \cdot \cos(1 \cdot jd[\mathrm{rad}]) + 0.070257 \cdot \sin(1 \cdot jd[\mathrm{rad}]) \\ &- 0.006758 \cdot \cos(2 \cdot jd[\mathrm{rad}]) + 0.000907 \cdot \sin(2 \cdot jd[\mathrm{rad}]) \\ &- 0.002697 \cdot \cos(3 \cdot jd[\mathrm{rad}]) + 0.001480 \cdot \sin(3 \cdot jd[\mathrm{rad}])\end{aligned} \tag{D.2}$$

D.2 Calculation of direct shortwave radiation (BASIS_DIR_RAD)

Parameterisation options for the calculation direct radiation at beam direction close to the ground:

(a) MITRAS (Gierisch, 2011, based on Bruse, 1999)

$$SW_{dir} = I_0 \cdot \mu_0 \frac{1}{1 + (\gamma/(1-\gamma))} \tag{D.3}$$

with $\gamma = 1/(1 + 8 \cdot \sin(\alpha)^{0.7})$ and $\mu_0 = 0.75$, being the amount of radiation lost due to the turbidity of the atmosphere, estimated from measurements in Northern Germany.

(b) VDI1994 (VDI, 1994)

$$SW_{dir} = I_0 \cdot \exp(-T_{L,am2} \cdot \delta_{R0} \cdot m_{r0} \cdot p/p_0) \tag{D.4}$$

with p being the actual pressure, p_0 the pressure of a standard atmosphere at sea level and m_{r0} the relative optical air mass

$$m_{r0} = 1/\sin(\alpha) + 0.50572 \cdot (\alpha + 6.07995)^{-1.6364} \tag{D.5}$$

and δ_{R0} being the vertical optical thickness of the clean and dry standard atmosphere

$$\delta_{R0} = \begin{cases} (9.4 + 0.9 \cdot m_{r0})^{-1} & \text{if } \alpha > 5° \\ f : \mathbb{R} \to \mathbb{R} \text{ (VDI, 1994)} & \text{else} \end{cases} \tag{D.6}$$

with $f : \mathbb{R} \to \mathbb{R}$ denoting a polynomial function. $T_{L,am2}$ is the Linke Turbidity factor of relative optical air mass 2 (see Section 3.1.3.1).

(c) ESRA (Rigollier et al., 2000; Remund et al., 2003) following Staiger (2014) without accounting for atmospheric refraction

$$SW_{dir} = I_0 \cdot \exp(-0.8662 \cdot T_{L,am2} \cdot m_{r0} \cdot p/p_0 \cdot \delta_{R0}/p_c) \tag{D.7}$$

with m_{r0} being the relative optical air mass (Eq. (D.5)), δ_{R0} being the vertical optical thickness of the clean and dry standard atmosphere

$$\delta_{R0} = \begin{cases} (10.4 + 0.718 \cdot m_{r0})^{-1} & \text{if } m_{r0} > 20 \\ (6.6296 + 1.7513 \cdot m_{r0} - 0.1202 m_{r0}^2 + 0.0065 m_{r0}^3 - 0.00013 m_{r0}^4)^{-1} & \text{else} \end{cases} \tag{D.8}$$

and p_c being the pressure correction for vertical optical thickness

$$p_c = \begin{cases} 1 + (p_{c,750} - 1) \cdot (1 - p/p_0) & \text{if } p > 750 \\ p_{c,750} + (p_{c,500} - p_{c,750}) \cdot (0.75 - p/p_0)/0.25 & \text{if } 500 < p \leq 750 \\ p_{c,500} & \text{if } p \leq 500 \end{cases} \tag{D.9}$$

with $p_{c,750} = 1.248274 - 0.011997 \cdot \delta_{R0} + 0.00037 \cdot \delta_{R0}^2$ and $p_{c,500} = 1.68219 - 0.03059 \cdot \delta_{R0} + 0.00089 \cdot \delta_{R0}^2$ and $T_{L,am2}$ being the Linke Turbidity factor of relative optical air mass 2 (see Section 3.1.3.1).

D.3 Calculation of diffuse shortwave radiation (BASIS_DIFF_RAD)

Parameterisation options for the calculation diffuse radiation close to the ground in SURM:

(a) MITRAS (Gierisch, 2011 after Bruse, 1999)

$$SW_{diff,s} = SW_{dir} \cdot \sin(\alpha) \cdot \frac{\gamma}{1-\gamma} \tag{D.10}$$

with $\gamma = 1/(1 + 8 \cdot \sin(\alpha)^{0.7})$

(b) VDI1994 (VDI, 1994)

$$SW_{diff,s} = 0.84 \cdot I_0 \cdot \sin(\alpha) \exp(-0.027 \cdot p/p_0 \cdot T_{L,am2}/\sin(\alpha)) - SW_{dir} \cdot \sin(\alpha) \tag{D.11}$$

(c) ESRA (Rigollier et al., 2000; Remund et al., 2003)

$$SW_{diff,s} = I_0 \cdot T_{rd} \cdot F_d \tag{D.12}$$

with T_{rd} being the diffuse transmission function with $T_{rd} = -0.015843 + 0.030543 \cdot T_L + 0.0003797 \cdot T_L^2$, F_d being the diffuse angular function with $F_d = a_0 + a_1 \cdot \sin(\alpha) + a_2 \sin(\alpha)^2$ and $a_0 = 0.26463 - 0.061581 \cdot T_L - 0.0031408 \cdot T_L^2$; if $a_0 \cdot T_{rd} < 0.002$ then $a_0 = 0.002/T_{rd}$, $a_1 = 2.04020 + 0.018945 \cdot T_L - 0.0111610 \cdot T_L^2$, $a_2 = -1.33025 + 0.0392311 \cdot T_L + 0.0085079 \cdot T_L^2$ and T_L being the height corrected Linke turbidity factor at air mass 2 (see Section 3.1.3.1) with $T_L = T_{L,am2} \cdot p/p_0$.

D.4 Calculation of longwave radiation from sky (BASIS_LON_SKY)

Parameterisation options for the calculation longwave radiation from sky close to the ground:

(a) MITRAS (Gierisch, 2011, based on Geiger et al. (2009))

$$LW_s = \sigma \cdot T_{a,k=2m}^4 \cdot (a - b \cdot 10^{-c \cdot e_{a,k=2m}[\mathrm{mmHg}]}) \tag{D.13}$$

with $a = 0.820$, $b = 0.250$, $c = 0.126$, taken from Bolz and Falckenberg (1949) in Geiger et al. (2009), measured for North Sea region and $e_{a,k=2m}$ being the vapour pressure at 2 m height in mmHg.

(b) Iso1981 (Oke, 1987)

$$LW_s = \sigma \cdot T_{a,k=2m}^4 \cdot (0.70 + 5.95 \cdot 10^{-5} \cdot (e_{a,k=2m}[\mathrm{Pa}]/100) \cdot \exp(1500/T_{a,k=2m})) \tag{D.14}$$

with $e_{a,k=2m}$ being the vapour pressure at 2 m height in Pa and σ being the Stefan-Boltzmann constant.

(c) vdi3789 (VDI, 1994)

$$LW_s = \sigma \cdot T^4_{a,k=2m} \cdot 9.9 \cdot 10^{-6} \cdot T^2_{a,k=2m} \tag{D.15}$$

with σ being the Stefan-Boltzmann constant.

D.5 Calculation of surface temperatures for ground and walls (BASIS_TS)

Two different parameterisation options are available for the calculation of the surface temperature of ground (T_g) and walls (T_w).

(a) prescribed surface temperatures

Prescribed input surface temperatures are used for the lit part of the ground ($i = g$) and wall ($i = w$), respectively, during the day and for all ground and wall surfaces during the night.

$$T_{i,lit} = T_{i,pre} \tag{D.16}$$

The temperature of shaded surfaces is assumed to be equal to air temperature:

$$T_{i,sha} = \begin{cases} T_a & \text{if } \alpha > 0 \\ T_{i,pre} & \text{else} \end{cases} \tag{D.17}$$

Eq. (D.17) is applied for wall surfaces both to the shaded part of the partly lit wall ($T_{w,sha}$) and to the entire shaded wall ($T_{w,shae}$). This option should be chosen, if ground and wall surface temperatures are known for instance from measurements.

(b) prognostic surface temperatures

Prognostic surface temperatures for ground and wall can be calculated if the surface temperatures are unknown. Both surface temperatures are calculated iteratively from air temperature (T_a) assuming immediate equilibrium of the energy fluxes. Although this method cannot account for the storage of heat, Staiger (2014) showed that this approach is sufficiently accurate to estimate T_{mrt} within an accuracy of ± 2 K in an non-obscured rural area.

Ground surface temperature

Ground surface temperature is calculated iteratively with the iterative Newton approach from

$$T_g = T_g - \frac{[SW_{net,g} + LW_{net,g}] \cdot (1 + b_{terr}) + (1 + Bo^{-1}) \cdot h_a \cdot (T_{a2m} - T_g)}{-4 \cdot \varepsilon_g \cdot \sigma \cdot T_g^3 \cdot (1 + b_{terr}) - (1 + Bo^{-1}) \cdot h_a}. \tag{D.18}$$

Bo is the Bowen ratio, which describes the ratio between sensible and latent heat fluxes. The following values may be used for the different surface type, if no better information is available.

$$Bo = \begin{cases} 0.5 & \text{for grass (AMS, 2012)} \\ 1.3 & \text{for urban (Jendritzky et al., 1990)} \end{cases} \tag{D.19}$$

h_a is a heat transfer coefficient describing the heat exchange between surface and atmosphere (Jendritzky et al., 1990; Staiger, 2014) with a simple drag approach:

$$h_a = 6.2 + 4.26 \cdot v_{10\ \mathrm{m}} \tag{D.20}$$

and b_{terr} is used to describe the soil heat flux with (Jendritzky et al., 1990; Staiger, 2014):

$$b_{terr} = \begin{cases} -0.19 & \text{during the day} \\ -0.32 & \text{during the night} \end{cases} \tag{D.21}$$

The longwave and shortwave radiation balance at ground surfaces needed in Eq. (D.18) are calculated from:

$$\begin{aligned} LW_{net,g} = VF_{g\to s} \cdot LW_s + VF_{g\to w,lit} \cdot \varepsilon_w \sigma T_{w,lit}^4 \\ + VF_{g\to w,sha} \cdot \varepsilon_w \sigma T_{b,sha}^4 + VF_{g\to w,shae} \cdot \varepsilon_w \sigma T_{w,shae}^4 \end{aligned} \tag{D.22}$$

$$SW_{net,g} = \begin{cases} (1-a_g)\cdot(SW_{dir}\cdot\cos(\Theta) & \\ \quad +VF_{g\to s}\cdot SW_{diff,s} & \\ \quad +VF_{g-w,lit}\cdot a_w\cdot SW_{dir}\cdot\cos(\eta_i) & \text{during the day} \\ \quad +VF_{g-w,lit}\cdot a_w SW_{diff,s} & \\ \quad +VF_{g-w,sha}\cdot a_w SW_{diff,s} & \\ \quad +VF_{g-w,shae}\cdot a_w SW_{diff,s}) & \\ 0 & \text{between sunset and sunrise} \end{cases} \tag{D.23}$$

with $VF_{g\to w,i}$ being view factors from the ground surface to i different wall surfaces as discussed in Section 3.1.3.3. For the shortwave radiation balance, sunny and shaded parts of the ground are differentiated; for shaded ground areas SW_{dir}=0 W m^{-2}.

Wall surface temperature

Wall surface temperature is calculated from (Gierisch, 2011)

$$T_b = T_b - \frac{SW_{net,w} + LW_{net,w} - C\cdot(T_{\mathrm{room}} - T_b) + h_a\cdot(T_a - T_b)}{-4\cdot\varepsilon_w\cdot\sigma\cdot T_b^3 + C - h_a}. \tag{D.24}$$

In Eq. (D.24) latent heat fluxes are neglected, which is a good approximation for non-vegetated buildings. C describes the heat transfer through the building wall and can be calculated according to Gierisch (2011):

$$C = \frac{1}{U^{-1} - 0.04} \tag{D.25}$$

where U is the total heat transfer coefficient of a building wall; it is set to $U = 1$ Wm^{-2}K^{-1} (Gierisch, 2011).

T_{room} is the indoor room air temperature and h_a heat transfer coefficient between the wall surface and the air (DIN EN ISO 6946 in Willems et al., 2006)

$$h_a = 4 + 4v_{10\ \mathrm{m}} \tag{D.26}$$

The longwave and shortwave radiation balance for the walls are calculated using surface-to-surface view factors (Section 3.1.3.3). Eq. (D.27) shows the longwave radiation balance for the entirely shaded wall as an example. The balances of the other walls are calculated similarly using the appropriate view factors.

$$\begin{aligned} LW_{net,w,shae} =& VF_{w\to s} \cdot LW_s \\ &+ VF_{w-g,lit} \cdot \varepsilon_g \cdot \sigma \cdot T^4_{g,lit} + VF_{w-g,sha} \cdot \varepsilon_g \cdot \sigma \cdot T^4_{g,sha} \\ &+ VF_{w-w,lit} \cdot \varepsilon_w \cdot \sigma \cdot T^4_{w,lit} + VF_{w-w,sha} \cdot \varepsilon_w \cdot \sigma \cdot T^4_{w,sha} \end{aligned} \tag{D.27}$$

Similarly the shortwave radiation balance is calculated from

$$SW_{net,lit} = \begin{cases} \begin{aligned} (1-a_w) \cdot (&SW_{dir} \cdot \cos(\Theta) \\ &+ VF_{w\to s} \cdot SW_{diff,s} \\ &+ VF_{w-g,lit} \cdot a_g \cdot \cos(\eta) \cdot SW_{dir} \\ &+ VF_{w-g,lit} \cdot a_g \cdot SW_{diff,s} \\ &+ VF_{w-g,sha} \cdot a_g \cdot SW_{diff,s} \\ &+ VF_{w-w,shae} \cdot a_w \cdot SW_{diff,s} \end{aligned} & \text{during the day} \\ 0 & \text{between sunset and sunrise} \end{cases} \tag{D.28}$$

Ground and wall temperature are adjusted to each other by iterating five times between Eq. (D.24) and Eq. (D.18). Based on selected test cases, five iteration was determined sufficient for ground and wall temperatures to be in balance with deviations smaller than 10^{-3}.

Appendix E

Table E.1: Parametric input distribution functions ('Distr') and corresponding parameters ('Param') for T_a used for the full-space analysis of the thermal indices with corresponding p-value for Kolmogorov-Smirnoff-test ('ks') and Anderson-Darling-test ('ad'). Index numbers at T_a denotes the hour, 'Su' summer and 'Wi' winter. The distribution names are shortened normal ('norm'), extreme value ('ev'), lognormal ('logn'), generalised extreme value ('gev'), weibull ('wbl'), gamma ('gam'), generalised pareto ('gp'), rayleigh ('rayl').

	Distr.	Param. 1	Param. 2	Param. 3	p-value (ks)	p-value (ad)
$T_{a,1,Su}$	gev	-0.50	3.85	13.72	0.93	0.99
$T_{a,2,Su}$	gev	-0.48	3.80	13.01	1.00	1.00
$T_{a,3,Su}$	gev	-0.47	3.73	12.47	0.94	0.99
$T_{a,4,Su}$	gev	-0.52	3.47	12.75	0.68	0.92
$T_{a,5,Su}$	wbl	16.29	6.23	-	0.28	0.45
$T_{a,6,Su}$	ev	18.84	2.45	-	0.67	0.52
$T_{a,7,Su}$	wbl	20.68	8.04	-	0.94	0.81
$T_{a,8,Su}$	wbl	22.62	8.40	-	0.80	0.80
$T_{a,9,Su}$	wbl	24.28	8.65	-	0.66	0.51
$T_{a,10,Su}$	ev	25.71	2.81	-	0.51	0.28
$T_{a,11,Su}$	wbl	26.55	8.89	-	0.45	0.61
$T_{a,12,Su}$	wbl	27.35	9.02	-	0.85	0.78
$T_{a,13,Su}$	norm	26.51	3.36	-	0.53	0.52
$T_{a,14,Su}$	norm	26.86	3.39	-	0.74	0.63
$T_{a,15,Su}$	wbl	28.45	8.98	-	0.97	0.89
$T_{a,16,Su}$	wbl	28.25	8.67	-	0.73	0.78
$T_{a,17,Su}$	norm	26.18	3.54	-	0.64	0.78
$T_{a,18,Su}$	wbl	26.67	7.87	-	0.84	0.88
$T_{a,19,Su}$	wbl	24.92	7.47	-	0.94	0.99
$T_{a,20,Su}$	ev	22.94	2.86	-	0.63	0.77
$T_{a,21,Su}$	ev	21.43	2.99	-	0.87	0.91
$T_{a,22,Su}$	wbl	20.09	5.96	-	0.87	0.85

	Distr.	Param. 1	Param. 2	Param. 3	p-value (ks)	p-value (ad)
$T_{a,23,Su}$	wbl	19.04	5.57	-	1.00	1.00
$T_{a,1,Wi}$	norm	-6.22	3.95	-	0.63	0.93
$T_{a,2,Wi}$	norm	-6.57	3.98	-	0.75	0.98
$T_{a,3,Wi}$	norm	-6.87	3.96	-	0.80	0.99
$T_{a,4,Wi}$	gev	-0.31	4.08	-8.47	0.91	0.98
$T_{a,5,Wi}$	norm	-7.30	4.00	-	0.92	1.00
$T_{a,6,Wi}$	gev	-0.29	3.95	-8.68	0.93	1.00
$T_{a,7,Wi}$	gev	-0.26	3.95	-8.73	0.87	0.98
$T_{a,8,Wi}$	norm	-6.58	4.35	-	0.91	0.99
$T_{a,9,Wi}$	norm	-5.20	4.46	-	0.64	0.88
$T_{a,10,Wi}$	norm	-3.75	4.61	-	0.93	0.97
$T_{a,11,Wi}$	norm	-2.48	4.68	-	0.90	0.93
$T_{a,12,Wi}$	norm	-1.49	4.81	-	0.65	0.84
$T_{a,13,Wi}$	gev	-0.14	4.36	-2.78	0.94	0.95
$T_{a,14,Wi}$	norm	-0.79	4.86	-	0.62	0.71
$T_{a,15,Wi}$	norm	-1.25	4.89	-	0.80	0.65
$T_{a,16,Wi}$	norm	-2.09	4.81	-	0.79	0.67
$T_{a,17,Wi}$	gev	-0.18	4.30	-4.77	0.98	0.93
$T_{a,18,Wi}$	norm	-3.69	4.42	-	0.94	0.93
$T_{a,19,Wi}$	norm	-4.21	4.28	-	0.99	0.98
$T_{a,20,Wi}$	norm	-4.71	4.22	-	0.95	0.93
$T_{a,21,Wi}$	norm	-5.13	4.06	-	0.99	0.99
$T_{a,22,Wi}$	norm	-5.64	4.03	-	0.86	0.99
$T_{a,23,Wi}$	norm	-5.99	4.25	-	0.97	0.94

Table E.2: As Table E.1 but for e.

	Distr.	Param. 1	Param. 2	Param. 3	p-value (ks)	p-value (ad)
$e_{1,Su}$	gev	-0.36	2.58	12.74	0.93	0.94
$e_{2,Su}$	norm	13.34	2.44	-	0.58	0.74
$e_{3,Su}$	norm	13.18	2.41	-	0.80	0.88
$e_{4,Su}$	norm	13.27	2.28	-	0.72	0.84
$e_{5,Su}$	wbl	14.75	6.76	-	0.50	0.76

	Distr.	Param. 1	Param. 2	Param. 3	p-value (ks)	p-value (ad)
$e_{6,Su}$	norm	14.18	2.50	-	0.71	0.80
$e_{7,Su}$	norm	14.19	2.79	-	0.96	0.97
$e_{8,Su}$	gam	21.75	0.65	-	0.66	0.66
$e_{9,Su}$	gam	19.34	0.71	-	0.88	0.85
$e_{10,Su}$	gam	18.95	0.70	-	0.93	0.72
$e_{11,Su}$	logn	2.53	0.24	-	0.91	0.95
$e_{12,Su}$	logn	2.50	0.23	-	0.96	1.00
$e_{13,Su}$	logn	2.49	0.22	-	0.88	0.83
$e_{14,Su}$	logn	2.48	0.22	-	0.47	0.69
$e_{15,Su}$	logn	2.47	0.23	-	0.93	0.97
$e_{16,Su}$	gam	19.01	0.64	-	0.97	0.97
$e_{17,Su}$	gam	18.18	0.68	-	0.59	0.79
$e_{18,Su}$	norm	12.76	2.91	-	0.89	0.87
$e_{19,Su}$	norm	13.50	3.05	-	0.98	0.99
$e_{20,Su}$	norm	14.18	3.08	-	0.87	0.87
$e_{21,Su}$	wbl	15.34	5.93	-	0.56	0.81
$e_{22,Su}$	norm	14.19	2.59	-	0.78	0.87
$e_{23,Su}$	norm	14.16	2.52	-	0.84	0.81
$e_{1,Wi}$	logn	1.10	0.35	-	0.95	0.99
$e_{2,Wi}$	gam	8.80	0.36	-	0.91	1.00
$e_{3,Wi}$	gam	9.04	0.34	-	0.95	1.00
$e_{4,Wi}$	gam	8.91	0.34	-	0.96	0.99
$e_{5,Wi}$	gam	8.84	0.34	-	0.98	0.99
$e_{6,Wi}$	gam	8.48	0.36	-	0.85	0.93
$e_{7,Wi}$	logn	1.05	0.35	-	0.81	0.90
$e_{8,Wi}$	gam	8.21	0.38	-	0.93	0.90
$e_{9,Wi}$	logn	1.11	0.35	-	0.89	0.91
$e_{10,Wi}$	logn	1.14	0.34	-	0.96	0.93
$e_{11,Wi}$	logn	1.14	0.33	-	0.93	0.98
$e_{12,Wi}$	logn	1.14	0.32	-	0.97	1.00
$e_{13,Wi}$	logn	1.13	0.34	-	0.98	1.00
$e_{14,Wi}$	gam	9.50	0.34	-	0.97	0.99
$e_{15,Wi}$	logn	1.11	0.32	-	0.99	1.00

	Distr.	Param. 1	Param. 2	Param. 3	p-value (ks)	p-value (ad)
$e_{16,Wi}$	logn	1.11	0.32	-	0.90	1.00
$e_{17,Wi}$	logn	1.13	0.31	-	0.94	0.99
$e_{18,Wi}$	logn	1.13	0.32	-	0.91	0.97
$e_{19,Wi}$	gam	10.03	0.32	-	0.86	0.98
$e_{20,Wi}$	gam	9.10	0.35	-	0.78	0.98
$e_{21,Wi}$	logn	1.11	0.32	-	0.81	0.90
$e_{22,Wi}$	gam	10.09	0.31	-	0.85	0.99
$e_{23,Wi}$	gam	9.53	0.33	-	0.89	0.98

Table E.3: As Table E.1 but for FF_{10}.

	Distr.	Param. 1	Param. 2	Param. 3	p-value (ks)	p-value (ad)
$FF_{10,1,Su}$	gam	2.06	0.91	-	0.40	0.69
$FF_{10,2,Su}$	gam	2.47	0.71	-	0.79	0.94
$FF_{10,3,Su}$	gam	2.57	0.71	-	0.84	0.82
$FF_{10,4,Su}$	gev	0.13	0.86	1.37	0.51	0.75
$FF_{10,5,Su}$	wbl	2.52	1.54	-	0.29	0.55
$FF_{10,6,Su}$	gam	2.77	1.00	-	0.91	0.95
$FF_{10,7,Su}$	gev	0.04	1.29	2.44	0.88	0.96
$FF_{10,8,Su}$	gam	3.64	1.00	-	0.48	0.48
$FF_{10,9,Su}$	gam	4.02	1.01	-	0.96	0.98
$FF_{10,10,Su}$	logn	1.36	0.53	-	0.54	0.63
$FF_{10,11,Su}$	gam	4.28	1.10	-	0.69	0.72
$FF_{10,12,Su}$	gp	-0.42	4.70	1.39	0.24	0.23
$FF_{10,13,Su}$	gam	4.33	1.10	-	0.94	0.98
$FF_{10,14,Su}$	rayl	3.76	-	-	0.33	0.32
$FF_{10,15,Su}$	wbl	5.60	2.38	-	0.94	0.97
$FF_{10,16,Su}$	wbl	5.69	2.41	-	0.63	0.75
$FF_{10,17,Su}$	norm	4.97	2.11	-	0.31	0.70
$FF_{10,18,Su}$	wbl	5.15	2.68	-	0.51	0.63
$FF_{10,19,Su}$	wbl	4.61	2.97	-	0.71	0.83
$FF_{10,20,Su}$	norm	3.55	1.42	-	0.48	0.90
$FF_{10,21,Su}$	wbl	3.55	2.30	-	0.84	0.95

	Distr.	Param. 1	Param. 2	Param. 3	p-value (ks)	p-value (ad)
$FF_{10,22,Su}$	wbl	3.15	1.85	-	0.56	0.58
$FF_{10,23,Su}$	wbl	2.85	1.71	-	0.98	0.98
$FF_{10,1,Wi}$	wbl	4.81	1.97	-	0.56	0.73
$FF_{10,2,Wi}$	rayl	3.35	-	-	0.95	0.94
$FF_{10,3,Wi}$	rayl	3.41	-	-	0.83	0.74
$FF_{10,4,Wi}$	wbl	4.72	1.88	-	1.00	0.99
$FF_{10,5,Wi}$	wbl	4.79	1.82	-	0.77	0.81
$FF_{10,6,Wi}$	wbl	4.79	1.82	-	0.96	0.94
$FF_{10,7,Wi}$	wbl	5.03	1.86	-	0.86	0.86
$FF_{10,8,Wi}$	rayl	3.90	-	-	0.80	0.82
$FF_{10,9,Wi}$	rayl	4.25	-	-	0.91	0.75
$FF_{10,10,Wi}$	wbl	6.29	1.97	-	0.83	0.75
$FF_{10,11,Wi}$	rayl	4.71	-	-	0.41	0.47
$FF_{10,12,Wi}$	rayl	4.79	-	-	0.48	0.54
$FF_{10,13,Wi}$	rayl	4.75	-	-	0.61	0.69
$FF_{10,14,Wi}$	wbl	6.64	2.32	-	0.37	0.62
$FF_{10,15,Wi}$	wbl	6.38	2.17	-	0.88	0.98
$FF_{10,16,Wi}$	wbl	5.79	2.10	-	0.86	0.98
$FF_{10,17,Wi}$	wbl	5.65	1.98	-	0.59	0.75
$FF_{10,18,Wi}$	wbl	5.46	1.90	-	0.35	0.61
$FF_{10,19,Wi}$	rayl	3.81	-	-	0.70	0.50
$FF_{10,20,Wi}$	wbl	5.32	1.91	-	0.75	0.96
$FF_{10,21,Wi}$	wbl	4.96	1.67	-	0.82	0.84
$FF_{10,22,Wi}$	wbl	5.06	1.75	-	0.78	0.93
$FF_{10,23,Wi}$	wbl	4.75	1.70	-	0.91	0.97

Appendix F

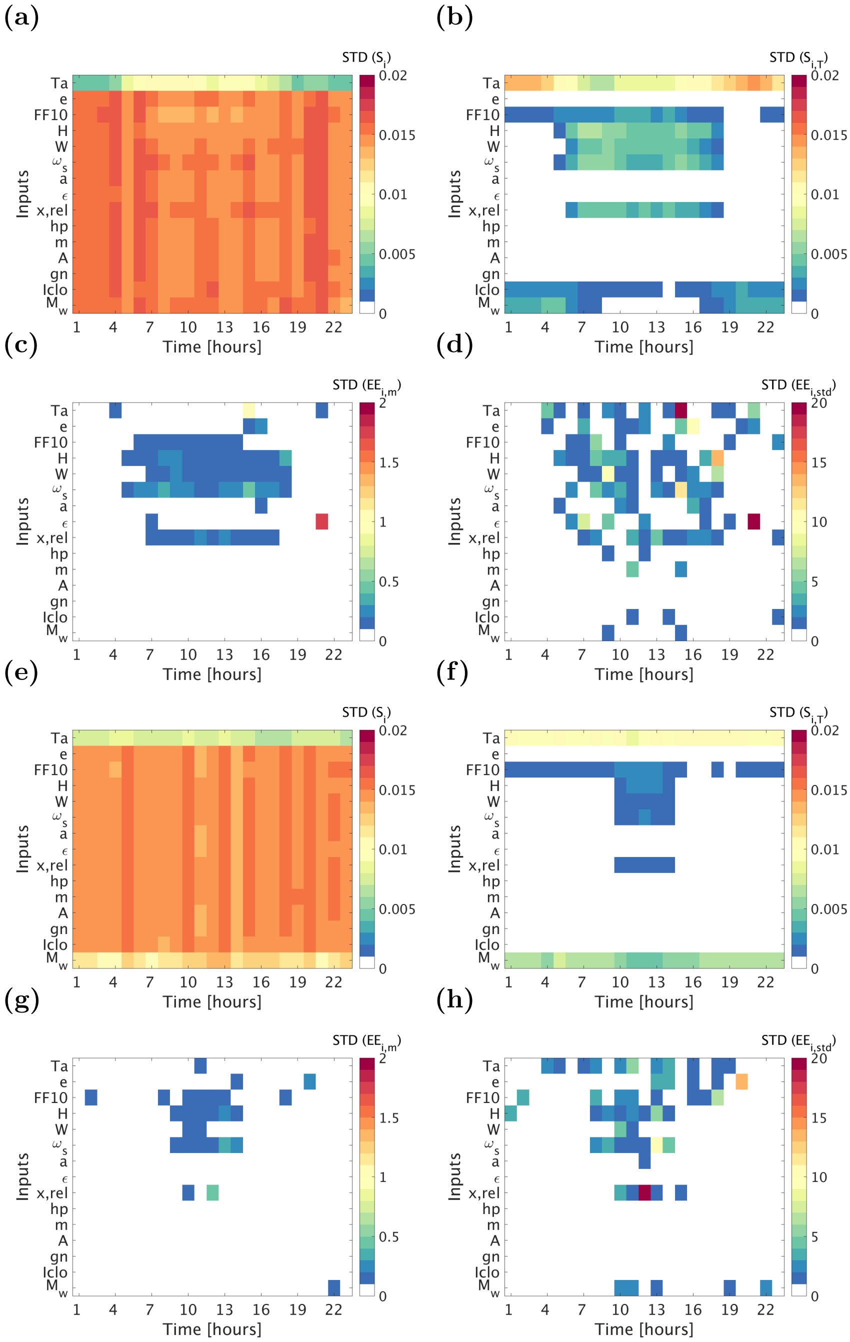

Figure F.1: Standard deviation of 500 bootstrap results for $\mathrm{PET}^*_{\mathrm{vdi}}$ for (a), (e) main (S_i) and (b), (f) total ($S_{i,T}$) sensitivity indices and (c), (g) mean elementary effects ($EE_{i,m}$) and (d), (h) standard deviation of elementary effects ($EE_{i,std}$) for (a) to (d) summer and (c) to (h) winter. For mean values see Figure 4.14; note the different scale.

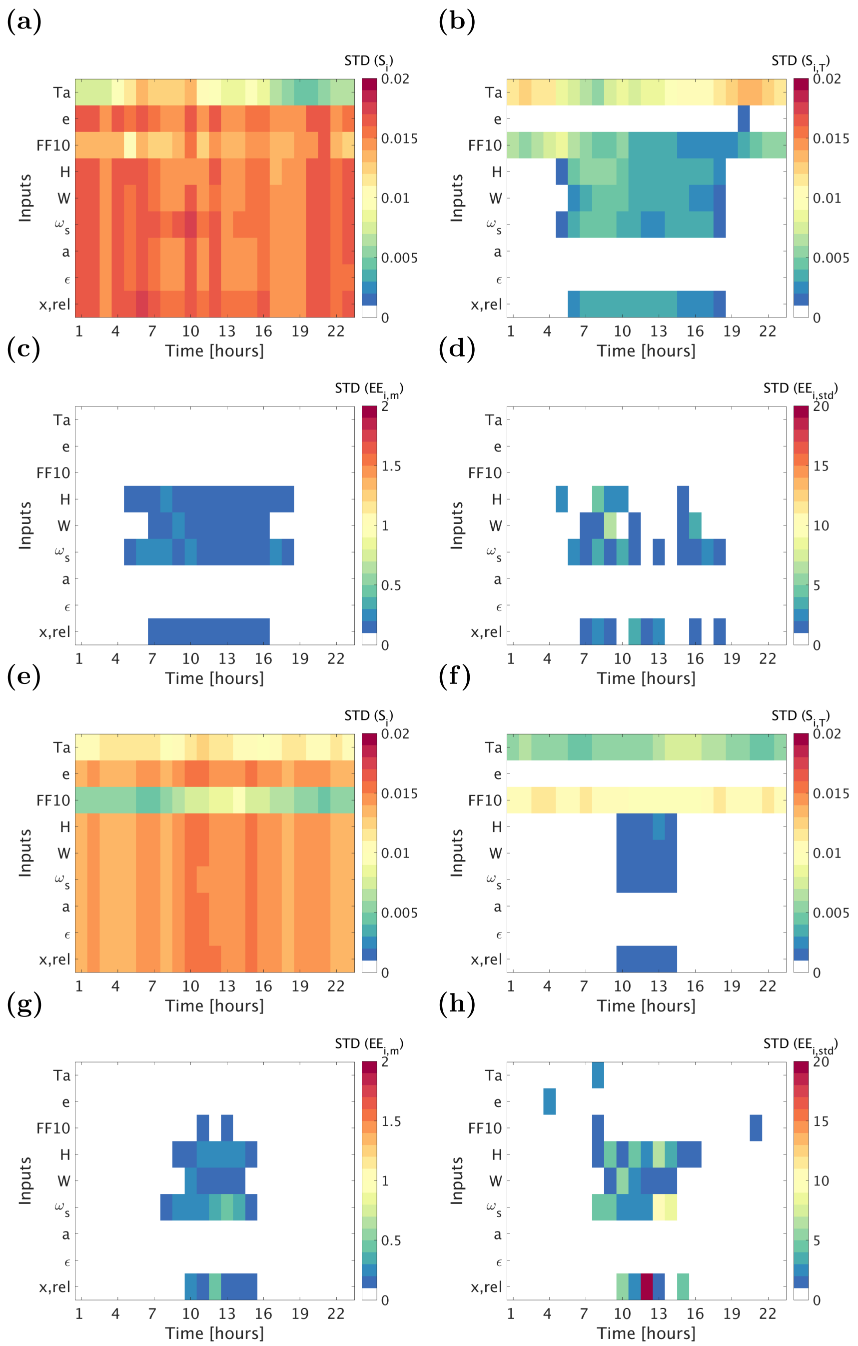

Figure F.2: Same as Figure F.1 but for UTCI. For mean values see Figure 4.15; note the different scale.

Appendix G

Table G.1: As Table 4.9 but for median input data accuracy.

	PET^*_{env}		PET^*_{vdi}				UTCI				Range
	Summer	Winter	Summer		Winter		Summer		Winter		
	Regr	Regr	Regr	EE	Regr	EE	Regr	EE	Regr	EE	
T_a [K]	1.1 ± 0.2	1.2 ± 0.2	1.2 ± 0.3	1.3 ± 0.06	1.2 ± 0.2	1.5 ± 0.08	0.8 ± 0.3	1.5 ± 0.1	1.0 ± 0.3	1.3 ± 0.06	
e [hPa]				16 ± 1.6		7.4 ± 0.7		7.1 ± 1.7		3.3 ± 0.1	
RH [%]	12 ± 6.6	208 ± 133	309 ± 242		977 ± 893		25 ± 20		43 ± 18		
FF_{10} [m/s]	3.4 ± 1.8	3.0 ± 1.6	4.2 ± 1.2	2.0 ± 0.6	3.1 ± 1.7	3.5 ± 0.4	0.5 ± 0.05	1.1 ± 0.2	0.6 ± 0.2	0.5 ± 0.03	
T_{mrt} [K]	2.9 ± 0.8	5.8 ± 3.2	3.5 ± 1.5		5.5 ± 3.3		4.1 ± 1.5		3.2 ± 0.2		
h_p [m]	1.2 ± 0.9	1.3 ± 0.8	2.3 ± 1.9	1.5 ± 0.3	1.1 ± 0.9	0.4 ± 0.01					1.5–2.0
m [kg]	91 ± 70	150 ± 87	169 ± 122	127 ± 26	97 ± 48	37 ± 0.5					50–100
A [y]	190 ± 128	101 ± 57	187 ± 125	209 ± 37	66 ± 19	80 ± 1.1					16–100
gn []				7.6 ± 1.2		5.2 ± 0.10					1– 2
I_{clo} [clo]	0.9 ± 0.6	1.5 ± 0.7	1.3 ± 0.9	0.5 ± 0.07	1.5 ± 0.8	0.7 ± 0.04					0.1–2.0
M_w [W]	60 ± 40	52 ± 35	131 ± 101	86 ± 22	49 ± 32	27 ± 0.2					0–300
H [m]				8.5 ± 3.2		120 ± 11		8.9 ± 2.5		81 ± 5.1	0–40
W [m]				18 ± 11		295 ± 55		19 ± 10		230 ± 16	5–50
ω_s [°]				24 ± 5.4		50 ± 9.7		30 ± 5.5		30 ± 5.2	0–180
a []				0.5 ± 0.2		1.4 ± 0.5		0.6 ± 0.3		1.0 ± 0.3	0.2–0.6
ε []				0.1 ± 0.01		0.3 ± 0.01		0.2 ± 0.02		0.2 ± 0.01	0.85–0.95
x_{rel} []				0.5 ± 0.3		12 ± 3.2		0.5 ± 0.3		10 ± 0.8	0.1–0.9

Appendix H

H.1 Governing equations of MITRAS

MITRAS is based on the conservation of momentum, mass and heat, water and other tracers. These conservations can be expressed on a rotating Earth with Eq. (H.1) to Eq. (H.3).

$$\frac{\partial \vec{v}}{\partial t} + (\vec{v} \cdot \nabla)\vec{v} = -\frac{1}{\rho}\nabla p - 2\left[\vec{\Omega} \times \vec{v}\right] - \nabla\Phi + \vec{F_m} \tag{H.1}$$

$$\frac{\partial \rho}{\partial t} + \nabla \cdot (\rho\vec{v}) = 0 \tag{H.2}$$

$$\frac{\partial \chi}{\partial t} + \vec{v} \cdot \nabla\chi = Q_\chi . \tag{H.3}$$

Here the three-dimensional wind velocity is defined as $\vec{v}$, the Nabla operator as ∇, air density as ρ, pressure as p and Time as t. The Earth's angular velocity Ω, the geopotential Φ and the Molecular forces F_m are used to define the Coriolis force, the gravitational force and the molecular friction respectively. χ represents scalar quantity such as potential temperature Θ, the temperature of an air parcel adiabatically brought to the reference pressure of 1000 hPa, or concentration q_1^k of atmospheric water, where k=1,2,3 is vapour, liquid and solid phase respectively. Possible sources and sinks of χ are described by Q_χ.

To close the system two additional equations are necessary: the ideal gas law (Equation H.4 and the equation for the potential temperature (Equation H.5).

$$v_i = \frac{R_i T}{p} \tag{H.4}$$

$$\Theta = T\left(\frac{1000 \cdot 10^2 \text{ Pa}}{p}\right)^{R_0/c_p} . \tag{H.5}$$

Here v_i stands for the specific volume of dry air ($i = 0$) and water ($i = 1$). R_i is the individual gas constant. c_p is used as a symbol for the Specific heat at constant pressure and T as a symbol for the temperature. Air can be treated as an ideal gas, because the volume of the molecules and the non-elastic impacts can be neglected for the temperature and pressure ranges in the troposphere.

H.2 Reynolds-Averaged-Navier–Stokes equations

Eq. (H.1) are averaged in space and time using the Reynold's averaging method to arrive at the Reynolds-Averaged-Navier–Stokes (RANS) equations. Within this method all prognostic variables are split into an averaged part (integrated over space and time) and its deviations. Pressure and density deviations from the average are assumed to be small. The averaged scalar quantities are further split into a large scale value, which corresponds to the domain averaged value, and a microscale value. The large scale value refers to a basic state. For numerical reasons average values of pressure are further split into the hydrostatic part p_1 and its deviation p_2, called dynamic pressure.

As a result of the Reynolds averaging new terms emerge, called Reynolds stresses for momentum, turbulent heat fluxes and turbulent mass fluxes (Blocken, 2015). Due to these additional terms the equations do not form a closed set anymore and therefore additional equations must be defined to close set. In MITRAS first-order closures, relating the turbulent fluxes to gradients of the mean flow are used for that above the surface layer (Appendix K, Salim et al., 2018). At the surface, Monin- Obukov surface layer similarity theory is applied (Appendix H.5).

H.3 Approximations

Besides the filtering, additional approximations are applied in MITRAS to lower the computational costs:

Neglecting of molecular friction Since turbulent fluxes are often much larger than molecular ones, this is a reasonable approximation.

Anelastic approximation The anelastic approximation is applied to filter sound waves, which have a large velocity and therefore require very small time step in the model (Pielke Sr., 2013, p. 28). Since on the microscale, air is close to being incompressible (Schlünzen et al., 2012b), the anelastic approximation is valid. Eq. (H.6) is used as a substitute for Equation H.2.

$$\nabla \cdot (\rho_0 \vec{v}) = 0 \tag{H.6}$$

Boussinesq approximation This approximation assumes that deviations in density from the basic state only contribute to the changes in buoyancy and can be replaced by the basic state density elsewhere.

Constant Coriolis parameter Since microscale model domains are small, using a constant Coriolis parameter f for the Coriolis force in Eq. (H.1) is a valid assumption.

Hydrostatic equilibrium and geostrophy In MITRAS all variables are splitted into a basic state and deviation from it (Section 5.1). The basic state is assumed to fulfil both the hydrostatic (Equation H.7) and the geostrophic equilibrium (Equation H.8).

$$\frac{\partial p}{\partial z} = -\rho_0 \cdot g \tag{H.7}$$

$$\begin{aligned} u_g &= -\frac{1}{\rho_0 f}\frac{\partial p}{\partial y} \\ v_g &= \frac{1}{\rho_0 f}\frac{\partial p}{\partial x}. \end{aligned} \tag{H.8}$$

Where g is the gravitational acceleration, and u_g and v_g are u- and v-components of the geostropic wind respectively.

H.4 Final model equations

Applying all above described approximations and filtering and performing the coordinate transformation from the Cartesian system (x, y, z) to a non-orthogonal coordinate system ($\dot{x}_1$, $\dot{x}_2$, $\dot{x}_3$), the RANS equations evolve to the following model equations (Salim et al., 2018):

$$\begin{aligned} \frac{\partial \rho_0 \alpha^* \overline{u}}{\partial t} = &- \frac{\partial}{\partial \dot{x}_1}\left(\overline{u}\frac{\partial \dot{x}_1}{\partial x}\rho_0\alpha^*\overline{u}\right) - \frac{\partial}{\partial \dot{x}_2}\left(\overline{v}\frac{\partial \dot{x}_2}{\partial y}\rho_0\alpha^*\overline{u}\right) - \frac{\partial}{\partial \dot{x}_3}\left(\overline{w}\frac{\partial \dot{x}_3}{\partial z}\rho_0\alpha^*\overline{u}\right) \\ &- \alpha^*\frac{\partial \dot{x}_1}{\partial x}\left(\frac{\partial p_1}{\partial \dot{x}_1} + \frac{\partial p_2}{\partial \dot{x}_1}\right) - \alpha^*\frac{\partial \dot{x}_3}{\partial x}\left(\frac{\partial p_2}{\partial \dot{x}_3}\right) + \widetilde{\rho}\alpha^* g\frac{\partial \dot{x}_3}{\partial x}\frac{\partial z}{\partial \dot{x}_3} \\ &+ f\rho_0\alpha^*(\overline{v} - v_g) - f'\cos\zeta\rho_0\alpha^*\overline{w} - \overline{F}_1 \end{aligned} \tag{H.9}$$

$$\begin{aligned}\frac{\partial \rho_0 \alpha^* \overline{v}}{\partial t} = & - \frac{\partial}{\partial \dot{x}_1}\left(\overline{u}\frac{\partial \dot{x}_1}{\partial x}\rho_0\alpha^*\overline{v}\right) - \frac{\partial}{\partial \dot{x}_2}\left(\overline{v}\frac{\partial \dot{x}_2}{\partial y}\rho_0\alpha^*\overline{v}\right) - \frac{\partial}{\partial \dot{x}_3}\left(\overline{w}\frac{\partial \dot{x}_3}{\partial z}\rho_0\alpha^*\overline{v}\right) \\ & - \alpha^*\frac{\partial \dot{x}_2}{\partial y}\left(\frac{\partial p_1}{\partial \dot{x}_2} + \frac{\partial p_2}{\partial \dot{x}_2}\right) - \alpha^*\frac{\partial \dot{x}_3}{\partial y}\left(\frac{\partial p_2}{\partial \dot{x}_3}\right) + \widetilde{\rho}\alpha^* g \frac{\partial \dot{x}_3}{\partial y}\frac{\partial z}{\partial \dot{x}_3} \\ & - f\rho_0\alpha^*(\overline{u} - u_g) + f'\sin\zeta\rho_0\alpha^*\overline{w} - \overline{F}_2\end{aligned} \tag{H.10}$$

$$\begin{aligned}\frac{\partial \rho_0 \alpha^* \overline{w}}{\partial t} = & - \frac{\partial}{\partial \dot{x}_1}\left(\overline{u}\frac{\partial \dot{x}_1}{\partial x}\rho_0\alpha^*\overline{w}\right) - \frac{\partial}{\partial \dot{x}_2}\left(\overline{v}\frac{\partial \dot{x}_2}{\partial y}\rho_0\alpha^*\overline{w}\right) - \frac{\partial}{\partial \dot{x}_3}\left(\overline{w}\frac{\partial \dot{x}_3}{\partial z}\rho_0\alpha^*\overline{w}\right) \\ & - \alpha^*\frac{\partial \dot{x}_3}{\partial z}\left(\frac{\partial p_2}{\partial \dot{x}_3}\right) + f'\rho_0\alpha^*(\overline{u}\cos\zeta - \overline{v}\sin\zeta) - \overline{F}_3\end{aligned} \tag{H.11}$$

$$\begin{aligned}\frac{\partial \rho_0 \alpha^* \overline{\chi}}{\partial t} = & - \frac{\partial}{\partial \dot{x}_1}\left(\overline{u}\frac{\partial \dot{x}_1}{\partial x}\rho_0\alpha^*\overline{\chi}\right) - \frac{\partial}{\partial \dot{x}_2}\left(\overline{v}\frac{\partial \dot{x}_2}{\partial y}\rho_0\alpha^*\overline{\chi}\right) - \frac{\partial}{\partial \dot{x}_3}\left(\overline{w}\frac{\partial \dot{x}_3}{\partial z}\rho_0\alpha^*\overline{\chi}\right) \\ & + \rho_0\alpha^*\overline{Q}_{\overline{\chi}} - \overline{F}_{\overline{\chi}}\end{aligned} \tag{H.12}$$

In the above equations ρ_0 is the large scale air density and $\widetilde{\rho}$ is the microscale air density. u, v and w are the velocity components in the Cartesian coordinate system and u_g and v_g are the geostrophic wind components. α^* is the grid volume, p_1 is the hydrostatic part of pressure and p_2 is the dynamic part of pressure. g is the Gravitational acceleration, f and f' are the Coriolis Parameter. $\overline{F}_1$, $\overline{F}_2$, $\overline{F}_3$, $\overline{F}_{\overline{\chi}}$ are the subgrid scale turbulent fluxes. χ is the scalar quantity and $\overline{Q}_{\overline{\chi}}$ are sources and sinks of χ.

H.5 Lower boundary conditions

The ground surface temperature (T_g, Eq. (H.13)) of all surfaces but water surfaces is determined from the shortwave and longwave radiation flux balances at the ground determine (term 1 and 2), sensible and the latent heat fluxes (term 3 and 4 in Eq. (H.13)) and the soil heat flux (term 5 in Eq. (H.13))

$$\frac{\partial T_g}{\partial t} = \frac{2\sqrt{\pi}k_s}{\nu_s h}\left(SW_{net} + LW_{net} + c_p\rho_0\vartheta_* u_* + l_{21}\rho_0 q_* u_* - \sqrt{\pi}\nu_s\frac{\overline{T}_s - \overline{T}(-h_\vartheta)}{h_\vartheta}\right). \tag{H.13}$$

Eq. (H.13) is solved based on the force restore method, with k_s being the thermal diffusivity and ν_s the thermal conductivity for each surface cover class (SCC). h is the elevation height, c_p is the Specific heat at constant pressure, l_{21} is the Specific heat of vaporisation ($2.5 \cdot 10^6$ J kg^{-1}) and h_ϑ the depths of daily temperature wave.

The scaling variables for the surface sensible and latent heat fluxes are calculated with the Parameter averaging method as:

$$u_* = \kappa \cdot v_{gr} \left\{ \ln\left(\frac{z_1}{z_0}\right) - \psi_{m,1}\left(\frac{z_1}{L}\right) \right\}^{-1} \tag{H.14}$$

$$\vartheta_* = \kappa \cdot \left(\overline{\Theta}_{z_1} - \overline{\Theta}_s\right) \left\{ \ln\left(\frac{z_1}{z_{0,\Theta}}\right) - \psi_{m,2}\left(\frac{z_1}{L}\right) \right\}^{-1} \tag{H.15}$$

$$q_* = \kappa \cdot \left(\overline{q}_{z_1} - \overline{q}_s\right) \left\{ \ln\left(\frac{z_1}{z_{0,q}}\right) - \psi_{m,3}\left(\frac{z_1}{L}\right) \right\}^{-1} \tag{H.16}$$

Here κ is the von Karman constant, v_{gr} is the wind speed parallel to ground in lowest model height (z_1), z_0, $z_{0,\Theta}$ and $z_{0,q}$ are the surface roughness lengths for momentum, temperature (Θ) and humidity (q), respectively, $\psi_{m,k}$ are stability functions for the different quantities, which depend on the stratification, and L is the Monin-Obukhov length. The index s denotes the scalar quantity at the surface, e.g. potential surface temperature (Θ_s) as calculated from Eq. (H.13) and surface humidity (q_s) as calculated from a budget equation according to Deardorff (Schlünzen et al., 2012b, p. 51):

$$\begin{aligned} \overline{q}^1_{1s} &= \alpha_q \quad \overline{q}^1_{1sat}(\overline{T}_s) + (1-\alpha_q)\overline{q}^1_1(z_k = 1) \\ \overline{q}^1_{1s} &\leq \qquad \overline{q}^1_{1sat}(\overline{T}_s) \end{aligned} \tag{H.17}$$

Here, $\overline{q}^1_{1sat}$ denotes the saturation humidity of the soil and $\overline{q}^1_1(z_k = 1)$ the specific humidity in the first model layer and α_q the soil water availability, which is ≤ 1, depending on the surface cover class (SCC, Schlünzen et al., 2012a, p. 11–14).

Appendix I

The preprocessor PREMASK is developed to create input files for the MITRAS preprocessor GRIMASK for idealised domains. It creates ascii-grid files with a predefined resolution and size at a specific reference point, with characteristics as defined from the input parameters.

I.1 Input

PREMASK requires as inputs information about the desired domain, e.g. reference point, resolution and grid type to calculate the required ascii-grid domain size. If desired, the domain size can be increased in downwind direction to avoid interactions of the inner domain with the model boundary. The surface cover class (SCC) of the outer part of the domain can be set to cropland.

To fill the domain as desired, horizontal lines of buildings with specific building types and street widths in between have to be defined. Building types can be either in form of a building block or in form of a terraced building with desired ground area, height and width. Several building types can be defined and mixed as desired within one horizontal line. The seperating streets can be of the same or different width to create regular and non-regular domains. For non-regular domains the street width is chosen randomly between the limits specified as inputs. The default SCC is asphalt. Areas with different SCC can be defined as well as the SCC around buildings can be chosen for instance to fill building blocks with grass. Similarly, areas of elevated terrain can be specified. Finally explicit vegetation can be defined both within the courtyard of a building and in form of horizontal tree lines.

I.2 Output

Output of the PREMASK are ASCII-grid files of building height, land-use, terrain height and vegetation at 1 m resolution, which can be used directly as inputs for GRIMASK. Additionally, the domain is evaluated for geometric and surface cover properties of a Local Climate Zone (LCZ) (Stewart and Oke, 2012). LCZs are defined "as regions of uniform surface cover, structure, material, and human activity that span hundreds of meters to several kilometres in horizontal scale" (Stewart and Oke, 2012). Therefore the entire MITRAS domain created with PREMASK corresponds in its horizontal extent to one

LCZ. Stewart and Oke (2012) list 7 properties for characterising a LCZ. In the following, their evaluation within PREMASK is briefly described.

I.2.1 Criterion 1: SVF

The SVF is calculated for one point in the centre of the street for every street canyon in the domain from the two respective wall view factors according to the summation theorem (Eq. (3.25)):

$$SVF = 1 - WVF_1 - WVF_2 \tag{I.1}$$

The wall view factors are calculated according to Johnson and Watson (1984) for a canyon of finite length from:

$$WVF_i = \frac{1}{\pi} + \frac{1}{2\pi} \cdot \{\cos\beta \cdot [\arctan(\cos\beta \cdot \tan(-\gamma)) - \arctan(\cos\beta \cdot \tan(\gamma))]\} \tag{I.2}$$

Here β is the elevation angle to the top of the wall as seen from the centre of the canyon with H being the building height and W being the street width:

$$\beta(H, W) = \arctan(H/(0.5 \cdot W). \tag{I.3}$$

and γ is the angle from the centre of the street to either end of the building wall with l being the street length:

$$\gamma(H, l) = \arctan(0.5 \cdot l/H). \tag{I.4}$$

To evaluate the SVF over the entire domain, the average SVF over all street canyons is calculated.

I.2.2 Criterion 2: Aspect ratio

The average aspect ratio ($\overline{ASP}$) is calculated for every street canyon (c) and then averaged over all street canyons (N_c) to calculate the mean aspect ratio within the model area:

$$\overline{ASP} = \frac{\sum_c^{N_c} H_c/W_c}{N_c} \tag{I.5}$$

I.2.3 Criterion 3 to 5: Surface fractions

Three surface fractions are used to characterise a LCZ: building surface fraction(f_b), impervious surface fraction (f_{iper}) and pervious surface fraction (f_{per}).

The building surface fraction is the ratio of building plan area to total plan area. This is calculated for the entire domain without the cropland boundaries, which are only added for numerical reasons.

The impervious surface fraction is the ratio of impervious plan area (paved, rock) to total plan area. In the current default implementation, asphalt is the only impervious surface. Similarly, the pervious surface fraction is the ratio of pervious plan area (bare soil, vegetation, water) to total plan area. Pervious surfaces in the current implementation are all surfaces except for asphalt, e.g. grass in courtyards and areas with special surface cover classes, such as water.

I.2.4 Criterion 6: Height of roughness elements

The height of roughness elements is the geometric average of building heights (H) for the entire domain.

I.2.5 Criterion 7: Davenport classification

The Davenport classification classifies areas according to their surface roughness length (z_0). However, the roughness length cannot be derived easily. Therefore, instead the ratio between building height and inter-spaced width for every street canyon (c) is used as an aid.

$$\overline{ASP} = \frac{\sum_c^{N_c} W_c/H_c}{N_c} \tag{I.6}$$

Appendix J

To ensure that the calculation of view factors has been correctly implemented and view factors can thus be used in MITRAS, the implementation of the calculation has been validated. Since view factors between two surfaces depend only on geometric properties of the surfaces, the calculated values can be compared against expected values. The results of these tests are shown in Section J.1. In Section J.1 and Section J.2 view factors for an idealised domain are calculated to ensure that also obscured surfaces are implemented correctly (Figure 5.11) and view factors for ground and wall surfaces are consistent. The idealised domain is used to validate the implementation for the surface-to-surface view factors as well as for the surface-to-person view factors.

J.1 Validation of surface-to-surface view factors

Test for the implementation of view factors between grid cells

To test the implementation of the calculation given in Eq. (5.34) and Eq. (5.36) to Eq. (5.38) tests cases are selected for which the resulting view factor is known. The applied and unit tests are shown schematically in Figure J.1 and described in Table J.4.

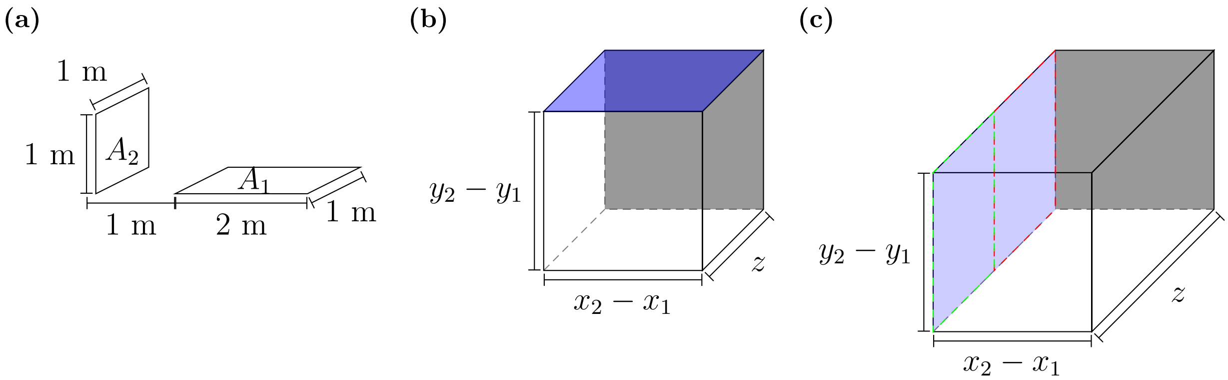

Figure J.1: Sketch of selected test cases for the implementation of view factors between grid cells.

For case U1, the model calculated $VF_{1\to2} = 0.0417$, when rounded to the same accuracy, and thus agrees perfectly with the expected results. For U2, view factors for two surfaces with a common edge are found to fulfil the values in Hamilton and Morgan (1952, p. 67), by manual comparison.

For `U3` to `U8` a random number generator has been used to randomly select a value for one side of the cuboid. This has been used, as used tests should be fulfilled independent of the actual side length. `U3` is based on the summation theorem (Eq. (3.25)). Results indicate that $VF_{w2w,per}$ and SVF agree to the forth decimal place ($|VF_{w2w,per} - SVF| < 10^{-4}$). The same accuracy has been used to check the results for `U4`, which is fulfilled. The two calculation methods of `U5` agree to the 10th decimal place. For test case `U6`, the view factor of the grey square (Figure J.1c) to the dashed red square ($VF_{\blacksquare-{\color{red}\square}}$), to the blue square ($VF_{\blacksquare-{\color{blue}\blacksquare}}$) and the green square ($VF_{\blacksquare-{\color{green}\square}}$) can be calculated according to Eq. (5.36) with $z/2$, Eq. (5.36) with z and Eq. (5.38), respectively. $VF_{\blacksquare-{\color{green}\square}} \stackrel{!}{=} VF_{\blacksquare-{\color{blue}\blacksquare}}$ and $-VF_{\blacksquare-{\color{red}\square}}$ agree to the forth decimal place. The values for `U7` and `U8` with 10^{-7}.

Table J.1: Test cases to validate the implementation of the view factor calculation.

Test	Aim	Domain	Comparison method
`U1`	Eq. 5.38	Fig. J.1a	Agreement of calculated value $VF_{1\to2}$ with $VF_{1\to2} = 0.0417$ take from Howell et al. (2016, 4.4 (b), p. 195).
`U2`	Eq. 5.36	Fig. J.2	Agreement of calculated common edge values with tabulated values in Hamilton and Morgan (1952, p. 67)
`U3`	Eq. 5.36	Fig. J.1b, i.e. $(x_2 - x_1) = (y_2 - y_1) = z$	Agreement of $VF_{w2w,per}$ with $SVF = 1 - VF_{w2g} - 2 \cdot VF_{w2w,per} - VF_{w2w,par}$
`U4`	Eq. 5.36	Fig. J.1b see `U3`	Agreement of $VF_{w2g} \stackrel{!}{=} VF_{w2w,per} \stackrel{!}{=} VF_{w2w,par}$
`U5`	Eq. 5.35	Fig. J.1b	Agreement of $VF_{w2w,per}$ with view factors calculated according to the equation given in Howell et al., 2016, p. 898, which is applicable to opposing surfaces of same size
`U6`	Eq. 5.38	Fig. J.1c Cuboid with side lengths $(x_2 - x_1) \cdot (y_2 - y_1)$ and $z = 2 \cdot (x_2 - x_1) = 2 \cdot (y_2 - y_1)$	According to the summation theorem (Eq. (3.25)) the following should be fulfilled: $VF_{\blacksquare-{\color{green}\square}} \stackrel{!}{=} VF_{\blacksquare-{\color{blue}\blacksquare}} - VF_{\blacksquare-{\color{red}\square}}$

Test	Aim	Domain	Comparison method
`U7`	Eq. 5.34	Fig. J.1b see `U3`	Agreement between Eq. (5.36) and Eq. (5.34) if $\xi = 10^{-7}$ and $x = 10^{-7}$ are used for Eq. (5.34)
`U8`	Eq. 5.37	Fig. J.1b see `U3`	Agreement between Eq. (5.36) and Eq. (5.37) if $\xi = 10^{-7}$ and $\eta_1 = y_2 + 10^{-7}$ are used for Eq. (5.37)

Idealised domain

The tests in Section J.1 ensure that the view factor calculation has been correctly implemented. To detect, whether obscured surfaces and view factors between ground and wall grid cell are calculated correctly for a more realistic urban domain, an idealised test domain is created. This domain consists of a block building with a height of one grid cell and a terraced building with a height of either one (`IS`, Figure J.2a) or two grid cells (`IH`, Figure J.2b) on an uniform grid with a vertical resolution of $\Delta z = 2$ m. A non-uniform grid is tested in cases `IHn` with the same domain as Figure J.2b but with a non-uniform grid at the boundaries of the domain (not shown).

The cells used for a particular test are denoted in the following way. To reference a view factor of a wall to another surface, the structures `nsurfcells` (red in Figure J.2) and `nsurfcount` (blue in Figure J.2) are used. In `nsurfcells` all surface cells are numbered consequentially. For each `nsurfcell`, `nsurfcount` indicates the number of building façades adjacent to that grid cell. To denote a view factor from façade number 1 of grid cell 13 (located within the courtyard in Figure J.2) is denoted $VF_{w13.1}$. In a similar way ground cells are referenced by the coordinate number in x-direction and the coordinate number in y-direction; for instance $VF_{11.0}$ denotes the cell 11th grid cell in x and the 0th cell in y.

Table J.2 shows all test cases performed for the domain with the small buildings Figure J.2a. Table J.3 show all test cases performed for the domain with the higher terraced buildings Figure J.2b. All tests have been successfully realised.

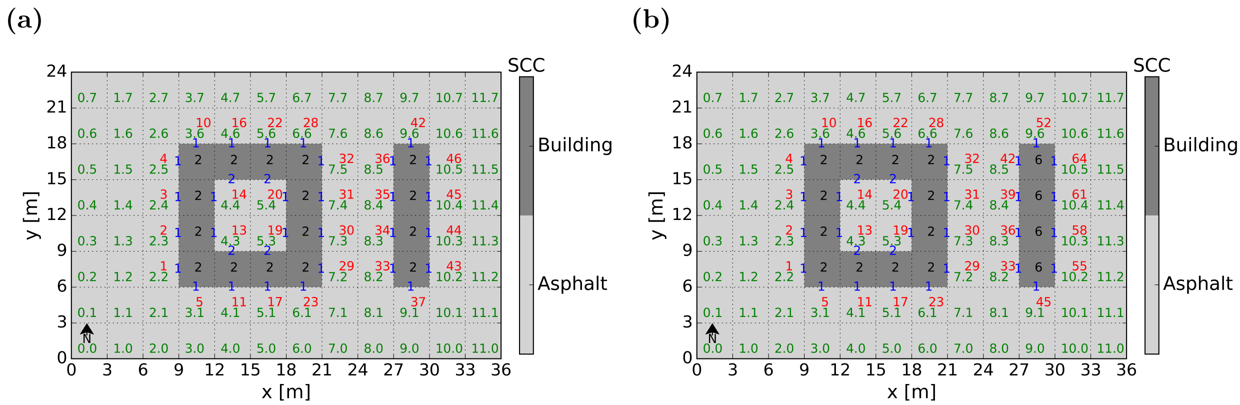

Figure J.2: Idealised domains for surface-to-surface view factor test case (a) `IS` and (b) `IH`. Numbers indicate building height (black), `nsurfcells` (red), `nsurfcount` (blue) and number of ground surface cell (green). See text for meaning of variables.

Table J.2: Performed tests for the idealised domains with a small terraced building (Figure J.2a). See text for the notation of $VF_{wi \to wj}$ and $VF_{gi \to wj}$.

Target VF	Test	Description (Evaluation target: result)
$VF_{wi \to wj}$	(a)	shading algorithm: each surface facing the courtyard has exactly 6 view factors (view factors of surfaces facing the courtyard to surfaces of the terraced building are 0).
	(b)	perpendicular view factors within courtyard: $VF_{w13.1-w14.2} = VF_{w13.1-w19.2} = VF_{w13.2-w14.1} = VF_{w13.2-w19.1} = VF_{w19.1-w20.2} = VF_{w19.2-w20.1}$
	(c)	perpendicular view factors with common edge within courtyard: $VF_{w13.1-w13.2} = VF_{w19.1-w19.2} = VF_{w20.1-w20.2} = VF_{w14.1-w14.2} = \max(VF_{\text{court}})$
	(d)	parallel view factors within domain: $VF_{w13.1-w19.1} = VF_{w14.1-w20.1} = VF_{w13.2-w14.2} = VF_{w19.2-w20.2} = VF_{w29.1-w33.1} = VF_{w30.1-w34.1} = VF_{w31.1-w35.1} = VF_{w32.1-w36.1}$

Target VF	Test	Description (Evaluation target: result)
	(e)	parallel view factors shifted by one grid cell within domain: $VF_{w13.1-w20.1} = VF_{w14.1-w19.1} = VF_{w13.2-w20.2} = VF_{w19.2-w14.2} = VF_{w29.1-w34.1} = VF_{w30.1-w33.1} = VF_{w30.1-w35.1} = VF_{w31.1-w34.1} = VF_{w31.1-w36.1} = VF_{w32.1-w35.1}$
	(f)	parallel view factors shifted by two grid cell within domain: $VF_{w29.1-w35.1} = VF_{w30.1-w36.1} = VF_{w31.1-w33.1} = VF_{w32.1-w34.1}$
$VF_{wi\to gj}$	(a)	shading algorithm: all surfaces facing the courtyard have exactly 4 view factors (view factors to ground surfaces outside the courtyard are 0).
	(b)	use correct surface orientation: $VF_{w1.1-g*}$ only faces ground surfaces with $i < 3$; $VF_{w29.1-g*}$ only faces ground surfaces with $i > 6$ (all other view factors are zero)
	(c)	check calculated value is consistent: $VF_{w1.1-g2.2} = VF_{w2.1-g2.3} = VF_{w30.1-g7.3} = VF_{w16.1-4.6}$
	(d)	check calculated value is consistent (x-direction): $VF_{w1.1-g2.2} > VF_{w1.1-g2.3} \geq VF_{w1.1-g2.1} \geq VF_{w1.1-g1.2} \geq VF_{w1.1-g1.1} \geq VF_{w1.1-g1.3} \geq VF_{w1.1-g0.2}$
	(e)	check calculated value is consistent (y-direction): $VF_{w22.1-g5.6} > VF_{w22.1-g4.6} \geq VF_{w22.1-g6.6} \geq VF_{w22.1-g4.7} \geq VF_{w22.1-g6.7}$
$VF_{gi\to wj}$		check consistency of $VF_{gi\to wj}$ and $VF_{wi\to gj}$ for all surfaces: $VF_{gi\to wj} = VF_{wi\to gj} \cdot 6/9$ (since $A_w = 6$ and $A_g = 9$)
$VF_{w\to s}$		check consistency: $(1 - VF_{wi-s}) = \sum VF_{wi\to gj} + \sum VF_{wi\to wj}$ for all i
$VF_{g\to s}$		check consistency: $(1 - VF_{gi-s}) = \sum VF_{gi\to wj}$ for all i

Table J.3: Performed tests for high terraced building (Figure J.2b). See text for the notation of $VF_{wi\to wj}$ and $VF_{gi\to wj}$.

Target VF	Test	Description (Target : result)
IH1		Fulfils tests IS2 to IS5 and IS1b to IS1f (when changing the numbering of the lowest model level) but fails IS1a, since surfaces of the uppermost row of the terraced building are also visible
IH2		shading algorithm: Only upper most row is visible from 13.1 and 14.1 (centre row between 2 m and 4 m is not visible). Reason: slope between surfaces is $\frac{2}{15}$ and distance to scalar grid point at 6.3 (or 6.4) is 7.5 and therefore the beam touches the top border of the cell
IHn1		check consistency of $VF_{gi\to wj}$ and $VF_{wi\to gj}$: since size of grid cell is different in non-uniform grid (grid spacing is between 3 and 4) for all surfaces it is true that $VF_{gi\to wj} = VF_{wi\to gj} \cdot i$ where i is either 6/9, 8/9, 6/12 or 6/16

J.2 Validation of the extensions for derivation of thermal indices

Similarly to the surface-to-surface view factors both tests against known values for person-to-surface view factors and tests for an idealised domain are performed. This ensures that both the calculation of the view factors is correctly implemented and the correct inputs are used in GRIMASK.

The view factor tests can be performed using GRIMASK by selecting the relevant module. The tests compare the calculated view factors for both vertical and horizontal surfaces to those presented in the diagrams in Fanger (1970) for specific combinations of person-to-surface distance and surface size. To test the correct derivation of input parameters for a realistic GRIMASK domain, the idealised domain of the surface-to-surface view factors (Figure J.2a) is used. The performed tests are summarised in Table J.4.

The results indicate that for IS1 and IS2 all values lie in the desired ranges.

Table J.4: Validation test cases for the view factor calculation for person-to-surface view factors $VF_{p\to i}$ for an idealised domain with small buildings (Figure J.2a). Tests are performed for all grid cells in the model domain that meet the described criteria.

Test		Description
`IS1` (VF_{p2w})	(a)	a quarter of the view factor half a grid cell apart from the wall ($VF_{p2w,0.5}$) is between $0.036 \leq 0.25 \cdot VF_{p2w,0.5} \leq 0.039$ (as read from Fanger (1970)) for vertical walls and between $0.048 \leq 0.25 \cdot VF_{p2w,0.5} \leq 0.05$ for roofs
	(b)	for the view factor to the vertical wall grid cell next to the person (e.g. blue grid cell 1 in Figure 5.23, $VF_{p2w,0.5+1}$): $0.05 \leq 0.5 \cdot VF_{p2w,0.5+1} + 0.25 \cdot VF_{p2w,0.5} \leq 0.053$ for vertical walls
`IS2` (VF_{p2g})		for $VF_{p2g,0.5}$ (defined as in `IS1`) the following is fulfilled: $0.048 \leq 0.25 \cdot VF_{p2g,0.5} \leq 0.05$

Appendix K

Table K.1: Parameterisations, numerical schemes and other settings applied for the simulations in Chapter 6. Boundary condition is abbreviated BC.

Parameter	Parameterisation / Numerical Scheme
Advection	Momentum: Adam-Bashforth in time, centred differences in space, scalar quantities: Advection with flux correction method (first order upstream in space with artificial diffusion) (Schlünzen et al., 2012b; Salim et al., 2018)
Diffusion	Prandtl-Kolmogorov closure based on TKE (Salim et al., 2018), Numerical scheme: horizontally and vertically: Adam-Bashforth in time, centred differences in space (Schlünzen et al., 2012b)
Pressure solver	BiCGSTAB (Maximum residuum 10^{-3}, maximum iterations (200) (Salim et al., 2018)
Sub-grid scale surface cover effects	Parameter averaging method (Schlünzen et al., 2012b)
Filter	Generally no filter, 7-points filter for `e220v0bb_18` and `e220v0bb_62` (Chapter 6, Appendix O)
BC: momentum (lateral)	Open (radiative) boundary conditions: Normal wind components: direct calculation as far as possible; parallel wind components: zero gradient
BC: momentum (bottom)	Horizontal wind: no slip; vertical wind: zero
BC: momentum (top)	Absorbing layers using a Rayleigh damping term: Normal wind components: large-scale values prescribed; parallel wind components: zero gradient
BC: temperature/ humidity (lateral, top)	No flux across boundary: zero gradient
BC: temperature/ humidity (bottom)	Budget equation (Section H.5)

Parameter	Parameterisation / Numerical Scheme
Clouds / Precipitation	Calculation is switched off

Table K.2: Setting for the calculation of surface temperature of buildings (Eq. (5.5)).

Parameter	Value
wall thickness (D)	0.3 m
thermal resistance of outer facade at inner building wall (R_{si})	0.17 $\mathrm{K\,m^2\,W^{-1}}$
thermal resistance of outer facade (R_{se})	0.04 $\mathrm{K\,m^2\,W^{-1}}$
volumetric heat capacity of the building wall (c_w)	1000 $\mathrm{J\,m^{-3}\,K^{-1}}$
Emissivity of the walls	0.95
Albedo of the walls (a_w)	0.15
U-value (U)	1 $\mathrm{W\,m^{-2}\,K^{-1}}$
heat transfer coefficient of the building wall (C)	0.962 $\mathrm{W\,m^{-2}\,K^{-1}}$
room air temperature (T_{room})	294 K

Appendix L

Table L.1: Studies included in the literature review on the influence of urban water surfaces.

Reference	Site	Type of water surface	Method	Impact
Ashie et al. (2006)	Tokyo, Japan	River	CFD (5 m), 31.07.2005	Distance 100 - 200 m, 1–2 K (air temperature)
Broadbent et al. (2017)	Adelaide, Australia	Several	Measurements	On average -1.8 cooling of daily maximum temperature, Distance 50 m, PET non linear relationship with water fraction
Chen et al. (2009)	Guangzhou, China	Pond /small Lake	ENVI-met (5 m) + observations, July 2007	Average cooling 1.3 K, 25 % less frequent of $T > 35$ K
Hathway and Sharples (2012)	Sheffield, UK	Small River	Measurements 24.04. to 12.08.2010	Distance 30 m, about 1–2 K (air temperature)
Heusinkveld et al. (2014)	Rotterdam, Netherlands	River	Measurements (also mobile on tropical day 06.08.2009)	During night: Observation at water side comparable to observations in city centre; during day: comparable to rural sites
Ishii et al. (1991)	Fukuoka, Japan	Large pond	Measurements	Cooling especially in the afternoon, less than 400 m, up to 3 K (air temperature)

Reference	Site	Type of water surface	Method	Impact
Katayama et al. (1991)	Fukuoka, Japan	Sea, river	Measurements, August 1991	Cooling due to interaction of sea breeze and river
Kim et al. (2008)	Seoul, Korea	River	Measurements summer 2003, 2004, 2005	Steam restoration lead to a 0.4 K cooling (air temperature)
Li and Yu (2014)	Chongqing, China	Lake	Measurements, July-August 2009 and 2010	Maximum cooling 3 K (air temperature)
Lopes et al. (2011)	Funchal, Madeira, Portugal	Sea	Measurements, May to October 2006	Ventilation paths for sea breezes; PET reduction
Manteghi et al. (2015)	Malacca, Malaysia	River	Measurements, June 2014	3–4 K cooling (air temperature)
Martins et al. (2016)	Toulouse, France	Pond	ENVI-met (3 m, 21.06., summer day	6 K cooling (air temperature); 2 K (PET) if fountains are included
Masiero and Souza (2013)	São José do Rio Preto, Brazil	Lake	Measurements	2 K cooling (air temperature), 7 $\mathrm{g\,m^{-3}}$ more humid, up to 1000 m
Mou and Fahim (2013)	Dhaka, Bangladesh	River	Measurements indoor, August	Near river, smaller T_a, larger RH, larger FF
Müller et al. (2013)	Oberhausen, Germany	Idealised	Measurements, ENVI-met (2 m), 10.7.2010	Distance at least 100 m, may be larger but restricted model area; 0.5 K cooling (PET)

Reference	Site	Type of water surface	Method	Impact
Murakawa et al. (1991)	Hiroshima, Japan	River	Measurements, specific dates each season	about 200 m, larger in some cases; 3–5 K cooling (air temperature)
Robitu et al. (2006)	Nantes, France	Pond	CFD, 15 July	Trees and pond together provide larger thermal comfort
Saaroni and Ziv (2003)	Tel Aviv, Israel	Pond (several hundred meter wide	Measurements, May / June 2000	1 K cooling (air temperature), more humidity, 0.8 to 1.1 K cooling (HSI), distance 40 m
Schatz and Kucharik (2014)	Madison, Wisconsin, US	Lake	Measurements (March 2012 – October 2013)	Lake effect up to 600 m, Almost always warming at night
Syafii et al. (2017)	Saitama Prefecture, Japan	Ponds, idealised city	Outdoor scale model	1.6 K cooling (PET)
Žuvela-Aloise et al. (2016)	Vienna /idealised, Austria	Several	MUKLIMO_3 100 m resolution, Cuboid method	1 K cooling (maximum, air temperature)

Appendix M

Preface

Figure M.4 and parts of this analysis have been published in **Wiesner S., Bechtel B., Fischereit J., Gruetzun V., Hoffmann P., Leitl B., Rechid D., Schlünzen K. H., and Thomsen S.** (2018): Is It Possible to Distinguish Global and Regional Climate Change from Urban Land Cover Induced Signals? A Mid-Latitude City Example. *Urban Science*, volume 2(1). ISSN 2413-8851. `http://dx.doi.org/10.3390/urbansci2010012` under the terms of the Creative Commons Attribution 4.0 International License (`http://creativecommons.org/licenses/by/4.0/`). I had the idea for this analysis and performed the calculations. For this thesis the font size of the figure has been increased.

Bio-climatic conditions in Hamburg

Throughout this thesis the city of Hamburg is used as an exemplary city for the different investigations. This appendix characterises the thermal bio-climatic conditions in Hamburg, to assess, whether and what kind of thermal stress occurs in Hamburg. Therefore, this section only deals with thermal aspects of the climate in Hamburg, characterisation of other climatological parameters can be found in Riecke and Rosenhagen (2010); Schlünzen et al. (2010); von Storch and Claussen (2011).

The metropolitan area of Hamburg is influenced from the maritime climates of the North and Baltic Sea, which due to their high heat capacity balance out temperature extremes on an annual basis (Riecke and Rosenhagen, 2010). Since the dominant wind direction is south west to west (Schlünzen et al., 2010), the maritime air is transported towards the city. Towards east and south the climate becomes more continental (Riecke and Rosenhagen, 2010). The region is relatively flat except for the Harburger Berge with 100 m above sea level (von Storch and Claussen, 2011).

In the years between 1891 and 2007 the temperature in Hamburg rose about on average 0.07 K/decade with recently increasing rates (Schlünzen et al., 2010). This is also reflected in the number of heat days ($T_{\mathrm{max}} \geq 30°\mathrm{C}$) and summer days ($T_{\mathrm{min}} \geq 20°\mathrm{C}$) per year at the station of the German Meteorological Service (DWD) Fuhlsbüttel (Figure M.1): the number of heat days increased by one day in 33 years in Fuhlsbüttel based on a linear trend analysis. However, from the standard deviations especially for the number of heat days, it becomes clear that a high temporal variability exist from year to year. This variability is much higher than the variability between the different stations in and around Hamburg (Figure M.2). Averaged over the entire measurement periods (Table M.1) and all stations an average number of 4 heat days and 0.4 tropical nights have been recorded. The number of tropical nights is much lower compared to the number of heat days, indicating that mostly relieve from day time heat stress can be found during the night. An exception is the inner city station Sankt Pauli (Figure M.2), where on average more tropical nights have been measured. This might be caused by the urban heat island effect as discussed in more detail in (Schlünzen et al., 2010; Arnds et al., 2015).

(a)

(b)

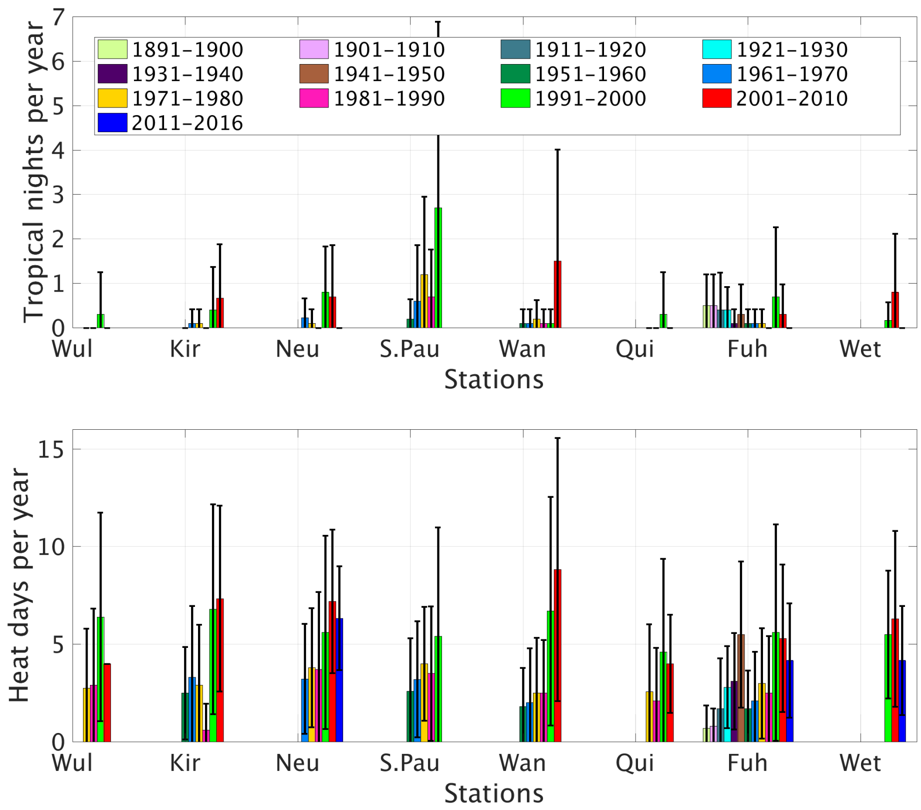

Figure M.1: Average number of tropical nights ($T_{\mathrm{min}} \geq 20$ °C, a) and heat days ($T_{\mathrm{max}} \geq 30$ °C, b) per year at different stations in and around Hamburg (Figure M.2). Error bars indicate standard deviation. Please note the different scales.

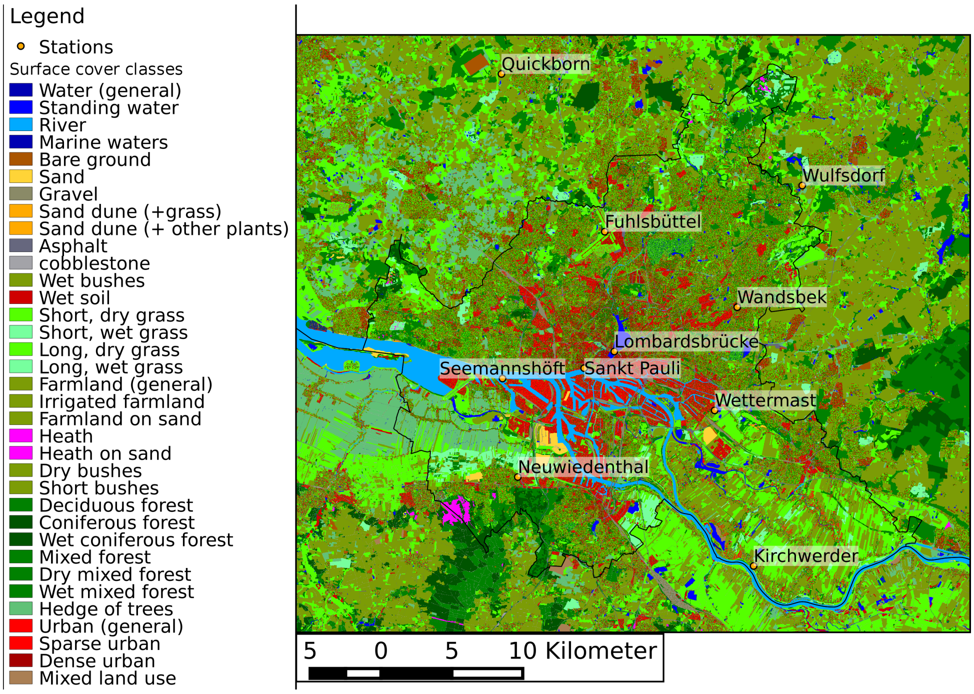

Figure M.2: Map of surface cover classes in and around Hamburg and location of measurement stations (orange dots, Table M.1) based on ATKIS Basis Digitales Landschaftsmodell von Niedersachsen, Schleswig Holstein, Hamburg, Mecklenburg Vorpommern.

Table M.1: Measurement periods of daily minimum and maximum temperature for different stations in and around Hamburg. Stations operated by the German Meteorological Service are indicated by DWD and stations operated by the University of Hamburg by MI-UHH.

Station	Begin	End
Ahrensburg Wulfsdorf (DWD)	01.01.1973	31.12.2001
Hamburg Kirchwerder (DWD)	01.01.1951	31.12.2006
Hamburg Neuwiedenthal (DWD)	01.05.1962	31.12.2016
Hamburg Sankt Pauli (DWD)	01.01.1956	29.02.2000
Hamburg Wandsbek (DWD)	01.01.1951	31.12.2006
Quickborn (DWD)	01.12.1974	31.12.2007
Hamburg Fuhlsbuettel (DWD)	01.01.1891	31.12.2016
Hamburg Wettermast (MI-UHH)	27.03.1995	21.07.2016

Compared to heat-related indicators, the number of cold-related indicators, e.g. ice days ($T_{\max} < 0$ °C) and frost days ($T_{\min} < 0$ °C), is much larger (Figure M.3). This indicates that cold-stress is in Hamburg as least as important as heat-stress. However, the warming trend found for the heat-related indicators is also apparent in the cold-related indicators: a linear trend analysis for Fuhlsbüttel suggests a decreasing trend for ice days (-1 day/38 years) and a corresponding increasing trend in frost days (+1 day/23 years). A thorough time series analysis is required for more detailed conclusions on trends, including an analysis of longer averaging periods. Additionally, the trend analysis should be viewed with care as measurements prior about 1945 are uncertain (von Storch and Claussen, 2011).

(a)

(b)

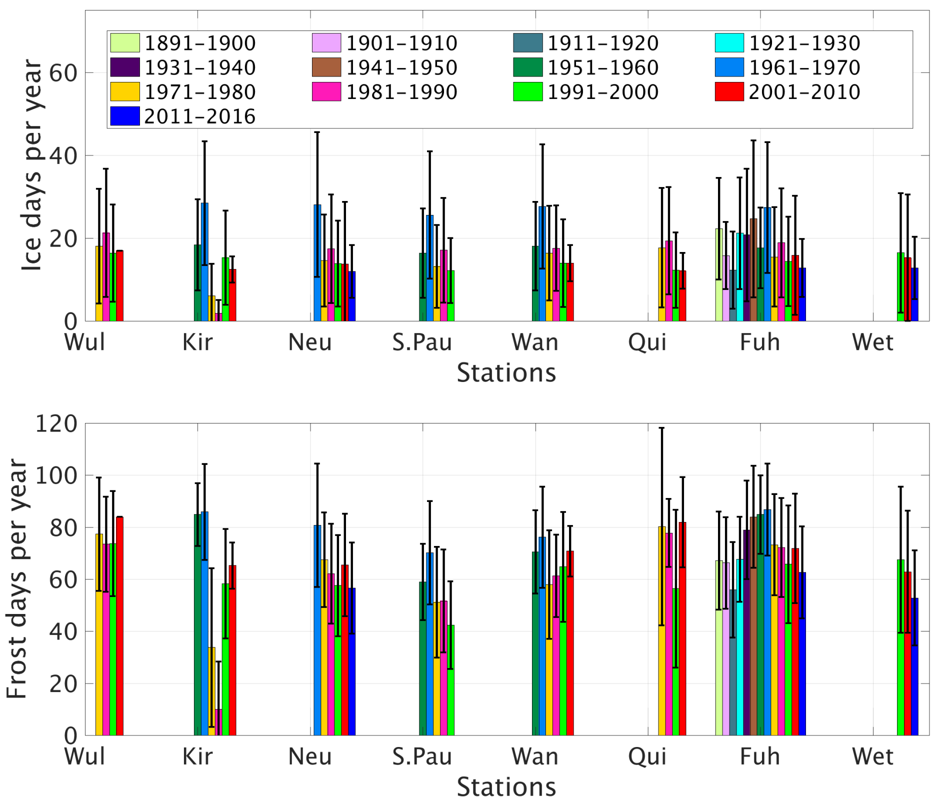

Figure M.3: Same as Figure M.1 but for ice days ($T_{\max} < 0$ °C, a) and frost days ($T_{\min} <$ 0 °C, b).

Although the analysis on threshold-days give a first impression of the frequency of hot and cold stress experienced in Hamburg, air temperature alone is a bad indicator for thermal stress since the human body reacts to the combination of heat, moisture, wind and radiative fluxes (Section 2.2.1). Therefore, a thermal index can better describe the amount of thermal stress experienced. Therefore, an additional bio-climatic analysis using the thermal index Physiologcial Equivalent Temperature (PET, Chapter 2) is used. With its fixed clothing ensemble it is well suited to compare different time periods. For the interpretation of the results, one has to keep in mind that the clothing insulation of 0.9 clo corresponds to indoor office clothing and is therefore higher than the average clothing insulation in summer and lower than in winter.

Measured hourly data of temperature, wind, humidity and cloudiness together with the Linke turbidity factor in Fuhlsbüttel between 1950 to 2015 have been used to estimate the mean radiant temperature (T_{mrt}) using a Fortran program by Staiger (2016) as described in Chapter 4. Using the derived T_{mrt} values and the other measured meteorological variables, hourly PET have been calculated between 1950 and 2015 using the VDI-version of PET (Section 4.2.1). Based on that data, Figure M.4 shows two 30-years-periods (1956–1985 (a) and 1986–2015 (b)) of PET-class-frequencies during daytime (06:00 to 22:00). During winter (December to February) mostly frosty to cold conditions are experienced (Table 2.4 with the frosty class added below the lowest existing class). In summer (June to August) during the day slightly cool to hot conditions dominate both between 1956–1985 as well as during 1986–2015. The difference plot in frequency of PET(1986-2015)-PET(1956-1985) per class shows that in almost every month the frequency of warmer PET classes increased for the recent 30-years-period compared to the former period, with significant changes based on the Chi-squared test indicated by stars. Smallest changes are experienced for June, September and October.

The changes in frequencies of PET-classes, reflect the trend analysis of the threshold days: on average cold to cool conditions are found in Hamburg with a trend to warmer PET-classes in recent years and periods with strong heat stress in summer. Since an indoor clothing ensemble is used for PET some of the uncomfortable cold conditions can be attributed to unsuitable clothing in these situations. In Chapter 4 an increase in clothing during cold conditions was shown to result in slightly higher PET values.

The changes in PET frequencies are caused by frequency changes in the input variables of PET (Figure M.5). Air temperatures (a) and mean radiant temperatures (d) increased in the period 1986–2015 compared to 1956–1985 in almost all months. Since PET is most sensitive to these variables (Chapter 4), those changes most likely dominant over the changes in vapour pressure (b). PET is also sensitive to wind speed (Chapter 4). On

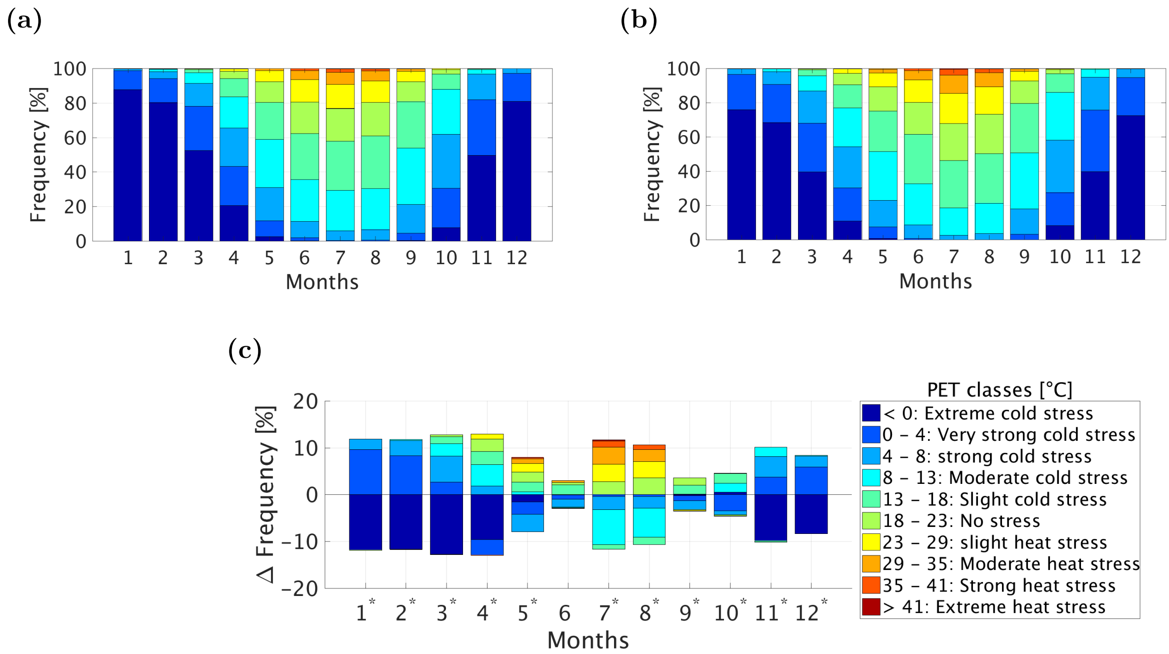

Figure M.4: Frequency of different PET classes during daytime (06:00 to 22:00) for 1956–1985 (a) and 1986–2015 (b) and changes in frequency of different classes between the two periods (PET(1986–2015)-PET(1956–1985)) (c). Significant changes as estimated from the Chi-squared test with a significance level of 5 % are indicated by '*' at the according months. Description of thermal stress classes can be found in 2.4.

average wind speed decreased from March to September (c) contributing to higher PET values.

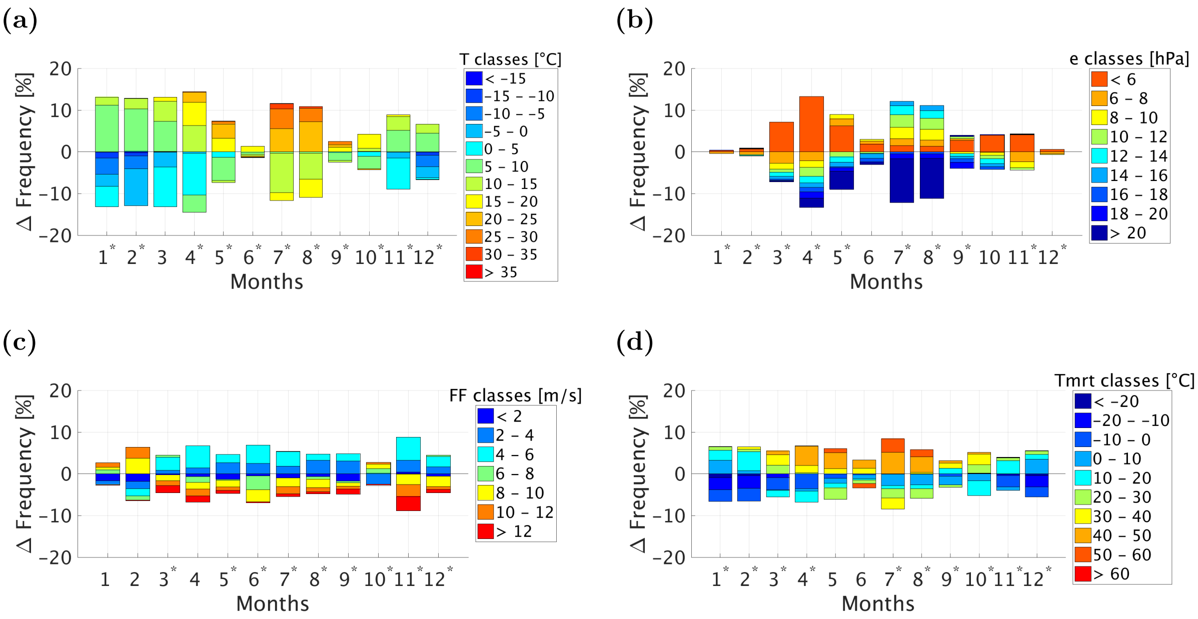

Figure M.5: Same as Figure M.4c but for air temperature (a), water vapour pressure (b), wind speed (c) and mean radiant temperature (d).

Overall, the summer thermal bio-climate in Hamburg can be summarised as mild with a few heat stress situations. The trend analysis of the threshold days and of the changes in PET-frequency for the suburban station Fuhlsbüttel indicated that warmer conditions have been experienced in recent years. Due to the limited measurement records at other stations (Table M.1) such an analysis was not performed for the stations closer to the city centre (Figure M.2), although at least the number of tropical nights (Figure M.1a) indicated higher frequencies in the inner city. For the future, regional climate projections indicate an increase of up to 1.5 tropical nights and up to 4 heat days per year for 2050 for the moderate RCP4.5 scenario without change in urban land use (Trusilova and Riecke, 2015). An additional change in surface cover from vegetation to buildings shows an additional increase in mean temperature especially for a dry summer month (Trusilova and Riecke, 2015). Furthermore the number of days with urban heat island and the duration and intensity of heat waves are projected to increase until the end of the century (Hoffmann et al., 2016; Trusilova and Riecke, 2015). Therefore, despite the mild temperatures in Hamburg it is worth to investigate heat stress related situations in summer.

Appendix N

Initial meteorological conditions for the simulations to test the sensitivity of the influence of water surfaces to meteorological conditions (Table N.1) and to urban morphology Table N.2.

Table N.1: Initial conditions for the simulations to test the sensitivity of the influence of water surfaces to the meteorological conditions with the four sampled inputs for 04:00 LST air temperature ($T_{a,4}$), wind speed in 10 m ($FF_{10,4}$), relative humidity (RH_4) and daily average temperature difference between air and water of daily average values ($\overline{T}_a - \overline{T}_{\mathrm{wat}}$) and the corresponding water temperature (T_{wat}). Additionally the input parameters for the other environmental parameters (ground surface temperature (T_g), stratification in the lowest 300 m ($\partial\Theta/\partial z(0-300)$) and stratification above ($\partial\Theta/\partial z(300-)$)) are given.

No	$T_{a,4}$	$FF_{10,4}$	$\overline{T}_a - \overline{T}_{\mathrm{wat}}$	RH_4	$\overline{T}_w$	T_g	$\partial\Theta/\partial z(0-300)$	$\partial\Theta/\partial z(300-)$
1	17.0	2.2	-1.9	89	26.2	18.1	0.0269	0.0035
2	10.8	2.2	-1.9	89	20.0	18.1	0.0269	0.0035
3	17.0	2.4	-1.9	89	26.2	18.1	0.0269	0.0035
4	17.0	2.2	-0.7	89	25.0	18.1	0.0269	0.0035
5	17.0	2.2	-1.9	79	26.2	18.1	0.0269	0.0035
6	15.6	1.2	-1.2	92	24.1	18.1	0.0269	0.0035
7	14.9	1.2	-1.2	92	23.4	18.1	0.0269	0.0035
8	15.6	1.0	-1.2	92	24.1	18.1	0.0269	0.0035
9	15.6	1.2	3.0	92	19.9	18.1	0.0269	0.0035
10	15.6	1.2	-1.2	98	24.1	18.1	0.0269	0.0035
11	9.7	0.8	1.3	83	15.7	18.1	0.0269	0.0035
12	12.3	0.8	1.3	83	18.3	18.1	0.0269	0.0035
13	9.7	1.2	1.3	83	15.7	18.1	0.0269	0.0035
14	9.7	0.8	0.3	83	16.6	18.1	0.0269	0.0035
15	9.7	0.8	1.3	93	15.7	18.1	0.0269	0.0035
16	13.1	2.0	5.2	96	15.1	18.1	0.0269	0.0035
17	17.5	2.0	5.2	96	19.5	18.1	0.0269	0.0035
18	13.1	3.4	5.2	96	15.1	18.1	0.0269	0.0035
19	13.1	2.0	0.0	96	20.4	18.1	0.0269	0.0035

No	$T_{a,4}$	$FF_{10,4}$	$\overline{T}_a - \overline{T}_{\text{wat}}$	RH_4	$\overline{T}_w$	T_g	$\partial\Theta/\partial z(0-300)$	$\partial\Theta/\partial z(300-)$
20	13.1	2.0	5.2	84	15.1	18.1	0.0269	0.0035
21	17.4	2.7	2.2	90	22.5	18.1	0.0269	0.0035
22	7.0	2.7	2.2	90	12.1	18.1	0.0269	0.0035
23	17.4	0.7	2.2	90	22.5	18.1	0.0269	0.0035
24	17.4	2.7	-3.4	90	28.0	18.1	0.0269	0.0035
25	17.4	2.7	2.2	82	22.5	18.1	0.0269	0.0035
26	16.2	0.7	1.1	80	22.4	18.1	0.0269	0.0035
27	12.6	0.7	1.1	80	18.9	18.1	0.0269	0.0035
28	16.2	1.9	1.1	80	22.4	18.1	0.0269	0.0035
29	16.2	0.7	-1.4	80	24.9	18.1	0.0269	0.0035
30	16.2	0.7	1.1	87	22.4	18.1	0.0269	0.0035
31	15.6	0.9	-0.4	90	23.3	18.1	0.0269	0.0035
32	11.2	0.9	-0.4	90	18.9	18.1	0.0269	0.0035
33	15.6	0.4	-0.4	90	23.3	18.1	0.0269	0.0035
34	15.6	0.9	-0.4	90	23.2	18.1	0.0269	0.0035
35	15.6	0.9	-0.4	91	23.3	18.1	0.0269	0.0035
36	14.3	1.8	1.8	83	19.8	18.1	0.0269	0.0035
37	11.6	1.8	1.8	83	17.1	18.1	0.0269	0.0035
38	14.3	3.2	1.8	83	19.8	18.1	0.0269	0.0035
39	14.3	1.8	0.2	83	21.4	18.1	0.0269	0.0035
40	14.3	1.8	1.8	94	19.8	18.1	0.0269	0.0035
41	8.9	1.5	0.7	72	15.5	18.1	0.0269	0.0035
42	14.1	1.5	0.7	72	20.7	18.1	0.0269	0.0035
43	8.9	3.9	0.7	72	15.5	18.1	0.0269	0.0035
44	8.9	1.5	-0.1	72	16.3	18.1	0.0269	0.0035
45	8.9	1.5	0.7	82	15.5	18.1	0.0269	0.0035
46	17.9	2.7	0.7	76	24.5	18.1	0.0269	0.0035
47	13.5	2.7	0.7	76	20.1	18.1	0.0269	0.0035
48	17.9	2.1	0.7	76	24.5	18.1	0.0269	0.0035
49	17.9	2.7	-2.7	76	27.9	18.1	0.0269	0.0035
50	17.9	2.7	0.7	78	24.5	18.1	0.0269	0.0035
51	16.4	1.4	-0.9	86	24.6	18.1	0.0269	0.0035
52	19.1	1.4	-0.9	86	27.3	18.1	0.0269	0.0035

No	$T_{a,4}$	$FF_{10,4}$	$\overline{T}_a - \overline{T}_{\text{wat}}$	RH_4	$\overline{T}_w$	T_g	$\partial\Theta/\partial z(0-300)$	$\partial\Theta/\partial z(300-)$
53	16.4	1.6	-0.9	86	24.6	18.1	0.0269	0.0035
54	16.4	1.4	2.5	86	21.2	18.1	0.0269	0.0035
55	16.4	1.4	-0.9	85	24.6	18.1	0.0269	0.0035
56	7.3	1.6	-0.9	63	15.4	18.1	0.0269	0.0035
57	14.8	1.6	-0.9	63	23.0	18.1	0.0269	0.0035
58	7.3	0.6	-0.9	63	15.4	18.1	0.0269	0.0035
59	7.3	1.6	-2.3	63	16.9	18.1	0.0269	0.0035
60	7.3	1.6	-0.9	88	15.4	18.1	0.0269	0.0035

Table N.2: Initial conditions for the simulations to test the sensitivity of the influence of water surfaces to urban morphology with the four sampled inputs for 04:00 LST air temperature ($T_{a,4}$), wind speed in 10 m ($FF_{10,4}$), relative humidity (RH_4) and daily average temperature difference between air and water of daily average values ($\overline{T}_a - \overline{T}_{\text{wat}}$) and the corresponding water temperature (T_{wat}). Additionally the input parameters for the other environmental parameters (ground surface temperature (T_g), stratification in the lowest 300 m ($\partial\Theta/\partial z(0-300)$) and stratification above ($\partial\Theta/\partial z(300-)$)) are given. Since the conditions are a subset of all simulated meteorological conditions, numbers (No) refer to numbers in Table N.1.

No	$T_{a,4}$	$FF_{10,4}$	$\overline{T}_a - \overline{T}_w$	RH_4	$\dot{\overline{T}}_w$	$\overline{T}_g$	$\partial\Theta/\partial z(0-300)$	$\partial\Theta/\partial z(300-)$
59	7.3	1.6	-2.3	63	16.9	18.1	0.0269	0.0035
20	13.1	2.0	5.2	84	15.1	18.1	0.0269	0.0035
57	14.8	1.6	-0.9	63	23.0	18.1	0.0269	0.0035

Appendix O

In two simulations (`e220v0bb_18` and `e220v0bb_62`) the stable stratification in combination with high wind speeds lead to numerical instabilities (waves) at about 500 m height at the very beginning of the simulation at about 07:00 LST. During the simulation the waves amplified, leading to very high vertical wind speeds. To avoid these instabilities, two options are tested: (1) increasing the minimal vertical diffusion coefficient from 10^{-4} to 10^{-3} and (2) implementing a 7-point filter for all wind components above two building heights. Two building heights have been chosen to apply the filter only outside of the near field of the buildings (VDI, 2017). Eq. (O.1) indicates the relationship between the unfiltered (ψ) and filtered values ($\ddot{\psi}$) (Schlünzen et al., 2012b):

$$\ddot{\psi}_i = \frac{1}{64}\left(\psi_{i+3} - 6\psi_{i+2} + 15\psi_{i+1} + 44\psi_i + 15\psi_{i-1} - 6\psi_{i-2} + \psi_{i-3}\right) \tag{O.1}$$

Increasing the vertical diffusivity only worked for `e220v0bb_62`. Therefore the 7-point filter simulations are used in the analysis of the impact of water surfaces.

Appendix P

P.1 Hovmöller diagrams for e30v0bb_57

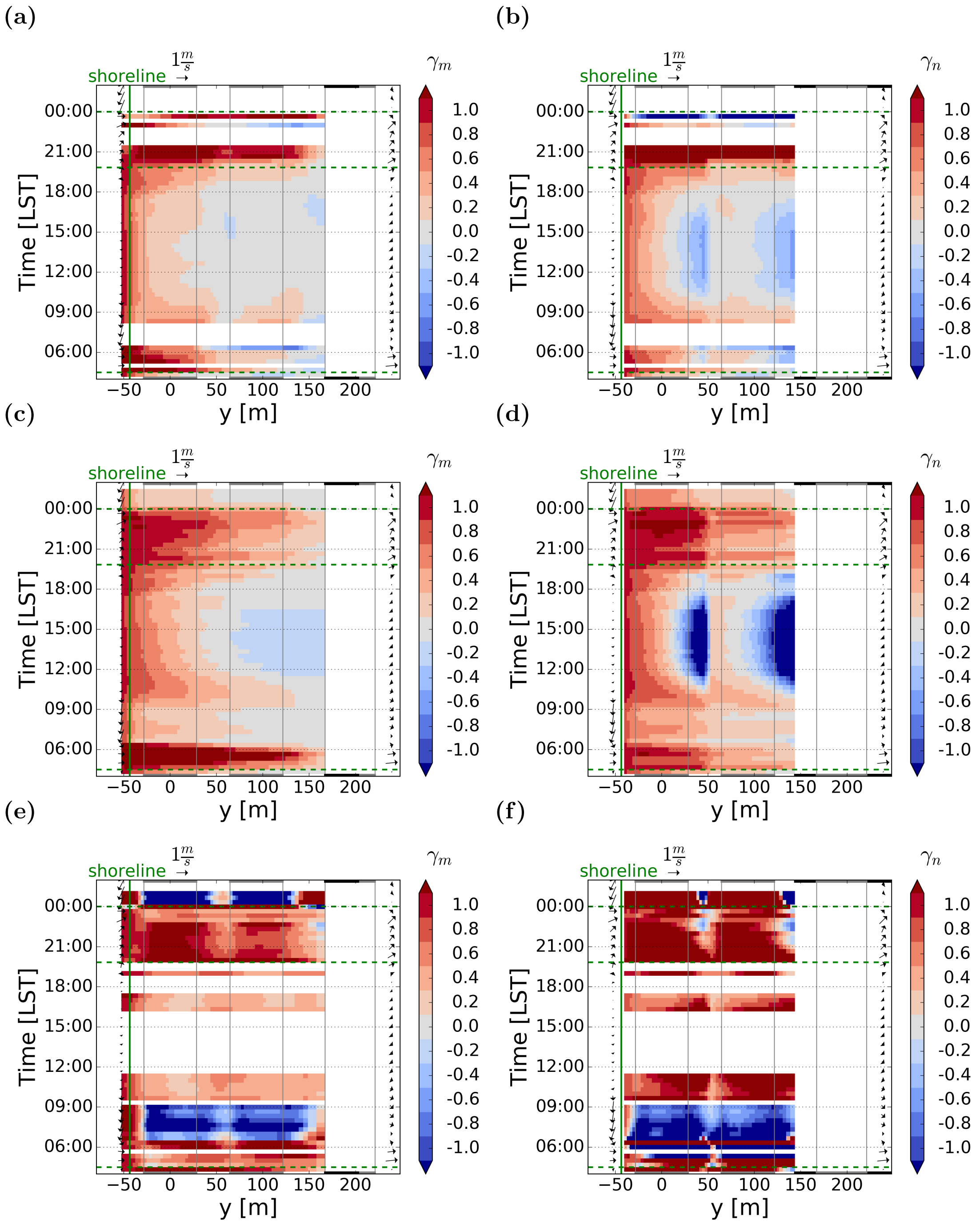

Figure P.1: Same as Figure 6.12 but for canal scenario e30v0bb_57.

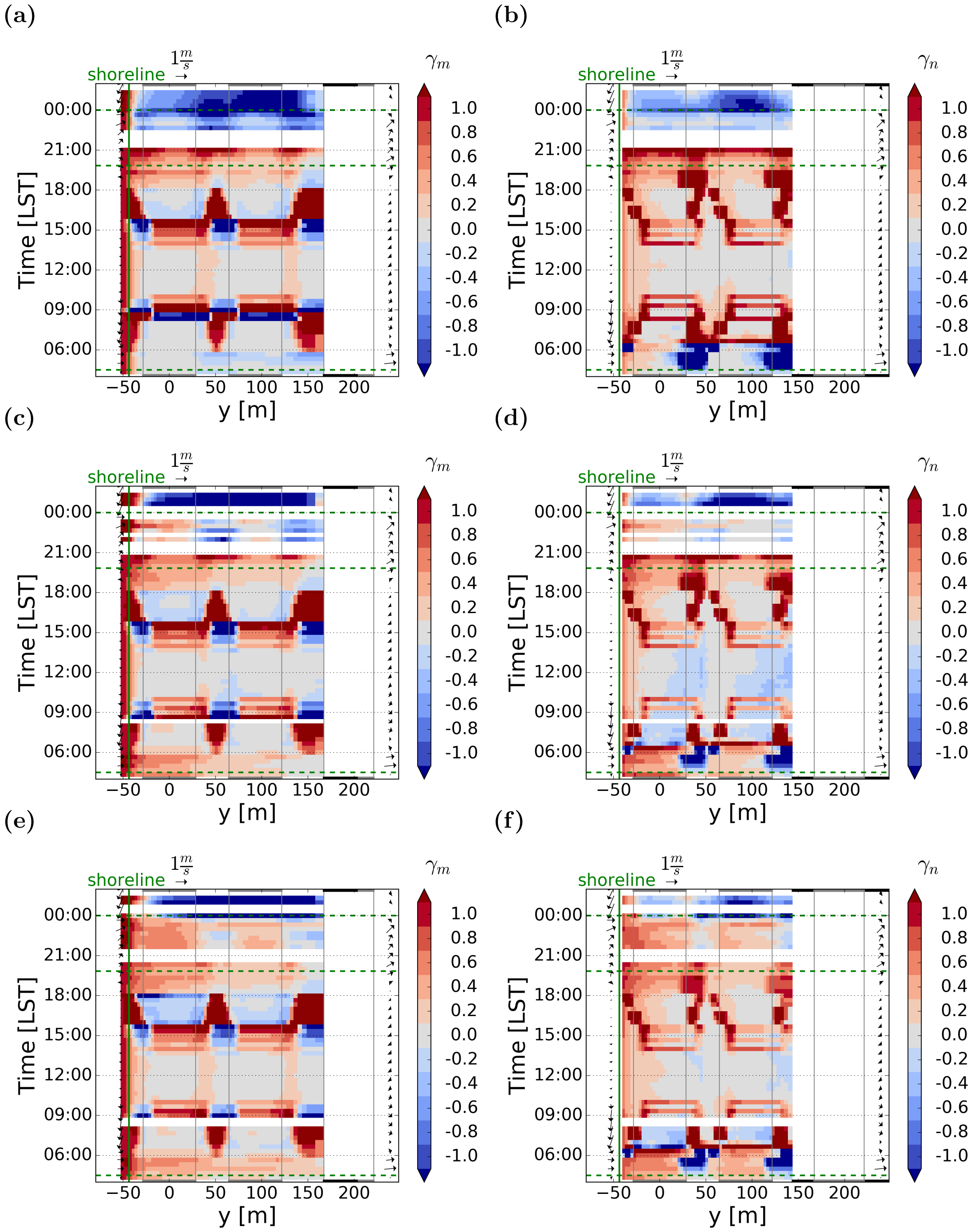

Figure P.2: Same as Figure 6.13 but for canal scenario e30v0bb_57.

P.2 Hovmöller diagrams for the different meteorological situations

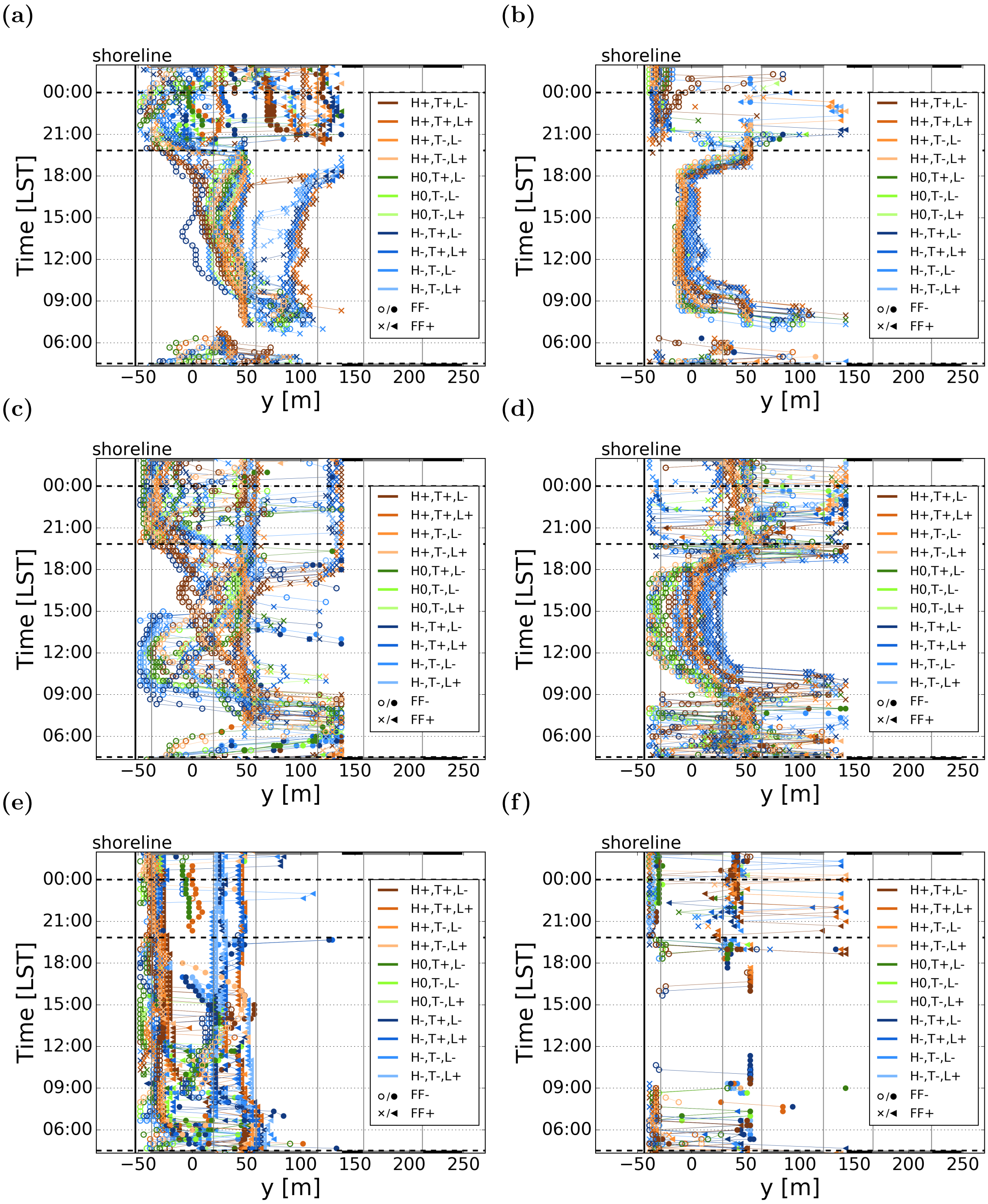

Figure P.3: Same as Figure 6.16 but for (a), (b) air temperature (reproduced from Figure 6.16 for convenience), (c), (d) vapour pressure, (e), (f) wind speed for (a), (c) and (e) for the lake (`e220v0bb`) and (b), (d) and (f) for the canal (`e30v0bb`).

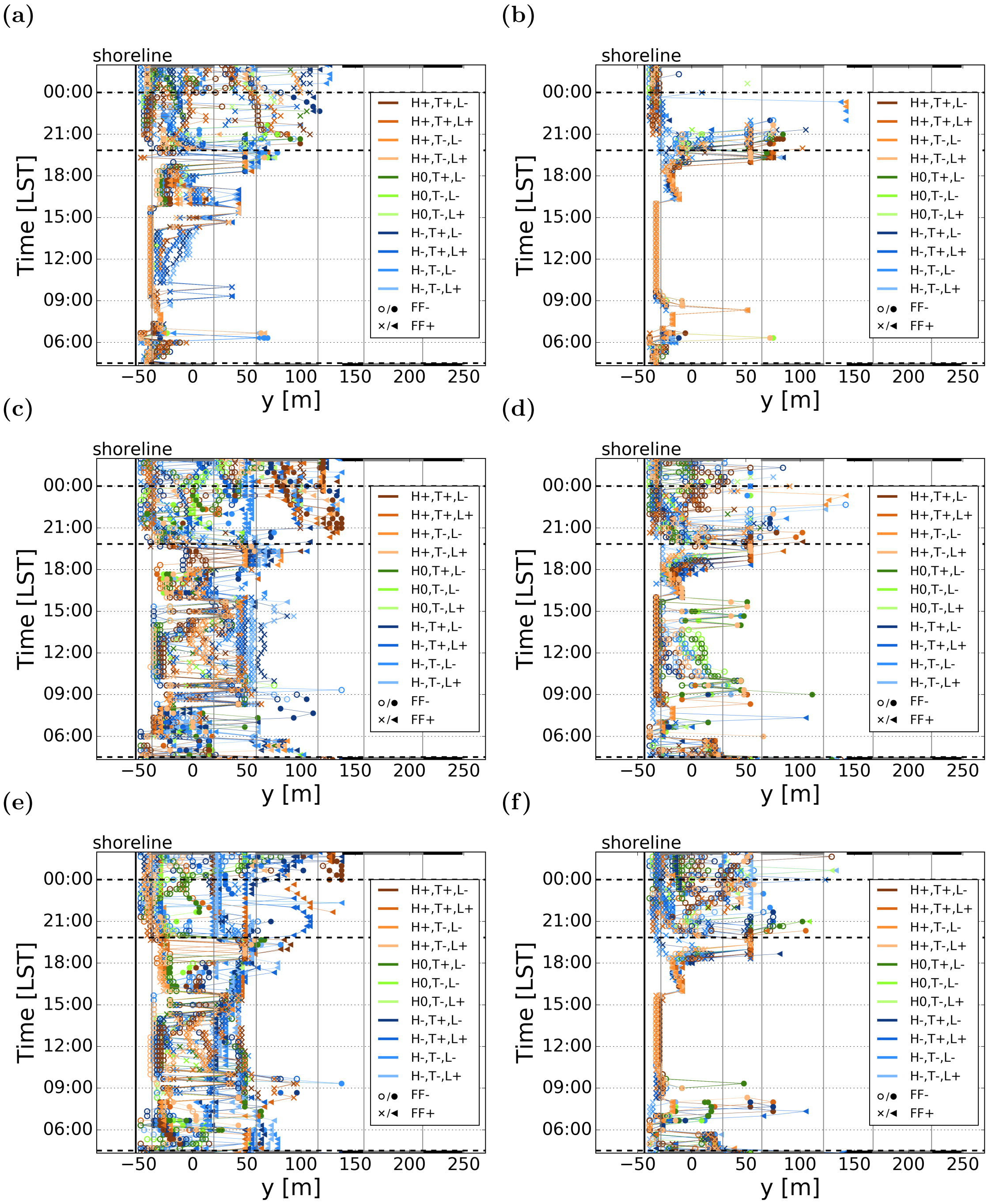

Figure P.4: Same as Figure P.3 but for (a), (b) mean radiant temperature, (c), (d) Physiological Equivalent Temperature, (e), (f) Universal Thermal Climate Index.

P.3 Hovmöller diagrams for magnitude of water influence for different meteorological conditions for the canal scenario

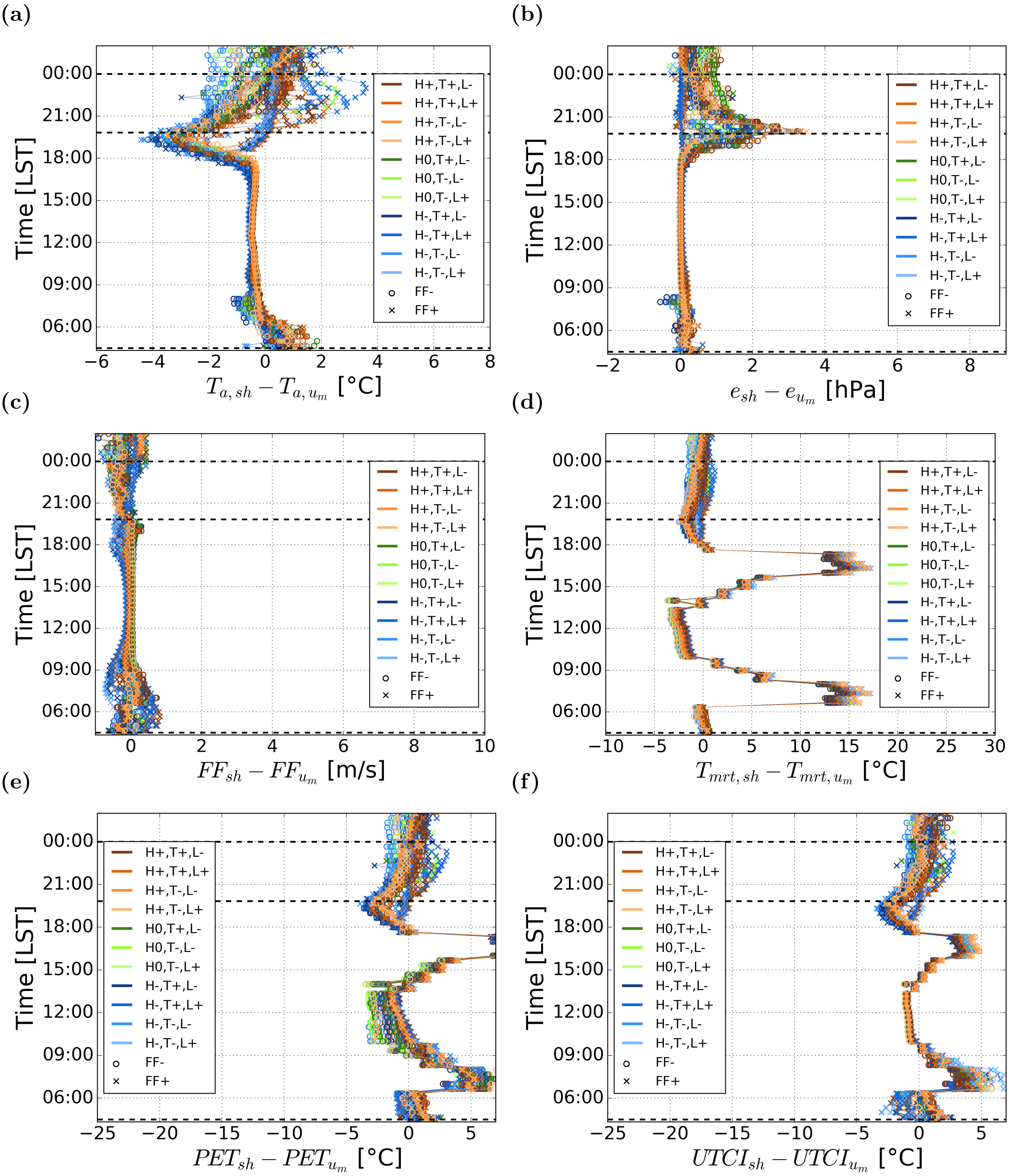

Figure P.5: Same as Figure 6.19 but for canal scenario (`e30v0bb`).

P.4 Hovmöller diagrams for penetration depth of water influence for different morphologies for the canal scenario

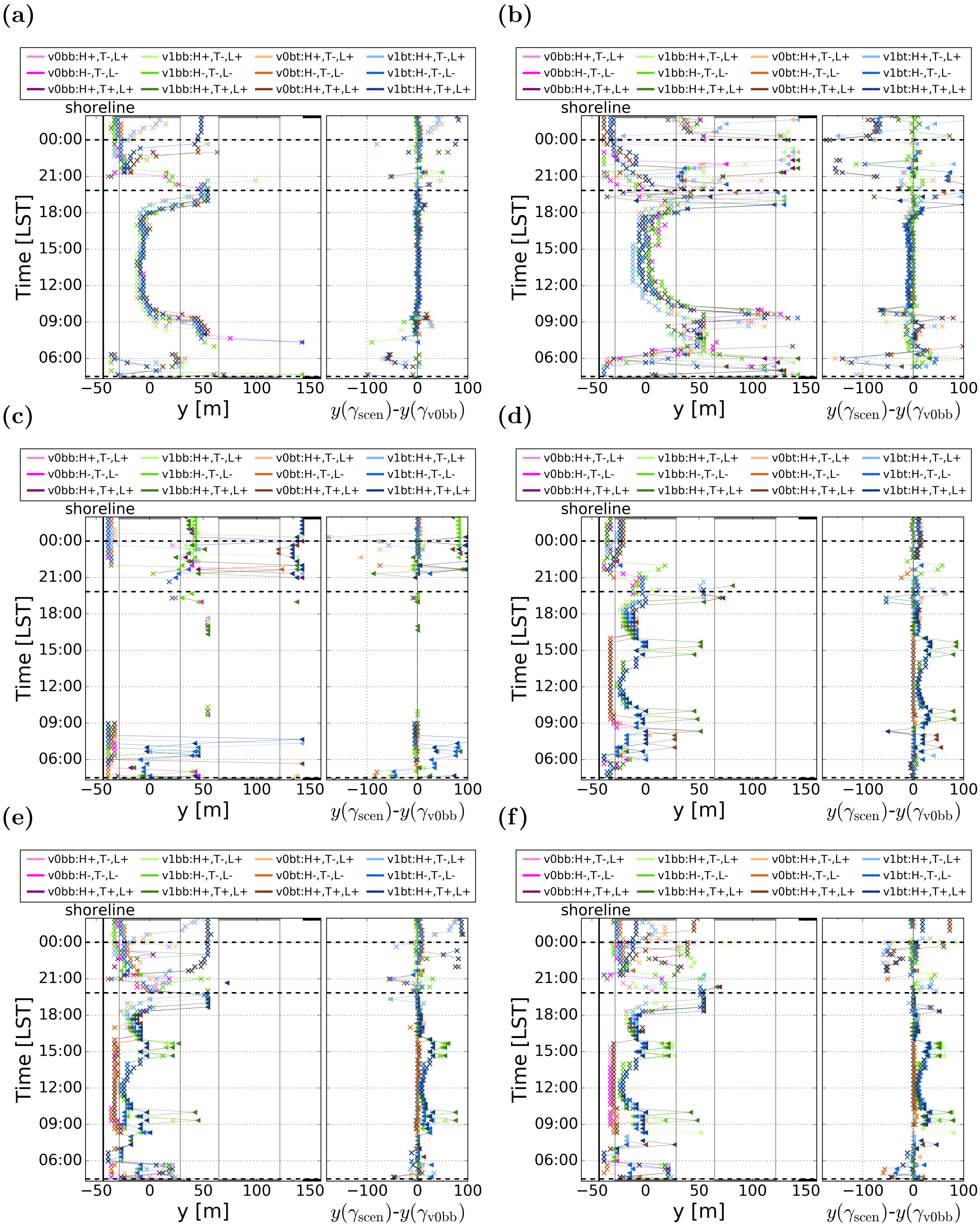

Figure P.6: Same as Figure 6.23 but for the lake scenario e30 for (a) air temperature, (b) vapour pressure, (c) wind speed, (d) mean radiant temperature, (e) Physiological Equivalent Temperature, (f) Universal Thermal Climate Index.

P.5 Hovmöller diagrams for magnitude of water influence at shoreline for different morphologies for the canal scenario

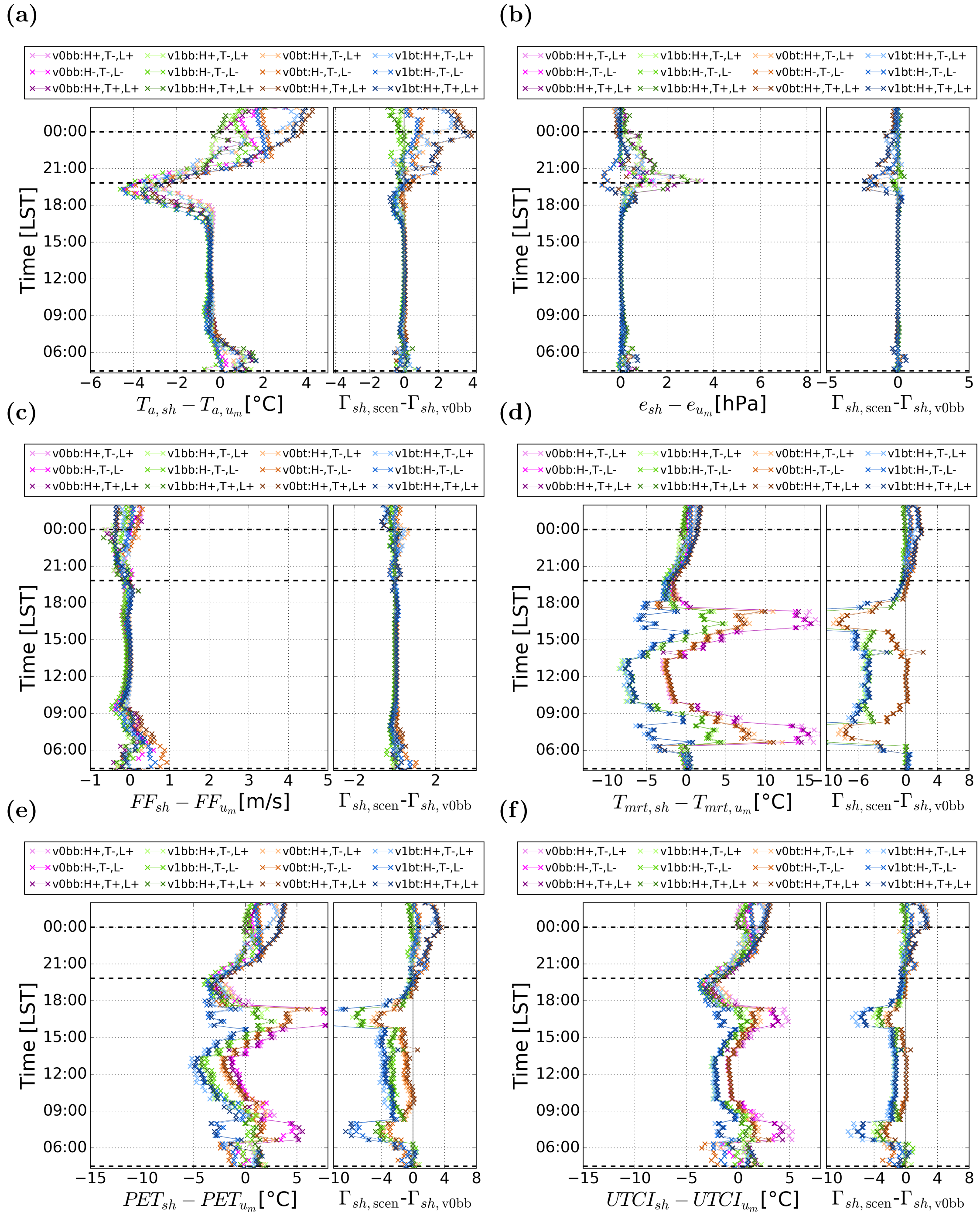

Figure P.7: Same as Figure P.6 but for the magnitude of the water influence at the shoreline, $\Gamma = \chi_{sh} - \chi_{u,m}$.

References

Acero J. A. and Herranz-Pascual K. (2015): A comparison of thermal comfort conditions in four urban spaces by means of measurements and modelling techniques. *Building and Environment*, volume 93(P2):pages 245–257. http://dx.doi.org/10.1016/j.buildenv.2015.06.028.

Adamenko V. N. and Khairullin K. S. (1972): Evaluation of conditions under which unprotected parts of the human body may freeze in urban air during winter. *Boundary-Layer Meteorology*, volume 2(4):pages 510–518. ISSN 1573-1472. http://dx.doi.org/10.1007/BF00821553.

Afanasieva R. (1977): *Hygienic theory of cold protection clothes projection*. Legkaya Industriya. Moscow.

Afanasieva R., Bobrov A., and Sokolov S. (2009): Cold Assessment Criteria and Prediction of Cooling Risk in Humans: The Russian Perspective. volume 47(3):pages 235–241. http://dx.doi.org/10.2486/indhealth.47.235.

Aikimovich N. and Balalla O. (1971): Sultry weathers at the south of Primorye and their influence on human body. *Izvestia ASc USSR, Geography*, volume 4:page 94–100.

Aizenshtat B. (1964): Methods for assessment of some bioclimate indices. *Meteorol Hydrol*, volume 12:pages 9 – 16.

Aizenshtat L. and Aizenshtat B. (1974): Equation for equivalent-effective temperature. *Questions of biometeorology, Hydrometeoizdat, Leningrad*, pages 81 – 83.

Ali-Toudert F. and Mayer H. (2006): Numerical study on the effects of aspect ratio and orientation of an urban street canyon on outdoor thermal comfort in hot and dry climate. *Building and Environment*, volume 41(2):pages 94 – 108. ISSN 0360-1323. http://dx.doi.org/10.1016/j.buildenv.2005.01.013.

Allegrini J., Dorer V., Defraeye T., and Carmeliet J. (2012): An adaptive temperature wall function for mixed convective flows at exterior surfaces of buildings in street canyons. *Building and Environment*, volume 49:pages 55 – 66. ISSN 0360-1323. http://dx.doi.org/10.1016/j.buildenv.2011.09.025.

AMS (American Meteorological Society) (2012): Glossary of Meteorology. https://web.archive.org/web/20170512114004/http://glossary.ametsoc.org/wiki/Bowen_ratio. last accessed, 03.12.2017 .

Andreou E. (2013): Thermal comfort in outdoor spaces and urban canyon microclimate. *Renewable Energy*, volume 55:pages 182 – 188. ISSN 0960-1481. http://dx.doi.org/10.1016/j.renene.2012.12.040.

Arnds D., Böhner J., and Bechtel B. (2015): Spatio-temporal variance and meteorological drivers of the urban heat island in a European city. *Theoretical and Applied Climatology*, pages 1–19. ISSN 1434-4483. http://dx.doi.org/10.1007/s00704-015-1687-4.

Arnfield A. J. (2003): Two decades of urban climate research: a review of turbulence, exchanges of energy and water, and the urban heat island. *International Journal of Climatology*, volume 23(1):pages 1–26. ISSN 1097-0088. http://dx.doi.org/10.1002/joc.859.

Arnoldy I. (1962): *Acclimatization of the man in north and south.* Medgiz, Moscow.

Ashie Y., Komatsu N., Kono T., and Takahashi K. (2005): *Annual Report of the Earth Simulator Center April 2005 – March 2006*, chapter Numerical Simulation of Urban Thermal Environment in the Waterfront Area of Tokyo, pages 83 – 87. Earth Simulator Center.

Ashie Y., Tokairin T., Kono T., and Takahashi K. (2006): *Annual Report of the Earth Simulator Center April 2006 – March 2007*, chapter Numerical Simulation of Urban Heat Island in a Ten-kilometer Square Area of Central Tokyo, pages 45 – 49. Earth Simulator Center.

ASHRAE (American Society of Heating and Air-Conditioning Engineers) (2001): *ASHRAE Handbook: Fundamentals.* Atlanta, GA.

Åström D. O., Forsberg B., and Rocklöv J. (2011): Heat wave impact on morbidity and mortality in the elderly population: A review of recent studies. *Maturitas*, volume 69(2):pages 99 – 105. ISSN 0378-5122. http://dx.doi.org/10.1016/j.maturitas.2011.03.008.

Auliciems A. and Kalma J. D. (1981): Human thermal climates of Australia. *Australian Geographical Studies*, volume 19(1):pages 3 – 24.

Auliciems A. and Szokolay S. V. (2007): *Thermal comfort*. PLEA in association with Dept. of Architecture, University of Queensland Brisbane, Qld, 2 edition. ISBN 0867767294.

Bakan S. (1994): Eine einfache Strahlungsparametrisierung für ein mesoskaliges Modell. Report, Max-Planck-Institut für Meteorologie, Hamburg, Internal paper.

Barry R. G. and Blanken P. D. (2016): *The Energy Balance*, page 99–125. Cambridge University Press. `http://dx.doi.org/10.1017/CBO9781316535981.007`.

Bechtel B., Alexander P. J., Böhner J., Ching J., Conrad O., Feddema J., Mills G., See L., and Stewart I. (2015): Mapping Local Climate Zones for a Worldwide Database of the Form and Function of Cities. *ISPRS International Journal of Geo-Information*, volume 4(1):pages 199–219. ISSN 2220-9964. `http://dx.doi.org/10.3390/ijgi4010199`.

Becker S. (2000): Bioclimatological rating of cities and resorts in South Africa according to the Climate Index. *International Journal of Climatology*, volume 20(12):pages 1403–1414. `http://dx.doi.org/10.1002/1097-0088(200010)20:12<1403::AID-JOC539>3.0.CO;2-V`.

Bedford T. (1936): Warmth factor in comfort at work. *Med Res Council, Industrial Health Research Board, Report*, (76).

Bedford T. (1951): Equivalent Tempeature - What it is - how it's measured. *Heating, Piping & Air Conditioning*, volume 8:pages 87 – 91.

Bedford T. (1957): Reactions of Mines-Rescue Personnel to Work in Hot Environments. *Occupational and Environmental Medicine*, volume 14(4):page 300. ISSN 0007-1072. `http://dx.doi.org/10.1136/oem.14.4.300`.

Bedford T. (1961): Researches on thermal comfort, Given at Bristol, 17 April. *Ergonomics*, volume 4(4):pages 289–310. `http://dx.doi.org/10.1080/00140136108930531`.

Bedford T. (1964): *Basic Principles of Ventilation and Heating*. H.K. Lewis and Co, London, London, 2 edition. `https://books.google.de/books?id=FWPInQAACAAJ`.

Belding H. S. and Hatch T. F. (1955): Index for evaluating Heat Stress in Terms of resulting Physiological Strains. *Heating, Piping and Air Conditioning*, volume 27(8):pages 129–36.

Belkin V. S. (1992): Biomedical Aspects of the Development of Mountain Regions: A Case-Study for the Gorno-Badakhshan Autonomous Region, Tajikistan. *Mountain Research and Development*, volume 12(1):pages 63–70. ISSN 02764741, 19947151. `http://www.jstor.org/stable/3673748`.

Best M. and Grimmond C. (2014): Key conclusions of the first international urban land surface model comparison project. *Bulletin of the American Meteorological Society*. `http://dx.doi.org/10.1175/BAMS-D-14-00122.1`.

Błażejczyk K. (2005): New Indices To Assess Thermal Risks Outdoors. In *Environmental Ergonomics XI, Proceedings of 11th International Conference*, pages 222–225. Holmér, I and Kuklane, I. and Gao, Ch., Ystat, Sweden.

Błażejczyk K. (2010): BioKlima - Universal tool for bioclimatic and thermophysiological studies. `http://www.igipz.pan.pl/Bioklima-zgik.html`, last accessed 27.10.2016.

Błażejczyk K. (2011): MENEX_2005 – the updated version of man-environment heat exchange model. `https://www.igipz.pan.pl/tl_files/igipz/ZGiK/opracowania/indywidualne/blazejczyk/MENEX_2005.pdf` (Last accessed: 21.05.2015).

Błażejczyk K., Epstein Y., Jendritzky G., Staiger H., and Tinz B. (2012): Comparison of UTCI to selected thermal indices. *International Journal of Biometeorology*, volume 56(3):pages 515–535. ISSN 0020-7128. `http://dx.doi.org/10.1007/s00484-011-0453-2`.

Błażejczyk K., Homér I., and Nilsson H. (1998): Absorption of Solar Radiation by an Ellipsoid Sensor Simulated the Human Body. *Applied Human Science*, volume 17(6):pages 267–273. `http://dx.doi.org/10.2114/jpa.17.267`.

Błażejczyk K. and Matzarakis A. (2007): Assessment of bioclimatic differentiation of Poland based on the human heat balance. *Geographia Polonica*, volume 80(1):pages 63–82.

Blazejczyk K. and Vinogradowa V. (2014): Adaptation Strain Index for tourists traveling from central and northern Europe to the Mediterranean. *Finisterra XLIX*, volume 98:pages 139–152.

Blocken B. (2015): Computational Fluid Dynamics for urban physics: Importance, scales, possibilities, limitations and ten tips and tricks towards accurate and reliable simulations. *Building and Environment*, volume 91:pages 219 – 245. ISSN 0360-1323.

http://dx.doi.org/10.1016/j.buildenv.2015.02.015. Fifty Year Anniversary for Building and Environment.

Bodman G. (1908): Das Klima als eine Funktion von Temperatur und Windgeschwindigkeit in ihrer Verbindung. Report, Lithographisches Institut des Generalstabs. Vol II.

Bogatkin O. and Tarakanov G. (2006): *Basics of Meteorology*. St Petersburg. http://elib.rshu.ru/files_books/pdf/img-306162302.pdf.

Bohnenstengel S., Schlünzen K. H., and Grawe D. (2004): Influence of thermal effects on street canyon circulations. *Meteorologische Zeitschrift*, volume 13(5):pages 381–386. http://dx.doi.org/10.1127/0941-2948/2004/0013-0381.

Borgonovo E. and Plischke E. (2016): Sensitivity analysis: A review of recent advances. *European Journal of Operational Research*, volume 248(3):pages 869 – 887. ISSN 0377-2217. http://dx.doi.org/10.1016/j.ejor.2015.06.032.

Brake D. J. and Bates G. P. (2002): Limiting Metabolic Rate (Thermal Work Limit) as an Index of Thermal Stress. *Applied Occupational and Environmental Hygiene*, volume 17(3):pages 176–186.

Brauner N. and Shacham M. (1995): Meaningful wind chill indicators derived from heat transfer principles. *International Journal of Biometeorology*, volume 39(1):pages 46–52. ISSN 1432-1254. http://dx.doi.org/10.1007/BF01320893.

Broadbent A. M., Coutts A. M., Tapper N. J., Demuzere M., and Beringer J. (2017): The microscale cooling effects of water sensitive urban design and irrigation in a suburban environment. *Theoretical and Applied Climatology*. ISSN 1434-4483. http://dx.doi.org/10.1007/s00704-017-2241-3.

Bröde P., Fiala D., Błażejczyk K., Holmér I., Jendritzky G., Kampmann B., Tinz B., and Havenith G. (2012): Deriving the operational procedure for the Universal Thermal Climate Index (UTCI). *International Journal of Biometeorology*, volume 56(3):pages 481–494. ISSN 0020-7128. http://dx.doi.org/10.1007/s00484-011-0454-1.

Brown R. D. and Gillespie T. J. (1986): Estimating outdoor thermal comfort using a cylindrical radiation thermometer and an energy budget model. *International Journal* *of Biometeorology*, volume 30(1):pages 43–52. ISSN 1432-1254. `http://dx.doi.org/10.1007/BF02192058`.

Bruse M. (1999): *Die Auswirkungen kleinskaliger Umweltgestaltung auf das Mikroklima – Entwicklung des prognostischen numerischen Modells ENVI-met zur Simulation der Wind-, Temperatur- und Feuchteverteilung in städtischen Strukturen.* Ph.D. thesis, Geowissenschaften, Ruhr-Universität Bochum, Bochum, Germany.

Bruse M. (2007): Simulating human thermal comfort and resulting usage patterns of urban open spaces with a Multi-Agent System. In S. Wittkopf and B. K. Tan, editors, *Proceedings of the 24th International Conference on Passive and Low Energy Architecture PLEA*. Singapore.

Bruse M. (2016): MEMI-model in ENVI-met. Personal communication.

Bruse and Team (2015): ENVI-met BioMet. `http://www.model.envi-met.com/hg2e/doku.php?id=apps:biomet`, last accessed 27.10.2016.

Bröde P., Kampmann B., and Fiala D. (2016): Extending the Universal Theraml Climate Index UTCI towards varying activity levels and exposure times.

Brüner H. (1959): Arbeitsmöglichkeiten unter Tage bei erschwerten klimatischen Bedingungen. *Int. Z. angew. Physiol. einschl. Arbeitsphysiol.*, volume 18:pages 31–61.

Budyko M. and Cicenko V. (1960): Climatic factors of human thermal sensation. *Izv AS USSR Ser Geogr*, volume 3:pages 3–11.

Burkart K., Meier F., Schneider A., Breitner S., Canário P., Alcoforado M. J., Scherer D., and Endlicher W. (2016): Modification of Heat-Related Mortality in an Elderly Urban Population by Vegetation (Urban Green) and Proximity to Water (Urban Blue): Evidence from Lisbon, Portugal. *Environmental Health Perspectives*, volume 124(7):pages 927 – 934. `http://dx.doi.org/10.1289/ehp.1409529`.

Burkart K., Schneider A., Breitner S., Khan M. H., Krämer A., and Endlicher W. (2011): The effect of atmospheric thermal conditions and urban thermal pollution on all-cause and cardiovascular mortality in Bangladesh. *Environmental Pollution*, volume 159(8–9):pages 2035 – 2043. ISSN 0269-7491. `http://dx.doi.org/10.1016/j.envpol.2011.02.005`. Selected papers from the conference Urban Environmental Pollution: Overcoming Obstacles to Sustainability and Quality of Life (UEP2010), 20-23 June 2010, Boston, USA.

Burton A. and Edholm O. (1955): *Man in a cold environment: physiological and pathological effects of exposure to low temperatures.* Arnold.

Buzan J. R., Oleson K., and Huber M. (2015): Implementation and comparison of a suite of heat stress metrics within the Community Land Model version 4.5. *Geoscientific Model Development*, volume 8(2):pages 151–170. `http://dx.doi.org/10.5194/gmd-8-151-2015`.

Böttcher M. (2017): *Selected climate mitigation and adaptation measures and their impact on the climate of the region of Hamburg.* Ph.D. thesis, Geowissenschaften, Universität Hamburg.

Cadarette B., Montain S., Kolka M., Stroschein L., Matthew W., and Sawka M. (1999): Cross validation of USARIEM heat strain prediction models. *Aviat Space Environ Med*, volume 70(10):pages 996 – 1006.

Cannistraro G., Franzitta G., Giaconia C., and Rizzo G. (1992): Algorithms for the calculation of the view factors between human body and rectangular surfaces in parallelepiped environments. *Energy and Buildings*, volume 19(1):pages 51 – 60. ISSN 0378-7788. `http://dx.doi.org/10.1016/0378-7788(92)90035-F`.

Chatzidimitriou A. and Yannas S. (2016): Microclimate design for open spaces: Ranking urban design effects on pedestrian thermal comfort in summer. *Sustainable Cities and Society*, volume 26:pages 27 – 47. ISSN 2210-6707. `http://dx.doi.org/10.1016/j.scs.2016.05.004`.

Chen L. and Ng E. (2012): Outdoor thermal comfort and outdoor activities: A review of research in the past decade. *Cities*, volume 29(2):pages 118 – 125. ISSN 0264-2751. `http://dx.doi.org/10.1016/j.cities.2011.08.006`.

Chen L. and Ng E. (2013): Simulation of the effect of downtown greenery on thermal comfort in subtropical climate using PET index: a case study in Hong Kong. *Architectural Science Review*, volume 56(4):pages 297–305. `http://dx.doi.org/10.1080/00038628.2012.684871`.

Chen L., Yu B., Yang F., and Mayer H. (2016): Intra-urban differences of mean radiant temperature in different urban settings in Shanghai and implications for heat stress under heat waves: A GIS-based approach. *Energy and Buildings*, volume 130:pages 829 – 842. ISSN 0378-7788. `http://dx.doi.org/10.1016/j.enbuild.2016.09.014`.

Chen Z., Krarti M., Zhai Z., Meng Q., and Zhao L. (2009): Sensitive Analysis Of Landscaping Effects On Outdoor Thermal Environment In A Residential Community Of Hot-Humid Area In China. In *The seventh International Conference on Urban Climate*. Yokohama, Japan.

Cheng Y., Niu J., and Gao N. (2012): Thermal comfort models: A review and numerical investigation. *Building and Environment*, volume 47:pages 13 – 22. ISSN 0360-1323. `http://dx.doi.org/10.1016/j.buildenv.2011.05.011`. International Workshop on Ventilation, Comfort, and Health in Transport Vehicles.

CIESIN (Center for International Earth Science Information Network) (2005): Gridded Population of the World, Version 3 (GPWv3): Population Count Grid. `http://dx.doi.org/10.7927/H4639MPP`.

Coccolo S., Kämpf J., Scartezzini J.-L., and Pearlmutter D. (2016): Outdoor human comfort and thermal stress: A comprehensive review on models and standards. *Urban Climate*, volume 18:pages 33 – 57. ISSN 2212-0955. `http://dx.doi.org/10.1016/j.uclim.2016.08.004`.

Cohen P., Potchter O., and Matzarakis A. (2013): Human thermal perception of Coastal Mediterranean outdoor urban environments. *Applied Geography*, volume 37:pages 1 – 10. ISSN 0143-6228. `http://dx.doi.org/10.1016/j.apgeog.2012.11.001`.

Coste L. and Eftimie E. (2010): Linke Turbidity Modelling for Brasov Urban Area . In *Proceedings of International Conference on Renewable Energies and Power Quality (ICREPQ'10)*. European Association for the Development of Renewable Energies, Environment and Power Quality, Granada, Spain.

Coutts A. M., Tapper N. J., Beringer J., Loughnan M., and Demuzere M. (2013): Watering our cities: The capacity for Water Sensitive Urban Design to support urban cooling and improve human thermal comfort in the Australian context. *Progress in Physical Geography: Earth and Environment*, volume 37(1):pages 2–28. `http://dx.doi.org/10.1177/0309133312461032`.

Cropper P. C., Yang T., Cook M., Fiala D., and Yousaf R. (2010): Coupling a model of human thermoregulation with computational fluid dynamics for predicting human–environment interaction. *Journal of Building Performance Simulation*, volume 3(3):pages 233–243. `http://dx.doi.org/10.1080/19401491003615669`.

Crosman E. T. and Horel J. D. (2010): Sea and Lake Breezes: A Review of Numerical Studies. *Boundary-Layer Meteorology*, volume 137:pages 1–29. http://dx.doi.org/10.1007/s10546-010-9517-9.

Dai Q. and Schnabel M. (2013a): Relationship between Mean Radiant Temperature and Building Type for Pedestrians in Rotterdam. In J. Zhang and C. Sun, editors, *Global Design and Local Materialization*, volume 369 of *Communications in Computer and Information Science*, pages 306–314. Springer Berlin Heidelberg. ISBN 978-3-642-38973-3. http://dx.doi.org/10.1007/978-3-642-38974-0_29.

Dai Q. and Schnabel M. A. (2013b): Relationship between mean radiant temperature and solar angle for pedestrians. In *Cutting Edge: 46th International Conference of the Architectural Science Association*, pages 251–260. The Architectural Science Association (ANZAScA), Australia. http://anzasca.net/wp-content/uploads/2014/08/67.pdf.

Dai Q. and Schnabel M. A. (2014): Thermal comfort levels classified by aspect ratio and orientation for three zones of a street in Rotterdam. *Architectural Science Review Reviews*, pages 1–9. http://dx.doi.org/10.1080/00038628.2014.930016.

Dai Q., Schnabel M. A., and Heusinkveld B. (2012): Influence of height-to-width ratio: Case study on mean radiant temperature for Netherlands buildings. In *Cutting Edge: 46th International Conference of the Architectural Science Association.* The Architectural Science Association (ANZAScA), Australia. http://anzasca.net/wp-content/uploads/2014/08/p661.pdf.

Dasler A. R. (1977): Heat stress, work function and physiological heat exposure limits in man. https://play.google.com/books/reader?id=49fL2qrLF8gC&printsec=frontcover&output=reader&authuser=0&hl=en&pg=GBS.PP2.

Dayal D. (1974): *An Index for assessing heat stress in terms of physiological strain.* Ph.D. thesis, Texas Tech University.

de Freitas, C. R. (1986): Human thermal climates of New Zealand. New Zealand Meteorological Service, Misk Publ, 190, Wellington.

Deardorff J. W. (1978): Efficient prediction of ground surface temperature and moisture, with inclusion of a layer of vegetation. *Journal of Geophysical Research: Oceans*, volume 83(C4):pages 1889–1903. http://dx.doi.org/10.1029/JC083iC04p01889.

Dimiceli V. E., Piltz S. F., and Amburn S. A. (2011): Estimation of Black Globe Temperature for Calculation of the Wet Bulb Globe Temperature Index. *Proceedings of the World Congress on Engineering and Computer Science*, volume 2.

Dufton A. F. (1929): The eupatheostat. *Journal of Scientific Instruments*, volume 6(8):page 249. http://stacks.iop.org/0950-7671/6/i=8/a=303.

Ehlert J. and Smith T. (1993): View Factors for Perpendicular and Parallel, Rectangular Plates. *J. Thermophys. Heat Trans.*, volume 7(1):pages 173–174.

Eissing G. (1995): Climate assessment indices. *Ergonomics*, volume 38(1):pages 47–57. http://dx.doi.org/10.1080/00140139508925084.

enviadmin (2017): Biomet_pet. http://www.envi-met.info/doku.php?id=apps:biomet_pet. Last accessed 11.06.2018.

Evans M. (1980): *Housing, climate, and comfort*. Architectural Press, London. ISBN 9780851391021.

Falconer R. (1968): Windchill, A Useful Wintertime Weather Variable. *Weatherwise*, volume 21(6):pages 227–255. http://dx.doi.org/10.1080/00431672.1968.9932829.

Fan Y. and van den Dool H. (2008): A global monthly land surface air temperature analysis for 1948 – present. *Journal of Geophysical Research*, volume 113:pages 1–18.

Fanger P., Melikov A., Hanzawa H., and Ring J. (1988): Air turbulence and sensation of draught. *Energy and Buildings*, volume 12(1):pages 21 – 39. ISSN 0378-7788. http://dx.doi.org/10.1016/0378-7788(88)90053-9.

Fanger P. O. (1970): *Thermal Comfort - Analysis and Applications in Environmental Engineering*. Danisch Technical Press, Copenhagen.

Fiala D. and Havenith G. (2015): Modelling Human Heat Transfer and Temperature Regulation. In *The Mechanobiology and Mechanophysiology of Military-Related Injuries*, Studies in Mechanobiology, Tissue Engineering and Biomaterials, pages 1–38. Springer Berlin Heidelberg. http://dx.doi.org/10.1007/8415_2015_183.

Fischereit J. and Schlünzen K. H. (2018): Evaluation of thermal indices for their applicability in obstacle resolving meteorology models. *International Journal of Biometeorology*, volume 62(10):pages 1887–1900. ISSN 1432-1254. http://dx.doi.org/10.1007/s00484-018-1591-6.

Foley R. and Kistemann T. (2015): Blue space geographies: Enabling health in place. *Health & Place*, volume 35:pages 157 – 165. ISSN 1353-8292. http://dx.doi.org/10.1016/j.healthplace.2015.07.003.

Frank A., Moran D., Epstein Y., Belokopytov M., and Shapiro Y. (1996): *The estimation of heat tolerance by a new cumulative heat strain index*, pages 194 – 197. Freund Publishing House, Tel Aviv-London.

Franke J., Hellsten A., Schlunzen K. H., and Carissimo B. (2011): The COST 732 Best Practice Guideline for CFD simulation of flows in the urban environment: a summary. *International Journal of Environment and Pollution*, volume 44(1-4):pages 419–427. http://dx.doi.org/10.1504/IJEP.2011.038443.

de Freitas C. (1987): Bioclimates Of Heat And Cold Stress In New Zealand. *Weather and Climate*, volume 7:pages 55–60.

de Freitas C. and Grigorieva E. (2016): A comparison and appraisal of a comprehensive range of human thermal climate indices. *Int J Biometeorology*. http://dx.doi.org/10.1007/s00484-016-1228-6.

de Freitas C. and Symon L. V. (1987): A Bioclimatic Index of Human Survival Times in the Antarctic. *Polar Record*, volume 23(147):pages 651–659. ISSN 0020-7128. http://dx.doi.org/10.1017/S0032247400008354.

de Freitas C. R. (1985): Assessment of human bioclimate based on thermal response. *International Journal of Biometeorology*, volume 29(2):pages 97–119. ISSN 1432-1254. http://dx.doi.org/10.1007/BF02189029.

de Freitas C. R. and Grigorieva E. A. (2009): The Acclimatization Thermal Strain Index (ATSI): a preliminary study of the methodology applied to climatic conditions of the Russian Far East. *International Journal of Biometeorology*, volume 53(4):pages 307–315. ISSN 1432-1254. http://dx.doi.org/10.1007/s00484-009-0215-6.

de Freitas C. R. and Grigorieva E. A. (2015): A comprehensive catalogue and classification of human thermal climate indices. *International Journal of Biometeorology*, volume 59(1):pages 109–120. ISSN 1432-1254. http://dx.doi.org/10.1007/s00484-014-0819-3.

de Freitas C. R. and Grigorieva E. A. (2017): A comparison and appraisal of a comprehensive range of human thermal climate indices. *International Journal of Biometeorology*, volume 61(3):pages 487–512. ISSN 1432-1254. `http://dx.doi.org/10.1007/s00484-016-1228-6`.

de Freitas C. R. and Ryken M. G. (1989): Climate and physiological heat strain during exercise. *International Journal of Biometeorology*, volume 33(3):pages 157–164. ISSN 1432-1254. `http://dx.doi.org/10.1007/BF01084600`.

Frey C. H. and Sumeet P. R. (2002): Identification and Review of Sensitivity Analysis Methods. *Risk Analysis*, volume 22(3):pages 553–578. ISSN 1539-6924. `http://dx.doi.org/10.1111/0272-4332.00039`.

Froehle A. W. (2008): Climate variables as predictors of basal metabolic rate: New equations. *American Journal of Human Biology*, volume 20(5):pages 510–529. ISSN 1520-6300. `http://dx.doi.org/10.1002/ajhb.20769`.

Fröhlich D. and Matzarakis A. (2015): A quantitative sensitivity analysis on the behaviour of common thermal indices under hot and windy conditions in Doha, Qatar. *Theoretical and Applied Climatology*, pages 1–9. ISSN 0177-798X. `http://dx.doi.org/10.1007/s00704-015-1410-5`.

Gabriel K. M. and Endlicher W. R. (2011): Urban and rural mortality rates during heat waves in Berlin and Brandenburg, Germany. *Environmental Pollution*, volume 159(8–9):pages 2044 – 2050. ISSN 0269-7491. `http://dx.doi.org/10.1016/j.envpol.2011.01.016`. Selected papers from the conference Urban Environmental Pollution: Overcoming Obstacles to Sustainability and Quality of Life (UEP2010), 20-23 June 2010, Boston, USA.

Gagge A., Fobelets A., and Berglund L. (1986): A standard predictive index of human response to the thermal environment. *ASHRAE Transactions*, volume 2B(92):pages 709–731.

Gagge A. P., Nishi Y., and Gonzalez R. R. (1973): Standard Effective Temperature - A single Temperature Index of Temperature Sensation and Thermal Discomfort. In U. HMSO, editor, *Symposium on thermal comfort and moderate heat stress*. Building Research Station.

Gagge A. P., Stolwijk J. A. J., and Nishi Y. (1971): An effective temperature scale based on a simple model of human physiological regulatory response. *ASHRAE TRANSACTIONS*, volume 77(1):pages 21–36. http://eprints.lib.hokudai.ac.jp/dspace/bitstream/2115/37901/1/13Suppl_21-36.pdf.

Gallagher M. J., Robertson R. J., Goss F. L., Nagle-Stilley E., Schafer M., Suyama J., and Hostler D. (2012): Development of a perceptual hyperthermia index to evaluate heat strain during treadmill exercise. *Europ J Appl Physiol*, volume 112(6):page 2025–2034.

Geiger R., Aron R. H., and Paul T. (2009): *The climate near the gorund*. Rowman & Littlefield Publishers, 7 edition.

Gennusa M. L., Nucara A., Pietrafesa M., Rizzo G., and Scaccianoce G. (2008): Angle Factors and Projected Area Factors for Comfort Analysis of Subjects in Complex Confined Enclosures: Analytical Relations and Experimental Results. *Indoor and Built Environment*, volume 17(4):pages 346–360. http://dx.doi.org/10.1177/1420326X08094621.

Gierisch A. (2011): *Mikroskalige Modellierung meteorologischer und anthropogener Einflüsse auf die Wärmeabgabe eines Gebäudes*. Diplomarbeit, Geowissenschaften, University of Hamburg, Hamburg, Germany. https://mi-pub.cen.uni-hamburg.de/fileadmin/files/forschung/techmet/nummod/thesis/diplom_andrea_gierisch.pdf.

Givoni B. (1976): *Man, Climate and Architecture*. Architectural Science Series. Applied Science Publ., Amsterdam, 2 edition.

Givoni B. and Goldman R. F. (1972): Predicting rectal temperature response to work, environment, and clothing. *Journal of Applied Physiology*, volume 32(6):pages 812–822. ISSN 8750-7587. http://jap.physiology.org/content/32/6/812.

Givoni B. and Goldman R. F. (1973): Predicting heart rate response to work, environment, and clothing. *Journal of Applied Physiology*, volume 34(2):pages 201–204. ISSN 8750-7587. http://jap.physiology.org/content/34/2/201.

Givoni B., Noguchi M., Saaroni H., Pochter O., Yaacov Y., Feller N., and Becker S. (2003): Outdoor comfort research issues. *Energy and Buildings*, volume 35(1):pages 77 – 86. ISSN 0378-7788. http://dx.doi.org/10.1016/S0378-7788(02)00082-8. Special issue on urban research.

Goldberg V., Kurbjuhn C., and Bernhofer C. (2013): How relevant is urban planning for the thermal comfort of pedestrians? Numerical case studies in two districts of the City of Dresden (Saxony/Germany). *Meteorologische Zeitschrift*, volume 22(6):pages 739 – 751. http://dx.doi.org/10.1127/0941-2948/2013/0463.

Golovina E. G. and Rusanov V. I. (1993): Some questions in biometeorology. Report, Russisches Staatshydrometeorologisches Institut, St. Petersburg. http://elib.rshu.ru/files_books/pdf/img-213173819.pdf.

Gonzalez R. R., Berglund L. G., and Gagge A. P. (1978): Indices of thermoregulatory strain for moderate exercise in the heat. *J Appl Physiol Respir Environ Exerc Physiol.*, volume 44(6):pages 889–899.

Gonzalez R. R., Nishi Y., and Gagge A. P. (1974): Experimental evaluation of standard effective temperature a new biometeorological index of man's thermal discomfort. *International Journal Biometeorology*, volume 18(1):pages 1–15. http://dx.doi.org/10.1007/BF01450660.

Graveling R. A., Morris L. A., and Graves R. J. (1988): Working in Hot Conditions in Mining: A Literature Review. Report 10, Institute of Occupational Medicine Ergonomics Branch. HSE Contract Research Report.

Grawe D., Thompson H. L., Salmond J. A., Cai X.-M., and Schlünzen K. H. (2013): Modelling the impact of urbanisation on regional climate in the Greater London Area. *International Journal of Climatology*, volume 33(10):pages 2388–2401. ISSN 1097-0088. http://dx.doi.org/10.1002/joc.3589.

Gregorczuk M. (1968): Bioclimates of the world related to air enthalpy. *International Journal of Biometeorology*, volume 12(1):page 35–39. ISSN 1432-1254. http://dx.doi.org/10.1007/BF01552976.

Gregorczuk M. and Cena K. (1967): Distribution of Effective Temperature over the Surface of the Earth. *International Journal of Biometeorology*, volume 11(2):pages 145–149.

Hall J. and Polte J. (1960): Physiological index of strain and body heat storage in hyperthermia. *Journal of Applied Physiology*, volume 15(6):pages 1027–1030. http://jap.physiology.org/content/15/6/1027.

Hamdi M., Lachiver G., and Michaud F. (1999): A new predictive thermal sensation index of human response. *Energy and Buildings*, volume 29:pages 167–178.

Hamilton D. C. and Morgan W. R. (1952): Radiant-interchange Configuration Factors. Technical Report NACA-TN-2836, NASA. https://ntrs.nasa.gov/archive/nasa/casi.ntrs.nasa.gov/19930083529.pdf. NACA Technical Note 2836.

Hathway E. and Sharples S. (2012): The interaction of rivers and urban form in mitigating the Urban Heat Island effect: A {UK} case study. *Building and Environment*, volume 58:pages 14 – 22. ISSN 0360-1323. http://dx.doi.org/10.1016/j.buildenv.2012.06.013.

Havenith G. (2005): Temperature Regulation, Heat Balance and Climatic Stress. In W. Kirch; R. Bertollini; and B. Menne, editors, *Extreme Weather Events and Public Health Responses*, pages 69–80. Springer Berlin Heidelberg. ISBN 978-3-540-24417-2. http://dx.doi.org/10.1007/3-540-28862-7_7.

Havenith G., Fiala D., Błażejczyk K., Richards M., Bröde P., Holmér I., Rintamaki H., Benshabat Y., and Jendritzky G. (2012): The UTCI-clothing model. *International Journal of Biometeorology*, volume 56(3):pages 461–470. ISSN 0020-7128. http://dx.doi.org/10.1007/s00484-011-0451-4.

He J. (2011): A design supporting simulation system for predicting and evaluating the cool microclimate creating effect of passive evaporative cooling walls. *Building and Environment*, volume 46(3):pages 584–596. ISSN 0360-1323. http://dx.doi.org/10.1016/j.buildenv.2010.09.005.

He J. and Hoyano A. (2010): Measurement and evaluation of the summer microclimate in the semi-enclosed space under a membrane structure. *Building and Environment*, volume 45(1):pages 230–242. ISSN 0360-1323. http://dx.doi.org/10.1016/j.buildenv.2009.06.006.

He X., Miao S., Shen S., Li J., Zhang B., Zhang Z., and Chen X. (2015): Influence of sky view factor on outdoor thermal environment and physiological equivalent temperature. *International Journal of Biometeorology*, volume 59(3):pages 285–297. ISSN 1432-1254. http://dx.doi.org/10.1007/s00484-014-0841-5.

Hedquist B. C. and Brazel A. J. (2014): Seasonal variability of temperatures and outdoor human comfort in Phoenix, Arizona, U.S.A. *Building and Environ-*

ment, volume 72:pages 377–388. ISSN 0360-1323. `http://dx.doi.org/10.1016/j.buildenv.2013.11.018`.

Heusinkveld B. G., Steeneveld G. J., van Hove L. W. A., Jacobs C. M. J., and Holtslag A. A. M. (2014): Spatial variability of the Rotterdam urban heat island as influenced by urban land use. *Journal of Geophysical Research: Atmospheres*, volume 119(2):pages 677–692. ISSN 2169-8996. `http://dx.doi.org/10.1002/2012JD019399`. 2012JD019399.

Hill L. and Hargood-Ash D. (1919): On the cooling and evaporative powers of the atmosphere, as determined by the kata-thermometer. *Proceedings of the Royal Society of London B: Biological Sciences*, volume 90(632):page 438–447. `http://dx.doi.org/10.1098/rspb.1919.0004`.

Hoffmann P., Fischereit J., Heitmann S., Schlünzen K. H., and Gasser I. (2018): Modeling Exposure to Heat Stress with a Simple Urban Model. *Urban Science*, volume 2(1). ISSN 2413-8851. `http://dx.doi.org/10.3390/urbansci2010009`.

Hoffmann P., Schoetter R., and Schlünzen K. (2016): Statistical-dynamical downscaling of the urban heat island in Hamburg, Germany. *Meteorologische Zeitschrift*, pages –. `http://dx.doi.org/10.1127/metz/2016/0773`.

Holmer I. (1988): Assessment of cold stress in terms of required clothing insulation—ireq. *International Journal of Industrial Ergonomics*, volume 3(2):pages 159–166. `http://dx.doi.org/10.1016/0169-8141(88)90017-0`.

Holst J. (2016): MEMI-model used in Holst and Mayer (2011). Personal communication.

Holst J. and Mayer H. (2010): Urban human-biometeorology: Investigations in Freiburg (Germany) on human thermal comfort. *Urban Climate News*, volume 38:pages 5–10.

Holst J. and Mayer H. (2011): Impacts of street design parameters on human-biometeorological variables. *Meteorologische Zeitschrift*, volume 20(5):pages 541–552. `http://dx.doi.org/10.1127/0941-2948/2011/0254`.

Hong B. and Lin B. (2015): Numerical studies of the outdoor wind environment and thermal comfort at pedestrian level in housing blocks with different building layout patterns and trees arrangement. *Renewable Energy*, volume 73:pages 18 – 27. ISSN

0960-1481. http://dx.doi.org/10.1016/j.renene.2014.05.060. Sustainable Development in Building and Environment (SuDBE) 2013.

Höppe P. (1984): *Die Energiebilanz des Menschen*. Ph.D. thesis, Geowissenschaften. Wissenschaftliche Mitteilungen, Meteorologisches Institut, Universität München, 49.

Höppe P. (1999): The physiological equivalent temperature – a universal index for the biometeorological assessment of the thermal environment. *International Journal of Biometeorology*, volume 43(2):pages 71–75. ISSN 0020-7128. http://dx.doi.org/10.1007/s004840050118.

Höppe P. (2002): Different aspects of assessing indoor and outdoor thermal comfort. *Energy and Buildings*, volume 34:pages 661–665.

Hori S. (1978): Index for the assessment of heat tolerance. *J. Human Ergol.*, volume 7:pages 135 – 144.

Hottel H. C. and Sarofim A. F. (1967): *Radiative transfer*. McGraw-Hill series in mechanical engineering. McGraw-Hill, New York u.a.

Hovmöller E. (1949): The Trough-and-Ridge diagram. *Tellus*, volume 1(2):pages 62–66. http://dx.doi.org/10.1111/j.2153-3490.1949.tb01260.x.

Howell J., Menguc M., and Siegel R. (2016): *Thermal Radiation Heat Transfer, 6th Edition*. Taylor & Francis. ISBN 9781466593268.

Howell J. R. (2010): *A Catalog of Radiation Heat Transfer Configuration Factors*. 3 edition. http://www.thermalradiation.net/sectionc.

Huang H., Ooka R., and Kato S. (2005): Urban thermal environment measurements and numerical simulation for an actual complex urban area covering a large district heating and cooling system in summer. *Atmospheric Environment*, volume 39(34):pages 6362–6375. ISSN 1352-2310. http://dx.doi.org/10.1016/j.atmosenv.2005.07.018.

Hubač M., Strelka F., Borský I., and Hubačová L. (1989): Application of the relative summary climatic indices during work in heat for ergonomic purposes. *Ergonomics*, volume 32(7):pages 733–750. http://dx.doi.org/10.1080/00140138908966839.

Hunter L., Watson I., and Johnson G. (1990): Modelling air flow regimes in urban canyons. *Energy and Buildings*, volume 15(3):pages 315 – 324. ISSN 0378-7788. `http://dx.doi.org/https://doi.org/10.1016/0378-7788(90)90004-3`.

Huttner S. (2012): *Further development and application of the 3D microclimate simulation ENVI-met*. Ph.D. thesis, Geographie, Johannes Gutenberg-Universität Mainz, Germany.

Hägerskog A., Clausen T., Holmgren T., and Lexén K. (2015): . Water for Development – Charting a Water Wise Path. Report No 35. Technical report, United Nations, SIWI, Stockholm. `http://alliance4water.org/resources/2015-WWW-report-digital.pdf`.

Iooss B. and Lemaître P. (2015): *A Review on Global Sensitivity Analysis Methods*, pages 101–122. Springer US, Boston, MA. ISBN 978-1-4899-7547-8. `http://dx.doi.org/10.1007/978-1-4899-7547-8_5`.

ISB Comission 6 (2012): UTCI Universal Thermal Climate Index - Documents. `http://www.utci.org/utci_doku.php`, last accessed 27.10.2016.

Ishii A., Iwamoto S., Katayama T., Hayashi T., Shiotsuki Y., Kitayama H., Tsutsumi J.-I., and Nishida M. (1991): A comparison of field surveys on the thermal environment in urban areas surroundings a large pond: when filled and when drained. *Energy and Buildings*, volume 16(3–4):pages 965 – 971. ISSN 0378-7788. `http://dx.doi.org/10.1016/0378-7788(91)90091-G`.

Jänicke B., Meier F., Hoelscher M.-T., and Scherer D. (2015): Evaluating the Effects of Façade Greening on Human Bioclimate in a Complex Urban Environment. *Advances in Meteorology*, volume 2015:pages 1–12. `http://dx.doi.org/10.1155/2015/747259`.

Jansen M. J. (1999): Analysis of variance designs for model output. *Computer Physics Communications*, volume 117(1):pages 35 – 43. ISSN 0010-4655. `http://dx.doi.org/10.1016/S0010-4655(98)00154-4`.

Jendritzky G. and de Dear R. (2009): Adaptation and Thermal Environment. In K. Ebi; I. Burton; and G. McGregor, editors, *Biometeorology for Adaptation to Climate Variability and Change*, volume 1 of *Biometeorology*, pages 9–32. Springer Netherlands. ISBN 978-1-4020-8920-6. `http://dx.doi.org/10.1007/978-1-4020-8921-3_2`.

Jendritzky G., de Dear R., and Havenith G. (2012): UTCI—Why another thermal index? *International Journal of Biometeorology*, volume 56(3):pages 421–428. ISSN 0020-7128. http://dx.doi.org/10.1007/s00484-011-0513-7.

Jendritzky G., Fiala D., Havenith G., Koppe C., Laschewski G., Staiger H., and Tinz B. (2007): Thermische Umweltbedingungen. *promet - Biometeorologie des Menschen*, volume 33(3):pages 83–94. ISSN 0340-4552. http://www.dwd.de/bvbw/generator/DWDWWW/Content/Oeffentlichkeit/PB/PBFB/Periodika/Promet/PDF/promet__33__3-4__en,templateId=raw,property=publicationFile.pdf/promet_33_3-4_en.pdf.

Jendritzky G., Menz G., Schmidt-Kessen W., and Schirmer H. (1990): Methodik zur raumbezogenen Bewertung der thermischen Komponente des Bioklima des Menschen (Fortgeschriebenes Klima-Michel-Modell). Technical Report 114, Akademie für Raumforschung und Landesplanung, Hannover.

Jendritzky G. and Nübler W. (1981): A model analysing the urban thermal environment in physiologically significant terms. *Archives for meteorology, geophysics, and bioclimatology, Series B*, volume 29(4):pages 313–326. ISSN 1434-4483. http://dx.doi.org/10.1007/BF02263308.

Jensen C. (2017): *Eine Stadtklimatologie für Hamburg aus mehrjährigen Messdaten automatischer Wetterstationen*. Masterarbeit, Geowissenschaften, University of Hamburg, Hamburg, Germany.

Johansson E., Thorsson S., Emmanuel R., and Krüger E. (2014): Instruments and methods in outdoor thermal comfort studies – The need for standardization. *Urban Climate*, volume 10, Part 2:pages 346 – 366. ISSN 2212-0955. http://dx.doi.org/10.1016/j.uclim.2013.12.002. ICUC8: The 8th International Conference on Urban Climate and the 10th Symposium on the Urban Environment.

Johnson G. T. and Watson I. D. (1984): The Determination of View-Factors in Urban Canyons. *Journal of Applied Meteorology and Climatology*, volume 23:pages 329–335. http://dx.doi.org/10.1175/1520-0450(1984)023<0329:TDOVFI>2.0.CO;2.

Jokl M. V. (1982): Standard Layers - A New Criterion of the Thermal Insulating Properties of Clothing. *Int. J. Biometeorology*, volume 26(1):pages 37 – 48.

Kakon A. N., Mishima N., and Kojima S. (2009): Simulation of the urban thermal comfort in a high density tropical city: Analysis of the proposed urban construction rules for Dhaka, Bangladesh. *Building Simulation*, volume 2(4):page 291. ISSN 1996-8744. http://dx.doi.org/10.1007/s12273-009-9321-y.

Kalkstein L. S. and Nichols M. C. (1996): A new spatial synoptic classification: Application to air-mass analysis. *International Journal Of Climatology*, volume 16:pages 983 – 1004.

Kalkstein L. S. and Valimont K. M. (1986): An evaluation of summer discomfort in the United States using a relative climatological index. *Bull. Amer. Meteor. Soc.*, volume 68:pages 1535 – 1540.

Kamon E. and Ryan C. (1981): Effective heat strain index using pocket computer. *American Industrial Hygiene Association Journal*, volume 42(8):pages 611–615. http://dx.doi.org/10.1080/15298668191420369.

Kántor N. and Unger J. (2011): The most problematic variable in the course of human-biometeorological comfort assessment — the mean radiant temperature. *Central European Journal of Geosciences*, volume 3(1):pages 90–100. ISSN 2081-9900. http://dx.doi.org/10.2478/s13533-011-0010-x.

Kántor N., Unger J., and Gulyás A. (2012): Subjective estimations of thermal environment in recreational urban spaces—Part 2: international comparison. *International Journal of Biometeorology*, volume 56(6):pages 1089–1101. ISSN 0020-7128. http://dx.doi.org/10.1007/s00484-012-0564-4.

Kasten F. (1983): Parametrisierung der Globalstrahlung durch Bedeckungsgrad und Trübungsfaktor. In *Deutsche Meteorologen-Tagung 1983 vom 16. bis 19. Mai 1983, Bad Kissingen, Germany.*

Kasten F. (1996): The linke turbidity factor based on improved values of the integral Rayleigh optical thickness. *Solar Energy*, volume 56(3):pages 239 – 244. ISSN 0038-092X. http://dx.doi.org/10.1016/0038-092X(95)00114-7.

Katayama T., Hayashi T., Shiotsuki Y., Kitayama H., Ishii A., Nishida M., Tsutsumi J.-I., and Oguro M. (1991): Cooling effects of a river and sea breeze on the thermal environment in a built-up area. *Energy and Buildings*, volume 16(3–4):pages 973 – 978. ISSN 0378-7788. http://dx.doi.org/10.1016/0378-7788(91)90092-H.

Ketterer C. and Matzarakis A. (2015): Comparison of different methods for the assessment of the urban heat island in Stuttgart, Germany. *International Journal of Biometeorology*, volume 59(9):pages 1299–1309. ISSN 1432-1254. `http://dx.doi.org/10.1007/s00484-014-0940-3`.

Kim Y.-H., Ryoo S.-B., Baik J.-J., Park I.-S., Koo H.-J., and Nam J.-C. (2008): Does the restoration of an inner-city stream in Seoul affect local thermal environment? *Theoretical and Applied Climatology*, volume 92(3):pages 239–248. ISSN 1434-4483. `http://dx.doi.org/10.1007/s00704-007-0319-z`.

Knez I., Thorsson S., Eliasson I., and Lindberg F. (2009): Psychological mechanisms in outdoor place and weather assessment: towards a conceptual model. *International Journal of Biometeorology*, volume 53(1):pages 101–111. ISSN 0020-7128. `http://dx.doi.org/10.1007/s00484-008-0194-z`.

Kobyscheva N. B., Stadnik B. B., Kljueva M. B., Pigolzina G. B., Akenteva E. M., Galjuk G. P., Rasova E. N., and Semenov J. A. (2008): Guidelines for specialized climatological services in economy. Report, Ministry of Natural Resources and Ecology RussianFederation, Federal Service for Hydrometeorology and Environmental Monitoring. `http://voeikovmgo.ru/download/publikacii/2008/Rukovodstvo.pdf`.

Koenigsberger O., Mahoney C., and Evans M. (1971): *Climate and House Design - Design of low-cost housing and cummunity facilities*, volume 1 of *United Nations Publication*. United Nations, New York.

Konzelmann T., van de Wal R. S., Greuell W., Bintanja R., Henneken E. A., and Abe-Ouchi A. (1994): Parameterization of global and longwave incoming radiation for the Greenland Ice Sheet. *Global and Planetary Change*, volume 9(1):pages 143 – 164. ISSN 0921-8181. `http://dx.doi.org/10.1016/0921-8181(94)90013-2`. Greenland ice margin experiment (GIMEx).

Kovatas R. S. and Hajat S. (2008): Heat Stress and Public Health: A Critical Review. *Annual Review of Public Health*, volume 29:pages 41–55. `http://www.annualreviews.org/doi/pdf/10.1146/annurev.publhealth.29.020907.090843`.

Krefis A. C., Augustin M., Schlünzen K. H., Oßenbrügge J., and Augustin J. (2018): How Does the Urban Environment Affect Health and Well-Being? A Systematic Review. *Urban Science*, volume 2(1). ISSN 2413-8851. `http://dx.doi.org/10.3390/urbansci2010021`.

Kucherenko S., Tarantola S., and Annoni P. (2012): Estimation of global sensitivity indices for models with dependent variables. *Computer Physics Communications*, volume 183(4):pages 937 – 946. ISSN 0010-4655. http://dx.doi.org/10.1016/j.cpc.2011.12.020.

Kummu M., de Moel H., Ward P. J., and Varis O. (2011): How Close Do We Live to Water? A Global Analysis of Population Distance to Freshwater Bodies. *PLoS ONE*, volume 6(6):pages 1–13. http://dx.doi.org/10.1371/journal.pone.0020578.

Kusaka H., Kondo H., Kikegawa Y., and Kimura F. (2001): A Simple Single-Layer Urban Canopy Model For Atmospheric Models: Comparison With Multi-Layer And Slab Models. *Boundary-Layer Meteorology*, volume 101(3):pages 329–358. ISSN 1573-1472. http://dx.doi.org/10.1023/A:1019207923078.

Kuttler W. (1991): *Urbane Gewässer*, chapter Zum klimatischen Potential urbaner Gewässer, pages 378–394. Westarp Verlagsservicegesellschaft mbH, 1 edition.

Lalic B. and Mihailovic D. T. (2004): An Empirical Relation Describing Leaf-Area Density inside the Forest for Environmental Modeling. *J. Appl. Meteorology*, volume 43:pages 641–645.

Landsberg H. (1972): The assessment of human bioclimate. A limited review of physical parameters. Report. http://ac.ciifen.org/omm-biblioteca/CCI_TECH/WMO-331.pdf.

Lecha E. and B. L. (1998): Biometeorological classification of daily weather types for the humid tropics. *Int J Biometeorology*, volume 42:pages 77 – 83.

Lee D. H. K. (1958): Proprioclimates of man and domestic animals. In *Climatology: reviews of research*. UNESCO Conf. Paris, 1956. Arid Zone Research Ser 10:102-125.

Lee D. H. K. and Henschel A. (1966): Effects of physiological and clinical factors on response to heat. *Annals of the New York Academy of Sciences*, volume 134(2):pages 743–749. ISSN 1749-6632. http://dx.doi.org/10.1111/j.1749-6632.1966.tb43059.x.

Lee D. H. K. and Vaughan J. A. (1964): Temperature Equivalent of Solar Radiation on Man. *Int. J. Biometeorology*, volume 8(1):pages 61–69.

Lee H. and Mayer H. (2016): Validation of the mean radiant temperature simulated by the RayMan software in urban environments. *International journal of biometeorology*, volume 60(11):page 1775—1785. ISSN 0020-7128. `http://dx.doi.org/10.1007/s00484-016-1166-3`.

Lee H., Mayer H., and Chen L. (2016): Contribution of trees and grasslands to the mitigation of human heat stress in a residential district of Freiburg, Southwest Germany. *Landscape and Urban Planning*, volume 148:pages 37 – 50. ISSN 0169-2046. `http://dx.doi.org/10.1016/j.landurbplan.2015.12.004`.

Lee H., Mayer H., and Schindler D. (2014): Importance of 3-D radiant flux densities for outdoor human thermal comfort on clear-sky summer days in Freiburg, Southwest Germany. *Meteorologische Zeitschrift*, volume 23(3):pages 315–330. `http://dx.doi.org/10.1127/0941-2948/2014/0536`.

Li C. and Yu C. W. (2014): Mitigation of Urban Heat Development by Cool Island Effect of Green Space and Water Body. In *Proceedings of the 8th International Symposium on Heating, Ventilation and Air Conditioning*. Xi'an, China. ISBN 978-3-642-39583-3. `http://dx.doi.org/10.1007/978-3-642-39584-0`. Lecture Notes in Electrical Engineering 261.

Libert J. P., Di Nisi J., Fukuda H., Muzet A., Ehrhart J., and Amoros C. (1988): Effect of Continuous Heat Exposure on Sleep Stages in Humans. *Sleep*, volume 11(2):pages 195–209. `http://dx.doi.org/10.1093/sleep/11.2.195`.

Lin T.-P. and Matzarakis A. (2008): Tourism climate and thermal comfort in Sun Moon Lake, Taiwan. *International Journal of Biometeorology*, volume 52(4):pages 281–290. ISSN 0020-7128. `http://dx.doi.org/10.1007/s00484-007-0122-7`.

Lind A. R. and Hellon R. F. (1957): Assessment of Physiological Severity of Hot Climates. *J Appl Physiol*, volume 11:pages 35–40.

Lindberg F. and Grimmond C. (2011): The influence of vegetation and building morphology on shadow patterns and mean radiant temperatures in urban areas: model development and evaluation. *Theoretical and Applied Climatology*, volume 105(3-4):pages 311–323. ISSN 0177-798X. `http://dx.doi.org/10.1007/s00704-010-0382-8`.

Lindberg F., Holmer B., and Thorsson S. (2008): SOLWEIG 1.0 – Modelling spatial variations of 3D radiant fluxes and mean radiant temperature in complex urban settings.

International Journal of Biometeorology, volume 52(7):pages 697–713. ISSN 0020-7128. http://dx.doi.org/10.1007/s00484-008-0162-7.

Linde M. (2011): *Modellierung des Einflusses von Windkraftanlagen auf das umgebende Windfeld.* Diplomarbeit, Geowissenschaften, University of Hamburg, Hamburg, Germany. https://mi-pub.cen.uni-hamburg.de/fileadmin/files/forschung/techmet/nummod/thesis/Diplomarbeit_M_Linde.pdf.

Linke F. (1926): Die Übertemperatur einer frei aufgestellten schwarzen Kugel. *Meteorologische Zeitschrift*, volume 42:pages 11–15.

Liopo T. and Cicenko G. (1971): *Climatic conditions and human thermal state.* Leningrad Hydrometeorological Publishing House.

Lobaccaro G. and Acero J. A. (2015): Comparative analysis of green actions to improve outdoor thermal comfort inside typical urban street canyons. *Urban Climate*, volume 14, Part 2:pages 251–267. ISSN 2212-0955. http://dx.doi.org/10.1016/j.uclim.2015.10.002.

Lopes A., Lopes S., Matzarakis A., and Alcoforado M. J. (2011): The influence of the summer sea breeze on thermal comfort in Funchal (Madeira). A contribution to tourism and urban planning. *Meteorologische Zeitschrift*, volume 20(5):pages 553–564. http://dx.doi.org/10.1127/0941-2948/2011/0248.

Lutz W., Sanderson W., and Scherbov S. (2008): The coming acceleration of global population ageing. *Nature*, volume 451:pages 716–719. http://dx.doi.org/10.1038/nature06516.

MacPherson R. K. (1962): The Assessment of the Thermal Environment. A Review. *British Journal of Industrial Medicine*, volume 19(3):pages 151–164. http://oem.bmj.com/content/19/3/151.abstract.

Malchaire J., Piette A., Kampmann B., Mehnert P., Gebhardt H., Havenith G., den Hartog E., Holmer I., Parsons K., Alfano G., and Griefahn B. (2001): Development and validation of the predicted heat strain model. *Annals of Occupational Hygiene*, volume 45(2):pages 123–135. http://dx.doi.org/10.1093/annhyg/45.2.123.

Maloney S. and Forbes C. (2011): What effect will a few degrees of climate change have on human heat balance? Implications for human activity. *International Journal of Biometeorology*, volume 55(2):pages 147–160. http://dx.doi.org/10.1007/s00484-010-0320-6.

Manteghi G., bin limit H., and Remaz D. (2015): Water Bodies an Urban Microclimate: A Review. *Modern Applied Science*, volume 9(6). http://dx.doi.org/10.5539/mas.v9n6p1.

Martins T. A., Adolphe L., Bonhomme M., Bonneaud F., Faraut S., Ginestet S., Michel C., and Guyard W. (2016): Impact of Urban Cool Island measures on outdoor climate and pedestrian comfort: Simulations for a new district of Toulouse, France. *Sustainable Cities and Society*, volume 26:pages 9 – 26. ISSN 2210-6707. http://dx.doi.org/https://doi.org/10.1016/j.scs.2016.05.003.

Marty C. and Philipona R. (2000): The clear-sky index to separate clear-sky from cloudy-sky situations in climate research. *Geophysical Research Letters*, volume 27(17):pages 2649–2652. http://dx.doi.org/10.1029/2000GL011743.

Masiero E. and Souza L. C. L. d. (2013): Variation of absolute humidity and air temperature in the urban canopy layer in the surroundings of a water body. *Ambiente Construado*, volume 13:pages 25 – 39. ISSN 1678-8621. http://dx.doi.org/10.1590/S1678-86212013000400003.

Masterson J. and Richardson F. A. (1979): Humidex, a method of quantifying human discomfort due to excessive heat and humidity. http://ptaff.ca/humidex/?lang=en_CA. Environment Canada.

Matyukhin V. and Kushnirenko E. (1987): Complex quality assessment of environmental influence on the human body. In *Proceedings of the WMO; WHO, UNEP-Symposium on Climate and Human Health*, volume 2, pages 33–37. WMO-WCP, Geneva.

Matzarakis A. and Fröhlich D. (2015): Sport events and climate for visitors—the case of FIFA World Cup in Qatar 2022. *International Journal of Biometeorology*, volume 59(4):pages 481–486. ISSN 1432-1254. http://dx.doi.org/10.1007/s00484-014-0886-5.

Matzarakis A. and Fröhlich D. (2009): RayMan. http://www.urbanclimate.net/rayman/, last acessed 27.10.2016.

Matzarakis A. and Gulyás A. (2011): A contribution to the thermal bioclimate of Hungary - mapping of the physiological equivalent temperature. In *Studies in Honour of Professor Ilona Bárány-Kevei on the Occasion of Her Birthday*, pages 479–488. Kiss, A. and Mezősi. G. and Sümeghy. Z., SZTE Éghajlattani és Tájföldrajzi Tanszék, Természeti Földrajzi és Geoinformatikai Tanszék, Szeged. http://www2.sci.u-szeged.hu/eghajlattan/baba/Matzarakis.pdf.

Matzarakis A. and Mayer H. (1996): Another kind of environmental stress: thermal stress. *WHO Colloborating Centre for Air Quality Management and Air Pollution Control Newsletter*, volume 18:pages 7–10.

Matzarakis A., Muthers S., and Rutz F. (2014): Application and comparison of UTCI and PET in temperate climate conditions. *Finisterra - Revista Portuguesa de Geografia*, volume XLIX(98):pages 21–31. http://dx.doi.org/10.18055/Finis6453.

Matzarakis A., Rutz F., and Mayer H. (2007): Modelling radiation fluxes in simple and complex environments—application of the RayMan model. *International Journal of Biometeorology*, volume 51(4):pages 323–334. ISSN 0020-7128. http://dx.doi.org/10.1007/s00484-006-0061-8.

Matzarakis A., Rutz F., and Mayer H. (2010): Modelling radiation fluxes in simple and complex environments: basics of the RayMan model. *International Journal of Biometeorology*, volume 54(2):pages 131–139. ISSN 0020-7128. http://dx.doi.org/10.1007/s00484-009-0261-0.

Mayer H., Holst J., Dostal P., Imbery F., and Schindler D. (2008): Human thermal comfort in summer within an urban street canyon in Central Europe. *Meteorologische Zeitschrift*, volume 17(3):pages 241–250. http://dx.doi.org/10.1127/0941-2948/2008/0285.

Mayer H. and Höppe P. (1987): Thermal comfort of man in different urban environments. *Theoretical and Applied Climatology*, volume 38(1):pages 43–49. ISSN 0177-798X. http://dx.doi.org/10.1007/BF00866252.

McArdle B., Dunham W., Holling H., Ladell W., Scott J., Thomson M., and Weiner J. (1947): The Prediciton of the physiological Effects of warm and hot environments. Report. RNP Rep. 47/391.

McIntyre D. (1973): A guide to thermal comfort. *Applied Ergonomics*, volume 4(2):pages 66–72. http://dx.doi.org/10.1016/0003-6870(73)90079-3.

McLaughlin J. T. and Shulman M. D. (1977): An Anthropocentric Summer Severity Index. *Int J Biometeorology*, volume 21(1):pages 16 – 28.

McPherson M. J. (1992): The generalization of air cooling power. In M. V. S. o. S. Africa, editor, *Proceedings of the 5th International Mine Ventilation Congress*, pages 27 – 35. Johannesburg:.

Mehnert P., Malchaire J., Kampmann B., Piette A., Griefahn B., and Gebhardt H. (2000): Prediction of the average skin temperature in warm and hot environments. *Eur J Appl Physiol.*, volume 82(1-2):pages 52–60.

Minella F. O., Krüger E., Honjo S., Goyette S., and Hedjazi A. (2014): Daytime microclimatic impacts of the SOVALP project in summer: A case study in Geneva, Switzerland. *Simulation*, volume 90(8):pages 857–873. ISSN 0037-5497. `http://dx.doi.org/10.1177/0037549714543085`.

Mochida T. (1979): Comfort Chart : An Index for Evaluating Thermal Sensation. *Memoirs of the Faculty of Engineering, Hokkaido University*, volume 15(2):pages 175 – 185. `http://hdl.handle.net/2115/37977`.

Moher D., Liberati A., Tetzlaff J., Altman D. G., and The P. G. (2009): Preferred Reporting Items for Systematic Reviews and Meta-Analyses: The PRISMA Statement. *PLOS Medicine*, volume 6(7):page e1000097. `http://dx.doi.org/10.1371/journal.pmed.1000097`.

Molenaar R. E., Heusinkveld B. G., and Steeneveld G. J. (2015): Projection of rural and urban human thermal comfort in The Netherlands for 2050. *International Journal of Climatology*, volume 36(4):pages 1708–1723. `http://dx.doi.org/10.1002/joc.4453`.

Moonen P., Defraeye T., Dorer V., Blocken B., and Carmeliet J. (2012): Urban Physics: Effect of the micro-climate on comfort, health and energy demand. *Frontiers of Architectural Research*, volume 1(3):pages 197 – 228. ISSN 2095-2635. `http://dx.doi.org/10.1016/j.foar.2012.05.002`.

Morakinyo T. E., Dahanayake K. K. C., Adegun O. B., and Balogun A. A. (2016): Modelling the effect of tree-shading on summer indoor and outdoor thermal condition of two similar buildings in a Nigerian university. *Energy and Buildings*, volume 130:pages 721 – 732. ISSN 0378-7788. `http://dx.doi.org/10.1016/j.enbuild.2016.08.087`.

Morakinyo T. E. and Lam Y. F. (2016): Simulation study on the impact of tree-configuration, planting pattern and wind condition on street-canyon's micro-climate and thermal comfort. *Building and Environment*, volume 103:pages 262–275. ISSN 0360-1323. http://dx.doi.org/10.1016/j.buildenv.2016.04.025.

Moran D. S., Castellani J. W., O'Brien C., Young D. T., and Pandolf K. B. (1999): Evaluating physiological strain during cold exposure using a new cold strain index. *Am J Physiol*, volume 277(46):page R556–R564.

Moran D. S., Pandolf K. B., Shapiro Y., Heled Y., Shani Y., Mathew W. T., and Gonzalez R. R. (2001): An environmental stress index (ESI) as a substitute for the wet bulb globe temperature (WBGT). *Journal of Thermal Biology*, volume 26:pages 427 – 431.

Moran D. S., Shitzer A., and Pandolf K. B. (1998): A physiological strain index to evaluate heat stress. *Am J Physiol Regul Integr Comp Physiol*, volume 275(R129 - R134).

Morris A. E. J. (1994): *History of urban form: Before the industrial revolutions.* Harlow, Longman.

Mou I. Z. H. and Fahim M. R. (2013): Relevance of Waterbody in Inducing Low Temperature in Residential Neighborhood: A Case of Dhanmondi, Dhaka. *Journal of Modern Science and Technology*, volume 1(1):pages 157–166.

Mount L. and Brown D. (1985): The calculation from weather records of the requirement for clothing insulation. *International Journal of Biometeorology*, volume 29(4):pages 311–321. http://dx.doi.org/10.1007/BF02189205.

Müller N., Kuttler W., and Barlag A.-B. (2013): Counteracting urban climate change: adaptation measures and their effect on thermal comfort. *Theoretical and Applied Climatology*, volume 115(1):pages 243–257. ISSN 1434-4483. http://dx.doi.org/10.1007/s00704-013-0890-4.

Müller N., Kuttler W., and Barlag A.-B. (2014): Counteracting urban climate change: adaptation measures and their effect on thermal comfort. *Theoretical and Applied Climatology*, volume 115(1):pages 243–257. ISSN 1434-4483. http://dx.doi.org/10.1007/s00704-013-0890-4.

Murakawa S., Sekine T., ichi Narita K., and Nishina D. (1991): Study of the effects of a river on the thermal environment in an urban area. *Energy and Buildings*, volume 16(3–4):pages 993 – 1001. ISSN 0378-7788. http://dx.doi.org/10.1016/0378-7788(91)90094-J.

Nagano K. and Horikoshi T. (2011): New index indicating the universal and separate effects on human comfort under outdoor and non-uniform thermal conditions. *Energy and Buildings*, volume 43(7):pages 1694 – 1701. ISSN 0378-7788. http://dx.doi.org/10.1016/j.enbuild.2011.03.012.

Nikolopoulou M., Baker N., and Steemers K. (2001): Thermal comfort in outdoor urban spaces: understanding the human parameter. *Solar Energy*, volume 70(3):pages 227 – 235. ISSN 0038-092X. http://dx.doi.org/10.1016/S0038-092X(00)00093-1. Urban Environment.

Norton J. (2015): An introduction to sensitivity assessment of simulation models. *Environmental Modelling & Software*, volume 69:pages 166 – 174. ISSN 1364-8152. http://dx.doi.org/10.1016/j.envsoft.2015.03.020.

Nossent J., Elsen P., and Bauwens W. (2011): Sobol' sensitivity analysis of a complex environmental model. *Environmental Modelling & Software*, volume 26(12):pages 1515 – 1525. ISSN 1364-8152. http://dx.doi.org/10.1016/j.envsoft.2011.08.010.

OFCM (Office of the Federal Coordinator for Meteorological services and supporting research) (2003): Report on Wind Chill Temperature and Extreme Heat Indices: Evaluation and Improvement Projects. Report, Washington, DC.

Oke T. R. (1987): *Boundary Layer Climates*. Routledge, London, 2 edition.

Oke T. R., Mills G., Christen A., and Voogt J. A. (2017): *Urban Climates*. Cambridge University Press. http://dx.doi.org/10.1017/9781139016476.

O'Neill M. S. and Ebi K. L. (2009): Temperature Extremes and Health: Impacts of Climate Variability and Change in the United States. *Journal of Occupational and Environmental Medicine*, volume 51(1):pages 13–25. http://dx.doi.org/10.1097/JOM.0b013e318173e122.

Ono H.-S. P. and Kawamura T. (1991): Sensible climates in monsoon Asia. *International Journal of Biometeorology*, volume 35(1):pages 39–47. http://dx.doi.org/10.1007/BF01040962.

Osczevski R. and Bluestein M. (2005): The New Wind Chill Equivalent Temperature Chart. *Bull. Amer. Meteor. Soc.*, volume 86:pages 1453–1458.

Pandolf K. B., Stroschein L. A., Drolet L. L., Gonzalez R. R., and Sawka M. N. (1985): Prediction Modeling of Physiological Responses and Human Performance in the Heat. Technical Report M1/86, US Army Rsch Inst of Env Med, Natick, Massachusetts.

Park S., Tuller S. E., and Jo M. (2014): Application of Universal Thermal Climate Index (UTCI) for microclimatic analysis in urban thermal environments. *Landscape and Urban Planning*, volume 125:pages 146 – 155. ISSN 0169-2046. `http://dx.doi.org/10.1016/j.landurbplan.2014.02.014`.

Parsons K. C. (2014): *Human thermal environments: the effects of hot, moderate, and cold environments on human health, comfort, and performance.* CRC Press, 3 edition.

Peng L. L. and Jim Y. C. (2013): Green-Roof Effects on Neighborhood Microclimate and Human Thermal Sensation. *Energies*, volume 6(2). ISSN 1996-1073. `http://dx.doi.org/10.3390/en6020598`.

Pepi J. W. (1987): The summer simmer index. *Weatherwise*, volume 40:pages 143–145.

Pepi J. W. (1999): The new Summer Simmer Index: a comfort index for the new millennium. `http://www.summersimmer.com/home.htm`.

Perini K. and Magliocco A. (2014): Effects of vegetation, urban density, building height, and atmospheric conditions on local temperatures and thermal comfort. *Urban Forestry & Urban Greening*, volume 13(3):pages 495 – 506. ISSN 1618-8667. `http://dx.doi.org/10.1016/j.ufug.2014.03.003`.

Pianosi F., Beven K., Freer J., Hall J. W., Rougier J., Stephenson D. B., and Wagener T. (2016): Sensitivity analysis of environmental models: A systematic review with practical workflow. *Environmental Modelling & Software*, volume 79:pages 214 – 232. ISSN 1364-8152. `http://dx.doi.org/10.1016/j.envsoft.2016.02.008`.

Pianosi F., Sarrazin F., and Wagener T. (2015): A Matlab toolbox for Global Sensitivity Analysis. *Environmental Modelling & Software*, volume 70:pages 80 – 85. ISSN 1364-8152. `http://dx.doi.org/10.1016/j.envsoft.2015.04.009`.

Pianosi F., Sarrazin F., and Wagener T. (2018): SAFE Toolbox – F.A.Q. `https://www.safetoolbox.info/faqs/`. Last accessed 18.06.2018.

Pianosi F. and Wagener T. (2015): A simple and efficient method for global sensitivity analysis based on cumulative distribution functions. *Environmental Modelling & Software*, volume 67:pages 1 – 11. ISSN 1364-8152. http://dx.doi.org/10.1016/j.envsoft.2015.01.004.

Pickup J. and de Dear R. J. (2000): An Outdoor Thermal Comfort Index (OUT_SET*) - Part I - The Model and its assumptions. In R. de Dear; J. Kalma; T. Oke; and A. Auliciems, editors, *Biometeorology and Urban Climatology at the Turn of the Millennium: Selected Papers from the Conference ICB-ICUC'99*. WCASP-50 WMO/TD-No. 1026. World Meteorological Organization: Geneva.

Pielke Sr. R. A. (2013): *Mesoscale Meteorological Modeling*. Elsevier Academic Press, 3 edition.

Provençal S., Bergeron O., Leduc R., and Barrette N. (2015): Thermal comfort in Quebec City, Canada: sensitivity analysis of the UTCI and other popular thermal comfort indices in a mid-latitude continental city. *International Journal of Biometeorology*, pages 1–13. ISSN 0020-7128. http://dx.doi.org/10.1007/s00484-015-1054-2.

Pulket C., Henschel A., Burg W. R., and Saltzman B. E. (1980): A comparison of heat stress indices in a hot-humid environment. *American Industrial Hygiene Association Journal*, volume 41(6):pages 442–449.

Qaid A., Bin Lamit H., Ossen D. R., and Raja Shahminan R. N. (2016): Urban heat island and thermal comfort conditions at micro-climate scale in a tropical planned city. *Energy and Buildings*, volume 133:pages 577–595. ISSN 0378-7788. http://dx.doi.org/10.1016/j.enbuild.2016.10.006.

Reindl D., Beckman W., and Duffie J. (1990): Diffuse fraction correlations. *Solar Energy*, volume 45(1):pages 1 – 7. ISSN 0038-092X. http://dx.doi.org/10.1016/0038-092X(90)90060-P.

Remund J., Wald L., Lefevre M., Ranchin T., and Page J. (2003): Worldwide Linke turbidity information. In *ISES Solar World Congress 2003,*. CD-ROM published by International Solar Energy Society.

Resler J., Krč P., Belda M., Juruš P., Benešová N., Lopata J., Vlček O., Damašková D., Eben K., Derbek P., Maronga B., and Kanani-Sühring F.

(2017): PALM-USM v1.0: A new urban surface model integrated into the PALM large-eddy simulation model. *Geoscientific Model Development*, volume 10(10):pages 3635–3659. http://dx.doi.org/10.5194/gmd-10-3635-2017.

Rida M., Ghaddar N., Ghali K., and Hoballah J. (2014): Elderly bioheat modeling: changes in physiology, thermoregulation, and blood flow circulation. *International Journal of Biometeorology*, volume 58(9):pages 1825–1843. ISSN 0020-7128. http://dx.doi.org/10.1007/s00484-013-0785-1.

Riecke W. and Rosenhagen G. (2010): Das Klima in Hamburg: Entwicklung in Hamburg und der Metropolregion. *Berichte des Deutschen Wetterdienstes*, volume 234.

Rigollier C., Bauer O., and Wald L. (2000): On the clear sky model of the ESRA - European Solar Radiation Atlas with respect to the Heliosat method. *Solar Energy*, volume 1(68):pages 33–48.

Rizzo G., Franzitta G., and Cannistraro G. (1991): Algorithms for the calculation of the mean projected area factors of seated and standing persons. *Energy and Buildings*, volume 17(3):pages 221 – 230. ISSN 0378-7788. http://dx.doi.org/10.1016/0378-7788(91)90109-G.

Robinson S., Turrell E. S., and Gerking S. D. (1944): Physiologically equivalent conditions of air temperature and humidity. *Am J Physiol*, volume 143:pages 21–32. http://ajplegacy.physiology.org/content/ajplegacy/143/1/21.full.pdf.

Robitu M., Musy M., Inard C., and Groleau D. (2006): Modeling the influence of vegetation and water pond on urban microclimate. *Solar Energy*, volume 80(4):pages 435–447. ISSN 0038-092X. http://dx.doi.org/10.1016/j.solener.2005.06.015.

Rodriguez C., Mateos J., and Garmendia J. (1985): Biometeorological comfort index. *International Journal of Biometeorology*, volume 29(2):pages 121–129. http://dx.doi.org/10.1007/BF02189031.

Rohles F. H., Hayter R., and Milliken G. (1975): Effective Temperature (ET*) as a predictor of thermal comfort. *ASHRAE Trans*, volume 81(2):pages 148–156.

Rohles F. H. and Nevis R. G. (1971): The nature of thermal comfort for sedentary man. *ASHRAE Trans*, volume 77(1):pages 239–246.

Rohles F. H., Woods J. E., and Nevis R. G. (1974): The Effects of Air Movement and Temperature on the Thermal Sensation of Sedentary Man. In *ASHRAE Semiannual Meeting*, 2298. ASHRAE, Los Angeles CA.

Rublack K., Medvedeva E. F., Gaebelein H., Noack H., and Schulz G. (1981): Integrative Bewertung der Wärmebelastung durch Arbeit und Klima. *Z. ges. Hyg*, volume 27:pages 12 – 17.

Rusanov V. (): Climate and human health. (1986). In *WMO; WHO, UNEP-Symposium on Climate and Human Health in*, volume 2, page 101–106. WMO-WCP, Geneva.

Rusanov V. (1981): Complex meteorological indices and methods of climate assessment in medical purposes – Handbook for students.

Saaroni H. and Ziv B. (2003): The impact of a small lake on heat stress in a Mediterranean urban park: the case of Tel Aviv, Israel. *International Journal of Biometeorology*, volume 47(3):pages 156–165. ISSN 1432-1254. `http://dx.doi.org/10.1007/s00484-003-0161-7`.

Salim M. H., Schlünzen K. H., Grawe D., Boettcher M., Gierisch A. M. U., and Fock B. H. (2018): The Microscale Obstacle Resolving Meteorological Model MITRAS: Model Theory. *Geoscientific Model Development Discussions*, volume 2018:pages 1–31. `http://dx.doi.org/10.5194/gmd-2017-250`.

Salim M. H., Schlünzen K. H., and Grawe D. (2015): Including trees in the numerical simulations of the wind flow in urban areas: Should we care? *Journal of Wind Engineering and Industrial Aerodynamics*, volume 144:pages 84 – 95. ISSN 0167-6105. `http://dx.doi.org/10.1016/j.jweia.2015.05.004`. Selected papers from the 6th International Symposium on Computational Wind Engineering CWE 2014.

Saltelli A. and Annoni P. (2010): How to avoid a perfunctory sensitivity analysis. *Environmental Modelling & Software*, volume 25(12):pages 1508 – 1517. ISSN 1364-8152. `http://dx.doi.org/10.1016/j.envsoft.2010.04.012`.

Saltelli A., Annoni P., Azzini I., Campolongo F., Ratto M., and Tarantola S. (2010): Variance based sensitivity analysis of model output. Design and estimator for the total sensitivity index. *Computer Physics Communications*, volume 181(2):pages 259 – 270. ISSN 0010-4655. `http://dx.doi.org/10.1016/j.cpc.2009.09.018`.

Sander H. A. and Zhao C. (2015): Urban green and blue: Who values what and where? *Land Use Policy*, volume 42:pages 194 – 209. ISSN 0264-8377. `http://dx.doi.org/10.1016/j.landusepol.2014.07.021`.

Saneinejad S., Moonen P., and Carmeliet J. (2014): Coupled CFD, radiation and porous media model for evaluating the micro-climate in an urban environment. *Journal of Wind Engineering and Industrial Aerodynamics*, volume 128:pages 1 – 11. ISSN 0167-6105. `http://dx.doi.org/10.1016/j.jweia.2014.02.005`.

Santee W. and Wallace R. F. (2003): Evaluation of weather service heat indices using the USARIEM heat strain decision aid (HSDA) model. Report, U.S. Army Research Institute of Environmental Medicine.

Scharlau K. (1943): Die Schwüle als meßbare Größe. *Bioklimatische Beiblätter (Meteorologische Zeitschrift)*, volume 10:pages 19–23.

Schatz J. and Kucharik C. J. (2014): Seasonality of the Urban Heat Island Effect in Madison, Wisconsin. *Journal of Applied Meteorology and Climatology*, volume 53(10):pages 2371–2386. `http://dx.doi.org/10.1175/JAMC-D-14-0107.1`.

Schellen L., van Marken Lichtenbelt W. D., Loomans M. G. L. C., Toftum J., and de Wit M. H. (2010): Differences between young adults and elderly in thermal comfort, productivity, and thermal physiology in response to a moderate temperature drift and a steady-state condition. *Indoor Air*, volume 20:pages 273 – 283. `http://dx.doi.org/doi:10.1111/j.1600-0668.2010.00657.x`.

Schlünzen K. H., Bungert U., Flagg D. D., Fock B. H., Gierisch A., Grawe D., Kirschner P., Lüpkes C., Reinhardt V., Ries H., Schoetter R., Spensberger C., and Uphoff M. (2012a): *Technical Documentation of the Multiscale Model System M-SYS*. Meteorological Institute, University of Hamburg. MEMI Technical Report 3, `https://www.mi.zmaw.de/fileadmin/files/forschung/techmet/nummod/metras/M-SYS_Technical_Documentation_2012-02-13.pdf`.

Schlünzen K. H., Flagg D. D., Fock B. H., Gierisch A., Lüpkes C., Reinhardt V., and Spensberger C. (2012b): *Scientific Documentation of the Multiscale Model System M-SYS*. Meteorological Institute, University of Hamburg. MEMI Technical Report 4.

Schlünzen K. H., Hinneburg D., Knoth O., Lambrecht M., Leitl B., López S., Lüpkes C., Panskus H., Renner E., Schatzmann M., Schoenemeyer T., Trepte S., and Wolke R. (2003): Flow and Transport in the Obstacle Layer: First Results of the Micro-Scale Model MITRAS. *Journal of Atmospheric Chemistry*, volume 44(2):pages 113–130. ISSN 1573-0662. `http://dx.doi.org/10.1023/A:1022420130032`.

Schlünzen K. H. and Sokhi R. S., editors (2008): *Overview of Tools and Methods for meteorological and air pollution mesoscale model evaluation and user training*. World Meteorological Organization. ISBN 978-1-905313-59-4. GAW Report No. 181.

Schlüter I. (2006): *Simulation des Transports biogener Emissionen in und über einem Waldbestand mit einem mikroskaligen Modellsystem*. Ph.D. thesis, Geowissenschaften, Universität Hamburg. `http://www.sub.uni-hamburg.de/opus/volltexte/2006/3054/`.

Schlünzen K., Ries H., Kirschner P., and Grawe D. (2011a): Machbarkeitsstudie Modellierung von Stadtklima – Abschlussbericht für Teil 1: Bewertung etablierter Methoden zur Einschätzung des Stadtklimas und Nutzung der vielfältigen Informationen zu vorhandenen Flächennutzungen für numerische Modelle. Technical report, Meteorological Institute, University of Hamburg. `https://www.mi.zmaw.de/fileadmin/files/forschung/techmet/nummod/Machbarkeitsstudie/BSU_AbschlussBericht_TeilI.pdf`.

Schlünzen K. H., Grawe D., Bohnenstengel S. I., Schlüter I., and Koppmann R. (2011b): Joint modelling of obstacle induced and mesoscale changes—Current limits and challenges. *Journal of Wind Engineering and Industrial Aerodynamics*, volume 99(4):pages 217 – 225. ISSN 0167-6105. `http://dx.doi.org/10.1016/j.jweia.2011.01.009`. The Fifth International Symposium on Computational Wind Engineering.

Schlünzen K. H., Hoffmann P., Rosenhagen G., and Riecke W. (2010): Long-term changes and regional differences in temperature and precipitation in the metropolitan area of Hamburg. *International Journal of Climatology*, volume 30(8):pages 1121–1136. ISSN 1097-0088. `http://dx.doi.org/10.1002/joc.1968`.

Schoen C. (2005): A New Empirical Model of the Temperature-Humidity Index. *J. Appl. Meteor.*, volume 44. ISSN 1413–1420. `http://dx.doi.org/10.1175/JAM2285.1`.

Schoetter R., Grawe D., Hoffmann P., Kirschner P., Grätz A., and Schlünzen K. H. (2013): Impact of local adaptation measures and regional climate change on perceived temperature. *Meteorologische Zeitschrift*, volume 22(2):pages 117–130. http://dx.doi.org/10.1127/0941-2948/2013/0381.

Schrijvers P. J. C., Jonker H. J. J., de Roode S. R., and Kenjereš S. (2016): The effect of using a high-albedo material on the Universal Temperature Climate Index within a street canyon. *Urban Climate*, volume 17:pages 284–303. ISSN 2212-0955. http://dx.doi.org/10.1016/j.uclim.2016.02.005.

Sheppard M. (2012): allfitdist. Matlab file exchange; https://de.mathworks.com/matlabcentral/fileexchange/34943-fit-all-valid-parametric-probability-distributions-to-data?s_tid=prof_contriblnk, last acessed 22.03.2017.

Sheridan S. C. (2002): The redevelopment of a weather-type classification scheme for North America. *International Journal Of Climatology*, volume 22(1):pages 51–68. ISSN 1097-0088. http://dx.doi.org/10.1002/joc.709.

Siple P. A. and Passel C. F. (1945): Measurements of Dry Atmospheric Cooling in Subfreezing Temperatures. *Proceedings of the American Philosophical Society*, volume 89(1):pages 177–199. ISSN 0003049X. http://www.jstor.org/stable/985324.

Smith F. E. (1952): Effective Temeprature as an index of physiological stress. Report, Medical Research Council, London.

SoDa Service (2017): Linke Turbidity factor, Ozone, Water Vapor and Angstroembeta - 2003. http://www.soda-pro.com/web-services/atmosphere/linke-turbidity-factor-ozone-water-vapor-and-angstroembeta. last accessed, 03.12.2017 .

Song X., Zhang J., Zhan C., Xuan Y., Ye M., and Xu C. (2015): Global sensitivity analysis in hydrological modeling: Review of concepts, methods, theoretical framework, and applications. *Journal of Hydrology*, volume 523:pages 739 – 757. ISSN 0022-1694. http://dx.doi.org/10.1016/j.jhydrol.2015.02.013.

Spagnolo J. C. and de Dear R. J. (2003): A human thermal climatology of subtropical Sydney. *International Journal of Climatology*, volume 23(11):pages 1383–1395. ISSN 1097-0088. http://dx.doi.org/10.1002/joc.939.

Spiessl S. M. and Becker D.-A. (2015): Sensitivity analysis of a final repository model with quasi-discrete behaviour using quasi-random sampling and a metamodel approach in comparison to other variance-based techniques. *Reliability Engineering & System Safety*, volume 134:pages 287 – 296. ISSN 0951-8320. http://dx.doi.org/10.1016/j.ress.2014.08.008.

Staiger H. (2014): *Die Strahlungskomponente im thermischen Wirkungskomplex für operationelle Anwendungen in der Human-Biometeorologie*. Ph.D. thesis, Geowissenschaften, Albert-Ludwigs-Universität Freiburg im Breisgau, Germany. https://www.freidok.uni-freiburg.de/dnb/download/9980.

Staiger H. (2016): Irradiance SYNOP. Fortran program received by personal communication, documented in Staiger (2014).

Staiger H., Laschewski G., and Grätz A. (2011): The perceived temperature – a versatile index for the assessment of the human thermal environment. Part A: scientific basics. *International Journal Biometeorology*, volume 56:pages 165–176.

Stavrakakis G. M., Tzanaki E., Genetzaki V. I., Anagnostakis G., Galetakis G., and Grigorakis E. (2012): A computational methodology for effective bioclimatic-design applications in the urban environment. *Sustainable Cities and Society*, volume 4:pages 41–57. ISSN 2210-6707. http://dx.doi.org/10.1016/j.scs.2012.05.002.

Steadman R. G. (1971): Indices of Windchill of Clothed Persons. *J. Appl. Meteor.*, volume 10:pages 674–683.

Steadman R. G. (1979): The Assessment of Sultriness. Part II: Effects of Wind, Extra Radiation and Barometric Pressure on Apparent Temperature. *J. Appl. Meteor.*, volume 18:pages 874–885. http://dx.doi.org/10.1175/1520-0450(1979)018<0874:TAOSPI>2.0.CO;2.

Steadman R. G. (1984): A Universal Scale of Apparent Temperature. *J. Climate Appl. Meteor*, volume 23:pages 1674–1687. http://dx.doi.org/10.1175/1520-0450(1984)023<1674:AUSOAT>2.0.CO;2.

Steadman R. G. (1994): Norms of apparent temperature in Australia. *Aust. Met. Mag.*, volume 43(1):pages 1–16. http://reg.bom.gov.au/amm/docs/1994/steadman.pdf.

Steeneveld G., Koopmans S., Heusinkveld B., and Theeuwes N. (2014): Refreshing the role of open water surfaces on mitigating the maximum urban heat island effect. *Landscape and Urban Planning*, volume 121:pages 92 – 96. ISSN 0169-2046. `http://dx.doi.org/10.1016/j.landurbplan.2013.09.001`.

Stewart I. D. and Oke T. R. (2012): Local Climate Zones for Urban Temperature Studies. *Bulletin of the American Meteorological Society*, volume 93(12):pages 1879–1900. `http://dx.doi.org/10.1175/BAMS-D-11-00019.1`.

von Storch H. and Claussen M., editors (2011): *Klimabericht für die Metropolregion Hamburg*. Springer Berlin Heidelberg. ISBN 978-3-642-16035-6. `http://dx.doi.org/10.1007/978-3-642-16035-6`.

Stull R. (2011): Wet-Bulb Temperature from Relative Humidity and Air Temperature. *Journal of Applied Meteorology and Climatology*, volume 50(11):pages 2267–2269. `http://dx.doi.org/10.1175/JAMC-D-11-0143.1`.

Syafii N. I., Ichinose M., Kumakura E., Jusuf S. K., Chigusa K., and Wong N. H. (2017): Thermal environment assessment around bodies of water in urban canyons: A scale model study. *Sustainable Cities and Society*, volume 34:pages 79 – 89. ISSN 2210-6707. `http://dx.doi.org/10.1016/j.scs.2017.06.012`.

von Szombathely M., Albrecht M., Antanaskovic D., Augustin J., Augustin M., Bechtel B., Bürk T., Fischereit J., Grawe D., Hoffmann P., Kaveckis G., Krefis A. C., Oßenbrügge J., Scheffran J., and Schlünzen K. H. (2017): A Conceptual Modeling Approach to Health-Related Urban Well-Being. *Urban Science*, volume 1(2). ISSN 2413-8851. `http://dx.doi.org/10.3390/urbansci1020017`.

Taleghani M., Kleerekoper L., Tenpierik M., and van den Dobbelsteen A. (2015): Outdoor thermal comfort within five different urban forms in the Netherlands. *Building and Environment*, volume 83:pages 65–78. ISSN 0360-1323. `http://dx.doi.org/10.1016/j.buildenv.2014.03.014`.

Taleghani M., Sailor D., and Ban-Weiss G. A. (2016): Micrometeorological simulations to predict the impacts of heat mitigation strategies on pedestrian thermal comfort in a Los Angeles neighborhood. *Environmental Research Letters*, volume 11(2):page 024003. ISSN 1748-9326. `http://stacks.iop.org/1748-9326/11/i=2/a=024003`.

Tennenbaum J., Sohar E., Adar R., Gilat T., and Yaski D. (1961): The physiological significance of the cumulative discomfort index (Cum DI). *Harefuah*, volume 60(10):pages 315–319.

Terjung W. (1966): Physiologic climates of the conterminous united states: A bioclimatic classification based on man. *Annals of the Association of American Geographers*, volume 56(1):pages 141–179. `http://dx.doi.org/10.1111/j.1467-8306.1966.tb00549.x`.

Terjung W. (1968): World patterns of distribution of the monthly comfort index. *Int J Biometeorology*, volume 12:pages 119–151.

Thilenius R. and Dorno C. (1925): Das Davoser Frigorimeter - ein Instrument zur Dauerregistrierung der physiologischen Abkühlungsgröße. *Meteorologische Zeitschrift*, volume 42:pages 57–60.

Thorsson H. T. Sofia, Lindberg F., Eliasson I., and Lim E.-M. (2007a): Thermal Comfort and Outdoor Activity in Japanese Urban Public Places. *Environment and Behavior*, volume 39(5). `http://dx.doi.org/10.1177/0013916506294937`.

Thorsson S., Lindberg F., Eliasson I., and Holmer B. (2007b): Different methods for estimating the mean radiant temperature in an outdoor urban setting. *International Journal of Climatology*, volume 27(14):pages 1983–1993. ISSN 1097-0088. `http://dx.doi.org/10.1002/joc.1537`.

Thorsson S., Rocklöv J., Konarska J., Lindberg F., Holmer B., Dousset B., and Rayner D. (2014): Mean radiant temperature – A predictor of heat related mortality. *Urban Climate*, volume 10, Part 2(0):pages 332 – 345. ISSN 2212-0955. `http://dx.doi.org/10.1016/j.uclim.2014.01.004`. ICUC8: The 8th International Conference on Urban Climate and the 10th Symposium on the Urban Environment.

Tikuisis P., Mclellan T., and Selkirk G. (2002): Perceptual versus physiological heat strain during exercise-heat stress. *Med Sci Sports Exerc*, volume 34(9):pages 1454 – 1461.

Tominaga Y., Sato Y., and Sadohara S. (2015): {CFD} simulations of the effect of evaporative cooling from water bodies in a micro-scale urban environment: Validation and application studies. *Sustainable Cities and Society*, volume 19:pages 259 – 270. ISSN 2210-6707. `http://dx.doi.org/10.1016/j.scs.2015.03.011`.

Tromp S. W. (1966): A Physiological Method for Determining the Degree of Meteorological Cooling. *Nature*, volume 210(5035):pages 486–487. http://dx.doi.org/doi:10.1038/210486a0.

Trusilova K. and Riecke W. (2015): Klimauntersuchung für die Metropolregion Hamburg zur Entwicklung verschiedener meteorologischer Parameter bis zum Jahr 2050. *Berichte des Deutschen Wetterdienstes*.

Tsitoura M., Tsoutsos T., and Daras T. (2014): Evaluation of comfort conditions in urban open spaces. Application in the island of Crete. *Energy Conversion and Management*, volume 86:pages 250 – 258. ISSN 0196-8904. http://dx.doi.org/10.1016/j.enconman.2014.04.059.

Tumini I., Higueras García E., and Baereswyl Rada S. (2016): Urban microclimate and thermal comfort modelling: strategies for urban renovation. *International Journal of Sustainable Building Technology and Urban Development*, volume 7(1):pages 22–37. ISSN 2093-761X. http://dx.doi.org/10.1080/2093761x.2016.1152204.

Tzenkova A., Ivancheva J., Koleva E., and Videnov P. (2007): The human comfort conditions at Bulgarian Black Seaside. http://www.urbanclimate.net/cctr/ws3/report/developTourCliml.pdf.

UN (United Nations) (2015): World Urbanization Prospects: The 2014 Revision. Technical Report ((ST/ESA/SER.A/366), United Nations, Department of Economic and Social Affairs, Population Division, New York.

VDI (Verein Deutscher Ingenieure) (1994): *Environmental Meteorology - Interactions between Atmosphere and Surfaces, Calculation of Short-wave and Long-wave Radiation*. VDI 3789. Part 2, Beuth, Berlin.

VDI (Verein Deutscher Ingenieure) (2001): *Environmental Meteorology - Interactions between Atmosphere and Surfaces, Calculation of spectral irradiances in the solar wavelength range*. VDI 3789. Part 3, Beuth, Berlin.

VDI (Verein Deutscher Ingenieure) (2005): *Prognostic microscale wind field models – Evaluation for flow around buildings and obstacles*. VDI 3783. Part 9, Beuth, Berlin.

VDI (Verein Deutscher Ingenieure) (2008): *Methods for the human biometeorological evaluation of climate and air quality for urban and regional planning at regional level, Part I: Climate*. VDI 3787. Part 2, Beuth, Berlin.

VDI (Verein Deutscher Ingenieure) (2017): *Prognostic microscale wind field models – Evaluation for flow around buildings and obstacles*. VDI 3783. Part 9, Beuth, Berlin.

Vernon H. and Warner C. G. (1932): The influence of the humidity of the air on capacity for work at high temperatures. *J Hyg*, volume 32:pages 431 – 462.

Vogt J. J., Candas V., and Libert J. P. (1982): Graphical determination of heat tolerance limits. *Ergonomics*, volume 25(4):pages 285–294. http://dx.doi.org/10.1080/00140138208924955.

Vogt J. J., Candas V., Libert J. P., and Daull F. (1981): Required Sweat Rate as an Index of Thermal Strain in Industry.

Vorre M. H., Jensen R. L., and Dréau J. L. (2015): Radiation exchange between persons and surfaces for building energy simulations. *Energy and Buildings*, volume 101:pages 110 – 121. ISSN 0378-7788. http://dx.doi.org/10.1016/j.enbuild.2015.05.005.

Völker S. and Kistemann T. (2011): The impact of blue space on human health and well-being – Salutogenetic health effects of inland surface waters: A review. *International Journal of Hygiene and Environmental Health*, volume 214(6):pages 449 – 460. ISSN 1438-4639. http://dx.doi.org/10.1016/j.ijheh.2011.05.001. The second European PhD students workshop: Water and health ? Cannes 2010.

Völker S. and Kistemann T. (2015): Developing the urban blue: Comparative health responses to blue and green urban open spaces in Germany. *Health & Place*, volume 35:pages 196 – 205. ISSN 1353-8292. http://dx.doi.org/10.1016/j.healthplace.2014.10.015.

Wallace R. F., Kriebel D., Punnett L., Wegman D. H., Wenger C. B., Gardner J. W., and Gonzalez R. R. (2005): The effects of continuous hot weather training on risk of exertional heat illness. *Med Sci Sports Exerc*, volume 37(1):pages 84–90. http://dx.doi.org/10.1249/01.MSS.0000150018.90213.AA.

Watanabe S., Nagano K., Ishii J., and Horikoshi T. (2014): Evaluation of outdoor thermal comfort in sunlight, building shade, and pergola shade during summer in a humid subtropical region. *Building and Environment*, volume 82(0):pages 556 – 565. ISSN 0360-1323. http://dx.doi.org/10.1016/j.buildenv.2014.10.002.

Watts J. D. and Kalkstein L. S. (2004): The Development of a Warm-Weather Relative Stress Index for Environmental Applications. *Journal of Applied Meteorology*, volume 43:pages 503 – 513.

Webb G. G. (1959): An Analysis Of Some Observations Of Thermal Comfort In An Equatorial Climate. *Brit. J. industr. Med.*, volume 16(4):pages 297–310.

Weiss M. (1982): The humisery and other measures of summer discomfort. *Nat Weather Digest*, volume 7(2):pages 10–18.

Wenzel H. G. (1978): Heat stress upon undressed man due to different combinations of elevated environmental temperature, air humidity, and metabolic heat production: a critical comparison of heat stress indices. *J Hum Ergol*, volume 7:page 185–206.

Wiesner S., Bechtel B., Fischereit J., Gruetzun V., Hoffmann P., Leitl B., Rechid D., Schlünzen K. H., and Thomsen S. (2018): Is It Possible to Distinguish Global and Regional Climate Change from Urban Land Cover Induced Signals? A Mid-Latitude City Example. *Urban Science*, volume 2(1). ISSN 2413-8851. `http://dx.doi.org/10.3390/urbansci2010012`.

Wiesner S., Eschenbach A., and Ament F. (2014): Urban air temperature anomalies and their relation to soil moisture observed in the city of Hamburg. *Meteorologische Zeitschrift*, volume 23(2):pages 143–157. `http://dx.doi.org/10.1127/0941-2948/2014/0571`.

Willems W. M., Schild K., and Dinter S. (2006): *Vieweg Handbuch Bauphysik Teil 1: Wärme- und Feuchteschutz, Behaglichkeit, Lüftung*. Vieweg, Wiesbaden, 1 edition.

Winslow C., Gagge A. P., Greenburg L., Moriyama I., and Rodee E. (1935): The calibration of the thermo-integrator. *Am J Hygiene*, volume 22:pages 137–156.

Winslow C. and Herrington L. (1949): *Temperature and Human Life*. Princeton University Press, Princeton.

Winslow C., Herrington L., and Gagge A. (1937): Physiological reactions of the human body to varying environmental temperatures. *Am J Physiol*, volume 120:pages 1–22.

WMO (World Meteorological Organization) (2018): OSCAR Observing Systems Capability Analysis and Review Tool – List of all Requirements. `https://www.wmo-sat.info/oscar/requirements`. last accessed, 07.06.2018 .

Wölki D. and van Treek C. (2013): Individualization of a mathematical manikin model in terms of gender, age and morphological issues for pedicting thermal comfort: A preliminary study. In *Proceedings of BS2013: 13th Conference of International Building Performance Simulation Association*. Chambéry, France. `http://www.ibpsa.org/proceedings/BS2013/p_1990.pdf`.

dePaula Xavier A. A. and Lamberts R. (2000): Indices of thermal comfort developed from field survey in Brazil. *ASHRAE Transactions*, volume 106(1):pages 1–14.

Yaglou C. and Minard D. (1957): Control of heat casualties atmilitary training centers. *Arch Indust Health*, volume 16:pages 302 – 316.

Yahia M. W. and Johansson E. (2014): Landscape interventions in improving thermal comfort in the hot dry city of Damascus, Syria—The example of residential spaces with detached buildings. *Landscape and Urban Planning*, volume 125:pages 1–16. ISSN 0169-2046. `http://dx.doi.org/10.1016/j.landurbplan.2014.01.014`.

Yang F., Lau S. S. Y., and Qian F. (2011): Thermal comfort effects of urban design strategies in high-rise urban environments in a sub-tropical climate. *Architectural Science Review*, volume 54(4):pages 285–304. ISSN 0003-8628. `http://dx.doi.org/10.1080/00038628.2011.613646`.

Yang W., Wong N. H., and Lin Y. (2015): Thermal Comfort in High-rise Urban Environments in Singapore. *Procedia Engineering*, volume 121:pages 2125–2131. ISSN 1877-7058. `http://dx.doi.org/10.1016/j.proeng.2015.09.083`.

Ye X., Wolff R., Yu W., Vaneckova P., Pan X., and Tong S. (2012): Ambient temperature and morbidity: A review of epidemiological evidence. *Environmental Health Perspectives*, volume 120(1):pages 19–28. `http://dx.doi.org/10.1289/ehp.1003198`.

Young K. C. (1979): The influence of environmental parameters on heat stress during exercise. *Journal of Applied Meteorology*, volume 18:pages 886–897.

Zaninović K. (1992): Limits of warm and cold bioclimatic stress in different climatic regions. *Theoretical and Applied Climatology*, volume 45(1):pages 65–70. `http://dx.doi.org/10.1007/BF00865996`.

Zhang K., Lu Z., Cheng L., and Xu F. (2015a): A new framework of variance based global sensitivity analysis for models with correlated inputs. *Structural Safety*, volume 55(Complete):pages 1–9. http://dx.doi.org/10.1016/j.strusafe.2014.12.005.

Zhang W., Mak C. M., Ai Z. T., and Siu W. M. (2012): A Study of the Ventilation and Thermal Comfort of the Environment Surrounding a New University Building under Construction. *Indoor and Built Environment*, volume 21(4):pages 568–582. ISSN 1420-326X. http://dx.doi.org/10.1177/1420326x11419871.

Zhang X.-Y., Trame M., Lesko L., and Schmidt S. (2015b): Sobol Sensitivity Analysis: A Tool to Guide the Development and Evaluation of Systems Pharmacology Models. *CPT: Pharmacometrics & Systems Pharmacology*, volume 4(2):pages 69–79. ISSN 2163-8306. http://dx.doi.org/10.1002/psp4.6.

Žuvela-Aloise M., Koch R., Buchholz S., and Früh B. (2016): Modelling the potential of green and blue infrastructure to reduce urban heat load in the city of Vienna. *Climatic Change*, volume 135(3):pages 425–438. ISSN 1573-1480. http://dx.doi.org/10.1007/s10584-016-1596-2.

Eidesstattliche Versicherung

Hiermit versichere ich an Eides statt, dass ich die vorliegende Dissertation mit dem Titel: "Influence of urban water surfaces on human thermal environments – an obstacle resolving modelling approach" selbstständig verfasst und keine anderen als die angegebenen Hilfsmittel – insbesondere keine im Quellenverzeichnis nicht benannten Internet-Quellen – benutzt habe. Alle Stellen, die wörtlich oder sinngemäß aus Veröffentlichungen entnommen wurden, sind als solche kenntlich gemacht. Ich versichere weiterhin, dass ich die Dissertation oder Teile davon vorher weder im In- noch im Ausland in einem anderen Prüfungsverfahren eingereicht habe und die eingereichte schriftliche Fassung der auf dem elektronischen Speichermedium entspricht.

Hamburg, den 03.08.2018

. . . .